Transactions of the ASME®

FLUIDS ENGINEERING DIVISION
Technical Editor
DEMETRI P. TELIONIS (1999)
Executive Secretary
PAT WHITE (1999)
Assistants to the Editor
N. W. SCHAEFFLER
J. E. POWELL
Calendar Editor
M. F. ACKERSON

Associate Technical Editors
P. R. BANDYOPADHYAY (1997)
P. W. BEARMAN (1998)
F. GIRALT (1997)
H. HASHIMOTO (1996)
J. A. C. HUMPHREY (1997)
F. HUSSAIN (1998)
J. KATZ (1998)
J. KIM (1996)
M. W. REEKS (1996)
P. M. SOCKOL (1998)
M. W. SINDIR (1997)
D. E. STOCK (1996)
M. S. TRIANTAFYLLOU (1998)
S. P. VANKA (1996)

BOARD ON COMMUNICATIONS
Chairman and Vice-President
R. MATES

Members-at-Large
T. BARLOW, N. H. CHAO, A. ERDMAN, G. JOHNSON, L. KEER, E. M. PATTON, S. PATULSKI, S. ROHDE, R. SHAH, F. WHITE, J. WHITEHEAD, K. T. YANG

OFFICERS OF THE ASME
President, **D. T. KOENIG**
Exec. Director
D. L. BELDEN
Treasurer
R. A. BENNETT

PUBLISHING STAFF
Managing Director, Engineering
CHARLES W. BEARDSLEY
Director, Technical Publishing
JANET M. WEINRIB
Managing Editor, Technical Publishing
CYNTHIA B. CLARK
Managing Editor, Transactions
CORNELIA MONAHAN
Production Assistant
MARISOL ANDINO

Transactions of the ASME, Journal of Fluids Engineering (ISSN 0098-2202) is published quarterly (Mar., June, Sept., Dec.) for $175.00 per year by The American Society of Mechanical Engineers, 345 East 47th Street, New York, NY 10017. Second class postage paid at New York, NY and additional mailing offices. POSTMASTER: Send address changes to Transactions of the ASME, Journal of Fluids Engineering, c/o THE AMERICAN SOCIETY OF MECHANICAL ENGINEERS, 22 Law Drive, Box 2300, Fairfield, NJ 07007-2300.
CHANGES OF ADDRESS must be received at Society headquarters seven weeks before they are to be effective. Please send old label and new address.
PRICES: To members, $40.00, annually: to nonmembers, $175.00. Add $30.00 for postage to countries outside the United States and Canada.
STATEMENT from By-Laws. The Society shall not be responsible for statements or opinions advanced in papers or . . . printed in its publications (B7.1, Par. 3).

COPYRIGHT © 1996 by The American Society of Mechanical Engineers. Authorization to photocopy material for internal or personal use under circumstances not falling within the fair use provisions of the Copyright Act is granted by ASME to libraries and other users registered with the Copyright Clearance Center (CCC). Transactional Reporting Service provided that the base fee of $3.00 per article is paid directly to CCC, 27 Congress St., Salem, MA 01970. Request for special permission or bulk copying should be addressed to Reprints/Permission Department.

INDEXED by Applied Mechanics Reviews and Engineering Information, Inc. Canadian Goods & Services Tax Registration #126148048.

Journal of Fluids Engineering

Published Quarterly by The American Society of Mechanical Engineers

VOLUME 118 • NUMBER 1 • MARCH 1996

1 **Editorial**

2 **Technical Forum**

4 **Particle Dispersion in Flowing Gases—1994 Freeman Scholar Lecture**
David E. Stock

18 **The Effects of Turbulence and Unsteadiness on Vortex Shedding From Sharp-Edged Bluff Bodies**
M. C. Wolochuk, M. W. Plesniak, and J. E. Braun

26 **Experiments on Turbulence Management Using Screens and Honeycombs**
Cesar Farell and Sadek Youssef

33 **Wall Suction Effects on the Structure of Fully Developed Turbulent Pipe Flow**
D. Sofialidis and P. Prinos

40 **Influences of Fluidic Interfaces on the Formation of Fine Scale Structures by Chaotic Mixing**
D. F. Zhang and D. A. Zumbrunnen

48 **Evaluation of Algebraic Stress Modeling in Free-Surface Jet Flows**
David T. Walker and Chao-Yi Chen

55 **The Structure of Shear Driven Mixing With an Unstable Thermal Stratification**
D. M. Snider and M. J. Andrews

61 **Flows Generated by the Impingement of a Jet on a Rotating Surface: Part I—Basic Flow Patterns**
S. Brodersen, D. E. Metzger, and H. J. S. Fernando

68 **Flows Generated by the Impingement of a Jet on a Rotating Surface: Part II—Detailed Flow Structure and Analysis**
S. Brodersen, D. E. Metzger, and H. J. S. Fernando

74 **Numerical Study of an Unsteady Confined Jet. Application to Crossflow Filtration**
C. Maranges, G. Arroyo, C. Fonade, and J. L. Estivalezes

81 **Laminar Fluid Flow in a Planar 90 Degree Bifurcation With and Without a Protruding Branching Duct**
T. G. Travers and W. M. Worek

85 **Exponential-Lagrangian Tracking Schemes Applied to Stokes Law**
I. E. Barton

90 **Elements of an Approach to the Assessment of Random Uncertainty in Transient Measurements**
P. K. Maciejewski

96 **Unsteady Heat Transfer From a Sphere at Small Peclet Numbers**
Zhi-Gang Feng and E. E. Michaelides

103 **On the Virtual Nonexistence of Multiple Instability Regions for Some Heat-Exchanger Arrays in Crossflow**
M. P. Païdoussis, S. J. Price, and N. W. Mureithi

110 **Flow Behavior Around Stayvanes and Guidevanes of a Francis Turbine**
Toshiaki Suzuki, Tomotatsu Nagafuji, Hiroshi Komiya, Takako Shimada, Toshio Kobayashi, and Nobuyuki Taniguchi

116 **Experimental and Computational Assessment of Windage Losses in Rotating Machinery**
P. M. Wild, N. Djilali, and G. W. Vickers

123 **Study of Vaneless Diffuser Rotating Stall Based on Two-Dimensional Inviscid Flow Analysis**
Yoshinobu Tsujimoto, Yoshiki Yoshida, and Yasumasa Mori

128 **Unstable Flow in Centrifugal Fans**
P. Chen, M. Soundra-Nayagam, A. N. Bolton, and H. C. Simpson

134 **Numerical and Experimental Study of the Propulsive Speed of the Three Joint Bending Propulsion Mechanism**
Motomu Nakashima and Kyosuke Ono

142 **Deformation and Rebounding Processes of a Water Droplet Impinging on a Flat Surface Above Leidenfrost Temperature**
Hitoshi Fujimoto and Natsuo Hatta

150 **General Equation for the Design of Capillary Tubes**
Tuncay Yilmaz and Saban Ünal

(Contents continued on p. 32)

Downloaded 03 Jun 2010 to 171.66.16.159. Redistribution subject to ASME license or copyright; see http://www.asme.org/terms/Terms_Use.cfm

(Contents continued)

155 Buoyant Convection During the Growth of Compound Semiconductors by the Liquid-Encapsulated Czochralski Process With an Axial Magnetic Field and With a Non-Axisymmetric Temperature
Nancy Ma and J. S. Walker

160 Enhanced Axial Dispersion in Oscillating Pipe Flow With Different Solute Concentrations at Its Ends
J. G. Zhang, W. C. Zegel, and U. H. Kurzweg

166 Effect of Branch Orientation on Annular Two-Phase Flow in T-Junctions (Data Bank Contribution)
F. Peng, M. Shoukri, and A. M. C. Chan

172 Modeling Hydrodynamic Nonequilibrium in Cavitating Flows
Yongliang Chen and S. D. Heister

179 Compressible Dusty-Gas Boundary-Layer Flow Over a Flat Surface
Ali J. Chamkha

186 On the Application of the Method of Landau and Lifshitz to Sonic Velocities in Homogeneous Two-Phase Mixtures
Joseph C. Leung

189 Calculations of Wall Shear Stress in Harmonically Oscillated Turbulent Pipe Flow Using a Low-Reynolds-Number k-ϵ Model
J. O. Ismael and M. A. Cotton

Technical Briefs

195 An Experimental Investigation of Buoyant Transient Cavity Collapse Near Rigid Cylindrical Boundaries
J. P. Best, W. K. Soh, and C. F. Yu

198 Effects of Flow Pulsation on a Single-Rotor Turbine Meter
Wiktor M. Jungowski and Marvin H. Weiss

202 Fluids Engineering Calendar

204 1995 List of Reviewers

207 1995 Journal of Fluids Engineering Index

Announcements and Special Notices

47 Transactions Change of Address Form

73 Subscription Notice

210 Call for Symposium Papers—1997 ASME Fluids Engineering Division Summer Meeting

213 Statement of Numerical Accuracy

213 Statement of Experimental Uncertainty

213 Access to the Electronic JFE

213 Submission of Papers

Downloaded 03 Jun 2010 to 171.66.16.159. Redistribution subject to ASME license or copyright; see http://www.asme.org/terms/Terms_Use.cfm

Journal of Fluids Engineering

Editorial

This is the annual report of the Technical Editor on the operation of this Journal. This report appears in every March issue and contains information on our efforts to disseminate more efficiently the archival material submitted by the authors and make it more accessible to our readership. This issue also contains a list of the papers published in different categories in the previous year and a list of all the reviewers who supported our effort. Authors' indices appear in a cumulative form every five years. The last author index was published in September, 1992 and was actually a ten-year index. The next will be a five-year index and will appear a year from now.

This year the Division of Fluids Engineering has undertaken special efforts to bring industry and academia closer. Some of the plans will be implemented in the upcoming summer meeting and will be announced in the preliminary program of the meeting. The Editorial Board of JFE has also been discussing how to make this Journal more accessible and more useful to industry. A first step in this direction is announced by the editorial that appears in the Technical Forum.

The number of papers submitted every year has been increasing for the past seven years. For a while, we were able to increase the number of our pages as well but as discussed in last year's editorial, due to the loss of some library subscriptions, ASME Publications Committee did not approve a commensurate increase in the number of allotted pages. As a result, last year we had a backlog that dictated delays of almost one year from the date of acceptance to the date of publication. The backlog has now been decreased somewhat, essentially due to a decrease of our acceptance rate from about 45% to 35% and by requesting that authors limit the length of their papers as much as possible. The situation has now improved. The backlog has been reduced and we publish papers three to six months after their formal acceptance. Moreover, we can relax somewhat our limitations on the number of pages allotted to each article. On this issue the authors should seriously consider the option of the Electronic JFE. Material which is not crucial for the continuity of the printed version of the paper like lengthy derivations, detailed descriptions of experimental methods or long numerical formulations, in short any material that would belong to an appendix can be included in the Electronic JFE. Authors are in fact encouraged to submit also results which would not fit in the printed version of their paper. These can be presented either in digital form through the Journal Data Bank, or in the form of figures and video, black and white or color through the Electronic JFE. Authors and readers should keep in mind that all this material is reviewed, archived and readily available to anyone who can access the Journal's home page. Directions are always listed on the last page of each issue.

We are happy to report here some very encouraging figures on the time required for review. The number of months from the date a paper was received until acceptance was reduced from 13.5 the year before to 8.1 last year. The number of months required from the time revisions were requested, until final acceptance was similarly reduced from 7.4 to 3.8 months. These are only averaged figures. Unfortunately, on occasion a paper may require much longer, mostly because it may run into negligent reviewers.

The Electronic JFE is continuing to provide space for data software, color figures and now also for lengthy appendices that accompany a paper. Moreover, readers can post their comments electronically. For directions, check the Electronic JFE box on the last page of each issue.

The next issue of this Journal will have turbulence modeling as its theme. A few contributed as well as two review articles will be published in this issue. The latter will be "Review: Advances in Three-Dimensional Turbulent Boundary Layers with Emphasis on Wall-Layer Regions," by James P. Johnston and Karen A. Flack and "Perspective: The Experimentalist in the Age of Supercomputers," by Morteza Gharib. The theme of the September issue will be micro-fluid mechanics. These issues are not dedicated exclusively to specific topics. Rather a topic of current interest is highlighted and some recent contributions are given prominence.

Finally we should acknowledge the valuable contribution of eight of our associate editors whose tenure has expired. They are (i) Wing Ng, in the area of fluid applications and systems; (ii) Morteza Gharib, in the area of fluid measurements, (iii) Ahmed F. Ghoniem (iv) George Em Karniadakis (v) Ralph W. Metcalfe, and (vi) William S. Saric, in the area of fluid mechanics; (vii) Roger E. A. Arndt and (viii) Michael W. Reeks, in the area of multiphase flow. We sincerely appreciate their hard work. We should also acknowledge the contribution of the individuals who reviewed papers for JFE this past year. Their names are listed in the last pages of this issue.

Five new associate editors have been nominated by the Executive Committee and their nominations have been approved by the ASME Board of Communications. These and the areas they will be working on are the following: Peter Bearman (Imperial College of Science, Technology and Medicine), Fazle Hussain (University of Houston) and Michael Triantafyllou (Massachusetts Institute of Technology) in fluid mechanics; Joseph Katz (Johns Hopkins University) in multiphase flow; Peter Sockol (NASA Lewis Research Center) in computational fluid dynamics. Two more individuals have been nominated more recently and their nomination will be considered by the ASME Board of Communications. These and the areas they will be working on are: Mark Cramer (Virginia Polytechnic Institute and State University) Technical Editor's Office, and Olivier Simonin (Laboratoire National d'Hydraulique/EDF) in multiphase flow. We should also express our appreciation to our Associate Editors, Dr. Jones and Dr. Nelik, who agreed to serve for one more year on our Editorial Board.

The Technical Editor

Copyright © 1996 by ASME

Downloaded 03 Jun 2010 to 171.66.16.125. Redistribution subject to ASME license or copyright; see http://www.asme.org/terms/Terms_Use.cfm

Journal of Fluids Engineering

Technical Forum

Industrial Perspective on Academic Research; An Experiment to Promote Constructive Dialogue

A. F. Ghoniem,[1] J. A. C. Humphrey,[2] L. Nelik[3], and M. M. Sindir[4]

Prologue

The Editorial Board of the *Journal of Fluids Engineering* has decided to conduct an experiment in which a selected number of accepted manuscripts will be sent to industrial experts soliciting their perspective on the relevance of the research described in the paper to technology and industry. The experts will be invited to write a paragraph highlighting the significance of the paper to industry, ways in which it can be utilized in applications, and directions which continuing work can take. Authors will be asked to respond, if they choose, to the industrial perspective and both will be published at the end of the paper. The purpose of this experiment is to foster/promote an ongoing constructive dialogue between academic researchers and practicing engineers, accelerate the process of conveying research results to industry and utilize industrial experience as an inspiration to academic researchers.

Background

As we move toward a new research paradigm in which the direct relevance of academic research to society, the role of research in improving the competitiveness of industry, and the fast transition of research results to market are vital to the continuing support of government and industry to engineering research, we recognize the need for an ongoing dialogue between academia and industry regarding research problems, tools, results, and how they all should be communicated to engineering practitioners. More and more research proposals are expected to include a section which highlights the value of the proposed research to industry and technology, often with one or more letters of endorsement from the targeted industry. Many major government supported research initiatives now request the participation of industry in writing the proposal, performing the research, and demonstrating convincingly the impact of the research on industrial products and processes. In many cases, industry matching funds are considered necessary. Many major corporations are more interested in establishing and maintaining closer ties with academic laboratories to benefit as early as possible from research results and to influence research directions. All signs point to the new reality that engineering research must maintain a positive view of its role in improving technological processes and products while industry must put more effort in shaping some of the near term directions of academic research.

Meanwhile, it should be recognized that some research must be done with the long term view that research for research, i.e., developing research tools and methodologies, is a necessary component of academic contribution. Moreover, the time scales governing academia and industry are different. Academic research is often conducted by graduate students who are pursuing degrees with various requirements and supervised by professors interested in succeeding academically. This somewhat limits the range of problems tackled in universities and forces academic researchers to focus on idealized problems whose solutions are directly useful in gleaning basic understanding of critical phenomena. Industry on the other hand is interested in solving real-life problems and getting products to the market as soon as possible, and before a competitor does so. These somewhat conflicting cultures have to be mutually appreciated if successful communications are to be enhanced.

Purpose

In exploring means by which the *Journal of Fluids Engineering* can enhance the communication and collaboration between the two communities and to maintain and publicize the dialogue between the providers and users of research, the Editorial Board has approved an experiment in which an industrial expert will be invited to write a paragraph assessing the relevance of an accepted paper to the applied engineering world. Our intention is to reaffirm the role of the Journal in disseminating research results published in its pages among the broader community, and especially in industry. We propose to re-introduce the idea that the Journal is not only a medium to disseminate research results, it is also a forum to debate the end use of research.

Policy and Implementation

Selected articles accepted for publication, following the normal review process, will be sent to carefully selected specialists in industry, currently active in the field of the paper. An industrial expert will be invited to write a paragraph highlighting his/her views concerning the relevance/significance of the research presented in a paper to practicing engineers. Depending on the nature of the article, the paragraph may discuss the value of the approach used, the model developed, the results obtained, the conclusions reached, and so on. The paragraph will be published at the end of the article, signed by the expert, as an integral

[1] A. F. Ghoniem, Department of Mechanical Engineering, Massachusetts Institute of Technology, Cambridge, MA 02139.
[2] J. A. C. Humphrey, Aerospace and Mechanical Engineering, University of Arizona, Tucson, AZ 85721.
[3] L. Nelik, Roper Pump, P.O. Box 269, Commerce, GA 30529.
[4] M. M. Sindir, Mail Code IB39, Rocketdyne Division/Rockwell International Corporation, P. O. Box 7922, Canoga Park, CA 91309-7922.

Copyright © 1996 by ASME
Downloaded 03 Jun 2010 to 171.66.16.125. Redistribution subject to ASME license or copyright; see http://www.asme.org/terms/Terms_Use.cfm

part of the paper. The industrial expert will be advised by the Editor that the purpose of "the industrial perspective" is not to critique the paper as such, but to identify/discuss the ways he/she sees the work is pertinent to the design/analysis of products and processes. The industrial perspective on academic research will then be sent to the author with a request for a response, and not a rebuttal since the paper has already been accepted for publication. If authors feel that a response is necessary, this will be published after the discussion, as "the authors' closure."

In order not to allow this process to delay the publication of an accepted article, the Associate Editor handling the paper will ask that the industrial expert write his/her perspective in no more than two weeks, and the author respond in no more than a week after receiving the communication. The selection of the industrial expert, like the selection of the reviewers, will be done by the Associate Editor. The author may be asked to provide names of potential industrial experts who can be contacted to perform this duty, and the Associate Editor may request more than one input. We emphasize that the primary goal here is to enhance the communications between academic researchers and practicing scientists and engineers. Thus we view this as a means to add to the value of the paper and the Journal.

The editorial board of the *Journal of Fluids Engineering* is interested to hear from the readers regarding the subject of this article. Please foward your comments to the Technical Editor, Demetri P. Telionis (e-mail: telionis@vt.edu) or the lead author, A. F. Ghoniem (e-mail: ghoniem@mit.edu) or post your comments on the JFE Electronic Bulletin Board (see directions on the last page of each issue).

Downloaded 03 Jun 2010 to 171.66.16.125. Redistribution subject to ASME license or copyright; see http://www.asme.org/terms/Terms_Use.cfm

David E. Stock
Department of Mechanical and Materials Engineering, Washington State University, Pullman, WA 99164-2920

Particle Dispersion in Flowing Gases—1994 Freeman Scholar Lecture

1 Introduction

Particle-laden gas flows are common in many man-made and natural environments. Their importance to industrial processes, agriculture, and human health has made them of great theoretical and practical interest over the past 50 years. Because particles are often carried by a turbulent gas stream, progress in understanding and predicting behavior of particle-laden flows has closely followed developments in understanding and prediction of turbulent flow. The motion of a particle in a gas flow is governed by gravity and the particle's interaction with the turbulent fluid surrounding it. However, to determine the location and thus the local turbulence surrounding the particle, the trajectory of the particle must be known. It is this nonlinear coupling between the particle motion and the turbulence that makes predicting particle dispersion in gas flow difficult. During the past two decades, fundamental understanding of the dispersion of particles in simple turbulent gas flows has been reached, and the capability of predictive tools has increased exponentially as a result. This review is an attempt to summarize our current state of knowledge about gas-particle flows, and to highlight areas where more research is needed.

Study of the motion of particles in a gas flow, often called gas-solid or gas-particle flows, is one branch of the general area of multiphase flow. Other branches of multiphase flow are gas-liquid flows, solid-liquid flows, and flows involving all three phases. This review focuses on gas-particle flows, with particle referring to either a solid sphere or a liquid droplet so small that internal circulation has no effect on its motion. Liquid droplets moving in air can meet this requirement if their diameter is less than about 500 μm. While the equations governing the motion of a particle have been developed for a rigid sphere, the resultant relationships can usually be extended empirically to account for particles that are rough or ellipsoidal in shape.

Aerosols are gas flows containing particles less than 1 μm in diameter. The forces that determine the motion of an aerosol in a gas flow are, in general, not the same as those in a gas flow containing larger particles. For this reason, aerosols are usually treated as a separate technology and will not be covered specifically in this review. However, there is some overlap between the two areas because, in both cases, the particles are being conveyed by a turbulent gas flow. The particles of major interest in this review are often called heavy particles, small particles of high density with a free-fall velocity or drift velocity on the order of the fluid rms velocity. Even without a drift velocity, a heavy particle being carried by a gas flow would not have the same trajectory as a fluid point because of the inertia of the heavy particle.

Examples of the transport and dispersion of heavy particles by a gas flow can be found in pollution control, power generation, agriculture, and industrial processes. Cyclone separators are used to remove sawdust, grain, water, etc. from an air stream by giving the flow a swirl as it enters a large cylindrical chamber. The particles move to the outer wall of the chamber and slide down and out the bottom, while the gas turns and exits out the top center. Cyclones operate best with particles larger than 20 μm. Smaller particles, such as fly ash from a coal-fired power plant, are collected with electrostatic precipitators that charge the particles and then use an electrostatic field to move the particles to a collecting wall. Control of the entrainment, dispersion, and deposition of agricultural soil in the form of air-borne heavy particles is an important environmental as well as agricultural concern. Examples of industrial applications include spray drying, pneumatic transport, and mixing. Fluidized beds and pneumatic transport with high particle loading are examples of gas-particle flows, but they will not be discussed here because momentum exchange in these cases is dominated by particle-to-particle collisions, rather than by fluid-to-gas exchange.

Heavy particles in a gas stream are carried by the turbulent flow, and dispersion of the particles is caused by turbulence. In fully developed turbulent flow, as found in the atmospheric boundary layer, in pipes, and in the far field of jets, wakes, and mixing layers, the particles are spread by the stochastic interaction of the turbulence with the particles. In these flows, the term dispersion will be used to denote either the chronological or spatial evolution of the particle distribution. In the initial region of shear layers, wakes, and jets, the dispersion is strongly influenced by the kinematics of the turbulence, and often a special definition of dispersion is used to quantify the distribution of the particles. In many applications, the number of particles in the flow is small enough that the turbulence of the gas is not affected by the particles. These flows are considered to be lightly loaded, in contrast to flows in which the turbulence is modified by the presence of the particles. However, these two types of flows represent ends of a spectrum; flows nearer the middle of this spectrum are more difficult to categorize.

Gas-particle flows are characterized by properties of the particles and by properties of the turbulent gas flow that carries the particles. Particles can be characterized by their density, ρ_p, and their response time, τ_p. The particle response time is the time required for the particle velocity to decrease to $1/e$ of its original value when viscous drag forces are the only forces acting on the particle and the particle velocity is low enough that Stokes flow can be assumed. The particle response time for a rigid sphere is

$$\tau_p = \frac{\rho_p d_p^2}{18\mu}, \tag{1}$$

where d_p is the particle diameter and μ the fluid viscosity. The particle response time is a reflection of the inertia and size of the particle. Particle Reynolds number is defined as

$$\mathrm{Re}_p = \frac{vd}{\nu} \quad \text{or} \quad \frac{wd}{\nu}, \tag{2}$$

Contributed by the Fluids Engineering Division for publication in the JOURNAL OF FLUIDS ENGINEERING. Manuscript received by the Fluids Engineering Division June 5, 1995. Associate Technical Editor: D. P. Telionis.

Copyright © 1996 by ASME

Downloaded 03 Jun 2010 to 171.66.16.125. Redistribution subject to ASME license or copyright; see http://www.asme.org/terms/Terms_Use.cfm

where v is the velocity of the particle and w is the velocity of the particle relative to the gas. Usually, the velocity of the particle relative to the gas is implied when Re_p is used. Stokes flow about the particle can be assumed when $\mathrm{Re}_p < 1$. The velocity given a particle as a result of gravitational force is often called a drift velocity, settling velocity, or a free-fall velocity, v_d, and in a stationary fluid the particle drift velocity (for $\mathrm{Re}_p < 1$) is

$$v_d = g\tau_p, \tag{3}$$

where g is the acceleration of gravity.

Because the particles are carried by the mean flow and dispersed by the turbulence, we need to define scales for both the mean flow and the turbulence that are important in gas-particle flows. The fluid mean flow can be scaled with a mean characteristic velocity, U, and a characteristic length scale, L. Both the turbulent Lagrangian and Eulerian scales (Hinze, 1975, p. 360) are important in describing particle dispersion because the dispersion of small particles is governed by Lagrangian scales, and larger particles are controlled by Eulerian scales. Two Eulerian integral time scales, the moving Eulerian time scale, T_{mE} (where the scale moves with the local mean velocity), and the fixed Eulerian integral time scale, T_{fE}, can be defined. The Lagrangian integral time scale is denoted by T_L. The integral spatial length scale of the turbulence, L_f, gives a relative size of the largest eddies in the turbulence, and the Kolmogoroff micro-length scale, η, gives the relative size of the smallest eddies in the turbulence. Experimentally, we can directly measure only the fixed Eulerian scales. We can then calculate the moving Eulerian scales, but there is no general method for relating the Eulerian scales to the Lagrangian scales. The rms velocity, u_0, can be measured in all three spatial directions which, for isotropic turbulence, are all equal.

The ratio of the response time of the particle, τ_p, to the time scale of the fluid is called the Stokes number. If the time scale of the mean flow, L/U, is used, the Stokes number indicates how closely the particles follow the mean fluid motion. The response of the particles to the turbulence is usually given by a Stokes number that is based on T_{mE}. Care must be taken when using the Stokes number, because a variety of definitions are used.

As a first step in predicting a particle-laden flow, only the mean motion of the particles and the effect of the particles on the mean motion of the fluid is of interest. In this case, dispersion of the particles due to the turbulence is neglected, but the effects of mean heat, mass, and momentum coupling can be included through empirical relations. Sirignano (1993) reviewed these effects for sprays. Numerical techniques for calculating the mean properties of a particle-laden flow were reviewed by Crowe (1982), who pointed out the advantages of the trajectory model (Crowe et al., 1977) for calculating the convection of particles and the mean coupling between the particles and the fluid. The focus of this review is on the dispersion of particles due to the turbulent flow; mean convection of particles will not be explicitly discussed. A listing or review all the work that has been done on gas-particle flow will not be given, but rather the emphasis will be on the fundamentals of the phenomena and our current state of knowledge (or lack thereof).

The following sections first review the equations governing particle motion in a gas and formally define particle dispersion and diffusivity. The results of analytical, experimental, and numerical studies of particle motion in simple flows are then used to create a clear picture of the parameters governing particle dispersion. Numerical techniques based on a trajectory or stochastic approach are described and their strengths and weaknesses discussed. The alternative approach to modeling gas-solid flows, the two-fluid model, is presented and the problem of finding and modeling the averaged equations discussed. The final sections give the present state of knowledge of turbulence modification by particles and the interaction of particles with large scale structures.

2 Particle Motion in a Turbulent Flow

The Lagrangian equation of motion for a particle in an unsteady laminar flow is developed in Appendix A. The same equation is assumed to hold for turbulent flow as long as the particle diameter is 20 to 100 times smaller than the smallest scales of the turbulence. The forces acting on the particle include Stokes drag, virtual mass, pressure gradient, Basset history, and gravity/buoyancy. For gas-particle flows with $\rho_f/\rho_p \approx 0.001$, the pressure gradient, virtual mass, and Basset history terms can usually be neglected and, in most computations, the initial conditions are either zero or go to zero very quickly. Assuming that gravity, g, is in the negative x_3 direction, the equation of motion for a particle, Eq. (4A), can be written as

$$\frac{dv_i}{dt} = \frac{[u_i(y(t), t) - v_i]f}{\tau_a} - g\delta_{i3}, \tag{4}$$

$$\frac{dy_i(t)}{dt} = v_i, \tag{5}$$

Nomenclature

d_p = particle diameter
$E(k)$ = scalar energy spectrum
$D(\tau)$ = one-point time correlation
f = ratio of drag coefficient to Stokes drag
k = wave number
L_f = longitudinal spatial integral length scale
L_g = transverse spatial integral length scale
L = characteristic length of the mean flow
m = turbulence structure function (21)
M = centerline distance between bars of a symmetric grid
g = acceleration of gravity
Re_p = particle Reynolds number (2)
R_L = Lagrangian velocity correlation coefficient
St = Stokes number, ratio of time scale of particle to time scale of fluid
T_{fE} = fixed Eulerian integral time scale
T_L = Lagrangian integral time scale
T_{mE} = moving Eulerian integral time scale
u_o = fluid rms fluctuating velocity
U = characteristic mean flow velocity
v = particle velocity
v_d = particle drift velocity (3)
w = particle velocity relative to the fluid velocity
y = particle location
ϵ_{ij}^p = particle diffusivity tensor
γ = drift parameter (8)
ρ_f = gas density
ρ_p = particle density
η = Kolmogoroff micro length scale
τ = delay time
τ_p = particle response time, (1)
μ = fluid dynamic viscosity
ν = fluid kinematics viscosity
ω = frequency

Superscripts

* = indicates a nondimensionalized term

Subscripts

f = fluid
fE = fixed Eulerian
L = Lagrangian
mE = moving Eulerian
0 = characteristic value
p = particle

Downloaded 03 Jun 2010 to 171.66.16.125. Redistribution subject to ASME license or copyright; see http://www.asme.org/terms/Terms_Use.cfm

where f is the ratio of the drag to Stokes drag and is given by Eq. (6A), and $y(t)$ is the location of the particle at time t. If the particle Reynolds number is less than one, f can be assumed to be equal to one. Equations (4) and (5) can be nondimensionalized using u_0 for the velocity, T_{me} for time, and $u_0 T_{me}$ for length to give

$$\frac{du_i^*}{dt^*} = \frac{[u_i^*(y^*(t^*), t^*) - v_i^*]f}{\mathrm{St}} - \frac{\gamma \delta_{i3}}{\mathrm{St}}, \tag{6}$$

$$\frac{dY_i^*(t^*)}{dt^*} = v_i^*. \tag{7}$$

The nondimensional equations of motion contain two parameters: St, the Stokes number, which is a measure of the relative importance of inertia; and γ, the drift parameter, which is a nondimensionalized drift velocity given by

$$\gamma = \frac{\tau_a g}{u_0} = \frac{v_d}{u_0}. \tag{8}$$

The Stokes number used to characterize the particle's response to the turbulence is the particle response time, τ_a, divided by the moving Eulerian integral time scale, T_{mE}, or $\mathrm{St} = \tau_a / T_{mE}$. The moving Eulerian integral time scale, T_{mE}, is used as the time scale because it is easier to determine experimentally than is the Lagrangian time scale. Also, at any point in the flow, there is a fixed, but unknown, relationship between the three fluid integral time scales.

Although the equation of motion for a solid particle in a gas, Eq. (6), looks like a simple linear ordinary differential equation, it is a complex nonlinear expression. If, for the moment, we neglect gravitational effects and assume Stokes drag, e.g., $f = 1$, the complexity still remains because we must know the particle trajectory to calculate the drag on the particle, and the drag must be known to find the particle trajectory. Thus, u_i^* represents the fluid velocity along the particle trajectory. The particle trajectory is not, in general, the same as the trajectory of a fluid point. Figure 1 shows the calculated trajectory for four different particles in the same homogenous turbulence when no gravitational force is present. Figure 1(a) shows a particle with St = 0.1. This closely represents the trajectory of a fluid point. The effect of increasing particle inertia, Stokes number, is clearly seen in Figs. 1(b) through 1(d). For each Stokes number, the fluid velocity along the particle trajectory is unique, even though each particle started in the same realization of the turbulence. If gravitational effects are included, the change in trajectory with increasing drift parameter, γ, is even more significant than is the change in trajectory with change in Stokes number (Fig. 2). Figures 1 and 2 illustrate the significant effect of particle inertia and drift velocity on the fluid velocity along a particle trajectory. The problem encountered when trying to calculate particle motion is determining the statistics of the fluid along the particle trajectory. In simple turbulent flows, the effect of Stokes number and drift parameter on particle trajectories can be quantified through a particle dispersion coefficient. Therefore, before discussing particle trajectory calculations and particle dispersion, the dispersion coefficient and other statistical measures related to dispersion will be explained.

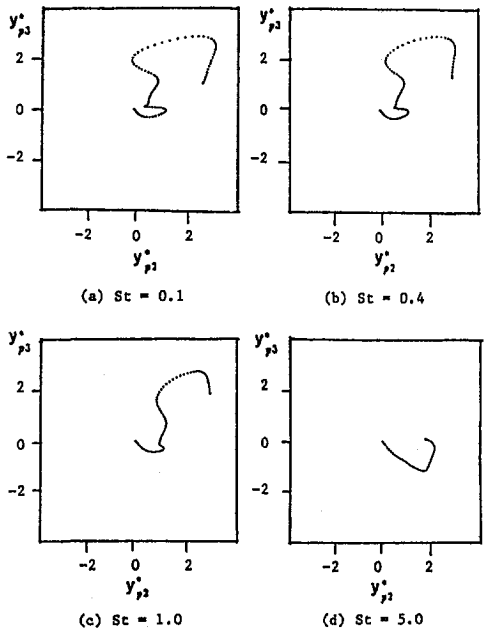


Fig. 1 Particle trajectories for Stokes numbers, St, of 0.1, 0.4, 1.0, and 5.0. In all cases the free-fall velocity is zero, $\gamma = 0$.

3 Turbulent Dispersion

In most turbulent flows, groups of particles that start in the same area will, on the average, have the distance between them increase with time due to the random action of the fluid turbulence. One way to quantify this spreading is to determine how the mean squared dispersion of the particles changes with time. First, consider the dispersion in uniform mean flow with the turbulence stationary and homogeneous. Considering first one direction (e.g., perpendicular to the mean flow direction), we can define the mean squared dispersion as

$$\langle y_2^2(t) \rangle = \langle y_2(t) y_2(t) \rangle, \tag{9}$$

where $\langle\ \rangle$ indicates ensemble averaging, which for a stationary flow would be the same as averaging over many particle trajectories all starting at the same location but at different times, with each particle trajectory lasting for time t. The particle displacement, y_2, is given by

$$y_2(t) = \int_0^t v_2(t')dt',$$

and Eq. (9) becomes

$$\langle y_2^2(t) \rangle = \left\langle \int_0^t dt' \int_0^t v_2(t') v_2(t'')dt'' \right\rangle$$

If the turbulence is stationary and homogeneous, the ensemble average can be moved inside the integral and replaced with a time average to give

$$\overline{y_2^2(t)} = \int_0^t dt' \int_0^t \overline{v_2(t') v_2(t'')}\, dt''.$$

If we now rewrite the limits of integration, recognizing that the integration plane was a square, we obtain

$$\overline{y_2^2(t)} = 2 \int_0^t dt' \int_0^{t'} \overline{v_2(t') v_2(t'')}\, dt''.$$

Finally, the two times, t' and t'', can be replaced by a single time and a time difference ($t''t' + \tau$) to give

$$\overline{y_2^2(t)} = 2 \int_0^t dt' \int_{-t'}^0 \overline{v_2(t') v_2(t' + \tau)}\, d\tau. \tag{10}$$

The time-averaged velocity correlation in Eq. (10) must be calculated along a particle trajectory (Lagrangian correlation) and, since the turbulence has been assumed to be homogeneous, it only depends on time difference τ, and is given by

$$R_L(\tau) = \frac{\overline{v_2(t) v_2(t + \tau)}}{\overline{v_2^2}}. \tag{11}$$

Downloaded 03 Jun 2010 to 171.66.16.125. Redistribution subject to ASME license or copyright; see http://www.asme.org/terms/Terms_Use.cfm

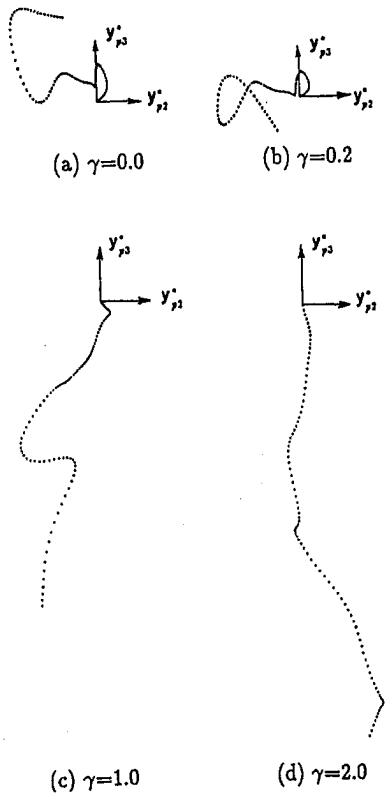


Fig. 2 Particle trajectories for drift parameters, γ, of 0, 0.2, 1.0, and 2.0. In all cases St = 0.2.

Substituting Eq. (11) into Eq. (10) and utilizing the symmetry of $R_L(\tau)$, we can obtain Taylor's (1921), equation for mean squared dispersion in terms of the Lagrangian correlation coefficient, R_L, as

$$\overline{y_2^2(t)} = 2\overline{v_2^2}\int_0^t dt' \int_0^{t'} R_L(\tau)d\tau. \tag{12}$$

Equations (11) and (12) are valid for either a fluid element or a particle as long as the corresponding velocities are used. The mean squared dispersion and the Lagrangian correlation tensor can be written as tensors in the form

$$\overline{y_i(t)y_j(t)} = 2v_{0i}v_{0j}\int_0^t dt' \int_0^{t'} R_{ij}(\tau)d\tau, \tag{13}$$

$$R_{ij} = \frac{\overline{v_i(t)v_j(t+\tau)}}{v_{0i}v_{0j}}, \tag{14}$$

where v_{0i} is the rms fluctuating velocity in the x_i direction. Particle diffusivity can now be defined in terms of the mean squared dispersion (Batchelor, 1949) as

$$\epsilon_{ij}(t) = \frac{1}{2}\frac{d}{dt}\overline{y_i(t)y_j(t)} = v_{0i}v_{0j}\int_0^t R_{ij}(\tau)d\tau. \tag{15}$$

For short times, the Lagrangian correlation coefficient is very close to one and the dispersion coefficient increases linearly with time. For long times, the integral of the Lagrangian correlation coefficient is a constant and is equal to the Lagrangian integral time scale. Therefore, for long times, the particle diffusivity tensor can be written as

$$\epsilon_{ij}^p = v_{0i}v_{0j}T_{Lij}^p, \tag{16}$$

where the superscript p is used to indicate the particle Lagrangian time scale and the particle diffusivity coefficient. Although Eq. (16) is limited to flows with a uniform mean velocity and homogeneous turbulence, it provides a means of quantifying dispersion and studying the effect of Stokes number and fall velocity on the dispersion. Understanding dispersion in this simple flow forms the basis for our examination of more complex flows. If we assume the turbulence is isotropic and that the mean velocity is uniform and in the x_1 direction with gravitational force in the $-x_3$ direction, the dispersion in the x_1 and x_2 direction will be the same and we can write Eq. (16) as

$$\epsilon_{11}^p = v_{01}^2T_{L11}^p, \quad \epsilon_{22}^p = v_{02}^2T_{L22}^p, \tag{17}$$

$$\epsilon_{33}^p = v_{03}^2T_{L33}^p. \tag{18}$$

From Eqs. (17) and (18) we see that dispersion is controlled by the particle rms velocity and the particle Lagrangian integral time scale. For a particle with no inertia and no free-fall velocity, the particle rms velocity will be equal to the fluid rms velocity, and the particle Lagrangian time scale will be equal to the fluid Lagrangian time scale. As the particle inertia and the fall velocity increase, both the particle rms velocity and the particle Lagrangian time scale will change. These changes are the subject of the next section.

4 Dispersion in Simple Flows

4.1 Analytical Solutions. The goal of this section is to develop a three-dimensional plot of the long-time particle dispersion coefficient as a function of particle inertia and drift velocity for a simple turbulent flow. In nondimensional terms, such a plot would give the particle diffusivity divided by the fluid diffusivity as a function of the Stokes number and the drift parameter, and for a particular structure of the turbulence. For homogeneous, isotropic, stationary turbulence, the structure of the turbulence is determined by the scalar energy spectrum, $E(k)$, and the moving Eulerian one-point time correlation, $D(\tau)$. Typical forms used for these two functions (Kraichnan, 1970) are

$$E(k) = \frac{u_o^2}{\sqrt{2\pi}}\frac{k^4}{k_o^5}\exp\left(-\frac{k^2}{2k_o^2}\right) \tag{19}$$

and

$$D(t) = \exp\left(-\frac{\pi t^2}{4T_{mE}^2}\right) = \exp\left(-\frac{\omega_0^2\tau^2}{2}\right). \tag{20}$$

Other shapes for $E(k)$ and $D(t)$ have been developed, but the long-time dispersion of particles is not very sensitive to the exact shape of the correlations used to describe the turbulence. With this in mind, we can specify the turbulence by specifying u_o, k_o, and T_{mE}. These three scales can be combined into a nondimensional parameter, m, and written as

$$m = \frac{2}{\sqrt{2\pi}}k_ou_oT_{mE} = \frac{u_0T_{mE}}{L_f}, \tag{21}$$

where L_f is the integral length scale of the turbulence in the longitudinal direction. Thus, the structure of this homogeneous, isotropic turbulence can be specified by giving the value for m. Reeks (1977) defined $\gamma_o = \omega_o/2k_ou_o$ as the structure parameter, making $m = 0.5/\gamma_o$. Since no general analytical solution exists for even this simple turbulent flow, approximate techniques must be employed. However, because we are concerned with very simple (Gaussian) turbulence, very good approximations have been developed. Reeks (1977) was the first to treat the interaction between the fluid and the particle correctly in his study of particle dispersion. He used a second-order approximation technique to find the fluid velocity along the particle trajectory and the response of the particle to this velocity. He included the effect of both gravity and inertia on the particle motion. His results are in the form of integral equations. The plotted exam-

Downloaded 03 Jun 2010 to 171.66.16.125. Redistribution subject to ASME license or copyright; see http://www.asme.org/terms/Terms_Use.cfm

ples are for $m = 0.5$. Nir and Pismen (1979) used Corrsin's (1959) independence approximation to obtain results similar to those of Reeks. Their results are in terms of integro-differential equations. While Reeks (1977) gives a complete representation of particle dispersion in an isotropic, homogeneous, stationary turbulence, the form of the equations makes them difficult to use. To overcome this difficulty, Wang and Stock (1993) started with the same equations used by Reeks, but employed a function for the velocity correlation along the particle trajectory that accounted for the effects of both inertia and drift velocity instead of the second-order perturbation technique, and developed the following equations:

$$\frac{\epsilon^p_{11}(\infty)}{u_0^2 T} = \frac{\epsilon^p_{22}(\infty)}{u_0^2 T} = \frac{\sqrt{1 + m_T^2\gamma^2} - 0.5 m_T \gamma}{1 + m_T^2 \gamma^2} \tag{22}$$

and

$$\frac{\epsilon^p_{33}(\infty)}{u_0^2 T} = \frac{1}{\sqrt{1 + m_T^2 \gamma^2}}. \tag{23}$$

The particle rms velocity is given by

$$\frac{v_{1o}}{u_1} = \frac{v_{2o}}{u_o} = \sqrt{\frac{1}{1 + \mathrm{St}_T\sqrt{1 + \gamma^2 m_T^2}} - \frac{0.5 m_T \gamma\ \mathrm{St}_T}{(1 + \mathrm{St}_T\sqrt{1 + \gamma^2 m_T^2})^2}}, \tag{24}$$

$$\frac{v_{3o}}{u_o} = \sqrt{\frac{1}{1 + \mathrm{St}_T\sqrt{1 + \gamma^2 m_T^2}}}. \tag{25}$$

Equations (22) through (25) are in terms of the drift parameter γ (given by Eq. (3)), a Stokes number, St_T, and a turbulence structure parameter, m_T, where T indicates that the time scale used in the parameter was the fluid time scale along the particle's trajectory. The time scale of the fluid along a particle trajectory is a function of the particle inertia and changes from the Lagrangian time scale for a fluid point to the moving Eulerian time scale for large particles. A curve fit to a numerical simulation for $m = 1$ gives (Wang and Stock, 1993)

$$\frac{T}{T_{mE}} = 1 - \frac{1 - \dfrac{T_L}{T_{mE}}}{(1 + \mathrm{St})^{0.4(1+0.01\mathrm{St})}} \quad \text{with} \quad \frac{T_L}{T_{mE}} = 0.356. \tag{26}$$

The usual Stokes number and structure parameter are related to ones defined in terms of T by

$$\mathrm{St}_T = \mathrm{St}\,\frac{T_{mE}}{T} \tag{27}$$

and

$$m_T = m\,\frac{T_{mE}}{T}. \tag{28}$$

Knowing the particle long-time diffusivity and the particle rms velocity, we can obtain the time scale of the particle using

$$\frac{T^p_{11}}{T_L} = \frac{T^p_{22}}{T_L} = \frac{\epsilon^p_{11}(\infty)}{v_{01}^2 T_L} = \frac{\epsilon^p_{22}(\infty)}{v_{02}^2 T_L}, \quad \text{and} \quad \frac{T^p_{33}}{T_L} = \frac{\epsilon^p_{33}(\infty)}{v_{01}^2 T_L}. \tag{29}$$

Using Eqs. (22) through (29), contour plots for long-time particle diffusivity, rms fluctuating velocity, and time scale in the $\mathrm{St} - \gamma$ plane can be drawn (Figs. 3–5). A clear understanding of particle dispersion can be gained by examining some asymptotic cases taken from these three plots.

Consider first the case of no drift velocity, $\gamma = 0$. The ratio of the particle diffusivity to the fluid diffusivity increases with Stokes number and is greater than one for all $\mathrm{St} > 0$. From Eq. (23) we have, for this special case,

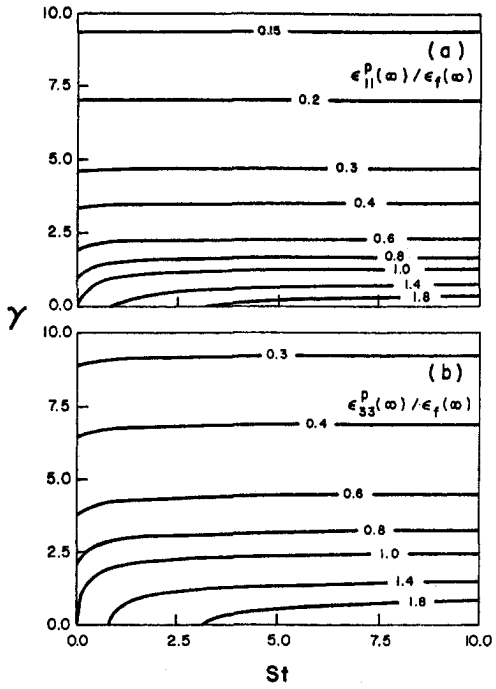


Fig. 3 Contour plots of dimensionless particle long-time diffusivity, Eqs. (22) and (23), showing the effects of Stokes number and drift parameter. The particle diffusivity is nondimensionalized by the fluid turbulent diffusivity, $\epsilon_f = u_0^2 T_L$. In this plot the structure parameter, m, was set equal to one.

$$\epsilon^p_{11} = \epsilon^p_{22} = \epsilon^p_{33} = u_0^2 T \tag{30}$$

and

$$\frac{\epsilon^p}{\epsilon^f} = \frac{T}{T_L}. \tag{31}$$

Because T changes from the Lagrangian time scale, T_L, to the Eulerian time scale, T_{mE}, as the Stokes number increases, the ratio of the particle diffusivity to the fluid diffusivity will change from 1 to T_{mE}/T_L. No theorem presently exists to give the ratio of the Eulerian to Lagrangian scales. However, for homogeneous turbulence, the ratio of the Eulerian to Lagrangian time scales has been found to depend on m and the shape of the energy spectrum. Values can range from 1 to 3, with 2.5 being a typical value for many flows. Reeks (1977) showed that the diffusivity ratio peaks at $m \approx 1.0$ and that the ratio goes to 1 for $m > 50$ and $m < 0.05$. For low drift velocities, the particle diffusivity can be greater than the fluid diffusivity, and the difference depends on the ratio of the moving Eulerian to Lagrangian time scales.

From Fig. 3 it is clear that the particle diffusivity decreases as the free-fall velocity of the particle increases. This is true for all Stokes numbers. The decrease in diffusivity with increasing free-fall velocity is known as the crossing trajectory effect and was first identified by Yudine (1959). The diffusivity decreases in all three directions. For a given Stokes number, the decrease in diffusivity with increasing drift parameter can be traced to a decrease in the particle rms velocity and a decrease in the particle integral time scale.

If we now look at the case of very small Stokes numbers and large drift velocity, Eqs. (22) through (25) reduce to

$$\epsilon^p_{11} = \epsilon^p_{22} = 0.5\,\frac{u_0^2 L_f}{v_d}, \quad \epsilon^p_{33} = \frac{u_0^2 L_f}{v_d}, \tag{32}$$

$$\frac{v_{01}}{u_0} = \frac{v_{02}}{u_0} = \frac{v_{03}}{u_0} = 1.0, \tag{33}$$

Downloaded 03 Jun 2010 to 171.66.16.125. Redistribution subject to ASME license or copyright; see http://www.asme.org/terms/Terms_Use.cfm

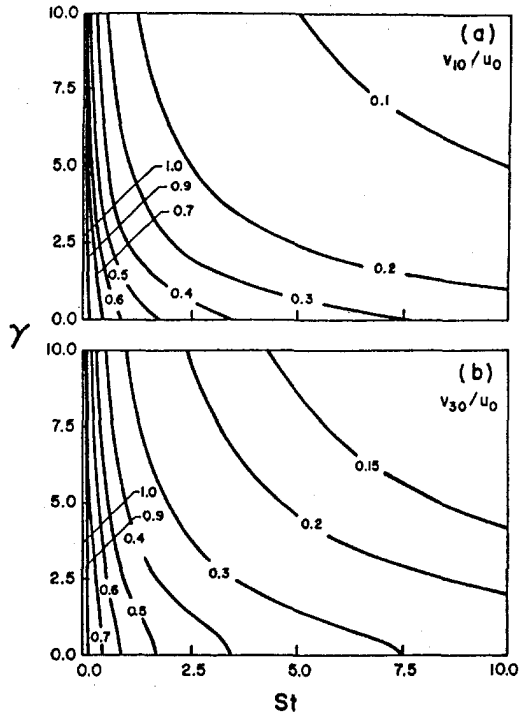


Fig. 4 Contour plots of dimensionless particle rms velocity, Eqs. (24) and (25), showing the effects of Stokes number and drift parameter. The particle rms velocity is nondimensionalized by the fluid rms velocity, u_0. In this plot the structure parameter, m, was set equal to one.

$$T_{11} = T_{22} = 0.5\,\frac{L_f}{v_d}, \quad T_{33} = \frac{L_f}{v_d}. \tag{34}$$

This limiting case of very small inertia and very large drift velocity corresponds to particles falling through the atmospheric boundary layer (Csanady, 1963), where the turbulence scales are very large.

Many interesting features of particle dispersion can be seen by examining Eqs. (32) through (34). The particle diffusivity in all three directions is inversely proportionally to the drift velocity, which is the crossing trajectory effect described by Yudine (1959). Also, the diffusivity in the particle free-fall direction is double that in the two transverse directions. This anisotropic diffusivity was first described by Csanady (1963) and was referred to by him as the continuity effect. When the drift velocity is large, diffusivity is controlled by the turbulence length scale because the particle moves through an eddy before the eddy decays. Therefore, it is the length scale of turbulence that limits the interaction time, not the time scale of the eddy. In the free-fall direction, the turbulence length scale corresponds to the longitudinal spatial velocity scale L_f and, in the two directions transverse to the fall direction, the turbulence length scale corresponds to the lateral spatial velocity scale L_g. For isotropic turbulence, continuity constrains the turbulence and requires that $L_f = 2L_g$. Thus, for this limiting case, the diffusivity in the fall direction is twice that in the two transverse directions. For the case of zero Stokes number and high drift velocity, the change in diffusivity with drift is caused by the reduction in the particle time scale; however, this is not the general case.

Now consider the case where the anisotropic nature of the dispersion is due solely to the difference in the velocity scales of the particle. If the Stokes number is not zero and the drift parameter is very large (St $\gamma \gg 1$), then the diffusivity is

$$\epsilon^p_{11} = \epsilon^p_{22} = 0.5\,\frac{u_0^2 L_f}{v_d}, \quad \epsilon^p_{33} = \frac{u_0^2 L_f}{v_d}, \tag{35}$$

and the particle velocity and time scales become

$$v_{01} = v_{02} = u_0\sqrt{\frac{0.5L_f}{\tau_a v_d}}, \quad v_{30} = u_0\sqrt{\frac{L_f}{\tau_a v_d}} \tag{36}$$

$$T_{11} = T_{22} = T_{33} = \tau_a. \tag{37}$$

In this case, the anisotropic dispersion originates from the difference in the velocity scale, not a difference in the time scales. This difference in the particle velocity scales is due to the difference in the fluid turbulence spatial velocity correlations, L_f and L_g. Because of the high free-fall velocity and finite Stokes number, the particle cannot respond to the fluid velocity fluctuations along the particle trajectory. The frequency of the fluctuations is set by the length scale of the turbulence and the fall velocity. Since the length scale of the turbulence in the free-fall direction is twice that in the transverse direction, the frequency of fluctuations in the fall direction will be only half that in the transverse direction and, in the limit of high free-fall velocities, the amplitude of the particle velocity fluctuations in the fall direction will be twice that in the transverse direction.

The dispersion of heavy particles in an isotropic, stationary turbulence is governed by the Stokes number, St, the drift parameter, γ, and the structure of the turbulence, m. Figures 3 through 5 give the full picture of the long-time particle diffusivity, the particle time scale, and the velocity scale. Because long-time diffusivity is the product of the particle time scale and the particle velocity scale squared, Eq. (16), the three plots are not independent, but each does provide a measure of understanding of the dispersion process. The plots are all for a single structure parameter, $m = 1$, and Stokes drag is assumed to apply. Particle diffusivity depends on the structure parameter (Reeks, 1977). For the approximate solution given by Eqs. (22) through (29), a unique form of Eq. (26) and of the ratio of the Lagrangian to moving Eulerian time scales is required for each m. For $m \to \infty$, the flow becomes frozen, the time scales go to infinity, and the dispersion is controlled by the spatial scales. As $m \to 0$, the moving Eulerian and Lagrangian scales become equal

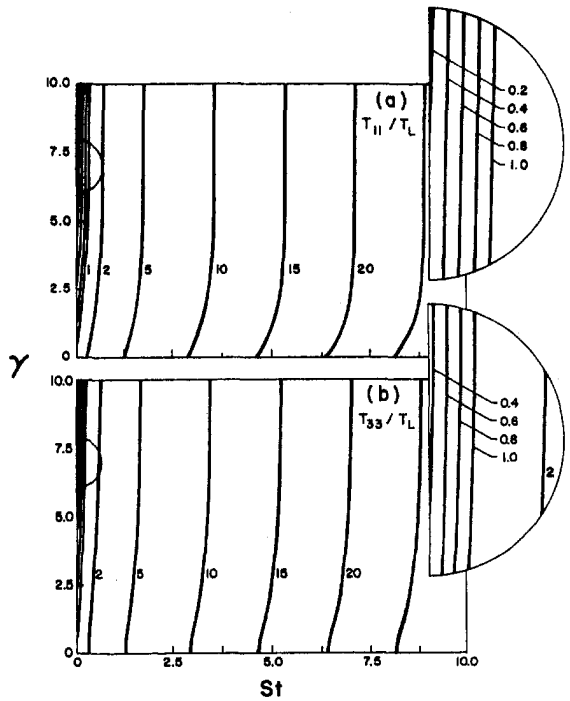


Fig. 5 Contour plots of dimensionless particle integral time scale, Eq. (29), showing the effects of Stokes number and drift parameter. The particle time scale is nondimensionalized by the fluid Lagrangian time scale, T_L. In this plot the structure parameter, m, was set equal to one.

Downloaded 03 Jun 2010 to 171.66.16.125. Redistribution subject to ASME license or copyright; see http://www.asme.org/terms/Terms_Use.cfm

and the particle diffusivity will always be equal to or less than the fluid particle diffusivity.

Particle dispersion depends on St and γ which, in turn, depend on the particle size, density, drift velocity, and the turbulence scales. The particle velocity scale (Fig. 4) is always less than the fluid velocity scale and depends on inertia and free-fall velocity. The velocity scale is a very strong function of Stokes number for St < 1. As the Stokes number increases, the particle velocity scale becomes a stronger function of the drift parameter. The time scale of the particle (Fig. 5) is larger than the fluid time scale except for St < 1, when it becomes mainly a function of the Stokes number. From numerical simulations of particle trajectories, we know that the particle time scale depends on the fluid spatial scales, except when the Stokes number and drift parameter are both small.

When particles have a free-fall velocity, the diffusivity in the fall direction will be greater than the diffusivity in the other two directions. Equations (32) through (34) show that when particles have a large γ and very small St, the diffusivity is twice as large in the direction of the free fall as it is in the other two transverse directions. Particles with large St reach this limit at lower drift velocities than do particles with small St.

A contour plot of diffusivity in the St-γ plane (Fig. 3) gives a clear picture of the crossing trajectories effect and the continuity effect; however, it is difficult to see how the diffusivity changes as the size of a particle changes. Figure 6 shows how the diffusivity (nondimensionalized by $u_0^2 T_{mE}$) changes as the diameter of a glass sphere increases. The diffusivity decreases in all three directions as the particle diameter increases, and the diffusivity becomes more anisotropic as the particle size increases. A 80 μm diameter glass sphere has one-fourth the diffusivity in the directions transverse to the fall direction as a fluid point, and the diffusivity in the fall direction is about twice that in the transverse direction. For a fixed particle size, the diffusivity will decrease as the fluid rms fluctuating velocity decreases. For this particular example, the effect of the free-fall velocity cannot be neglected for particles larger than 20 μm, and the anisotropy of the diffusivity must be taken into account.

4.2 Experiments in Grid-Generated Turbulence. Three experiments (Snyder and Lumley, 1971; Wells and Stock, 1983; and Ferguson, 1986) support the analytical work described in Section 4.1. All were done in decaying grid-generated turbulent flow with a 2.45 cm grid spacing ($M = 2.54$ cm) and a mean velocity of 6.5 m/s. Wells and Stock measured the effect of free-fall velocity on dispersion in the fall direction (the crossing trajectory effect); Ferguson measured the difference between the dispersion in the fall direction and the dispersion in the direction transverse to the fall direction (the continuity effect); while Snyder and Lumley measured Lagrangian statistics for particles for a range of Stokes numbers and fall parameters in the direction transverse to the fall direction. Each of the experiments was conducted in grid-generated turbulence, which differs from the flow considered by Reeks (1977), Nir and Pismen (1979), and Wang and Stock (1993) (discussed in Section 4.1) because it decays. If the particle relaxation time is small compared to the flow decay, the flow can be considered locally stationary. This is a good assumption for fluid points because, for grid-generated turbulence, the rms fluctuating velocity decays as $x^{-1/2}$ and the time scale grows as x; therefore, the diffusivity of a fluid element (the product of u_0^2 and T_L) is nearly constant. For some of the larger particles used in the experiments described below, the long relaxation time of the particle relative to the decay time of the turbulence must be taken into account when the experimental results are compared with the analytical predictions given in Section 4.1. While the flow fields used in the experiments were generated with a similar grid and mean velocity, the three flow fields were not identical. The source of the difference might be traced to different initial conditions (George, 1990).

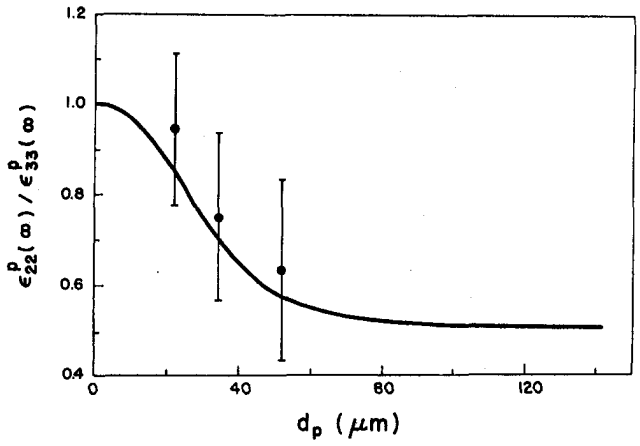


Fig. 6 Change in particle diffusivity ratio (the ratio of diffusivity in fall direction to diffusivity in transverse direction) with particle diameter for the dispersion of glass beads in homogeneous, isotropic turbulence. Solid points show experimental measurements and the line shows the results of a Gaussian random modes simulation. Nonlinear drag effects were included in the simulation. Vertical bars indicate experimental uncertainty.

Wells and Stock (1983) used a horizontal wind tunnel, injected charged particles at the plane of the grid, and measured the vertical dispersion of the particles. An electric field was used to control the fall velocity of the charged particles. With the electric field, the free-fall velocity could be reduced to zero or increased beyond that due to gravity, thus allowing the drift parameter to be changed without changing the Stokes number. Glass beads of 57 μm and 5 μm were used, giving St $\sim$ 0.5 for the 57 μm particles and St $\sim$ 0.004 for the 5 μm particles. Estimated drift parameters for the experiment ranged from zero to 4. Because of the flow decay and the experimental problems involved in measuring T_{mE}, it is difficult to give exact values for St or γ. A single-component laser Doppler anemometer was used to measure velocities in the mean flow direction, v_1, and to measure the relative particle number density. Particle diffusivity, ϵ^g_{33}, was calculated from the slope of the mean squared dispersion curve, Eq. (15), and was found to depend strongly on the particle drift parameter and not on the Stokes number. This supports the analytical finding that dispersion is a strong function of the particle free-fall velocity. The experimental uncertainty was too large to determine if the dispersion of the large particles was greater than that of the small particles when the attraction of gravity was canceled by the force due to the electric field. Numerical simulations (discussed in Section 4.3), which included the effects of flow decay and nonlinear drag, reproduce the findings for the 57 μm particles of this experiment if the data from the 5 μm particle are used to find the scales of the turbulence.

Ferguson (1986, 1995) used the same tunnel as Wells, but did not use charged particles or an electric field. Ferguson measured the particle concentration in the $x_2 - x_3$ plane at several x_1 locations (the mean flow was in the x_1 direction and gravity was in the negative x_3 direction). Dispersion experiments were conducted with 29 μm particles and a mean gas velocity of 4.5 m/s, and 62 μm particles and a mean velocity of 4.5 m/s. The small particles had Stokes numbers ranging from 0.12 to 0.03 and, with a drift velocity of 6.1 cm/s, the drift parameter, γ, was 0.2 to 0.39. The Stokes number for the 62 μm particles ranged between 0.2 to 0.14 and, with a drift velocity of 30 cm/s, the drift parameter was 2.2 to 2.5. The Stokes numbers and drift parameter varied in the mean flow direction because the fluid turbulence intensity decreased and the length scale increased due to turbulence decay. Dispersion coefficients in both the x_2 and x_3 directions were calculated from the mean squared dispersion. The small particles, with a low drift parameter, exhibited symmetric dispersion ($\epsilon_{22}/\epsilon_{33} \approx 1$) and the larger particles exhibited asymmetric dispersion ($\epsilon_{22}/\epsilon_{33} \approx .53$). This finding supports the analytical studies and demonstrates the continuity effect, the second effect of drift velocity on particle dispersion.

Downloaded 03 Jun 2010 to 171.66.16.125. Redistribution subject to ASME license or copyright; see http://www.asme.org/terms/Terms_Use.cfm

Using the same experimental facility, Wang and Stock (1995a) extended the measurements of Ferguson. Wang made comparisons between the experimental results and the analytical predictions for the diffusivity ratio, the particle rms velocity ratio, and the particle time scale ratio for three particle sizes (Figs. 6, 7, and 8). These figures also illustrate the large uncertainty in the measurement of particle diffusivity ratio and time scale ratio.

Snyder and Lumley (1971) measured the horizontal particle velocity autocorrelation function in a vertical grid-generated flow (M = 2.54 cm). The mean velocity was 6.5 m/s and the particles were injected at x/M = 20. Single particle trajectories were tracked photographically from x/m = 68 to 168, digitized, and displacement and velocities determined. From the velocities, the particle autocorrelation along the particle trajectory was determined and then corrected for the flow decay. Because measurements were taken in a region where the decay rate was low, the particles were able to follow the decay, in contrast to the situation in the experiments of Wells where the decay rate was higher and the decay of the larger particles lagged behind the fluid decay. Snyder and Lumley found that the heavier particles had the smallest integral time scale. This result can be explained in terms of the combined effect of the Stokes number and the drift parameter as discussed in Section 4.1.

The three experiments described above all have considerable experimental uncertainty, but they provide the data needed to support the analytical studies of particle dispersion in stationary, homogeneous turbulent flow. They show the effect of Stokes number and drift parameter on the particle velocity scale, time scale, and diffusivity. They show that the crossing trajectories effect reduces the dispersion and makes it anisotropic. The experimental studies do not show the effect of the turbulent structure parameter, m, because all the studies were conducted using the same mean velocity and the same grid to generate the turbulence. We need at least one more experimental study of particle dispersion in grid turbulence, but with a very different turbulence structure than the ones used in past studies. The analysis of Mei and Adrian (1993) can be used as a guide for designing such an experiment. We also need experimental studies in a uniform shear flow so that the effect of shear on particle dispersion can be determined. Numerical simulations cannot completely replace experiments because, in the simulations, particle motion is governed by the forces included in the particle equation of motion, and the choice of forces to include and their functional form is at the discretion of the modeler.

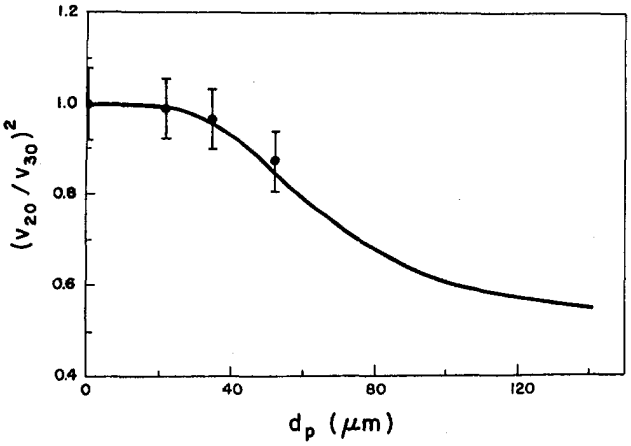


Fig. 7 Change in velocity scale ratio (the ratio of the particle rms velocity in the fall direction to the particle rms velocity in the transverse direction) with particle diameter for the dispersion of glass beads in a homogeneous, isotropic turbulence. Solid points show experimental measurements and the line shows the results of a Gaussian random modes simulation. Nonlinear drag effects were included in the simulation. Vertical bars indicate experimental uncertainty.

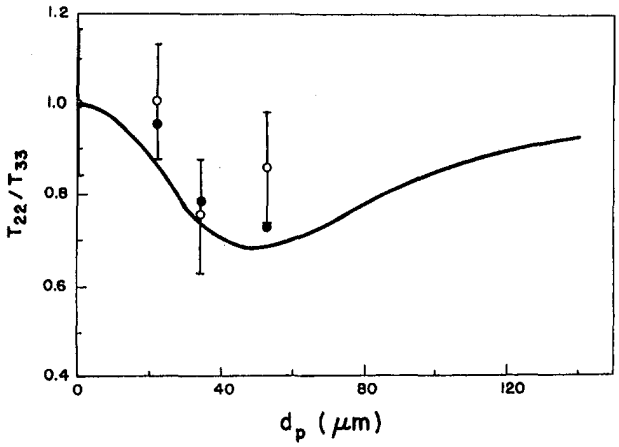


Fig. 8 Change in particle time scale ratio (the ratio of the particle integral time scale in the fall direction to the particle integral time scale in the transverse direction) with particle diameter for the dispersion of glass beads in a homogeneous, isotropic turbulence. Open points show the measured fixed Eulerian time scale ratio, solid points show the Lagrangian time scale ratio calculated from measured particle diffusivity and rms velocity, and the line shows the results of a Gaussian random modes simulation. Nonlinear drag effects were included in the simulation. Vertical bars indicate experimental uncertainty.

4.3 Numerical Simulation of Dispersion in Simple Flows. Particle dispersion in simple flows can be studied by numerically generating the time-dependent turbulent flow field and then numerically tracking particles through the flow. A simple three-dimensional turbulent flow field, such as stationary homogeneous turbulence or decaying homogeneous turbulence, can be generated by direct numerical simulation (DNS) or stochastic methods that use a linear superposition of random Fourier modes. Before a particle can be tracked through the turbulence, the equation of motion for the particle must be specified. This is not a problem when simulating flows with uniform mean velocity in which the particles do not come near the wall. The correct form of the equation of motion for a flow with a mean shear or for particles nearing a wall is still being studied (Appendix A).

DNS simulation has been used to study heavy particle dispersion in low Reynolds number isotropic turbulence. Riley and Patterson (1974) found that the particle diffusivity increased as the particle response time increased for heavy particles with no free-fall velocity. This same trend is predicted by the analysis in Section 4.1 for γ = 0. Elghobashi and Truesdell (1992) simulated Snyder and Lumley's (1971) experiment by scaling the particle drift time scale. After proper scaling, they were able to simulate the experimental results. They found that the diffusivity of the heavy particles in the absence of gravity was less than the fluid point diffusivity; this indicates that the Lagrangian integral time scale was greater than the Eulerian integral time scale. The analytical work and the stochastic simulations used flows with the Lagrangian time scale less than the Eulerian time scale. Both the DNS and the stochastic simulation were able to predict the experimental results of Snyder and Lumley.

Squires and Eaton (1991a) simulated homogeneous nondecaying turbulence by applying steady forcing at low wave numbers, and investigated the effects of particle inertia and free-fall velocity. They also used DNS to study the preferential microconcentration structure of the particles as a function of Stokes number (Squires and Eaton, 1991b). The preferential concentration was also studied by Wang and Maxey (1993) and reviewed by Eaton and Fessler (1994). Preferential concentrations were found to be strongest at intermediate Stokes numbers and for no drift velocity.

Downloaded 03 Jun 2010 to 171.66.16.125. Redistribution subject to ASME license or copyright; see http://www.asme.org/terms/Terms_Use.cfm

An alternative method for generating an instantaneous flow field is to use linear superposition of random Fourier modes. This method was developed by Kraichnan (1970) and has the advantage of being able to simulate high turbulent Reynolds number flows and to provide the instantaneous fluid velocity at any desired location and time; thus no interpolation is required as it is in DNS simulations. The disadvantages are that the generated turbulence is Gaussian (the third moments are zero) and does not include interaction between the small and large eddies. Any desired scalar energy spectrum and Eulerian one-point time correlation can be used, but most studies used the forms given by Eqs. (19) and (20) and use about 80 modes. Reeks (1980) used a random modes simulation to test the dispersion prediction obtained using Eulerian direction interaction, and Reeks and McKee (1984) used the same method to study the effect of the Basset history force on long-time particle dispersion. Maxey (1987) used a random modes simulation to study the fall velocity of particles through a turbulent field. He found that the average settling velocity of heavy particles was a few percent higher in a turbulent flow than in still air. Wang (1990) made extensive use of Kraichnan's random modes method to simulate the analytical work of Reeks and the experiments of Wells, Ferguson, and Snyder, and to gain a better understanding of particle motion.

To simulate the flow field used in an experiment with the random modes technique, the structure of the flow given by Eq. (21) must be known. However the experimental measurements are not usually complete enough to allow m to be calculated directly. An example of how m can be determined is given by Wang and Stock (1994b). Figure 9 shows a comparison between Snyder and Lumley's (1971) data and their random modes simulation. Because Snyder and Lumley's measurements were taken in the region were flow decay ($x/M = 70$) was small, the simulations with flow decay not included reproduce the experimental data. Figure 10 gives a comparison of the results of their random-modes simulation and the data of Wells and Stock (1983). In this simulation the effect of the decay must be included because the measurements were made near the grid were flow decay is significant. Random modes simulations were also used to determine when nonlinear drag should be included in a simulation (Wang and Stock, 1989) and to check a suggested method for including nonlinear drag in analytical predictions (Wang and Stock, 1993). The use of random mode simulations allows us to better understand and extend experimental studies.

5 Dispersion in Complex Flows

Most gas-particle flows of importance in fluids engineering are more complex than the simple flows discussed in Section

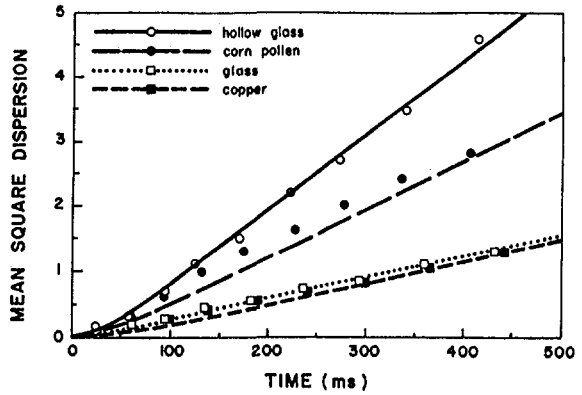


Fig. 9 Comparison of mean squared dispersion in grid turbulence calculated using a Gaussian random modes simulation with the experimental results of Snyder and Lumley (1971). Lines show the simulations and points the experimental data for various types and sizes of particle: ○ hollow glass spheres, ● corn pollen, □ glass spheres, ■ copper spheres.

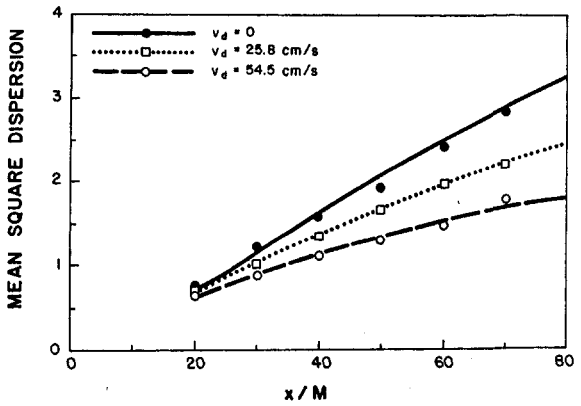


Fig. 10 Comparison of mean squared dispersion in grid turbulence calculated using a Gaussian random modes simulation with the experimental results of Wells and Stock (1983). Lines show the simulations and points the experimental data for 57 μm glass beads with various drift velocities: ● v_d = 0, □ v_d = 25.8 cm/s, ○ v_d = 54.5 cm/s.

4. Complex flows are flows in which the turbulent velocity and length scales change significantly with location. Examples include jets, sprays, wakes, mixing layers, boundary layers, and sudden expansions. Sirignano (1993) reviewed the computational methods that have been used to study sprays. Flows that exhibit clearly defined large-scale structures (e.g., plane mixing layers, jets) also fall into this class. Complex flows found in industrial processes and in the environment can have particle loadings large enough to change the turbulent character of the flow. In this section, the numerical methods used to model these flows are classified and discussed.

Particle-laden flows often involve the transfer of mean and turbulent momentum, heat, and mass between the fluid and the particles. In this review, the focus is on the exchange of turbulent momentum between the gas and the particles. One-way coupling implies that the mass per unit volume of the particles is less than that of the fluid, and that gas phase turbulence is assumed not to be affected by the presence of the particles. As the particle loading increases and we move into two-way coupling, the fluid turbulence can be either damped or increased by the presence of the particles. Finally, when the loading becomes even higher, we can have four-way coupling, with particle-to-particle collisions being an important source of momentum transfer. This subsection will treat only one-way coupling; Section 6 covers two-way coupling, and four-way coupling is beyond the scope of this review.

Numerical prediction of complex flows uses an Eulerian formulation for the gas phase and either a Lagrangian (also called the trajectory method) or an Eulerian formulation (also called the two-fluid model) for the particulate phase. Most Eulerian solution schemes for the gas phase use a k-ϵ turbulence closure model because it gives a good balance between computing time and accuracy. While the solution might give an acceptable solution for the mean fluid flow field, it often falls short of providing the information on the turbulent aspects of the flow that are needed to model particle dispersion. The k-ϵ model assumes that the turbulence is isotropic which, in turn, would make the dispersion of particles in the absence of gravity also isotropic. In many applications this is not a problem, because the flow field is considered two-dimensional with the dispersion normal to the main flow direction. In these cases, the turbulence structure calculated as part of the k-ϵ model is sufficient to model the dispersion. However, the k-ϵ closure does not provide adequate turbulence information to model particle dispersion in two-dimensional recirculation zones or in three-dimensional flows unless auxiliary schemes are used to supplement the turbulence data. Numerical turbulence models only provide a rough approximation of the statistics for the turbulence in complex flows

Downloaded 03 Jun 2010 to 171.66.16.125. Redistribution subject to ASME license or copyright; see http://www.asme.org/terms/Terms_Use.cfm

and, in most cases, experimentally determined time and length scales have considerable uncertainty as well.

5.1 Lagrangian Models. Numerical techniques that use the Lagrangian frame of reference for the particle phase track individual particles through a numerically determined turbulent flow field. The Lagrangian or trajectory method is conceptually simple in that we know the equations of motion for the particles, Eqs. (4) and (5), and if the complete flow field is known for all locations and times, the particles could be tracked through the flow and statistics of the particle motion generated. This can be done for simple flows using DNS. The challenge with the Lagrangian technique is reproducing the essence of the turbulent flow from the limited information provided by the numerical scheme used to solve the gas phase flow. In one of the first heavy particle trajectory calculations, Gosman and Ioannides (1981) used a k-ϵ simulation for the fluid and a one-step-per-eddy, Monte-Carlo simulation for the particles. This technique, which has been widely used to simulate long-time dispersion, can account for particle inertia and particle free-fall velocity (crossing trajectory effect), but it does not account for the non-isotropic dispersion (continuity effect). Short-time dispersion (short-time meaning less than a few fluid integral time scales) depends on the shape of the fluid correlation spectrum (Berlemont et al., 1990). Berlemont et al. (1993) give examples of the effect of the velocity correlation on short-time dispersion and of the effect of the fluid time scale on both the short and long-time mean squared dispersion. The first step in understanding the trajectory method is to consider fluid point dispersion.

Wang and Stock (1992) compared the Monte Carlo process (also called a random walk model), which uses one time step per eddy, with the Langevin equation, which uses many steps per eddy. Both had limitations and they suggested a model that combines the two techniques. MacInnes and Bracco (1992) compared the random walk models and the Langevin equation for fluid point dispersion. Most models reproduced dispersion in homogeneous turbulence, but could not predict a uniform particle distribution if the turbulence was inhomogeneous. They explain the source of the spurious drift and methods to correct for it.

Most of the trajectories models only simulate one-dimensional heavy particle dispersion and cannot predict non-isotropic dispersion (continuity effect), because account is not taken of the directional difference between the motion of the eddy containing the particle and the motion of the particle. If the particle and eddy are moving in the same or opposite directions and the relative motion is large enough that the particle travels through the eddy before it decays, then the length scale that governs the motion will be L_f (longitudinal length). However, if the eddy and the particle are moving perpendicular to one another and the particle moves through the eddy before it decays, then the motion is governed by L_g (transverse length scale). Huang et al. (1993) implement this idea in a simple Monte-Carlo simulation that reproduces the full St-γ plane.

Lagrangian models are well suited to modeling dispersion from a point source. They can correctly simulate the mean squared dispersion as it changes from being a function of time squared to a function of time as the dispersion progresses. They do, however, become computationally expensive if the particles start with a broad spatial or size distribution.

5.2 Two-Fluid Models. Two-fluid models solve Eulerian equations for both the gas and the particulate phases. This is similar to solving equations for two-gas species in a binary mixture, except the momentum transfer between the two fluids is not the same. The time-dependent equations for both the gas and particle phase, including a symbolic representation for the interaction force between the two phases, can easily be written, but must be time-averaged before they can be used. The advantage of the two-fluid model is that once the equations have been averaged and a closure scheme developed, the resulting equations can be solved using the same numerical techniques used for a single-phase flow. Another advantage of the two-fluid approach is that no extra computation is required for flows that start with a spatial distribution of particles. The disadvantage is that a closure scheme must be developed.

Until recently, most applications of the two-fluid formulation used a volume-averaged velocity when the governing equations were time averaged. This type of averaging can lead to many new terms that involve a fluctuating volume fraction-fluctuating velocity correlation (Elghobashi and Abou-Arab, 1983; Chung, et al., 1986). In a single-phase variable density flow, considerable simplification can be obtained if density weight velocity is used when the equations are time averaged (Laufer, 1969). Several investigators have recently been using the density weighted velocity when time averaging (Simonin, 1991; Reeks, 1992).

To close the time-averaged two-fluid equations, relations must be developed for the interphase force terms. Many models rely on a gradient transport scheme. Recent use of the Fokker-Plank equations and modeling in phase-space (where the dispersed phase density is given in terms of position, velocity, and time) have shown the limitations of the gradient diffusion models (Reeks, 1993) and have led to prediction of particle dispersion in a simple shear flow (Hyland et al., 1993). We are only beginning to understand two-fluid modeling, but important steps have been made.

5.3 Discrete Vortex Methods. Discrete vortex methods have been used to model particle transport in two-dimensional flows that are dominated by large-scale organized structures. This technique captures the essential features of the flow without the complexity and time requirements of DNS. It has been used to model jets (Chung and Troutt, 1988), plane mixing layers (Wen et al., 1992), etc. A recent review by Eaton and Fessler (1994) gives a detailed discussion of the use of discrete vortex methods and points out the role of the Stokes number in understanding particle dispersion in flows with large organized structures.

6 Flows With Two-Way Coupling

Many industrial and environmental flows have particle loadings high enough that the presence of the particles alters the gas phase mean velocity and turbulence. Crowe (1982) reviewed techniques that can be used to model the coupling between the gas phase mean velocity and the mean particle velocity field. He pointed out the advantages of using a trajectory method for the particles. Recently, research has been directed toward understanding the effect of the presence of the particles on the gas phase turbulence. Elghobashi (1991) gives a map of the possible flow regimes. Small particles tend to decrease the gas phase turbulence because they follow the turbulent fluctuations and add mass to the fluid. Large particles, on the other hand, do not follow the gas phase turbulent fluctuations and generate turbulence in the gas phase as a result of the instantaneous relative velocity between the particles and the gas. Gore and Crowe (1989) found that when the ratio of the particle diameter to the turbulence length scale was less than 0.1, the turbulence intensity of the fluid phase along the centerline of a pipe or jet was not modified by the particles. Hetsroni (1989) found a similar effect when $\mathrm{Re}_p < 400$, but his results were not conclusive. The effect of particles on the turbulence length scales is unclear. DNS has been used to investigate the effect of the particles on the fluid energy spectrum and on the fluid turbulent kinetic energy (Squires and Eaton, 1990; Elghobashi and Truesdell, 1993). The results of these studies add to our understanding of turbulence modification, but no simple picture of the phenomenon has emerged. Two recent reviews (Eaton and Fessler, 1994; McLaughlin, 1994) summarize the DNS studies of the effect of particles on the gas phase turbulence.

Downloaded 03 Jun 2010 to 171.66.16.125. Redistribution subject to ASME license or copyright; see http://www.asme.org/terms/Terms_Use.cfm

Various extensions of the k-ϵ model have been made to allow numerical prediction to account for turbulence modification in the gas phase (Elghobashi et al., 1984; Chen and Wood, 1985), but, as pointed out by Crowe (1993), none of these models predicts an increase in the gas phase turbulence for large particles. The best method to model turbulence modification due to the presence of particles, as found in dust storms and many other industrial and environmentally important flows, is still unresolved.

7 Conclusions

Particle dispersion in a uniform flow field with homogenous turbulence is well understood. There is general agreement among experiments, analytical predictions, and numerical simulations. Recently, simple Lagrangian methods have been use to predict both the crossing-trajectory effect and the non-isotropic dispersion for homogeneous turbulence when the mean flow velocity is uniform. The validation of extensions of this method to flows with a mean shear or non-homogeneous turbulence requires experimental data that clearly show how these gradients affect particle dispersion. Recent advances in two-fluid modeling provide a sound basis for this modeling technique, which could develop into a useful tool for predicting industrially and environmentally important flows. In all modeling development, it is important to be able to show the effects of particle inertia and free-fall velocity in both the plane of the free-fall velocity and in the plane perpendicular to the free-fall velocity. To complete our understanding of particle dispersion in simple flows, experiments need to be done to understand the effect of a shear in the mean flow and the effect of a gradient in the fluid turbulence.

Acknowledgments

The opportunity to prepare this review and present a lecture at the ASME Winter Annual Meeting, November 1994, were made possible by the ASME Freeman Scholar Program in Fluids Engineering. I am grateful to the Freeman Scholar Committee: Drs. J. Hoyt (chair), C. Brennen, and F. White. I am also very grateful to Dr. Michael W. Reeks, Berkeley Technology Centre, Nuclear Electric, UK, who has provided sound advice and encouragement over many years, and who hosted my visit to the Berkeley Technology Centre in fall 1994. I thank Dr. Clayton Crowe for introducing me to gas-solid flows, and Drs. J. Eaton and John Jurewicz for their support. I am also very grateful for having had the opportunity to work with several past Ph.D. students at Washington State University: Drs. Michael Wells, John Ferguson, Greg Kallio, Gylfi Arnason, and Lian-Ping Wang; and with present Ph.D. student, Ms. Xiaoyan Huang.

References

Auton, T. R., Hunt, J. C. R., and Prud'homme, M., 1988, "The Force Exerted on a Body in Inviscid Unsteady Non-Uniform Rotational Flow," *Journal of Fluid Mechanics,* Vol. 197, pp. 241–257.

Basset, A. B., 1888, *Treaties on Hydrodynamics,* London, Deighton Bell, Vol. 2, Chapter 22, pp. 285–297.

Batchelor, G. K., 1949, "Diffusion in a Field of Homogeneous Turbulence I. Eulerian, Analysis," *Aust. Journal of Scientific Research,* Vol. 2, pp. 437–459.

Berlemont, A., Desjonqueres, P., and Gouesbet, G., 1990, "Particle Lagrangian Simulation in Turbulent Flows," *International Journal of Multiphase Flow,* Vol. 16, No. 1, pp. 19.

Berlemont, A., Desjonquères, P., and Gouesbet, G., 1993, "Particle Tracking in Turbulent Flows," ASME/FED, *Gas-Solid Flows,* Vol. 166, pp. 121–129.

Boussinesq, J., 1885, "Applications a l'etudes des Potentiels" [Re-edition 1969 ed.], Paris, Blanchard, pp. 413–416.

Boussinesq, J., 1903, *Theorie Analytique de la Chaleur,* Paris, L'Ecole Polytechnique, Vol. 2, pp. 224.

Chen, C. P., and Wood, P. E., 1985, "A Turbulence Closure Model for Dilute Gas-Particle Flows," *Canadian Journal of Chemical Engineering,* Vol. 63, pp. 349–360.

Cherukat, P., McLaughlin, J. B., and Graham, A. L., 1994, "The Inertial Lift on a Rigid Sphere Translating in a Linear Shear Flow Field," *International Journal of Multiphase Flow,* Vol. 20, No. 2, pp. 339–353.

Chung, J. N., and Troutt, T. R., 1988, "Simulation of Particle Dispersion in an Axisymmetric Jet," *Journal of Fluid Mechanics,* Vol. 186, pp. 199–222.

Chung, M. K., Sung, H. J., and Lee, K. B., 1986, "Computational Study of Turbulent Gas-Particle Flow in a Venturi," ASME JOURNAL OF FLUIDS ENGINEERING, Vol. 108, pp. 248.

Clift, R., and Gauvin, W. H., 1970, *Proc. Chemeca '70,* Vol. 1, pp. 14–28.

Clift, R., Grace, J. R., and Weber, M. E., 1978, *Bubbles, Drops and Particles,* New York, Academic Press.

Corrsin, S., 1959, "Progress Report on Some Turbulent Diffusion Research," *Advances in Geophysics,* Vol. 6, pp. 161–184.

Corrsin, S., and Lumley, J. L., 1956, "On the Equation of Motion for a Particle in Turbulent Fluid," *Applied Scientific Research A,* Vol. 6, pp. 114–116.

Cox, R. G., and Brenner, H., 1967, "The Slow Motion of a Sphere Through a Viscous Fluid Toward a Plane Surface II. Small Gap Widths, Including Inertial Effects," *Chemical Engineering Sciences,* Vol. 22, pp. 1753–1777.

Crowe, C. T., 1982, "Review-Numerical Models for Dilute Gas-Particle Flows," ASME JOURNAL OF FLUIDS ENGINEERING, Vol. 104, pp. 297.

Crowe, C. T., 1993, "Modeling Turbulence in Multiphase Flows," Rodi, W. and Martelli, F., eds., *Engineering Turbulence Modeling and Experiments 2,* Elsevier Science Publishers, pp. 899–913.

Crowe, C. T., Sharma, M. P., and Stock, D. E., 1977, "The Particle-Source-in Cell (PSI-CELL) Model for Gas-Droplet Flows," ASME JOURNAL OF FLUIDS ENGINEERING, Vol. 99, pp. 325.

Csanady, G. T., 1963, "Turbulent Diffusion of Heavy Particles in the Atmosphere," *Journal of Atmospheric Sciences,* Vol. 20, pp. 201–208.

Cunningham, E., 1910, "On the Velocity of Steady Fall of Spherical Particles Through Fluid Medium," *Proc. Roy. Soc. Ser. A.,* Vol. 83, pp. 357–365.

Dandy, D. S., and Dwyer, H. A., 1990, "A Sphere in Shear Flow at Finite Reynolds Number: Effect of Shear on Particle Lift, Drag, and Heat Transfer," *Journal of Fluid Mechanics,* Vol. 216, pp. 381–410.

Eaton, J. K., and Fessler, J. R., 1994, "Preferential Concentration of Particles by Turbulence," *International Journal of Multiphase Flow,* Vol. 20, No. Supplement, pp. 169–209.

Elghobashi, S. E., and Abou-Arab, T. W., 1983, "A Two-Equation Turbulence Model for Two-Phase Flows," *Physics of Fluids,* Vol. 26, pp. 931–938.

Elghobashi, S., 1991, "Particle-Ladden Turbulent Flows: Direct Simulation and Closure Models," *Applied Science Research,* Vol. 48, pp. 301–314.

Elghobashi, S., and Truesdell, G. C., 1992, "Direct Simulation of Particle Dispersion in a Decaying Isotropic Turbulence," *Journal of Fluid Mechanics,* Vol. 242, pp. 655–700.

Elghobashi, S., and Truesdell, G. C., 1993, "On the Two-Way Interaction Between Homogeneous Turbulence and Dispersed Solid Particles. 1: Turbulence Modification," *Physics of Fluids A,* Vol. 5, pp. 1790–1801.

Elghobashi, S. E., A. Arab, T. W., Rizk, M., and Mostafa, A., 1984, "Prediction of the Particle Laden Jet with a Two Equation Turbulent Model," *International Journal of Multiphase Flow,* Vol. 10, pp. 697–710.

Faxen, H., 1922, Arkiv foef Mathematik, Astronomi och Fysik, Vol. 17, pp. 1.

Ferguson, J. R., 1986, "Effect of Fluid Continuity on the Turbulent Dispersion of Particles," Ph.D. dissertation, Washington State University, Pullman.

Ferguson, J. R., and Stock, D. E., 1995, "Effects of Fluid Continuity on Turbulent Particle Dispersion," *Journal of Fluid Mechanics,* Vol. submitted.

George, W. K., 1990, "Governing Equations, Experiments and the Experimentalist," *Experimental Thermal and Fluid Sciences,* Vol. 1990 (3), pp. 557–566.

Gore, R. A., and Crowe, C. T., 1989, "Effect of Particle Size on Turbulence Intensity," *International Journal of Multiphase Flow,* Vol. 15, pp. 279–285.

Gosman, A. D., and Ioannides, E., 1981, "Aspects of Computer Simulation of Liquid-Fuelled Combustors," pp. AIAA-81-0323.

Harper, E. Y., and Chang, I.-D., 1968, "Maximum Dissipation Resulting From Lift in Slow Viscous Flow," *Journal of Fluid Mechanics,* Vol. 33, pp. 209–225.

Hetsroni, G. M., 1989, "Particle-Turbulence Interaction," *International Journal of Multiphase Flow,* Vol. 15, pp. 315–327.

Hinze, J., 1975, *Turbulence,* McGraw-Hill, New York.

Hogg, A. J., 1994, "The Inertial Migration of Non-Neutral Buoyant Spherical Particles in Two-Dimensional Shear Flows," *Journal of Fluid Mechanics,* Vol. 272, pp. 285–318.

Huang, X., Stock, D. E., and Wang, L.-P., 1993, "Using the Monte-Carlo Process to Simulate Two-Dimensional Heavy Particle Dispersion," ASME/FED, *Gas-Solid Flows,* Vol. 166, pp. 153–167.

Hyland, K. E., McKee, S., and Reeks, M. W., 1993, "The Dispersion of Particles in a Simple Shear Flow," ASME/FED, *Gas-Solid Flows,* Vol. 166, pp. 177–182.

Kallio, G. A., 1993, "Random-Walk Modeling of Particle Deposition," ASME/FED, *Gas-Solid Flows,* Vol. 166, pp. 161–167.

Kallio, G. A., and Reeks, M. W., 1989, "A Numerical Simulation of Particle Deposition in Turbulent Boundary Layers," *International Journal of Multiphase Flow,* Vol. 15, pp. 433–446.

Kraichnan, R. H., 1970, "Diffusion by a Random Velocity Field," *Physics of Fluids,* Vol. 13, pp. 22–31.

Landau, L. D., and Lifshitz, E. M., 1959, *Fluid Mechanics,* Oxford, Pergamon Press.

Laufer, J., 1969, "Turbulent Shear Flows of Variable Density," *AIAA Journal,* Vol. 7, pp. 706.

MacInnes, J. M., and Bracco, F. V., 1992, "Stochastic Particle Dispersion Modeling and Tracer-Particle Limit," *Physics of Fluids A,* Vol. 4, pp. 2809–2824.

Downloaded 03 Jun 2010 to 171.66.16.125. Redistribution subject to ASME license or copyright; see http://www.asme.org/terms/Terms_Use.cfm

Maxey, M. R., 1987, "The Gravitational Settling of Aerosol Particles in Homogeneous Turbulence and Random Flow Fields," *Journal of Fluid Mechanics,* Vol. 174, pp. 441–465.

Maxey, M. R., 1993, "The Equation of Motion for a Small Rigid Sphere in a Nonuniform or Unsteady Flow," ASME/FED, *Gas-Solid Flows,* Vol. 166, pp. 57–62.

Maxey, M. R., and Riley, J. J., 1983, "Equation of Motion for a Small Rigid Sphere in a Nonuniform Flow," *Physics of Fluids,* Vol. 26, pp. 883–889.

McLaughlin, J. B., 1991, "Inertial Migration of a Small Sphere in Linear Shear Flows," *Journal of Fluid Mechanics,* Vol. 224, pp. 261–275.

McLaughlin, J. B., 1993, "The Lift on a Small Sphere in Wall-Bounded Linear Shear Flows," *Journal of Fluid Mechanics,* Vol. 246, pp. 249–265.

McLaughlin, J. B., 1994, "Numerical Computation of Particle-Turbulence Interaction," *International Journal of Multiphase Flow,* Vol. 20, No. Supplement, pp. 211–231.

Mei, R., and Adrian, R. J., 1993, "Effect of Turbulence Structure on the Dispersion of Fluid and Particles," ASME/FED, *Gas-Solid Flows,* ASME FED-Vol. 166, pp. 131–143.

Nir, A., and Pismen, L. M., 1979, "The Effect of a Steady Drift on the Dispersion of a Particle in Turbulent Fluid," *Journal of Fluid Mechanics,* Vol. 94, pp. 369–381.

Oseen, C. W., 1927, *Hydrodynamik,* Leipzig, 132 p.

Reeks, M. W., 1977, "On the Dispersion of Small Particles Suspended in an Isotropic Turbulent Field," *Journal of Fluid Mechanics,* Vol. 83, pp. 529–546.

Reeks, M. W., 1980, "Eulerian Direct Interaction Applied to the Statistical Motion of Particles in a Turbulent Field," *Journal of Fluid Mechanics,* Vol. 97, pp. 569–590.

Reeks, M. W., 1992, "On the Continuum Equations for Dispersed Particles in Nonuniform Flows," *Physics of Fluids A,* Vol. 4, pp. 1290–1303.

Reeks, M. W., 1993, "On the Constitutive Relations for Dispersed Particles in Nonuniform Flows 1: Dispersion in a Simple Shear Flow," *Physics of Fluids A,* Vol. 5, pp. 750–761.

Reeks, M. W., and McKee, S., 1984, "The Dispersive Effect of Basset History Forces on Particle Motion in a Turbulent Flow," *Physics of Fluids,* Vol. 27, pp. 1573–1582.

Riley, J. J., 1971, Ph.D. dissertation, The Johns Hopkins University, Baltimore, MD.

Riley, J. J., and Patterson, G. S., 1974, "Diffusion Experiments with Numerically Integrated Isotropic Turbulence," *Physics of Fluids,* Vol. 17, pp. 292–297.

Rivero, M., Magnaudet, J., and Fabre, J., 1991, "Quelques résultats nouveaux concernant les forces exercées sur une inclusion sphérique par un écoulement accéléré," C. R. Acad. Sci. Paris, t. 312, pp. 1499–1506.

Rubinow, S. I., and Keller, J. B., 1961, "The Transverse Force on a Spining Sphere Moving in a Viscous Fluid," *Journal of Fluid Mechanics,* Vol. 11, pp. 447–459.

Saffman, P. G., 1965, "The Lift on a Small Sphere in a Slow Shear Flow," *Journal of Fluid Mechanics,* Vol. 22, pp. 285–400.

Saffman, P. G., 1968, "The Lift on a Small Sphere in a Slow Shear Flow-Corrigendum," *Journal of Fluid Mechanics,* Vol. 31, pp. 624.

Simonin, O., 1991, "Prediction of the Dispersed Phase Turbulence in Particle-Laden Jets," ASME/FED, *Gas-solid Flows,* Vol. 121, pp. 197–206.

Sirignano, W. A., 1993, "Fluid Dynamics of Sprays—1992 Freeman Scholar Lecture," ASME JOURNAL OF FLUIDS ENGINEERING, Vol. 115, pp. 345–378.

Snyder, W. H., and Lumley, J. L., 1971, "Some Measurements of Particle Velocity Autocorrelation Functions in a Turbulent Flow," *Journal of Fluid Mechanics,* Vol. 48, pp. 41–71.

Squires, K. D., and Eaton, J. K., 1990, "Particle Response and Turbulence Modification in Isotropic Turbulence," *Physics of Fluids A,* Vol. 2, pp. 1191–1203.

Squires, K. D., and Eaton, J. K., 1991a, "Measurements of Particle Dispersion Obtained From Direct Numerical Simulations of Isotropic Turbulence," *Journal of Fluid Mechanics,* Vol. 226, pp. 1–35.

Squires, K. D., and Eaton, J. K., 1991b, "Preferential Concentration of Particles by Turbulence," *Physics of Fluids, A,* Vol. 3, pp. 1169–1178.

Taylor, G. I., 1921, "Diffusion by Continuous Movements," *Proc. London. Math. Soc.,* Vol. 20, pp. 196–212.

Tchen, C. M., 1947, "Mean and Correlation Problems Connected With the Motion of Small Particles Suspended in a Turbulent Fluid," Ph.D. dissertation, Delft University, Martinus Nujhoff, The Hague.

Vojir, D. J., and Michaelides, E. E., 1994, "Effect of the History Term on the Motion of Rigid Spheres in a Viscous Fluid," *International Journal of Multiphase Flow,* Vol. 20, No. 3, pp. 547–556.

Wang, L. P., 1990, "On the Dispersion of Heavy Particles by Turbulent Motion," Ph.D. dissertation, Dept. of Mech. & Materials Eng., Washington State University, Pullman, 241 pp.

Wang, L. P., and Maxey, M. R., 1993, "Settling Velocity and Concentration Distribution of Heavy Particles in Homogeneous Isotropic Turbulence," *Journal of Fluid Mechanics,* Vol. 256, pp. 27–68.

Wang, L. P., and Stock, D. E., 1989, "Numerical Simulation of Heavy Particle Dispersion Time Step and Nonlinear Drag Consideration," ASME JOURNAL OF FLUIDS ENGINEERING, Vol. 114, pp. 100–106.

Wang, L. P., and Stock, D. E., 1992, "Stochastic Trajectory Models for Turbulent Diffusion: Monte Carlo Process Versus Markov Chains," *Atmospheric Environment,* Vol. 26A, pp. 1599–1607.

Wang, L. P., and Stock, D. E., 1993, "Dispersion of Heavy Particles by Turbulent Motion," *Journal of the Atmospheric Sciences,* Vol. 50, pp. 1897–1913.

Wang, L. P., and Stock, D. E., 1994b, "Numerical Simulation of Heavy Particle Dispersion-Scale Ratio and Flow Decay Considerations," ASME JOURNAL OF FLUIDS ENGINEERING, Vol. 116, pp. 154–163.

Wang, L. P., and Stock, D. E., 1995a, "Anisotropy in Dispersion Statistics of Glass Beads in a Grid-Generated Turbulent Air Flow," *Journal of Fluid Mechanics,* Vol. submitted.

Wells, M. R., and Stock, D. E., 1983, "The Effects of Crossing Trajectories on the Dispersion of Particles in a Turbulent Flow," *Journal of Fluid Mechanics,* Vol. 136, pp. 31–62.

Wen, F., Kamalu, N., and Chung, J. N., 1992, "Particle Dispersion by Vortex Structures in Plane Mixing Layers," ASME JOURNAL OF FLUIDS ENGINEERING, Vol. 114, pp. 657–666.

Yudine, M. I., 1959, "Physical Consideration on Heavy-Particle Dispersion," *Advances in Geophysics,* Vol. 6, pp. 185–191.

APPENDIX A

Particle Equation of Motion

The equation governing the motion of a particle in a stationary fluid is generally attributed to Basset (1888), Boussinesq (1903), and Oseen (1927) and called the BBO equation.[1] The BBO equation was derived by assuming that the fluid flow near the particle can be split into two parts: the original fluid flow without the particle, and the disturbance flow due to the particle. The forces acting on a particle are found by assuming that the disturbance flow can be treated as creeping flow and the inertia terms neglected. The resulting BBO equation shows that the acceleration of the particle depends on the sum of three forces: viscous drag, added mass, and the Basset history. The added mass term is the inertial response to the displacement of the surrounding fluid by the particle, and the Basset history term arises from the diffusion of vorticity away from the particle as the particle changes velocity. The BBO equation is only valid for a particle starting at rest relative to the fluid. A derivation of the equation can be found in Landau and Lifshitz (1959). Tchen (1947) modified the BBO equation to allow for fluid motion by including the force due to a pressure gradient in the fluid. Tchen also wrote the equation in terms of the relative velocity between the particle and the fluid. Corrsin and Lumley (1956) and Riley (1971) made corrections to the term accounting for the effect of the pressure gradient in the fluid flow field. The equation of motion was rederived by Maxey and Riley (1983). They included the Faxen correction (Faxen, 1922), to the steady drag term to account for the effect of nonlinear changes in the velocity of the fluid flow across the particle. The development by Maxey and Riley is the most recent full derivation of the equation of motion for an isolated particle in nonuniform, unsteady flows with the particle starting at rest relative to the fluid. In the derivation, Maxey and Riley attempt to keep all approximations to the same order and to discuss the limitations on the final equation. The limitation of requiring that the particle start with a velocity equal to that of the fluid has been removed in recent work by Maxey (1993) and Vojir and Michaelides (1994). Reeks and McKee (1984) showed that excluding the effect of the initial velocity resulted in initial conditions having an effect on the long-time dispersion of particles.

The most recent form for the equation of motion for an isolated particle, as given by Maxey (1993), is

$$m_p \frac{d\mathbf{v}}{dt} = (m_p - m_F)\mathbf{g} - m_F \frac{D\mathbf{u}}{Dt}$$

$$-\frac{1}{2} m_F \frac{d}{dt}\left[\mathbf{v} - \mathbf{u}(y(t), t) - \frac{1}{10}\nabla^2\mathbf{u}\right]$$

[1] Vojir and Michaelides (1994) noted that Boussinesq (1885) derived an equation of motion for a particle that included an integral history effect term before Basset.

Downloaded 03 Jun 2010 to 171.66.16.125. Redistribution subject to ASME license or copyright; see http://www.asme.org/terms/Terms_Use.cfm

$$- 6\pi a\mu \mathbf{H}(t) - 6\pi a^2 \mu \int_0^t \frac{d\mathbf{H}}{D\tau}\left[\pi \frac{\mu}{\rho^f}(t-\tau)\right]^{-1/2} d\tau$$

$$- 6\pi a^2 \mu \left[\pi \frac{\mu}{\rho^f} t\right]^{-1/2} \mathbf{H}(0), \quad (1A)$$

where

$$\mathbf{H}(t) = \mathbf{v}(t) - \mathbf{u}(y(t), t) - \tfrac{1}{6}a^2 \nabla^2 \mathbf{u}. \quad (2A)$$

In equation (1A), $\mathbf{v}$ represents the velocity of the particle and $\mathbf{u}$ the velocity of the gas. The equation could be rewritten in terms of the relative velocity $\mathbf{w}$. The derivative d/dt is the derivative following the particle and D/Dt is the derivative following the fluid. The constraints on Eq. (1A) are

$$\frac{2aw}{\nu} \ll 1, \quad \frac{a^2}{\nu}\left(\frac{U}{L}\right) \ll 1, \quad \text{and} \quad \frac{2a}{L} \ll 1, \quad (3A)$$

where $2aw/\nu$ is the Reynolds number of the particle based on the relative velocity, and U/L is the velocity gradient. The first constraint limits the particle Reynolds number to less than one; the second constraint limits the gradients in the fluid velocity field; and the third constraint requires that the particle be much smaller than the length scale of the surrounding fluid.

Before specializing the equation of motion of a particle to the case of gas-solid flow, the terms in Eq. (1A) will be identified. The first term on the right represents the gravity/buoyancy force. The second term, often called the pressure gradient term, is the force due to the acceleration of the surrounding fluid. The third term, the added mass term, on the right-hand side of equation (1A) represents the force on the particle caused by the surrounding fluid being deflected around the particle. At present, there is not complete agreement on the form of the added mass term (Auton et al., 1988; Rivero et al., 1991); however, the differences among the formulations is small for particle Reynolds numbers less than 1. The fourth term on the right-hand side of equation (1A) represents the force due to quasi-steady Stokes drag. The fifth term, which involves an integral over time, is the Basset history term, which arises from the diffusion of vorticity from the particle as the particle changes relative velocity. The final term on the right-hand side of equation (1A) accounts for the particle having an initial velocity not equal to that of the surrounding fluid. The Laplacian term in the added mass term and $H(t)$ are referred to as the Faxen correction terms and account for the nonlinear changes in fluid velocity in the vicinity of the particle.

Many of the forces that act on a particle are important when the density of the fluid and the density of the particle are about the same, and not important for gas-particle flows when there is a big difference between the density of the particle and the density of the fluid. Therefore, before discussing the wealth of research that has been conducted to understand the motion of an isolated particle, the equation of motion will be reduced to apply only to the case of gas-particle flows. In a typical gas-particle flow, the ratio of the density of the fluid to the density of the particles, ρ_f/ρ_p, is on the order of 0.001. Based on density ratio alone, one would expect the pressure gradient term and the added mass terms to be small in Eq. (1A). The Basset term and the initial velocity effect (the second term in the brackets) vary as ρ^f/ρ^p and are small except for very small times after the beginning of the motion. Therefore, the motion of a heavy particle in a gas is governed by the effects of viscous drag and gravity (Vojir and Michaelides, 1994). In the original derivation, the viscous drag was limited to Stokes drag by conditions given in equation (3A) requiring the particle Reynolds number to be less than one. If only viscous drag and gravity affect the particle motion, then empirical relations can be used to account for the drag force on the particle, and we can write the equation of motion for a heavy particle in dimensional form as

$$\frac{dv_i}{dt} = \frac{[u_i(y(t), t) - v_i]f}{\tau_p} - g\delta_{i3}, \quad (4A)$$

where τ_p is the particle aerodynamic response time (assuming Stokes drag applies) and is given by

$$\tau_p = \frac{2\rho_p a_p^2}{9\mu}. \quad (5A)$$

The factor f is the ratio of the drag coefficient to the Stokes drag and is given by Clift et al. (Clift and Gauvin, 1970; Clift et al., 1978) as

$$f = 1 + 0.15\ \mathrm{Re}_p^{0.687}. \quad (6A)$$

The relations given above for the viscous drag on a particle will overpredict the drag if the particle size is comparable to the mean free path of the surrounding gas particles due to slip flow at the particle surface. In atmospheric air, this effect is not important until the particle is less than 1 μm in diameter (Cunningham, 1910).

The Maxey-Riley equation (1A) for the motion of a particle in an infinite fluid does not include the effect of molecules colliding with the particle (Brownian motion), the effect of a velocity gradient in a direction perpendicular to the particle motion, the effect of particle spin, or the effect of confining walls. Each of these effects can be important under a specific set of fluid and particle parameters, but they can often be neglected in a gas-particle flow.

This review covers particles that are large enough to have a significant free-fall velocity, which usually implies a diameter of 1 μm or larger. Since Brownian motion does not become significant for particles with a diameter of less than 1 μm, the forces due to molecular collisions can be neglected in most gas-solid flows. They are, however, often important in aerosol dynamics.

Particles can acquire a spin as a result of the collisions with walls, other particles, or from shear in the surrounding fluid. The spin created by particle-wall or particle-particle collisions can cause a particle to experience a lift force similar to that experienced by a spinning particle being injected into a stagnant fluid (Rubinow and Keller, 1961). This lift due to spin is often called the Magnus effect. However, it is usually impossible to compute or measure the spin on individual particles and, therefore, this term is usually not included in a calculation of a particle's trajectory.

A shear in the mean velocity field can exert a lift force on a particle, where lift means a force in the direction perpendicular to the relative velocity between the particle and the fluid. This effect is often called inertial migration because the lift or migration is caused by changes in the far field of the flow around the particle and must be accounted for by the inertia terms in the equation of motion for the disturbance flow. Saffman (1965, 1968) developed a relation for the lift force by using matched asymptotic expansions and matching the large distance behavior of the inner expansion to the small distance terms of the outer expansion, giving

$$F_L = -6.46\mu w a^2 \left(\frac{\alpha}{\nu}\right)^{1/2}, \quad (7A)$$

where α is the mean velocity shear and w is the velocity of the particle relative to the fluid. The shear is assumed to be perpendicular to the relative velocity of the particle and the lift force, F_L, is in the direction of the shear. The direction of the lift force is such that if the particle is moving faster than the fluid, the lift force will be in the direction of decreasing shear. In deriving equation (7A), four major assumptions were made:

Downloaded 03 Jun 2010 to 171.66.16.125. Redistribution subject to ASME license or copyright; see http://www.asme.org/terms/Terms_Use.cfm

$$\mathrm{Re}_\alpha = \frac{4a^2\alpha}{\nu} \ll 1, \quad \mathrm{Re}_w = \frac{2aw}{\nu} \ll 1,$$

$$\mathrm{Re}_\Omega = \frac{4a^2\Omega}{\nu} \ll 1 \quad \text{and} \quad \mathrm{Re}_\alpha^{1/2} \gg \mathrm{Re}_w, \qquad (8A)$$

where Ω is angular velocity of the particle and w is the relative velocity of the particle. McLaughlin (1991) removed the restriction between the shear Reynolds number, Re_α, and the slip velocity Reynolds number, Re_w. The equation for the lift force is still limited to laminar flow, linear shear with the motion of the particle parallel to the mean velocity, and $\mathrm{Re}_w > 1$. In general, the velocity of the particle and the fluid are not parallel and the Saffman equation only accounts for the component of the particle velocity that is parallel to the mean flow. The component of the particle velocity perpendicular to the mean velocity will also cause a lift force, and the other components will cause a change in the drag force (Harper and Chang, 1968; Hogg, 1994). Cherukat et al. (1994) experimentally measured particle drift in a laminar, uniform shear flow. They corrected their results for the effect of the wall and found, for $\mathrm{Re}_w > 1$, the Saffman equation for lift modified by McLaughlin (1991) to remove restriction, $\mathrm{Re}_\alpha^2 \gg \mathrm{Re}_w$, agreed to within experimental uncertainty with the measurements. Interestingly, for higher particle Reynolds numbers, the equations of Rubinow and Keller (1961), which only account for the lift due to particle spin, gave reasonable agreement with the experimental results. Dandy and Dwyer (1990) numerically determined the drag and lift for a fixed, nonrotating particle in a steady, laminar, linear shear for particle Reynolds numbers between 0.1 and 100. They found excellent agreement between the computed lift and that predicted by Saffman's equation for $\mathrm{Re}_p = 0.1$. They also found that the computational domain had to be extended to 25 particle radii before the calculated lift force was unaffected by the edge of the domain. This indicates that a linear shear has to extend about 25 particle radii beyond the particle before the Saffman equation can be used to predict the lift force.

In a turbulent shear flow, the fluid surrounding the particle does not in general have a shear equal to the mean shear, since the length scale of the local shear would be on the order of the Kolmogoroff scale. There is not sufficient evidence to suggest that a lift force calculated from Saffman's equation (8A) would be correct. Until experimental or DNS studies at high turbulence Reynolds numbers can be carried out, it seems more realistic not to include a lift force when calculating particle motion in a fully turbulent shear flow.

As a particle approaches a wall, the drag force on the particle will increase as a/y (Cox and Brenner, 1967), where y is the distance from the wall. The drag increase has the same functional dependence for particles moving parallel or perpendicular to the wall, but with a slightly different magnitude. This increase in drag becomes important when the distance to the wall is less than about 20 particle diameters, (Kallio, 1993). The presence of a wall will also influence the lift (McLaughlin, 1993). Kallio and Reeks (1989) numerically simulated particle deposition in pipe flow using the Monte-Carlo method incorporating both lift and the change in drag as the particle approached the wall. A summary of our present understanding of the forces acting on a particle as it nears a wall in a strongly sheared viscous flow is given by (McLaughlin, 1994). He points out the lack of rigor surrounding equations of motion for a particle in the near-wall region of a shear flow.

Although the equation of motion for a particle in a viscous flow with arbitrary velocity gradients has still not been worked out in general, the equation of motion for a solid particle in a gas flow is much simpler than the general case, since only viscous drag and lift due to shear need to be considered. If we consider a turbulent flow and exclude the region very near the wall, the lift forces would be small and it is unclear how to calculate them since the instantaneous shear surrounding the particle is not linear and, in most computations, is unknown. Therefore, we can use equation (4A) to calculate the trajectory of a particle in a turbulent flow field if we know the instantaneous fluid velocity along the particle trajectory.

Downloaded 03 Jun 2010 to 171.66.16.125. Redistribution subject to ASME license or copyright; see http://www.asme.org/terms/Terms_Use.cfm

The Effects of Turbulence and Unsteadiness on Vortex Shedding From Sharp-Edged Bluff Bodies

M. C. Wolochuk

M. W. Plesniak

J. E. Braun

School of Mechanical Engineering,
Purdue University,
West Lafayette, IN 47907

Motivated by a desire to evaluate vortex shedding flow meters for measuring velocity in unsteady turbulent flow applications, the objective of our work was to study the effects of flow disturbances on vortex shedding from sharp-edged bluff bodies. In particular, the combined effects of turbulence and unsteadiness were examined, as well as their separate effects using controlled wind tunnel tests. After causing an initial and sudden decrease in the Strouhal number, increasing turbulence intensity from 2.5 to 10 percent resulted in only a 2.4 percent increase in the Strouhal number, for turbulence with a length scale of 0.5 bluff body diameters. Turbulence integral length scale had a significant influence on the Strouhal number, with the greatest effect exhibited for length scales near 3 bluff body diameters. Turbulence of this length scale caused a 26 percent decrease in the Strouhal number, as compared to a low-turbulence base case. Fluctuating pressure amplitude and signal-to-noise ratio were also affected by turbulence, and decreased significantly when the integral length scale was increased from 0.25 to 0.75 bluff body diameters for a turbulence intensity of 10 percent. Unsteadiness caused lock-on for forcing at the Strouhal frequency, twice and four times the Strouhal frequency, while no lock-on was observed for forcing at half the Strouhal frequency. The range of lock-on increased with increasing perturbation amplitude and was asymmetric about the resonant frequency. For the cases investigated, the effects of combined turbulence and unsteadiness were additive, with the turbulence shifting the Strouhal frequency, and the unsteadiness causing lock-on about the shifted Strouhal frequency. The results of this study suggest that vortex shedding flow meters should be calibrated in turbulent flows and turbulence length scale must be controlled at the bluff body. Lock-on can be avoided by sizing the bluff body so that the shedding frequency is always much greater than any disturbance frequency in the flow.

I Introduction

The phenomenon of vortex shedding from bluff bodies has been studied since the pioneering work of Strouhal (1878) and Von Kármán (1912). When a bluff body is placed in a flow stream, vortices form behind it and shed alternately from each side. The nondimensional shedding frequency, the Strouhal number, is defined as:

$$\mathrm{St} = \frac{fD}{U} \tag{1}$$

where f is the vortex shedding frequency, D is the bluff body diameter, and U is the mean free-stream velocity. Over a wide range of Reynolds numbers, the Strouhal number is constant, implying a linear relationship between shedding frequency and mean velocity.

The idea of building a flow meter based on the assumption of a constant Strouhal number was first proposed by Roshko (1953, 1955), who studied vortex shedding from a circular cylinder in a Reynolds number range of $40 < \mathrm{Re} < 10{,}000$. For $\mathrm{Re} > 300$ (the "irregular" range), the Strouhal number remains at an almost constant value of 0.2, independent of Reynolds number. Roshko (1961) also showed that as Re is increased beyond a critical value of 2×10^5 for a circular cylinder, the Strouhal number increases rapidly. Gerrard (1966) proposed that the constant Strouhal number results from a balance between two length scales in the near-wake: shear layer thickness (diffusion length) and vortex formation length, i.e., the distance behind the bluff body at which entrained fluid first crosses the wake centerline. Bearman (1967) suggested that the lateral distance between vortex rows is an appropriate characteristic length scale.

Vortex shedding flow meters have been used in steady flows for over two decades and have proven themselves to be reliable and accurate. The benefits of this type of flow meter include high accuracy, linearity, wide dynamic range, and high reliability (no moving parts). However, in many potential applications, disturbances in the form of free stream turbulence and periodic unsteadiness may degrade meter performance by changing the Strouhal number, decreasing signal-to-noise ratio, or forcing the shed vortices to "lock-on" to the periodic disturbance frequency. Hot-wire measurements by Wolochuk et al. (1995) confirmed that both turbulence and periodic unsteadiness are present in the flow of air through ducts used in air conditioning (HVAC) systems. Turbulence intensities (Tu) of about 8 percent and periodic unsteadiness at frequencies less than 10 Hz were measured in a long straight section of duct, as well as downstream of a bend.

Motivated by the desire to use vortex shedding flow meters to monitor velocity in unsteady turbulent flow applications, the objective of our work was to study the individual and combined effects of these disturbances on vortex shedding from sharp-

Contributed by the Fluids Engineering Division for publication in the JOURNAL OF FLUIDS ENGINEERING. Manuscript received by the Fluids Engineering Division October 18, 1994; revised manuscript received June 6, 1995. Associate Technical Editor: M. Gharib.

Copyright © 1996 by ASME

Downloaded 03 Jun 2010 to 171.66.16.125. Redistribution subject to ASME license or copyright; see http://www.asme.org/terms/Terms_Use.cfm

edged bluff bodies. Previous studies concerning the effects of free stream turbulence and unsteadiness on vortex shedding from bluff bodies provide important background for the results presented in this paper and are discussed below.

Free stream turbulence has been reported to weaken vortex shedding and to alter shedding frequency. Malard et al. (1991) showed that for small-scale free stream turbulence (characterized by an integral length scale of $L_x/D \approx 0.25$), an increase in turbulence intensity (Tu) from 3.3 to 10.3 percent increased the Strouhal number for a trapezoidal cylinder by 2 percent. The authors found that an increase in turbulence intensity was accompanied by a decrease in the signal to noise ratio (SNR), due to an increase in background turbulence noise and a decrease in the vortex shedding signal.

Nakamura and Ohya (1984) found that two length scales are important in the interaction of free stream turbulence with vortex shedding from rectangular cylinders: the thickness of the separated shear layers (small-scale) and the size of the near-wake (large-scale). Small-scale turbulence tended to strengthen vortex shedding for shorter (i.e., in depth) cylinders, while it weakened shedding for longer cylinders. Large-scale turbulence weakened shedding for all cylinders and decreased the spanwise coherence of vortex formation. This effect was most pronounced for $L_x/D \approx 3$.

Norberg (1986) used hot-wire anemometry to determine the length scales present in the near-wake of a circular cylinder and found a strong coupling of shear layer thickness and formation length with vortex shedding frequency. He found that increasing turbulence intensity (from 0.1 to 1.3 percent) caused the formation length to decrease and the diffusion length to increase. The changes in these length scales were accompanied by an increase in the Strouhal number. The interaction of vortex shedding and free stream turbulence was shown to be dependent on complex feedback mechanisms in the near-wake.

The data of Malard et al. (1991) and Norberg (1986) exhibit a trend of a slightly increasing Strouhal number with turbulence intensity, with a more pronounced effect at higher Reynolds numbers. The sharp-edged bluff body studied by Malard et al. appears to be less sensitive to changes in Tu than the circular cylinder. However, since the ratio of turbulence length scale to bluff body diameter (L_x/D) ranges only from 0.2 to 0.3 in both studies, no conclusions can be drawn about length scale effects on the Strouhal number.

Periodic unsteadiness in the mean flow can cause the vortex shedding to lock-on to the perturbation frequency or its subharmonic. While the shedding is locked-on, the shedding frequency remains constant over a range of changing velocities. Various types of forcing mechanisms have been used to induce lock-on (see the review by Griffin and Hall, 1991). These include oscillating the bluff body either transverse-to or in-line with the flow, acoustic waves, and periodic velocity fluctuations imposed on the mean velocity field. Periodic unsteadiness is characterized by its frequency (f_p) and its amplitude (A). In this work, A is defined as the ratio of the streamwise rms periodic fluctuating velocity to the mean velocity.

Clements (1975) used a two-dimensional discrete vortex computer model to simulate vortex shedding from a blunt-based body in a flow with a sinusoidal velocity perturbation in the flow direction. It was shown that lock-on occurs for f_p near twice and four times the natural shedding frequency, f_{SO}. Furthermore, the range of f_p over which lock-on occurs increases as the perturbation amplitude is increased.

Blevins (1985) studied the effects of transverse sound waves on vortex shedding from a circular cylinder and found that it is the fluctuating velocity rather than pressure that causes lock-on. This result implies that velocity fluctuations, rather than pressure fluctuations, should be measured when studying lock-on. Blevins also observed that greater shifts in shedding frequency could be obtained when f_p was below f_{SO} than above it. Therefore, the range of frequencies over which shedding remains locked is not symmetric about f_{SO}. Finally, it was found that free stream turbulence tended to decrease the influence of acoustic forcing. This effect was attributed to the fact that the turbulence velocities were comparable to the sound-induced velocities.

Armstrong et al. (1986) studied lock-on for a circular cylinder, a D-section cylinder, and a flat plate in a Reynolds number range of $15{,}000 < \mathrm{Re} < 35{,}000$ for various disturbance amplitudes, with f_p near $2f_{SO}$. The velocity range of lock-on increased with increasing perturbation amplitude. The lock-on range for the circular cylinder was twice as great as that for the sharp-edged bluff bodies. It was also found that the lock-on range did not depend on whether the velocity had been successively increased or decreased. In addition, lock-on was achieved when the velocity was held constant and f_p was varied. Thus, lock-on can be induced by varying f_p or by varying U.

Barbi et al. (1986) measured vortex shedding from circular cylinders in perturbed flows in the range $3000 < \mathrm{Re} < 40{,}000$ and longitudinal velocity pulsation amplitudes ranging from 10 to 50 percent of the mean flow velocity. Holding the mean velocity constant and varying the perturbation frequency, lock-on occurred for f_p near f_{SO} and $2f_{SO}$; there was some evidence of lock-on for f_p near $4f_{SO}$. Transitions to and from lock-on were shown to be gradual, rather than sudden jumps.

Most recently, Hall and Griffin (1993) performed a direct numerical simulation of the incompressible Navier-Stokes equations to investigate vortex shedding from a circular cylinder in a flow with a sinusoidal velocity perturbation superimposed on the mean flow. They investigated the range of lock-on frequencies as a function of perturbation amplitude and showed that there is a transition range between lock-on and no lock-on, in which the dominant frequency in the flow is neither the natural

Nomenclature

A = unsteadiness amplitude of flow velocity
b = turbulence-generating grid bar diameter
D = bluff body width (diameter)
f = vortex shedding frequency
f_p = perturbation frequency
f_{SO} = natural (Strouhal) shedding frequency
H = test section height
L = length (span) of bluff body
L_x = turbulence streamwise integral length scale, approximated as $L_x = Ut^*$
M = turbulence-generating grid mesh size
P_g = static pressure (gage)
p' = fluctuating static pressure
R_{xx} = autocorrelation function, $R_{xx}(t) = \int_{-\infty}^{\infty} U(t)U(t+\tau)d\tau$
Re = Reynolds number
rms = root-mean-square
S_{xx} = power spectral density function
S.R. = grid solidity ratio
SNR = signal-to-noise ratio, Eq. (2)
St = Strouhal number, Eq. (1)
St_o = natural (undisturbed) Strouhal number
St_p = perturbation Strouhal number, Eq. (3)
t^* = zero crossing of the autocorrelation, $R_{xx}(t)$
Tu = streamwise turbulence intensity, $\mathrm{Tu} = u'/U$
U = mean flow velocity
u' = fluctuating streamwise velocity component
x = distance between turbulence grid and bluff body

Superscripts

$(\bar{\ })$ = mean value
$(\tilde{\ })$ = smoothed quantity

Downloaded 03 Jun 2010 to 171.66.16.125. Redistribution subject to ASME license or copyright; see http://www.asme.org/terms/Terms_Use.cfm

Table 1 Bluff body characteristics

Bluff #	Geometry	D (cm)	L/D	D/H
1		5.08	6.0	16.7%
2		2.54	12.0	8.33%
3		1.49	20.5	4.88%
4		0.325	93.8	1.07%

shedding frequency nor half the perturbation frequency. In this transition range, the dominant frequency is the sum of these two frequencies. They also found that the formation length increases (compared to unforced shedding) when lock-on occurs for $f_p < 2f_{SO}$, and decreases when $f_p > 2f_{SO}$. Their results agree quite well with previous experimental results, including those of Barbi et al. (1986), and the numerical results of Karniadakis and Triantafyllou (1989).

Most of the previous work, which was aimed at understanding the effects of flow disturbances on vortex shedding, has focused on circular cylinders. The effects of these disturbances on sharp-edged bluff bodies should be less significant since their separation points are fixed, whereas they move randomly on a circular cylinder. As a result, sharp-edged bluff bodies should be more suitable for measurements in unsteady and turbulent environments.

This paper presents the results obtained in controlled wind tunnel experiments in which turbulence and periodic unsteadiness were independently generated to determine their effects on vortex shedding from sharp-edged bluff bodies. The effect of varying both turbulence intensity and length scale on the Strouhal number is presented. For periodic approach flow, the range of lock-on is presented as a function of perturbation amplitude. In addition, results are presented from combined turbulence and unsteadiness experiments, an issue which has not been addressed in previous work. Finally, some implications of these results on the design and application of vortex shedding flow meters are discussed.

II Experimental Facility and Techniques

Experiments were performed in an open-circuit, low-speed wind tunnel described by Wolochuk (1994). Flow is conditioned upstream of the test section by a turbulence management section consisting of a bell-mouth inlet followed by a honeycomb flow straightener, four screens, and a 5:1, two-dimensional contraction section. The test section is 30 cm wide by 30 cm high by 91 cm long. Flow through the test section has a mean uniformity of ±2.4 percent and a free stream turbulence intensity of less than 0.7 percent over a velocity range of 2 to 30 m/s.

Four different bluff bodies were used in this study: three triangular-section bluff bodies (an equilateral triangle and two right triangles) and a square-section bluff body. The bluff bodies spanned the entire width of the test section (30.48 cm), with the tunnel walls terminating each bluff body. The geometric characteristics of the bluff bodies are presented in Table 1. The bluff body diameter is given by D, aspect ratio (length over width) by L/D, and tunnel blockage ratio (bluff body width over test section height) by D/H. All four bluff bodies were used in the turbulence experiments, but only bluff body #1 was used in the unsteadiness experiments.

Hot-wire anemometry was used to characterize the mean flow, as well as to measure velocity profiles and spectra in the wake for all four bluff bodies. A low-pass anti-aliasing filter conditioned the anemometer output signal, which was then acquired by a MacADIOS II A/D board on a Macintosh Quadra 900 personal computer. The digitized signal was analyzed using LabVIEW 2® data acquisition software. Typically, 2048 points were acquired for each realization at a sampling frequency of at least twice the maximum frequency of interest to meet the Nyquist criterion. The vortex shedding frequency was inferred from the dominant peak in the power spectral density of the streamwise fluctuating velocity signal. Bluff body #1 was instrumented with static pressure taps on its three sides, so shedding frequency could also be determined by analyzing the fluctuating pressure on this bluff body. The approach velocity was monitored with a pitot-static probe connected to a differential pressure transducer, the output of which was also acquired by the computer.

Turbulence was generated with square-mesh biplanar grids of circular-section bars, whose geometric characteristics are given in Table 2. The parameters in the table are grid mesh size (M, defined as the space between each bar), bar diameter (b), and solidity ratio (S.R.), which is defined as the ratio of the blocked area to the total cross-sectional area.

Turbulence intensity at the bluff body was varied by changing the distance of the grid relative to the bluff body (x), and integral length scale (L_x) was varied by using grids of different mesh sizes (M). By varying the combinations of the three grids and the four sharp-edged bluff bodies, the ratio of integral length scale to bluff body diameter, L_x/D, was varied from 0.25 to 11.7. Turbulence integral length scale was approximated as the mesh size of the particular turbulence-generating grid being used, and the approximation was confirmed with hot-wire measurements.

Periodic unsteadiness was produced by a set of 5 continuously rotating shutters downstream of the test section. As the shutters rotated, the variable blockage caused fluctuations in the static pressure, which in turn drove the velocity fluctuations, generating a near-sinusoidal velocity variation in the test section. The shutters were driven by a 1.5 hp dc motor that allowed continuous adjustment of the rotational speed to produce a longitudinal velocity perturbation between 10 and 180 Hz. An EMF feedback motor controller was used to keep the frequency constant to ±1 percent. Perturbation amplitude was varied by changing the amount of blockage (i.e., the shutter width). Four sets of shutters were used, producing maximum blockages of 51, 61, 71, and 82 percent; root-mean-square perturbation amplitude of the velocity, A, ranged from 1 to 16 percent. The amplitude of the fluctuation was dependent on perturbation frequency and increased linearly with mean flow speed.

III Experimental Results and Discussion

A. Low-Turbulence Base Case. In order to establish a reference for comparison, approach velocity and shedding frequency were measured for a low-turbulence base case for each bluff body over a velocity range of 2 to 25 m/s. Using air as the working fluid and the bluff body diameter range of 0.325 to 5.08 cm, the Reynolds number varied from $480 < \mathrm{Re} < 83{,}000$. A plot of Strouhal number versus Reynolds number for the four bluff bodies studied is shown in Fig. 1, along with the data of Igarashi (1985). For a given bluff body, the Strouhal number is fairly constant over the entire Reynolds number range tested. The constant values of the Strouhal number in this range

Table 2 Turbulence grid characteristics

Grid #	M (mm)	b (mm)	S.R.
1	12.7	3.175	0.527
2	25.4	6.35	0.498
3	38.1	9.525	0.510

Downloaded 03 Jun 2010 to 171.66.16.125. Redistribution subject to ASME license or copyright; see http://www.asme.org/terms/Terms_Use.cfm

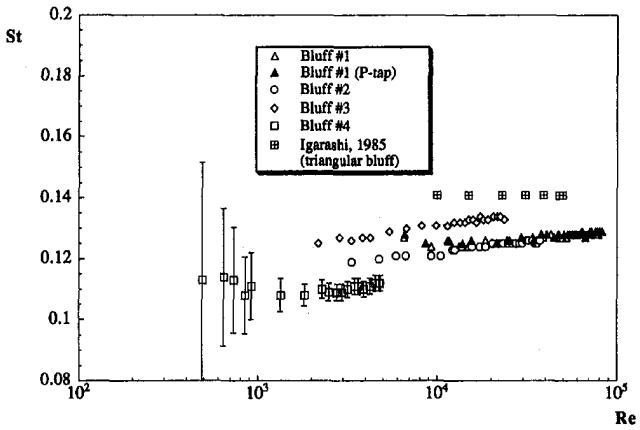


Fig. 1 Strouhal number versus Reynolds number for low-turbulence, base case

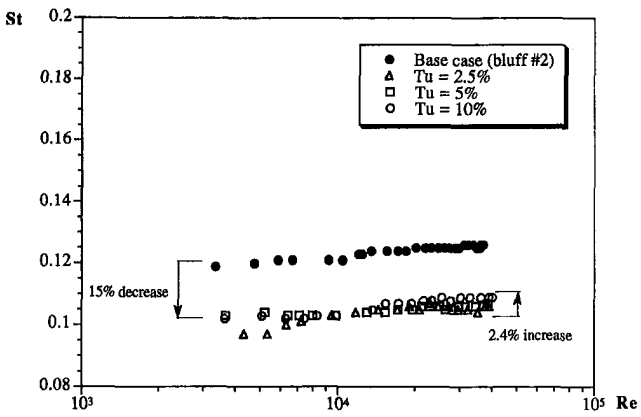


Fig. 3 The effect of turbulence intensity on Strouhal number

are 0.127, 0.124, 0.131, and 0.111 for bluff bodies #1–4, respectively. A Strouhal number value of 0.141 (in the range 12,000 $<$ Re $<$ 50,000) is quoted by Igarashi (1985) for a triangular bluff body with an aspect ratio of 5.0 and a wind tunnel blockage of 7.5 percent. The values of St quoted above for the triangular cylinders (0.124–0.131) are about 10 percent lower. This slight discrepancy may be due to differences in background turbulence, tunnel blockage, bluff body aspect ratio, and end conditions.

In Figure 1, the open symbols represent data in which shedding frequency was inferred from a hot-wire signal, while the filled symbols represent pressure tap data from bluff body #1. As expected, the pressure and velocity measurements yield nearly identical results. Figure 1 also shows error bars for data points associated with bluff body #4 to illustrate the trend of the experimental uncertainty (see Appendix A for an uncertainty analysis). The uncertainty in the Strouhal number results mainly from the uncertainty in the measured velocity. For U greater than 10 m/s, the uncertainty in the Strouhal number is less than 3 percent. At low velocities, the uncertainty in the pitot-static probe measurements is very large, leading to large errors in the Strouhal number. Most of the results presented in this study are for $U > 10$ m/s.

Figure 2 demonstrates the linear relationship between flow velocity and shedding frequency that is implied by a constant Strouhal number. For each bluff body, the least-squares correlation coefficient, R, is greater than 0.999, indicating a high degree of linearity. The greater uncertainty at low velocities is also illustrated in the results of Fig 2. For velocities greater than 10 m/s, the uncertainty in U for bluff body #4 is less than 2 percent (see Appendix A).

B. Freestream Turbulence Effects. The effect of elevated turbulence intensity on the Strouhal number is shown in Fig 3 for $L_x/D = 0.5$. After an initial drop of 15 percent in the Strouhal number at Tu of 2.5 percent, further increasing the turbulence intensity to 10 percent results in a slight (2.4 percent) increase in the Strouhal number. The trend of a slightly increasing Strouhal number with increasing turbulence intensity is consistent with the results of Malard et al. (1991). However, the large drop in St compared to a low-turbulence base case has not been reported previously. Since a grid-generated intensity of 2.5 percent was the lowest that could be achieved in the wind tunnel (due to the short test section, the maximum distance between the grid and the bluff body was about 27 M), it is not known whether St drops suddenly at some threshold value of Tu (lower than 2.5 percent), or if the decrease is continuous at very low intensities. Even though the background turbulence level, 0.7 percent, was lower than 2.5 percent, the length scale was not the same. Therefore, the threshold Tu for $L_x/D = 0.5$ may be lower than 0.7 percent. The trend in St with varying Tu in the low-turbulence range ($<$2.5%) remains to be investigated in future work.

The effect of varying the turbulence length scale (L_x/D) was examined by using various combinations of grids (to vary L_x) and bluff bodies (to vary D). Figure 4 illustrates how variation in turbulence integral length scale affects the Strouhal number. The trend is for the Strouhal number to decrease with increasing length scale for the range considered. For the conditions plotted in this figure, Tu was held constant at 10 percent, and L_x/D was varied from 0.25 to 1.5. For each length scale considered, the Strouhal number remains fairly constant over the range of Reynolds numbers tested. Thus, for the sharp-edged bluff bodies studied in this work, the Strouhal number is nearly independent

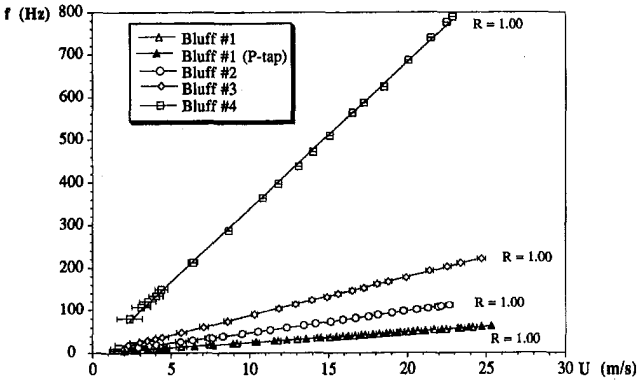


Fig. 2 Shedding frequency versus approach velocity for low-turbulence, base case

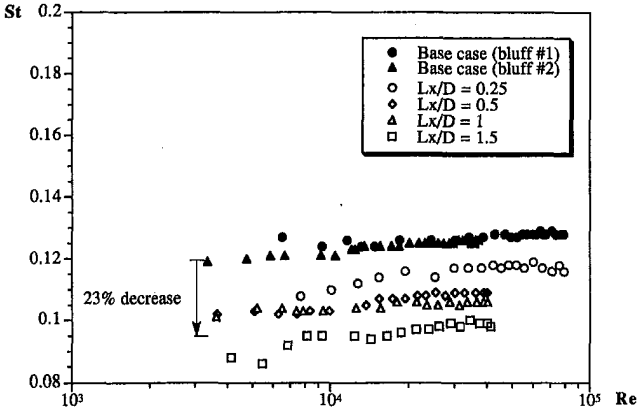


Fig. 4 The effect of turbulence length scale on Strouhal number

Downloaded 03 Jun 2010 to 171.66.16.125. Redistribution subject to ASME license or copyright; see http://www.asme.org/terms/Terms_Use.cfm

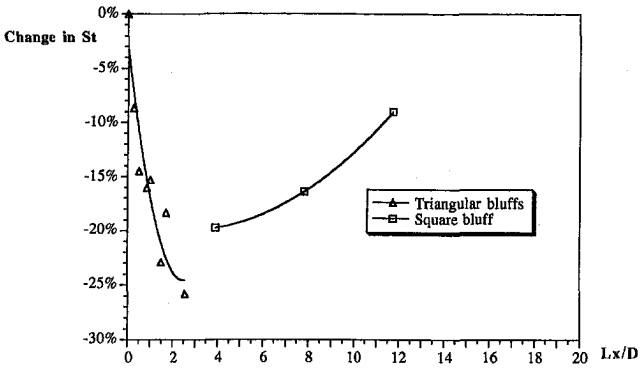


Fig. 5 Percent decrease in Strouhal number with turbulence length scale

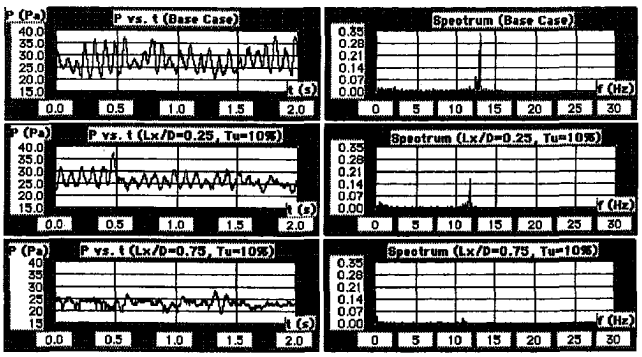


Fig. 6 Time traces and power spectra of fluctuating pressure signals (U = 5.1 m/s)

of Reynolds number (over the range tested), even for turbulent approach flow. This result differs from the results presented by Norberg (1986) for a circular cylinder, in which the Strouhal number increased with increasing Reynolds number for small-scale, moderate-intensity turbulence. The Reynolds number dependence of Norberg is most likely due to the randomly moving separation points on the circular cylinder.

Figure 5 shows the percent decrease in the Strouhal number (as compared to a low-turbulence base case) as a function of the length scale of the incoming turbulence (L_x/D). All four sharp-edged bluff bodies were used to generate this plot, so that a wide range of L_x/D could be covered. The square-section bluff body was used to obtain large values of L_x/D because of the difficulty in machining such a small triangular bluff body. It is assumed that the minor change in geometry does not significantly affect the trends. The base case for each bluff body is represented by the point (0,0) and Tu = 10 percent for all turbulence cases. For $L_x/D < 3$, the Strouhal number decreases with increasing length scale. Increasing L_x/D beyond 3 causes the Strouhal number to increase toward its undisturbed value. Nakamura and Ohya (1984) found that the relationship between mean base pressure and turbulence length scale exhibited the same trend, with a minimum base pressure occurring for $L_x/D \approx 3$.

The strong interaction of turbulence with vortex shedding at $L_x/D \approx 3$ may be due to the fact that this length scale is close to the natural length scales in the near-wake of the bluff body (e.g., formation length, diffusion length, wake width, vortex street wavelength). It is not surprising that the length scales of the incoming turbulence and the near-wake must be commensurate for the two to interact. Also, the turbulence most likely affects the spanwise structure of the shed vortices, since it is a three-dimensional disturbance. The specific mechanism of the interaction between large-scale turbulence and vortex shedding commands further study.

In addition to causing changes in the Strouhal number, free stream turbulence also affected the fluctuating pressure amplitude, p', and the signal-to-noise ratio, SNR, measured with a pressure tap on the back of bluff body #1. Fluctuating pressure amplitude is simply the standard deviation of a pressure-time signal. The signal-to-noise ratio was computed from the power spectrum of the signal and is defined herein as:

$$\text{SNR} \equiv 20 \log_{10} \frac{S_{xx}(f_{vsf})}{\bar{S}_{xx}(f)} \qquad (2)$$

where $S_{xx}(f_{vsf})$ is the amplitude of the spectrum (power spectral density) at the vortex shedding frequency (signal strength), and $\bar{S}_{xx}(f)$ is the mean amplitude at all other frequencies (noise).

Temporal fluctuations of base pressure were recorded from a transducer connected to a static pressure tap on the back of bluff body #1 and the time records were processed to obtain the power spectral density of the pressure signals. Figure 6 shows time traces and the corresponding power spectra (referenced with respect to atmospheric pressure) for the base case and two different turbulence length scales at turbulence intensities of 10 percent. Table 3 summaries the values of the SNR, mean base pressure, and fluctuating pressure amplitude for the three test cases.

For the base case, the time trace is highly periodic and the spectrum contains a large peak at the shedding frequency, giving a SNR of 48 dB. When grid generated turbulence is introduced with Tu = 10 percent and L_x/D = 0.25, there are noticeable reductions in both the fluctuating pressure amplitude and the spectral peak at the shedding frequency as compared with the base case. However, the periodic nature of the pressure fluctuations is still apparent and there is only a slight decrease in the SNR (from 48 to 46 dB). The effect of turbulence on the pressure measurements becomes much more pronounced when L_x/D is increased to 0.75 for the same turbulence intensity. In this case, there is a 64% decrease in the fluctuating pressure amplitude and a 9 dB decrease in the SNR as compared with the low-turbulence base case. In fact, the spectral peak at the shedding frequency is barely noticeable in Figure 6 for the larger length scale, L_x/D = 0.75, case. Table 3 further shows that the magnitude of the mean base pressure also decreases with increasing L_x/D.

The trend of a decreasing base pressure and SNR with increasing L_x/D is consistent with the results of Nakamura and Ohya (1984). Undoubtedly, turbulence with length scales that are close to the natural length scales in the near-wake of the bluff body has a stronger influence on the formation of vortices. These results are also consistent with the results of Fig 5, where values of L_x/D of about 3 appeared to have the largest effect on the Strouhal number.

Spanwise coherence of the vortex shedding is another indicator of signal quality. Nakamura and Ohya (1984) showed that a decrease in the spanwise coherence of vortex shedding was accompanied by a decrease in the SNR. High coherence ($\approx$100 percent) at the shedding frequency implies that single spanwise vortex filaments form along the bluff body, parallel to the bluff body axis. Low spanwise coherence could result from various three-dimensional effects such as oblique shedding or vortex splitting.

In this study, spanwise coherence at the shedding frequency was measured in the near-wake with two hot-wires separated

Table 3 Pressure tap signal parameters (U = 5.1 m/s)

L_x/D	Tu	$-P_g$ (Pa)	p' (Pa)	SNR (dB)
No grid	0.7%	27.8	3.9	48
0.25	10%	26.4	2.4	46
0.75	10%	23.3	1.4	39

Downloaded 03 Jun 2010 to 171.66.16.125. Redistribution subject to ASME license or copyright; see http://www.asme.org/terms/Terms_Use.cfm

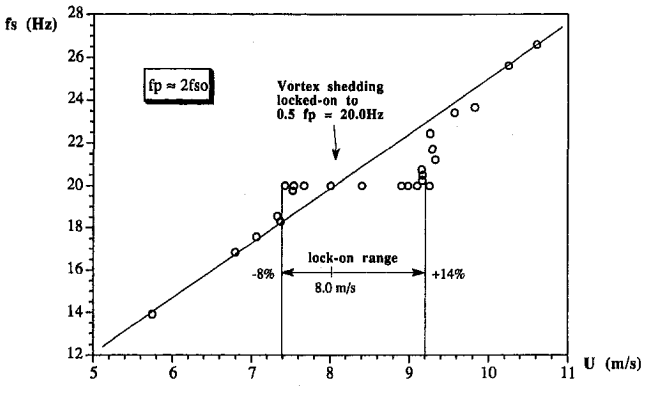


Fig. 7 Shedding frequency versus approach velocity in unsteady flow for forcing at twice the Strouhal frequency (f_p = 40 Hz, A = 5 percent)

along the span, Wolochuk (1994). A stationary hot-wire was positioned at the center-span of bluff body #3 just above the trailing edge and one bluff body diameter behind it, while a second hot-wire was traversed along the span. It was found that the coherence at the shedding frequency decreases with increasing spanwise separation distance between the two hot-wires for all cases. Elevated freestream turbulence results in a decrease of the spanwise coherence (at the shedding frequency) over the entire span of the bluff body, especially at large separation distances. The highest coherence (0.85 to 1.0) is found for the low turbulence base case, while the lowest coherence (as low as 0.6) is observed for the large scale turbulence case (L_x/D = 2.56). Generally, as L_x/D increases the coherence decreases, although the trend is not monotonic with turbulence length scale (L_x/D).

C. Periodic Unsteadiness. This section presents results of periodic unsteadiness tests performed in the absence of grid-generated turbulence. The effect of periodic unsteadiness on the frequency of vortex shedding is illustrated in Fig 7, where the lock-on phenomenon is clearly demonstrated. The freestream was oscillated at a frequency (f_p) of 40 Hz with shutters that produced an rms amplitude (A) of 5 percent of the mean velocity at the upper range of lock-on (9.2 m/s). For these conditions, vortex shedding locked-on to 20 Hz (half the perturbation frequency) over a mean velocity range of 7.4 to 9.2 m/s. Furthermore, the extent of the lock-on range is not symmetric about the forcing frequency. Greater shifts in shedding frequency occur when the forcing frequency is less than the natural frequency. Part of this shift may be due to the lower perturbation amplitudes that occur with lower mean velocities for a given set of shutters operating at a given forcing frequency.

In addition to lock-on, there is a transition range in which the forced shedding frequency is neither the natural shedding frequency nor half the perturbation frequency. This is most apparent for an approach velocity between 9.2 and 10.0 m/s. In this range, the shedding frequency rises gradually from the locked frequency (20 Hz) to the unforced value, f_{SO}. The presence of a transition range between lock-on and no lock-on is consistent with the findings of Barbi et al. (1986), Karniadakis and Triantafyllou (1989) and Hall and Griffin (1993).

The free stream was oscillated at a number of forcing frequencies in order to determine which harmonics and subharmonics of the Strouhal frequency would cause lock-on. A summary of results for these unsteadiness tests is given in Table 4. No lock-on was observed for forcing at half the Strouhal frequency ($f_p \approx 0.5 f_{SO}$), which is consistent with the findings of Malard et al. (1991). This result is significant in that it implies that lock-on will not occur for $f_p < f_{SO}$ (even at high disturbance amplitudes, A up to 16%), since lock-on in this frequency range would most likely have occurred for forcing at the first subharmonic of f_{SO}. In addition, lock-on did not occur at odd multiples of the natural frequency for the low disturbance amplitudes considered (other investigators have reported lock-on at these harmonics for large amplitude forcing). However, lock-on did occur at even multiples of the natural frequency for relatively low perturbation amplitudes.

Table 4 Lock-on results summary

fp/fso	A	Lock-on?
0.5	16%	no
1	3%	yes
2	1–16%	yes
3	4.5%	no
4	2.5%	yes
8	3%	no

The influence of perturbation amplitude on lock-on range is illustrated in Fig. 8 for forcing frequencies near twice the natural shedding frequency ($f_p \approx 2 f_{SO}$). The solid line represents the envelope over which lock-on occurs for a particular disturbance amplitude. The extent of the range of lock-on is shown on the horizontal axis as the ratio of the perturbation Strouhal number (St_p) to the undisturbed "natural" Strouhal number (St_o). Perturbation Strouhal number is defined as:

$$St_p \equiv \frac{f_p D}{U} \tag{3}$$

Using this notation, the lock-on range can be decomposed in terms of either velocity (f_p constant) or frequency (U constant).

Figure 8 shows that there is a minimum perturbation amplitude that is necessary to establish lock-on. As the disturbance amplitude is increased beyond this threshold, the range of frequencies over which vortex shedding is locked-on to the forcing frequency increases. The extent of the lock-on range is not symmetric about the forcing frequency. Even for constant perturbation amplitude, greater shifts in shedding frequency occur when the forcing frequency is less than the natural frequency. The shape of the forcing amplitude versus perturbation frequency ratio curve is typical of that reported by a number of investigators, e.g., the experimental work of Koopmann (1967), Blevins (1985) and Barbi et al. (1986) and the numerical work of Karniadakis and Triantafyllou (1989) and Hall and Griffin (1993). The results of a number of other studies are summarized in the review paper of Hall and Griffin (1991), where the shape of the lock-on boundary is further discussed. Karniadakis and Triantafyllou (1989) discuss the shape of the lock-on envelope (or state selection diagram) for a laminar wake, as well as that of the receptivity boundary of the wake to flow disturbances. The lock-in region with its characteristic asymmetric inverted triangular shape is known as a resonant horn or an Arnol'd

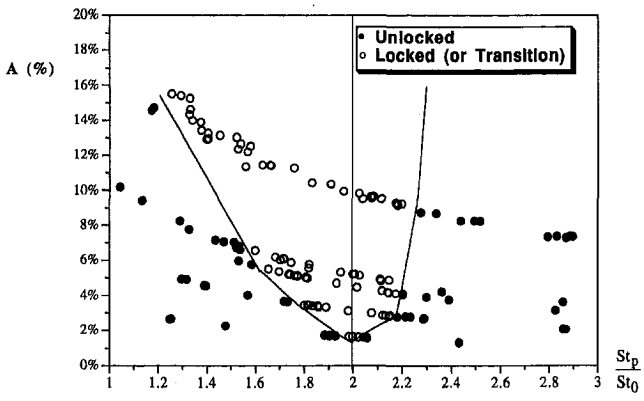


Fig. 8 Influence of perturbation amplitude on lock-on range

Downloaded 03 Jun 2010 to 171.66.16.125. Redistribution subject to ASME license or copyright; see http://www.asme.org/terms/Terms_Use.cfm

Table 5 Comparison of lock-on results with those of Armstrong et al. (1986)

	Bluff geometry	A	Lock-on range (St_p/St_o)
Armstrong et al. (1986)	○	1.2%	1.85–2.04
	▯	1.5%	1.93–2.04
	D	1.4%	1.94–2.02
Present investigation	▷	1.7%	1.96–2.03

tongue. In the region between the receptivity boundary (which extends beyond the lock-in boundary) and the lock-in boundary, the flow loses stability giving rise to quasi-periodic and chaotic states, which have also been observed experimentally by Olinger and Sreenivasan (1988).

In Table 5, the range of lock-on for the lowest amplitude disturbance (1.7 percent) is compared to the range calculated using the data of Armstrong et al. (1986). The range for the triangular bluff body used in this study agrees quite well with that for the sharp-edged bluff bodies used by Armstrong et al. Note that the extent of lock-on for the circular cylinder is roughly twice as great as for the sharp-edged bluff bodies.

D. Combined Turbulence and Periodic Unsteadiness. In order to examine the combined effects of turbulence and unsteadiness, the free stream was oscillated at a frequency near twice the Strouhal frequency ($f_p \approx 2f_{SO}$), and a turbulence grid was placed upstream of the bluff body. The unsteadiness conditions (f_p, A) were the same as for the case presented in Fig 7, while two different turbulence length scales and intensities were tested.

Figure 9 shows shedding frequency as a function of mean velocity for Tu of 10 percent and L_x/D of 0.75. These results demonstrate that the presence of free stream turbulence does not inhibit lock-on. However, the center of the lock-on range (i.e., the velocity corresponding to 20 Hz for unforced shedding) for this case was 9.0 m/s, compared to 8.0 m/s for the low-turbulence case. In addition, the extent of the lock-on range increases slightly. The increase in the lock-on range results from the shift to higher velocities, where the perturbation amplitude, A, is larger.

Table 6 summarizes the results of the combined turbulence and unsteadiness tests. The effects of unsteadiness and turbulence appear to be additive for the cases tested: turbulence shifts the Strouhal frequency and unsteadiness causes lock-on about

Table 6 Results from combined turbulence and unsteadiness tests

Figure	f_p (Hz)	A	L_x/D	Tu	U_{center} (m/s)	Lock-on range
7	40	5%	No Grid	0.7%	8.0	−8% to +14%
N/A	40	5%	0.25	5.4%	8.1	−6% to +14%
9	40	5%	0.75	10%	9.0	−9% to +20%

the shifted Strouhal frequency. When the results are normalized to remove the turbulence effect, the lock-on range is the same for all three cases.

The normalized lock-on range for each case is plotted in Fig. 10. The abscissa was normalized as in Fig. 8, except that now St_o is the value of the Strouhal number for the given turbulence condition without periodic forcing. The effect of turbulence on St is thereby removed from the results and the lock-on range is relatively constant for all three cases. The asymmetry of the range of lock-on about the disturbance frequency is somewhat exaggerated, due to an increase in A with decreasing St_p.

Conclusions

Turbulence at intensities up to 10 percent did not inhibit vortex shedding from sharp-edged bluff bodies, nor did it destroy the linear relationship between shedding frequency and mean velocity. Furthermore, it was found that the Strouhal number is fairly insensitive to changes in turbulence intensity in the range 2.5 percent ≤ Tu ≤ 10 percent (2.4 percent increase in St over the range) for a given turbulent length scale. However, a dramatic drop in St occurred for Tu between 0.7 percent (base case) and Tu = 2.5 percent. The magnitude of St is dependent upon the integral length scale of the turbulence. The greatest influence of turbulence on vortex shedding was found for $L_x/D \approx 3$. For turbulence intensities of 10 percent at this length scale, the Strouhal number was 26 percent lower than for a low-turbulence (0.7 percent) base case. Although the trend of a slightly increasing Strouhal number with increasing turbulence intensity is well known, the large change in St compared to a low-turbulence base case has not been previously reported.

Periodic unsteadiness was studied for the low turbulence base case and was found to cause lock-on for forcing at various harmonics of the Strouhal frequency ($f_p \approx f_{SO}$, $2f_{SO}$, $4f_{SO}$). However, for amplitudes up to 16 percent, no lock-on occurred for subharmonic forcing ($f_p \approx 0.5f_{SO}$), implying that lock-on does not occur for forcing frequencies in the range $f_p < f_{SO}$. For forcing at twice the Strouhal frequency ($f_p \approx 2f_{SO}$), the range of lock-on increased with increasing perturbation amplitude. The extent of the lock-on range was not symmetric about the resonant frequency. Greater shifts in shedding frequency occur when the forcing frequency is less than the natural frequency.

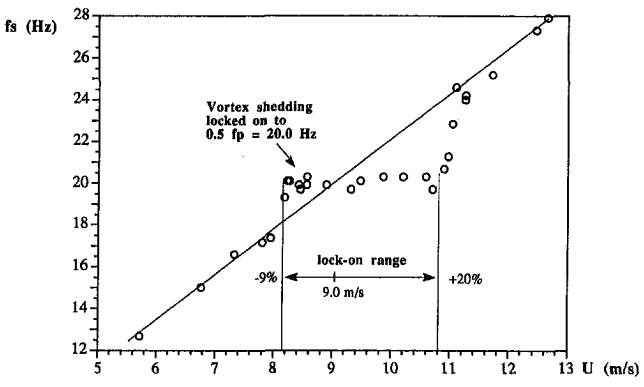


Fig. 9 Shedding frequency versus approach velocity for unsteady turbulent flow (Tu = 10 percent, L_x/D = 0.75, f_p = 40 Hz, A = 5 percent)

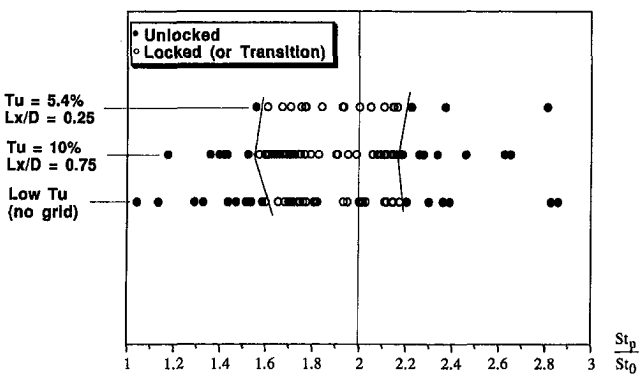


Fig. 10 Influence of turbulence on the lock-on range

Downloaded 03 Jun 2010 to 171.66.16.125. Redistribution subject to ASME license or copyright; see http://www.asme.org/terms/Terms_Use.cfm

The combined effects of turbulence and unsteadiness were found to be additive for the cases studied. For the range of parameters investigated, the turbulence caused a decrease in the Strouhal frequency, and the unsteadiness caused lock-on about this shifted Strouhal frequency.

The results of this study indicate that flow meters based on vortex shedding from sharp-edged bluff bodies can be used in unsteady turbulent flows, but care must be taken in their design and application. In particular, a meter should be calibrated in turbulent flows with turbulent length scales and intensities similar to those encountered in the application. The length scale could be controlled through the use of a shroud or mesh. Alternatively, the bluff body could be sized much smaller or larger than the length scale of the turbulence for the application. It does not appear necessary to control the turbulence intensity, if it is in the range of 2.5 to 10 percent. Lock-on could be avoided for a flow meter by sizing the bluff body so that all periodic disturbances in the flow are at frequencies less than half of the lowest natural shedding frequency for the velocity range of interest. This implies the use of a small bluff body, which is also appropriate for minimizing the effects of turbulence. Furthermore, turbulence was found to decrease the amplitude and signal-to-noise ratio (SNR) of a fluctuating pressure signal, compared to a low-turbulence base case (64% decrease in amplitude, 9 dB decrease in SNR). The greatest effects occur when the turbulence integral length scale is approximately the same size as the bluff body ($L_x/D \approx 3$).

References

Armstrong, B. J., Barnes, F. H., and Grant, I., 1986, "The Effect of a Perturbation on the Flow Over a Bluff Cylinder," *Physics of Fluids,* Vol. 29 (7), pp. 2095–2102.

Barbi, C., Favier, D. P., Maresca, C. A., and Telionis, D. P., 1986, "Vortex Shedding and Lock-On of a Circular Cylinder in Oscillatory Flow," *Journal of Fluid Mechanics,* Vol. 170, pp. 527–544.

Bearman, P. W., 1967, "On Vortex Street Wakes," *Journal of Fluid Mechanics,* Vol. 24 (4), pp. 625–641.

Blevins, R. D., 1985, "The Effect of Sound on Vortex Shedding from Cylinders," *Journal of Fluid Mechanics,* Vol. 161, pp. 217–237.

Clements, R. R., 1975, "On Vortex Shedding in a Flow with Perturbations Parallel to the Main Stream," *Journal of Sound and Vibration,* Vol. 40 (4), pp. 563–565.

Gerrard, J. H., 1966, "The Mechanics of the Formation Region of Vortices Behind Bluff Bodies," *Journal of Fluid Mechanics,* Vol. 25 (2), pp. 401–413.

Griffin, O. M., and Hall, M. S., 1991, "Review—Vortex Shedding Lock-On and Flow Control in Bluff Body Wakes," ASME JOURNAL OF FLUIDS ENGINEERING, Vol. 113, pp. 526–537.

Hall, M. S., and Griffin, O. M., 1993, "Vortex Shedding and Lock-On in a Perturbed Flow," ASME JOURNAL OF FLUIDS ENGINEERING, Vol. 115, pp. 283–291.

Igarashi, T., 1985, "Fluid Flow Around a Bluff Body Used for a Kármán Vortex Flowmeter," *Proceedings, Fluid Control and Measurement Conference,* Tokyo, pp. 1003–1008.

Karniadakis, G. E., and Triantafyllou, G. S., 1989, "Frequency Selection and Asymptotic States in Laminar Wakes," *Journal of Fluid Mechanics,* Vol. 199, pp. 441–469.

Kline, S. J., and McClintock, F. A., 1953, "Describing Uncertainty in Single-Sample Experiments," *Mechanical Engineering,* Vol. 73, pp. 3–8.

Koopmann, G. H., 1967, "The Vortex Wakes of Vibrating Cylinders at Low Reynolds Numbers," *Journal of Fluid Mechanics,* Vol. 28 (3), pp. 501–512.

Malard, L., Wisnoe, W., Strzelecki, A., Gajan, P., and Hebrard, P., 1991, "Air Visualizations and Flow Measurements Applied to the Study of a Vortex Flowmeter: Influence of Grid Turbulence and Acoustical Effects," *Proceedings, Flucome '91,* ASME 1991, pp. 689–704.

Nakamura, Y., and Ohya, Y., 1984, "The Effects of Turbulence on the Mean Flow Past Two-Dimensional Rectangular Cylinders," *Journal of Fluid Mechanics,* Vol. 149, pp. 255–273.

Norberg, C., 1986, "Interaction Between Freestream Turbulence and Vortex Shedding for a Single Tube in Cross-Flow," *Journal of Wind Engineering and Industrial Aerodynamics,* Vol. 23, pp. 501–514.

Olinger, D. J., and Sreenivasan, K. R., 1988, "Nonlinear Dynamics of the Wake of an Oscillating Cylinder," *Physical Review Letters,* Vol. 60 (9), pp. 797–800.

Roshko, A., 1953, "On the Development of Turbulent Wakes from Vortex Streets," NACA Technical Note 2913, 77 pages.

Roshko, A., 1955, "On the Wake and Drag of Bluff Bodies," *Journal of Aeronautical Sciences,* Vol. 22, pp. 124–132.

Roshko, A., 1961, "Experiments on the Flow Past a Circular Cylinder at Very High Reynolds Number," *Journal of Fluid Mechanics,* Vol. 10, pp. 345–356.

Strouhal, V., 1878, "Über Eine Besondere Art Der Tonerregung," *Ann. Phys. und Chemie, Neue Folge, Bd. 5,* Heft 10, pp. 216–251.

Von Kármán, Th., and Rubach, H., 1912, "Über Den Mechanismus Des Flussigkeits und Luftwiderstandes," *Phys. Zeitschr.,* Bd. 13, Heft 2, pp. 49–59.

Wolochuk, M. C., 1994, "Evaluation of Vortex Shedding Flow Meters for HVAC Applications," M.S. thesis, Purdue University.

Wolochuk, M. C., Braun, J. E., and Plesniak, M. W., 1995, "Evaluation of Vortex Shedding Flow Meters for Monitoring Air Flows in HVAC Applications," *ASHRAE International Journal of Heating, Ventilating, Air-Conditioning and Refrigerating Research,* Vol. 1, No 4, pp. 282–307.

APPENDIX A

Uncertainty Analysis

Using the methods of Kline and McClintock (1953), the relative uncertainty in estimating the Strouhal number depends on the relative uncertainties in the measurements of velocity, bluff body diameter, and shedding frequency according to:

$$u_{St} = [u_U^2 + u_D^2 + u_f^2]^{1/2} \qquad (A.1)$$

Velocities were computed from pitot-static probe measurements using Bernoulli's equation. For the equipment used in this study, Wolochuk (1994) showed that the relative uncertainty in velocity can be estimated as:

$$u_U = \frac{1}{2}\left[\frac{\left(\frac{2}{\rho} \times 0.0025 \times (\Delta P_{max} + c)\right)^2}{U^4} + u_\rho^2\right]^{1/2} \qquad (A.2)$$

At high flow speeds, the second term in Equation A.2 dominates, and the uncertainty in the measured velocity asymptotically approaches the uncertainty in the air density. As U approaches zero, the first term dominates, resulting in very high uncertainty at low velocities. Table A-1 gives values of the constants associated with the conditions of this study used to estimate the relative uncertainties in the velocity and the Strouhal number. The relative uncertainty in velocity is less than 2 percent for $U > 10$ m/s, but increases dramatically for lower velocities. According to Eq. (A.1), the uncertainty in velocity dominates the uncertainty in the Strouhal number at low velocities, since u_D and u_f are both less than 2 percent. The relative uncertainty in Strouhal number is less than 3 percent for $U > 10$ m/s and is acceptable, since most of the studies were conducted in the range where $U > 10$ m/s.

Table A-1 Data used to calculate uncertainties

Symbol	Definition	Value
ΔP_{max}	Diaphragm maximum pressure	860 Pa
ρ	Air density (22 C)	1.18 kg/m^3
u_ρ	Uncertainty in air density	± 0.02
c	Transducer calibration constant	0.054 Pa
N	Number of samples per realization	2048
U	Velocity measured by pitot probe	2–30 m/s
∂_V	Error in voltage = $\pm 0.25\% E_{max}$	±0.037 volts
u_D	Uncertainty in bluff diameter	± 0.02
u_f	Uncertainty in vortex shedding frequency	<0.005
u_U	Uncertainty in U	$= f(U, \Delta P_{max}, u_\rho, c)$
u_{St}	Uncertainty in St	$= f(u_U, u_D, u_\rho)$

Downloaded 03 Jun 2010 to 171.66.16.125. Redistribution subject to ASME license or copyright; see http://www.asme.org/terms/Terms_Use.cfm

Experiments on Turbulence Management Using Screens and Honeycombs

Cesar Farell

Sadek Youssef

St. Anthony Falls Laboratory,
Department of Civil Engineering,
University of Minnesota
Minneapolis, MN 55414

The results of some experiments on turbulence management using combinations of honeycombs of different lengths and coarse and fine screens, carried out in highly nonuniform and turbulent flows generated in a 127-mm plexiglas pipe by an upstream fan, are presented. The performance of the devices as single manipulators and in combination is evaluated through hot-wire measurements of the mean and rms values of the longitudinal velocities over the pipe cross section. The results show that relatively short honeycombs, preceded by a coarse screen and followed by one or more fine screens, can be used for effective management of such flows.

Introduction

Traditionally, screens have been widely used to remove or create flow nonuniformities, and to control turbulence scale and intensity. Because fine wire screens are not effective in removing swirl or large scale eddy motions, and because of "singing" problems in water tunnel applications, honeycombs alone or combinations of screens and honeycombs have also been used extensively as turbulence control devices. Two important uses of these turbulence management systems are in wind and water tunnel circuits and as conditioning devices in flow metering applications.

In the present work the results of some experiments on turbulence management using combinations of coarse and fine screens and honeycombs of different lengths are presented. The investigation was carried out in highly nonuniform and turbulent flows generated in a 127-mm plexiglas pipe by an upstream fan and diffuser.

Literature Review

Honeycombs. While reducing the turbulence level of the incoming flow, a honeycomb creates also additional turbulence of its own. Analyses have been developed (Lumley, 1964; Lumley and McMahon, 1967; Robbins, 1978) for prediction of these effects under the assumption of fully-developed flow in the honeycomb cells. Because the small cell size and large length-to-diameter ratio necessary to achieve fully developed laminar flow are usually prohibitive in practice, Lumley's analysis developed conditions to achieve fully developed turbulent cell flow. At Re near turbulence transition in the cells, incidentally, higher levels of turbulence and mean velocity nonuniformity may result as a consequence of transition occurring nonuniformly across the honeycomb (Robbins 1978).

The experiments of Loehrke and Nagib (1972, 1976), on the other hand, were carried out with laminar honeycomb cell flow ($\mathrm{Re}_d = 1{,}203$), not necessarily fully developed. Under these conditions, the thwarting of the transverse velocity components by the cell walls was found to be particularly effective. In fact, the results suggest that the major part of the suppression occurred within a short distance from the leading edge of the cells, and thus that much shorter cells than required to reach fully developed laminar flow can be used in design. A major finding of this work was the suppression effect that a fine mesh screen placed downstream from the honeycomb (recommended distance less than 5 cell sizes) had on the honeycomb wake shear layer instability responsible for downstream turbulence generation.

Screens. The flow through a screen can be characterized as subcritical or supercritical depending on the fluctuation levels immediately downstream from it. In the subcritical regime no eddies are shed by the screen and the levels are lower than those in the oncoming stream. For larger Re, in the supercritical regime, the levels are above those in the oncoming stream, but decrease rapidly with distance and reach values significantly below the original free-stream turbulence intensity. The critical Re depends on the screen solidity ratio (Schubauer et al., 1950). Tan-atichat et al. (1982) recommend that screens not be operated at subcritical Re because the performance of the screen is strongly dependent on the free-stream velocity. Subcritical screens introduce substantial pressure drops and are prone to clogging by small particles. While they have been used in wind tunnels with apparent success, the velocity dependence and pressure drop must obviously be kept in mind for design purposes. Near the critical Re, on the other hand, the screen damping characteristics can change abruptly with small changes in flow conditions, and this situation must be avoided.

Existing theories lump screen characteristics in experimental coefficients of pressure drop, K, and refraction, α. Available theories and data show only limited agreement, and consideration of the structure of the upstream flow and the mechanisms of turbulence generation and suppression by the screen may be necessary to improve the predictions (Loehrke and Nagib, 1972). Plots of the longitudinal (μ) and lateral (ν) turbulence energy reduction factors predicted by Taylor and Batchelor's (1949) theory are given in Corrsin (1963) and Batchelor (1967), assuming $\alpha = 1.1/\sqrt{(1 + K)}$ for $K > 0.7$ and $\alpha = (8 - K)/(8 + K)$ for $K < 0.7$ (Dryden and Schubauer, 1949). The data of Townsend (1951) are also shown. The theory predicts too great a degree of anisotropy downstream from the screen, but the total energy reduction given by $(\mu + 2\nu)$ appears to be predicted more accurately by it. Debatable assumptions of the theory are that the wake turbulence produced by the screen wires can be neglected and that the turbulence intensities are small.

As Corrsin observed, the factors μ and ν are approximately equal to the reduction factors for spatial variations in mean velocity if use is made of the noted empirical relations between α and K. Under these conditions, $\sqrt{\nu} = \alpha = 1.1/\sqrt{(1 + K)}$ for $K > 0.7$. Experimental agreement with the comparable expression $\sqrt{\nu} = 1/\sqrt{(1 + K)}$, originally proposed by Dryden and

Contributed by the Fluids Engineering Division for publication in the JOURNAL OF FLUIDS ENGINEERING. Manuscript received by the Fluids Engineering Division March 22, 1994; revised manuscript received May 1, 1995. Associate Technical Editor: W. S. Saric.

Copyright © 1996 by ASME

Downloaded 03 Jun 2010 to 171.66.16.125. Redistribution subject to ASME license or copyright; see http://www.asme.org/terms/Terms_Use.cfm

Schubauer (1947) for both longitudinal and lateral component turbulence reduction, has been reported by Scheiman and Brooks (1981). For longitudinal component reduction, however, these authors reported agreement with the expression $\sqrt{\mu} = 1/(1 + K)$, proposed originally by Prandtl (1933) as reduction factor for longitudinal spatial mean velocity variations. The total longitudinal and lateral turbulence reduction factors for screens in series were found to be fairly well predicted by the product of the factors $1/(1 + K)$ and $1/\sqrt{(1 + K)}$, respectively, for each screen.

Considerable reductions in turbulence intensities by combinations of up to five screens have been reported by Groth and Johannson (1988). For a three-screen combination a reduction of the initial 5.5 percent longitudinal turbulence intensity to 0.78 percent was observed 1 m downstream of the last screen (reduction factor $\approx$0.14). For a five-screen combination the reduction factor was approximately 0.083. These measured reductions were compared by the authors with the product of the factors $1/\sqrt{(1 + K)}$ for each screen, assuming the validity of Dryden and Schubauer's (1947) formulas for both longitudinal and lateral component turbulence reduction. For the five-screen combination, this prediction gave a reduction factor of 0.164, almost double the measured value. A better prediction can be obtained, however, if the different effects of a screen on lateral and axial turbulence are taken into account, as discussed later.

Honeycomb-Screen Combinations. Measurements of the turbulence characteristics behind combinations of screens and honeycombs have been carried out by Scheiman and Brooks (1981). The length-to-diameter ratio of the honeycombs was chosen as 6 or 8 on the basis of the laminar cell flow results of Loehrke and Nagib cited earlier. But the cell Re of these experiments are in the transition range or higher and, furthermore, the first screen behind the honeycomb was placed so that the honeycomb turbulence was almost completely decayed before encountering it. These data are then essentially different from Loehrke and Nagib's. In general, the turbulence reduction of a screen when placed downstream of a honeycomb was found to be better than that for the screen alone. There appear to be some inconsistencies in the data, however, which require elucidation for comparison with other results.

Results of an exploratory examination of the mechanism of turbulence generation by a honeycomb and a fine screen have been reported by Xia et al. (1990). Velocity fluctuation spectra measured downstream of the honeycomb disclosed the presence of organized flow structures, which persisted for some distance and were particularly well defined for the smaller Re tested. No organized motion was observed for $\mathrm{Re}_d > 3{,}900$. For $\mathrm{Re}_d < 3{,}900$, installation of the screen immediately downstream of the honeycomb was effective in thwarting the instability growth responsible for the organized motion, in agreement with the findings of Loehrke and Nagib (1972) cited earlier.

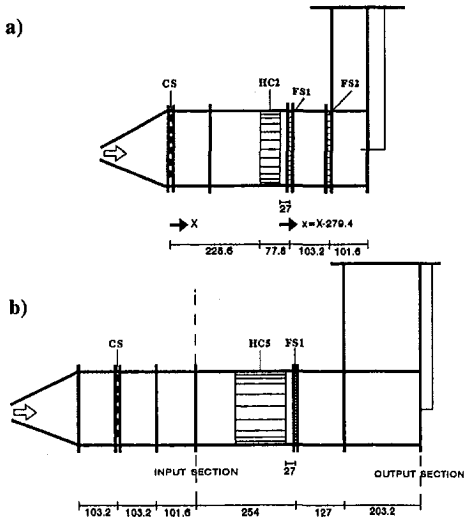


Fig. 1 General arrangement of screens and honeycombs (dimensions in mm)

Instrumentation and Experimental Procedure

A plexiglas pipe ($D = 127$ mm) was used to study the effect of honeycombs and screens on the flow produced by an upstream fan, connected to the pipe by a 66-cm long diffuser with an included angle of 5 degrees. Three honeycombs made of plastic straws ($d = 5.95$ mm, $\beta = 0.88$) were used: HC2 ($l = 50.8$ mm, $K = 0.90$), HC5 ($l = 127$ mm, $K = 1.85$), and HC10 ($l = 254$ mm, $K = 2.9$). The honeycomb pressure drop coefficients were estimated at $\mathrm{Re}_D = 51{,}300$ ($U = 6.1$ m/s, $\mathrm{Re}_{\mathrm{cell}} = 2{,}730$) on the basis of limited measurements carried out with nonuniform approach flows and may be in error by ± 15 percent (the value of K and the accuracy of the experimental determination of U depend strongly on the characteristics of the approach flow). A coarse screen (CS: $M = 8.47$ mm, $d_w = 2.03$ mm, $\beta = 0.578$) and two fine screens (FS1: $M = 1.588$ mm, $d_w = 0.254$ mm, $\beta = 0.706$; and FS2: $M = 1.27$ mm, $d_w = 0.229$ mm, $\beta = 0.672$) were used. When used, screen CS was installed always before the honeycomb. Estimated K values at $U = 6.1$ m/s were 0.95 (CS), 0.70 (FS1), and 0.85 (FS2). All screens operated in the supercritical regime.

The general arrangement of screens and honeycombs is shown in Fig. 1. When honeycomb HC10 was tested, the arrangement was the same as in Fig. 1(b) except that an extra section of pipe was added to accommodate the longer honeycomb. For the experiments without screen CS, the input and output sections of Fig. 1(b) were at the same positions, but the end of the diffuser was brought 206.4 mm closer. Longitudinal velocities were measured using a TSI 1054A hot-wire anemom-

Nomenclature

D = pipe internal diameter
d = honeycomb internal cell diameter
d_w = wire diameter
I = input section
K = pressure drop coefficient ($K = \Delta p/\frac{1}{2}\rho U^2$)
l = honeycomb length
M = mesh size of a screen
O = output section
Re = Reynolds number
R_e = estimated turbulence reduction factor
$\mathrm{Re}_{\mathrm{cell}} = 1/\beta(Ud/\nu)$
Re_D = pipe Reynolds number ($\mathrm{Re}_D = UD/\nu$)
$\mathrm{Re}_d = Ud/\nu$
R_m = measured turbulence reduction factor
U = average cross-sectional velocity
$\bar{u}$ = mean local velocity
u' = rms value of longitudinal velocity fluctuations
X = longitudinal distance from the coarse screen
x = longitudinal distance from the end of honeycomb
y = vertical distance
z = horizontal distance
α = refraction coefficient
β = open area ratio
μ = longitudinal turbulence energy reduction factor
ν = lateral turbulence energy reduction factor
ρ = density of air

Downloaded 03 Jun 2010 to 171.66.16.125. Redistribution subject to ASME license or copyright; see http://www.asme.org/terms/Terms_Use.cfm

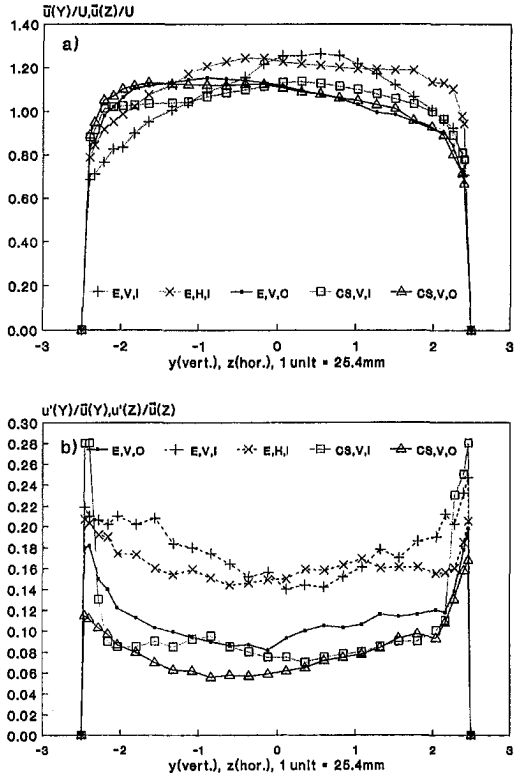


Fig. 2 (*a*) **Mean velocity and** (*b*) **velocity fluctuation profiles in empty pipe (E) and in pipe with coarse screen (CS). (H, horizontal traverse; V, vertical traverse; I, input section; O, output section).**

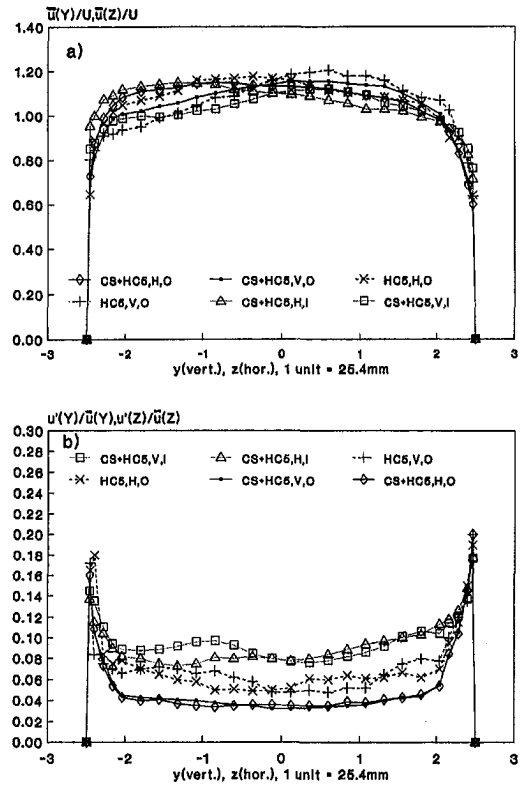


Fig. 3 (*a*) **Mean velocity and** (*b*) **velocity fluctuation profiles in pipe with *honeycomb HC5 and in pipe with coarse screen and honeycomb HC5* (CS + HC5). Other symbols as in Fig. 2.**

eter. Mean and rms values were obtained by means of digital multimeters. Other equipment included a manometer with a 0.025 mm resolution and a digital signal analyzer. For a more detailed description of the experimental setup reference is made to Farell and Youssef (1992) and Saxena (1989).

Presentation of Results

Representative mean velocity and turbulence intensity profiles are shown in Figs. 3 through 7. Additional results can be found in Farell and Youssef (1992) and Saxena (1989). The following notation has been used: E, empty pipe; W, combination CS + HC5 + FS1; W2, combination CS + HC2 + FS1 + FS2.

Experiments With Honeycombs HC5 and HC10. For the pipe without manipulators (see Fig. 2, E) the profiles were rather nonuniform and asymmetric. A longitudinal swirling motion appeared to be present. Comparison of input profiles measured in the empty pipe with and without manipulators showed differences in mean velocities and turbulence intensities of at most 5 and 10 percent, respectively, with smaller differences near the pipe centerline. Given the high turbulence levels, the strong cross-sectional nonuniformity of the flow, and the errors in hot-wire measurements under these conditions, it was concluded that the presence of the manipulators affected only slightly, if at all, the oncoming flow as produced by the blower.

Figure 2 presents also the vertical velocity distributions with screen CS installed. The comparable input profiles for the combination CS + HC5 are shown in Fig. 3. All E and CS profiles showed significant asymmetry. The CS results suggested again the presence of longitudinal swirl in the pipe, but the CS output horizontal profile was not available for additional evidence. The input turbulence intensities decreased markedly after installation of the screen. The change in output section intensities was less but still significant.

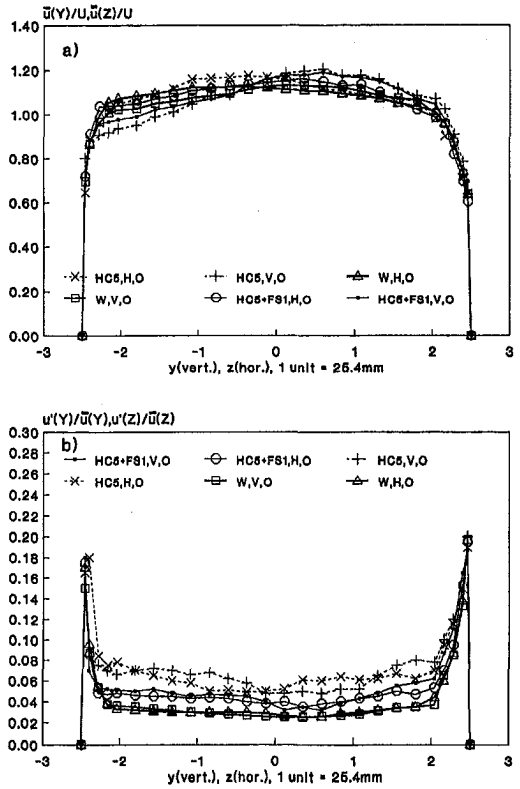


Fig. 4 (*a*) **Mean velocity and** (*b*) **velocity fluctuation profiles in pipe with honeycomb HC5, in pipe with HC5 and fine screen FS1 (HC5 + FS1), and in pipe with coarse screen, HC5 and FS1 (W). Other symbols as in Fig. 2.**

Downloaded 03 Jun 2010 to 171.66.16.125. Redistribution subject to ASME license or copyright; see http://www.asme.org/terms/Terms_Use.cfm

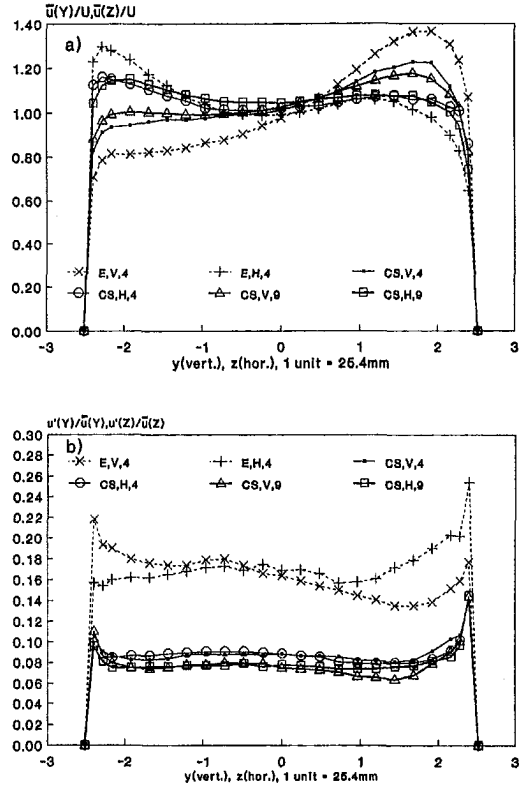


Fig. 5 (*a*) Mean velocity and (*b*) velocity fluctuation profiles in new facility in empty pipe (E) and in pipe with coarse screen (CS), at distances $X = 4$ in. (101.6 mm) and $X = 9$ in (228.6 mm). Other symbols as in Fig. 2.

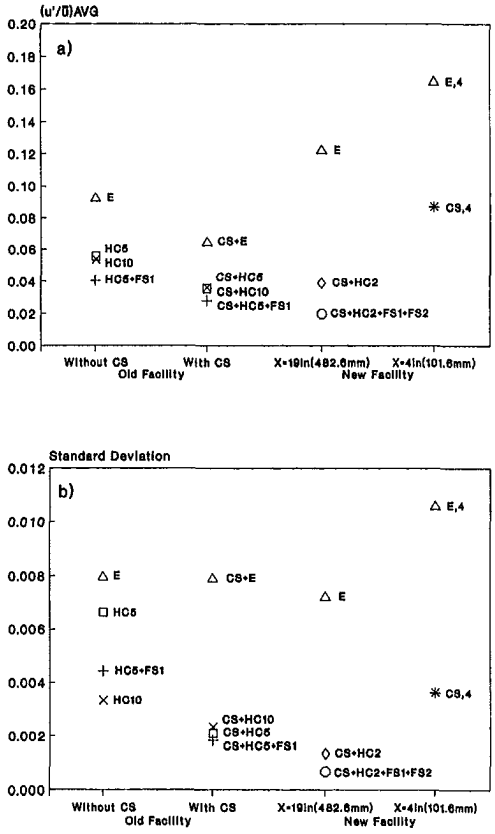


Fig. 7 (*a*) Average and (*b*) standard deviation of $u'/\bar{u}$ values over 55-mm-diameter center portion of the pipe.

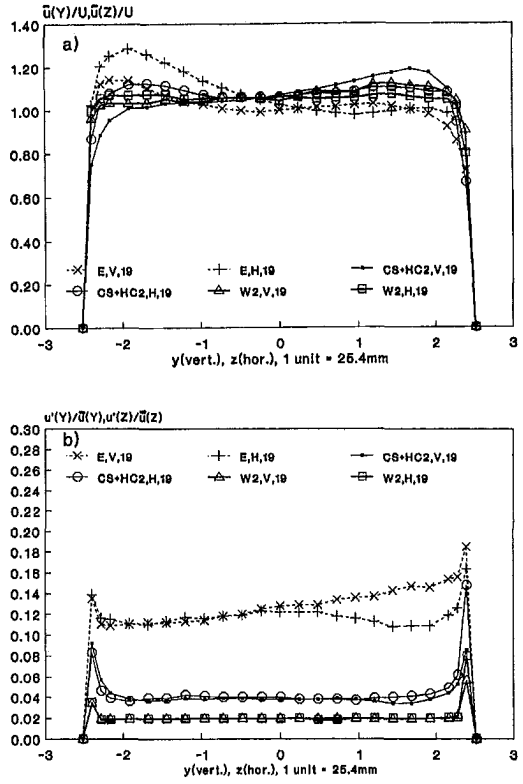


Fig. 6 (*a*) Mean velocity and (*b*) velocity fluctuation profiles in new facility in empty pipe (E), in pipe with coarse screen and honeycomb HC2 (CS + HC2), and in pipe with CS, HC2, and screens FS1 and FS2 (W2), at distance $X = 19$ in (482.6 mm). Other symbols as in Fig. 2.

The performance of honeycomb HC5 as a single manipulator is depicted in Fig. 3. The profiles for honeycomb HC10 were not significantly different from the HC5 profiles and are not shown. Comparison of the E input profiles in Fig. 2 with the HC5 and HC10 output profiles suggested a reduction of the swirling motion in the pipe by the honeycombs, a conclusion supported by single point measurements at other longitudinal locations. On the other hand, the HC5 and HC10 profiles showed no significant improvement in uniformity over the empty pipe profiles: for example, the momentum defect in the vertical input profile (Fig. 2, $y < 0$) was still present in the HC5 and HC10 output profiles. The turbulence intensities were lower, however, and about the same for both honeycombs, with HC10 showing somewhat better uniformity.

The effect of adding screen CS on the performance of honeycomb HC5 is also shown in Fig. 3. The performance of the honeycomb was improved by the addition of the coarse screen. This was also true for honeycomb HC10, but there was no advantage in using the longer over the shorter honeycomb, and the remainder of the tests were carried out with HC5. The output profiles obtained with screen FS1 placed a distance 5d downstream from honeycomb HC5 are shown in Fig. 4, together with the corresponding profiles for HC5 alone. The effect of adding screen CS to HC5 and FS1 to form combination *W* is also shown in this figure. There was a distinct improvement in profile uniformity for this combination, and the turbulence intensities became significantly lower.

With individual loss coefficients of 1.85 for HC5, 0.95 for CS, and 0.70 for FS1, the overall loss coefficient of the *W* combination was $K = 3.50$. The output mean velocities at distances y, z less than 80 percent of the pipe radius were within 5 percent from their mean value, while the turbulence levels were between 2.5 percent (near the pipe centerline) and 3.5 percent. Under these conditions, it would be possible to achieve

Downloaded 03 Jun 2010 to 171.66.16.125. Redistribution subject to ASME license or copyright; see http://www.asme.org/terms/Terms_Use.cfm

further improvement in uniformity and reduction in turbulence levels through addition of more fine screens, at the expense of a larger pressure loss. Because comparison of the HC5 and HC10 results showed no advantage of using the longer honeycomb, it was decided instead to investigate the performance of the even shorter honeycomb HC2 ($1/d = 8.53$) which, with a lower $K = 0.95$, would allow the use of one additional screen for about the same overall K.

Experiments Using Honeycomb HC2. The centrifugal blower used to produce the flow had to be replaced when the facility was moved to another building, midway through the experiments with honeycomb HC2. Initial mean velocity profiles measured in the old facility at $X = 482.6$ mm for combination $W2$ (CS + HC2 + FS1 + FS2, overall $K = 3.40$) showed significant improvement in uniformity in comparison with the profiles for combination W (overall $K = 3.50$). The $W2$ mean velocities at distances y, z less than 80 percent of the pipe radius were within 1.5 percent from their mean value. Replacement of the blower changed the oncoming flow conditions. As illustrated by the representative profiles shown in Figs. 5 and 6 for the empty pipe flow, flow nonuniformity and asymmetry were much more pronounced in the new installation. The profiles shown, together with profiles measured at other cross sections up to $X = 889$ mm, suggested that a longitudinal swirling motion was present in the pipe without manipulators. Turbulence intensities near the pipe centerline varied from around 17 percent at $X = 101.6$ mm to 10 percent at $X = 889$ mm. The profiles with screen CS only in the pipe are also shown for reference in Fig. 5.

A comparison of the profiles produced at $X = 482.6$ mm by combinations CS + HC2 and W2 is shown in Fig. 6. The W2 mean velocities in this figure, at distances y, z less than 80 and 40 percent of the pipe radius are, respectively, within 3.8 and 2.1 percent from their mean value. The deviations are larger than those measured for the same combination in the old installation, but the nonuniformity and asymmetry of the empty pipe profiles were much more pronounced in the new facility.

Discussion

Mean Velocity Profiles. The large momentum defect present in the flow in the pipe without manipulators for $y < 0$ (Fig. 2) was still present in the output profiles for honeycombs HC5 (Fig. 3) and HC10, which produced only a slight improvement in flow uniformity. One can see in Fig. 3 that HC5 actually preserved to a considerable extent the shape of the $\bar{u}$ profiles. On the other hand, both honeycombs were effective as expected in reducing pipe swirl. The output profiles without manipulators showed the evolution of the pipe flow itself, the $\bar{u}$ profiles becoming less nonuniform and the turbulence intensities decreasing with distance downstream.

These results suggest that the energy losses in the honeycomb cells were not large enough to produce significant flow uniformization through redistribution of the oncoming flow. On the other hand, the channeling of the flow by the cells prevented the momentum exchange that would otherwise result from the dynamics of the energy containing eddies of the approach flow. The scale of these eddies, of the order of, say, the pipe radius, is the relevant length scale in the interaction of the turbulence with the mean flow. These large eddies are responsible for the relative decrease in $\bar{u}$ nonuniformity as the flow proceeds along the empty pipe, while the reduction in turbulence energy results from the generation of smaller eddy scales and subsequent dissipation of energy toward the small scale end of the spectrum.

Installation of screen CS in the pipe resulted in a modification of the eddy structure and a considerable reduction in flow nonuniformity and turbulence levels. The mesh size of screen CS was sufficiently large to enhance, via the large-scale eddy structure it produced, the interaction of the turbulence with the oncoming mean flow inhomogeneities. The choice of screen mesh size and diameter is critical to ensure the correct performance of a screen. In fact, a screen may be very inefficient in reducing mean flow nonuniformity and turbulence levels if the oncoming flow contains gross inhomogeneities and large scale turbulence and the screen dimensions are much smaller than the size of the oncoming flow features (Tan-atichat et al., 1982). On the other hand, screens are generally not effective in reducing large scale swirling, and indeed longitudinal swirl was still detected in the pipe with screen CS installed.

The preceding discussion suggests that in order to use a relatively short honeycomb to reduce large scale swirling motions and turbulence levels, it is best to install a coarse screen upstream from it so that the flow reaching the honeycomb cells is as uniform as possible. The $\bar{u}$ data for honeycomb HC5 (see Figs. 3 and 4) show the improvement in performance when CS was added to the system. The performance of CS + HC10 (results not shown) was very close to that of CS + HC5. For the shorter honeycomb HC2, under the rather nonuniform approach flow conditions in the new facility, there was only a small reduction on $\bar{u}$ nonuniformity due to the honeycomb itself, as illustrated by a comparison of the coarse screen profiles in Fig. 5 at $X = 228.6$ mm (the position of the honeycomb inlet) and profiles CS + HC2 in Fig. 6. On the other hand, the reduction in turbulence intensity due to honeycomb HC2 and the intervening length of pipe between these two positions was considerable, from about 7 to 4 percent.

Velocity Fluctuation Profiles. To summarize the velocity fluctuation data, the average and the standard deviation of the $u'/\bar{u}$ values measured within the 55-mm-diameter center portion of the pipe were calculated for each manipulator combination and are presented in Fig. 7, plotted along four vertical lines. The first and second lines contain the output section averages and standard deviations for the experiments in the old facility, without and with screen CS, with honeycombs HC5 or HC10 as one of the manipulators. The third and fourth lines contain the averages and standard deviations at $X = 482.6$ mm and 101.6 mm for the experiments in the new facility using honeycomb HC2.

Both with and without the upstream screen CS, the performance of honeycombs HC5 and HC10 was about the same. The turbulence intensity was reduced by a factor between 1.7 and 1.8 relative to the intensity at the same section without either honeycomb. Without the coarse screen, the cross section profiles were slightly more uniform and the reduction factor slightly larger for HC10 (see Fig. 7(b)). The results of Lumley and McMahon (1967) can be applied to honeycomb HC10, which had fully developed turbulent cell flow as defined in their Fig. 2. Assuming an integral length scale $L \approx 75$ mm for the incoming turbulence, we have $L/1 \approx 0.30$, and the rms turbulence reduction factor obtained from their Fig. 1 is $\sqrt{\eta} \approx 0.16$ ($\sqrt{\eta}$ varies between about 0.165 for $K = 2.2$ and 0.15 for $K = 2.9$). Adding the contributions from the residual turbulence and the turbulence generated by the honeycomb one gets $u'/\bar{u} \approx 0.03$ for HC10 alone (input section $u'/\bar{u} \approx 0.16$, see Fig. 2) and $u'/\bar{u} \approx 0.02$ for HC10 downstream of CS (input $u'/\bar{u} \approx 0.09$, see Fig. 3). The measured values (about the same as the values for HC5) are about 80 percent larger. One can conjecture that the rather nonuniform nature of the flow may be responsible for this difference, resulting perhaps in non-negligible turbulence production by the mean flow. Elucidation of these results requires however further investigation.

The results for the shorter HC2 showed a large decrease in turbulence intensity at $X = 482.6$ mm due to installation of CS + HC2 in the pipe, from $u'/\bar{u} \approx 0.12$ to $u'/\bar{u} \approx 0.04$. The empty pipe flow in the new installation contained gross inhomogeneities (still present to a considerable extent at $X = 482.6$ mm after installation of CS + HC2, see Fig. 6) and large scale turbulence and swirl. The addition of fine screens downstream of honeycomb HC2 served then not only to reduce further the

Downloaded 03 Jun 2010 to 171.66.16.125. Redistribution subject to ASME license or copyright; see http://www.asme.org/terms/Terms_Use.cfm

turbulence intensities but also, through improvement in the flow uniformity, to prevent the generation of additional turbulence through nonzero mean flow gradients.

For a comparison of screen performance with the existing theories and measurements reviewed briefly earlier, values of the turbulence energy reduction factors μ and ν were obtained by three methods: the expressions $\sqrt{\mu} = 1/(1 + K)$ and $\sqrt{\nu} = 1/\sqrt{(1 + K)}$ (Scheiman and Brooks, 1981), Taylor and Batchelor's (1949) theory, and the data of Townsend (1951). The reduction in total energy given by $(\mu + 2\nu)$ and the reduction factor $R = \sqrt{(\mu + 2\nu)/3}$ were then calculated. Inspite of the differences in the predicted individual values of μ and ν, the estimates for total energy reduction provided by the three methods were reasonably close. The estimates R_e were, respectively for the three methods: for CS, 0.66, 0.68, and 0.63 (average $R_e \approx 0.66 \pm 0.03$); for FS1, 0.71, 0.72, and 0.69 (average $R_e \approx 0.71 \pm 0.02$); and for FS2, 0.68, 0.70, and 0.66 (average $R_e \approx 0.68 \pm 0.02$). It should be noted that if this prediction method for total energy reduction is applied to the five-screen combination of Groth and Johannson (1988) (see literature review), one obtains $R_e = 0.097$ using the K values given in this reference and $R_e = 0.079$ using K values estimated from published data, to be compared with the measured value of 0.083. The R_e estimates for CS, FS1, and FS2 can be correlated with the measurements depicted in Fig. 7.

For screen CS, comparison of the intensity values with and without the screen at the input and output sections in the old installation gave a measured reduction factor R_m between 0.70 and 0.75. This estimate is subject to some error, firstly because it required interpolation, secondly because only vertical profiles were measured at the output section with CS installed, and both the $\bar{u}/U$ and $u'/\bar{u}$ distributions were rather nonuniform. In the new installation, the reduction factors at $X = 101.6$ mm and $X = 228.6$ mm, obtained by division of the intensity values with and without the screen, were about the same, approximately equal to 0.53. This large reduction is likely due to the rather disturbed nature of the approach flow and the direct effect that screen CS, placed at the exit section of the diffuser, had on the diffuser flow.

For screen FS1 (placed 27 mm downstream from HC5) the measured reduction factor, R_m, can be obtained by direct division of the results in Fig. 7, since these represent measurements at the same cross section with and without FS1. One gets $R_m = 0.79$ with screen CS in the system and $R_m = 0.73$ with screen CS removed. While the last value is close to the average estimate of 0.71, the reason for the smaller turbulence reduction in the case of the more uniform flow with screen CS in the pipe is not clear. For screens FS1 and FS2 together, finally, the measurements in the new installation give $R_m \approx 0.51$ at a cross section 76.2 mm (60 M) downstream of the position of FS2, about 6 percent larger than the product of the average estimates $(0.71)(0.68) \approx 0.48$. Multiplying, on the other hand, $R_m \approx 0.79$ for screen FS1 by the estimate 0.68 for FS2 yields about 0.54, somewhat larger than the measured $R_m \approx 0.51$. It is noted here also that measurements in the old facility appeared to show that the turbulence reduction due to both screens FS1 and FS2 was unchanged by a 127 mm downstream shift of both screens. This last result would imply that the separation between honeycomb and first screen is not critical in the case of turbulent honeycomb cell flow, contrary to the case of laminar cell flow (Loehrke and Nagib, 1976; also Xia et al., 1990).

Conclusions

The performance of combination W2 (the shorter honeycomb HC2 and screens CS, FS1, and FS2; total $K \approx 3.4$) may be satisfactory for many applications, in particular given the disturbed nature of the oncoming flow in the new facility. The $\bar{u}$ values measured in the old and new facilities over the central core of the pipe cross section, at distances y, z less than 80 percent of the pipe radius, were within 1.5 and 3.8 percent, respectively, from their means. The smallness of these deviations allows for further improvement in flow uniformity, if necessary, through addition of one or more fine screens, at the expense of an increase in K of about 0.75 per screen. Relative turbulence intensities were reduced from about 12 to 2 percent by this combination. Questions remain regarding optimum honeycomb length, screen sizes, and manipulator spacings, all likely dependent on the quality of the oncoming flow. The effect of approach flow characteristics on manipulator performance requires in particular further investigation.

Both with and without the upstream screen CS, the performance of honeycombs HC5 and HC10 as single manipulators was about equal. The large momentum defect present in the flow in the empty pipe was still present in the output profiles for both honeycombs, which produced only a slight improvement in flow uniformity. The honeycombs, on the other hand, were effective in reducing pipe swirl. The turbulence intensity was reduced by a factor between 1.7 and 1.8 relative to the intensity at the same section without either honeycomb. Application of Lumley and McMahon's (1967) theory to honeycomb HC10 resulted in much smaller turbulence intensities than the measured values.

Screen energy reduction factors estimated by existing theories and data showed some differences with the measured values, of the order of 10 percent, due likely to the dependence of a screen performance on approach flow conditions. The estimates reviewed can be used as a first approximation for screen selection. The results and analyses suggest that in order to use a relatively short honeycomb to reduce large scale swirling motions and turbulence levels, it is best to install an upstream coarse screen so that the flow reaching the honeycomb is as uniform as possible.

Acknowledgments

The study reported herein is part of work done in conjunction with the design and construction of the St. Anthony Falls Atmospheric Boundary Layer Wind Tunnel, supported partially by National Science Foundation under Grants NSF/ECE-8410532 and NSF/ECE-6613554, and by the State of Minnesota under a Stripper Well Oil Overcharge Grant.

References

Batchelor, G. K., 1967, *The Theory of Homogeneous Turbulence,* Cambridge University Press.

Corrsin, S., 1963, "Turbulence: Experimental Methods," *Handbuch der Physik,* Vol. 8, No. 2.

Dryden, H. I. and Schubauer, G. B., 1949, Appendix 2 in Taylor, G. I. and Batchelor, G. K.

Dryden, H. I. and Schubauer, G. B., 1947, "The Use of Damping Screens for the Reduction of Wind Tunnel Turbulence," *Journal of Aeronautical Sciences,* Vol. 14, pp. 221–228.

Farell, C., and Youssef, S., 1992, "Experiments on Turbulence Management Using Screens and Honeycombs," St. Anthony Falls Hydraulic Laboratory Project Report No. 338, University of Minnesota.

Groth, J., and Johansson, A., 1988, "Turbulence Reduction by Screens," *Journal of Fluids Mechanics,* Vol. 197, pp. 139–155.

Loehrke, R. I., and Nagib, H. M., 1972, "Experiments on Management of Free-Stream Turbulence," AGARD Report No. 598.

Loehrke, R. I., and Nagib, H. M., 1976, "Control of Free Stream Turbulence by Means of Honeycombs: A Balance Between Suppression and Generation," ASME JOURNAL OF FLUIDS ENGINEERING, Vol. 98, pp. 342–353.

Lumley, J. L., 1964, "Passage of a Turbulent Stream Through Honeycomb of Large Length-to-Diameter Ratio," ASME *Journal of Basic Engineering,* Vol. 86, pp. 218–220.

Lumley, J. L., and McMahon, J. F., 1967, "Reducing Water Tunnel Turbulence by Means of a Honeycomb," ASME *Journal of Basic Engineering,* Vol. 89, pp. 764–770.

Prandtl, L., 1933, "The Attainment of a Steady Air Stream in Wind Tunnels," NACA Technical Memo No. 726 (translation).

Robbins, Basil E., 1978, "Water Tunnel Turbulence Measurements Behind a Honeycomb," *Journal of Hydronautics,* Vol. 12, pp. 122–128.

Saxena, V., 1989, "Reduction of Turbulence in a 5-inch Conduit Using Honeycombs and Screens," M. S. thesis, University of Minnesota.

Downloaded 03 Jun 2010 to 171.66.16.125. Redistribution subject to ASME license or copyright; see http://www.asme.org/terms/Terms_Use.cfm

Scheiman, J., and Brooks, J. D., 1981, "Comparison of Experimental and Theoretical Turbulence Reduction from Screens, Honeycomb, and Honeycomb-Screen Combinations," *Journal of Aircraft,* Vol. 18, No. 8, pp. 638–643.

Schubauer, G. B., Spangenberg, W. G. and Klebanoff, P. S., 1950, "Aerodynamic Characteristics of Damping Screens," NACA TN 2001.

Tan-atichat, J., Nagib, H. M., and Loehrke, R. I., 1982, "Interaction of Free-Stream Turbulence with Screens and Grids: A Balance Between Turbulence Scales," *Journal of Fluid Mechanics,* Vol. 114, pp. 501–528.

Taylor, G. I., and Batchelor, G. K., 1949, "The Effect of Wire Gauze on Small Disturbances in a Uniform Stream," *Quarterly Journal of Mechanics and Applied Mathematics,* Vol. 2, pp. 1–29.

Townsend, A. A., 1951, "The Passage of Turbulence Through Wire Gauzes," *Quarterly Journal of Mechanics and Applied Mathematics,* Vol. 4, p. 308.

Xia, L., Farell, C., and Kavanagh, P., 1990, "Experimental Investigation of the Unsteady Flow Behind Screens and Honeycombs," *Proceedings, 36th International Instrumentation Symposium,* Instrument Society of America, pp. 367–376.

Downloaded 03 Jun 2010 to 171.66.16.125. Redistribution subject to ASME license or copyright; see http://www.asme.org/terms/Terms_Use.cfm

Wall Suction Effects on the Structure of Fully Developed Turbulent Pipe Flow

D. Sofialidis

P. Prinos

Hydraulics Laboratory,
Department of Civil Engineering,
Aristotle University of Thessaloniki,
Thessaloniki, Greece

The effects of wall suction on the structure of fully developed pipe flow are studied numerically by solving the Reynolds averaged Navier-Stokes equations. Linear and nonlinear k-ϵ or k-ω low-Re models of turbulence are used for "closing" the system of the governing equations. Computed results are compared satisfactorily against experimental measurements. Analytical results, based on boundary layer assumptions and the mixing length concept, provide a law of the wall for pipe flow under the influence of low suction rates. The analytical solution is found in satisfactory agreement with computed and experimental data for a suction rate of A = 0.46 percent. For the much higher rate of A = 2.53 percent the above assumptions are not valid and analytical velocities do not follow the computed and experimental profiles, especially in the near-wall region. Near-wall velocities, as well as the boundary shear stress, are increased with increasing suction rates. The excess wall shear stress, resulting from suction, is found to be 1.5 to 5.5 times the respective one with no suction. The turbulence levels are reduced with the presence of the wall suction. Computed results of the turbulent shear stress $\overline{uv}$ are in close agreement with experimental measurements. The distribution of the turbulent kinetic energy k is predicted better by the k-ω model of Wilcox (1993). Nonlinear models of the k-ϵ and k-ω type predict the reduction of the turbulence intensities u', v', w', and the correct levels of v' and w' but they underpredict the level of u'.

1 Introduction

The study of wall suction effects on the structure of turbulent pipe flow has both practical and theoretical interest. Turbulent pipe flow with mass withdrawal from the wall (i.e., suction) is encountered in a variety of engineering applications and it is well known that wall suction has a significant effect on mass, momentum and heat transfer rates. From a theoretical viewpoint, wall suction, even at low rates, affects considerably the near-wall mean velocities and causes an alteration of the logarithmic law of the wall. In addition, it increases the wall shear stress in the suction region and reduces the turbulence levels across the pipe radius.

Studies regarding the effects of wall suction on turbulent pipe flow are rather limited in comparison with those conducted in boundary layers under zero pressure gradient (Verollet et al., 1977; Antonia et al., 1988; Antonia and Fulachier, 1989; Fulachier et al., 1991, among others).

Weissberg and Berman (1955) studied experimentally the effect of uniform wall suction on the structure of fully developed pipe flow for suction rates A ($A = V_w/U_{bo}$, where V_w = suction velocity and U_{bo} = inlet bulk velocity) up to 2 percent. They found that the suction effect was to reduce the longitudinal turbulence intensity across the pipe radius.

Kinney and Sparrow (1970) developed a turbulent transport model, based on the mixing-length concept, to calculate the mean streamwise velocity profile, as well as heat and mass transfer rates, in turbulent pipe flow with wall suction rates up to $A = 2$ percent. Friction factor, pressure drop, heat and mass transfer coefficients were calculated for $A = 0$ percent to 2 percent and were found to be affected considerably even by very low suction rates. Merkine et al. (1971) used the same analytical method with the previous investigators but they applied a modified damping function. Their model yielded better results than those of Kinney and Sparrow (1970) especially when the pressure drop was compared with the experimental measurements of Weissberg and Berman (1955).

Aggarwal et al. (1972) applied uniform wall suction rates up to $A = 2$ percent to a fully developed turbulent pipe flow for a length of 10D (D is the pipe diameter). They measured pressure drop, mean velocity profiles, and turbulent intensities and found that the latter, normalized with the local mean velocity, decreased in the central part of the pipe for low suction rates but increased for higher suction rates. However, the absolute levels of turbulence intensities were found to decrease in both situations. Brosh and Winograd (1974) presented experimental results for suction rates up to $A = 0.4$ percent applied for various pipe lengths (up to 40D). They showed that a suction length more than 40D results in a decrease of turbulence levels as compared with those of pipe flow with no suction. They also suggested that mixing-length models may be inadequate to describe turbulent momentum transport in such flow conditions.

Also, suction effects on turbulence statistics in a heated pipe flow were studied by Elena (1984). Taylor's microscale, integral length scale, skewness and flatness factors were measured for $A = 0.3$ percent and the suction effect on such quantities was exploited to gain understanding of the turbulence generation near the wall.

To the authors' knowledge, the most complete experimental study reported in the literature was performed by Schildknecht et al. (1979). Suction rates up to $A = 2.53$ percent were induced into a fully developed turbulent pipe flow using a 2.7D long porous pipe. Detailed results of mean and turbulence characteristics along the suction region are given for a suction rate of $A = 0.46$ percent which are used in the present study for comparison purposes. Their results indicate that turbulent intensities are reduced by suction, as well as the maxima of the terms in the turbulent kinetic energy equation. Also, more uniform axial mean velocity distributions were measured, since due to suction the near-wall layers are accelerated and the core flow is decelerated by the increasing radial velocity component.

Contributed by the Fluids Engineering Division for publication in the JOURNAL OF FLUIDS ENGINEERING. Manuscript received by the Fluids Engineering Division November 15, 1994; revised manuscript received May 25, 1995. Associate Technical Editor: S. P. Vanka.

Copyright © 1996 by ASME

Downloaded 03 Jun 2010 to 171.66.16.125. Redistribution subject to ASME license or copyright; see http://www.asme.org/terms/Terms_Use.cfm

Numerical studies of the suction effects on turbulent pipe flow are rather scarce. To the authors' knowledge, the only study is that of So and Yoo (1987) who tested a low-Re stress model of turbulence as well as the low-Re k-ϵ model of Chien (1982). The latter model overpredicted the axial pressure drop and underestimated the mean velocity in the region away from the wall. Near-wall predictions of mean velocity were similar in both models; however, the former model did not predict the peak of turbulence intensity near the wall for all suction rates examined.

In the present work the wall suction effects on the fully developed turbulent pipe flow are studied numerically by solving the Reynolds-averaged Navier-Stokes equations in conjunction with k-ϵ and k-ω eddy-viscosity models (EVM) of turbulence of the low-Re type. Models of this kind are capable of describing all the flow features up to the wall which is necessary since conventional wall functions are known to be inappropriate for flow conditions with wall mass transfer.

The k-ϵ models used are those of Launder and Sharma (1974) and Craft et al. (1993) slightly modified according to Suga (1993), while the k-ω models employed are those of Wilcox (1993) and Sofialidis (1993). These models are assigned for brevity as LS, CLS, W93 and SOF, respectively. The CLS and SOF models differ from LS and W93 models in two aspects. First, they employ a nonlinear constitutive relation with strain and vorticity invariant dependency for the description of the Reynolds stresses. Second, in order to simulate the turbulence damping that occurs near solid boundaries they do not only use empirical damping functions, f_μ, but they also introduce damping caused by the strain rate of the flow.

The two nonlinear models (LS and W93) were selected as the most commonly used two-equation, low-Re EVM's of the k-ϵ and k-ω type respectively. The two non-linear models (CLS and SOF) can be considered to be the non-linear counterparts of the linear models and hence the comparison of the computed results enables to investigate potential advantages of the nonlinear over the conventional ones. Also, such a comparison indicates the differences between the k-ϵ and k-ω schemes.

Computational results are compared against detailed experimental measurements performed by Schildknecht et al. (1979). Also numerical and experimental results are compared with analytical solutions, based on the model of Kinney and Sparrow (1970) and the improved version of Merkine et al. (1971) and limitations and inadequacies of the analytical models are highlighted. The effects of wall suction on the mean and turbulence characteristics are examined at selected stations in the suction region where detailed experimental measurements are available for $A = 0.46$ percent. The comparison entails profiles of the mean velocity, turbulent shear stress, turbulent kinetic energy and turbulent intensities along the pipe radius. Attention is given to the distribution of the wall shear stress in the suction region and finally comparison of mean velocities is presented for a much higher suction rate of $A = 2.53$ percent.

2 Governing Equations and Theoretical Considerations

The equations governing the steady, incompressible, two-dimensional turbulent pipe flow are the Reynolds-averaged Navier-Stokes equations which can be written in cylindrical coordinates as follows:

continuity eq.

$$\frac{\partial}{\partial x}(rU) + \frac{\partial}{\partial r}(rV) = 0 \tag{1}$$

x-momentum eq.

$$\frac{\partial}{\partial x}(rU^2) + \frac{\partial}{\partial r}(rVU) = -r\frac{\partial P}{\partial x} + r\frac{\partial}{\partial x}\left[\nu\left(\frac{\partial U}{\partial x} + \frac{\partial U}{\partial x}\right) - \overline{u^2}\right] + \frac{\partial}{\partial r}\left\{r\left[\nu\left(\frac{\partial U}{\partial r} + \frac{\partial V}{\partial x}\right) - \overline{uv}\right]\right\} \tag{2}$$

r-momentum eq.

$$\frac{\partial}{\partial x}(rUV) + \frac{\partial}{\partial r}(rV^2) = -r\frac{\partial P}{\partial r} + r\frac{\partial}{\partial x}\left[\nu\left(\frac{\partial V}{\partial x} + \frac{\partial U}{\partial r}\right) - \overline{uv}\right] + \frac{\partial}{\partial r}\left\{r\left[\nu\left(\frac{\partial V}{\partial r} + \frac{\partial V}{\partial r}\right) - \overline{v^2}\right]\right\} - \frac{2\nu V}{r} - \overline{w^2} \tag{3}$$

where x, r = axial and radial co-ordinates, U, V = corresponding mean velocity components, P = mean pressure, ν = kinematic viscosity of the fluid and $\overline{u^2}$, $\overline{v^2}$, $\overline{w^2}$ and $\overline{uv}$ = Reynolds stresses.

Kinney and Sparrow (1970), applied boundary layer assumptions ($V \ll U$ and $\partial/\partial x \ll \partial/\partial y$) and postulated that locally self-similar U-velocity profiles (i.e., $U/U_b = f(r/R)$, where R = pipe radius) exist for uniform suction. They derived a nonlinear integrodifferential equation for the velocity using a mixing length distribution modified under the influence of suction. They solved the equation iteratively for suction rates up to 2 percent. Similarly, Merkine et al. (1971) used the same equation but with a slightly modified damping function in the mixing length relationship. The above methodology is expected to hold for low suction rates where the boundary layer assumptions are valid. In case that streamwise gradients are significant all the terms in the x-momentum equation should be included otherwise the method may lead to significant errors.

In the present study Eqs. (1) (2), and (3) are solved numerically with all terms included in the calculation without making any assumptions (elliptic problem). In addition the calculation of the turbulent shear stress is not based on the mixing-length concept; instead the eddy viscosity, ν_t, is estimated through the calculation of the turbulent kinetic energy, k, and a second variable that is related to its dissipation rate, ϵ. The models of turbulence employed use transport equations for k and $\tilde{\epsilon}$ or ω. Their exact formulation and their features are described in the next section.

3 Turbulence Models

3.1 The Eddy-Viscosity Concept; Linear and Nonlinear Formulations. In the present investigation, the turbulence models used for calculating the Reynolds stresses are of the "eddy viscosity" type and they employ two transport equations, one for the turbulent kinetic energy, k, and a second for a variable that is related to ϵ, the dissipation rate of k.

The description of the turbulent stresses is made through the eddy viscosity concept which links them with ν_t and the mean strain tensor, $S_{ij} \equiv (\partial U_i/\partial x_j + \partial U_j/\partial x_i)$:

$$\overline{u_i u_j} = -\nu_t S_{ij} + \tfrac{2}{3}\delta_{ij}k \tag{4}$$

Equation (4) is used in the linear models of this study; the LS k-ϵ model and the W93 k-ω model. The other two models, the CLS and SOF models, use the same relation with additional non-linear terms, namely quadratic and cubic terms of the strain,

Downloaded 03 Jun 2010 to 171.66.16.125. Redistribution subject to ASME license or copyright; see http://www.asme.org/terms/Terms_Use.cfm

Table 1 Constants of the nonlinear Reynolds stress expression

Model	c_I	c_{II}	c_{III}	c_{IV}	c_V	c_{VI}	c_{VII}
CLS	−0.1	0.1	0.26	$-10c_\mu$	0	$-5c_\mu$	$5c_\mu$
SOF	−0.08	0.08	0.18	−1.0	0	−0.1	0.1

S_{ij}, and vorticity, $\Omega_{ij} \equiv (\partial U_i/\partial x_j - \partial U_j/\partial x_i)$, tensors, as proposed by Craft et al. (1993).

$$\overline{u_i u_j} = -\nu_t S_{ij} + \frac{2}{3}\delta_{ij}k + c_I\nu_t\frac{k}{\epsilon}\left(S_{ik}S_{kj} - \frac{1}{3}S_{kl}S_{kl}\delta_{ij}\right) + c_{II}\nu_t\frac{k}{\epsilon}(\Omega_{ik}S_{kj} + \Omega_{jk}S_{ki}) + c_{III}\nu_t\frac{k}{\epsilon}\left(\Omega_{ik}\Omega_{jk} - \frac{1}{3}\Omega_{lk}\Omega_{lk}\delta_{ij}\right) + c_{IV}c_\mu\nu_t\frac{k^2}{\epsilon^2}\left(S_{ki}\Omega_{lj} + S_{kj}\Omega_{li}\frac{2}{3} - S_{km}\Omega_{lm}\delta_{ij}\right)S_{kl} + c_V c_\mu\nu_t\frac{k^2}{\epsilon^2}\left(S_{ik}S_{jl} - \frac{1}{3}S_{mk}S_{ml}\delta_{ij}\right)S_{kl} + c_{VI}c_\mu\nu_t\frac{k^2}{\epsilon^2}S_{ij}S_{kl}S_{kl} + c_{VII}c_\mu\nu_t\frac{k^2}{\epsilon^2}S_{ij}\Omega_{kl}\Omega_{kl} \quad (5)$$

In the case of the SOF k-ω model the ratio (k/ϵ), appearing in Eq. (5), is replaced by definition with $(1/\omega)$. The values of the constants of Eq. (5) are given in Table 1.

The eddy viscosity, appearing in Eqs. (4) and (5) is expressed as a function of k and $\tilde{\epsilon}$ (isotropic dissipation rate of k, $\tilde{\epsilon} \equiv \epsilon - 2\nu(\partial\sqrt{k}/\partial x_j)^2$) or ω for the k-ϵ and k-ω models, respectively:

$$\nu_t = c_\mu f_\mu \frac{k^2}{\tilde{\epsilon}} \quad \text{or} \quad \nu_t = c_\mu f_\mu \frac{k}{\omega} \quad (6)$$

where c_μ and f_μ = constants or functions. Conventional low-Re models use damping functions, $f\mu$, for the approximation of the near-wall turbulence damping which are related to a viscosity-dependent parameter, the local turbulent Reynolds number, R_t ($R_t \equiv k^2/(\nu\tilde{\epsilon})$ or $R_t \equiv k/(\nu\omega)$). Models of this type are the LS k-ϵ and W93 k-ω models used in the present investigation. On the other hand, the CLS and SOF models use strain and vorticity parameters, S and Ω, respectively, ($S \equiv (k/\epsilon)\sqrt{0.5S_{ij}S_{ij}} = (1/\omega)\sqrt{0.5S_{ij}S_{ij}}$, $\Omega \equiv (k/\epsilon)\sqrt{0.5\Omega_{ij}\Omega_{ij}} = (1/\omega)\sqrt{0.5\Omega_{ij}\Omega_{ij}}$), to simulate the turbulence damping, allowing c_μ to vary with S or Ω. Nevertheless, this is not sufficient to introduce the necessary damping effect and damping is supplemented by the use of damping functions, f_μ. The constants or functions c_μ and f_μ of the various models used are given in Table 2.

3.2 k and $\tilde{\epsilon}$ or ω Transport Equations. The modeled equation for the turbulent kinetic energy, k, obtains the following form, in cylindrical coordinates, for all four models employed in this study:

k-eq.

$$\frac{\partial}{\partial x}(rUk) + \frac{\partial}{\partial r}(rVk) = r\frac{\partial}{\partial x}\left[\left(\nu + \frac{\nu_t}{\sigma_k}\right)\frac{\partial k}{\partial x}\right] + \frac{\partial}{\partial r}\left[r\left(\nu + \frac{\nu_t}{\sigma_k}\right)\frac{\partial k}{\partial r}\right] + r(P_k - \epsilon) \quad (7)$$

where P_k = production of k due to shear, $P_k \equiv -\overline{u_i u_j}(\partial U_i/\partial x_j)$, and σ_k = model constant (=1.0 for both LS and CLS models, 2.0 for the W93 model and 1.2 for the SOF model). The production term, P_k, is evaluated through Eq. (4) or Eq. (5) depending on the choice of the model.

The second transport equation used is that of $\tilde{\epsilon}$, when the LS and CLS models are employed. ϵ and $\tilde{\epsilon}$ take quite different values near solid boundaries and tend to coincide away from them. An ω-equation is used in the models of W93 and SOF. From Eq. (6) it is evident that the relation between ϵ (and equivalently $\tilde{\epsilon}$) and ω is simply $\omega = \epsilon/k = \tilde{\epsilon}/k$. The corresponding equations are shown below:

$\tilde{\epsilon}$*eq.*

$$\frac{\partial}{\partial x}(rU\tilde{\epsilon}) + \frac{\partial}{\partial r}(rV\tilde{\epsilon}) = r\frac{\partial}{\partial x}\left[\left(\nu + \frac{\nu_t}{\sigma_\epsilon}\right)\frac{\partial\tilde{\epsilon}}{\partial x}\right] + \frac{\partial}{\partial r}\left[r\left(\nu + \frac{\nu_t}{\sigma_\epsilon}\right)\frac{\partial\tilde{\epsilon}}{\partial r}\right] + r\left(c_{\epsilon 1}\frac{\tilde{\epsilon}}{k}Pk - c_{\epsilon 2}f_\epsilon\frac{\tilde{\epsilon}^2}{k}\right) + E \quad (8)$$

Table 2 c_μ and f_μ constants/functions appearing in the eddy viscosity relation

Model	f_μ	c_μ
LS	$\exp[-3.4/(1 + R_t/50)^2]$	0.09
CLS	$1 - 0.9\exp[-(R_t/30)^2]$	$\frac{0.3}{1 + 0.35\,S'^{1.5}}\left\{1 - \exp\left[-\frac{0.36}{\exp[-0.75\,S']}\right]\right\}$
W93	$\frac{0.025 + (R_t/6.0)}{1.0 + (R_t/6.0)}$	$0.09\frac{(5.0/18.0) + (R_t/8.0)^4}{1.0 + (R_t/8.0)^4}$
SOF	$1 - 0.72\exp(-0.0056\,R_t)$	$0.09\left[\frac{3.89}{S'} - 0.089\right](1 - \exp[-0.3S' - 0.15\,S'^2])$

where $S' \equiv \max(S, \Omega)$

Downloaded 03 Jun 2010 to 171.66.16.125. Redistribution subject to ASME license or copyright; see http://www.asme.org/terms/Terms_Use.cfm

Table 3 Model constants/functions appearing in the appearing in the $\tilde{\epsilon}$ and ω transport equations

k-ϵ	f_e	E
LS	$1 - 0.3 \exp(-R_t^2)$	$2\nu\ \nu_t \left(\frac{\partial^2 U_i}{\partial x_k \partial x_l}\right)^2$
CLS	$1 - 0.3 \exp(-R_t^2)$	$2\nu\ \nu_t \left(\frac{\partial^2 U_i}{\partial x_k \partial x_l}\right)^2, R_t > 100$
		$0.0095\ S \frac{k^2}{\tilde{\epsilon}}\ \nu_t \left(\frac{\partial^2 U_i}{\partial x_k \partial x_l}\right)^2, R_t < 100$

k-ω	$c_{\omega 1}$	$c_{\omega 2}$
W93	$\frac{5}{9} \frac{0.1 + (R_t/2.7)}{1.0 + (R_t/2.7)} \frac{1}{f_\mu}$	3/40
SOF	$0.435 + 2.17\ [\exp(-0.3\ R_t)]$	$0.833 + 2.17\ [\exp(-R_t/3.0)]$

ω-*eq.*

$$\frac{\partial}{\partial x}(rU\omega) + \frac{\partial}{\partial r}(rV\omega) = r\frac{\partial}{\partial x}\left[\left(\nu + \frac{\nu_t}{\sigma_\omega}\right)\frac{\partial \omega}{\partial x}\right] + \frac{\partial}{\partial r}\left[r\left(\nu + \frac{\nu_t}{\sigma_\omega}\right)\frac{\partial \omega}{\partial r}\right] + r\left(c_{\omega 1}\frac{\omega}{k}P_k - c_{\omega 2}\omega^2\right) \quad (9)$$

where σ_ϵ, $c_{\epsilon 1}$, $c_{\epsilon 2}$ = constants of the LS and CLS models (=1.3, 1.44 and 1.92, for both models), σ_ω = constant of the k-ω models (=2.0 for the W93 model and 0.8 for the SOF model), $c_{\omega 1}$, $c_{\omega 2}$, f_ϵ and E = model functions given in Table 3.

4 Computational Aspects and Solution Procedure

4.1 Flow Geometry. The flow geometry used in the computations is shown in Fig. 1. Although at the domain inlet initial profiles for all the variables were inserted (taken from parabolic computations corresponding to the fully developed turbulent pipe flow) a significant upstream length was decided to be given to eliminate errors resulting from the interpolation of these profiles to the grid arrangement used in the elliptic solution. Finally, the length from the suction outlet to the domain outlet was proven long enough to allow fully developed state to be reached again (i.e., uniform streamwise pressure gradient across the pipe radius). This was necessary for convenient boundary conditions to be imposed at the domain outlet.

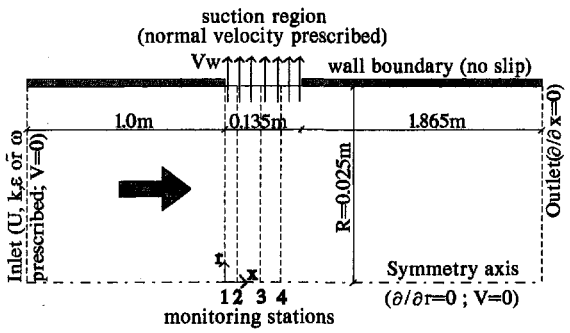


Fig. 1 Flow geometry and boundary conditions

4.2 Initial Profiles. At the domain inlet, profiles of U, k, $\tilde{\epsilon}$ or ω were inserted taken from parabolic computations for fully developed turbulent pipe flow. The PASSABLE parabolic code was used (Leschziner, 1982) employing the same models with those used in the subsequent elliptic computations. With no suction the solutions with the various models resulted in slightly different inlet Reynolds numbers, Re_{bo}, while in the experiment the measured value was 17250. The three models (LS, CLS, and SOF) predicted the inlet bulk velocity and the respective Reynolds number with high accuracy (error less than ± 1 percent) while the W93 model underestimated the above quantities (error -7.8 percent). Also all models provide a velocity distribution at the domain inlet that reproduces well the laminar sublayer and the logarithmic region for the fully developed pipe flow.

4.3 Grid Arrangement. An orthogonal, nonuniform grid of 190×128, in the axial and radial direction respectively, was employed. The grid was particularly fine at the suction inlet and outlet planes. It employed 51 grid nodes upstream of the suction region, 116 nodes covered the suction region and finally 23 nodes were used downstream up to the domain outlet. Computations with all the models and for suction rates up to $A = 3$ percent proved that at least 30 grid nodes were located inside the viscous sublayer ($y^+ < 2$) and therefore the assumptions involved in the low-Re models were satisfied. With the above grid arrangement the results are considered to be grid independent since subsequent calculations with doubling the grid (400×300) did not produce considerable changes. For the sake of brevity no results are presented from the grid independence checks.

4.4 Numerical Method—Boundary Conditions. The governing equations (1), (2), (3), (7), and (8) or (9) were solved by a finite volume method for elliptic flows as described by Huang and Leschziner (1983). The main characteristics of the numerical method are: (a) The QUICK scheme is used for the discretization of the advection terms, (b) the PISO method is applied for the pressure correction, and (c) the TDMA algorithm is used for solving the algebraic equations resulting after the discretization of the partial differential equations.

With reference to Fig. 1 the boundary conditions are the following: At the domain inlet profiles of U, V, k, and $\tilde{\epsilon}$ or ω were prescribed, while along the symmetry axis the $\partial/\partial r$ gradients were set to zero as well as the radial velocity component, V. At the domain outlet all the $\partial/\partial x$ gradients were set to zero corresponding to the assumption for fully developed flow. V was not set to zero but it was obtained from local continuity. However, U profile was corrected to satisfy the overall continu-

Downloaded 03 Jun 2010 to 171.66.16.125. Redistribution subject to ASME license or copyright; see http://www.asme.org/terms/Terms_Use.cfm

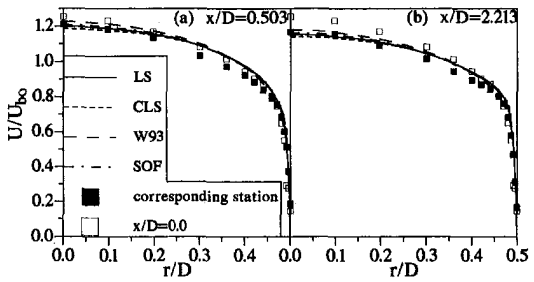


Fig. 2 Experimental and computed axial velocity distribution for A = 0.46 percent

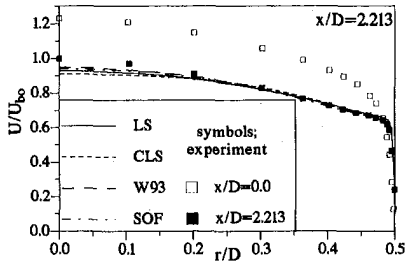


Fig. 4 Experimental and computed axial velocity profiles for A = 2.53 percent

ity, taking into account the abstracted flow. On the wall the no-slip condition was employed for U, V, k and $\tilde{\varepsilon}$ except along the suction region where V was given a constant value corresponding to the uniform suction rate under investigation. ω at the first node adjacent to the wall is given by the boundary condition, $\omega = 6\nu/(c_{\omega 2} y^2)$ where y is the distance from the wall, assuming that molecular diffusion balances dissipation in the viscous sublayer.

5 Analysis of Results

The response of the mean and turbulence characteristics of the fully developed pipe flow to wall suction is examined at selected stations along the suction region where detailed experimental measurements (Schildknecht et al., 1979) are available for A = 0.46 percent. In addition, measurements for a higher suction rate are available (A = 2.53 percent). Finally, analytical results, based on the model of Kinney and Sparrow (1970) and the improved version of Merkine et al. (1971), are compared with experimental and computed results which indicate the validity of the assumptions involved in the analysis.

Figure 2 shows the computed and measured axial velocity profiles at x/D = 0.503 and 2.213 for A = 0.46 percent. Also the experimental data at x/D = 0.0 are included and hence the development of the U-velocity profile along the suction region is clearly shown. The effect of the wall suction on the mean axial velocity distribution is to increase the near-wall values and to reduce the velocities near the centreline, since the wall layers are accelerated and the central flow is decelerated due to the increasing radial velocity component. The increase of near-wall velocities is clearly shown, especially at x/D = 0.503 due to the non-uniformity of the wall suction imposed in the experiments. Such non-uniformity occurs because of difficulties with the construction of the porous material. However, as measurements of radial velocity indicate (Fig. 3), a "fully developed" state is achieved at about x/D = 1.3. At x/D = 2.213 the velocity profile has become more uniform and the near-wall velocities are slightly higher than those with no suction due to the low suction rate. The computed velocity distributions by the various models are similar and have the same features observed in the experiments. The results computed by the W93 k-ω model are shown to be closer to the experimental ones, especially near the wall.

A comparison between experimental and computed (LS model) radial velocities V at all stations is shown in Fig. 3 for A = 0.46 percent. It is evident that, due to the construction of the suction region, the suction velocities are much higher in the entrance region while they relax to a "fully developed" state at about x/D = 1.3. The computed normalized radial velocity, V/V_W, due to the "numerical" uniformity of the mass transfer takes the value of one at the wall in all stations and increases in the near-wall accelerating flow region. In this region, due to local continuity, the magnitude of V must increase with increasing distance from the wall. This is clearly observed in the computations, as well as in the experimental results.

For the higher suction, A = 2.53 percent, computed velocities are compared with experimental ones at x/D = 2.213 where measurements are available (Fig. 4). It is shown that for such a high suction rate the velocity profile becomes quite flat, when compared with that at the suction inlet, exhibiting increased velocities near the pipe wall. All models reproduce well the effects of such a high suction rate on the velocity distribution with a slight overestimation of the velocities near the wall and respective underestimation in the central region. Also, for this suction rate the W93 k-ω model is shown to perform slightly better than the other models.

Computed and experimental velocities are compared against analytical results in Fig. 5. At x/D = 2.213, where "fully developed" state prevails, such a comparison is possible for both suction rates. The local velocities have been normalised with the local bulk value since analytical results are based on the assumption of local similarity. Analytical results are in close agreement with both computational and experimental measurements for A = 0.46 percent indicating that the assumptions involved in the analysis are valid for such suction rates. For A = 2.53 percent the analytical velocity profile is similar with that of the smaller suction rate. It differs, however, from the computed ones and the experimental measurements especially near the wall indicating that the boundary layer assumptions involved in the analysis are not valid for such high mass transfer rates due to the significant axial gradients. Such a behaviour has also been reported in similar studies of open channels with high suction rates (MacLean, 1991).

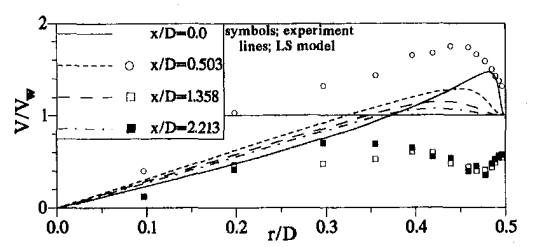


Fig. 3 Experimental and computed radial velocity distribution for A = 0.46 percent

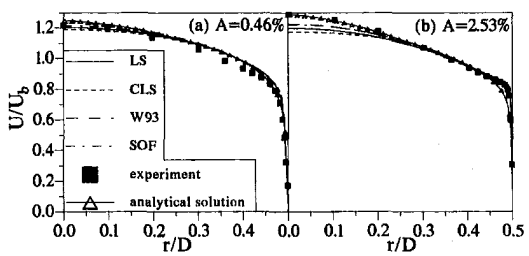


Fig. 5 "Fully developed" axial velocity profiles with suction at x/D = 2.213

Downloaded 03 Jun 2010 to 171.66.16.125. Redistribution subject to ASME license or copyright; see http://www.asme.org/terms/Terms_Use.cfm

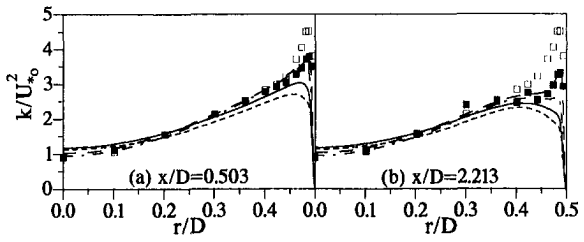


Fig. 6 Experimental and computed profiles of k for A = 0.46 percent. For legend see Fig. 2.

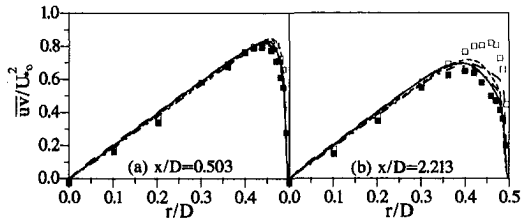


Fig. 8 Experimental and computed profiles of the turbulent shear stress, for A = 0.46 percent. For legend see Fig. 2.

The effects of the wall suction on the turbulent kinetic energy is shown in Fig. 6 where computed and experimental k profiles are plotted for A = 0.46 percent. The wall suction effect is to decrease the near-wall turbulent kinetic energy as it is indicated by both the experimental and computed results. Upstream of the suction region the maximum value of k/U_{*0}^2 is approximately 4.5, equal to that observed in fully developed pipe flow (Laufer, 1954) while at the downstream stations the maximum value is reduced down to 3.5. The predictions of W93 model are shown to be superior than those of the other models and follow the shape of the experimental distribution. The other models, and especially both k-ϵ models, predict lower levels of k at all stations. However, all models, together with the experimental data, indicate that the effects of suction propagate from the wall to the internal flow and penetrate up to approximately $r/D = 0.3$ at the last station. The absolute reduced levels of turbulent kinetic energy along the suction region, together with the turbulent shear stresses presented later, indicate that for a considerably long suction region flow laminarization is expected to take place.

The performance of the nonlinear CLS k-ϵ and SOF k-ω models in predicting the turbulence intensities u', v', and w' is highlighted in Fig. 7. Both models underestimate the axial turbulence intensity at both stations due to the underprediction of the total turbulent kinetic energy. The other two components (v' and w') are captured better by both models with the CLS k-ϵ performing better than the SOF k-ω. A general remark is that since the flow remains a shear layer, particularly for the low suction rate, and therefore does not demonstrate strong straining, the effect of the additional non-linear elements in the stress-strain relation is negligible.

The wall suction effects on the turbulent shear stress $\overline{uv}$ are shown in Fig. 8 for the same suction rate. A reduction of the absolute levels in the suction region is observed in both experimental and computed results which indicates that even small suction rates tend to destroy turbulence and inverse transition to laminar flow is expected to occur for a long suction length. This reduction is in accordance with the reduction observed in the turbulent kinetic energy. The propagation of the suction effects from the wall to the interior of the flow, especially in the last station, is well captured by all models with those of LS and SOF performing better than the others.

Finally the effect of the wall suction on the wall shear stress, τ_w, is shown in Fig. 9 for both suction rates. The increase in τ_w is significant even for the smallest suction rate (approximately 50 percent). For A = 2.53 percent such an increase is much higher and the excess wall shear stress resulting from suction is found to be 5 times the respective one with no suction. The W93 model produces a smaller increase of τ_w than that of the other three models. In the same figure the analytical values of τ_w, based on the respective analytical velocity profiles (Fig. 5), are included at the location of the "fully developed" flow. It is shown that for the low suction rate analytical and computed results indicate similar levels of increased τ_w. However, for the high suction rate the analytical results tend to underestimate the τ_w since the gradient of the analytical velocity profile (Fig. 5(b)) at the wall is smaller than that of the computed (or the experimental) velocity profile. In the same figure empirical values, derived from a simple relation, based on the work of Silver and Wallis (1965), are presented which indicate similar increase with that observed in the analytical solution. This is due to the same assumptions involved in both methods for calculating τ_w.

6 Conclusions

The numerical study of the turbulent pipe flow with wall suction rates ranging from 0.46 to 2.53 percent, in conjunction with experimental measurements and analytical solutions indicates the following:

(a) Wall suction effects on fully developed pipe flow lead to more uniform velocity distribution with increased near-wall values and reduced ones near the centreline. Linear and nonlinear EVM's used in the study are capable of predicting correctly the flow characteristics observed in the experiment.

(b) Computed and analytical velocity distributions are in satisfactory agreement with experimental measurements for the lowest suction rate indicating the validity of the boundary assumptions involved in the analytical solution. For high suction rates these assumptions are not valid and analytical results deviate from the computed and experimental ones especially near the wall.

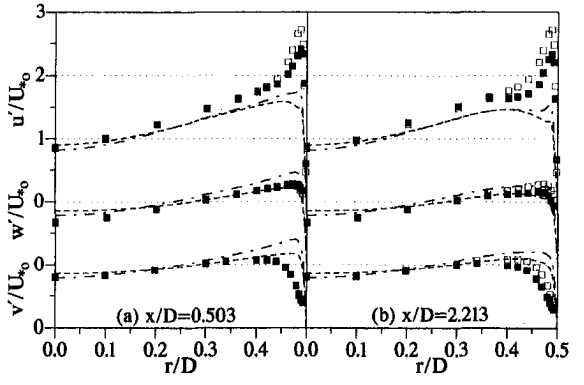


Fig. 7 Experimental and computed turbulence intensities. For legend see Fig. 2.

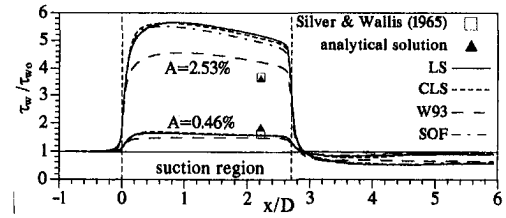


Fig. 9 Variation of wall shear stress along the suction region

Downloaded 03 Jun 2010 to 171.66.16.125. Redistribution subject to ASME license or copyright; see http://www.asme.org/terms/Terms_Use.cfm

(*c*) The experimental and computed near-wall radial component of velocity, V, increases with increasing distance from the wall due to the accelerating fluid layers in the longitudinal direction (V component increases to satisfy local continuity).

(*d*) The absolute levels of turbulent kinetic energy decrease with increasing suction rate. Wall suction effects are evident up to $r/D = 0.3$ in both experimental and computational results.

(*e*) All near-wall turbulence intensities (up to $r/D = 0.3$) decrease due to wall suction effects, with the vertical component v' affected more by the presence of the wall suction. The nonlinear models used in this study (CLS and SOF) underpredict the main component, u', due to the underprediction of k, but they reproduce better the other two components (v' and w'), as well as the region of influence of the wall suction.

(*f*) Wall suction tends to decrease the levels of the turbulent shear stress $\overline{uv}$, indicating that reverse transition from turbulent to laminar flow would take place for a longer suction length. The propagation of the suction effects in the interior of the flow is simulated by the turbulence models.

(*g*) Increased boundary shear stress along the suction region is calculated for both suction rates. The increase in τ_w is significant even for the smallest suction rate (up to 50 percent) while such an increase is much higher for $A = 2.53$ percent (up to 500 percent). Analytical results and empirical relationships indicate similar levels of increase for the low suction rate but tend to underestimate τ_w for the high suction rate, where the boundary layer assumptions cease to be valid.

References

Aggarwal, J. K., Hollingsworth, M. A., and Mayhew, Y. R., 1972, "Experimental Friction Factors for Turbulent Flow with Suction in a Porous Tube," *International Journal of Heat and Mass Transfer,* Vol. 15, pp. 1585–1602.

Antonia, R. A., Fulachier, L., Krishnamoorthy, L. V., Benabid, T., and Anselmet, F., 1988, "Influence of Wall Suction on the Organised Motion in a Turbulent Boundary Layer," *Journal of Fluid Mechanics,* Vol. 190, pp. 217–240.

Antonia, R. A., and Fulachier, L., 1989, "Topology of a Boundary Layer with and without Wall Suction," *Journal of Fluid Mechanics,* Vol. 198, pp. 429–451.

Brosh, A., and Winograd, Y., 1974, "Experimental Study of Turbulent Flow in a Tube with Wall Suction," ASME *Journal of Heat Transfer,* Vol. 94, pp. 338–342.

Chien, K. Y., 1982, "Predictions of Channel and Boundary Layer Flows with a Low-Reynolds Number Two-Equation Model of Turbulence," *AIAA Journal,* Vol. 28, pp. 33–38.

Craft, T. J., Launder, B. E., and Suga, K., 1993, "Extending the Applicability of Eddy Viscosity Models through the use of Deformation Invariants and Non-Linear Elements," *Proceedings of the 5th International Symposium on Refined Flow Modelling and Turbulence Measurements,* Paris, pp. 125–132.

Elena, M., 1984, "Suction Effects on Turbulence Statistics in a Heated Pipe Flow," *Physics of Fluids,* Vol. 27 (4), pp. 861–866.

Fulachier, L., Anselmet, F., Benabid, T., and Antonia, R. A., 1991, "Normalisation for a Turbulent Boundary Layer with Wall Suction," *Physics of Fluids,* Vol. A3 (1), pp. 213–235.

Huang, P. G., and Leschziner, M. A., 1983, "An Introduction and Guide to the Computer Code TEAM," Report TFD/83/09, Thermofluids Division, Department of Mechanical Engineering UMIST.

Kinney, R. B., and Sparrow, E. M., 1970, "Turbulent Flow, Heat Transfer and Mass Transfer in a Tube with Surface Suction," ASME *Journal of Heat Transfer,* Vol. 92, pp. 117–125.

Laufer, J., 1953, "The Structure of Turbulence in Fully Developed Pipe Flow," NACA Technical Note no. 2954.

Launder, B. E., and Sharma, B. L., 1974, "Application of the Energy-Dissipation Model of Turbulence to the Calculation of Flow Near a Spinning Disk," *Letters in Heat and Mass Transfer,* Vol. 1, pp. 131–138.

Leschziner, M. A., 1982, "An Introduction and Guide to the Computer Code PASSABLE," Report TFD/82/11, Thermofluids Division, Department of Mechanical Engineering, UMIST.

MacLean, A. G., 1991, "Open Channel Velocity Profiles over a Zone of Rapid Infiltration," *Journal of Hydraulic Research,* Vol. 29, pp. 15–27.

Merkine, L., Solan, A., and Winograd, Y., 1971, "Turbulent Flow in a Tube with Wall Suction," ASME *Journal of Heat Transfer,* Vol. 93, pp. 242–244.

Schildknecht, M., Miller, J. A., and Meier, G. E. A., 1979, "The influence of Suction on the Structure of Turbulence in Fully Developed Pipe Flow," *Journal of Fluid Mechanics,* Vol. 90, pp. 67–107.

Silver, R. S., and Wallis, G. B., 1965, "A Simple Theory for Longitudinal Pressure Drop in the Presence of Lateral Condensation," *Proceedings of the Institution of Mechanical Engineers,* Vol. 180, pp. 36–40.

So, R. M. C., and Yoo, G. J., 1987, "Low Reynolds Number Modelling of Turbulent Flows with and without Wall Transpiration," *AIAA Journal,* Vol. 25, pp. 1556–1564.

Sofialidis, D., (1993), "The Strain-Dependent, Non-Linear k-ω Model of Turbulence and its Application," M.Sc. thesis, Thermofluids Division, Department of Mechanical Engineering, UMIST.

Suga, K., 1993, "Personal Communication."

Verollet, E., Fulachier, L., and Dekeyser, I., 1977, "Etude Phenomenologique d'une Couche Limite Turbulente avec Aspiration et Chauffage a la Paroi," *International Journal of Heat and Mass Transfer,* Vol. 20, pp. 107–112.

Weissberg, H. L., and Berman, A. S., 1955, "Velocity and Pressure Distributions in Turbulent Pipe Flow with Uniform Wall Suction," *Proceedings of the Heat Transfer Fluid Mechanics Institute,* University of California, Los Angeles, Vol. 14, pp. 1–30.

Wilcox, D. C., 1993, "Comparison of Two-Equation Turbulence Models for Boundary Layers with Pressure Gradient," *AIAA Journal,* Vol. 31, pp. 1414–1421.

Downloaded 03 Jun 2010 to 171.66.16.125. Redistribution subject to ASME license or copyright; see http://www.asme.org/terms/Terms_Use.cfm

D. F. Zhang
Research Assistant.

D. A. Zumbrunnen
Associate Professor. Mem. ASME

Thermal and Fluid Sciences
Research Laboratory,
School of Mechanical and
Industrial Engineering,
Clemson University,
Clemson, SC 29634-0921

Influences of Fluidic Interfaces on the Formation of Fine Scale Structures by Chaotic Mixing

A numerical model has been developed of two-dimensional chaotic mixing of immiscible Newtonian fluids. A computationally efficient numerical methodology is employed which is well-suited to complex, evolving interfaces. Mixing was confined to a rectangular cavity with periodically driven upper and lower surfaces. Interfacial forces and the transient flow fields in each phase were considered to assess specifically the influences on interfacial morphology of interfacial tension and phase viscosity ratio under creeping flow conditions. Predicted morphologies are compared to those of solidified specimens synthesized by chaotic mixing in companion studies.

Introduction

In recent studies, chaotic mixing has been investigated (Zumbrunnen et al., 1996; Liu and Zumbrunnen, 1995) as a means to directly synthesize fine-scale fibrillar and lamellar composites. Molten discrete phase clusters surrounded by a molten continuous phase intertwine on progressively finer scales due to recursive stretching and folding processes associated with chaos. Emergent structures, as defined by interfaces between phases, can be subsequently captured by solidification. Interfacial tension and phase viscosity ratio influence the ultimate emergent morphology as chaotic mixing proceeds. A micrograph of fine-scale composite structures formed with low density polyethylene (LDPE) is indicated in Fig. 1. The structure, which is shown in cross-section and corresponds to negligible interfacial tension, has a lamellar morphology and reveals patterns associated with chaos extending to microscopic scales which resemble those reported at much larger scales by Ottino (1989). As for a dissimilar polymeric system with appreciable interfacial tension, folding and contracting flows during chaotic mixing promote instabilities such as those indicated by the sinuous pattern in Fig. 2. Large minor phase bodies subdivide rapidly due to the instabilities to yield smaller bodies and extensional flows cause these bodies to become stretched into high aspect ratio fibrils. The interfacial structures in Figs. 1 and 2 are cross-sections of long sheets. Consequently, many of their features can be modeled in two-dimensions.

In order to employ chaotic mixing effectively to produce in-situ fine scale composite structures or to improve mixing processes in industrial applications, interfacial interactions must be understood. A numerical model has therefore been developed in this study which is particularly well suited to investigate the emerging complex morphologies of interfaces between fluid phases under chaotic mixing conditions. Numerical simulations are necessarily restricted to early mixing times due to rapid reductions in length scales. In order to gain insights applicable to later mixing times, results are presented in terms of applicable dimensionless parameters. Changes in interfaces at smaller length scales can be inferred by examining behavior corresponding to higher dimensionless interfacial tensions since effects due to interfacial tension are more significant for smaller minor phase bodies.

Chaotic mixing has been investigated in two-dimensional flows within cavities. Much of this work has been done to elucidate fundamental mixing processes with passive interfaces. Chien et al. (1986) experimentally studied the chaotic advection of a passive dye in a variety of trapezoidal cavity flows. Chaotic flows were confirmed by detecting Smale horseshoe maps. Chaotic mixing in a rectangular cavity with movable upper and lower walls was further studied experimentally and numerically by Leong and Ottino (1989). The abatement of regions of regular motion (i.e., islands) was assessed for different mixing protocols. Liu et al. (1994b) examined in detail the stretching field in a similar rectangular cavity filled with a single fluid. It should be noted that chaotic mixing with active interfaces is considered in the present work in contrast to these prior investigations. Mixing with an active interface is a complex process in which interfaces modify the flows within all phases and are themselves influenced by the modified flows. Interfacial dynamics becomes more significant as the interfacial area increases during mixing or when several minor phase clusters are present and can interact.

Numerical simulations of morphological evolution in chaotic mixing of immiscible fluids involve the solution of the Navier-Stokes equations for two or more fluid phases with specified boundary and interfacial conditions. The major difficulty in these numerical simulations is the unknown location of the moving interface, which must be found together with the pressure and velocity fields within the different fluid phases. Several recent and established approaches to solve these types of moving interface problems are available in the literature, although none has been used previously to investigate chaotic mixing conditions. A semi-analytical numerical boundary-integral method was used by Rallison and Acrivos (1978) to study the deformation and burst of a viscous drop freely suspended in an immiscible fluid in which the far exterior velocity field was a known linear one. Using the integral approach, Stone and Leal (1989) numerically studied the relaxation and breakup of an initially extended drop in an otherwise quiescent fluid. With the same method, Tjahjadi et al. (1992) investigated the interfacial tension-driven fragmentation of a very long fluid filament in a quiescent viscous fluid. Satellite and subsatellite formations of broken droplets observed in a companion experimental study were successfully predicted.

In the MAC [Marker-And-Cell] method (Harlow and Welch, 1965; Hirt and Shannon, 1968; Chan and Street, 1970; Vafai and Chen, 1992), massless particles are used which are referred to as markers. The markers move with the fluid and determine whether a cell is occupied by one fluid or the other, or by a mixture of the two fluids. The markers thereby identify cells where the interface is located. Though the MAC method has been verified to be a powerful numerical tool, computational

Contributed by the Fluids Engineering Division for publication in the JOURNAL OF FLUIDS ENGINEERING. Manuscript received by the Fluids Engineering Division December 10, 1994; revised manuscript received November 6, 1995. Associate Technical Editor: Jong H. Kim.

Copyright © 1996 by ASME

Downloaded 03 Jun 2010 to 171.66.16.125. Redistribution subject to ASME license or copyright; see http://www.asme.org/terms/Terms_Use.cfm

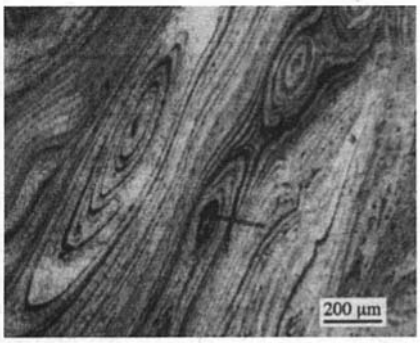


Fig. 1 Micrograph of cross-sections of emergent lamellar structures for LDPE as the major phase and pigmented LDPE distributed initially in 4 mm pellet form revealing signatures of chaos at microscopic scales (Zumbrunnen et al., 1996)

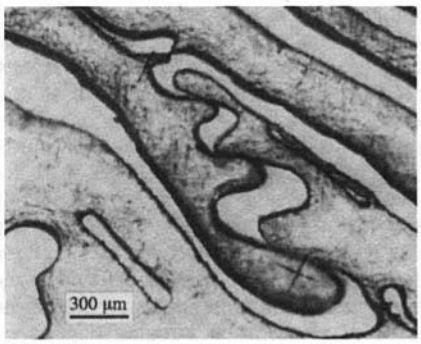


Fig. 2 Micrograph of intermediate interfacial morphologies shown in cross-section during the chaotic mixing of low density polyethylene and polystyrene as the minor phase (Liu and Zumbrunnen, 1995)

storage requirements can become excessive and the association between markers may become ambiguous when interface morphology is complex. The VOF [Volume of Fluid] method (Hirt and Nichols, 1981; Bugg and Rowe, 1991, 1993) overcomes deficiencies of the MAC method by associating with the interface one scalar function f instead of massless markers. The function f is defined as the fractional volume of a computational cell occupied by a certain fluid. Cells with f values between zero and one identify interface locations. Thus, the VOF method provides the same interface information available to the MAC method, but computational storage requirements are consistent with requirements for all other dependent variables.

In the aforementioned approaches, a separate representation of interfacial forces must be incorporated. Consequently, these methods have suffered from difficulties in modeling morphologically complex interfaces, especially when interfacial tension is important. Recently, a two-dimensional continuum surface force (CSF) method for modeling interfacial tension has been introduced by Brackbill et al. (1992). In this method, interfacial tension is interpreted as a continuous, three-dimensional effect across an interface, rather than as a boundary condition on the interface. With interfacial forces replaced by a volumetric force, the CSF technique is ideally suited for Eulerian interfaces that are not in general aligned with the computational grid. Richards et al. (1993) demonstrated that the CSF method can alleviate topological constraints on modeling interfaces having surface tension without sacrificing accuracy.

In the present study, the evolution of active interfaces under chaotic mixing conditions was numerically simulated within a two-dimensional rectangular cavity. A general numerical code has been developed based on the VOF method (Hirt and Nichols, 1981), finite volume method (Patankar, 1980), and an updated CSF technique (Kothe et al., 1991). The major incentive for using the VOF method in conjunction with the CSF technique, as previously discussed, is that the description of highly complex interfaces is facilitated. Reconstruction of interfaces to evaluate interfacial forces is unnecessary which provides computational efficiency. Its use in this study of fluid interfaces under chaotic mixing conditions was therefore deemed appropriate.

Governing Equations and Numerical Modeling

Numerical modeling was performed in accordance with the following assumptions: (i) unsteady, laminar flow, (ii) constant thermophysical properties, (iii) immiscible fluids, (iv) incompressible, Newtonian fluids, (v) no-slip conditions at both cavity walls and fluidic interfaces, (vi) absence of gravitational and

Nomenclature

A = aspect ratio of the mixing cavity = H/L
C_μ = ratio of viscosity of minor phase B to the viscosity of the major phase A = μ_B/μ_A
C_ρ = ratio of density of minor phase B to the density of the major phase A = ρ_B/ρ_A = 1
f = volume fraction of minor phase fluid B in a computational cell
H = height of mixing cavity
L = length of mixing cavity
N = number of periods, where one period comprises the movement of both cavity walls
P = dimensionless pressure = p/P_0
p = pressure (N/m^2)
P_0 = scale factor for pressure = $\mu_A\mu_0/L$
Re = Reynolds number = $\rho_A\mu_0 L/\mu_A$
St = Strouhal number = $T_0/T = L/Tu_0$
t = time (s)
T = time interval equivalent to one period (s)
T_0 = scale factor for time = L/u_0
u = velocity component in x-direction (m/s)
u_B = velocity of lower wall of mixing cavity (m/s)
u_T = velocity of upper wall of mixing cavity (m/s)
u_0 = scale factor for velocity equivalent to the constant nonzero speed of the moving walls (m/s)
U = dimensionless velocity component in x-direction = u/u_0
v = velocity component in y-direction (m/s)
V = dimensionless velocity component in y-direction = v/u_0
x = horizontal coordinate (m) (Fig. 3)
X = dimensionless horizontal coordinate = x/L
y = vertical coordinate (m) (Fig. 3)
Y = dimensionless vertical coordinate = y/H
τ = dimensionless time = t/T_0
μ = dynamic viscosity (kg/m s)
ρ = mass density of fluid (kg/m^3)
σ = interfacial tension (N/m)
σ^* = dimensionless interfacial tension = $\sigma/\mu_A\mu_0$
κ = curvature of fluid-fluid interface (1/m)
K = dimensionless curvature of fluid-fluid interface = κL
$\Delta\tau$ = dimensionless computational time step
M = dimensionless mass density for fluid in a computational cell
Γ = dimensionless viscosity for fluid in a computational cell

Subscripts

A = major phase
B = minor phase

Downloaded 03 Jun 2010 to 171.66.16.125. Redistribution subject to ASME license or copyright; see http://www.asme.org/terms/Terms_Use.cfm

other external body forces. The computational domain (Fig. 3) is of a two-dimensional rectangular cavity. The upper and lower walls move according to assigned velocity functions $u_T(t)$ and $u_B(t)$. The lateral walls are fixed. A discontinuous velocity protocol, in which the upper wall moves for one-half time period while the lower wall is stationary followed by an identical motion in the opposite direction by the lower wall, was selected since chaotic particle motion can be achieved under this periodic flow condition (Leong and Ottino, 1989). A minor phase fluid B, with mass density ρ_B and viscosity μ_B, was initially suspended in immiscible fluid A of mass density ρ_A and viscosity μ_A. Since interfacial tension maintains an equilibrium circular form for a motionless condition, circular shapes were specified for the initial interfaces of the minor phase (fluid B) clusters. While the model is described for two fluids, methods are adaptable to three or more fluids.

The aforedescribed VOF method was used to define and track the moving interfaces. The approach is summarized here for completeness. A scalar function $f(X, Y, t)$ was introduced and defined as the volume fraction of the minor phase fluid B within the computational cells. The two-dimensional evolution equation of f was obtained by noting that f is in essence an advected quantity and is thereby governed by the equation $Df/Dt = 0$. Therefore, the dimensionless evolution equation for f in Cartesian coordinates for a cavity of aspect ratio A is given by

$$\frac{\partial f}{\partial \tau} + U\frac{\partial f}{\partial X} + \frac{1}{A} V \frac{\partial f}{\partial Y} = 0 \tag{1}$$

Since f changes abruptly from zero to unity across the interface and over a distance comparable to the resolution afforded by the computational mesh, a special approach must be used to solve numerically Eq. (1). In each of the computational cells in the finite volume approach employed in this study, Eq. (1) is integrated over a finite volume and thereby a discretization equation is obtained which includes the change of f over the cell and the volumetric flow of fluid B across the finite volume. The change of f for each grid point was determined by the net flow of fluid B across the four surfaces in the computational cell in accordance with a donor-acceptor algorithm (Hirt and Nichols, 1981).

An updated CSF technique (Kothe et al., 1991) was adopted to deal with the effect of interfacial tension at moving interfaces. The CSF technique is valid for moving interfaces between incompressible fluids where the interfacial tension coefficient is constant. For these conditions, interfacial tension is balanced by pressures p_A and p_B within individual phases according to

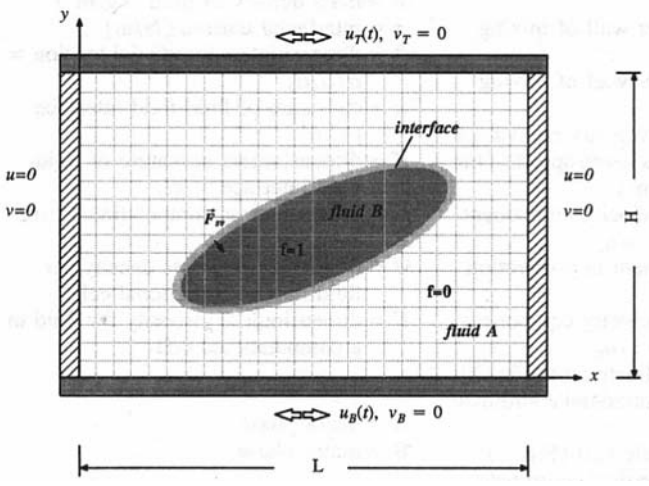


Fig. 3 Computational domain and boundary conditions employed in the numerical model

$$p_s \equiv p_B - p_A = \sigma\kappa \tag{2}$$

where p_s is the so-called surface pressure. The corresponding normal force per unit interfacial area at a position $\mathbf{x}_s$ is given by

$$\mathbf{F}_{sa}(\mathbf{x}_s) = \sigma\kappa(\mathbf{x}_s)\hat{n}(\mathbf{x}_s) \tag{3}$$

where $\hat{n}(\mathbf{x}_s)$ is the unit normal vector at $\mathbf{x}_s$. In the CSF method, the discontinuous sharp interface is replaced by a transition region with a distance of $O(h)$, where h is a length comparable to the resolution afforded by a computational mesh. It is thereby no longer appropriate to apply a pressure jump induced by interfacial tension at an interface. Rather, interfacial tension acts everywhere within this transition region via a volumetric force $\mathbf{F}_{sv}(\mathbf{x})$. Integration of the volumetric force $\mathbf{F}_{sv}(\mathbf{x})$ over a volume encompassing the transition region must equate to the integration of $\mathbf{F}_{sa}(\mathbf{x}_s)$ over a corresponding interface area. The volumetric force $\mathbf{F}_{sv}(\mathbf{x})$ is then related to $\mathbf{F}_{sa}(\mathbf{x}_s)$ via a distribution function which can be conveniently related to the volume fraction f (Brackbill et al., 1992). The volumetric force is then given by

$$\mathbf{F}_{sv}(\mathbf{x}) = \sigma\kappa(\mathbf{x})\frac{\nabla f(\mathbf{x})}{[f]} \tag{4}$$

In Eq. (4), $[f] = f_2 - f_1 = 1 - 0 = 1$, given the physical definition of f. The x and y components of $\mathbf{F}_{sv}(\mathbf{x})$ are:

$$F_{svx}(\mathbf{x}) = \sigma\kappa(\mathbf{x})\frac{\partial f(\mathbf{x})}{\partial x}; \quad F_{svy}(\mathbf{x}) = \sigma\kappa(\mathbf{x})\frac{\partial f(\mathbf{x})}{\partial y} \tag{5a, b}$$

More information about intermediate mathematical steps of the CSF technique is available in recent papers (Kothe et al., 1992; Richards et al., 1992).

With interfacial forces obtained with the VOF method and CSF technique, the continuity equation and the momentum equations in Cartesian coordinates were nondimensionalized in terms of suitable dimensionless parameters and variables (see Nomenclature). Since modeling was performed under creeping flow conditions, the scale factor P_0 for pressure relates to viscous forces instead of inertial forces, for example. Additionally, the steady speed u_0 of the upper and lower walls, the mixing period T, and cavity length L defined a dimensionless time τ and a dimensionless frequency in terms of a Strouhal number St for the mixing process. The resulting dimensionless equations, with body forces from Eq. (5), are given below.

$$\frac{\partial U}{\partial X} + \frac{1}{A}\frac{\partial V}{\partial Y} = 0 \tag{6}$$

$$\mathrm{Re}\left(\frac{\partial (MU)}{\partial \tau} + U\frac{\partial (MU)}{\partial X} + \frac{1}{A}V\frac{\partial (MU)}{\partial Y}\right) = -\frac{\partial P}{\partial X} + \frac{\partial}{\partial x}\left(\Gamma\frac{\partial U}{\partial X}\right) + \frac{1}{A^2}\frac{\partial}{\partial Y}\left(\Gamma\frac{\partial U}{\partial Y}\right) + \sigma^* K\frac{\partial f}{\partial X} \tag{7}$$

$$\mathrm{Re}\left(\frac{\partial (MV)}{\partial \tau} + U\frac{\partial (MV)}{\partial X} + \frac{1}{A}V\frac{\partial (MV)}{\partial Y}\right) = -\frac{1}{A}\frac{\partial P}{\partial Y} + \frac{\partial}{\partial X}\left(\Gamma\frac{\partial V}{\partial X}\right) + \frac{1}{A^2}\frac{\partial}{\partial Y} \times \left(\Gamma\frac{\partial V}{\partial Y}\right) + \frac{1}{A}\sigma^* K\frac{\partial f}{\partial Y} \tag{8}$$

The dimensionless mass density M and viscosity Γ in Eqs. (7) and (8) are properties of computational cells in which both fluid A and fluid B may be contained. Given the fact that the

Downloaded 03 Jun 2010 to 171.66.16.125. Redistribution subject to ASME license or copyright; see http://www.asme.org/terms/Terms_Use.cfm

sharp interface is replaced by a transition region, these two properties were obtained by linearly combining the properties of two different fluids according to the volume fraction f.

$$M = 1 + f(C_\rho - 1) \tag{9a}$$

$$\Gamma = 1 + f(C_\mu - 1) \tag{9b}$$

Inertial force terms were included in the governing equations in order to obtain a general model. In companion experimental studies (Miles et al., 1996; Zumbrunnen et al., 1996; Liu and Zumbrunnen, 1996) and prior related studies with passive interfaces (e.g., Leong and Ottino, 1989), results pertained to Reynolds numbers on the order of unity so that inertial forces would not be large in comparison to viscous forces. For consistency with these prior studies, the numerical calculations of this study were also performed with Re = 1 and $C_\rho = 1$. The influence of inertial forces at higher Reynolds numbers in this two-phase flow is the subject of ongoing work.

Physically appropriate boundary conditions were specified at the cavity walls as shown in Fig. 3. Protocols for the wall velocities u_T and u_B to give chaotic mixing conditions were discussed above. Equations (7) and (8) were discretized using the finite volume approach and were solved according to the SIMPLE method (Patankar, 1980). A uniform mesh was used in both the X and Y directions in order to disclose accurately the interfacial morphology everywhere in the mixing cavity. Finite volume representations of the momentum equations [Eqs. (7) and (8)] were used to calculate new approximate velocities at a future time level $(n + 1)$ using initial conditions or previous time level (n) values. A fully implicit formulation, using first-order backward differencing for temporal terms, was used to avoid instability problems. The hybrid scheme (Spalding, 1972) was used to discretize advective and diffusive terms. Pressures and velocities in each mesh cell were adjusted iteratively by the successive over-relaxation method to satisfy continuity [Eq. (6)]. This iteration process continued until convergence criteria (below) were satisfied in the entire computational domain. Finally, based on the convergent velocity field, Eq. (1) and the donor-acceptor algorithm were used to update the fractional values in the VOF method. It should be noted that interface reconstruction was not necessary during the computations since interfacial forces were calculated according to Eq. (5).

The mesh was successively refined to ensure grid independence through two criteria. To satisfy the first criterion, the mesh was refined so that the calculated velocity components at three unique reference points differed by less than 0.1 percent. The three reference points were located on the symmetric lines ($X = 0.5$ or $Y = 0.5$) where velocity gradients were highest. To satisfy the second criterion, the mesh was refined until the locations of an interface, which was initially located near the center of the cavity, and of tracked particles differed by less than 1% after the maximum elapsed mixing time. As will be demonstrated, clusters were situated initially near a period-1 hyperbolic point in a chaotic region. Folding and stretching thereby correspond to chaotic mixing conditions. Meshes that satisfied both criteria were 120×160 for $A = 1.333$ and 200×120 for $A = 0.6$. Time-step independence was assessed by successively refining the time step $\Delta\tau$ in accordance with the criteria above. For most cases, $\Delta\tau = 10^{-3}$. Iterations in the line-by-line tridiagonal matrix algorithm within each time step were continued until convergency criteria were satisfied. Two convergence criteria were used. First, the maximum relative differences in velocity components in the entire computational domain for each time step should be less than 10^{-5}. Second, the maximum mass balance error of each computational cell for each time step should be less than 5×10^{-5}. The amount of CPU time on a Sun Microsystems, Inc. (Mountain View, California) Sparc 10 Workstation (12 MFLOP) ranged from 20 to 36 hours for the chaotic mixing cases.

Several available solutions were used to test the accuracy and validate the numerical code. Steady flow fields with one wall moving and the other wall stationary or with two walls simultaneously moving were solved. The motion of passive tracers during chaotic mixing conditions after six periods ($N = 6$) was determined by tracking 20,000 fluid particles which comprised a small simulated passive discrete phase cluster. The geometry of the deformed cluster was easily discerned from patterns formed in the positions of the many tracked particles. Numerical results were compared with the experimental results reported by Leong and Ottino (1989). Excellent agreement with the patterns was obtained and thereby validated the code for single phase flows. The VOF algorithm was assessed by comparing the interface location predicted with the VOF algorithm to that given by particle tracking with passive interfaces. The results differed by less than 1 percent after one time period. The VOF results were also compared and found to be in excellent agreement with the experimental results obtained by Chien et al. (1986). The examples given by Brackbill et al. (1992) were used to test the CSF algorithm. The surface tension-driven flow for an initially square drop within a quiescent fluid was used and the equilibrium circular form was correctly predicted.

Results and Discussion

Prior to considering evolving interfacial morphologies in a time-varying flow, it is informative to first consider the interaction between a single minor phase cluster and a steady flow field. A previously investigated (Leong and Ottino, 1989) tall rectangular cavity ($A = 1.333$) was selected, since simultaneous and steady motion in opposing directions of both upper and lower walls established a stationary hyperbolic point within the flow field and associated homoclinic orbits, as depicted in Fig. 4(a). As a demonstration of the influence of active interfaces, a circular minor phase cluster with initial diameter of $1/6L$ was placed at the center of the mixing cavity. Calculations were performed for different interfacial tensions and a phase viscosity ratio C_μ of unity. The location of the interface at $\tau = 5.0$ is shown in Fig. 4(b) for a dimensionless interfacial tension $\sigma^* = 0.5$. Shear stresses in the flow field acting on the cluster interface tend to stretch the cluster. However, interfacial tension resists this deformation. When the interfacial tension is small, the shear stress overcomes the effect of interfacial tension and large deformations occur. Notably, the flow field is similar to that without the cluster (Fig. 4(a), and the hyperbolic point still exists at the center of the mixing cavity. In this case, the cluster behaves essentially as a passive tracer. At still higher values of σ^*, strong interfacial interactions induce a much different evolution in the interface. The interface location at $\tau = 5.0$ for $\sigma^* = 2.0$ is shown in Fig. 4(c). This interfacial structure is stable in that shear, pressure, and interfacial forces have become balanced. Far away from the cluster, the flow characteristics of the case for $\sigma^* = 0.5$ persist. Adjacent to and inside the cluster, however, the flow field is strongly modified and inspection reveals that the hyperbolic point has vanished. Flow velocities inside the cluster are very small. It should be noted that the disappearance of hyperbolic points due to the presence of a minor phase cluster is detrimental to efficient mixing in steady flows.

Chaotic mixing conditions are demonstrated in Fig. 5 and subsequent figures for a shorter cavity ($A = 0.6$) where the upper and lower walls move periodically as previously described with a Strouhal number St = 0.16. In Fig. 5, a circular passive ($\sigma^* \approx 0.0$, $C_\mu = 1$) minor phase cluster with diameter of $0.2L$ was placed initially at the location of a period-1 homoclinic point [$(x_0, y_0) = (0.825L, 0.5H)$]. Characteristic stretching and folding processes of chaotic mixing can be clearly observed after one mixing period, which consisted of alternate movements of the upper and lower walls for equal time intervals. In Fig. 5a, the initially circular cluster is stretched and

Downloaded 03 Jun 2010 to 171.66.16.125. Redistribution subject to ASME license or copyright; see http://www.asme.org/terms/Terms_Use.cfm

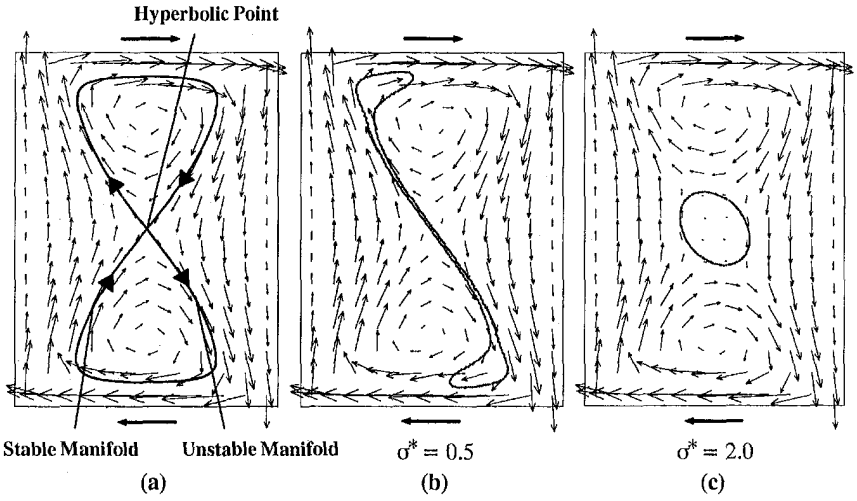


Fig. 4 Flow structures, velocity fields, and interfacial morphologies which arise due to the simultaneous and steady motion of upper and lower walls to a cavity with $A = 1.333$ and $C_\mu = 1.0$: (*a*) hyperbolic point in a single phase flow, (*b*) intermediate interfacial morphology at $\tau = 5.0$ with $\sigma^* = 0.5$, (*c*) emergence of a stable interfacial morphology with $\sigma^* = 2.0$

returned folded after one period ($N = 1$) in reverse and forward mappings to yield horseshoes. Transverse intersections in the manifolds become evident with $N = 2$. The existence of horseshoe maps and transverse intersections are confirmations of chaotic behavior (Ottino, 1989).

The influence of a chaotic flow field on the morphological development of an active interface is considered in Fig. 6 for a minor phase cluster of identical initial size and location as the one considered in Fig. 5. The phase viscosity ratio C_μ was selected to be 0.2, given that less viscous fluids are normally used as the minor phases in actual mixing processes. The deformed interfaces are shown at the completion of one period ($N = 1$) for different interfacial tensions (σ^*) and Eulerian velocity vectors are overlaid to show the effect of the active interface on the velocity field. At the completion of one period, the lower cavity surface is moving and the upper surface is stationary. The flow is not steady and responds to interfacial motions and periodic changes in the cavity wall movements. Thus, the flow is both externally and interfacially driven. When interfacial tension is very small ($\sigma^* = 0.05$), the interaction of the minor phase cluster with the flow field is very weak and the interface is almost passively advected. Significant stretching and folding are observed, showing the same characteristic behaviors of chaotic mixing with passive interfaces. Because of the stretching and folding, a lamellar structure would emerge if mixing continued such as the one in the micrograph of Fig. 1 where $\sigma^* \approx 0$. Interfacial effects yield a bulbous end as disclosed by comparing the morphology with the one in Fig. 5. Similar bulbous ends have been described for the relaxation of extended droplets (Stone and Leal, 1989). Repetitive stretching and folding processes would continue if mixing proceeds until counteracted by the increasing influence of interfacial tension at smaller length scales. A dependence on length scale is associated with the dimensionless interface curvature K in Eqs. (7) and (8). With $\sigma^* = 0.10$ in Fig. 6, interfacial interactions strongly influence the evolution of the interface. The folding that was evident with $\sigma^* = 0.05$ does not arise due to the higher resistive forces associated with curvatures within folds. Interestingly, significant stretching still occurs along the major axes of the deformed bodies. Such elongated, unfolded shapes are not subject to appreciable interfacial tension forces since radii of curvature are comparatively large in the stretching direction. However, the stretching rate is ultimately reduced at higher interfacial tensions, as shown for $\sigma^* = 0.25$. When the interfacial tension increases further, such as when $\sigma^* = 1.0$, the cluster was found to essentially move within the cavity as an autonomous body. It is likely that such minor phase bodies can disrupt KAM curves in the manner demonstrated by Liu et al. (1994a) with solid particles.

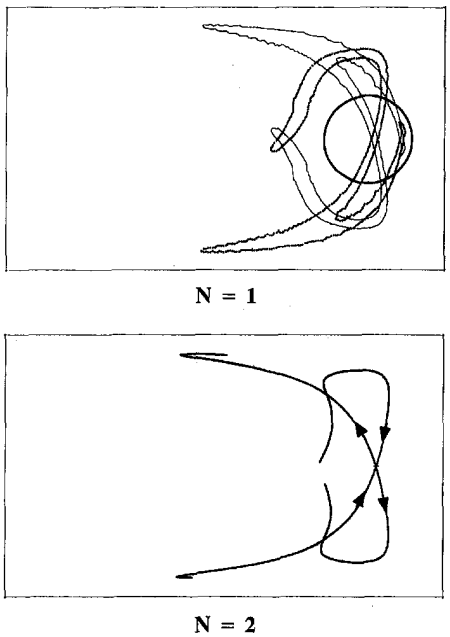


Fig. 5 Numerically generated horseshoe maps and associated transverse intersections in the manifolds of a period-1 hyperbolic point for a passive cluster of initial circular shape with $A = 0.6$, $C_\mu = 1.0$, $\sigma^* = 0.0$, and $St = 0.16$

The results of Fig. 6 demonstrate that the magnitude of interfacial tension has a strong influence on the interfacial morphology during chaotic mixing processes. In consideration of the mathematical form of the interfacial force in Eqs. (5), (7), and (8), the effect of interfacial tension is very sensitive to the scale of a cluster via the dimensional curvature κ of a fluid-fluid interface which is multiplicative with σ^*. The interfacial curvature κ increases with decreasing scale. In the case of negligible interfacial tension at the beginning of mixing (Fig. 6, $\sigma^* = 0.05$), the effect of interfacial tension will eventually become significant as chaotic mixing proceeds until lesser deformations

Downloaded 03 Jun 2010 to 171.66.16.125. Redistribution subject to ASME license or copyright; see http://www.asme.org/terms/Terms_Use.cfm

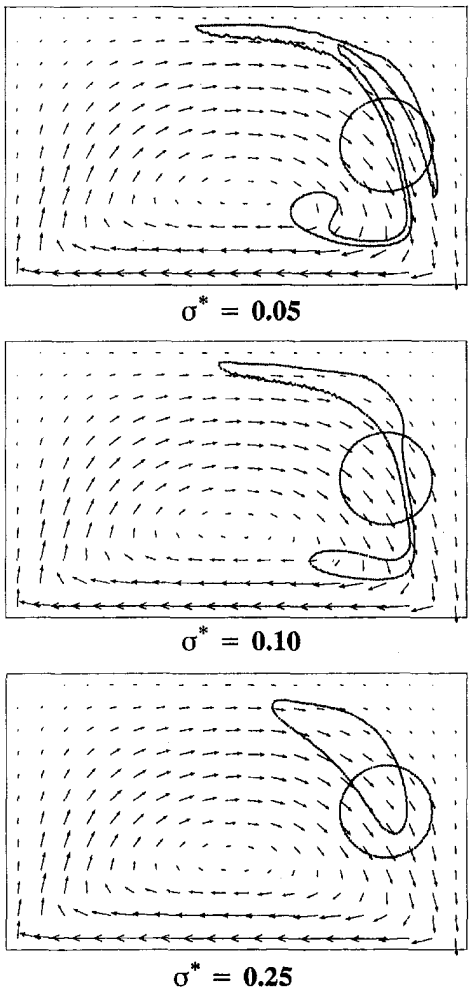


Fig. 6 Influence of interfacial tension on interfacial morphologies at the completion of one period ($N = 1$) indicating a degradation of folding and stretching within the mixing cavity with $A = 0.6$, $St = 0.16$, and $C_\mu = 0.2$

become possible (Fig. 6, $\sigma^* = 0.25$). Thus, the results of Fig. 6 are representative of mixing conditions at different length scales as well as different interfacial tensions when interpreted in the context of the governing equations. Decreasing scales arise due to stretching and folding and also due to break-up associated with instabilities (Stone and Leal, 1989.) Consequently, the interfacial dynamics can be represented by any of the general behaviors in Fig. 6 depending on the elapsed mixing time, so long as σ^* is sufficiently small to permit morphological changes in the early interface.

The effect of phase viscosity ratio C_μ on the interfacial morphology at a low interfacial tensions of $0 < \sigma^* < 0.1$ was examined for $0.2 < C_\mu < 2.0$. The phase viscosity ratio within this range was found to have little influence on interfacial morphology prior to the onset of instabilities in the interface. For example, for the extreme case where $\sigma^* = 0$, interfacial forces are solely due to shear forces. Although small differences existed in the deformed interfaces, results were qualitatively similar to those with $\sigma^* = 0.1$. Insensitivity to phase viscosity ratio at low interfacial tensions and prior to the onset of instabilities is due to the creeping flow conditions. Under creeping flow conditions, inertial force terms in the momentum equations can be neglected and the velocity field can be obtained by solving a harmonic equation simplified from the Navier-Stokes equations. In this harmonic equation, fluid viscosity does not appear explicitly and the velocity field is thereby independent of it. Morphological developments of interfaces are similar since relative velocities between phases are minimized under creeping flow conditions. (Indeed, relative velocities are one outcome of inertial effects.) Additionally, since the morphological development is influenced strongly by the action of hyperbolic points where the flow is extensional instead of shear, shear stresses may be small when the morphology is undergoing the most substantial changes.

Whereas viscosity ratio has little influence on the morphology prior to the onset of interfacial instabilities, numerical results indicated that interfacial instabilities which may lead to breakup occur more readily (i.e., at larger length scales) for $C_\mu < 1$. This result is consistent with the experimental findings by Tjahjadi and Ottino (1991). Such instabilities are evident in Fig. 2 where a sinuous pattern is formed near a fold. An example of model predictions of similar sinuous interfacial morphologies are shown in Fig. 7 with $C_\mu = 0.2$, where an interfacial morphology of Fig. 6 has been used as a convenient starting point in the computations. As in Fig. 2, a sinuous interface arises preferentially near folds. Instabilities grow rapidly and lead to breakup. The single, original elongated body is transformed to four bodies which relax to more nearly circular shapes. These bodies can be regarded as elongated structures since the flow is two-dimensional. In a three-dimensional mixing process, such as the one employed by Liu and Zumbrunnen (1995) to produce fibrillar composites, these bodies can be stretched along their axes (i.e., along the direction perpendicular to the figure) into high aspect ratio fibrils before succumbing themselves to break up preferentially within folds. Such stretching along major axes is consistent with the results of Fig. 6.

In actual mixing processes, several minor phase clusters instead of a single cluster may be dispersed within a major phase and therefore interactions among clusters can occur. As a demonstration of the suitability of the numerical approach to such cases, calculations were performed to study the interfacial evolution of three identical adjacent clusters with initial locations shown in Fig. 8 by the circular forms. The initial location of cluster 1 is identical to the one in Fig. 6 for comparison purposes. Since interfacial tension has a strong influence on interfacial morphology while the phase viscosity ratio C_μ has lesser influence prior to the onset on interfacial instabilities, a value of unity for C_μ was selected and two different interfacial tensions were considered. The results at the completion of one period are given in Fig. 8 for $\sigma^* = 0.10$ and $\sigma^* = 0.25$. Due to interfacial motions, the velocity fields in the vicinities of each minor phase cluster are modified. Upon comparing Fig. 6 and Fig. 8, it is evident that the locations and shapes of cluster 1 have changed appreciably due to the presence of adjacent clusters. In both cases, cluster 1 is less deformed. Stretching facilitates an interaction between clusters 1 and 3 so that deformations in cluster 3 are induced which resemble folds. Cluster 1 is, however, stretched less than in Fig. 6 due to impeding influences of the adjacent cluster interfaces. Cluster 3 has effectively displaced a portion of cluster 1 and has developed a morphology near the upper wall resembling the one for cluster 1 in Fig. 6. This displacement has mitigated the influence of the wall motion on cluster 1 as evidenced by its more central location in the cavity and the elongated forms of clusters 2 and 3. If reduced deformations and lessened stretching persist at later mixing times, mixing would be slowed by the minor phase interactions.

Conclusions

A numerical model has been developed which is particularly well suited to study the emerging complex morphologies of interfaces between fluid phases under chaotic mixing conditions. The model was implemented in specific examples to demonstrate model performance and also to assess effects of interfacial tension, phase viscosity ratio, and minor phase body interactions in the vicinity of a period-1 hyperbolic point. At very small interfacial

Downloaded 03 Jun 2010 to 171.66.16.125. Redistribution subject to ASME license or copyright; see http://www.asme.org/terms/Terms_Use.cfm

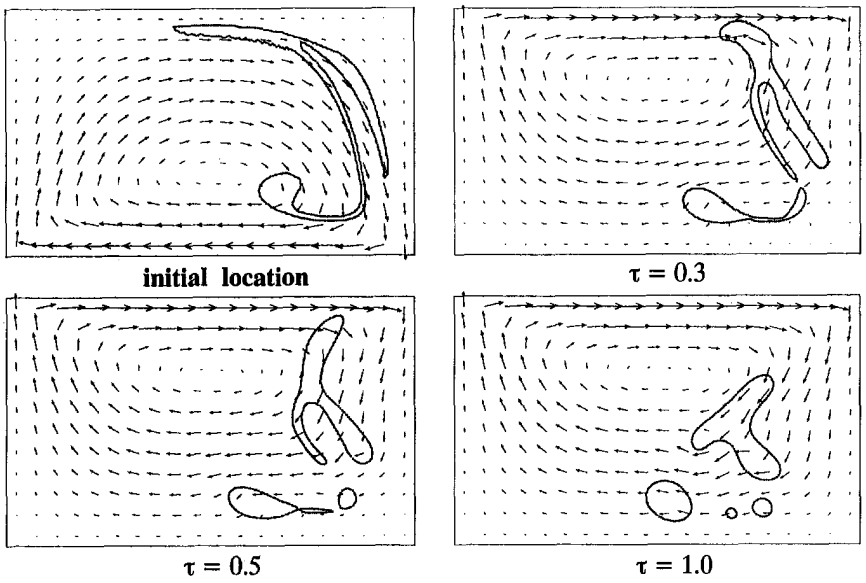


Fig. 7 Sinuous interfacial instabilities and breakup within folds leading to the formation of smaller circular bodies for $A = 0.6$, $C_\mu = 0.2$, $St = 0.16$, and $\sigma^* = 0.5$. (Compare to Fig. 2)

tensions, results show that minor phase clusters act nearly as passive tracers and thereby readily stretch and fold to yield fine-scale interfacial morphologies with lamellar structures. At high interfacial tensions, minor phase clusters can more effectively alter the flow field while undergoing little change in interfacial morphology. At intermediate interfacial tensions, stretching remains effective but folding is suppressed as interfacial tension resists the small curvatures associated with folds. Interactions between multiple minor phase clusters induce changes in mixing rates principally since stretching may be countered by deflected or reduced flows in the vicinity of adjacent interfaces. For low interfacial tensions and prior to the onset of interfacial instabilities, the interfacial morphology under creeping flow conditions is relatively insensitive to phase viscosity ratio within the range $0.2 < C_\mu < 2.0$. As length scales decrease, sinuous instabilities in interfaces arise preferentially near folds and lead to breakup. Such instabilities occur at larger length scales for lower viscosity ratios as found by prior researchers with simpler flow fields. Predicted interfacial morphologies are in good agreement with those observed in micrographs of composite materials produced by chaotic mixing of thermoplastics.

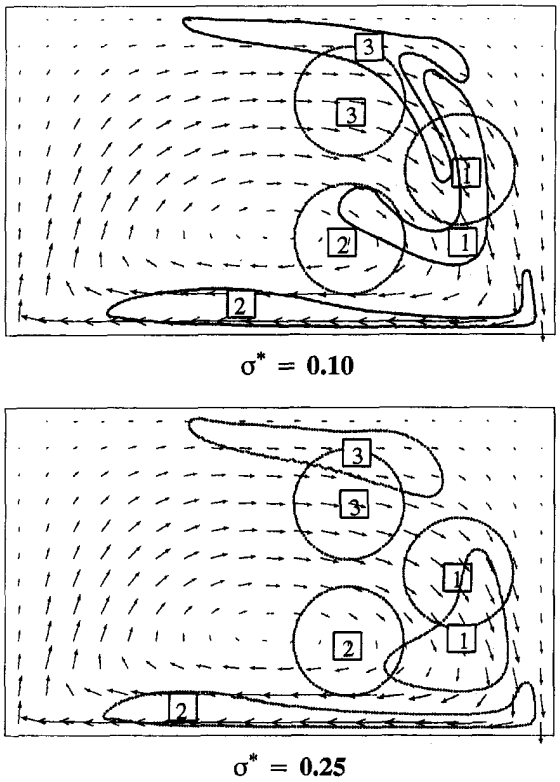


Fig. 8 Influence of interactions between multiple minor phase clusters on interfacial morphology at the completion of one period ($N = 1$) under chaotic mixing conditions with $A = 0.6$, $St = 0.16$, and $C_\mu = 0.2$

Acknowledgment

Support for this work was provided by the National Science Foundation of the United States under grant no. CMS-9253640 and is gratefully acknowledged. The authors also express appreciation to Dr. D. B. Kothe of Los Alamos National Laboratory for useful suggestions.

References

Brackbill, J. U., Kothe, D. B., and Zemach, C., 1992, "A Continuum Method for Modeling Surface Tension," *Journal of Computational Physics,* Vol. 100, pp. 335–354.

Bugg, J. D., and Rowe, R. D., 1991, "Modeling the Initial Motion of Large Cylindrical and Spherical Bubbles," *International Journal for Numerical Methods in Fluids,* Vol. 13, pp. 109–129.

Bugg, J. D., and Rowe, R. D., 1993, "Modeling Large-Bubble Formation at Submerged Orifices," *International Journal for Numerical Methods in Fluids,* Vol. 16, pp. 813–825.

Chan, R. K.-C., and Street, R. L., 1970, "A Computer Study of Finite Amplitude Water Waves," *Journal of Computational Physics,* Vol. 6, pp. 68–94.

Chien, W.-L., Rising, H., and Ottino, J. M., 1986, "Laminar Mixing and Chaotic Mixing in Several Cavity Flows," *Journal of Fluid Mechanics,* Vol. 170, pp. 355–377.

Harlow, F. H., and Welch, J. E., 1965, "Numerical Calculation of Time-Dependent, Viscous, Incompressible Flow of Fluid with Free Surface," *Physics of Fluids,* Vol. 8, pp. 2182–2189.

Hirt, C. W., and Shannon, J. P., 1968, "Free-Surface Stress Condition Incompressible-Flow Calculation," *Journal of Computational Physics,* Vol. 2, pp. 403–411.

Hirt, C. W., and Nichols, B. D., 1981, "Volume of Fluid (VOF) Method for the Dynamics of Free Boundaries," *Journal of Computational Physics,* Vol. 39, pp. 201–225.

Kothe, D. B., Mjolsness, R. C., and Torrey, M. D., 1991, "RIPPLE: A Computer Program for Incompressible Flows with Free Surfaces," Los Alamos National Laboratory Report LA-12007-MS.

Leong, C. W., and Ottino, J. M., 1989, "Experiments on Mixing Due to Chaotic Advection in a Cavity," *Journal of Fluid Mechanics,* Vol. 209, pp. 463–499.

Downloaded 03 Jun 2010 to 171.66.16.125. Redistribution subject to ASME license or copyright; see http://www.asme.org/terms/Terms_Use.cfm

Liu, M., Peskin, R. L., and Muzzio, F. J., 1994a, "Fractal Structure of a Dissipative Particle-Fluid System in a Time-Dependent Chaotic Flow," *Physical Review Letters,* Vol. 50, pp. 4245–4248.

Liu, M., Peskin, R. L., Muzzio, F. J., and Leong, C. W., 1994b, "Structure of the Stretching Field in Chaotic Cavity Flows," *AIChE Journal,* Vol. 40, pp. 1273–1286.

Liu, Y. H., and Zumbrunnen, D. A., 1995, "Emergence of Fibrillar Composites Due to Chaotic Mixing of Molten Polymers," *Proceedings of the 1995 Annual Technical Conference of the Society of Plastics Engineers,* Vol. II, pp. 3104–3108; also: *Polymeric Composites* (in press).

Miles, K. C., Nagarajan, B., and Zumbrunnen, D. A., 1996, "Three-Dimensional Chaotic Mixing of Fluids in a Cylindrical Cavity," ASME JOURNAL OF FLUIDS ENGINEERING (in press).

Ottino, J. M., 1989, *The Kinematics of Mixing: Stretching, Chaos, and Transport,* Cambridge University Press, Cambridge, Great Britain.

Patankar, S. V., 1980, *Numerical Heat Transfer and Fluid Flow,* Hemisphere Publishing, New York.

Rallison, J. M., and Acrivos, A., 1978, "A Numerical Study of the Deformation and Burst of a Viscous Drop in an Extensional Flow," *Journal of Fluid Mechanics,* Vol. 89, pp. 191–200.

Richards, J. R., Beris, A. N., and Lenhoff, A. M., 1993, "Steady Laminar Flow of Liquid-Liquid Jets at High Reynolds Numbers," *Physics of Fluids,* Vol. A5, pp. 1703–1717.

Spalding, D. B., 1972, "A Novel Finite Difference Formulation for Differential Expressions Involving Both First and Second Derivatives," *International Journal of Numerical Methods in Engineering,* Vol. 4, pp. 551–559.

Stone, H. A., and Leal, L. G., 1989, "Relaxation and Breakup of an Initially Extended Drop in an Otherwise Quiescent Fluid," *Journal of Fluid Mechanics,* Vol. 198, pp. 399–427.

Tjahjadi, M., and Ottino, J. M., 1991, "Stretching and Breakup of Droplets in Chaotic Flows," *Journal of Fluid Mechanics,* Vol. 232, pp. 191–219.

Tjahjadi, M., Stone, H. A., and Ottino, J. M., 1992, "Satellite and Subsatellite Formation in Capillary Breakup," *Journal of Fluid Mechanics,* Vol. 243, pp. 297–317.

Vafai, K., and Chen, S. C., 1992, "Analysis of Free Surface Transport Within a Hollow Glass Ampule," *Numerical Heat Transfer, Part A,* Vol. 22, pp. 21–49.

Zumbrunnen, D. A., Miles, K. C., and Liu, Y. H., 1996, "Auto-Processing of Very Fine-Scale Composite Materials by Chaotic Mixing of Melts," *Composites Part A,* Vol. 27A, pp. 37–47.

Downloaded 03 Jun 2010 to 171.66.16.125. Redistribution subject to ASME license or copyright; see http://www.asme.org/terms/Terms_Use.cfm

Evaluation of Algebraic Stress Modeling in Free-Surface Jet Flows

David T. Walker

Chao-Yi Chen

Department of Naval Architecture
& Marine Engineering,
University of Michigan, Ann Arbor, MI
48109-2145

This study evaluated three algebraic stress models for predicting turbulent stresses near the free surface in a free-surface jet at nonzero Froude number, by comparing to experiments. The models examined included one with no explicit near-surface modeling, one which specified model coefficients in terms of invariants of the anisotropy tensor, and a third model which employed a surface correction with an ad-hoc damping function. Experiment showed that at low Froude number, the anisotropy near the free surface did not attain the limiting behavior characteristic of two-dimensional turbulence and the anisotropy increased with streamwise distance. At high Froude number the surface can have little effect on the anisotropy. Far from the free surface, all the models performed well. For the model with no explicit free-surface modeling, the turbulence near the free surface was predicted to be isotropic. For the "anisotropy-invariant" model, the predicted anisotropy was too small and confined to locations too near the free surface. The model with the ad-hoc damping function captured the anisotropy near the free surface best, but specification of the decay constant in the damping function is an open question.

1 Introduction

Great strides have been made in recent years in the direct simulation of turbulence; however, for engineering purposes, Reynolds-averaged turbulence modeling is the generally accepted approach. Large-eddy simulation is the most-likely next step for engineering predictions, but the high Reynolds numbers associated with marine applications (in particular, full-scale ship-related flows) relegate this approach to the distant future. As a result, closure of the Reynolds-averaged Navier-Stokes (RANS) equations, using appropriate turbulence models, is of direct relevance for the foreseeable future in the area of ship hydrodynamics.

Only recently have investigators begun to examine turbulence modeling in the context of free-surface flows. Rodi (1984) discusses it briefly, and proposes that the modeling of terms in the transport equations for the Reynolds stresses can be modified in a manner similar to that in near-wall flow to account for the effect of the free surface (see Naot and Rodi, 1982). Tahara et al. (1991) presented calculations for flow around a ship using a standard k-ϵ model (isotropic eddy viscosity) and observed that the anisotropy of the turbulence near the free surface was not represented by the model. The SURFWAKE program used in calculations of evolving surface-ship wakes (Miner et al., 1988) relies on an algebraic stress model and, in principal, can predict anisotropy in the turbulent stresses; however, free-surface effects are not explicitly modeled. The model proposed by Swean et al. (1991) employs recent ideas on specifying model coefficients in terms of invariants of the anisotropy tensor, and nonlinear behavior in the 'slow' part of the pressure-strain correlation. It was developed using simulation results for open channel flow. Miner et al. (1993) proposed a model which employs a surface correction with an ad-hoc damping function (similar to Naot and Rodi 1982) which captures the effect of the free surface in a turbulent planar free-surface jet.

All of these models have been developed for, and verified in flows with zero, or very low, Froude-numbers. For these cases, the free surface can be treated as a flat shear-free boundary. This requires that the vertical velocity fluctuations vanish at the surface. For finite Froude-number flows, the surface deforms and waves are generated. As a result, the vertical velocity fluctuations are no longer required to vanish at the surface (see Anthony and Willmarth, 1992; Walker et al., 1995).

This study examines the performance of algebraic stress models in predicting non-zero-Froude-number flows. The goals will be to determine overall performance, as well as applicability near the free surface, and the dependence of these characteristics on Froude number. The flows examined will be initially round jets which issue beneath and parallel to the free surface. Two Froude numbers will be examined, one low (but nonzero) and one high. Experimental measurements of the three mean velocities and the six Reynolds stresses reported in Walker et al. (1995) will be used to evaluate the modeling of the Reynolds stresses using three algebraic stress models: the SURFWAKE model, that of Swean et al. (1991), and that of Miner et al. (1993). Using measured velocity statistics, algebraic relationships for the Reynolds stresses can be evaluated. These models use the dissipation rate ϵ for modeling of the turbulent stresses; however, so one piece of information is unknown. Using experimental data for all the Reynolds stresses at a given spatial location, a "best-fit" value for ϵ can be determined which results in the minimum root-mean-square (r.m.s.) error in the predicted Reynolds stresses. The r.m.s. error in the predicted stresses represents the minimum obtainable error for the model in question when compared to the given data.

In what follows, we first examine algebraic stress models, then the data which will be used in the evaluation and, finally, the evaluation of the models is presented.

2 Algebraic Stress Models

Algebraic stress models (Rodi, 1984) require only solution of transport equations for the turbulence kinetic energy $k = \frac{1}{2}\overline{u_i u_i}$ and the isotropic dissipation rate $\epsilon = 2\nu(\partial u_i/\partial x_k)^2$. Algebraic equations for the Reynolds stresses can be derived from the full transport equations for the Reynolds stresses by neglecting advection and both viscous and turbulent diffusion. The resulting equations are of the form:

$$0 = P_{ij} + \Phi_{ij} - \epsilon_{ij} \qquad (1)$$

Contributed by the Fluids Engineering Division for publication in the JOURNAL OF FLUIDS ENGINEERING. Manuscript received by the Fluids Engineering Division October 5, 1994; revised manuscript received June 30, 1995. Associate Technical Editor: D. P. Telionis.

Copyright © 1996 by ASME

Downloaded 03 Jun 2010 to 171.66.16.125. Redistribution subject to ASME license or copyright; see http://www.asme.org/terms/Terms_Use.cfm

where P_{ij} is production of Reynolds stress

$$P_{ij} = -\overline{u_j u_k}\frac{\partial \bar{U}_i}{\partial x_k} - \overline{u_i u_k}\frac{\partial \bar{U}_j}{\partial x_k}, \quad (2)$$

Φ_{ij} is the gain or loss of Reynolds stress due to interaction between the fluctuating pressure and strain fields (the pressure-strain correlations)

$$\Phi_{ij} = \overline{\frac{p}{\rho}\left(\frac{\partial u_i}{\partial x_j} + \frac{\partial u_j}{\partial x_i}\right)}, \quad (3)$$

and ϵ_{ij} is the dissipation tensor

$$\epsilon_{ij} = 2\nu\,\overline{\frac{\partial u_i}{\partial x_k}\frac{\partial u_j}{\partial x_k}}. \quad (4)$$

The latter two of these terms, (3) and (4), contain fluctuating velocity gradients and the fluctuating pressure and require modeling. Launder et al. (1975) decomposed the pressure-strain correlations into three parts

$$\Phi_{ij} = \Phi_{ij}^{(1)} + \Phi_{ij}^{(2)} + \Phi_{ij}^{(S)}. \quad (5)$$

Almost invariably $\Phi_{ij}^{(1)}$ (the slow part) is modeled in the manner proposed by Rotta (1951)

$$\Phi_{ij}^{(1)} = -C_1\epsilon a_{ij} \quad (6)$$

where $a_{ij} = (\overline{u_i u_j} - \frac{2}{3}k)/k$ is the Reynolds-stress anisotropy tensor. The second component (the rapid part) is generally modeled as

$$\Phi_{ij}^{(2)} = -C_2(P_{ij} - \tfrac{2}{3}P\delta_{ij}) - C_3 k S_{ij} - C_4(D_{ij} - \tfrac{2}{3}P\delta_{ij}) \quad (7)$$

(Launder et al., 1975) where

$$P = \frac{1}{2}P_{ii}, \quad S_{ij} = \frac{\partial \bar{U}_i}{\partial x_j} + \frac{\partial \bar{U}_j}{\partial x_i},$$

$$D_{ij} = -\overline{u_j u_k}\frac{\partial \bar{U}_k}{\partial x_i} - \overline{u_i u_k}\frac{\partial \bar{U}_k}{\partial x_j}.$$

Some models include only the first term of (7) while others include only the first two terms. The third term in (5) captures the effects of the free surface. It varies from model to model and so will be discussed below. The C_i coefficients contained in (6) and (7) also are specified in various ways-either as pure constants (Launder et al., 1975) or as functions of various invariants of a_{ij} (e.g., Launder and Shima, 1989). Usually, dissipation is modeled as isotropic

$$\epsilon_{ij} = \tfrac{2}{3}\epsilon\delta_{ij} \quad (8)$$

where $\epsilon = \frac{1}{2}\epsilon_{ii}$.

Substitution of these models, along with appropriate expressions for the constants and $\Phi_{ij}^{(S)}$, into (1) yields algebraic equations for the Reynolds stresses in terms of the mean velocity gradients, k and ϵ. These are then used along with transport equations for k and ϵ to close the RANS equations.

2.1 The SURFWAKE Model. The code SURFWAKE, described by Miner et al. (1988), is used to calculate the evolution of free-surface turbulent flows (in particular, the wakes of surface ships). SURFWAKE is used to solve the parabolized form of the RANS equations along with transport equations for the turbulence kinetic energy k and its dissipation rate ϵ. The algebraic stress model used in SURFWAKE models $\Phi_{ij}^{(1)}$ using (6), models $\Phi_{ij}^{(2)}$ using only the first two terms of (7) and has no surface correction ($\Phi_{ij}^{(S)}$). Dissipation is assumed to be isotropic as shown in (8). The resulting model, as presented in Miner et al. (1988), is

$$\overline{u_i u_j} = \frac{2}{3}k\delta_{ij} + C_2'\frac{k}{\epsilon}\left(P_{ij} - \frac{2}{3}P\delta_{ij}\right) + C_1' C_2'\frac{k^2}{\epsilon}S_{ij} \quad (9)$$

where the constants are $C_1' = 0.16$ and $C_2' = 0.23$.

2.2 The Swean et al. 1991 Model. Swean et al. (1991) proposed modeling for the pressure-strain correlations specifically designed for free-surface turbulent flows. The model was evaluated using the results from a direct simulation of turbulent open-channel flow in the zero-Froude-number limit. They assumed a Rotta-type model for $\Phi_{ij}^{(1)}$ where, following Launder and Shima (1989), the constant is given as $C_1 = 1.3AA_2^{1/4}$. Here, $A = 1 - \frac{9}{8}(A_2 - A_3)$ ($A_2 = a_{ij}a_{ij}$ and $A_3 = a_{ij}a_{jk}a_{ki}$ are the second and third invariants of a_{ij}). The modeling of $\Phi_{ij}^{(2)}$, the portion of the pressure-strain correlations resulting from the mean strain field, retains the first and last terms of the Launder et al. (1975) model with $C_2 = 0.76$ and $C_4 = 0.11$ (both from $c_2 = 0.4$ in the original form of the model), but multiplies both by $A_2^{1/2}$. This yields

$$\Phi_{ij}^{(2)} = -C_2 A_2^{1/2}(P_{ij} - \tfrac{2}{3}P\delta_{ij}) - C_4 A_2^{1/2}(D_{ij} - \tfrac{2}{3}P\delta_{ij}). \quad (10)$$

A near-surface correction is applied in the model presented by Swean et al. (1991). It is given by the following expression:

$$\Phi_{ij}^{(S)} = -C_1\tfrac{9}{8}(A_3 - |A_3|)\epsilon[2.2a_{ij} + 9.8(a_{ik}a_{kj} - \tfrac{1}{3}A_2\delta_{ij})] \quad (11)$$

Here, C_1 is the same as was used in modeling $\Phi_{ij}^{(1)}$, and the constants were chosen for best fit to simulations of turbulent open-channel flow. The term in square brackets includes a Rotta (1951) type term and a nonlinear term similar to that used by Speziale et al. (1991), among others.

2.3 The Miner, Stewart, and Swean 1993 Model. Miner et al. (1993) presented an alternative algebraic stress model and used it to calculate the evolution of the two-dimensional planar surface jet of Swean et al. (1991). In Miner et al. (1993), (6) was used to model $\Phi_{ij}^{(1)}$ and the first term of (7) was used to model $\Phi_{ij}^{(2)}$ with $C_1 = 1.8$ and $C_2 = 0.6$. The effect of the free surface was modeled by

$$\Phi_{ij}^{(S)} = -C_S\frac{\epsilon}{k}\left(\overline{u_n u_n}\delta_{ij} - \frac{3}{2}\overline{u_i u_n}\delta_{nj} - \frac{3}{2}\overline{u_n u_j}\delta_{in}\right)F(l/x_n) \quad (12)$$

where $C_S = 0.6$, l is the length scale of the energy-containing eddies, and x_n is the distance from the surface. The "damping" function is taken as $F = \exp(-4x_n/l)$ with l set equal to one-fourth of the local jet half-width. This is a "wall-reflection" term attributed to Shir (1973) and originating with the work of Daly and Harlow (1970).

The dissipation is modeled as isotropic using (8), but is corrected at the surface to account for observed anisotropy in the normal stress dissipation. The dissipation term including the correction is

$$\epsilon_{ij} = \tfrac{2}{3}\epsilon\delta_{ij} - C_S\epsilon(\delta_{ij} - \tfrac{3}{2}\delta_{nj} - \tfrac{3}{2}\delta_{in})\delta_{ij}F(l/x_n). \quad (13)$$

This model is similar in many respects to that of Naot and Rodi (1982), but has been optimized to some extent for free-surface jet flows.

3 Evaluation of the Reynolds Stress Models

Modeling of the turbulent stresses will be evaluated using three-component laser velocimeter data obtained in a turbulent jet issuing parallel to the free surface. These data were obtained as part of a larger study investigating the turbulent structure in free-surface jet flows (see Walker et al., 1995). Two sets of results will be examined in detail: Those for a single Reynolds number (Re = 12700) and two Froude numbers (Fr = 1.0 and 8.0). In both cases, the jet was located two jet-exit diameters beneath the free surface and, as a result, was fully turbulent

Downloaded 03 Jun 2010 to 171.66.16.125. Redistribution subject to ASME license or copyright; see http://www.asme.org/terms/Terms_Use.cfm

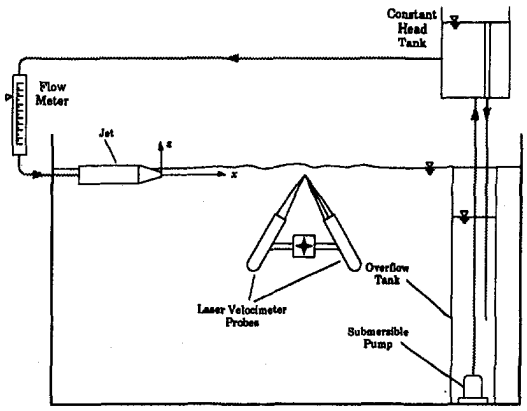


Fig. 1 Schematic of experimental apparatus

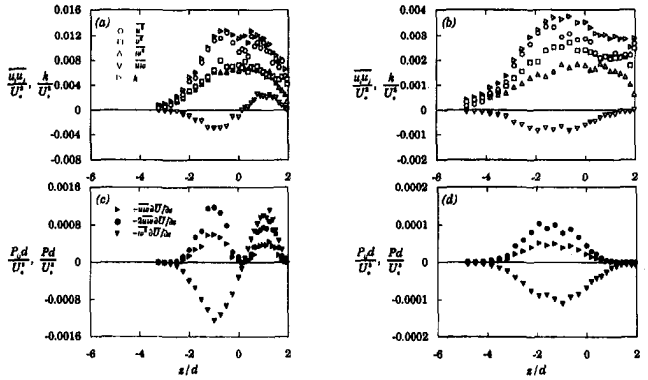


Fig. 3 Profiles of Reynolds stress (±0.03k) and turbulence kinetic energy (±3 percent) for Fr = 1.0 at (a) x/d = 16, and (b) x/d = 32. Profiles of production (±5 percent) for Fr = 1.0 at (c) x/d = 32 and (d) x/d = 1.

where it first interacted with the free surface. The experimental arrangement is shown in Fig. 1. These data show the effect of the free surface on the turbulence structure for extreme differences in Froude number. The high-Froude-number case exhibits large turbulence-generated surface disturbances and a resulting decrease in turbulence kinetic energy. For the low-Froude-number jet, the free-surface behaves more as a flat shear-free boundary. Two streamwise locations will be examined, $x/d = 16$, just downstream of the initial interaction of the jet with the free surface, and $x/d = 32$, where the maximum in the streamwise velocity has reached a location near the free surface.

Vertical profiles of turbulence quantities will be presented for the centerplane of the jet, $y = 0$. These locations were chosen since they show the behavior of the turbulence as the free surface is approached. For these locations, some of the Reynolds stresses and mean velocity gradients are identically zero. This fact will be used in the following analysis. Some of the terms in the model expressions for the individual Reynolds stresses are not identically zero, but make no significant contribution to the model. These terms were identified by ordering the terms in the model expressions. Only the terms of the first two leading orders were retained. This results in model equations for the Reynolds stresses which are applicable for the flow in question and are accurate to roughly one percent.

In the following sections, we first examine the experimental data, and then the performance of each model in turn. For the evaluations, each model was used as specified by the original authors. All quantities to be presented are normalized using the jet exit velocity U_0 and jet diameter d. In all the figures, the jet axis is located at $z/d = 0$ and the free-surface is located at the right edge of the figure, $z/d = 2$.

3.1 Experimentally Determined Quantities. In this section we present the experimental data upon which the evaluation of the turbulent stress modeling will be based. These include the mean velocity profiles ($\bar{U}$, $\bar{W}$), the Reynolds stresses ($\overline{u^2}$, $\overline{v^2}$, $\overline{w^2}$, $\overline{uw}$), and the turbulence kinetic energy (k). Estimates of the production terms and the anisotropy of the Reynolds stresses are also presented.

Estimated uncertainties (95% confidence) are $\pm 0.02\bar{U}$ for the three mean velocity components ($\bar{U}$, $\bar{V}$, $\bar{W}$), $\pm 0.03k$ for the Reynolds stresses ($\overline{u^2}$, $\overline{v^2}$, $\overline{w^2}$, $\overline{uw}$). Uncertainty of the production terms is estimated at 5 percent, due to smoothing associated with the curve-fits used for differentiation (discussed below).

Figure 2 shows vertical profiles of the mean streamwise velocity $\bar{U}$ and the mean vertical velocity $\bar{W}$ for $x/d = 16$ and 32. Figures 2(a) and 2(c) are for $x/d = 16$ and results for $x/d = 32$ are shown in Figs. 2(b) and 2(d). The vertical velocity $\bar{W}$ is at least an order of magnitude smaller than $\bar{U}$. The lines passing through the data are fifth-order polynomial fits to the experimental data used to calculate the necessary derivatives of $\bar{U}$. For all cases the correlation coefficient R^2 was greater than 0.98.

Figures 3 and 4 show the nonzero Reynolds stresses and turbulence kinetic energy on the centerplane of the jet for the low- and high-Froude-number jets, respectively. In both figures, (a) and (b) show the Reynolds stresses for $x/d = 16$ and 32, respectively. These quantities are used to calculate the various production terms, as well as for comparison to the predicted results. The production terms which appear in the expressions for the Reynolds stresses are also shown in Figures 3 and 4 for the low- and high-Froude-number jets, respectively. The

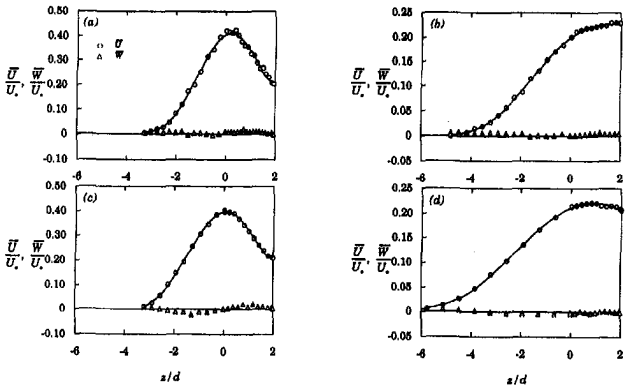


Fig. 2 Vertical profiles of mean velocity $\bar{U}$ (±2 percent) and $\bar{W}$ (±0.02 $\bar{U}$) for (a) Fr = 1.0, x/d = 16; (b) Fr = 1.0, x/d = 32; (c) Fr = 8.0, x/d = 16; (d) Fr = 8.0, x/d = 32

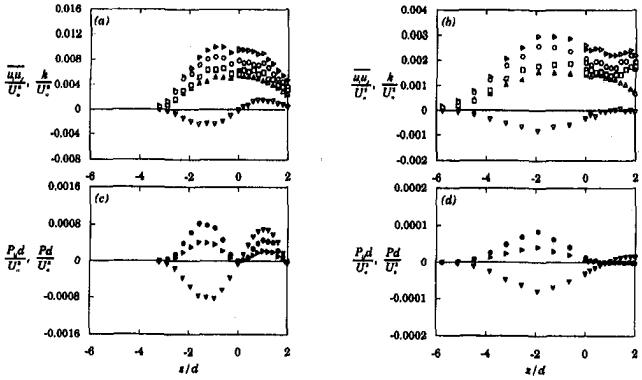


Fig. 4 Profiles of Reynolds stress (±0.03k) and turbulence kinetic energy (±3 percent) for Fr = 8.0 at (a) x/d = 16, and (b) x/d = 32. Profiles of production (±5 percent) for Fr = 8.0 at (c) x/d = 32, and (d) x/d = 1. Symbols as in Fig. 3.

Downloaded 03 Jun 2010 to 171.66.16.125. Redistribution subject to ASME license or copyright; see http://www.asme.org/terms/Terms_Use.cfm

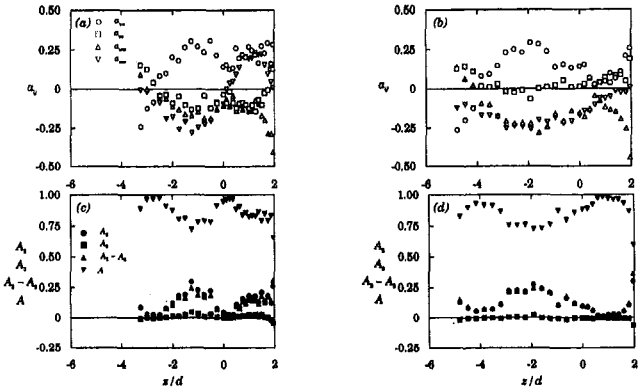


Fig. 5 Reynolds stress anisotropy a_{ij}, anisotropy invariant, and flatness parameter profiles for Fr = 1.0. Anisotropy at (*a*) x/d = 16 and (*b*) x/d = 32. Anisotropy invariant and flatness parameter at (*c*) x/d = 16 and (*d*) x/d = 32.

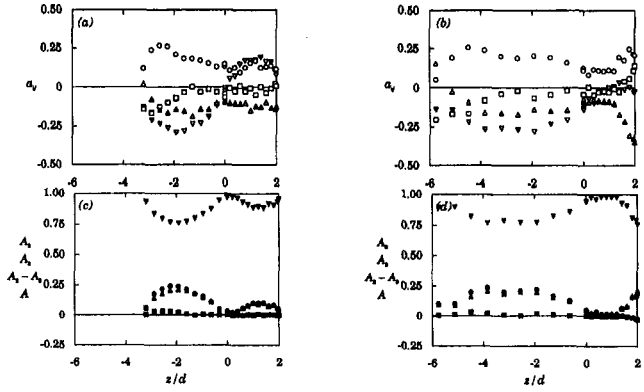


Fig. 6 Reynolds stress anisotropy a_{ij}, anisotropy invariant, and flatness parameter profiles for Fr = 8.0. Anisotropy at (*a*), x/d = 16 and (*b*) x/d = 32. Anisotropy invariant and flatness parameter at (*c*) x/d = 16 and (*d*) x/d = 32. Symbols as in Fig. 5.

production terms are shown in (*c*) and (*d*), for x/d = 16 and 32, respectively. The production term for $\overline{u^2}$, $-2\overline{uw}\partial\bar{U}/\partial z$, is everywhere positive. The production term for the $\overline{uw}$ shear stress, $-\overline{w^2}\partial\bar{U}/\partial z$, is negative for locations below the maximum $\bar{U}$ and positive above. Also shown is the production term for k, $-\overline{uw}\partial\bar{U}/\partial z$.

Recent attempts at modeling the pressure-strain correlations (Swean et al., 1991, Speziale et al., 1991, and others) have made use of the anisotropy tensor a_{ij} and its various invariants (A_2, A_3) as well as the "flatness" function A presented above. Figures 5 and 6 show these quantities on the centerplane. In both figures, (*a*) and (*b*) show the elements of the anisotropy tensor a_{ij} for x/d = 16 and 32, respectively. At both locations for the low Froude number the anisotropy in $\overline{u^2}$ and $\overline{v^2}$ rises and that of $\overline{w^2}$ decreases as the free surface is approached. The region in which these changes occurs is about twice as large at x/d = 32 as it is at 16, roughly following the growth of the characteristic length scale of the jet. For the high-Froude-number jet, the anisotropy is largely unaffected by the free surface at x/d = 16. However, at x/d = 32, the near-surface behavior is similar to that of the low-Froude-number jet. These results show that the anisotropy of the turbulence at the free surface is strongly dependent on the Froude-number and evolves in the streamwise direction-with the turbulence becoming more anisotropic with increasing distance downstream.

Figures 5 and 6, (*c*) and (*d*) show quantities related to the invariants of a_{ij}. In these results, A_3 is near zero everywhere except near the free-surface, where it becomes slightly negative (except for x/d = 16 at high Froude number). This indicates that the turbulence is approaching two-component, isotropic turbulence at the surface. For all the cases, except x/d = 16 at high Froude number, A_2 increases as the surface is approached indicating that the turbulence is becoming more anisotropic. The quantity ($A_2 - A_3$) is also shown and it rises near the surface but does not reach the limiting value of $\frac{8}{9}$ for two-component turbulence. The maximum value attained is about 0.3 at x/d = 32 for the low-Froude-number jet. The flatness parameter A remains larger than about 0.75, except near the free surface in the low-Froude-number jet. It decreases only to about 0.5 for x/d = 32 in this case.

3.2 Evaluation of the Stress Models. We now examine the behavior of the models presented above. In the results to be presented, estimates of ϵ have an uncertainty of roughly 7 percent when calculated using all four Reynolds stresses with Eq. (6) and (7) substituted into Eq. (5), and Eqs. (5), (8), and (2) then substituted into (1). The resulting estimates of the individual Reynolds stresses will have an uncertainty of roughly $\pm 0.05k$, again based on (1). This would yield an r.m.s. error of roughly ± 0.075 in the estimates of all the Reynolds stresses at a given location when normalized with $2k/3$ (the form in which they will be presented below). Hence, an r.m.s. error in the predicted Reynolds stresses larger than about 0.07–0.08 (normalized with $2k/3$) represents a failure of the model

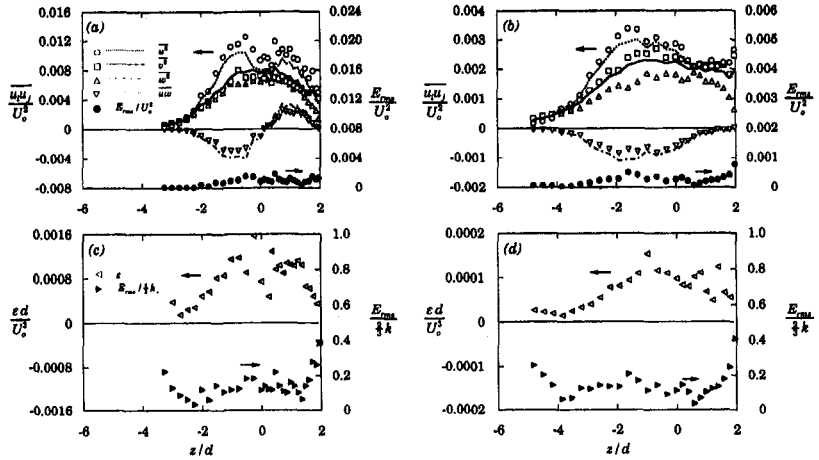


Fig. 7 Performance of the SURFWAKE model for Fr = 1.0: Reynolds stress and absolute error at (*a*) x/d = 16 and (*b*) x/d = 32. Symbols represent experimental data; lines represent model prediction. Best fit dissipation and relative error at (*c*) x/d = 16 and (*d*) x/d = 32.

Downloaded 03 Jun 2010 to 171.66.16.125. Redistribution subject to ASME license or copyright; see http://www.asme.org/terms/Terms_Use.cfm

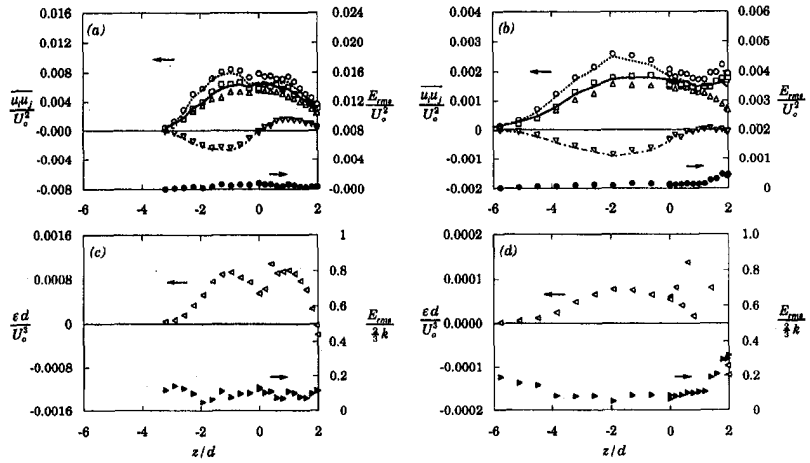


Fig. 8 Performance of the SURFWAKE model for Fr = 8.0: Reynolds stress and absolute error at (*a*) $x/d = 16$ and (*b*) $x/d = 32$. Symbols represent experimental data; lines represent model prediction. Best fit dissipation and relative error at (c) $x/d = 16$ and (*d*) $x/d = 32$. Symbols and lines as in Fig. 7.

in question to capture the observed behavior. Errors smaller than this can be attributed to the uncertainty of the experimental data being used for comparison.

Figures 7 and 8 show the results from the SURFWAKE model for the four sets of data. The experimentally determined Reynolds stresses are plotted in (a) and (b) along with lines representing the model predictions for the stresses. Also shown in (a) and (b) is the r.m.s. error incurred in the Reynolds stress predictions. The error is scaled identically to the Reynolds stresses and plotted on the same scale, therefore it indicates the absolute error in the predictions. In all the cases, due to the limitations of the model, the predicted $\overline{v^2}$ and $\overline{w^2}$ levels are identical; they also lie between the experimental values. As the free surface is approached, the prediction for $\overline{u^2}$ converges to that for the other two normal stresses, and the turbulence is modeled as isotropic. This results from the absence of production near the surface. For $x/d = 16$ at the high Froude number (Fig. 8(a)) this behavior is correct; however, in the other cases the anisotropy due to the free surface is not captured. The Reynolds shear stress $\overline{uw}$ is predicted quite well by this model across the entire flow, since it is not significantly affected by the free surface.

Figures 7 and 8, (c) and (d) show the estimated dissipation and the relative error in the predictions of the Reynolds stresses for the four cases. Some of the estimated dissipation values are outside the range of the plot. This can occur when one or more components of the anisotropy tensor and the associated production rates approach zero. Under these conditions ϵ is nearly indeterminate. Also notable is the occurrence of negative values for dissipation. Since ϵ is a positive-definite function, this makes no sense physically; however, in the context of the models examined here, the occurrence of negative dissipation simply indicates that the model does not capture some source of Reynolds stress which exists in the flow. This could be due to inadequate modeling assumptions or the inappropriate specification of a model parameter. The negative values for dissipation (which occur only near the free surface) indicate the failure of this particular model to adequately capture free-surface effects. The relative error shown in (c) and (d) shows that the model does well modeling the Reynolds stresses far from the free surface, with r.m.s. error approaching that due to the uncertainty of the data (0.07–0.08). Near the free surface, the error rises to as much as 0.4 in the low-Froude-number case (Fig. 7(c, d)).

Figures 9 and 10 show the results from the Swean et al. (1991) model. In all the cases, the predicted $\overline{v^2}$ and $\overline{w^2}$ levels are different due to the inclusion of the third term in (7) in the model for $\Phi_{ij}^{(2)}$. This results in improved performance and re-

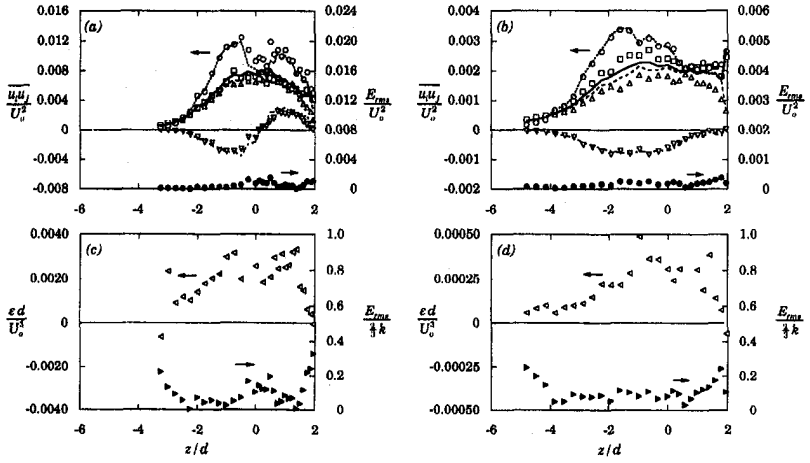


Fig. 9 Performance of the Swean et al. (1991) model for Fr = 1.0: Reynolds stress and absolute error at (*a*) $x/d = 16$ and (*b*) $x/d = 32$. Symbols represent experimental data; lines represent model prediction. Best fit dissipation and relative error at (c) $x/d = 16$ and (*d*) $x/d = 32$. Symbols and lines as in Fig. 7.

Downloaded 03 Jun 2010 to 171.66.16.125. Redistribution subject to ASME license or copyright; see http://www.asme.org/terms/Terms_Use.cfm

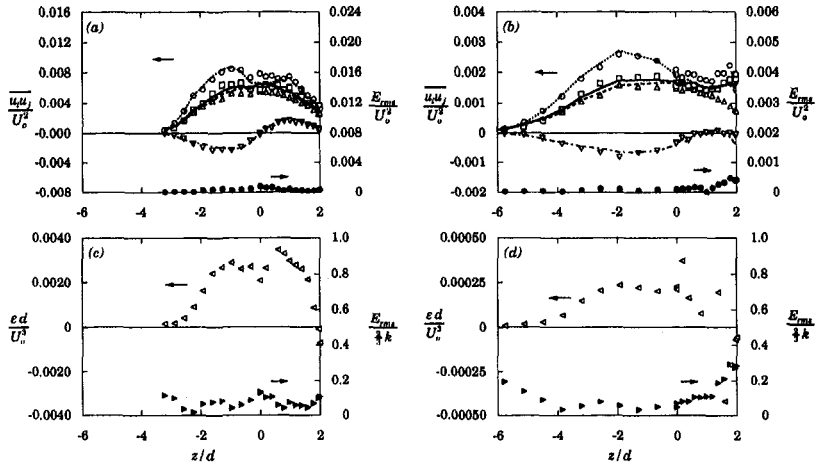


Fig. 10 Performance of the Swean et al. (1991) model for Fr = 8.0: Reynolds stress and absolute error at (*a*) $x/d = 16$ and (*b*) $x/d = 32$. Symbols represent experimental data; lines represent model prediction. Best fit dissipation and relative error at (c) $x/d = 16$ and (*d*) $x/d = 32$. Symbols and lines as in Fig. 7.

duces the r.m.s. error in all cases below that seen for the SURFWAKE model. At $x/d = 16$ for high Froude number (Figure 10(*a*)), as the free surface is approached, the prediction for $\overline{u^2}$ converges to that for the other two normal stresses, and the turbulence is modeled as isotropic. For the low-Froude-number case (Fig. 9(*a*)) some anisotropy is seen in $\overline{w^2}$ but there is still a relative error of more than 0.3. For low Froude number at $x/d = 32$ (Fig. 9(*b*)) the anisotropy due to the free surface is captured, but the layer is too thin. The small vertical extent of this region reflects the behavior of A_3 shown in Fig. 6(*d*). (The near-surface turbulence modeling is only active for $A_3 < 0$.) For the high-Froude-number case (Fig. 10(*b*)) at the free surface, A is relatively large and A_3 is nearly zero. As a result, the anisotropy of the predicted Reynolds stresses is small for this case. Again, the Reynolds shear stress $\overline{uw}$ is predicted quite well across the entire flow.

Figures 9 and 10, (*c*) and (*d*) show the estimated dissipation and the relative error in the predictions of the Reynolds stresses for the four cases. There is still negative dissipation in the near surface region which indicates that additional modeling is required. In general the dissipation levels are higher (by a factor of 2.5) than those obtained with either of the other two models. This is due to the effective magnitude of C_1 (the Rotta constant) for this model. (The magnitude of the estimated dissipation will be inversely proportional C_1. In the context of algebraic stress models, only the relative magnitudes of the various C_i affect the result. The absolute dissipation levels for the flow are unknown, and so this ambiguity is tolerated.) The relative error shown in (*c*) and (*d*) shows that near the free surface, the error has decreased to about 0.3, or less—a small performance improvement relative to the predictions based on the SURFWAKE model.

Figures 11 and 12 show the results from the Miner et al. (1993) model. In all the cases, the predicted $\overline{v^2}$ and $\overline{w^2}$ levels are again the same since the modeling of $\Phi_{ij}^{(2)}$ is identical to that for the SURFWAKE model for these stresses. As a result, the performance well below the surface is similar to that seen in the SURFWAKE model. For all cases the anisotropy of the Reynolds stresses is captured quite well and the r.m.s. error is lower near the free surface than for either of the other models. Relative errors less than 0.2 are obtained near the surface for all cases, with little in the way of negative dissipation. This indicates that the model is capturing more of the dynamics at the free surface. Just below the free surface the error increases slightly. This is due to an overly large decay constant in the damping function F in (13).

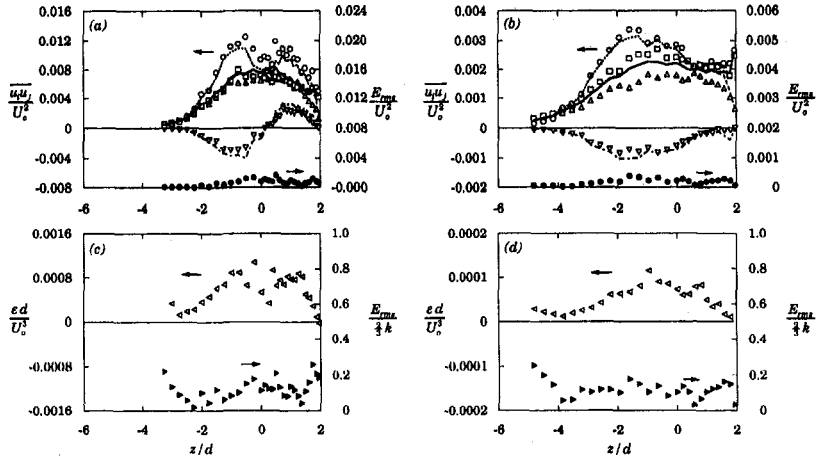


Fig. 11 Performance of the Miner et al. (1993) model for Fr = 1.0: Reynolds stress and absolute error at (*a*) $x/d = 16$ and (*b*) $x/d = 32$. Symbols represent experimental data; lines represent model prediction. Best fit dissipation and relative error at (c) $x/d = 16$ and (*d*) $x/d = 32$. Symbols and lines as in Fig. 7.

Downloaded 03 Jun 2010 to 171.66.16.125. Redistribution subject to ASME license or copyright; see http://www.asme.org/terms/Terms_Use.cfm

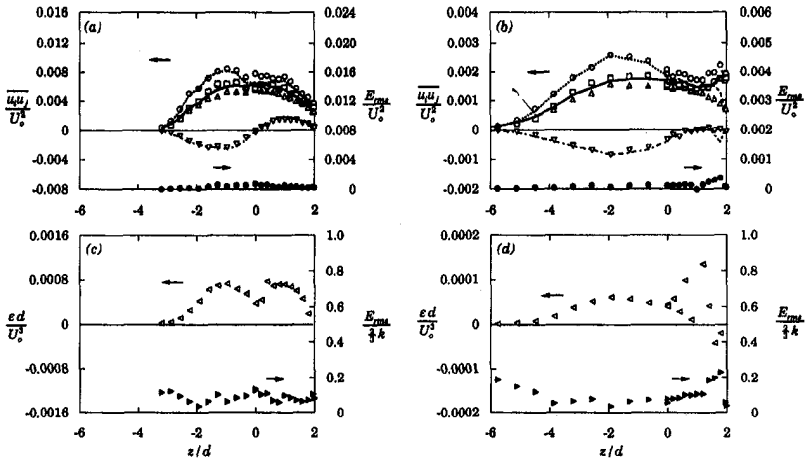


Fig. 12 Performance of the Miner et al. (1993) model for Fr = 8.0: Reynolds stress and absolute error at (*a*) $x/d = 16$ and (*b*) $x/d = 32$. Symbols represent experimental data; lines represent model prediction. Best fit dissipation and relative error at (*c*) $x/d = 16$ and (*d*) $x/d = 32$. Symbols and lines as in Fig. 7.

4 Summary and Conclusions

This study evaluated three algebraic stress models for predicting turbulent stresses near a free surface in a turbulent free-surface jet by comparing to experimental data. The measurements were done at a single Reynolds number and a low and a high Froude number. The models examined included one with no near-surface modeling (the SURFWAKE model), one which employed recent ideas on the specifying model coefficients in terms of invariants of the anisotropy tensor, and nonlinear behavior in the slow part of the pressure-strain correlation (Swean et al., 1991), and a third model which employed a surface correction with an ad-hoc damping function (Miner et al., 1993).

Experimental results showed that, at high Froude numbers, there was no significant anisotropy introduced by the free surface initially, but the anisotropy evolved with downstream distance. For low Froude number the anisotropy was larger, and increased with downstream distance. For all cases $(A_2 - A_3)$ was less than 0.3 and did not approach the limiting value of $\frac{8}{9}$ for two-dimensional turbulence near the surface. The flatness parameter remained larger than 0.75 for all cases and did not approach zero at the free surface. This is because in these finite-Froude-number flows, the vertical velocity fluctuations are small, but do not vanish.

All the models predicted well the near-surface behavior for the high-Froude-number jet at $x/d = 16$. At this location, there was no significant anisotropy caused by the free surface and, hence, no near-surface modeling is needed. The SURFWAKE model predicted well the stresses far from the free surface, (the r.m.s. errors approached the experimental accuracy) but did not capture the strong anisotropy near the free surface, nor the mild anisotropy far from the free surface. The Swean et al. (1991) model captured the anisotropy far from the free surface due to better modeling of the rapid portion of the pressure-strain correlation, but the region affected by the free surface was too thin and the predicted anisotropy was smaller than seen in the experiments. This is due to the behavior of A_3 (used in the near-surface modeling) as the surface is approached. For both these models, negative dissipation occurred near the free surface; this indicates that there is a near-surface stress production mechanism which is not accounted for in the models. Finally, the model of Miner et al. (1993) captures the anisotropy near the free surface better than the Swean et al. model, but the decay constant in the model is too large and, as a result, the region of anisotropy near the free surface is again too thin. With this model, however, little negative dissipation was seen.

Acknowledgment

This work was supported by the Fluid Dynamics Program of the Office of Naval Research under Grant No. N00014-92-J-1750, monitored by Dr. E. P. Rood. The helpful comments and guidance of T. F. Swean of the Office of Naval Research were greatly appreciated.

References

Anthony, D. G., and Willmarth, W. W., 1992, "Turbulence Measurements in a Round Jet Near a Free Surface," *Journal of Fluid Mechanics,* Vol. 243, pp. 699–720.

Daly, B. J., and Harlow, F. H., 1970, "Transport Equations of Turbulence," *Physics of Fluids,* Vol. 13, p. 2634.

Launder, B. E., and Shima, N., 1989, "A Second Moment Closure for the Near-Wall Sublayer: Development and Application," *AIAA Journal,* Vol. 27, pp. 1319–1325.

Launder, B. E., Reece, G. J., and Rodi, W., 1975, "Progress in Development of a Reynolds-Stress Closure," *Journal of Fluid Mechanics,* Vol. 68, pp. 537–566.

Miner, E. W., Stewart, M. B., and Swean, T. F., 1993, "Modeling and Computation of Turbulent Free-Surface Jets," AIAA Paper No. 93-0201.

Miner, E. W., Swean, T. F., and Troesch, A. W., 1988, "Evaluation and Additional Documentation of the Parabolic Marching Code SURFWAKE," NRL Memorandum Report 6331, Naval Research Laboratory, Washington, D.C.

Naot, D., and Rodi, W., 1982, "Calculation of Secondary Currents in Channel Flow," *Journal of the Hydraulics Division* ASCE, Vol. 108, pp. 948–968.

Rodi, W., 1984, *Turbulence Models and their Application in Hydraulics,* IAHR, Delft.

Rotta, J. C., 1951, "Statistiche Theorie nichtmonger Turbulenz," *Z. Physics,* Vol. 129, p. 547.

Shir, C. C., 1973, "A Preliminary Model of Atmospheric Turbulent Flow in an Idealized Turbulent Boundary Layer," *Journal of Atmospheric Science,* Vol. 30, pp. 1327–1329.

Speziale, C. G., Sarkar, S., and Gatski, T. B., 1991, "Modeling the Pressure-Strain Correlation of Turbulence: An Invariant Dynamical Systems Approach," *Journal of Fluid Mechanics,* Vol. 227, pp. 245–272.

Swean, T. F., Leighton, R. I., Handler, R. A., and Swearingen, J. D., 1991, "Turbulence Modeling Near the Free Surface in Open Channel Flow," AIAA Paper No. 91-0613.

Swean, T. F., Ramberg, S. E., and Miner, E. W., 1991, "Anisotropy in a Turbulent Jet Near a Free Surface," ASME JOURNAL OF FLUIDS ENGINEERING, Vol. 113, pp. 430–438.

Tahara, Y., Stern, F., and Rosen, B., 1991, "An Interactive Approach for Calculating Ship Boundary Layers and wakes for Nonzero Froude Number," *Eighteenth Symposium on Naval Hydrodynamics,* National Academy Press, Washington, D.C., pp. 699–719.

Walker, D. T., Chen, C.-Y., and Willmarth, W. W., 1995, "Turbulent Structure in Free-Surface Jet Flows," *Journal of Fluid Mechanics,* Vol. 291, pp. 223–262.

Downloaded 03 Jun 2010 to 171.66.16.125. Redistribution subject to ASME license or copyright; see http://www.asme.org/terms/Terms_Use.cfm

The Structure of Shear Driven Mixing With an Unstable Thermal Stratification

D. M. Snider

M. J. Andrews

Department of Mechanical Engineering,
Texas A&M University,
College Station, TX 77843

A water channel experiment was used to study the turbulent mixing structure of shear and buoyancy. Density differences between fluid layers were produced by thermal stratification. The experiment was statistically steady and provided a long time period to study the mixing behavior and record data. The mixing process was studied using dye and digitized photographs. Individual images gave a two-dimensional view of the mixing structure. An ensemble average of images gave averaged mixing layer growth rate and the distribution of light and heavy fluid in the mixing layer. The experiment gave a space-time transformation in the streamwise direction which permitted a continuous study of the mixing evolution. The structure of the early growth of a compound shear and buoyancy mixing layer is presented. For the range of flows (ΔU = 0 to 1 cm/s) and density differences (0.38 to 2.4 kg/m^3), buoyancy was the dominant mixing mechanism.

Introduction

Free shear mixing can be accompanied by buoyancy mixing. Unstable thermal stratification occurs in both environmental and in industrial processes (Sharp, 1984). Shear and buoyancy mixing occurs in nature from effluent discharge into rivers and estuaries or from the flow of rivers into lakes, reservoirs or the ocean (Turner, 1973). Furnaces and combustion chambers introduce cool fuel mixtures over hot gasses, and chemical reactors mix chemicals of different densities. Swirl in pipes and internal combustion engines produces an unstable thermal layer and promotes heat transfer (Dhir and Chang, 1992).

A shear layer forms when two streams of different velocity come in contact. In the shear layer, Kelvin-Helmholtz instabilities lead to quasi-two-dimensional spanwise vortices (rollers) (Brown and Roshko, 1974; Dimotakis and Brown, 1976; Lasheras and Choi, 1988). Superimposed on the spanwise eddies are counter rotating streamwise vortices (Lasheras and Choi, 1988). The large coherent structures initially produce little global mixing (Koochesfahani and Dimotakis, 1986). As the mixing width grows, the effect of initial condition is lost as structures pair, giving larger structures. A "mixing transition" is reached where small scale, vigorous turbulence produces a well mixed state (Roshko, 1991).

Buoyancy mixing is produced by a unstable density stratification that produces a pressure imbalance normal to the interface as opposed to shear flow which results from tangential forces. A density difference with the potential energy of heavy fluid above light fluid under gravity, produces small Rayleigh-Taylor instabilities at the interface which grow exponentially (Taylor, 1950; Chandrasekhar, 1961). Short wavelength perturbations appear first. As the wave's amplitude becomes significant compared with its wavelength, the instability saturates and the growth rate slows. Longer wavelength perturbations continue their exponential growth and overtake shorter waves, so that successively larger wavelengths dominate the mixture growth rate. Interaction between growing structures leads to "bubble" combination or pairing (Emmons et al., 1963) which produces even larger structures. As the mixture evolves, the memory of the initial perturbation is lost and a similarity behavior is expected.

Limited experimental data are available on compound shear and buoyancy mixing layers. Lawrence et al. (1991) described the visual character of an unstable density, shear layer. The flow was observed to initially develop as a free shear layer and eventually transform to large billows characteristic of buoyancy. This paper presents experimental observations on compound buoyancy and shear mixing in a plane layer. The structure of compound mixing is contrasted with shear or buoyancy mixing alone. An ensemble average of images is used to quantify the average distribution of fast and slow and heavy and light fluids in the mixing layer.

Experiment

Experiment Apparatus and Operation. The experimental system used in this study resembled that used in free shear layer studies. The system is illustrated in Fig. 1. Two water streams at different temperatures flow parallel to each other separated by a thin splitter plate. At the end of the splitter plate, the flows meet. An unstable interface forms and buoyancy mixing begins. If the velocities are different, a compound buoyancy and shear mixing layer forms. It can be shown that this statistically steady problem is parabolic in the streamwise direction if the mixing spread angle is small. The time axis, which is associated with a buoyant mixing layer, is transformed by $t = x/U$, where x is the axial distance and U is the mean axial velocity.

The apparatus consisted of an inlet and exit plenum connected by a Plexiglas flow channel. The channel was 30.5 cm wide, 38 cm deep and 244 cm long. The flow area was adjusted by adding a vertical divider and a floor. Figure 1 shows the two channel cross sections used in this study. One cross section width was 11.4 cm and the other was 15.4 cm. The inlet plenum was divided into two compartments. One section fed cold water, and the other fed hot water to the test channel. A Plexiglas horizontal "splitter" plate extending from the channel entrance to the start of the test section separated the incoming hot and cold water. The splitter plate was 0.32 cm thick, 89 cm long, and had a 2.5 deg knife edge at the end. The test section following the splitter plate was 155 cm long.

Cold water was supplied to the upper inlet plenum, and hot and cold water were supplied to the lower inlet plenum. The cold water was pumped from storage tanks. Hot water was taken

Contributed by the Fluids Engineering Division for publication in the JOURNAL OF FLUIDS ENGINEERING. Manuscript received by the Fluids Engineering Division May 27, 1994; revised manuscript received June 6, 1995. Associate Technical Editor: M. Gharib.

Copyright © 1996 by ASME

Downloaded 03 Jun 2010 to 171.66.16.125. Redistribution subject to ASME license or copyright; see http://www.asme.org/terms/Terms_Use.cfm

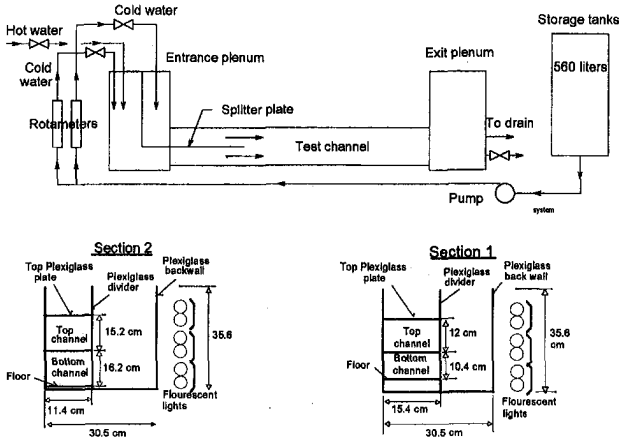


Fig. 1 Experimental system

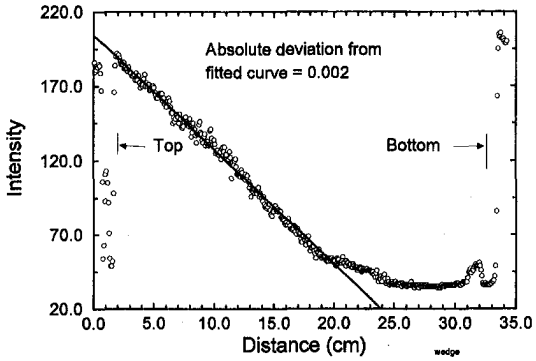


Fig. 2 Calibration wedge measured intensity versus concentration (distance along wedge)

from a hot water heater connected to the building water supply. The separated channels each contained screens and flow straighteners to produce a uniform flow, dissipate free stream turbulence, and minimize the boundary layer on the splitter plate and walls (Koop, 1976). The cold water flow rates were measured by calibrated rotameters. The hot water flow rate was measured from the time to fill a known size container. The test section was back lit with a row of 6 fluorescent lamps. Drafting paper velum was placed against the Plexiglas divider wall to diffuse the light. Nigrosene dye was added to one channel, and the mixing layer photographed. The fluid temperatures in the hot and cold channels were measured using thermocouples and a digital meter.

A problem in our test system was bubbles forming on screens, walls and in the flow straighteners. Prior to starting a test, a water jet was used to clean all screens and walls. The flow rate for no shear tests was adjusted so that the fluid interface between streams was visually flat (no Kelvin-Helmholtz waves). This procedure indicated flow velocities above and below the interface were close, and was more precise than setting the flow rates solely using the rotameters. A density difference (temperature difference) was added to the flows and the mixing layer was photographed at approximately 20 s intervals. Photographs were digitized using a scanner. Using a calibration wedge filled with water and dye, the scanned intensities (pixel values) were found to be linearly proportional to concentration over a wide intensity range as shown in Fig. 2. From 6 to 25 photographs were taken for each test. The digitized images were processed to eliminate non-uniform back-lighting and to linear map images to the same reference location. Images were then ensemble averaged.

Method of Mixture Fraction Measurement. The mixing structure is observed using a passive scalar (dye). Dye was introduced in one stream, and as the streams mixed, the dye dispersed. A measure of the average distribution of the upper and lower streams in the mixing layer can be made from the dye in terms of the mixture fraction, defined as:

$$f_1 = \frac{V_1}{V} \tag{1}$$

where V_1 is the volume occupied by fluid from stream 1 and V is the total volume. The measured minimum intensity (dark) corresponds to a mixture fraction of 0, and the maximum intensity (clear) corresponds to a mixture fraction of 1. Andrews and Spalding (1990) used a densitometer (measured transmitted light) to measure the mixture fraction from photographic negatives. In this study, a scanner (measures reflected light) is used to measure the intensity and a discussion of the process is given by Snider and Andrews (1994). From the linear relation between digitized intensity and concentration (color-wedge data), the mixture fraction in terms of the intensity is

$$f_1(x, y) = \frac{i(x, y) - i_{\min}}{i_{\max} - i_{\min}} \tag{2}$$

where i is the ensemble averaged intensity at position (x, y), and $i_{\min}$ and $i_{\max}$ are the ensemble average minimum and maximum intensities outside the mixing layer. The mixture fraction for the other stream is $f_2 = 1 - f_1$.

Figure 3 shows the ensemble average warm fluid mixture fraction variation across the channel at two axial locations. The mixing is from pure buoyancy. The mixture fraction varies approximately linearly across the mixing region with a diffusion like profile at the edges. The linear mixture fraction variation indicates that, in the ensemble average of the turbulent mixing process, cold and hot water are near linearly distributed across the mixing layer.

Method of Mixing Width Measurement. The mixing width envelope is a common measured parameter in plane mixing layers and provides information on the average growth rate

Nomenclature

A = Atwood number = $(\rho_2 - \rho_1)/(\rho_2 + \rho_1)$
f_1, f_2 = mixture fraction of fluids 1 and 2
g = gravity acceleration
h = mixture half width
$i(x, y)$ = intensity at location x, y in the image (8 bits)
$i_{\max}$ = maximum intensity outside the mixing layer
$i_{\min}$ = minimum intensity outside the mixing layer
t = time or time scale $t = 2x/(U_1 + U_2)$
τ = time constant $\tau = \Delta U/Ag$
Ri = Richardson number Ri = $(hgA/\Delta U^2)$
U_1, U_2 = freestream velocity for fluids 1 and 2
U = freestream mean velocity $(U = (U_1 + U_2)/2)$
V = volume
x = distance from end of splitter plate
x_0 = the projected virtual origin where the mixture width goes to zero
α = acceleration constant in the buoyancy equation
η = nondimensional similarity time for buoyancy $\eta = (gA/W)[(x - x_0)/U]^2$
ρ_1, ρ_2 = density of fluids 1 and 2

Downloaded 03 Jun 2010 to 171.66.16.125. Redistribution subject to ASME license or copyright; see http://www.asme.org/terms/Terms_Use.cfm

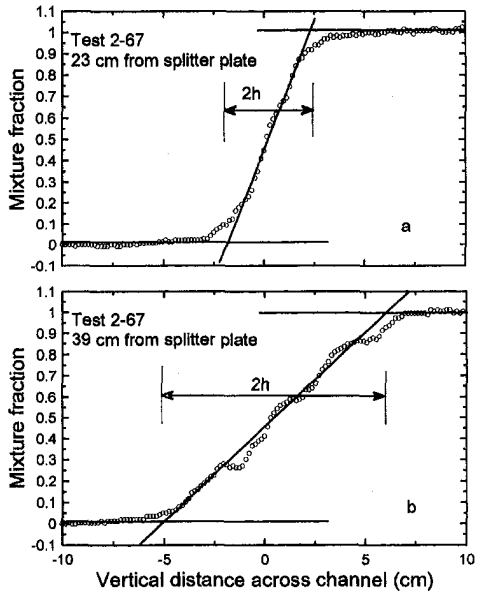


Fig. 3 Mixture fraction distribution across the mixing layer. Test 2-67: U_t = 4.4 cm/s, U_b = 4.4 cm/s, Atwood no. = 0.00080. (*a*) 23 cm from splitter plate, (*b*) 39 cm from splitter plate.

of structures, the amount of entrainment into the mixing region and to some extent the degree of mixing. An automatic method to measure the mixing width from mixture fraction data is used. If the mixing width is less than 60 percent of the channel vertical height, many sets of data around the original interface are linearly fitted using an absolute deviation. The set with the most data and a deviation below a prescribed small deviation is chosen to represent data in the mixing region. The mixture width is the distance between the intersection of the best fit line through the data set and the two horizontal lines through mixture fractions of zero and unity. This method is illustrated in Figure 3. If the criterion for fitting fails, the mixing width is determined manually. For mixture widths greater than or equal to 60 percent the channel height, the mixture width is measured between the locations of 0.05 and 0.95 mixture fraction. The mixture fraction profile and consequently the mixture width is measured from the ensemble average image.

Mixture half width data, h, are presented normalized by the vertical channel width, W, of test Section 1 (W = 31.4 cm). The axial channel distance is transformed to time, $t = (x - x_0)/U$, where x is the axial distance offset by a virtual origin x_0, and U is the mean axial fluid velocity. Mixing width data are plotted versus the buoyancy similarity variable:

$$\eta = \frac{gA}{W}\left(\frac{x - x_0}{U}\right)^2 \qquad (3)$$

where A is the Atwood number defined as $A = (\rho_2 - \rho_1)/(\rho_2 + \rho_1)$ and g is gravity. A larger Atwood number (larger density difference) gives a larger buoyancy driven mixing.

The effect of sample size on the mixture width is evaluated by comparing the mixture width from 25 averaged images to widths from 5, 10 and 15 averaged images for the same test. Figure 4 compares the mixture width data for the four sample sizes. An average of 10 and 15 images gives nearly the same mixture width as 25 averaged images. For large flow structures, the mixture width from 5 averaged images is observed to vary from that from 25 averaged images (at the right in Fig. 4).

The size of samples was limited by the work involved in processing images. The ensemble average from 10 to 25 samples used in this study produced reasonably invariant mixture widths. A higher sample rate is expected to produce the same

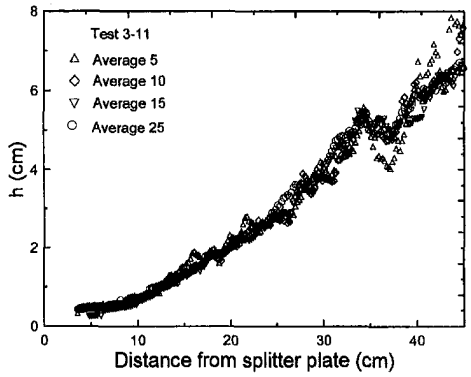


Fig. 4 Effect of number of images in average on the mixing width. Test 3-11: U_t = 4.1 cm/s; U_b = 4.7 cm/s; Atwood no. = 0.00078.

mixture widths with smoother curves. While the averaged data curves show some fluctuations, such as seen in Figure 4, the curves follow repeatable mixture growth patterns when compared with other tests.

The intensity density population (histogram) provides an estimate of the error in measuring concentration from intensity (Andrews and Spalding, 1990). The population density curve has two spikes. One at the minimum intensity corresponding to the dyed layer of water and one at the maximum intensities corresponding to the undyed layer of water. The gradation between the peaks is the mixing layer. The lower side of the minimum peak and the upper side of the maximum peak ideally should have a step change (dyed and undyed layers should be at a constant concentration giving a single intensity). Variation from a step represents an error in measured concentration of either warm or cold fluid at each measurement time (over the entire test section). Population densities for the tests are given by Snider (1994), and the percent variation over the measured intensity ranged from 3 to 7 percent.

The Structure of the Developing Buoyancy and Shear Mixing Layers

Photographs in Fig. 5(*a*), 5(*b*), and 5(*c*) show the side view of the mixing layer from shear alone, compound shear and

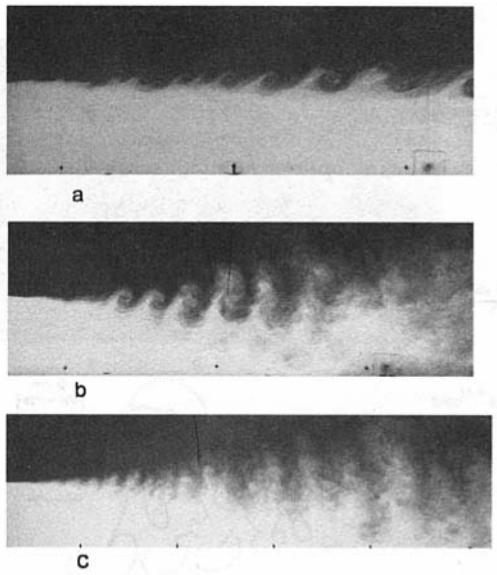


Fig. 5 (*a*) Test 3-13, U_t = 5.2 cm/s, U_b = 3.8 cm/s, Atwood no. = 0, (*b*) Test 3-09, U_t = 5.2 cm/s, U_b = 4.3 cm/s Atwood no. = 0.00074, (*c*) Test 2-68, U_t = 4.9 cm/s, U_b = 4.8 cm/s, Atwood no. = 0.00064.

Downloaded 03 Jun 2010 to 171.66.16.125. Redistribution subject to ASME license or copyright; see http://www.asme.org/terms/Terms_Use.cfm

buoyancy, and buoyancy alone. From the side, the shear mixing layer (Fig. 5(a)), shows the large two-dimensional spanwise vortices observed in other studies (Brown and Roshko, 1974; Koochesfahani and Dimotakis, 1986). Jimenez et al. (1985) showed that for the low Reynolds number the rollers were only quasi-two-dimensional with an array of streamwise vortices forming on them. The buoyancy alone mixing layer, shown in Fig. 5(c), begins with small, vertical structures followed by larger structures downstream. Predominantly vertical, coherent structures are observed amongst the turbulent mixing. The compound buoyancy and shear flow (Fig. 5(b)) is observed to initially form large spanwise vortices (rollers) seen in shear flow alone (Fig. 5(a)). There is an overall vertical stretching of these shear vortices as the heavy and light fluids interpenetrate, and the amplitude of the rollers grows faster in the compound flow than in the free shear flow. By the interchange of axial distance and time, each of the large structures in Fig. 5(b) can be considered as a growth history of a single structure. Looking at the first structure from compound mixing, a spanwise vortex spiral is formed. The spiral is composed of fluid from the heavy upper and light lower layers. As the shear layer grows, the heavy fluid (dyed) follows the spanwise vortex stream path and surrounds the light fluid (not-dyed). This locally unstable condition leads to a vertical stretching of the vortex center and its destruction which is seen as the elongated second and third large structures in the photograph. As time progresses, buoyancy plumes become the dominant structure with only remnants of the surface shear vorticity being seen at the top and bottom boundary of the mixing layer (the fourth large structure in the photograph).

The three-dimensional character of the mixing layer can be seen from a perspective view. For a shear layer, numerous experimental studies have examined the mixing layer from a variety of perspectives. Photographs by Lasheras and Choi (1988) show spanwise vortices with imposed pairs of counter rotating streamwise vortices. In this study, a side perspective view of the developing unstable buoyancy layer is shown in Fig. 6. A side perspective view of the compound buoyancy and shear mixing layer is shown in Fig. 7.

Viewed from the side, buoyancy mixing begins with small regular, vertical structures translating with the uniform flow as seen in Fig. 5(c). The structures are fairly distinct suggesting a two-dimensional structure extending spanwise across the channel. Figure 6 shows that from a perspective view looking

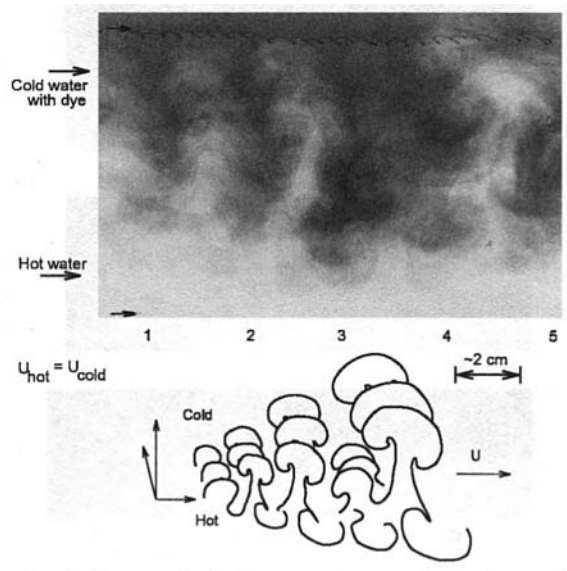


Fig. 6 View of three-dimensional plumes across channel. Test 3-28: U_t = 4.1 cm/s; U_b = 4.0 cm/s; Atwood no. = 0.00026.

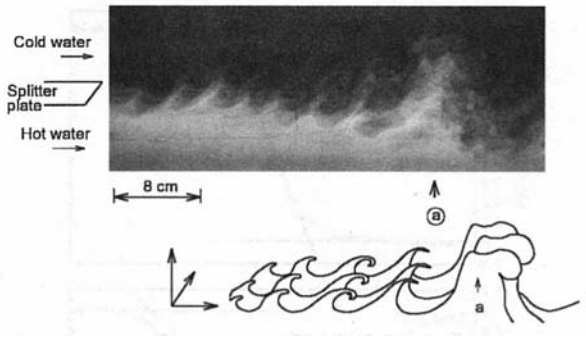


Fig. 7 Perspective view of the three-dimensional compound shear and buoyancy mixing layer. Test 3-23: U_t = 6.0 cm/s, U_b = 4.4 cm/s, Atwood no. = 0.00065.

down on the mixing layer, the structures are three-dimensional. From the close view of the developing buoyant structures, distinct ascending and descending plumes are visible across the channel. The regular spanwise row of plumes gives the two-dimensional appearance when viewed from the side. The interpenetrating heavy and light structures form mushroom heads typical of buoyant plumes produced from an underlying heated plate. Transient unstable buoyant layer studies by Read (1984) with large accelerations and large density differences produced cases of "spikes" and "bubbles" of interpenetrating fluids instead of mushroom headed plumes.

As structures grow, the magnitude of the plumes becomes significant compared with the coherence length (streamwise distance between major large structures), and structures begin to combine. The onset of this pairing of structures is visible in Fig. 6. Figure 6 shows five rows of major structures at a regular frequency. The last two structures in the series (right) are beginning to pair. Following the idea of bubble competition, the retarded plume (second from right) combines with the advanced plume (far right). The pairing produces a larger structure with longer wavelength. As mixing progresses, the size of structures become significant compared with the channel dimensions and the quasi-two-dimensional spanwise row of structures is replaced by large individual structures.

Figure 7 shows a perspective view of the compound shear and unstable buoyancy mixing. The initial mixing is observed to have many plane shear mixing characteristics. Initial spanwise vortices form; however, unlike shear flow, the spanwise vortices are not tightly wound. Buoyancy pulls apart the vortices formed from heavy (dark in the photograph) and light (light in the photograph) fluids winding about each other. The initial flow is quasi-two-dimensional with dark troughs stretching axially between vortices. The spanwise vortices, enhanced by buoyancy, grow quickly as seen from the side view in Figure 5(b). Eventually the vortex behavior gives way to a buoyant upheaval. Figure 7 at location a, shows the first distinct large upheaval from buoyancy. The light fluid erupts in a row of bubbles, originating from the crest of spanwise vorticies. The appearance of the mixing structures changes from spirals of free shear flow to the blunt plumes typical of an unstable buoyancy mixing layer.

Mixing Width Growth Rate

We relate the observations in this study to other work, in part, by examining the measured growth rate of the mixing layer. It is shown below that this study produces mixing growth rates comparable to other studies for shear mixing and for transient unstable buoyancy layers. No known data are available on the growth of compound shear and unstable buoyancy mixing.

Figure 5(a) shows the free shear mixing layer which has the familiar spanwise vortices. From photographs similar to that in Fig. 5(a), the growth rate of the mixing layer was measured.

Downloaded 03 Jun 2010 to 171.66.16.125. Redistribution subject to ASME license or copyright; see http://www.asme.org/terms/Terms_Use.cfm

The measured growth rates in this study compare favorably with the linear rate from Gortler's (1942) self-similar solution using an empirical mixing constant by Sabin (1965), and with the measured growth rate by Brown and Roshko (1974).

Figure 5(*c*) shows a photograph of the buoyancy mixing layer which is characterized by large vertical plumes. A numerical buoyancy study by Youngs (1984) and buoyancy experimental data by Read (1984) showed that the buoyant mixing width depends on the similarity length Agt^2. With loss of memory of initial conditions, the half width of the mixture fits the relation:

$$h = \alpha A g t^2 \tag{4}$$

In this study, an imposed uniform flow gives an inertial frame of reference traveling with the vertically expanding mixing layer. Applying the Galilean transformation (Drazin and Reid, 1982) the axial variation of mixing width is:

$$h = \alpha A g \left(\frac{x - x_0}{U} \right)^2 \tag{5}$$

where h is the half width of the mixture, g is the gravity acceleration, t is time and A is the Atwood number. The x_0 is a virtual origin which accounted for the effect of the splitter plate and non-similarity of the initial mixing layer. The acceleration constant, α, has been experimentally found to range from 0.05 to 0.077 (Youngs, 1992). Figure 8 compares the mixing widths from five tests at different Atwood numbers and no shear. The Atwood number ranged from 0.00034 to 0.0012. The acceleration constant for each test was found from a best fit curve through the data. The percent mean deviation of measured data from the fitted curve is typically 2.2 percent with minimum and maximum values of 1.3 and 4.8 percent. The average acceleration constant $\alpha = 0.070$ with a standard deviation of 0.007 compares well with prior transient studies. The Atwood number in this study is lower and more typical of that in the environment than in previous experiments. Prior transient experiments were directed towards inertially confined fusion, and high accelerations and large density differences gave large Atwood numbers. Growth rates measured in this study extend the lower range of buoyancy driven mixing layers.

Figure 5(*b*) shows the structure of compound shear and buoyancy mixing. The structure of the compound shear and buoyancy mixing initially resembled shear layer mixing and downstream migrated to buoyancy mixing. For individual shear mixing and buoyancy mixing, the growth rate can be expressed in terms of their self-similar variables. Because of the quadratic and linear self-similar scales for shear and buoyancy mixing, a self-similar scale for compound mixing is not expected. However, it was reasoned that because the pure buoyancy layer grows quadratically, the buoyancy self-similar variable may produce a reasonable scaling variable far downstream. Figure

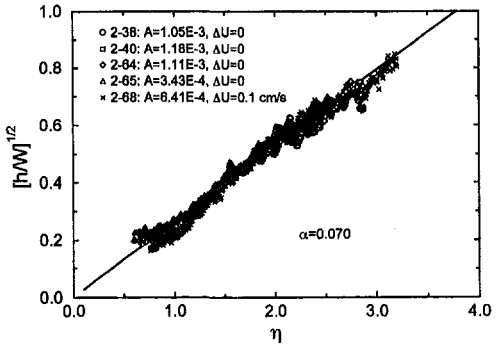


Fig. 8 Mixture width from buoyancy alone

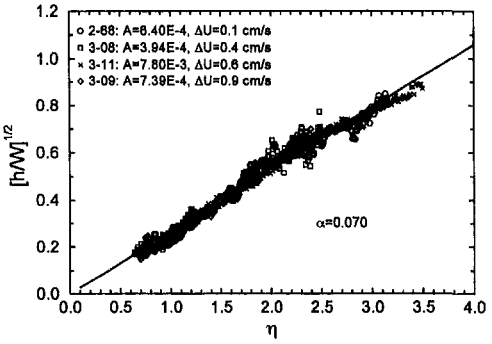


Fig. 9 Comparison of buoyancy mixing width from tests with upper and lower channel velocity differences

9 shows the compound mixing growth rate as a function of the buoyancy self-similar variable, η. The Atwood number is nearly the same for the three tests. The compound mixing width is described by the same quadratic curve as that for pure buoyancy, with the same acceleration constant, $\alpha = 0.070$.

The Richardson number (Ri), provides a measure of the influence of shear and buoyancy on the plane mixing layer. The Richardson number used in this study is the ratio between kinetic energy produced from buoyancy potential energy and inertial kinetic energy:

$$\mathrm{Ri} = \frac{hg\mathrm{A}}{\Delta U^2} \tag{6}$$

In the limiting cases, the mixing width grows linearly for the shear layer and quadratically for the unstable buoyancy layer (Eq. (5)). The Richardson numbers for shear and buoyancy mixing widths, respectively, are:

$$\mathrm{Ri}_S = -0.25c(t/\tau) \quad \text{and} \quad \mathrm{Ri}_B = -\alpha(t/\tau)^2 \tag{7}$$

The time scale is $t = 2x/(U_1 + U_2)$ and it is normalized by the time constant $\tau = \Delta U/Ag$. Measured values of the constants are $c = 0.38$ and $\alpha = 0.07$. Traditionally the Ri number has been reported as positive for a stable buoyancy layer. Here gravity and the time scale are positive and the Richardson number is reported negative (unstable buoyancy). A Ri ~ -1 (equal energy from shear and buoyancy) would be expected to give a mixing layer driven by both shear and buoyancy. The larger the negative Ri number, the stronger the influence of buoyancy.

Equations (7) for the shear and buoyancy Ri numbers suggest that once buoyancy becomes significant, the Ri number will grow (negatively) quickly which in turn would indicate the dominance of buoyancy. Experimentally, the Ri number at $\eta = 1$ in Fig. 9 where the mixing width data begin collapsing onto a single curve are much less than -1 indicating buoyancy dominated mixing. The Richardson numbers at $\eta = 1$ for the four tests shown are:

Test	2-68	3-08	3-11	3-09
Ri number	−138	−5.38	−47	−2

For flow rates and density differences in this study, the Ri numbers on the order of -1 or greater occurred as the mixing layer transited towards self-similar buoyancy mixing.

This study used both a modest density difference (0.38 kg/m^3) and a low velocity difference (1 cm/s). The modest density difference produced significant mixing. However, the velocity difference was not large enough to resolve whether shear with buoyancy increases the mixing layer growth rate beyond that of either of the pure growth rates, or whether mixing widths lie somewhere between the pure mixing growth rates. Experiments at higher velocity differences are needed and are currently being

Downloaded 03 Jun 2010 to 171.66.16.125. Redistribution subject to ASME license or copyright; see http://www.asme.org/terms/Terms_Use.cfm

pursued. The dominance of one mechanism over the other at streamwise locations will be further characterized by a nondimensional parameter such as the Richardson number.

Conclusions

A statistically steady experiment has been developed that allows independent control of buoyancy and shear driven mixing. This versatile, but mechanically noncomplicated, experiment allows a heavy fluid to be easily placed above a light fluid and allows a long time duration in which to study mixing structure.

While the shear rates were relatively low, we were still surprised by the overwhelming dominance of buoyancy in the compound buoyancy and shear mixing experiments. Shear produced spanwise vortices composed of heavy and light fluid early in the mixing layer development. Buoyancy expands the shear produced vortices, and as mixing progresses downstream, buoyant structures become dominant. For the density and velocity ranges in this study, the mixture width from compound shear and buoyancy grows at the same quadratic rate as that from buoyancy alone. The average acceleration constant from tests with buoyancy and with compound buoyancy and shear is 0.070 with a standard deviation of 0.007.

Acknowledgments

Thanks are due to Dr. D. L. Youngs, Dr. J. Glimm, and Dr. David Sharp for their helpful comments throughout this work. This work was supported from an Engineering Excellence Grant from Texas A&M University, and by an Interdisciplinary Research Initiative grant from the office of the Vice President for Research and associate Provost for Graduate Studies at Texas A&M University.

References

Andrews, M. J., and Spalding, D. B., 1990, "A Simple Experiment to Investigate Two-Dimensional Mixing by Rayleigh-Taylor Instability," *Physics of Fluids A,* p. 922.

Brown, G. L., and Roshko, A., 1974, "On Density Effects and Large Structures in Turbulent Mixing Layers," *J. Fluid Mech.,* Vol. 64, p. 775.

Chandrasekhar, S., 1961, *Hydrodynamic and Hydromagnetic Stability,* Oxford University Press.

Comte, P., Lesieur, M., Laroche, H., and Normand, X., 1989, "Numerical Simulation of Turbulent Plane Shear Layers," *Turbulent Shear Flow 6,* Springer-Verlag, Berlin, pp. 360–380.

Dimotakis, P., and Brown, G. L., 1976, "The Mixing Layer at High Reynolds Number: Large Structure Dynamics and Entrainment," *J. Fluid Mech.,* Vol. 78, p. 535.

Dhir, V. K., and Chang, F., 1992, "Heat Transfer Enhancement Using Tangential Injection," *ASHRAE Transactions,* BA-92-4-1.

Drazin, P. G., and Reid, W. H., 1982, *Hydrodynamic Stability,* Cambridge Univ. Press, p. 324.

Emmons, H. W., Chang, C. T., and Watson, B. C., 1963, "Taylor Instability of Finite Surface Waves," *J. Fluid Mech.,* Vol. 7, p. 177.

Gortler, H., 1942, "Berechnung von auffaben der freien turbulenz auf grund eines neuen naherungsansatzes," *Z. Agnew. Math. Mech.,* Vol. 22, pp. 244–254.

Jimenez, J., Cogollos, M., and Bernal, L. P., 1985, "A Perspective View of the Plane Mixing Layer," *J. Fluid Mech.,* Vol. 152, p. 125.

Koochesfahani, M. M., and Dimotakis, P. E., 1986, "Mixing and Chemical Reactions in a Turbulent Liquid Mixing Layer," *J. Fluid Mech.,* Vol. 170, p. 83, 1986.

Koop, G. K., 1976, "*Instability and Turbulence in a Stratified Shear Layer,*" Ph.D. thesis, Univ. So. Calif.

Lasheras, J. C., and Choi, H., 1988, "Three-Dimensional Instability of a Plane Free Shear Layer: An Experimental Study of the Formation and Evolution of Streamwise Vortices," *J. Fluid Mech.,* Vol. 189, p. 53.

Lawerence, G. A., et al., 1991, "The Stability of a Shear Density Interface," *Phys. Fluids A,* Vol. 3, No. 5, pp. 2360–2370.

Read, K. I., 1984, "Experimental Investigation of Turbulent Mixing by Rayleigh-Taylor Instability," *Physica 12D,* pp. 45–58.

Roshko, A., 1991, "The Mixing Transition in Free Shear Flows," *The Global Geometry of Turbulence,* J. Jimenez, ed., Plenum Press, NY, p. 3.

Sabin, C. M., 1965, "Analytical and Experimental Study of the Plane Incompressible Turbulent Free Shear Layer with Arbitrary Velocity Ratio and Pressure Gradient," *ASME Journal of Basic Engineering,* pp. 421–428.

Sharp, D. H., 1984, "An Overview of Rayleigh-Taylor Instability," *Physica,* p. 3.

Snider, D. M., and Andrews, M. J., 1995, "An Inexpensive Method for Quantitative Data Collection From Photographic Prints," *Meas. Sci. Technol.,* Vol. 6, pp. 502–506.

Snider, D. M., 1994, "A Study of Compound Buoyancy and Shear Mixing," Ph.D. thesis, Texas A&M Univ., College Station.

Taylor, G. I., 1950, "The Instability of Liquid Surfaces When Accelerated in a Direction Perpendicular to Their Planes I," *Proc. Royal Soc. A,* Vol. CCI, p. 192.

Turner, J. S., 1973, *Effects in Fluids,* Cambridge University Press, p. 165.

Youngs, D. L., 1992, "Numerical Simulation of Turbulent Mixing by Experimental Investigation of Turbulent Mixing by Rayleigh-Taylor Instability," *Advances in Compressible Turbulent Mixing,* W. P. Danevik, et al., eds., p. 607.

Youngs, D. L., 1984, "Numerical Simulation of Turbulent Mixing by Rayleigh-Taylor Instability," *Physica 12D,* p. 32.

Downloaded 03 Jun 2010 to 171.66.16.125. Redistribution subject to ASME license or copyright; see http://www.asme.org/terms/Terms_Use.cfm

Flows Generated by the Impingement of a Jet on a Rotating Surface: Part I—Basic Flow Patterns

S. Brodersen
Present Address:
KSB AG,
67225 Frankenthal, Germany

D. E. Metzger[1]

H. J. S. Fernando

Arizona State University,
Environmental Fluid Dynamics Program,
Department of Mechanical and
Aerospace Engineering,
Tempe, AZ 85287-6106

The results of an experimental study of the flow field resulting from the interaction between an impinging jet and a rotating disk are presented. The resulting flow configuration has applications in turbomachinery, for example, to intensify the local heat transfer at turbine disks. The experiments cover separate measurements of the disk-wall flow, the jet flow and interaction between the two. The flow patterns are investigated over a range of jet Reynolds numbers $Re_{jet} = 0.66 \cdot 10^4 - 6.80 \cdot 10^4$ *(based on jet diameter) and disk Reynolds number* $Re_{disk} = 3.4 \cdot 10^5 - 6.2 \cdot 10^5$ *(based on impingement radius), achieved by varying the jet nozzle diameter, jet flow rate, rotational disk speed and the impingement radius. The measurements included the depth of jet penetration into the wall boundary layer, the travel distance of the jet against the direction of disk rotation, and the turbulent and mean velocity distribution. Another objective of this study concerns the type of flow at the impingement region (jet dominated flow or rotation dominated flow) and the conditions for the transition from one to the other. In the first part of the study, the flow structure of the jet and disk flows as well as the three-dimensional flow fields resulting from the interaction are presented.*

1 Introduction

During the manufacture of gas turbines, a detailed knowledge of heat transfer mechanisms is imperative especially in designing highly thermally stressed components such as the turbine disk. A disk cooling scheme which can intensify local heat transfer rates with a relatively low coolant flow rate consists of squirting a coolant jet at the rotating disk. This scheme is especially attractive if jet impingement is used at the blade attachment region (i.e., at the rim of the disk). This scheme is currently applied in the space shuttle main engine turbopumps. In addition to their applications in turbomachinery, the disk-jet flows also have a great variety of general applications (Littell and Eaton, 1994). Owing to its vast applications, numerous studies have been reported on this topic. Most of these studies are of experimental nature and deal with fluid mechanics and heat transfer aspects of jet impingement on stationary surfaces. One of the early studies on the flow structure and heat transfer of jets impinging on a stationary plate was reported by Gardon and Akfirat (1965). Other experimental investigations, particularly on the flow characteristics, were carried out, for example, by Baines and Keffer (1976) and Glowacki (1989). Experimental studies on the heat transfer aspects have been done by Goldstein and Behbahani (1982), Hrycak (1983) and by Baughn and Shimizu (1989). Some reported numerical investigations are Wolfshtein (1970), Amano and Brandt (1984), Rabel (1980), and Huang et al. (1984); in the latter study, the effect of crossflow and wall motion were also included.

The case of jet impingement on a moving surface is different from that of jet impingement on a stationary surface, with or without a cross flow. The thin wall boundary layer, established by disk rotation and pumping, has its maximum velocity at the wall, when viewed from the laboratory frame of reference (i.e., from which the jet is discharged), see Fig. 1. This flow configuration has been studied by several investigators as a means of cooling the rotating surface. The studies were mainly concentrated on large area-averaged heat transfer measurements and flow visualization tests (see Ruby, 1972; Henry, 1976; Grochowsky, 1975; Metzger et al., 1977, 1979; and Metzger and Partipilo, 1989). Measurements of local heat transfer rates have also been carried out by Popiel et al. (1974), Bogdan (1982), Popiel and Boguslawski (1986) and Metzger et al. (1989). These measurements covered both laminar and turbulent wall boundary layers. A numerical study on laminar flow impingement on a rotating disk has been done by Nakata (1989). The main finding is that for both laminar and turbulent wall boundary layers the heat transfer rate can be increased significantly when there is "jet-dominated" flow, i.e., when the jet penetration into the disk wall boundary layer is sufficiently deep. In the opposite case, when the jet is too weak and is deflected from the disk surface flow, there is no influence of the jet on the rotating surface heat transfer, and the flow is "disk-dominated". Although some of the studies on the jet-wall flow interaction include smoke flow visualizations to facilitate the understanding of heat transfer results, there are no detailed studies on the flow structure in the interaction region. Some questions that need to be addressed are: how deep into a wall boundary layer an impinging jet can penetrate? How far against the direction of the disk rotation can it expand? What is the level and distribution of turbulence intensity? In the present study, the distribution of mean velocity and turbulence intensity fields are investigated through localized laser-Doppler velocimetry measurements with the aim to obtain a better understanding of the jet-rotating disk interaction phenomenon. Because of its practical interest, only turbulent flows (jet and disk flow) are considered in this study.

2 Experimental Facility

Figure 2 shows a cross-sectional view of the test apparatus. It was connected to a flow and temperature controlled water

[1] Professor Darryl E. Metzger, a well-known educator and researcher, died on August 1, 1993 after a short but courageous battle with cancer. He was instrumental in initiating the research program of which the results are presented herein. S. Brodersen and H. J. S. Fernando wish to dedicate these two papers (Parts I and II) in memory of their dear colleague and friend, Darryl E. Metzger.

Contributed by the Fluids Engineering Division for publication in the JOURNAL OF FLUIDS ENGINEERING. Manuscript received by the Fluids Engineering Division August 23, 1994; revised manuscript received June 7, 1995. Associate Technical Editor: H. Hashimoto.

Copyright © 1996 by ASME

Downloaded 03 Jun 2010 to 171.66.16.125. Redistribution subject to ASME license or copyright; see http://www.asme.org/terms/Terms_Use.cfm

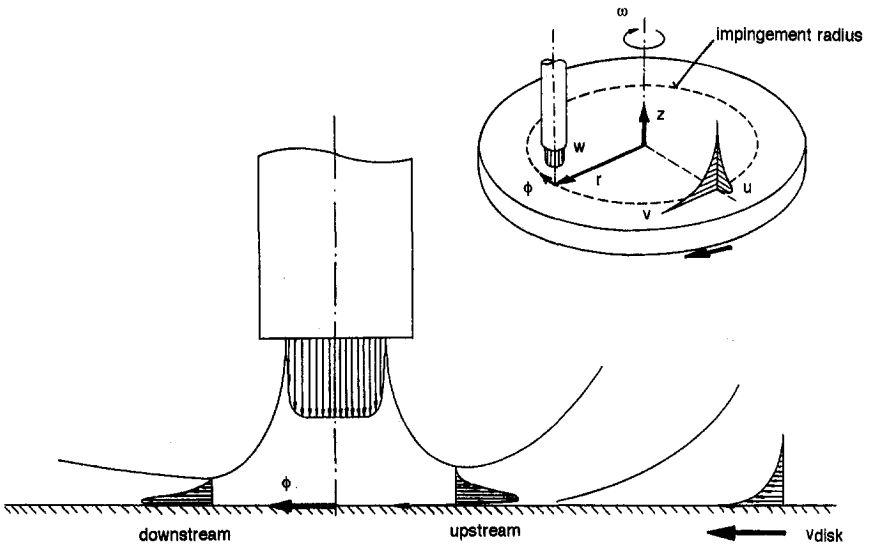


Fig. 1 A schematic of the jet-rotating disk interaction

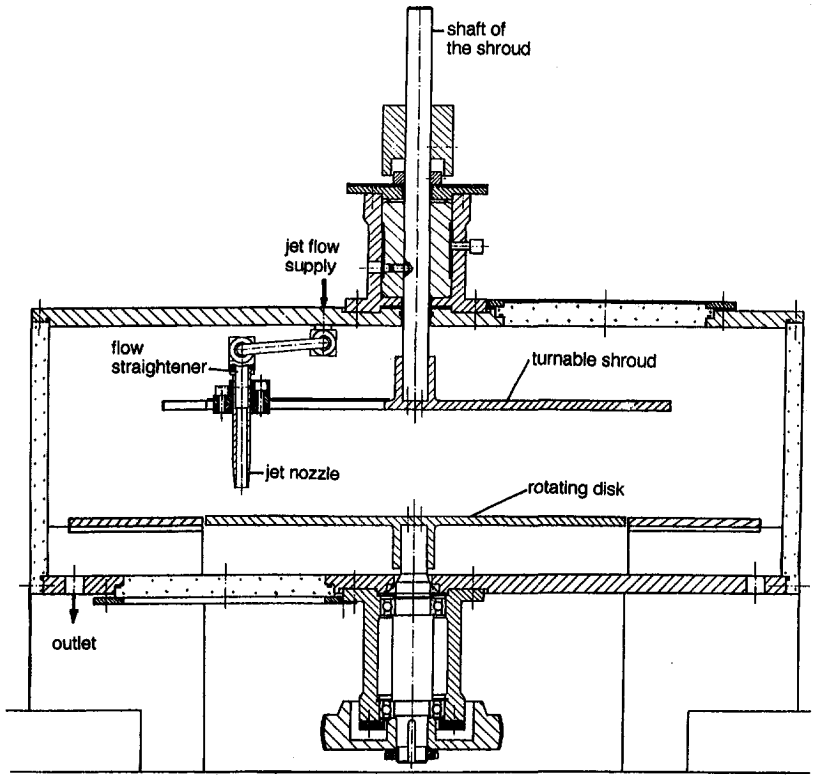


Fig. 2 A diagram of the test section

loop and consisted of the enclosing chamber, rotating disk and turnable shroud where the nozzle was mounted and could be traversed in radial and axial directions. Two side walls made from plexiglas provided optical access for LDV-measurements. The jet flow was supplied from a hose coupling at the top plate and was drained via eight hose couplings in the bottom plate;

Nomenclature

d = diameter (m)
n = rotational speed (Hz)
Q = flow rate (ml/s)
$\mathrm{Re}_{\mathrm{disk}}$ = disk Reynolds number (−)
$\mathrm{Re}_{\mathrm{jet}}$ = jet Reynolds number (−)
u, v, w = mean velocity components (m/s)
u', v', w' = r.m.s. turbulent velocities (m/s)
r, ϕ, z = polar coordinates (m, deg, m)
α = ratio of Reynolds numbers $\mathrm{Re}_{\mathrm{jet}}/\mathrm{Re}_{\mathrm{disk}}$ (−)
δ = boundary layer thickness (m)
ν = kinematic viscosity (m^2/s)
ω = angular speed ($2\pi n$)

Downloaded 03 Jun 2010 to 171.66.16.125. Redistribution subject to ASME license or copyright; see http://www.asme.org/terms/Terms_Use.cfm

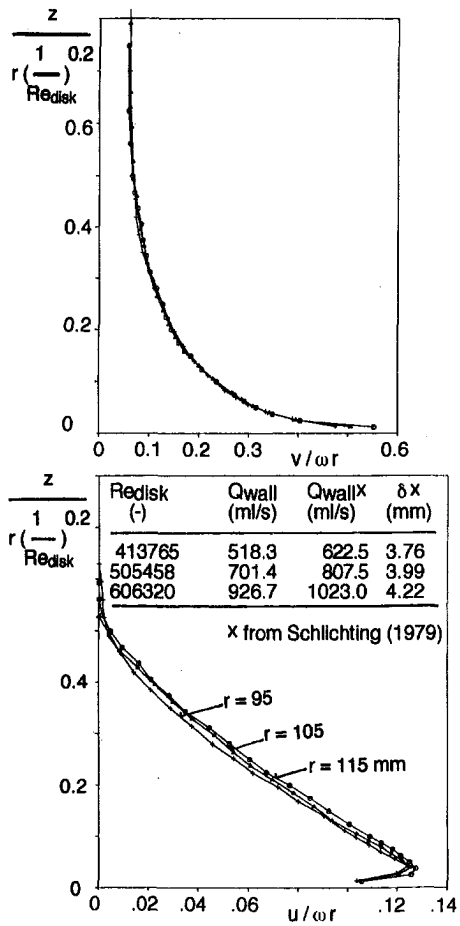


Fig. 3 Dimensionless azimuthal and radial velocity distributions at various radii in the absence of a jet

the working fluid used was water. The wobble at the rim of the test disk (250 mm o.d.) was always less than 0.05 mm peak-to-peak. The shaft of the shroud was fixed into a bearing device, which allowed circumferential and axial adjustments. Two nozzles were used with inner diameters of 6 and 8 mm, and each had a blunt nozzle tip of 12.7 mm outer diameter. Both were provided with a flow straightener positioned 57 mm upstream of the nozzle tip. The distance between the nozzle and the disk was maintained at 1.5 jet diameters. The wall flow leaving the upper side of the rotating disk was separated from the lower flow by a plexiglas sheet that was ribbed on its lower side; this reduced the circumferential flow inside the chamber and prevented the development of unsteady flow phenomena at the disk rim.

The flow field measurements were carried out by means of a single-component laser-Doppler velocimeter. Experimental uncertainties in the velocity measurements were 3 percent for the center of the interaction flow field and 4 percent in the periphery. Since the jet-rotating disk interaction is a three-dimensional phenomenon, the measurement of all three velocity components are desired but because of experimental difficulties only 2 components were measured. Since the flow field is essentially steady, successive measurements of single velocity components, made at different times, could be used to construct the velocity field. For measurements of the radial components in a r, ϕ-grid, where r is the radius and ϕ is the azimuthal angle of a polar coordinate system with origin at the disk center (see Fig. 1), the LDV-system was traversed in the radial direction. The circumferential position of the nozzle was set by rotating the shroud around its center-line. The azimuthal velocity components at different radii were measured after the optical path of the LDV-system was aligned to pass through the disk center; the probe volume was traversed along the optical path only. The nozzle was then turned by 90 deg and measurements were repeated for different circumferential positions relative to the probe volume thus covering a large spacial extent of measurements.

3 Experimental Results for Rotating Disks Without Jets

Before the jet-disk interaction measurements were carried out, some preliminary tests were conducted in order to check

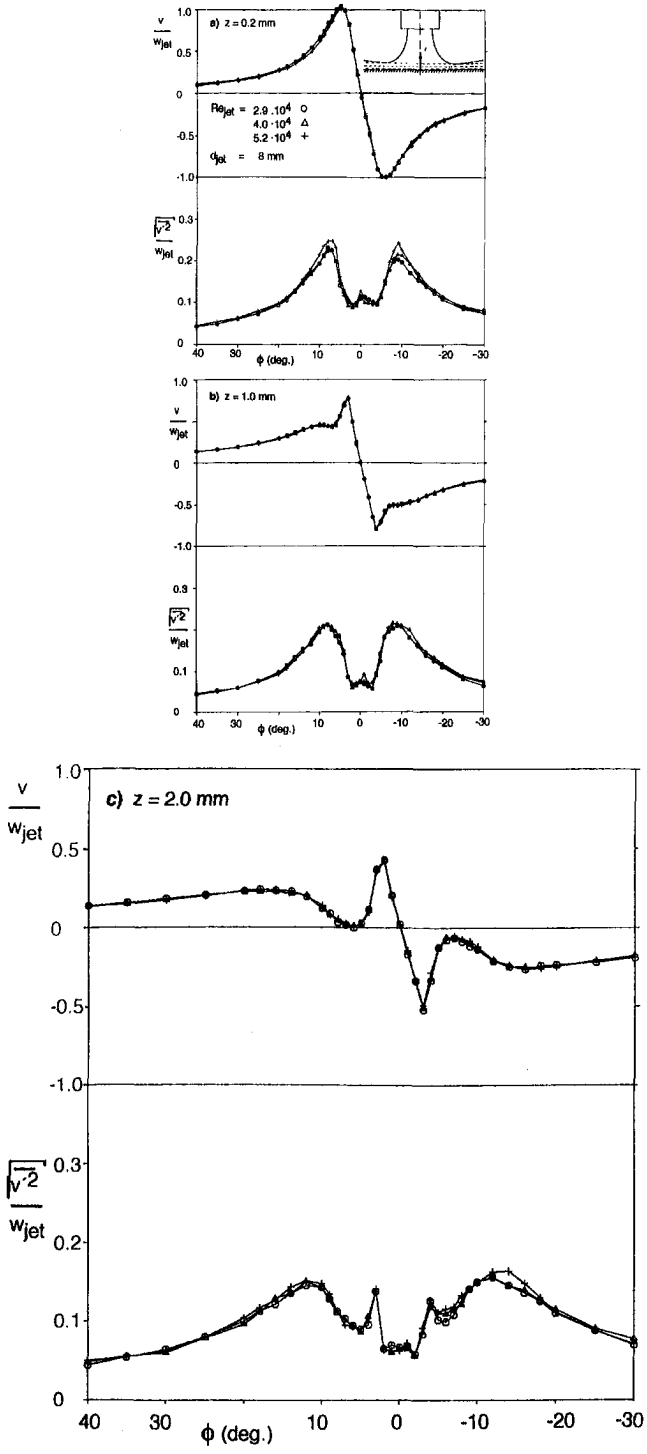


Fig. 4 Azimuthal mean (v) and normalized r.m.s. ($(v'^2)^{1/2}$) velocity distributions, measured at different heights z from the disk surface

Downloaded 03 Jun 2010 to 171.66.16.125. Redistribution subject to ASME license or copyright; see http://www.asme.org/terms/Terms_Use.cfm

how the experimental configuration inside the casing influenced the disk wall flow. Fig. 3 shows the azimuthal v and radial u mean velocity profiles over z for different radii, i.e., for different disk Reynolds numbers $\mathrm{Re}_{\mathrm{disk}}$ after the fluid has spun up. The normalized profiles are based on Eq. (1) and the disk velocity; a reasonably good collapse of the data can be seen. Due to the presence of the shroud and the enclosure, the azimuthal velocity exhibits a constant value above the boundary layer (about 6 percent of v_{disk}). Assuming that the azimuthal velocity above the flat plate follows the $\frac{1}{7}$ velocity power law, von Karman (1956) evaluated the thickness δ of the turbulent boundary layer over a flat, rotating disk in an infinite environment as

$$\delta \sim r(\nu/r_\omega^2)^{1/5} \sim r\,\mathrm{Re}_{\mathrm{disk}}^{-0.2} \tag{1}$$

Experimental measurements of Schmidt (1921) and Kempf (1924) have been used to evaluate the proportionality constant of Eq. (1) as 0.526. Thus, the axial volume flow rate above the disk can be evaluated as (Schlichting, 1979)

$$Q = 0.219 r_\omega^3\,\mathrm{Re}_{\mathrm{disk}}^{-0.2} \tag{2}$$

A comparison between the axial flow rate calculated using Eq. (2) and the measured value gave the result that the pumped wall flow is between 83 and 90 percent of that for a disk rotating in an infinite environment.

4 Experimental Results for Jet Impinging on a Stationary Disk

As already mentioned, the nozzle was placed 1.5 nozzle diameters above the disk; this is a small distance compared to the initial development regime of a jet, but was chosen with potential cooling applications in mind. Previous studies report that "a submerged circular jet propagates as a free jet to within a distance of roughly 1.2 nozzle diameters from the impacted surface" (Gardon and Akfirat, 1965). For the present case this means that the jet travels as a free jet only about 2 mm until it is affected by the presence of the disk. Since the mixing at the outer edge of the jet and thus the production of high turbulence levels has just started at this time, the structure of the present jet can be described as one having a small "mixed region" and a large "potential core" (see, Gardon and Akfirat, 1965).

In Fig. 4, the flow characteristics of the 8 mm-jet impinging on a stationary disk and then moving along the surface as a wall jet are shown. The distributions of the azimuthal velocity component v parallel to the surface and $(v'^2)^{1/2}$ are plotted over the azimuthal coordinate ϕ of the disk; these results will be compared with the results of the jet impingement experiments with the disk in rotation; the exit mean jet velocity w_{jet} has been used for normalization and the results are presented for different z. The velocity distribution at $z = 0.2$ mm shows an almost linear acceleration of fluid elements from the stagnation point to $\phi = 5$ to 6 deg where it reaches the level of the jet mean velocity. This distance corresponds, on the average, to 1.1 jet diameter and coincides with the value which Gardon and Akfirat (1965) referred to as the radius of the "stagnation region." This is the region of a strong pressure gradient which causes the acceleration. Away from the jet center-line the turbulence intensity first decreases and then, with decreasing velocity and diminishing pressure gradient, tends to increase again. The monotonically decreasing velocity for distances greater than $\phi = 5$ to 6 deg is caused by increased flow area, wall friction and turbulent mixing of momentum with ambient fluid. Despite the decrease of velocity, the velocity fluctuations increase until about $\phi = 8$ to 9 deg, i.e., at approximately 1.8 jet diameters. This is a very interesting detail; Gardon and Akfirat (1965) have found that a secondary peak in the heat transfer rate appears at 1.9 diameters from the jet axis, when the jet flow is not fully developed. Their experiments with an artificially increased turbulence intensity in the jet center showed the disappearance of

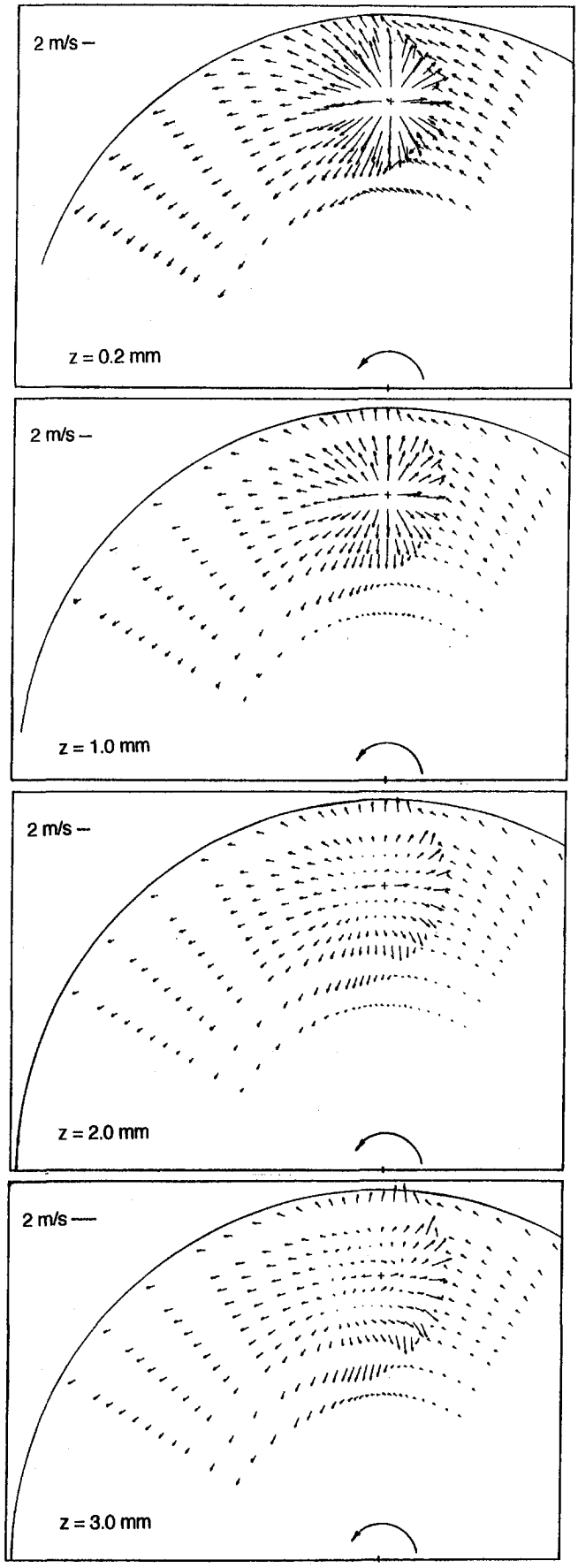


Fig. 5 Vector plots of velocity fields resulting due to jet-rotating disk interactions at various distances from the disk surface. $\mathrm{Re}_{\mathrm{disk}} = 3.98 \cdot 10^5$, $v_{\mathrm{disk}} = 4.18\ \mathrm{ms}^{-1}$, $n = 7$ Hz, $\mathrm{Re}_{\mathrm{jet}} = 3.84 \cdot 10^4$, $d_{\mathrm{jet}} = 6$ mm, $\mathrm{Re}_{\mathrm{jet}}/\mathrm{Re}_{\mathrm{disk}} = 0.097$ and $r_{\mathrm{jet}} = 95$ mm. The scale of the plot is also shown

Downloaded 03 Jun 2010 to 171.66.16.125. Redistribution subject to ASME license or copyright; see http://www.asme.org/terms/Terms_Use.cfm

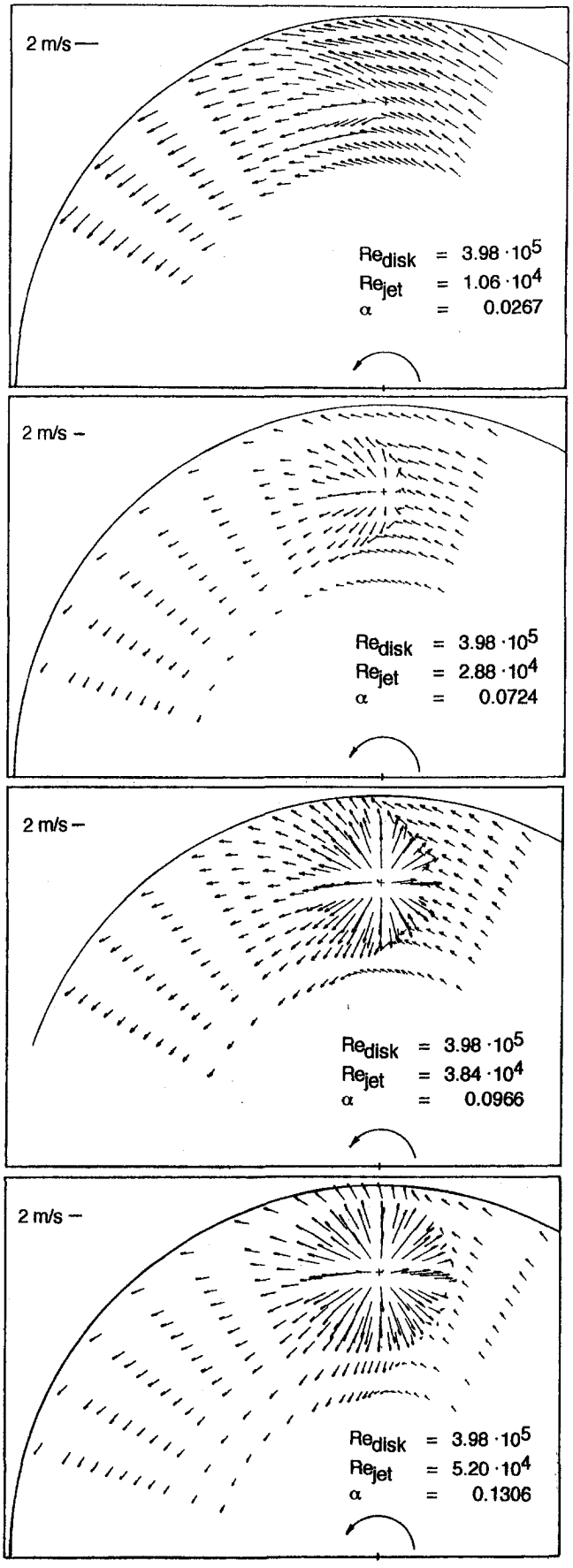


Fig. 6 Velocity vector diagrams showing the variation of the velocity field resulting from jet-rotating disk interaction with the ratio of jet and disk Reynolds numbers α. The measurements have been taken at z = 0.2 mm

the peaks to yield an overall increase of heat transfer. Gardon and Akfirat attributed this increase of heat transfer to transition from laminar to turbulent flow. The numerical studies of Amano and Brandt (1984) on jet impingement also show a secondary maximum in the distribution of skin friction at 2 jet diameters. Their calculations show that for small distances from the nozzle surface ($<2\ d_{jet}$), the fluid particles with high kinetic energy produced at the shear layer of the jet cause a secondary "disturbance" at the wall, thus affecting the distribution of skin friction. This peak was found to expand radially outwards with increased Reynolds number or with higher jet turbulence intensity. In the present study, however, no such expanding effect could be observed.

5 Jet-Wall Flow Interaction

The flow field measurements presented in this section were carried out in several planes parallel to the disk surface to obtain information about the three-dimensional flow structure. The jet flow rate, jet diameter and impingement radius were varied so as to obtain Reynolds numbers of $Re_{jet} = 0.66 \cdot 10^4$ to $5.2 \cdot 10^4$ and $Re_{disk} = 4.0 \cdot 10^5$ to $4.90 \cdot 10^5$. Preliminary tests showed that for $z_{jet}/d_{jet} < 1.5$ the flow patterns become independent of z_{jet}/d_{jet}. Figure 5 shows an example for a jet-rotating disk interaction where the jet is quite strong as quantified by high Re_{jet}; a vector plot of the velocity field at different heights from the rotating disk are shown. As evident from these plots, the jet penetrates deep into the wall boundary layer and is observed to expand in the upstream direction ($-v_{disk}$ direction) even in the lowest measuring plane z = 0.2 mm.

In the velocity vector plots shown in Fig. 6, the dependence of the flow patterns on the relative strengths of the jet and wall flows is illustrated; here the strengths are signified by Re_{jet} and Re_{disk}, respectively, and the relative strength is given by $\alpha = Re_{jet}/Re_{disk} \sim M^{1/2}/\omega r^2$. For small α (Fig. 6(a)) the jet does not appear to really penetrate into the wall boundary layer, but seems to mix with it downstream of the nozzle center-line. At what appears to be the outer edge of this mixing region the wall flow is slightly deflected. With increasing α, the jet becomes more capable of disturbing the wall flow (Fig. 6(b)), and starts to expand against the direction of disk rotation. Note that this transition is rather gradual and there is no sudden change of behavior. Additional measurements made at constant jet flow rates with slow increases and decreases of disk flow did not indicate the presence of hysteresis for the transition. However, for low Re_{jet} the radial wall flow appeared to become significant, the jet flow is moved radially outwards (Fig. 6(a)). When the jet starts to penetrate into the wall boundary layer at high Re_{jet}, this influence vanishes (Fig. 6(b)). In this case, the flow patterns are quite symmetric with respect to the impingement radius, which indicates that the azimuthal component of the wall flow is of major influence, with the radial component playing a minor role. The flow structure does not change appreciable when α is increased above 0.07, except for an extended jet flow expansion in the upstream direction. It was also found that the azimuthal velocity profile above the disk, at the upstream of the interaction region, is not affected by the presence of the jet. Downstream of the interaction region, the wall profile between z = 0.2 mm and 1.5 mm is redeveloped into a one similar to that observed in the absence of the jet, with the difference between the cases being only 5 percent. The radial velocity profile, however, is more affected by the presence of the jet, especially close to the center of the disk and at high jet flow rates.

Typical turbulence intensity distributions corresponding to the above flow fields are shown in Fig. 7. Since the axial velocity component was not measured in the disk boundary layer, the turbulence intensity was determined using the radial and azimuthal velocity fluctuations and is presented as a fraction of the jet mean velocity. For α = 0.07, the lines of constant turbulence

Downloaded 03 Jun 2010 to 171.66.16.125. Redistribution subject to ASME license or copyright; see http://www.asme.org/terms/Terms_Use.cfm

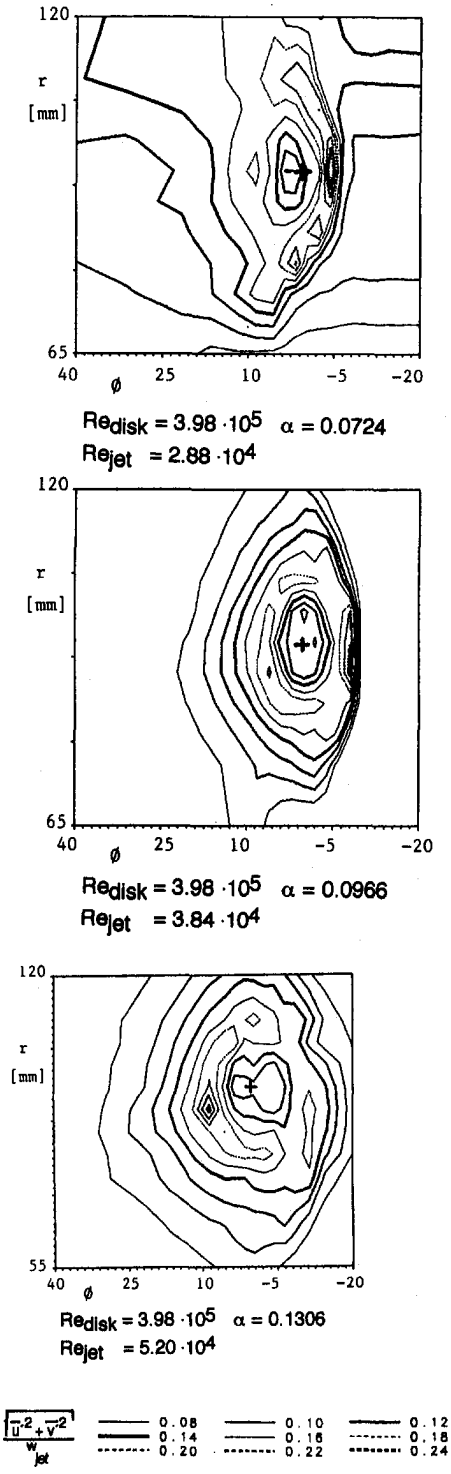


Fig. 7 Distribution of turbulence intensity (as a fraction of jet mean velocity w_{jet}) for various jet and disk Reynolds numbers, impinging radii and jet diameters; $z = 0.2$ mm

intensity are compressed upstream of the jet very close to the jet center, as a result of the interaction with the oncoming wall flow. The downstream maximum is always located at approximately 1.8 jet diameters, which is the same as that for the case of jet impingement on a stationary surface. Upstream of the jet, the turbulence intensity decreases with increasing α with the location of the maximum moving away from the jet center. For the highest α investigated ($\alpha = 0.13$), the turbulence intensity distribution gained an almost totally symmetric pattern, which indicates the total dominance of jet flow over wall flow.

6 Summary

Measurements were carried out to investigate the flow field generated by the impingement of a jet on a rotating disk. The essential findings of this study can be summarized as follows. The structure of the flow field and the distribution of the turbulence intensity are mainly determined by the ratio of the jet and disk Reynolds numbers α. When the jet is capable of expanding upstream, it usually can penetrate very deep into the wall boundary layer (closer to the disk than 0.2 mm). With increasing α ($\alpha > 0.125$), the jet characteristics become similar to those of jets impinging on a stationary surface. The main conclusions of the entire study are reported in part II of this paper, where detailed velocity and turbulence measurements are discussed.

Acknowledgments

This study was supported by a post-doctoral fellowship from the Alexander von Humboldt-Foundation, Federal Republic of Germany. Additional funding was provided by NASA Marshall Space Flight Center through a contract with the Rocketdyne Division of Rockwell International, Allied Signal Aerospace Corporation and the National Science Foundation.

References

Amano, R. S., and Brandt, H., 1984, "Numerical Study of Turbulent Axisymmetric Jets Impinging on a Flat Plate and Flowing into an Axisymmetric Cavity," ASME JOURNAL OF FLUIDS ENGINEERING, Vol. 106, pp. 410–417.

Baines, W. D., and Keffer, J. F., 1976, "Shear Stress and Heat Transfer at a Stagnation Point," *International Journal of Heat Mass Transfer,* Vol. 19, pp. 21–26.

Baughn, J. W., and Shimizu, S., 1989, "Heat Transfer Measurements From a Surface With Uniform Heat Flux and an Impinging Jet," AMSE JOURNAL OF HEAT TRANSFER, Vol. 111, pp. 1096–1098.

Bogdan, Z., 1982, "Cooling of a Rotating Disk by Means of an Impinging Jet," *Proceedings of the 7th International Heat Transfer Conference,* Munich, Vol. 3, pp. 333–336.

Gardon, R., and Akfirat, J. C., 1965, "The Role of Turbulence in Determining the Heat Transfer Characteristics of Impinging Jets," *International Journal of Heat Mass Transfer,* Vol. 8, pp. 1261–1272.

Glowacki, P., 1989, "Turbulence Characteristics of Impinging Jets Near the Deflecting Surface. The Effect of Polymer Additives," *Journal of Non-Newtonian Fluid Mechanics,* Vol. 33, pp. 25–38.

Goldstein, R. J., and Behbahani, A. I., 1982, "Impingement of a Circular Jet With and Without Cross Flow," *International Journal of Heat Mass Transfer,* Vol. 25, No. 9, pp. 1377–1382.

Grochowsky, L. D., 1975, "An Investigation of Flow Interactions and Heat Transfer Characteristics For Single Jet Impingement on Rotating Disks," MS thesis, Arizona State University, Tempe, AZ.

Henry, R. W., 1976, "Heat Transfer on a Rotating Disk with Single Axisymmetric Jet Impingement Cooling," MS thesis, Arizona State University, Tempe, Ariz.

Hrycak, P., 1983, "Heat Transfer From Round Impinging Jets To a Flat Plate," *International Journal of Heat Mass Transfer,* Vol. 26, No. 12, pp. 1857–1865.

Huang, P. G., Mujumdar, A. S., and Douglas, W. J. M., 1984, "Numerical Prediction of Fluid Flow and Heat Transfer Under a Turbulent Impingement Slot Jet With Surface Motion and Crossflow," ASME Paper No. 84-WA/HT-33.

Karman, Th. von, 1956, *Collected Works II,* Butterfields Scientific Publishing, London, pp. 91–97.

Kempf, G., 1924, "Über den Reibungswiderstand rotierender Scheiben," Vortrage auf dem Gebiet der Hydro- und Aerodynamik, Innsbrucker Kongress, 1922, Berlin, p. 168.

List, E. J., 1982, "Turbulent Jets and Plumes," *Annual Review of Fluid Mech.,* Vol. 14, Annual Review. Inc., Palo Alto, CA, pp. 189–212.

Littell, H., and Eaton, J. K., 1994, "Turbulence Characteristics of the Boundary Layer on a Rotating Disk," *Journal of Fluid Mechanics,* Vol. 266, pp. 175–207.

Metzger, D. E., and Grochowsky, L. D., 1977, "Heat Transfer Between an Impinging Jet and a Rotating Disk," ASME *Journal of Heat Transfer,* Vol. 99, pp. 663–667.

Metzger, D. E., Mathis, W. J., and Grochowsky, L. D., 1979, "Jet Cooling at the Rim of a Rotating Disk," ASME *Journal of Engineering for Power,* Vol. 101, pp. 68–72.

Metzger, D. E., Bunker, R. S., and Bosch, G., 1989, "Transient Liquid Crystal Measurements of Local Heat Transfer on a Rotating Disk with Jet Impingement," ASME paper 89-GT-287.

Metzger, D. E., and Partipilo, V. A., 1989, "Single and Multiple Jet Impingement Heat Transfer on Rotating Disks," AIAA paper 89-0174.

Nakata, Y., 1989, "Laminar Impingement Heat Transfer on an Enclosed Rotating Disk," MS thesis, Arizona State University, Ariz.

Downloaded 03 Jun 2010 to 171.66.16.125. Redistribution subject to ASME license or copyright; see http://www.asme.org/terms/Terms_Use.cfm

Papanicolaou, P. N., and List, E. J., 1988, "Investigations of Round Vertical Turbulent Buoyant Jets," *Journal of Fluid Mechanics,* Vol. 195, pp. 341–391.

Popiel, C. O., Tuliszka, L., and Boguslawski, L., 1974, "Heat Transfer From a Rotating Disk in an Impinging Round Air Jet," *Proceedings of the 5th International Heat Transfer Conference,* Tokyo 1974, Vol. 3, pp. 212–216.

Popiel, C. O., and Boguslawski, L., 1986, "Local Heat Transfer From a Rotating Disk in an Impinging Round Jet," ASME *Journal of Heat Transfer,* Vol. 108, pp. 357–364.

Rubel, A., 1980, "Computations of Jet Impingement on a Flat Surface," *AIAA Journal,* Vol. 18, No. 2, pp. 168–175.

Ruby, W. A., 1972, "Cooling Effect of the Impingement of Axisymmetric Air Jets on a Rotating Disk," MS thesis, Arizona State University, Tempe, Ariz.

Schlichting, H., 1979, *Boundary Layer Theory,* 7th ed., McGraw-Hill, p. 596.

Schmidt, W., 1921, "Ein einfaches Messverfahren für Drehmomente," *Z. VDI,* Vol. 65, pp. 411–444.

Tani, I., and Komatsu, Y., 1966, "Impingement of a Round Jet on a Flat Surface," *The International Congress of Applied Mechanics,* Munich, Springer, pp. 672–676.

Wolfshtein, M., 1970, "Some Solutions of the Plane Turbulent Impinging Jet," ASME Paper No. 70-FE-27.

Downloaded 03 Jun 2010 to 171.66.16.125. Redistribution subject to ASME license or copyright; see http://www.asme.org/terms/Terms_Use.cfm

Flows Generated by the Impingement of a Jet on a Rotating Surface: Part II—Detailed Flow Structure and Analysis

S. Brodersen
Present Address:
KSB AG,
67225 Frankenthal, Germany

D. E. Metzger

H. J. S. Fernando

Arizona State University,
Environmental Fluid Dynamics Program,
Department of Mechanical and
Aerospace Engineering,
Tempe, AZ 85287-6106

In Part I of this investigation, the basic flow patterns resulting from the interaction of a turbulent jet and a rotating disk flow were presented paying particular attention to mean and turbulent velocity fields around the jet impingement point on the disk and the flow patterns above the disk in the absence of the jet. The latter was used as a base flow pattern, on which the influence of the jet impingement could be assessed. In Part II, further details of the jet/disk flow interaction problem are discussed in the context of potential turbomachinery cooling applications and previous experimental results.

1 Introduction

In a companion paper (henceforth referred to as Part I), the basic flow patterns resulting from the impingement of a jet on a rotating disk were presented. The r.m.s. and mean velocities in and around the jet impingement region were presented for various disk and jet Reynolds numbers. The experimental apparatus was discussed in detail and the measurements in the presence of the jet were compared with the case where the jet is absent, i.e., only the rotating disk is present. It was shown that the distributions of the velocity as well as their fluctuations, for jet to disk Reynolds number ratios $\alpha > 0.03$, are nearly symmetric with respect to the impingement radius. More detailed flow field measurements showed that the distribution of the radial and azimuthal velocity fluctuations along the impingement radius are comparable in magnitude. Thus the measurements of the azimuthal velocity distribution along the impingement radius may yield valuable information on the jet-wall interaction; the present investigation deals with this aspect. The working fluid used was water, the experimental uncertainties in the velocity measurements were 3 percent for the center of the interaction flow field and 4 percent in the periphery (mixing with ambient fluid).

2 Comparison Between Jet Impingement on Rotating and Nonrotating Disks

The results presented here are based on the experiments with the 8 mm-nozzle positioned at $r_{jet} = 95$ mm and $z_{nozzle} = 1.5$ $d_{jet} = 12$ mm. The distance between the disk and shroud is $Z = 58.5$ mm (23.4 percent of disk diameter), Fig. 1. The measurements have been carried out for axial distances $z = 0.2–2.0$ mm, i.e., for 0.025 to 0.25 jet diameters. The jet flow rate was varied over $Q_{jet} = 67$ to 394 ml/s. With the rotational disk speed ranging from $n = 7$ to 9 Hz, this covers $\alpha = \mathrm{Re}_{jet}/\mathrm{Re}_{disk} = 0.26$ to 0.158 and $w_{jet}/v_{disk} = 0.32$ to 1.87. The measured azimuthal velocities and their fluctuations as a function of r, ϕ and z are presented in Fig. 2 in the order of increasing α. For the lowest Re_{jet} ($\mathrm{Re}_{jet} = 1.06 \cdot 10^4$), the jet does not penetrate into the wall boundary layer, but rather smears out within it (Fig. 2(a)). Negative velocities upstream of the jet occur first at $z = 1$ mm. The increase of the azimuthal velocity further downstream of the jet position can be explained by the drag effect of the moving surface. At $\phi = 40$ deg the profiles have again assumed the shape of the wall flow before the interaction. Two details of the velocity distribution in Fig. 2 at $z = 2.0$ mm are noteworthy: first, it shows zero velocity at the nozzle centerline, indicating that the jet has not yet been deflected, and it starts to expand almost equally on both sides, in the direction of and opposite to the disk rotation; a second point of zero velocity at $\phi = 6$ deg corresponds to the upper boundary of the wall jet in the z direction, which is thinnest at this point. The location of this zero velocity point is the same as the boundary layer thickness for the jet impinging case without the rotation of the disk (shown in Part I, Fig. 4). As far as the peaks downstream are concerned, the distribution of the velocity fluctuations in Fig. 2(a) also has some resemblance to the results for the jet impingement on a stationary surface. Close to the disk, at $z = 0.2$ mm, the maximum of the velocity fluctuations is located at $\phi = 9$ to 10 deg, which is equivalent to a distance of two jet diameters. For the jet impinging on a non-rotating disk, this maximum was found at approximately 1.8 jet diameters. Upstream of the jet, the fluctuations are 1.2 to 2 times higher due to the strong shear associated with the disk rotation and wall flow. Beyond some distance away from the jet center ($\phi \sim 20$ deg), the turbulence intensity is not affected at all by the jet and approaches the same levels as for the disk flow without the jet.

Some results for $\alpha = 0.07$ to 0.13 are shown in Figs. 2(b–f), which signify typical characteristics of jet-wall flow interaction; here the jet is able to expand in the upstream direction. In the comparison of these results with those in Fig. 2(a), lower relative velocities and turbulent intensities are evident. Here the wall flow velocities close to the disk ($z = 0.2$ mm) are only 30 to 50 percent of the average jet velocity w_{jet}. The upstream development of the azimuthal jet flow shows an increasing expansion with increasing α; i.e., the upstream velocity distribution becomes similar to the downstream flow, but the velocities are lower. With increasing influence of the jet, it is apparent that the flow pattern begins to separate into two regions. In the first, within approximately one jet diameter, the flow is governed by the features of the jet deflected at the wall (velocities

Contributed by the Fluids Engineering Division for publication in the JOURNAL OF FLUIDS ENGINEERING. Manuscript received by the Fluids Engineering Division August 23, 1994; revised manuscript received June 7, 1995. Associate Technical Editor: H. Hashimoto.

Copyright © 1996 by ASME

Downloaded 03 Jun 2010 to 171.66.16.125. Redistribution subject to ASME license or copyright; see http://www.asme.org/terms/Terms_Use.cfm

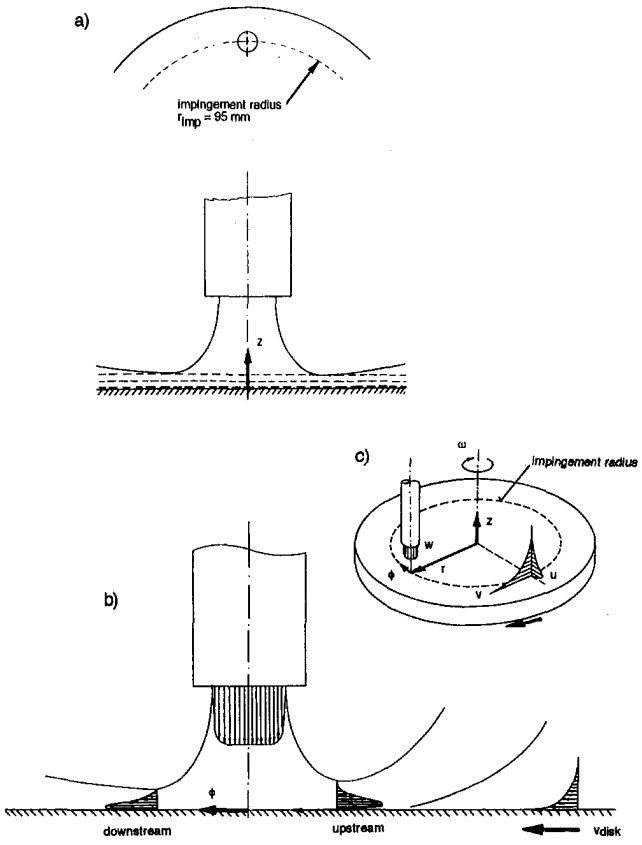


Fig. 1 A schematic of the jet-rotating disk interaction and measuring planes

scale well with w_{jet}). The second region is characterized by the collision of the jet flow with the wall flow. Close to the nozzle center the velocity distributions show a symmetrical acceleration in both directions with respect to the nozzle center-line. An interesting fact is the coincidence of the symmetry plane of acceleration with the nozzle center-line (Figs. 2(*b*) to 2(*f*)). This implies that the jet is not at all deflected by the wall flow, down to the lowest measuring plane at $z = 0.2$ mm. At $z = 0.2$ mm, the acceleration in the direction of disk rotation reaches a maximum at 1.1 jet diameter, which is identical with the point of maximum velocity in the case without rotation (see Part I, Fig. 4). This also corresponds to the area where the pressure gradient generated by the jet when impacting on the surface becomes most effective. At the same circumferential position the normalized velocity becomes zero for $z = 2.0$ mm, i.e., one quarter jet diameter in the axial direction, which also coincides with the non-rotating case. Further downstream, the velocity profile approaches the shape of the pre-interaction profile.

The peaks of the turbulence intensity, upstream of the jet, are located where the deceleration is greatest. In Fig. 2(*b*) these peaks are close to the nozzle axis but far enough away not to affect the jet center. It can be conjectured that the upstream turbulence intensity is determined by the collision of jet and wall flows as well as by the shear between the jet flow and ambient fluid. For all cases investigated, the location of the downstream peak of the turbulence intensity is found to be identical with the results of the non-rotating case. Further downstream, the turbulence intensity at $z = 0.2$ mm approaches the same values as before the interaction. However, with increasing Re_{disk}, the turbulence intensity far downstream becomes greater at $z > 0.2$ mm. Higher jet exit velocity at the nozzle produces greater shearing with the ambient fluid, and thus the mixing with ambient fluid becomes more intense. The above-mentioned flow properties can best be seen in the sample shown in Fig. 2(*f*). It exhibits the flow pattern of a fully jet-dominated interaction. Between the cases shown in Figs. 2(*c*) and 2(*f*), there is a distinct change in flow pattern for $\alpha > 0.125$. For $\alpha > 0.125$, the jet first expands as if there is no disk flow and then collides with the oncoming wall flow. The distribution of the turbulence intensity exhibits two separate peaks. The first reflects the axisymmetric deflection and lateral expansion of the jet flow, and the second the collision, shearing and mixing with the wall flow. This is consistent with the measured velocity distribution.

All of the above results are summarized in Fig. 3, which includes the measurements in the planes $z = 0.2$ and 2.0 mm. The results obtained without the disk rotation are also included. Once the jet is strong enough to expand against the disk flow, an increase in jet strength causes the flow to approach the non-rotating case. From Fig. 3 it is clear that for the case of highest α ($\alpha = 0.158$), the normalized turbulence intensities match almost everywhere with the non-rotating case, except for the peak magnitude. This is surprising, since this effect can also be found at $z = 0.2$ mm, which is just 2.5 percent of the jet diameter and very close to the wall. It also shows that for the case of $z = 0.2$ mm, the turbulence intensity far downstream from the jet center is not strongly determined by the wall motion, but by the properties of the jet. In Fig. 4, the maximum normalized turbulence intensities of all investigated cases are plotted as a function of α. Though there is a slight uncertainty with regard to the maximum values (the point of the real maximum might not have been investigated), a principal dependence is visible. At large α ($\alpha > 0.125$), values of $(v'^2)^{1/2}/w_{jet}$ approach the values of the non-rotating case. This means, that for $\alpha < 0.125$ the maximum turbulence intensity is determined by the interaction of the wall flow and jet flow.

The development of the azimuthal velocity profiles with varying jet flow rate is shown in Figs. 5(*a–c*) for three circumferential positions. In these plots, the distance z from the disk surface is normalized with the impingement radius, in order to compare the results with the case of no jet impingement. The experiments cover the range of $0.019 < \alpha < 0.131$. Again, the results show the thinness of the shear layer between the moving disk and the upstream jet. It should be noted, that the diameter of the LDV-probe volume (0.18 mm) is of the same order as the smallest distance between the probe volume and rotating disk (0.2 mm) and that the disk could wobble up to 0.05 mm peak-to-peak. Therefore, the data cannot be used to evaluate the shear stress. For $\phi = -5$ deg (Fig. 5*a*), the azimuthal velocity profiles correspond to the change from fully developed jet domination (with the smallest wall jet thickness at about −5 deg) to a

Nomenclature

d = diameter (m)
f = flow property, see Eq. (1)
g_1, g_2, g_3 = functions (−)
M = momentum flux (m^4/s^2)
n = rotational speed (Hz)
Q = flow rate (ml/s)
Re_{disk} = disk Reynolds number (−)
Re_{jet} = jet Reynolds number (−)
u, v, w = velocity components (m/s)
u', v', w' = r.m.s. turbulent velocities (m/s)
r, ϕ, z = polar coordinates (m, deg, m)
Z = distance between disk and shroud (m)
α = ratio of Reynolds numbers Re_{jet}/Re_{disk} (−)
ν = kinematic viscosity (m^2/s)
ω = angular speed ($2\pi n$)

Downloaded 03 Jun 2010 to 171.66.16.125. Redistribution subject to ASME license or copyright; see http://www.asme.org/terms/Terms_Use.cfm

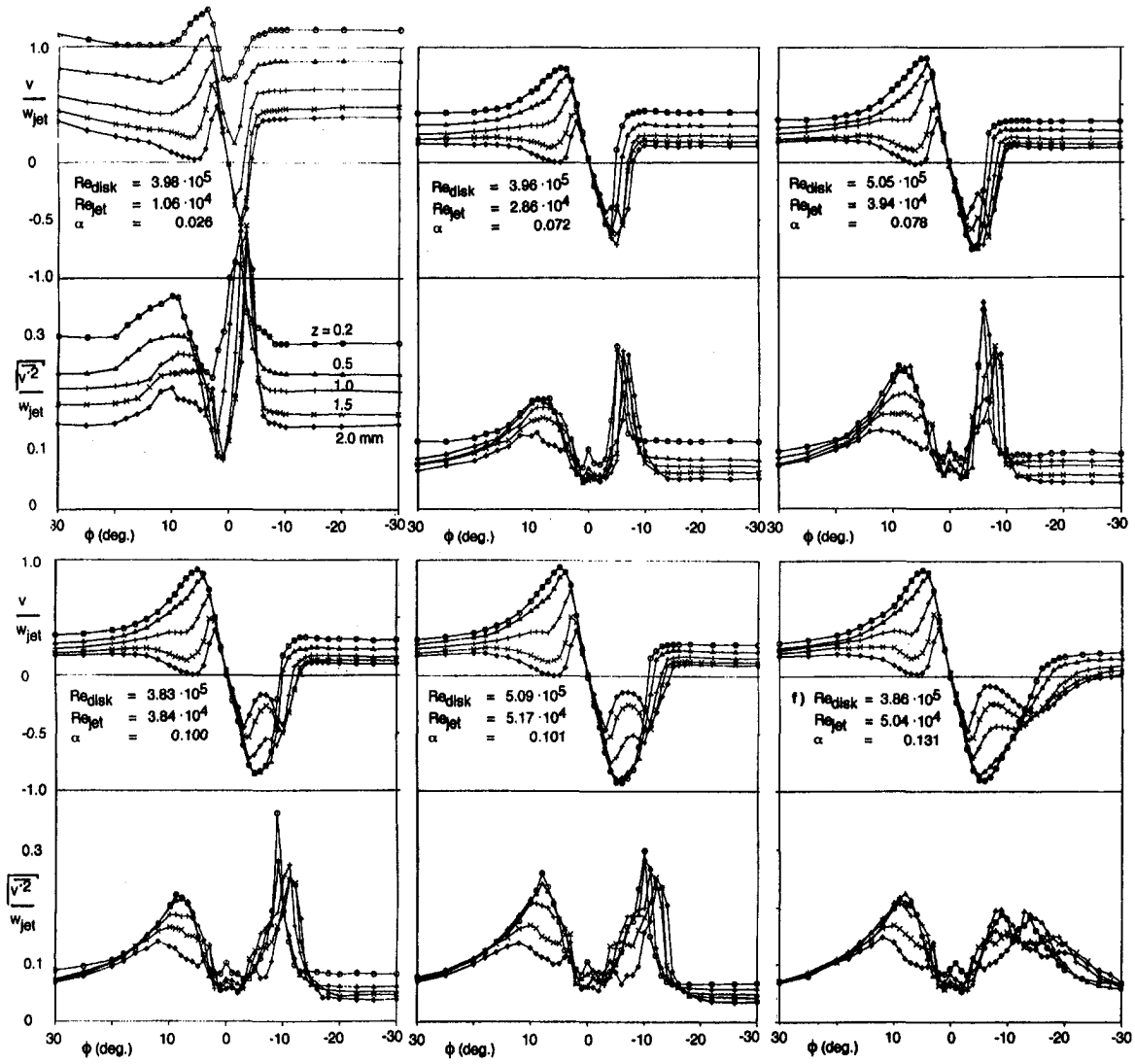


Fig. 2 Distribution of dimensionless azimuthal velocity and turbulence intensity along impingement radius for various jet and disk Reynolds numbers; d_{jet} = 8 mm, r_{jet} = 95 mm

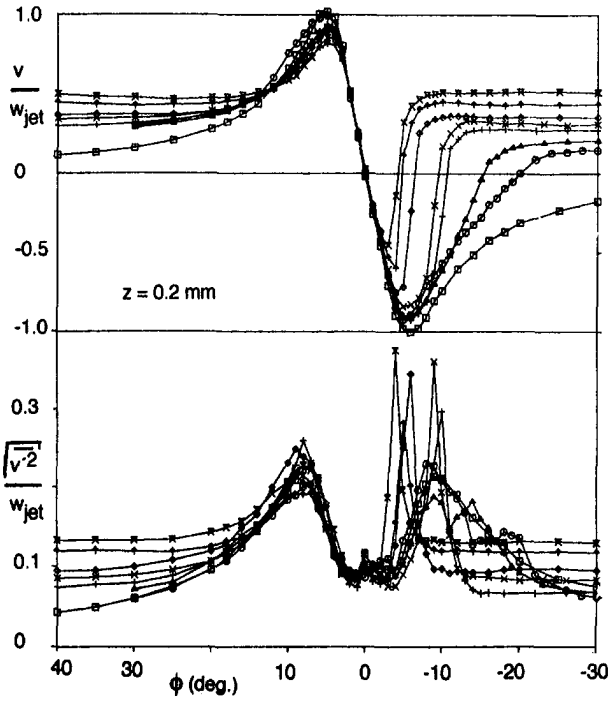
decelerated, lifted and eventually totally deflected jet flow. For positions at the jet outer diameter ($\phi = -3$ deg) and within the jet core ($\phi = -1$ deg) the flow partially remains unaffected by the changes that occur upstream of it. Because of the smooth change of the flow pattern from the jet dominated to undisturbed wall flow and vice versa, it is difficult to draw an exact demarcation that separates jet dominated and disk-rotation dominated regimes. However, it seems reasonable to consider the case no. 7 in Fig. 5(b) ($\alpha = 0.055$) as jet dominated, since the velocity profile has developed the typical shape of a starting wall jet; the profile of case no. 6 ($\alpha = 0.045$) lacks this character. Thus, the separation between jet and wall domination appears to occur at $\alpha \sim 0.05$. The locations of ϕ for $v = 0$, as an indicator for the jet flow expansion, are shown in Fig. 6 for different z values. All collision fronts over z are similar except for the changes which take place between $\alpha = 0.12$ and 0.13. Then the gradient of the jet flow expansion becomes much steeper. From these and other measurement points that are not included here, ϕ ($v = 0$) points at $z = 0.5$ mm were extracted and are plotted in Fig. 7 as a function of α. The circumferential distance from the jet center is not measured in degrees but in equivalent millimeters to compare the results with those obtained with higher impingement radii. The dependence of the jet expansion on α is very clear from this plot.

3 Transition From Disk-Flow Dominated to Jet-Flow Dominated Regime

As mentioned before, the transition from a disk-flow dominated to a jet-flow dominated regime is important because it is associated with a sharp rise in the cooling rate of the disk. The difference of the flow patterns was discussed in Part I (e.g., Fig. 6), and the profiles depicted in Fig. 5(b) were used in Section 2 to define the boundary between the regimes. The detailed velocity profile measurements of the present study complements the previous work of Grochowsky (1975) who used smoke flow visualization to observe flow patterns near the jet impingement on unshrouded disks. Further, Grochowsky (1979) classified the flow patterns based on whether the jet expands into the upstream flow or not. The transition values of Re_{disk} between the two regimes were presented as a function of the ratio of jet flow rate to pumped wall flow rate, but the data were widely scattered.

For sufficiently large disks and confining boundaries far away from the jet location, it is possible to write any property f at a given location (r, ϕ, z) as a function of the local disk velocity $v_{disk} = \omega r$, kinematic viscosity of the fluid ν, location of the jet (r_{jet}, 0, z_{jet}) and the properties of the jet; the jet can be represented using its specific momentum flux M (List, 1982) and

Downloaded 03 Jun 2010 to 171.66.16.125. Redistribution subject to ASME license or copyright; see http://www.asme.org/terms/Terms_Use.cfm



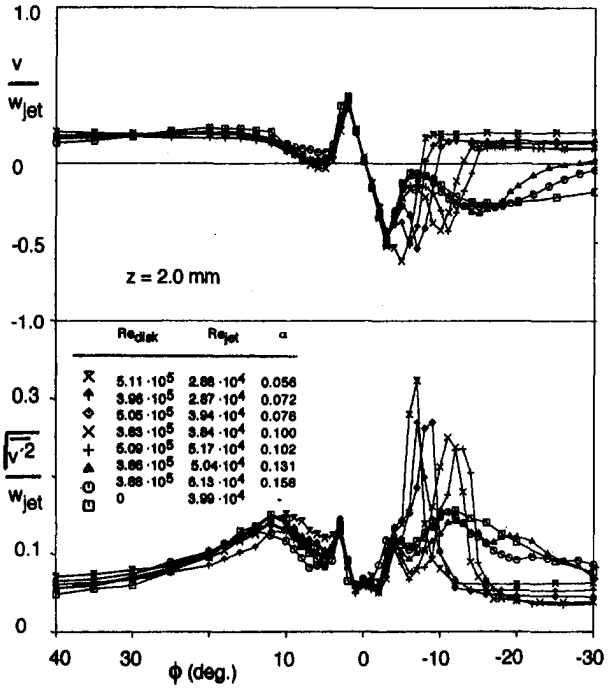


Fig. 3 Comparison of flow characteristics along the impingement radius for various jet flow rates with jet impingement on a stationary surface; d_{jet} = 8 mm, r_{jet} = 95 mm

the jet diameter d_{jet}, where $M = \pi/4 d_{jet}^2 w_{jet}^2$ and w_{jet} is the velocity at the jet exit. Thus we obtain

$$f = f(r\omega, r, \phi, z, M, z_{jet}, r_{jet}, \nu, d_{jet}) \quad (1)$$

or

$$f = f(r^2\omega/\nu, M^{1/2}/\nu, z/z_{jet}, \phi, r/r_{jet}, r/z_{jet}, z/d_{jet}) \quad (1a)$$

Note that $Re_{disk} = r^2\omega/\nu$ is the local disk Reynolds number at a radius r and $Re_{jet} = (2/\pi^{1/2})M^{1/2}/\nu$ is the jet Reynolds

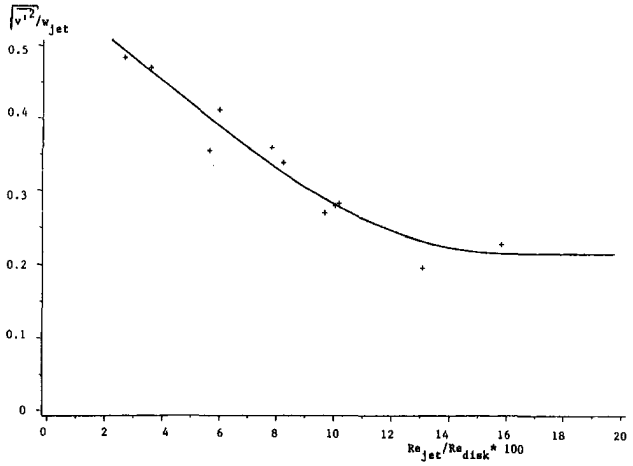


Fig. 4 Maximum turbulence intensity measured upstream of the jet over a range of α; d_{jet} = 6 and 8 mm

number. Based on Eq. (1a), it is possible to conclude that the transition between the regimes near the disk, at $z = \phi = 0$, should be governed by an expression of the form

$$0 = g_1(r^2\omega/\nu, M^{1/2}/\nu, r/z_{jet}). \quad (2)$$

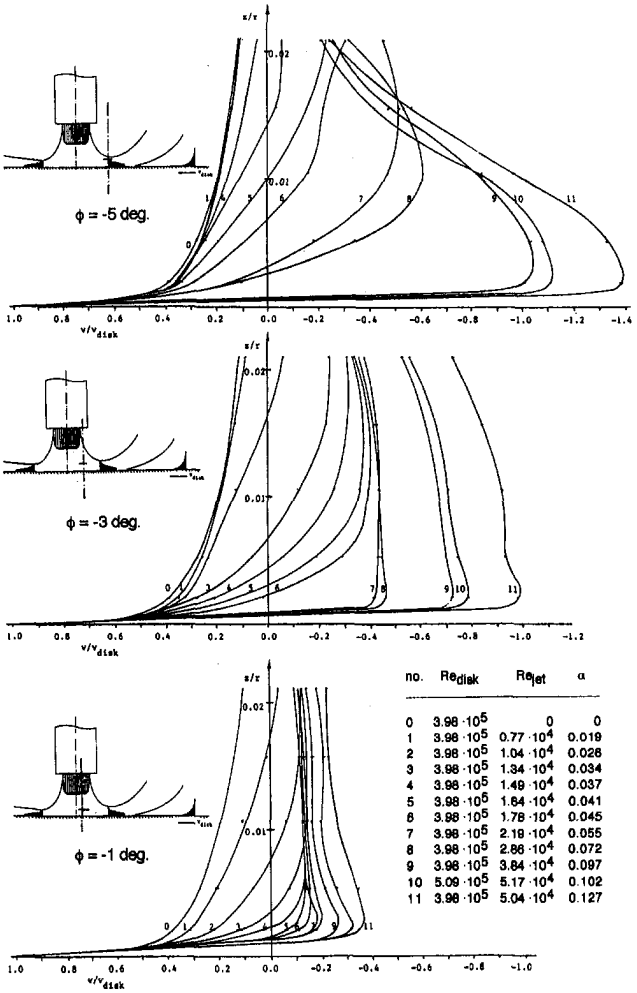


Fig. 5 Azimuthal velocity profiles; v/v_{disk} versus z/r_{jet}, for different disk and jet Reynolds numbers; d_{jet} = 8 mm, r_{jet} = 95 mm; (a) $\phi = -5$ deg, (b) $\phi = -3$ deg, (c) $\phi = -1$ deg (ϕ values are indicated in the upper left-hand corner)

Downloaded 03 Jun 2010 to 171.66.16.125. Redistribution subject to ASME license or copyright; see http://www.asme.org/terms/Terms_Use.cfm

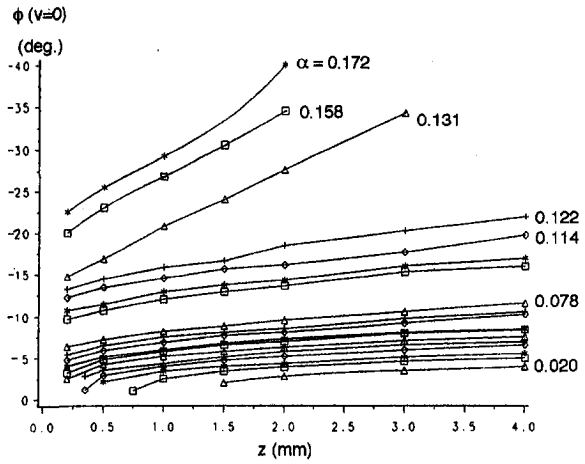


Fig. 6 Flow expansion upstream of the jet at different heights; d_{jet} = 8 mm, r_{jet} = 95 mm

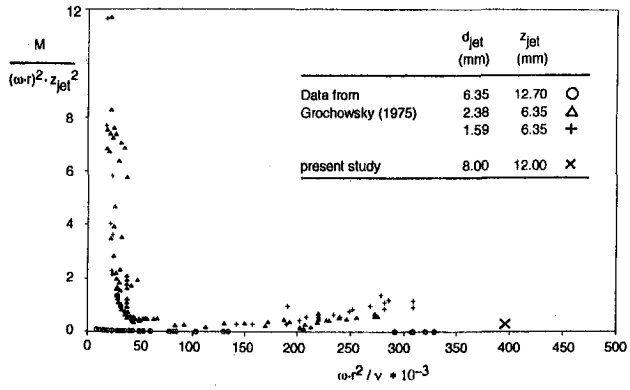


Fig. 8 A plot of $M/((\omega r)^2 z_{jet}^2)$ versus $Re_{disk} = r^2\omega/\nu$ at the transition between jet domination and disk-rotation domination

This can be arranged to include a parameter that signifies the relative magnitude of the velocity of the jet ($\sim M^{1/2}/z_{jet}$) and the velocity of the disk surface, as

$$M/((\omega r)^2 z_{jet}^2) = g_2(r^2\omega/\nu,\ r/z_{jet}). \quad (3)$$

Another possible form is

$$M^{1/2}/\omega r^2 = g_3(r^2\omega/\nu,\ r/z_{jet}). \quad (4)$$

Note that $M^{1/2}/\omega r^2$ signifies the ratio of eddy viscosities within the jet and in the wall boundary layer, which can be parameterized as $M^{1/2}$ and ωr^2, respectively. The data of Grochowsky (1975) are plotted in Figs. 8 and 9 based on Eqs. (3) and (4). The data, when plotted between the variables $M/((\omega r)^2 z_{jet}^2)$ versus $r^2\omega/\nu$ or $M^{1/2}/\omega r^2$ versus $r^2\omega/\nu$, collapse exceedingly well, particularly in the latter case, except for the experimental run with d_{jet} = 6.35 mm. The data point obtained in the present study (x), with water as a working fluid, also collapses with Grochowsky's data. During these experiments, r/z_{jet} was widely varied but no apparent effect could be discerned. The offset of Grochowsky's data for d_{jet} = 6.35 mm (o) is due to his definition of a transition smoke pattern. For this jet size, smoke patterns were classified as rotation-dominated, which are comparable with case no. 8 of Fig. 5, but here they are considered as jet dominated. For Grochowsky's smaller jet diameters it is apparent, based on close inspection of the smoke pattern photographs, that the definition for the transition matches the one in Fig. 5. The interaction phenomenon appears to be governed by either $M^{1/2}/\omega r^2$ or $M/((\omega r)^2 z_{jet}^2)$. Figure 9 shows that for $Re_{disk} > 10^5$ the transition occurs at $M^{1/2}/\omega r^2 = 0.05$ (or within a narrow band around this value). Considering the symmetry of the flow pattern relative to the impingement area (Part I), this result might extend to cases where a jet interacts with linearly moving surfaces.

4 Conclusions

Detailed flow field measurements have been carried out to investigate the flow field generated by the impingement of a jet on a rotating disk. The jet flow rate, impingement radius, rotational speed of the disk and the jet diameter were varied to obtain a range of disk (Re_{disk}) and jet Reynolds numbers (Re_{jet}). The jet flow and the wall boundary layer are fully turbulent over this range. The essential findings of this study can be summarized as follows. The structure of the flow field and the distribution of the turbulence intensity appear to be governed by either of the parameters $M/((\omega r)^2 z_{jet}^2)$ or $M^{1/2}/\omega r^2$, where the latter is identical to the ratio of the Reynolds numbers α. The ratio α determines the distance over which the jet expands against the disk flow. When the jet expands against the disk flow it simultaneously penetrates deep into the wall boundary layer and the jet center-line coincides with the nozzle center-line; the jet expansion occurs axisymmetrically around it. At large α, expanding jet characteristics become much the same as that of jet impingement on a stationary surface. The maximum velocities occur at approximately 1.1 jet diameters measured from the jet center, and there is a positive pressure gradient

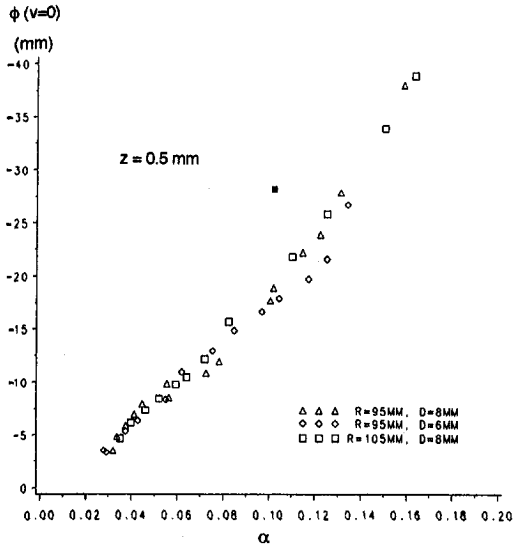


Fig. 7 Flow expansion upstream of the jet at z = 0.5 mm (circumferential coordinate is in mm)

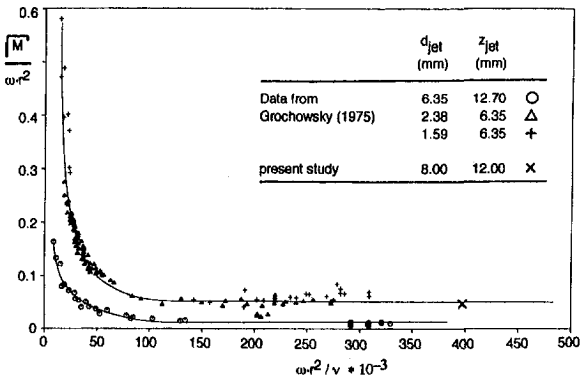


Fig. 9 A plot of $M^{1/2}/\omega r^2$ versus $Re_{disk} = r^2\omega/\nu$ at the transition between jet domination and disk-rotation domination

Downloaded 03 Jun 2010 to 171.66.16.125. Redistribution subject to ASME license or copyright; see http://www.asme.org/terms/Terms_Use.cfm

within this deflection area. This pressure gradient can be regarded as the source for the axisymmetric flow pattern, even in the presence of disk rotation. At the outer edge of the impingement zone, the boundary-layer thickness of the wall jet is about one quarter of a jet diameter. The distribution of turbulence intensities is mainly governed by α and the jet structure. For high α, the interaction flow field can be separated into three zones: (i) the collision zone, where collision, mixing and lifting of the wall jet and disk wall flow occurs and where the level of turbulence intensity is determined only by α, (ii) an extended deflection zone around the jet center-line where the distribution of turbulence intensity is only dependent on the jet flow structure and geometry, and (iii) a zone downstream of the jet center where the turbulence depends on both the jet flow structure and disk surface velocity. The jet flow structure is basically dependent on mixing of the jet flow with the ambient fluid, and the maximum turbulent intensity for both rotating and nonrotating disk cases occurs at about 1.8 jet diameters away from the jet center-line. For low values of α, the first two zones come closer and finally merge, but the downstream area remains mainly uninfluenced by this change. The above flow patterns can be considered as typical of jet-wall flow interactions. The demarcation between rotation-dominated and jet-dominated cases appears to be determined by a certain relationship between $M^{1/2}/\omega r^2$ and $\mathrm{Re}_{\mathrm{disk}}$ or $M/((\omega r)^2 z_{\mathrm{jet}}{}^2)$ and $\mathrm{Re}_{\mathrm{disk}}$. Within the accuracy of present measurements, it was not possible to determine which relationship is most appropriate. In any event, it was found that this transition is unaffected by $\mathrm{Re}_{\mathrm{disk}}$ when $\mathrm{Re}_{\mathrm{disk}} > 10^5$; then the transition occurs for $M^{1/2}/\omega r^2 = 0.05$.

Acknowledgments

This study was supported by a post-doctoral fellowship from the Alexander von Humboldt-Foundation, Federal Republic of Germany. Additional funding was provided by NASA Marshall Space Flight Center through a contract with the Rocketdyne Division of Rockwell International, Allied-Signal Aerospace Corporation and the National Science Foundation.

References

Grochowsky, L. D., 1975, "An Investigation of Flow Interactions and Heat Transfer Characteristics For Single Jet Impingement on Rotating Disks," MS thesis, Arizona State University, Tempe, Ariz.

List, E. J., 1982, "Turbulent Jets and Plumes," *Annual Review of Fluid Mechanics,* Vol. 14, Annual Review Inc., Palo Alto, Calif., pp. 189–212.

Downloaded 03 Jun 2010 to 171.66.16.125. Redistribution subject to ASME license or copyright; see http://www.asme.org/terms/Terms_Use.cfm

C. Maranges
Institut National des Sciences Appliquées,
Centre de Bioingénierie G. Durand
(URA CNRS 544, L.A. INRA),
Complexe Scientifique de Rangueil,
F31077 Toulouse Cedex, France

G. Arroyo
Research Engineer.
Centre National du Machinisme Agricole,
Division Technologie,
17 avenue de Cucillé,
F35044 Rennes Cedex, France

C. Fonade
Professor.
Institut National des Sciences Appliquées,
Centre de Bioingénierie G. Durand
(URA CNRS 544, L.A. INRA),
Complexe Scientifique de Rangueil,
F31077 Toulouse Cedex, France

J. L. Estivalezes
Research Engineer.
CERT-ONERA,
Dpt de mécanique et energétique
des systèmes,
2 avenue E. Belin,
F31055 Toulouse Cedex, France

Numerical Study of an Unsteady Confined Jet. Application to Crossflow Filtration

This paper deals with the influence of a new flow unsteadiness on the permeate flux in crossflow filtration. A pneumatically controlled valve generates intermittent jets from the main flow, leading to the formation of large vortices moving downstream along the tubular membrane. A numerical calculation of this flow is achieved using a finite difference scheme. Influences of tube diameter and jet velocities are discussed. Application of this technique is carried out by filtering a bentonite suspension through an ultrafiltration membrane.

1 Introduction

Crossflow filtration is increasingly used in biochemical and food industries for concentration, purification, and separation of macromolecules, colloids, and suspended particles from solutions. Indeed, in many industrial applications, crossflow filtration systems are favored over other traditional separation methods due to their athermal character. However, the rapid fall in permeate flux, which is attributed to membrane fouling and concentration polarisation, limits their industrial development. In most cases, the main cause of the flux decline is the formation of an external fouling layer on the surface of the membrane. For that reason, specific hydrodynamic conditions have been proposed for maintaining high fluxes by reducing the thickness of that layer (Belfort and Nagata, 1985; Schulz and Ripperger, 1989). The most common way to increase the wall shear stresses which control the thickness of the boundary layer is to use high crossflow velocities (up to 5 or 6 $m \cdot s^{-1}$). However, this results in high pressure drops, transmembrane pressure changes along the membrane and, of course, energy consumption increase. Other techniques, such as turbulence promoters (Poyen et al., 1984), rotating membranes (Kroner et al., 1987) or pulsating flows (Finnigam and Howell, 1989; Doubrovine, 1992), have been proposed but they often remain as complex technologies. However, all these studies have shown that a significant flux enhancement can be obtained from high turbulence intensities or flow unsteadiness.

The present paper deals with another type of unsteadiness which can be expected to increase the average transverse convection outward from the membrane. A detailed description of the unsteadiness principle was given by Arroyo and Fonade (1993) but, for convenience, it is briefly recalled here. A circular nozzle is coaxially located upstream of the filtration tube. By means of a pneumatically controlled valve, the flow passes periodically either through the entire section of the tube (annulus part and jet nozzle) or only through the nozzle (Fig. 1). The period of this switching process is T and each sequence lasts for T/2. The aim of the unsteadiness principle is to periodically generate large vortices which can sweep the surface of the membrane when moving downstream. In order to find out the best technical conditions for the generation and conservation of strong vortices along the tube wall, we have carried out a preliminary numerical study of which the conclusions are given in Section 3.

The flow field generated by a free intermittent jet has been investigated experimentally in a plane configuration (Abd-Elmessih, 1985). It was found that the effect of the unsteadiness is maintained over a long distance, more than 60 slot widths, and that very high transient turbulence intensities exist inside the vortices. These two properties are interesting in the filtration process, provided that confinement by the tube does not damp the vortices too rapidly.

2 Basic Equations and Solution Procedure

The flow considered in the present study was assumed to be Newtonian, laminar and incompressible with a constant kinematic viscosity, taken as being equal to that of water. The dimensionless Navier-Stokes equations written in Cartesian tensor notation may be expressed as follows:

Contributed by the Fluids Engineering Division for publication in the JOURNAL OF FLUIDS ENGINEERING. Manuscript received by the Fluids Engineering Division July 15, 1994; revised manuscript received November 6, 1995. Associate Technical Editor: A. F. Ghoniem.

Copyright © 1996 by ASME

Downloaded 03 Jun 2010 to 171.66.16.125. Redistribution subject to ASME license or copyright; see http://www.asme.org/terms/Terms_Use.cfm

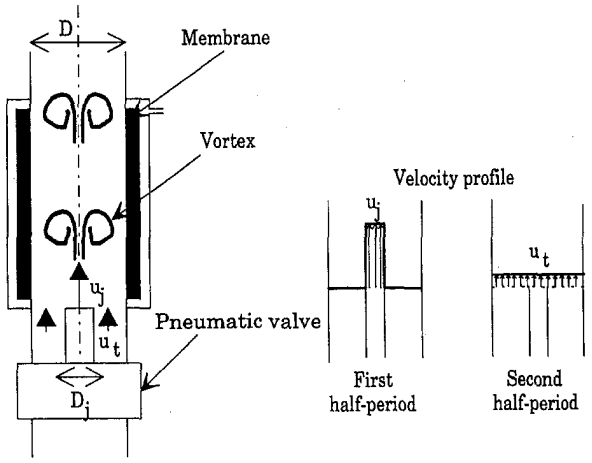


Fig. 1 Generation of vortices in a tubular membrane by means of an intermittent jet

$$\frac{\partial(yu)}{\partial x} + \frac{\partial(yv)}{\partial y} = 0 \tag{1}$$

$$\frac{\partial u}{\partial t} + u\frac{\partial u}{\partial x} + v\frac{\partial u}{\partial y} = -\frac{1}{\rho}\frac{\partial p}{\partial x} + \nu\left[\frac{\partial^2 u}{\partial x^2} + \frac{1}{y}\frac{\partial}{\partial y}\left(y\frac{\partial u}{\partial y}\right)\right] \tag{2a}$$

$$\frac{\partial v}{\partial t} + u\frac{\partial v}{\partial x} + v\frac{\partial v}{\partial y} = -\frac{1}{\rho}\frac{\partial p}{\partial y} + \nu\left[\frac{\partial^2 v}{\partial x^2} + \frac{\partial}{\partial y}\left(\frac{1}{y}\frac{\partial(yv)}{\partial y}\right)\right] \tag{2b}$$

$$\frac{\partial c}{\partial t} + u\frac{\partial c}{\partial x} + v\frac{\partial c}{\partial y} = D_s\left[\frac{\partial^2 c}{\partial x^2} + \frac{1}{y}\frac{\partial}{\partial y}\left(y\frac{\partial c}{\partial y}\right)\right] \tag{3}$$

In the above, u and v denote the velocity in the axial and radial directions, respectively, p the pressure, and c the solute concentration.

In order to solve the system of partial differential equations governing the mean flow, the solution algorithm of Shimizu and Wada (1985) was appropriately modified. The code, in its original form, embodied a centered difference scheme for both convection and diffusion terms. In this, the Marker and Cell method (MAC method) due to Harlow and Welch (1965) was used. Because of the problem of stability posed by the FTCS formulation, an alternative scheme, proposed by Viecelli (1971), was incorporated into the basic code: it is a backward difference scheme for the convection terms. With regard to the concentration equation, we adopted a fully explicit calculation based on a forward-in-time and centered-in-space scheme. But, as for the Navier-Stokes equations, we modified the convection terms with a two points backward scheme in order to increase the procedure stability. It would go beyond the scope of this paper to discuss the scheme and its performance in detail; such a discussion is provided in reference (Shimizu and Wada, 1985) so that it may suffice here to provide a brief description of the salient features of the scheme. It is based on solving accurately, at the beginning of each time step a Poisson equation for the pressure under the additional constraint that the updated velocity field is divergence-free. The resulting pressure is then inserted in the Navier-Stokes equations to compute the true velocity field.

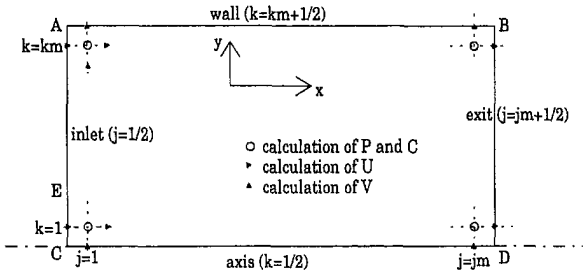


Fig. 2 Flow field for computing and coordinates system

Figure 2 shows the computational flow field and boundaries. The boundary AB is a no-slip wall ($u = 0$) through which filtration can take place ($v \neq 0$). As it is difficult to predict the spatial filtration velocity variations in a fouled system, we took in our simulations a uniform and overestimated filtration velocity ($10^{-3}\ u_j$). The boundary CD is a symmetric axis ($v = 0$, $\partial/\partial y$ of all other quantities $= 0$). At the inlet AC, the flow is assumed parallel to the x-axis. It consists of a primary flow entering through CE and a secondary flow entering through EA. The wall separating the two flows (E) is assumed to be without thickness. AE and EC contain a whole cell number and the inlet velocity profiles are uniform ($v = 0$). The exit boundary BD is in the flow field. Therefore, we cannot specify the velocity along this boundary. Ikeda (1977) assumed that the disturbance travelled downstream with a constant velocity to specify quantities along the boundary. However, we adopted the plausible assumption that the longitudinal component u may vary linearly in the flow direction, and that $\partial^2 u/\partial^2 x$ tends to zero on the boundary. This condition is not consistent with the pressure condition (uniform profile) but was the most satisfactory we found. One of its main advantages was that, unlike the classical condition $\partial u/\partial x = 0$, it allowed the tracking of the vortices until they reached the exit or, more precisely, until negative longitudinal velocity components appeared on the outflow boundary.

As we simulate an unsteady flow where the high gradient areas move in the whole field, all the calculations were done with a uniform grid in each direction. But, in order to save computation time, the cells were 3 times larger in the x direction than the y direction. The effect of mesh size on the results was examined by performing computations in three different cases, where the total number of grid points are, respectively, 80 by

Nomenclature

C = solute concentration ($g \cdot l^{-1}$)
D = tubular filter diameter (m)
D_j = nozzle or jet diameter (m)
D_s = solute diffusivity ($m^2 \cdot s^{-1}$)
J = permeate flux ($m \cdot s^{-1}$)
J_0 = initial permeate flux for each filtration run ($m \cdot s^{-1}$)
J_R = relative flux for each filtration run, $J_R = J/J_0$
p = pressure (Pa)
R = relative hydraulic resistance, $R = (J_0/J) - 1$
T = period of the jet intermittence (s)
u = x-directed velocity ($m \cdot s^{-1}$)
u_j = jet velocity ($m \cdot s^{-1}$)
v = y-directed velocity ($m \cdot s^{-1}$)
v_p = velocity filtration ($m \cdot s^{-1}$)
V_{tot} = velocity magnitude $(u^2 + v^2)^{0.5}$
Δx = axial grid spacing (m)
Δy = radial grid spacing (m)
ρ = fluid density ($kg \cdot m^{-3}$)
ν = kinematic viscosity ($m^2 \cdot s^{-1}$)
Ψ = angle made by the local velocity vector with the axial direction (rad)

Downloaded 03 Jun 2010 to 171.66.16.125. Redistribution subject to ASME license or copyright; see http://www.asme.org/terms/Terms_Use.cfm

20, 160 by 20 and 160 by 40. Although no observable influence was found, the finest mesh size was used in the remaining computations in order to be on the safe side. To assess the extent of the numerical error, the numerical coefficient suggested by De Vahl Davis and Mallinson (1976) $\mu_f = \rho V_{tot} \Delta x \Delta y \sin 2\Psi / 4(\Delta y \sin^3 \Psi + \Delta x \cos^3 \Psi)$ was evaluated for the entire flowfield. As it is always one order of magnitude less than the fluid viscosity, we can say that numerical viscosity does not influence significantly the numerical results.

3 Results and Discussion

3.1 Preliminary Examination. Preliminary studies were made on several points, prior to the main study, to avoid possible misinterpretation of the computed results. The points studied are briefly mentioned in the following paragraphs.

Flow Structure. In the case of crossflow filtration application, the following guidelines can be deduced (Fig. 3):

When an intermittent jet is used, the generation and characteristics of the vortices essentially arise from the inertial effects due to the difference in velocity between the jet and the surrounding fluid. The shear stresses arising from viscosity effects or turbulence will affect the development of these vortices and the rapidity of transfer of the energy they contain into smaller and smaller eddies.

These vortices are transported downstream by the main flow. Their velocity was found to be in the range [0.25 u_j; 0.4 u_j], a little less rapid than in free jets where the vortex velocity is approximately 0.5 u_j. This transport results in turbulence intensity values higher than the ones which can be expected from turbulence generation by the tube wall effect alone. However, this effect is only valid along a certain tube length, depending on geometric parameters and viscosity. This point is also under investigation.

In the first part of the tube, where the vortices are still coherent, both radial and axial components of the velocity periodically change their direction. In absolute values, it is the x-component which is the more affected but the negative values taken by the y-component are very interesting because they are of the same order of magnitude as a high filtration velocity.

Finally, when the jet is stopped, the flow recirculation is amplified. However, this positive effect is balanced by the vortex weakening which cannot be compensated by a rapid reopening of the jet because the new vortex quickly catches up the previous one and the two rotations interfere. It means that the frequency of the jet intermittence must not be too high. Moreover, the part of the period during which the jet remains open must be long enough to maintain the rotation of the vortex while it moves forward along the tube.

Program Validation. In order to validate the program, comparison of the numerical results was carried out with specific experimental data relative to the formation and displacement of the first vortex generated in the still fluid. Using a hot film anemometer (DISA 56B10), the amplitudes of velocity were recorded in several transverse sections and radial positions for 3 different flowrates ($1.4\ 10^{-5}$ m$^3 \cdot$s^{-1}, $2.7\ 10^{-5}$ m$^3 \cdot$s^{-1} and $4.2\ 10^{-5}$ m$^3 \cdot$s^{-1}) that is, jet velocities of $23\ 10^{-2}$ m$\cdot$s^{-1}, $44\ 10^{-2}$ m$\cdot$s^{-1} and $68\ 10^{-2}$ m$\cdot$s^{-1}. The experimental setup consists of a vertical tube ($4.4\ 10^{-2}$ m internal diameter) supplied at its bottom by a jet of diameter $8.8\ 10^{-3}$ m. At the same time, simulations are carried out for each of the velocity values on a field length which represents 16.8 times the tube diameter. Figure 4 shows an example of the variation with time of the measured and calculated velocities. Good agreement was obtained, especially for the displacement velocity and the characteristics of the front edge of the vortex. However, this validation is acquired within a very short distance after the jet exit: the vortex is experimentally detected only at a distance of 2.7 D. Beyond this value, we could not identify the presence of a coherent structure, only a higher turbulence intensity was noted. It is probable that the vortex has turned into a more turbulent form, not detected by the hot film probe, but it cannot be fully concluded whether a coherent structure still existed or not. Only an unsteady turbulence calculation could allow us to answer this question. Another important difference exists between experiment and simulation: experiments showed systematically more disturbances and higher velocities on the rear edge of the vortex. As the flow is not strictly axisymetric, these fluctuations are due both to the helicoidal circulation which causes large turbulent structures and to the periodic emission of two rows of vortices along the side of the jet which increases the turbulence. In the case of crossflow filtration applications, this phenomenon turns out to be very effective.

3.2 Results and Discussion. The numerical study principle consists in the velocity and solute concentration analysis on the last cell nearest the wall. As the calculation times were very large, the work was limited to a sample case allowing us to take out general principles. All the simulations were based on the hot film anemometer experiment for which we have changed velocity and geometry parameters. Table 1 summarizes the parameters characterizing the simulation conditions. The initial state of each simulation is obtained after a 1000 time interval simulation with the velocity and the solute concentration maintained uniform on the whole inlet section, respectively, at $u = u_t$ and $C = 1$.

Influence of the Jet Velocity. Six simulations were made with the following jet velocities: $0.44\ 10^{-2}$ m$\cdot$s^{-1}, $0.88\ 10^{-2}$ m$\cdot$s^{-1}, $1.32\ 10^{-2}$ m$\cdot$s^{-1}, $1.76\ 10^{-2}$ m$\cdot$s^{-1}, $2.2\ 10^{-2}$ m$\cdot$s^{-1} and $4.4\ 10^{-2}$ m$\cdot$s^{-1}. When the jet velocity increases, the vortex advance is not modified in dimensionless time. On the other hand, the velocity fluctuation amplitudes and the highest negative velocities at the wall are multiplied by a factor at least proportional to the jet velocity, and this takes place in both radial and axial directions. However, these disturbances do not have any influence on the polarisation concentration layer. Indeed, the concentration profile trough is of the same order of magnitude whatever the jet velocity. Moreover, after the passage of the vortex, the wall concentration rises and reaches the same value as a nondisrupted accumulation: the matter removal due to the vortex is rapidly cancelled out by an accelerated accumulation of which the explanation is given in Figs. 5 through 7. On these figures the axial and radial velocities and concentration variations with time are shown at the same mesh point ($j = 40$; $k = 40$) for 4 of the 6 cases studied. We notice a peak narrowing with time: the increase in the vortex velocity leads to an increase in the accelerations experienced. This effect, which must be positive, is compensated by a decrease in the time during which the inversions of velocity are close to the membrane. When we look at the solute concentration near the wall, higher jet velocities appear to cause a decrease of the same amplitude but lasting for a shorter time. Therefore, if we are only interested in wall matter removal, there is no point in increasing the jet velocity, unless we work with suspensions for which we must overcome the agglomerated particle inertia by high wall accelerations.

In order to explain why the concentration increases so rapidly after having fallen, we have tried to emphasise the mechanism of material removal by the vortex. For this, we have studied how the concentration variations were synchronized with the vortex passage (Fig. 8). At time (a), the concentration decrease begins while the vortex is still in mesh co-ordinate "j" below 33. The decrease in concentration is caused by the arrival of less concentrated liquid from the centre of the tube. At time (b), the concentration velocity decrease is at a maximum due to the axial velocity inversion. The vortex edge reaches the reference mesh point ($j = 40$; $k = 40$). Then the dilute liquid flowrate from the tube centre is at its highest. At time (c),

Downloaded 03 Jun 2010 to 171.66.16.125. Redistribution subject to ASME license or copyright; see http://www.asme.org/terms/Terms_Use.cfm

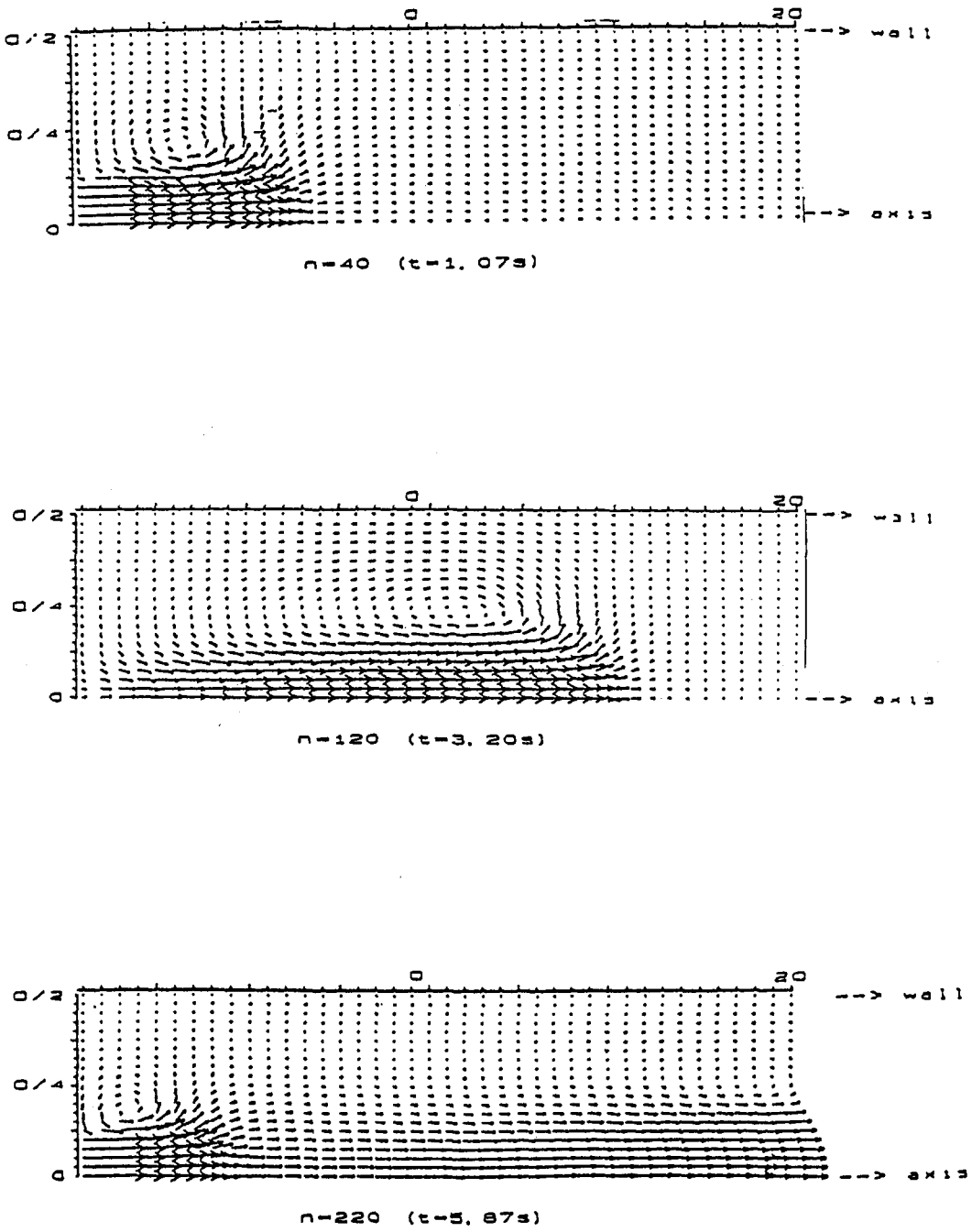


Fig. 3 Numerical simulation of the vortices generated by an intermittent confined jet (plane geometry). Velocity fields at different times (*a*) $t = 0.3T$, (*b*) $t = 0.7T$, (*c*) $t = 1.2T$. Calculation parameters: $D = 4.4\ 10^{-2}$ m, $D_j = 0.88\ 10^{-2}$ m, $u_j = 3.75\ 10^{-2}\ m \cdot s^{-1}$, $T = 5.4s$ and filtration velocity $V_p = 0.15\ 10^{-3}\ m \cdot s^{-1}$.

the rate of change in concentration falls because the velocities sweeping the reference point stop being orientated towards the wall and become parallel to it. There is no more movement from the tube centre and the convection now carries material from the wall layer. Finally at time (d), the concentration rises rapidly. As a matter of fact, the highest negative axial velocities are just downstream from the reference point and therefore this point receives high levels of the matter removed from the superior "j." At this time, the point $j = 40$ receives matter from points which are between states (b) and (c) on their concentration curve. In conclusion, we can say that this sweeping mechanism is mainly dominated by longitudinal movements. Under these conditions, the concentrated layer regains its original value and the time period of the drop in concentration is very short. But, we must underline that we have only simulated the action of a single vortex on a concentration layer established in stationary flow. Indeed, in real filtration conditions with an intermittent jet working from the start of filtration, we must have rapidly arrived at an "unsteady-permanent" state in which vortices act successively bringing matter from behind and pushing it forwards. Each vortex will contribute to decreasing the quantity of matter that the following vortex can bring back.

Influence of the Jet Diameter. Three new simulations have been made with the same jet velocity and different jet diameters: $D_j = 0.3D$, $D_j = 0.5D$, and $D_j = 0.7D$. As in the study on the influence of jet velocity, we have investigated the variation with time of both velocity and concentration at a reference mesh

Downloaded 03 Jun 2010 to 171.66.16.125. Redistribution subject to ASME license or copyright; see http://www.asme.org/terms/Terms_Use.cfm

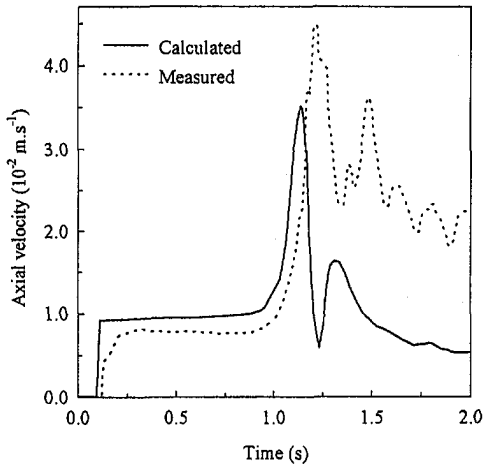


Fig. 4 Comparison between calculated velocities and hot film anemometer measurements. $D = 4.4\ 10^{-2}$ m, $D_j = 0.88\ 10^{-2}$ m, $u_j = 23\ 10^{-2}$ m · s^{-1}. Measurement points: axial distance from the nozzle x = 2.7D, radial distance from the axis r = 0.25D.

Table 1 Simulation conditions

Tube diameter	$4.4\ 10^{-2}$ m
Simulated length	$26.4\ 10^{-2}$ m
Jet velocity	$44\ 10^{-2}$ m.s^{-1}
Jet diameter	$8.8\ 10^{-3}$ m
Filtration velocity	$0.44\ 10^{-3}$ m.s^{-1}
Solute diffusivity	10^{-10} m^2.s^{-1}

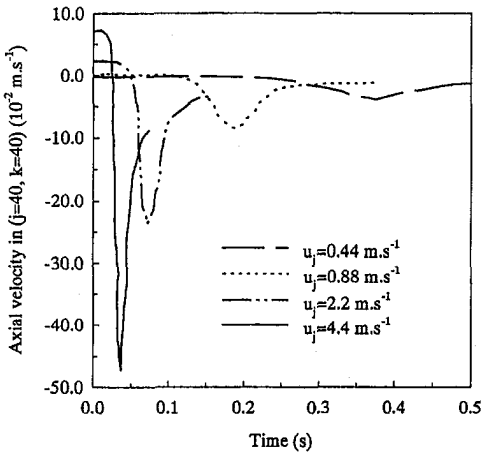


Fig. 5 Variation of the axial velocity with jet velocity

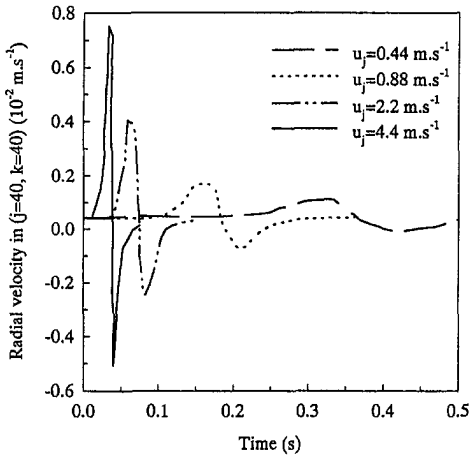


Fig. 6 Variation of the radial velocity with jet velocity

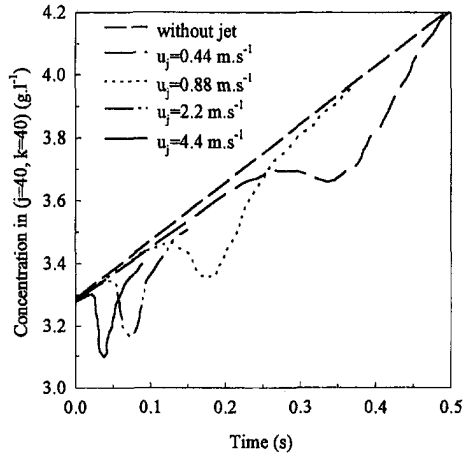


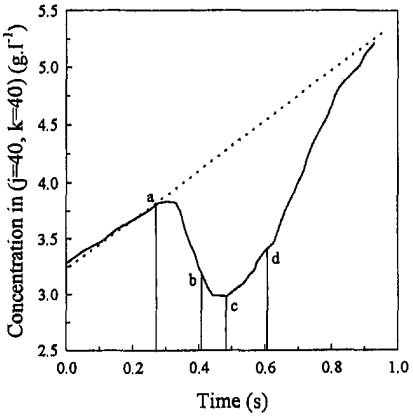
Fig. 7 Variation of the solute concentration with jet velocity

point ($j = 40$; $k = 40$). Figures 9 through 11 show this variation with time. When the diameter ratio is increased, the space decrease between the edge of the jet and the wall confines the vortex to a more restricted area. Thus the recirculated flowrate causes higher negative velocities between the tube center and the wall. Meanwhile, the translational velocity of the vortex is greatly decreased. Furthermore, the jet diameter increase allows, thanks to the vortex slowing down and lengthening, the negative peak height to enlarge without reducing the width of the base, both for radial and axial velocity. Concerning the solute concentration, increasing the jet diameter has a very positive effect because the more pronounced curve deflection affects a greater membrane length. Therefore, the quantity of removed matter is larger and this, even if the sweeping mechanism is the same: whatever the jet diameter, the solute concentration rapidly rises after the passage of the vortex. Increasing jet diameters leads to increasing velocity fluctuations whilst maintaining the same gradient. Therefore, the acceleration rates are comparable but the time which they last is longer. However, when the simulation is continued beyond the vortex passage, oscillations appear in the velocity curve for the higher jet diameters. These oscillations are caused by secondary vortices occurring behind the initial vortex. Indeed, beyond this time, the initial vortex is broken up and therefore the downstream disturbances are weaker. This phenomenon is of value for the reduction in the polarisation layer since, as soon as it appears, there is no further concentration accumulation at the wall and the reduction in the initial concentration is maintained. However, the existence of this vortex breakdown must be confirmed by a turbulence simulation.

In the conclusion to this numerical study, we can say that the choice of jet dimensions must take into consideration the expected type of external fouling. Indeed, in the case of a dense deposit, small jet diameters ($D/D_j < 0.4$) are preferred because they ensure high velocity and acceleration rates near the wall, even for moderate crossflow flowrates. In the opposite case of sparse deposits, a large jet diameter leads to a better concentration reduction but the breakdown of the vortex strongly decreases the tube length affected by the disturbance.

Filtration Application. In order to validate our numerical results, we have applied this unsteady method to the filtration of a bentonite suspension ($1\text{g} \cdot \text{l}^{-1}$). Ultrafiltration axisymmetric zirconia-coated alumina membranes whose characteristics are: length 0.25 m, tube diameter $15\ 10^{-3}$ m, pore diameter $20\ 10^{-6}$ m were used. 3 nozzle jet diameters were used: 4, 6, and 7.5

Downloaded 03 Jun 2010 to 171.66.16.125. Redistribution subject to ASME license or copyright; see http://www.asme.org/terms/Terms_Use.cfm



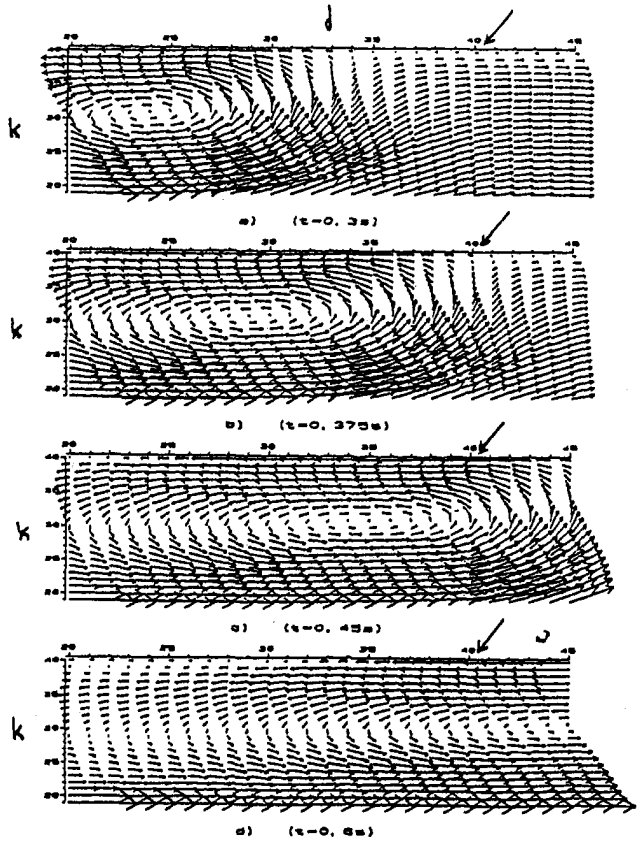


Fig. 8 Mechanism of wall sweeping by the vortex. Conditions of calculations: D = 4.4 10^{-2} m, D_j = 2.2 10^{-2} m and u_j = 44 10^{-2} m·s^{-1}.

mm. The intermittence frequency was 0.5 Hz, a value chosen in order to avoid the interaction between two successive vortices. The experimental setup used for the filtration experiments was given by Arroyo and Fonade (1993) as well as the whole of the filtration results. We will mention here only the main results.

Figure 12 shows the variation of the relative flux $J_R = J/J_0$ with time for the steady and unsteady conditions, where J_0 is the initial value of the permeate flux. We can see two effects of the unsteady operating conditions. Firstly, the fall in the initial flux was less rapid: 30 min were needed to reach J_R = 0.5 but only 10 min under steady conditions. Secondly, the final flux value was higher and seemed more stable. This long term effect can also be seen through the relative hydraulic resistance R, defined as $R = (J_0/J) - 1$, which represents the additional resistance due to the concentration polarization (Fig. 13). In most cases this parameter remained nearly constant, showing

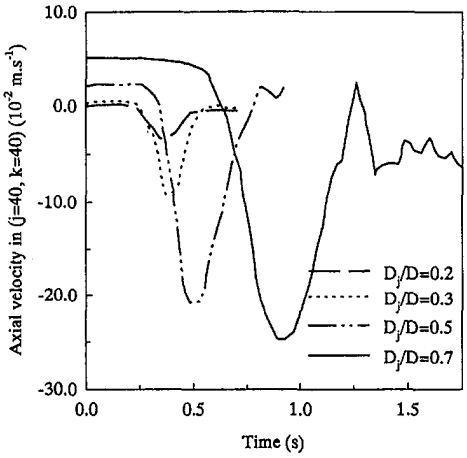


Fig. 9 Variation of the axial velocity with jet diameter

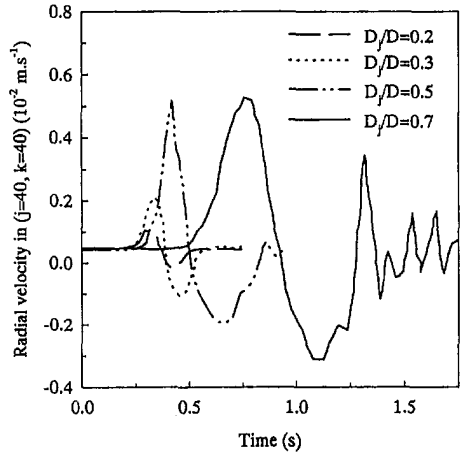


Fig. 10 Variation of the radial velocity with jet diameter

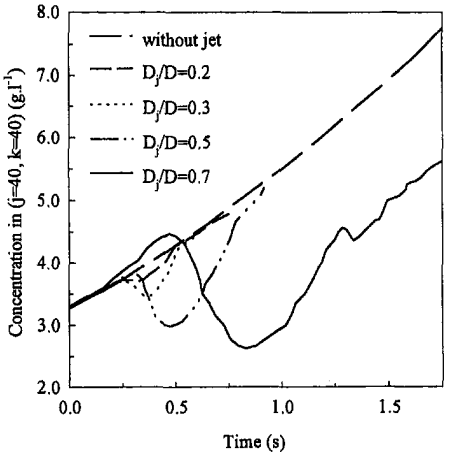


Fig. 11 Variation of the solute concentration with jet diameter

that the jet caused a reduction in the rate of increase of the hydraulic resistance. This means that, under unsteady conditions, the flux remains higher for at least a prolonged period of time and perhaps indefinitely.

4 Conclusions

In order to enhance the flux in crossflow filtration processes, a new principle of main flow unsteadiness was investigated on

Downloaded 03 Jun 2010 to 171.66.16.125. Redistribution subject to ASME license or copyright; see http://www.asme.org/terms/Terms_Use.cfm

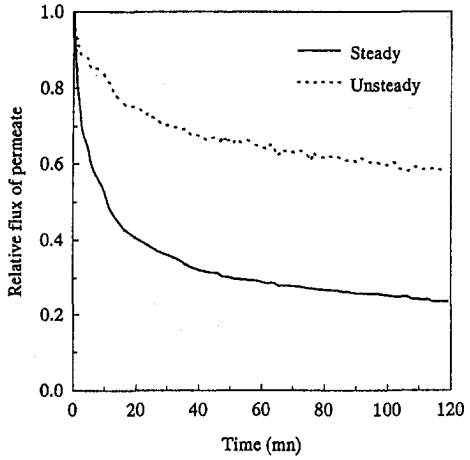


Fig. 12 Flux decline under steady and unsteady conditions. $D_j = 4\ 10^{-3}$ m, $Q = 0.7$ m^3/h.

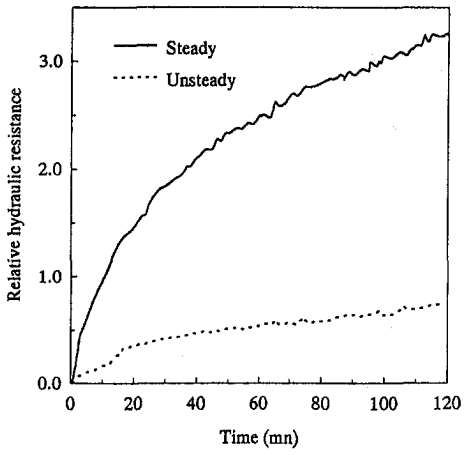


Fig. 13 Relative hydraulic resistance variation under steady and unsteady conditions. $D_j = 4\ 10^{-3}$ m, $Q = 0.7$ m^3/h.

the basis of numerical flow calculations and experimental work. This principle involves the generation of large vortices upstream of the tubular membrane, which are able to sweep periodically the surface of the membrane when moving downstream.

The numerical study of the flow highlights the influence of jet diameter and jet velocity, not only on the intensities but also on the nature of the disturbances near the wall. Moreover, the polarization layer sweeping mechanism of the vortices was analyzed.

This principle was applied to the filtration of a bentonite suspension through an ultrafiltration mineral membrane. It was shown that the intermittent jet principle can efficiently enhance the flux since the relative hydraulic resistance could be divided by a factor of more than 4.

Other studies will be necessary to allay the uncertainties which exist on the real membrane length affected by the vortices. For this, we need to cross an important threshold both in the field of experiment and calculation.

References

Abd-Elmessih, R. N., 1985, "Etude expérimentale des caractéristiques dynamiques d'un jet plan intermittent," Ph.D. thesis, Institut National Polytechnique, Toulouse, France, 164 pp.

Arroyo, G., and Fonade, C., 1993, "Use of Intermittent Jets to Enhance Flux in Crossflow Filtration," *Journal of Membrane Science,* Vol. 80, pp. 117–129.

Belfort, G., and Nagata, N., 1985, "Fluid Mechanics and Crossflow Filtration: Some Thoughts," *Desalination,* Vol. 53, pp. 57–79.

De Vahl Davis, G., and Mallinson, G. D., 1976, "An Evaluation of Upwind and Central Difference Approximations by a Study of Recirculating Flow," *Computers and Fluids,* Vol. 4, pp. 29–41.

Doubrovine, N., 1992, "Influence d'un écoulement instationnaire intermittent sur les performances d'un procédé de filtration tangentielle," Ph.D. thesis, Institut National des Sciences Appliquées, Toulouse, France, 209 pp.

Finnigam, S. M., and Howell, J. A., 1989, "The Effect of Pulsed Flow on Ultrafiltration Fluxes in a Baffled Tubular Membrane System," *Chemical Engineering Research and Design,* Vol. 67, pp. 278–282.

Harlow, F. H., and Welch, J. E., 1965, "Numerical Calculation of Time-Dependent Viscous Incompressible Flow of Fluid with Free Surface," *Physics Fluids,* Vol. 8, pp. 2182–2189.

Ikeda, M., 1977, "Finite Disturbances and Growing Vortices in a Two-Dimensional Jet," *Journal of Fluid Mechanics,* Vol. 80, pp. 401–421.

Kroner, K. H., Nissinen, V., and Ziegler, H., 1987, "Improved Dynamic Filtration of Microbial Suspensions," *Biotechnology,* Vol. 5, pp. 921–926.

Poyen, S., Quemeneur, F., and Bariou, B., 1984, "Amélioration du flux en ultrafiltration par promoteurs de turbulence," *Entropie,* Vol. 120, pp. 50–55.

Schulz, G., and Ripperger, S., 1989, "Concentration Polarization in Crossflow Microfiltration," *Journal of Membrane Science,* Vol. 40, pp. 173–187.

Shimizu, A., and Wada, T., 1985, "A Numerical Analysis of Vortex Growth in a Two-Dimensional Jet," *Computers and Fluids,* Vol. 13, pp. 83–97.

Viecelli, J. A., 1971, "A Computing Method for Incompressible Flows Bounded by Moving Walls," *Journal of Computational Physics,* Vol. 8, pp. 119–143.

Downloaded 03 Jun 2010 to 171.66.16.125. Redistribution subject to ASME license or copyright; see http://www.asme.org/terms/Terms_Use.cfm

Laminar Fluid Flow in a Planar 90 Degree Bifurcation With and Without a Protruding Branching Duct

T. G. Travers[1]

W. M. Worek

Department of Mechanical Engineering (m/c 251), The University of Illinois at Chicago, 842 West Taylor Street, Chicago, IL 60607-7022

The laminar flow field in a planar, ninety degree bifurcation is examined. This numerical study uses the computational-fluid-dynamics software Fluent Version 4.11. First, the velocity field in a bifurcation without a protruding branching duct is modeled, and the results are successfully compared to experimental data. Next, the flow field is studied in bifurcations that have branching ducts that protrude into the main duct. The velocity field and pressure drop are documented, and are found to be strongly influenced by the extent of the branching duct protrusion.

Introduction

Ninety degree bifurcated flows can occur in piping systems, HVAC ducts, heat exchangers, and other applications. In the basic, two-dimensional geometry, flow enters the main duct inlet with a mass flow rate $\dot{m}_1$, and this flow then divides between the branching duct ($\dot{m}_2$) and the main duct outlet ($\dot{m}_3$). Karino et al. (1979) have shown that three areas of recirculation may be formed in this laminar flow field, depending on the inlet flow rate and the dividing flow ratio $\dot{m}_2/\dot{m}_1$.

A variation on this geometry is shown in Fig. 1, where the branching duct protrudes into the main duct. This arrangement can be found on some heat transfer equipment. For example, when a cylindrical branch is brazed or welded into a cylindrical main duct or header, the connecting end of the branching duct often fits into the main duct and is not contoured to the main duct inner diameter.

It is the influence on planar, laminar flow of a ninety degree branching duct that protrudes into the main duct that is the topic of this study. The flow will be analyzed computationally. It is the goal of this work to compare the flow field characteristics of bifurcations with protrusions to those with no protrusions, and to develop results giving the dependence of pressure drop on the extent of the protrusion.

A search of the literature revealed no studies of the flow characteristics of the ninety degree bifurcation with a protruding branching duct. However, the bifurcation with the non-protruding branching duct has been studied extensively. Karino et al. (1979) and Karino and Goldsmith (1985) studied the paths of neutrally buoyant rigid spheres in steady, laminar flow in cylindrical ducts. A number of investigators have numerically simulated steady, laminar, two-dimensional flow. Kawaguti and Hamano (1979), using a finite-difference method, computed streamlines and pressure variations.

Liepsch et al. (1982) also used a finite-difference method, and additionally measured velocities using laser Doppler anemometry. Khodadadi et al. (1986), using the same computational approach as Liepsch et al. (1982), examined air flow and heat transfer in the bifurcation. Hayes et al. (1989) used a finite element method to solve the governing equations for the 90 degree bifurcation.

The pressure field has been experimentally examined. Cho et al. (1985) measured pressure distribution along the main branch for laminar flow in cylindrical ducts. Kawaguti and Hamano (1979), Liepsch et al. (1982), and Hayes et al. (1989) reported similar pressure field results from their two-dimensional computations.

Verification of the Mathematical Model

The experimental results of Liepsch et al. (1982) are used to verify the mathematical model.

Governing Equations. The assumptions placed on the flow field are: two-dimensional, incompressible, steady state, constant properties, and no body forces. The resulting set of governing equations is:

$$\frac{\partial u}{\partial x} + \frac{\partial v}{\partial y} = 0 \tag{1}$$

$$u\frac{\partial u}{\partial x} + v\frac{\partial u}{\partial y} = -\frac{1}{\rho}\frac{\partial P}{\partial x} + \nu\left(\frac{\partial^2 u}{\partial x^2} + \frac{\partial^2 u}{\partial y^2}\right) \tag{2}$$

$$u\frac{\partial v}{\partial x} + v\frac{\partial v}{\partial y} = -\frac{1}{\rho}\frac{\partial P}{\partial y} + \nu\left(\frac{\partial^2 v}{\partial x^2} + \frac{\partial^2 v}{\partial y^2}\right) \tag{3}$$

Computational Approach. The boundary conditions for the modeling are as follows. The flow at the inlet is modeled as hydrodynamically fully developed. Along the walls, the no-slip condition exists. The lengths of the outlet ducts are chosen to ensure fully developed flow at the exit boundaries. Of course, the experimental results indicated the approximate lengths required for these outlet ducts. The expression presented by Shah and London (1978) for laminar entrance length for such flows, that is

$$\frac{L_e}{2H} = \frac{0.315}{0.0175\ \mathrm{Re} + 1} + 0.011\ \mathrm{Re} \tag{4}$$

was used, with a generous safety factor, to ensure fully developed flow at the outlets.

Three different computational grids were used to simulate the experimental conditions. The first was 65 × 51, with 9.8 percent of the grid lines forming active computational cells. The second, 74 × 71, and the third, 107 × 128 had 8.4 and 3.2 percent of grid lines forming active cells respectively. The computational procedure is the SIMPLE (Semi-Implicit Method

[1] Current address: Standard Refrigeration Co., 2050 N. Ruby Street, Melrose Park, IL 60160-1133.

Contributed by the Fluids Engineering Division for publication in the JOURNAL OF FLUIDS ENGINEERING. Manuscript received by the Fluids Engineering Division July 20, 1994; revised manuscript received June 6, 1995. Associate Technical Editor: S. P. Vanka.

Copyright © 1996 by ASME

Downloaded 03 Jun 2010 to 171.66.16.125. Redistribution subject to ASME license or copyright; see http://www.asme.org/terms/Terms_Use.cfm

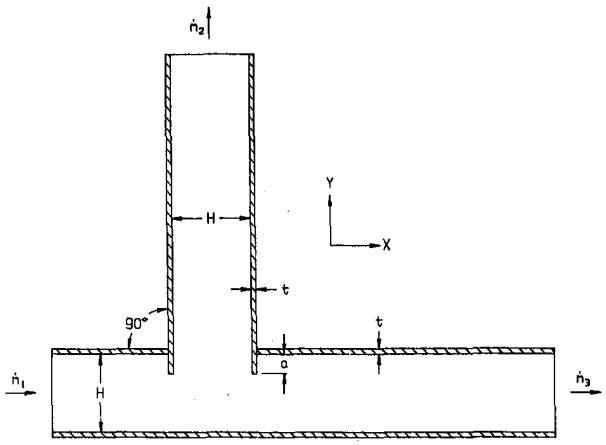


Fig. 1 The basic flow geometry and a branching duct protruding into the main duct

for Pressure-Linked Equations) algorithm of Patankar (1980), as implemented by Fluent Version 4.11. For each of the control volumes, the governing equations are integrated, yielding finite-difference equations for the unknowns u, v, and P. A nonstaggered grid is used in Fluent Version 4.11, so that all the unknowns are computed at the control volume centers. The calculations were performed on a Cray Y-MP4/464. The solutions were deemed well converged when the sum of the normalized residuals for P, u, and v were less than 1.0E-03.

Comparison of Computed to Experimental Results. The experimental conditions of Re = 496 and dividing flow ratio $\dot{m}_2/\dot{m}_1 = 0.44$ were chosen for comparison. The value of Re = 496 was based on the experimental hydraulic diameter, and corresponds to Re = 558 using $2H$ as the hydraulic diameter. Figure 2 shows the comparison between the measured and computed x and y velocity fields for all three grids.

The agreement between the experimental and computational results for the x-direction profiles is very good. Indeed, all three grids yield results that closely match the experimental findings. The agreement between the numerical and measured results for the y-direction profiles, in the region of recirculation, is not quite as good. Further, the computed results for the various grids do not match as closely as they did for the x-direction profiles. Liepsch et al. (1982), using a similar numerical procedure, observed similar discrepancies between their computed and measured results. They concluded that three-dimensional effects in the bifurcation region of the test section was the most likely cause. An additional computational reason for these discrepancies may be false numerical diffusion (Patankar, 1980), which occurs when the flow direction is not aligned with the computational grid.

As Fig. 2 illustrates, the 65 × 51 grid generates reasonably accurate results, with considerable computational savings over the other two grids. The maximum error in the velocity field of the 65 × 51 grid with respect to the 107 × 128 grid is less than 13%. The 65 × 51 grid will be used to investigate the effects on laminar flow of a branching duct that protrudes into the main duct.

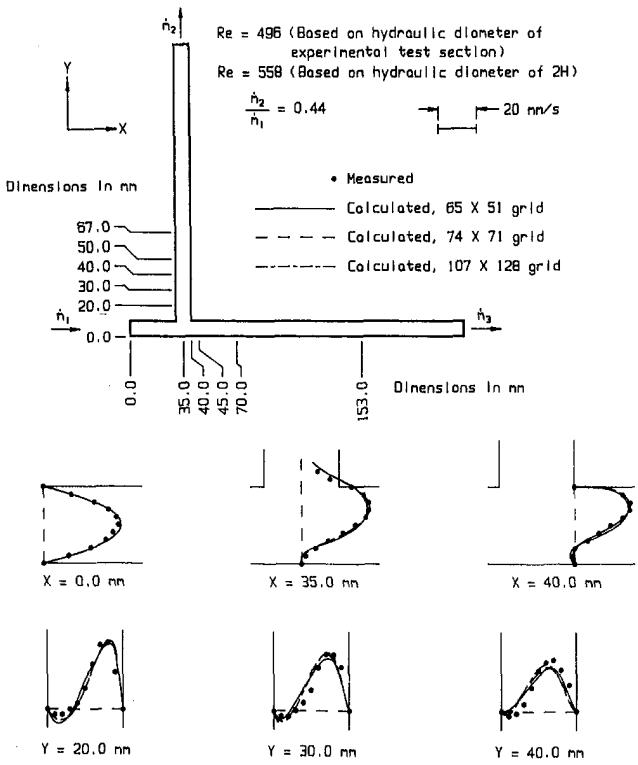


Fig. 2 Comparison between calculated and measured x and y direction velocity profiles

Results and Discussion

The flow conditions of Re = 50, 250, and 500, and $\dot{m}_2/\dot{m}_1 = 0.2$ were chosen for the simulations. The geometric configurations of $a = 0$, $a = H/8$, and $a = H/4$ are studied, and the protrusion thickness, t, is 0.6 mm. The working fluid is air. The boundary conditions remain identical to the verification runs.

The extent of the branching duct protrusion has a significant effect on the pressure field. Figures 3 and 4 show the variation of the centerline pressure for the main duct and the branching duct, respectively, for Re = 500.

The effects on overall centerline pressure drop of the extent of protrusion for three Reynolds numbers and $\dot{m}_2/\dot{m}_1 = 0.2$ are shown in Figs. 5 and 6. Figure 5 depicts the main duct, and Fig. 6 the branching duct. In both cases, the inlet pressure is taken at the main branch inlet (three channel heights upstream of the branching duct upstream wall). In Fig. 5, the outlet pressure is taken at ten channel heights downstream of the branching duct downstream wall. In Fig. 6, the outlet pressure is taken at ten channel heights downstream of the main duct top wall.

The flow in a bifurcation with $a = 0$ is complicated, and the addition of protrusions adds to the flow complexity. In the main duct, when $a = 0$, the flow enters fully developed, but near the branch, the flow in the upper part of the main duct accelerates and in the lower part decelerates as 20 percent of the mass flow is directed into the branch. As shown in Fig. 3, the centerline

Nomenclature

a = length of branching duct protrusion
H = height of duct
$\dot{m}_1$ = mass flow rate at main duct inlet
$\dot{m}_2$ = mass flow rate at branching duct outlet
$\dot{m}_3$ = mass flow rate at main duct outlet
P = pressure
Re = Reynolds number ($2HU_m/\nu$)
t = duct wall thickness
U_m = mean velocity at main duct inlet
u = x-direction velocity component
v = y-direction velocity component
x = coordinate direction
y = coordinate direction
ρ = density
ν = kinematic viscosity

Downloaded 03 Jun 2010 to 171.66.16.125. Redistribution subject to ASME license or copyright; see http://www.asme.org/terms/Terms_Use.cfm

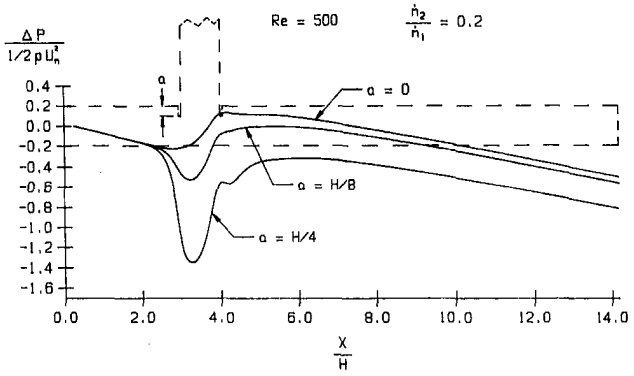


Fig. 3 Centerline pressure variation in the main duct

pressure recovers somewhat in the branching region, and then quickly resumes a pressure drop as the flow returns to the fully-developed state. This is exactly the pressure variation behavior observed by Cho et al. (1985) and the numerical investigators cited earlier. As for the flow that enters the branching duct, it initially forms a significant flow reversal region. In Fig. 4, the effects on centerline pressure of this recirculation region are very clear. A recovery in pressure occurs just past the recirculation zone, after which the fully developed flow and pressure variation characteristics return.

With the addition of protrusions ($a > 0$), the main duct flow is initially forced to accelerate through the area under the upstream protrusion. The pressure loss due to this protrusion is clearly documented in Fig. 3. The main duct pressure then recovers, but the recovery is dampened by the effects of the downstream protrusion. As in the case of no protrusions, the flow and pressure drop in the main duct resume a fully developed profile, but the overall pressure drop is greater than if there had been no protrusions. In the entrance to the vertical

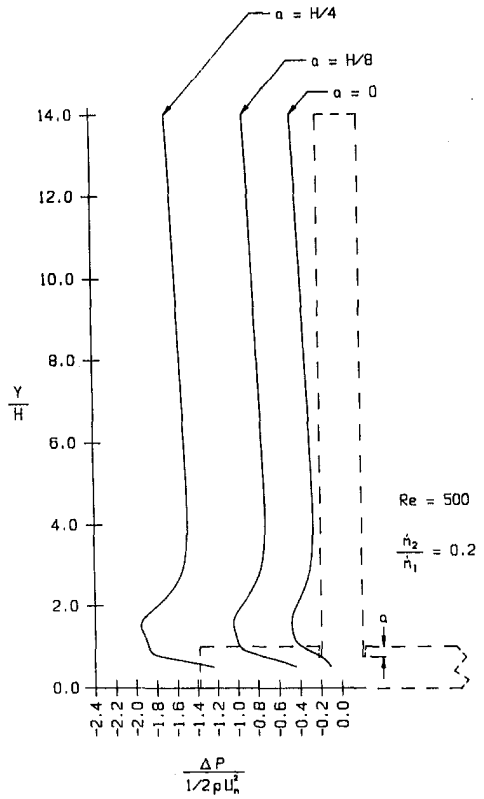


Fig. 4 Centerline pressure variation in the branching duct

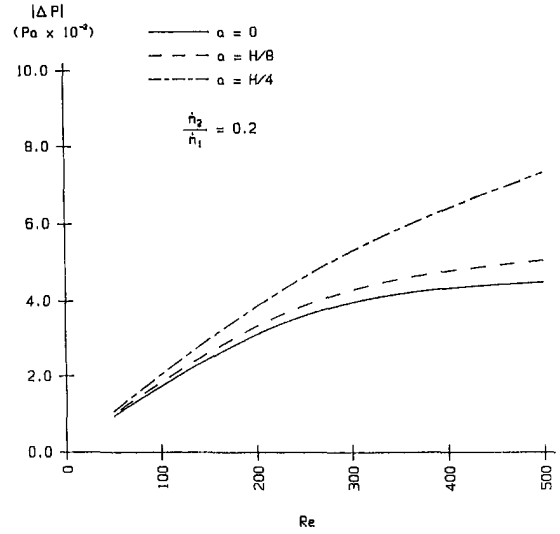


Fig. 5 Overall centerline pressure drop in the main duct

branch, the recirculation region has greater intensity, (i.e., larger local velocities) when the protrusions are present. The impact on the centerline pressure is shown in Fig. 4. The larger the protrusion, the larger the recirculation zone pressure drop. Also, the overall pressure drop in the branching duct is clearly a function of protrusion size.

In Fig. 5, the influence of the Reynolds number and the amount of protrusion on overall centerline pressure drop across the main duct is documented. At Re = 50, the difference in pressure drop between $a = 0$, $a = H/8$, and $a = H/4$ is quite small. As the Reynolds number increases to 250, the effects of protrusions on the pressure drop become more significant. At Re = 500, these protrusion effects are even greater. For example, the increase in pressure drop between $a = 0$ and $a = H/4$ at Re = 50 is 12.9 percent. However, at Re = 500, this increase in pressure loss is 63.5 percent. Also, increasing the extent of

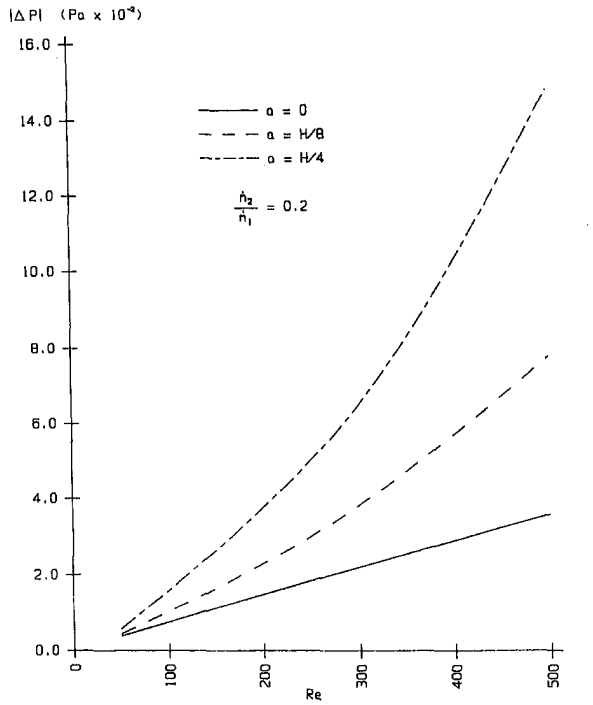


Fig. 6 Overall centerline pressure drop in the branching duct

Downloaded 03 Jun 2010 to 171.66.16.125. Redistribution subject to ASME license or copyright; see http://www.asme.org/terms/Terms_Use.cfm

protrusion from $a = H/8$ to $a = H/4$ dramatically increases the overall main duct centerline pressure loss. For example, at Re = 500, the increase in pressure drop between $a = 0$ and $a = H/8$ is 12.3 percent, whereas between $a = H/8$ and $a = H/4$ this increase is 45.6 percent. This trend is observed at lower Reynolds numbers as well.

The influence of Reynolds number and extent of protrusion on the overall centerline pressure loss through the branching duct can be seen in Fig. 6. At Re = 50, the effects of the protrusion are more significant than for the same conditions in the main duct. Note that at Re = 50, the recirculation region at the upstream wall of the branching duct is considerably smaller than at Re = 500. The trend of this recirculation region increasing in size with increasing Reynolds number has been observed experimentally by Karino et al. (1979), and numerically by Khodadadi et al. (1986). As in the main duct, with increasing Reynolds number, a greater effect of the protrusions on overall pressure loss is observed. For example, at Re = 50, the increase in pressure drop between $a = 0$ and $a = H/4$ is 47.5 percent, but at Re = 500 this increase is 314.0 percent. For the pressure loss through the branching duct, increasing of the extent of protrusion from $a = H/8$ to $a = H/4$ does not necessarily cause a greater relative pressure loss than the increase from $a = 0$ to $a = H/8$, as was the case in the main duct. For example, at Re = 50, the increase in pressure loss between $a = 0$ and $a = H/8$ is 15.0 percent, and the increase between $a = H/8$ and $a = H/4$ is 28.3 percent. However, at Re = 500, the rise in pressure drop between $a = 0$ and $a = H/8$ is 116.8 percent, and the increase between $a = H/8$ and $a = H/4$ is 91.0 percent.

Conclusions

The influence of the extent of branching duct protrusion on the laminar flow field of a ninety degree bifurcation has been computationally examined. For a given flow rate, increasing the extent of the protrusion intensifies the local pressure drop in the region of the protrusions, and results in a greater overall pressure drop for both branches. Also, with increasing Reynolds numbers, the effects on overall pressure drop of the protrusions also increases for both branches. In the main duct, the protrusion $a = H/4$ has a relatively larger impact on overall pressure drop than the $a = H/8$ protrusion. However, this trend is only observed at Reynolds numbers less than 250 in the branching duct.

Acknowledgment

This work was partially supported by the National Science Foundation under grant number CBT920038N and utilized the Cray Y-MP4/464 at the National Center for Supercomputing Applications, University of Illinois at Urbana-Champaign.

References

Cho, Y. I., Back, L. H., and Crawford, D. W., 1985, "Experimental Investigation of Branch Flow Ratio, Angle, and Reynolds Number Effects on the Pressure and Flow Fields in Arterial Branch Models," ASME JOURNAL OF BIOMECHANICAL ENGINEERING, Vol. 107, pp. 257–267.

Hayes, R. E., Nandakumar, K., and Nasr-El-Din, H., 1989, "Steady Laminar Flow in a 90 Degree Planar Branch," *Computers & Fluids,* Vol. 17, pp. 537–553.

Karino, T., Kwong, H. H. M., and Goldsmith, H. L., 1979, "Particle Flow Behaviour in Models of Branching Vessels: I. Vortices in 90° T-Junctions," *Biorheology,* Vol. 16, pp. 231–248.

Karino, T., and Goldsmith, H. L., 1985, "Particle Flow Behavior in Models of Branching Vessels II. Effects of Branching Angle and Diameter Ratio on Flow Patterns," *Biorheology,* Vol. 22, pp. 87–104.

Kawaguti, M., and Hamano, A., 1979, "Numerical Study on Bifurcating Flow of a Viscous Fluid," *Journal of the Physical Society of Japan,* Vol. 46, pp. 1360–1365.

Khodadadi, J. M., Nguyen, T. M., and Vlachos, N. S., 1986, "Laminar Forced Convective Heat Transfer in a Two-Dimensional 90° Bifurcation," *Numerical Heat Transfer,* Vol. 9, pp. 677–695.

Liepsch, D., Moravec, S., Rastogi, A. K., and Vlachos, N. S., 1982, "Measurement and Calculations of Laminar Flow in a Ninety Degree Bifurcation," *Journal of Biomechanics,* Vol. 15, pp. 473–485.

Patankar, S. V., 1980, *Numerical Heat Transfer and Fluid Flow,* Hemisphere Publishing Corp., Washington D.C.

Shah, R. K., and London, A. L., 1978, *Laminar Flow Forced Convection in Ducts, A Source Book For Compact Heat Exchanger Analytical Data,* Academic Press, New York.

Downloaded 03 Jun 2010 to 171.66.16.125. Redistribution subject to ASME license or copyright; see http://www.asme.org/terms/Terms_Use.cfm

I. E. Barton[1]
Division of Aerospace Engineering,
Manchester School of Engineering,
Simon Building,
Oxford Road,
The University of Manchester,
M13 9PL, United Kingdom

Exponential-Lagrangian Tracking Schemes Applied to Stokes Law

The exponential-Lagrangian tracking scheme applied to Stokes Law is developed by introducing a predictor-corrector formulation. The new predictor-corrector schemes are more accurate than the original scheme and are estimated to give a better performance taking into account the increased computational effort. The schemes are tested on two simple problems and the results are compared with the analytical solutions.

Introduction

The capability to predict the motion of particles in a fluid flow has many diverse applications ranging form industrial combustion processes to biological artery systems. Fundamentally, the motion of a particle that is heavier than the fluid is described by a dominant drag force, as well as other forces, refer to Clift et al. (1978). If the velocity slip is small the drag force can be expressed as Stokes Law, refer to Clift et al. (1978), (additional effects are considered later):

$$\frac{\partial U_p}{\partial t} = \frac{U_f - U_p}{\tau_p} \tag{1}$$

where U_p is the velocity of the particle, U_f is the velocity of the fluid at the particle's location and τ_p is the particle relaxation time which characterizes the aerodynamic behaviour of the particle. Particles with large τ_p values have large inertia and their motion is dominated by inertial effects whereas, particles with small τ_p values tend to follow the flow. The equation of motion is therefore a simple first-order differential equation which has a particular complexity in that the fluid velocity is a function of position and/or time for all but simple cases.

For most cases, Eq. (1) and the subsequent equation for the particle's position can be accurately solved using a high-order Runge-Kutta technique, see Chow (1979) for further details. The Runge-Kutta scheme has the draw-back that it is limited to the stability requirement that $\Delta t < 2\tau_p$ similar to other explicit Eulerian schemes discussed in Anderson et al. (1984). Alternatively, Eq. (1) can be integrated using a less accurate exponential-Lagrangian tracking scheme which was partly developed to overcome this stability requirement, refer to Boris and Oran (1987). The present study considers integrating Eq. (1) using the well-established exponential scheme and develops the scheme to give improved accuracy.

The exponential-Lagrangian tracking scheme has been extensively used in numerical studies such as the study by Boysan et al. (1982). It has a reasonable local truncation error of Δt^2 but more importantly the scheme is inherently stable. The scheme simply assumes that the fluid velocity remains constant until the next time-step. This allows equation (1) to be integrated to form the solution:

$$U_p^{n+1} = U_p^n \exp\frac{-\Delta t}{\tau_p} + U_f^n\left(1 - \exp\frac{-\Delta t}{\tau_p}\right) \tag{2}$$

where Δt is the time-step interval, $n + 1$ is the final time-level and n is the initial time-level. Equation (2) can then be integrated again to find the position of the particle.

$$x_p^{n+1} = x_p^n - \tau_p(U_f^n - U_p^n)\left(1 - \exp\frac{-\Delta t}{\tau_p}\right) + U_f^n\Delta t \tag{3}$$

Equation (2) predicts particles with a large τ_p values tend to give the limit $U_p^{n+1} = U_p^n$ and for small τ_p values the equation tends to the limit $U_p^{n+1} = U_f^n$. The first limit is physically acceptable (a particle with large inertia will have constant velocity). The second limit is not acceptable because the particle's velocity lags behind the fluid's velocity by the time of the numerical time-step. A physically acceptable limit would be $U_p^{n+1} = U_f^{n+1}$ but the U_f^{n+1} term is unknown until the particle steps forward in time and displacement. This is the fundamental problem of the exponential scheme which the present study addresses with three new exponential schemes. In keeping with the original scheme the new exponential schemes are simple, unlike the original scheme the new schemes use a predictor-corrector technique to improve their accuracy. A predictor-corrector approach is well-established for finite-difference schemes for the solution of Eq. (1) refer to Ruetsch and Meilburg (1993) for example. The classical two-stage Lax-Wendroff and MacCormack finite-difference schemes have a truncation error of Δt^2 and are also stable, refer to Anderson et al. (1984) nonetheless the exponential scheme has been applied more extensively to Lagrangian tracking problems and for this reason the exponential scheme has been developed.

The Predictor-Corrector Exponential Schemes

All the predictor-corrector exponential schemes use the original exponential scheme to give the initial prediction level. The original exponential scheme is referred to as scheme [1].

Scheme [2] is the simplest proposed scheme. After the prediction level the correction level is calculated from using equations in the same form as Eqs. (2) and (3) where the U_f^n term in Eq. (2) is replaced with U_f^{n+1*}. The U_f^{n+1*} term is the predicted fluid velocity at the time level $n + 1$. The U_f^n terms in Eq. (3) are replaced with $(U_f^{n+1*} + U_f^n)/2$. The correction level now has physically correct limits when τ_p tends to zero namely $U_p^{n+1} = U_f^{n+1*}$ and $\Delta x_p = (U_f^{n+1*} + U_f^n)\Delta t/2$.

Schemes [3] and [4] are conceptually very similar both assume that the fluid velocity varies in someway with time. The time derivatives are calculated using U_f^{n+1*} and other terms. An alternative approach would be to assume the fluid velocity varied in someway with position however, although this is more appropriate for the majority of applications, this has not been adopted for the following reasons:

(i) Equation (1) is numerically integrated with time. It follows that a time-variation scheme can be applied to either steady-state or temporal problems.

[1] Presently: Engineering University Department, Cambridge University, Trumpington Street, Cambridge CB2 1PZ.

Contributed by the Fluids Engineering Division for publication in the JOURNAL OF FLUIDS ENGINEERING. Manuscript received by the Fluids Engineering Division December 19, 1994; revised manuscript received June 8, 1995. Associate Technical Editor: M. W. Reeks.

Copyright © 1996 by ASME

Downloaded 03 Jun 2010 to 171.66.16.125. Redistribution subject to ASME license or copyright; see http://www.asme.org/terms/Terms_Use.cfm

(ii) The spacial derivatives using U_f^{n+1*} require Δx_p^{n+1*} which could lead to instabilities.

(iii) Equation (1) can no longer be solved directly as a first-order partial differential equation but would have to be extended to form a second-order or higher partial differential equation.

(iv) Extending the scheme to include additional forces is straight-forward, this is discussed later.

None of the above problems are encountered with a time-variation approach. Scheme [3] assumes that the fluid velocity varies linearly which is expressed as:

$$U_f(t) = U_f^n + At$$
$$A = \frac{U_f^{n+1*} - U_f^n}{\Delta t} \tag{4}$$

Scheme [4] assumes a quadratic variation, for constant time-step values this is expressed as:

$$U_f(t) = U_f^n + At + Bt^2$$
$$A = \frac{U_f^{n+1*} - U_f^{n-1}}{2\Delta t}$$
$$B = \frac{U_f^{n+1*} - 2U_f^n + U_f^{n-1}}{2\Delta t^2} \tag{5}$$

Most applications use non-uniform time-step values found from the present particle's velocity and a length scale. Non-uniform time-steps mean the A and B terms are slightly more complex and are given in appendix I. The U_f^{n-1} term is stored from the last time-level, for spacial-variation problems the U_f^{n-1} term is unknown for the initial time-step ($n = 0$) a reasonable initial value in this case is to set $U_f^{-1} = U_f^0$.

When the above $U_f(t)$ equations are substituted into Eq. (1) then the general solution for the particle's velocity and position can be expressed as:

$$U_p^{n+1} = U_p^n \exp\frac{-\Delta t}{\tau_p} + U_f^n\left(1 - \exp\frac{-\Delta t}{\tau_p}\right) + A\left\{\Delta t - \tau_p\left(1 - \exp\frac{-\Delta t}{\tau_p}\right)\right\} + B\left\{\Delta t^2 - 2\tau_p\Delta t + 2\tau_p^2\left(1 - \exp\frac{-\Delta t}{\tau_p}\right)\right\} \tag{6}$$

and

$$x_p^{n+1} = x_p^n - \tau_p(U_f^n - U_p^n)\left(1 - \exp\frac{-\Delta t}{\tau_p}\right) + U_f^n\Delta t + A\left\{\frac{\Delta t^2}{2} - \tau_p\Delta t + \tau_p^2\left(1 - \exp\frac{-\Delta t}{\tau_p}\right)\right\} + B\left\{\frac{\Delta t^3}{3} - \tau_p\Delta t^2 + 2\tau_p^2\Delta t - 2\tau_p^3\left(1 - \exp\frac{-\Delta t}{\tau_p}\right)\right\} \tag{7}$$

By setting $A = 0$, $B = 0$ the general solution reduces to the original solution which is a direct consequence of choosing a time-variation approach. Clearly, by setting A equal to the value in Eq. (4) and setting $B = 0$ gives scheme [3] while setting A and B to the values in Eq. (5) gives scheme [4]. The limits for both schemes [3] and [4] for small τ_p values are $U_p^{n+1} = U_f^{n+1*}$ and $\Delta x_p^{n+1} = (U_f^{n+1*} + U_f^n)\Delta t/2$.

The local truncation error associated with the exponential schemes [1] and [2] is $O(\Delta t^2)$ caused by assuming no variation in the U_f term. The local truncation error associated with schemes [3] and [4] is problem dependent. If U_f is only a function of time then scheme [3] will have a truncation error of $O(\Delta t^3)$ and scheme [4] a truncation error of $O(\Delta t^4)$. A steady-state problem with spacial-variation will have a truncation error of $O(\Delta t^3)$ for schemes [3] and [4]. The stability of schemes [2], [3], and [4] should not, in general, be any less stable than scheme [1].

The various schemes are tested for two idealistic problems—an oscillating fluid flow problem and a simple vortex problem. The oscillating fluid flow problem examines the behaviour of the schemes for a time-dependent flow. The vortex problem is a steady-state problem which has a reasonably complex flow field that can be analytically solved.

The Oscillating Fluid Flow Problem

The particle is assumed to be in oscillating fluid-flow, governed by a sinusoid motion similar to a problem studied by Schöneborn (1975):

$$U_f(t) = U_f^{\mathrm{MAX}} \sin(\omega t) \tag{8}$$

The particle's velocity terms are non-dimensionalized using the U_f^{MAX} term, ω is set to unity. The equation of the particle's velocity has the exact solution:

$$U_p = \frac{1}{1 + \tau_p^2}\left(\sin(t) + \tau_p\left\{\exp\frac{-t}{\tau_p} - \cos(t)\right\}\right) \tag{9}$$

assuming the initial particle's velocity is the same as the fluid. The time varies from $t = 0$ s to $t = 2\pi$ s for a set of results.

Time-dependent problems may seem trivial partly because analytical solutions are usually available and partly because the U_f^{n+1} term is known. It should be emphasized that although U_f^{n+1} is known U_p^{n+1} is not and this problem tests how the various schemes (except scheme [1]) model the behaviour of the particle when acted on by the terms U_f^n and U_f^{n+1}.

A set of results of U_p for all the schemes are shown in Fig. 1 as well as the exact solution. The particle relaxation time is set to 1 s. The time-step interval is set to 0.2π s (0.628 s) e.g., there are ten steps for a complete set of results. The figure shows the non-physical time-lag behaviour of scheme [1]. The error is noticeable at $t = 0$ s where the scheme simply predicts $U_p = 0$ over the first time-step. The other predictor-corrector schemes do not suffer from the time-lag problem. Results for scheme [2] are almost as poor as scheme [1] but appear to display the reverse behaviour instead of time-lagging the particle's velocity appears to be ahead of the exact solution. The principle of scheme [2] that U_f^n should be replaced by U_f^{n+1} is of course only really valid for small particle relaxation times and it is not surprising it performs badly for a moderate τ_p value. This demonstrates how scheme [2] is very crude in principle and the replaced U_f^n terms should be a function of τ_p.

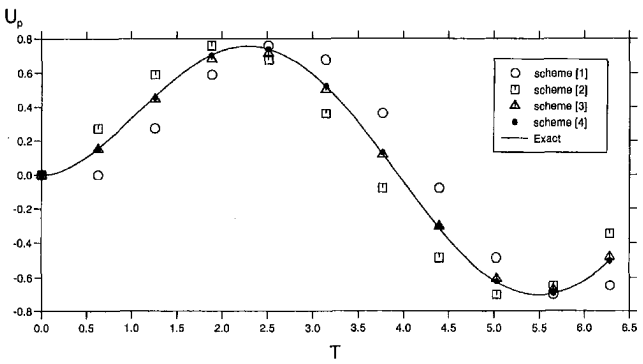


Fig. 1 The particle velocity against time for the oscillating flow problem, a comparison of various schemes

Downloaded 03 Jun 2010 to 171.66.16.125. Redistribution subject to ASME license or copyright; see http://www.asme.org/terms/Terms_Use.cfm

Table 1 Average difference from the exact solution for various time-step values

time-step/s	scheme [1]	scheme [2]	scheme [3]	scheme [4]
0.6283	0.1496	0.1244	1.486E-2	4.321E-3
0.3142	6.804E-2	6.077E-2	3.853E-3	5.348E-4
0.0628	1.238E-2	1.210E-2	1.524E-4	4.044E-6
0.0314	6.124E-3	6.053E-2	3.801E-5	5.019E-7
6.28E-3	1.212E-3	1.211E-3	1.517E-6	3.991E-9

This is not investigated in the present study but may be considered a more feasible and less expensive approach than schemes [3] and [4]. Schemes [3] and [4] give excellent results in comparison with the exact solution. It is just noticeable that scheme [4] has sharper peaks than scheme [3] which are in better agreement with the exact solution. The average difference between the exact U_p solution and the various schemes are summarized for $\tau_p = 1$ s in table I using a variety of time-step values. The results in table I broadly agrees with the truncation analysis. Schemes [1] and [2] converge to similar results for decreasing time-steps this simply shows that U_f^{n+1} tends to U_f^n for small time-steps. Clearly, the error associated with the various schemes is dependent on the time-step as well as the particle relaxation time, τ_p. The ratio of the average difference between the various schemes and the exact solution in comparison with scheme [1] are shown in table 2 for various particle relaxation times. The time-step interval is fixed to 0.2π s (0.628 s). The results show that scheme [1] and [2] are virtually identical for $\tau_p > 1$ s but for smaller particle relaxation times scheme [2] gives a reasonable improvement. Whereas, schemes [3] and [4] give better results than scheme [1] for all τ_p values improving for small τ_p values because scheme [1] tends to fail for this case.

The Vortex Problem

The oscillating fluid-flow problem has a rather limited application for in general, particle tracking studies use steady-state flow-fields or pseudo steady-state flow-fields such as a turbulent flow where the velocity-field varies with position. As previously discussed such problems should be dealt with using $(\partial U_f/\partial x)$ and higher terms but this introduces a number of problems which are not encountered using $(\partial U_f/\partial t)$ and higher terms. The time derivative for steady-state problems no longer refers to the real physical derivative but refers to the time-marching integration term.

The vortex test uses solid-body rotation with the angular velocity, ω_r, fixed at unity. A similar problem has been studied by Ruetsch and Meilburg (1993). Initially the particle is at $(x = 0, y = 1)$ and has the velocity components $(v_x = 1, v_y = 0)$. The path is integrated from $t = 0$ s to $t = 2\pi$ s. The fluid velocity components can be described as $(\omega_r y, -\omega_r x)$ when these terms are substituted into a vector equation in the form of Eq. (1) an exact analytical solution for (x, y) can be found which is in the form of an exponentially increasing spiral. The exact solution of (x, y) is summarized in the Appendix II. Figure 2 shows three exact solutions for the particle relaxation times of 0.01 s, 1 s and 100 s for the total time of flight. The particle with the smallest τ_p value has an almost circular path whereas the particle with the largest τ_p value has only a very slight curve maintaining its initial velocity over the time of flight. The particle with $\tau_p = 1$ s spirals outwards which causes the particle to travel further by experiencing the faster fluid flow velocities away from the centre.

In the oscillating flow problem the U_f^{n+1} term is known but in the vortex flow problem the term is only a prediction U_f^{n+1*} where the prediction is initially found using scheme [1]. The prediction can be poor in comparison with the exact solution which appears to be a major draw-back with schemes [2], [3], and [4]. This problem can be overcome by using more than one prediction level. (It may be possible to improve the prediction level for schemes [3] and [4] by using equations in the form of Eqs. (6) and (7) and assuming for the prediction level that $A^n = A^{n-1}$ and $B^n = B^{n-1}$.) After the appropriate scheme is applied ([2], [3] or [4]) the correction result can be treated as the prediction result. Indeed, this procedure can be repeated a number of times until the correction result converges. A large number of predictions are unnecessary as the predicted value (U_f^{n+1*}) tends to a stable converged result. The number of prediction levels required to produce a stable result is dependent on the time-step value as well as the particle relaxation time. Small time-step values only require the initial prediction from scheme [1] because the prediction is reasonably accurate. Small τ_p values tend to require at least one further prediction level using scheme [2], [3], or [4] because scheme [1] tends to fail for this condition. Generally, two prediction levels were found to give acceptable results, that is to say one prediction from scheme [1] and one further prediction from the advanced schemes.

The ratio of the average distance between the exact solution and the schemes [2], [3], and [4] in comparison with scheme [1] are summarized in Table 3 for a range of particle relaxation times, the time-interval is fixed to 0.2π s (0.628 s) e.g., there are ten steps for a complete set of results. In the table the results of schemes [2], [3], and [4] are shown using one, two and three orders of predictions (expressed as superscripts). The deviation from the exact solution tends to increase with smaller particle relaxation times. Scheme [1] is the most inaccurate

Table 2 The ratio of the average difference from the exact solution for schemes [2], [3], and [4] in comparison with scheme [1] for various particle relaxation times

τ_p/s	scheme [2]	scheme [3]	scheme [4]
100	0.9944	0.1498	3.325E-2
10	0.9975	0.1364	3.352E-2
1	0.8316	9.936E-2	3.022E-2
0.1	0.1912	3.871E-2	1.521E-2
0.01	1.684E-2	4.755E-3	2.082E-3

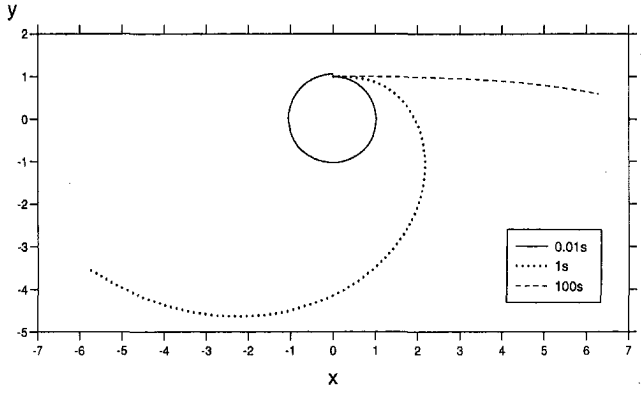


Fig. 2 Exact solutions of the particle tracks for the vortex problem for various particle relaxation times

Downloaded 03 Jun 2010 to 171.66.16.125. Redistribution subject to ASME license or copyright; see http://www.asme.org/terms/Terms_Use.cfm

Table 3 The ratio of the average difference from the exact solution for schemes [2], [3], and [4] in comparison with scheme [1] for various particle relaxation times

τ_p/s	$[2]^1$	$[2]^2$	$[2]^3$	$[3]^1$	$[3]^2$	$[3]^3$	$[4]^1$	$[4]^2$	$[4]^3$
100	0.947	0.947	0.947	1.80E-3	1.80E-3	1.80E-3	0.208	0.208	0.208
10	0.929	0.929	0.929	9.91E-3	1.62E-2	1.62E-2	0.192	0.191	0.191
1	0.718	0.707	0.696	1.84E-2	6.68E-2	6.69E-2	0.111	7.07E-2	6.96E-2
0.1	0.141	0.148	0.124	8.91E-2	7.03E-2	7.84E-2	0.144	1.18E-2	3.23E-2
0.01	0.122	6.86E-2	7.38E-2	0.121	6.16E-2	7.26E-2	0.154	1.01E-2	3.77E-2

scheme. Scheme [2] can give solutions that are an order of magnitude more accurate than scheme [1] provided τ_p is small else the scheme has a similar accuracy as scheme [1]. The most accurate schemes are schemes [3] and [4] predicting solutions that are up to three orders of magnitude more accurate. If $\tau_p <$ 1 s then scheme [4] is the most accurate however if $\tau_p > 1$ s then scheme [3] is the most accurate scheme. It is worth noting this demonstrates a flaw in the current test as opposed to a general result. The fluid velocity increases linearly with component distances this allows scheme [3] to outperform scheme [4] for large particle relaxation times. Generally, however, scheme [4] should give better predictions than scheme [3]. Unlike schemes [2] and [3], scheme [4] gave accurate solutions that were fairly independent of τ_p.

Decreasing the time-step interval for a complete set of results confirmed the global truncation error of scheme [1] is $O(\Delta t)$. Scheme [2] has a global truncation very nearly $O(\Delta t^2)$ for small τ_p values. Schemes [3] and [4] has a global truncation error of at least $O(\Delta t^2)$ for all τ_p values.

The computational performance of the various schemes can be estimated by considering the improved accuracy in ratio with the increase computational cost. The required CPU time is very dependent on computer coding nevertheless a rough estimate has been obtained. Assuming scheme [1] requires 1 CPU unit of time then scheme $[2]^1$ requires about 1.2, $[2]^2$ about 1.9, $[3]^1$ about 1.3, $[3]^2$ about 2.0, $[4]^1$ about 1.5 and scheme $[4]^2$ requires about 2.4 CPU units of time. Scheme [2] only gives a better performance than scheme [1] for small τ_p values. Schemes $[3]^2$ and $[4]^2$ give an improved accuracy of about one order of magnitude (sometimes more) and therefore they give a better performance than scheme [1], in particular scheme $[4]^2$ gives very accurate solutions for small τ_p values. This is significant because for small τ_p values Eq. (1) becomes very stiff; also there is a greater likelihood that the stability $\Delta t < 2\tau_p$ will be invoked. Clearly, scheme $[4]^2$ is a suitable replacement for the original exponential scheme. Extending scheme [4] for additional effects is considered below although similar arguments are applicable to other schemes.

Additional Effects

The present study has only dealt with the problem of integrating Stokes Law which describes the fundamental difficulty in integrating the equation of motion for a particle. Generally, additional forces such as gravity and a pressure gradient across the particle have to be included as well as ultra-Stokeian drag.

Extending scheme [4] to incorporate additional forces is straight-forward. A constant force such as gravity, $-g$, is incorporated by replacing U_f^n in Eqs. (6) and (7) with $U_f^n - \tau_p g$. A time or spacial varying force such as the pressure gradient force, $h \equiv (\pi d_p^3/6)(\partial p/\partial x)$ where d_p is the particle's diameter, is assumed to vary in the same way as the fluid's velocity which is expressed as:

$$h(t) = h^n + At + Bt^2$$

$$A(h) = \frac{h^{n+1^*} - h^{n-1}}{2\Delta t}$$

$$B(h) = \frac{h^{n+1^*} - 2h^n + h^{n-1}}{2\Delta t^2} \qquad (10)$$

The U_f^n terms in Eqs. (6) and (7) are now replaced with $U_f^n - \tau_p g + \tau_p h^n$. The A and B terms in Eqs. (6) and (7) are now set so $A = \tau_p A(h) + A(U_f)$ and $B = \tau_p B(h) + B(U_f)$. Incorporating the additional forces does not significantly increase the computational cost as the U_f^n, A and B terms are simply replaced and a few additional calculations are required.

When the particle Reynolds number, $\mathrm{Re}_p = d_p|U_f - U_p|/\nu$ where ν is the kinetic viscosity, is above unity then Stokes Law is no longer applicable and the drag coefficient is modified by replacing τ_p with $\tau_p fn(\mathrm{Re}_p) \equiv \tau_{pfn}$. The fn term is an empirical modification which describes ultra-Stokeian drag, refer to Clift et al. (1978). As the particle Reynolds number varies with time so does τ_{pfn}. This is usually incorporated by assuming the modification does not vary over the succeeding time-step e.g., τ_p is replaced with τ_{pfn}^n. A predictor-corrector scheme gives the predicted velocity values and the τ_p terms in Eqs. (6) and (7) can therefore be replaced by a combination of $\tau_{pfn}^{n+1^*}$ and τ_{pfn}^n. Replacing the τ_p terms in Eqs. (6) and (7) with $(\tau_{pfn}^{n+1^*} + \tau_{pfn}^n)/2$ is appropriate for schemes [2] and [3] but this is computationally expensive as the exponential terms have to be re-evaluated. Fortuitously, as scheme [4] uses a quadratic fit through the preceding and succeeding time-steps the τ_p terms can be replaced by τ_{pfn}^n with some validity provided the τ_p terms which form the coefficients for the constant force terms are replaced by $(\tau_{pfn}^{n+1^*} + \tau_{pfn}^n)/2$ e.g. $U_f^n \to U_f^n - (\tau_{pfn}^{n+1^*} + \tau_{pfn}^n)g/2$ elsewhere $\tau_p \to \tau_{pfn}^n$. This means exponential terms do not have be re-evaluated and scheme [4] is reasonably efficient.

Concluding Remarks

The exponential-Lagrangian tracking scheme tends to fail for small particle relaxation numbers; fundamentally because of the explicit nature of the scheme. The original exponential scheme was therefore developed by introducing a predictor-corrector element to remove this problem and improve the scheme's accuracy. The predictor-corrector schemes have been tested on two simple problems (which have analytical solutions) one has only time-variation and the other only spacial-variation.

Time-variation problems have a rather limited scope. The problem demonstrated a very good improvement in accuracy for schemes [3] and [4]. Increasing the order of the polynomial fit for the fluid velocity reduces the local truncation error by $O(\Delta t)$ and therefore scheme [4] gave the best results. It follows that a higher-order scheme may be worth considering for a time-variation application. Scheme [2] only gave better results in comparison with scheme [1] for small particle relaxation times.

The spacial-variation problem has greater importance in terms of general applications. In general, all the schemes are problem-dependent. Extremely small time-steps (with moderate particle relaxation times) are probably most efficiently solved using the original exponential scheme where the most important issue is simply the time required to solve the problem. When moderate and large time-steps are used the original exponential scheme gives poor accuracy. For all cases this can be improved using schemes [3] or [4]. Scheme [3] gives particularly good results for large particle relaxation times in the vortex test because the particle moves linearly through the flow which scheme [3] coincidentally models. Nevertheless, the problem can be solved with greater accuracy for moderate/large time-steps and

Downloaded 03 Jun 2010 to 171.66.16.125. Redistribution subject to ASME license or copyright; see http://www.asme.org/terms/Terms_Use.cfm

large particle relaxation times using a high-order Runge-Kutta scheme because the stability condition ($\Delta t < 2\tau_p$) is not invoked. When small particle-relaxation times are considered the classical Runge-Kutta scheme is not suitable and therefore schemes [2] and [4] are of particular interest. Scheme [2] tends to be out-performed by scheme [3] but it is very similar to the original scheme. Indeed, the original exponential scheme only requires minor additions to formulate scheme [2] and for this reason it may be of interest but as previously discussed it requires further development. Scheme [4] gives excellent results in comparison with the original scheme, even taking into account the increased computational cost, but the scheme does have draw-backs involving mainly increased computer coding. Generally, schemes [3] and [4] need two prediction levels for desirable results.

Introducing additional forces and ultra-Stokeian drag for the various schemes is straight-forward (in particular for scheme [4]) and their application is not limited to the integration of Stokes law.

In conclusion, scheme [4] is recommended as a suitable replacement for the origin exponential-Lagrangian tracking scheme.

Acknowledgment

The author is grateful for comments from a referee which initiated the present study. The author would like to thank Ms A. Field for her comments on the original manuscript and also would like to express thanks to Dr. I. M. Hall for helpful comments on the subject.

References

Anderson, D. A., Tannehill, J. C., and Pletcher, R. H., 1984, *Computational Fluid Mechanics and Heat Transfer*, Hemisphere.

Boris, J. P., and Oran, E. S., 1987, *Numerical Simulation of Reactive Flow*, Elsevier.

Boysan, F., Ayers, W. H., and Swithenbank, J., 1982, "A Fundamental Mathematical Modelling Approach to Cyclone Design," *Transactions for the Institute of the Chemical Engineering*, Vol. 60, pp. 222–230.

Chow, C. Y., 1979, *An Introduction to Computational Fluid Mechanics*, John Wiley.

Clift, R., Grace, J. R., and Weber, M. E., 1978, *Bubbles, Drops and Particles*, Academic Press.

Ruetsch, G. R., and Meilburg, E., 1993, "On the Motion of Small Spherical Bubbles in Two-Dimensional Vortical Flows," *Physics of Fluids A*, Vol. 5, pp. 2326–2341.

Schöneborn, P.-R., 1975, "The Interaction Between a Single Particle and an Oscillating Fluid," *International Journal of Multiphase Flow*, Vol. 2, pp. 307–317.

APPENDIX I

The coefficient terms A and B for Eq. (5) are expressed as:

$$A(\phi) = \frac{\phi^{n+1*}(\Delta t^{n-})^2 + \phi^n((\Delta t^{n+})^2 - (\Delta t^{n-})^2) - \phi^{n-1}(\Delta t^{n+})^2}{\Delta t^{n-}\Delta t^{n+}(\Delta t^{n-} + \Delta t^{n+})}$$

$$B(\phi) = \frac{\phi^{n+1*}\Delta t^{n-} - \phi^n(\Delta t^{n-} + \Delta t^{n+}) + \phi^{n-1}\Delta t^{n+}}{\Delta t^{n-}\Delta t^{n+}(\Delta t^{n-} + \Delta t^{n+})} \quad (11)$$

in general terms for nonuniform time intervals where Δt^{n+} is the succeeding time step and Δt^{n-} is the preceding time step.

APPENDIX II

The solution of x and y in terms of time can be expressed in the following form:

$$(x \vee y) = \cos\frac{bt}{\tau_p}\left(A \exp\left(-\tfrac{1}{2} + a\right)\frac{t}{\tau_p} + B \exp - \left(\tfrac{1}{2} + a\right)\frac{t}{\tau_p}\right) + \sin\frac{bt}{\tau_p}\left(C \exp\left(-\tfrac{1}{2} + a\right)\frac{t}{\tau_p} + D \exp - \left(\tfrac{1}{2} + a\right)\frac{t}{\tau_p}\right) \quad (12)$$

where the terms a and b are dependent on the particle relaxation time.

$$a = \left(\frac{1 + (1 + 16\tau_p^2)^{1/2}}{8}\right)^{1/2}$$

$$b = \left(\frac{-1 + (1 + 16\tau_p^2)^{1/2}}{8}\right)^{1/2} \quad (13)$$

The A, B, C, D terms have the following values for the x solution.

$$A_x = -B_x = \frac{12a^2 - 4b^2 - 3}{16a(a^2 + b^2)}\tau_p$$

$$C_x = \frac{3a + 4a^2 - 4a^3 + 12ab^2 + 4b^2}{16ab(a^2 + b^2)}\tau_p$$

$$D_x = \frac{3a - 4a^2 - 4a^3 + 12ab^2 - 4b^2}{16ab(a^2 + b^2)}\tau_p \quad (14)$$

The constant terms A, B, C, D for the y solution can be expressed in terms of the x-constant terms:

$$A_y = \frac{2ab}{\tau_p}C_x$$

$$B_y = \frac{-2ab}{\tau_p}D_x$$

$$C_y = D_y = \frac{-2ab}{\tau_p}A_x \quad (15)$$

Downloaded 03 Jun 2010 to 171.66.16.125. Redistribution subject to ASME license or copyright; see http://www.asme.org/terms/Terms_Use.cfm

Elements of an Approach to the Assessment of Random Uncertainty in Transient Measurements

P. K. Maciejewski
Mechanical Engineering Department,
University of Pittsburgh,
Pittsburgh, PA 15261

This paper presents an approach to the assessment of random uncertainty in transient measurements based on the modeling of a time series that is representative of the variable of interest. The recommended approach employs conventional regression techniques to estimate all parameters that appear in a model for a given time series. Assessments of random uncertainty are based on the residual deviations associated with an adequate model for a given time series. The approach also incorporates a treatment of the dynamic response of a measurement system as it pertains to random uncertainty in transient measurements.

Introduction

Although many experiments and tests involve the measurement of variables whose values are time-dependent during the period of the experiment or test, at present there is no standard method for assessing measurement uncertainty for time-dependent variables. In fact, the entire literature that is explicitly devoted to the topic of uncertainty in transient measurements may consist of a single paper presented by Alwang (1991). The present paper will explore some of the issues associated with the specification of random uncertainty in transient measurements, and will recommend an approach to assessing random uncertainty for time-dependent measured variables.

Conceptually, perhaps the most direct approach to assessing random uncertainty for a time-dependent measured variable is to replicate an experiment or test, defining a set of random variables Q_t such that Q_t estimates the value of the time-dependent variable at time t, the time from the initiation of the test. The ensemble average value of Q_t is then an estimate of the mean value of the time-dependent variable at time t, and the standard deviation in Q_t divided by the square-root of the number of replications is an estimate of the standard deviation in the average value of Q_t at time t. While replications of the experiment or test may prove to be costly, as few as two such replications would permit a statistically sound estimate of a confidence interval for the mean value of the time-dependent variable at any time t.

While the ensemble averaging approach to the problem of assessing random uncertainty for a time-dependent measured variable does appear to have its merits, its success in practice rests on at least two assumptions. First of all, it assumes that the average value of Q_t is an unbiased estimate of the mean value of the time-dependent variable at time t. In practice, Q_t may not be a variable that is directly measured, but rather one that ought to be calculated in terms of the output variable and transfer function for the measurement system. If Q_t is merely the output variable from a measurement system, then the expected value for Q_t is likely to be a biased estimate for the mean value of the time-dependent variable of interest at time t, with the magnitude of the bias determined by the values of the "true" but unknown time-dependent input variable and the model employed for the dynamic response of the measurement system. (It should be noted that this concern regarding the influence of the measurement system on one's estimate of a variable of interest is not a concern restricted to an ensemble averaging approach to the assessment of uncertainty in transient measurements per se, but only a concern regarding a naive employment of an ensemble averaging approach.) Second, the ensemble averaging approach presupposes one can construct replications of an experiment or test that are identical in every respect. The "uncertainty" in a time-dependent measured variable associated with replications of an experiment or test will be higher than the "uncertainty" in that variable associated with the measurement itself, since other factors will influence the value of the measured variable if each replication of the experiment or test is not identical to every other replication.

As a practical matter, the ensemble averaging approach to the problem of assessing random uncertainty for a time-dependent measured variable ought to be rejected on the ground that it confounds run-to-run variation in a test result with the uncertainty in the test result. In many contexts, the run-to-run variation in a test result can be employed to decide whether the test is controlled. (If the results of independent replications of a test are not significantly different, then the test is controlled. If the results of independent replications of a test are significantly different, then the test is uncontrolled.) The issue here is one of placing the experimenter in a position to statistically test whether or not a test result is repeatable, i.e., in a position to test whether or not an experiment is controlled. If one has a method for assessing the uncertainty of a measured result that is independent of the process of the replication of a test, e.g., a method that can be applied to a single realization of the test, then one is in a position to compare the variability in the results of a set of replications directly to the measurement uncertainty associated with a single realization of the result for the purpose of deciding whether or not the test is repeatable. On the other hand, if one uses the variability in the results of a set of replications for the purpose of assessing the uncertainty in the result, as required by the ensemble averaging approach, then one cannot check, by means of some statistical test, whether or not the test in question is repeatable, because there is no independent method for determining the uncertainty in the result of a single realization of the test for the purpose of comparison. An estimate of measurement uncertainty for the result of a test that is independent of the assessment of the variability of the results of a set of replications of the test is essential in maintaining the

Contributed by the Fluids Engineering Division for publication in the JOURNAL OF FLUIDS ENGINEERING. Manuscript received by the Fluids Engineering Division December 5, 1994; revised manuscript received November 6, 1995. Associate Technical Editor: Jong H. Kim.

Copyright © 1996 by ASME

Downloaded 03 Jun 2010 to 171.66.16.125. Redistribution subject to ASME license or copyright; see http://www.asme.org/terms/Terms_Use.cfm

"repeatability of a test" as a diagnostic tool for experimentation.

Any adequate method for assessing random uncertainty for a time-dependent measured variable should meet the following criteria: (1) it should permit the construction of a confidence interval for the measured variable at any given time, (2) it should account for the dynamic response of the measurement system, and (3) it should be applicable to a single test run. The aim of this paper will be to propose a method for assessing random uncertainty for a time-dependent measured variable that meets these criteria.

Scope of the Present Enquiry

The aim of this paper is to provide an overview of an approach to the assessment of random uncertainty in transient measurements made at discrete time intervals. A presentation of the treatment of the dynamic response of measurements systems as it pertains to an assessment of random uncertainty is deferred until after the proposed approach has been presented for the case in which the observed time series is directly representative of the variable of interest. Issues pertaining to the treatment of deterministic uncertainty in transient measurements are not addressed by this study.

Given the nature of this topic, a completely satisfying presentation of the approach would presuppose an extensive understanding of probability theory, statistical principles and applied modeling techniques. However, this paper aims to introduce an approach to the assessment of random uncertainty in transient measurements that could be developed more rigorously, but that addresses a community that may not yet have a thorough background in these areas. Throughout the text, the language employed falls somewhere between statistical rigor and common understanding.

Models for Random Uncertainty

What is it that constitutes an error in the measurement of a variable that is presumed to be a function of time? In the case of a steady-state measurement, in which the value of the measured variable is presumed to be independent of time, the issue of what constitutes an error is greatly simplified: All variation in the data is attributed to measurement error. In the case of a measurement of an unsteady variable, however, all variation in the data cannot be attributed to measurement error. The total variation in the data must be partitioned into a component that can be modeled as a function of time and a component that cannot be modeled as a function of time. One must distinguish variation in the data due to the time dependence of the variable from the variation in the data due to measurement error.

Conceptually, an error in measurement may be defined as the difference between the true value of the measured variable and the observed value. This is the conception of an error in measurement presented in ANSI/ASME PTC 19.1 (1985). The difficulty with this conception of an error in measurement is that it does not allow one to assign a value to the error, since the true value of the measured variable is in practice unknown and must be estimated by the observed value. The assessment of measurement uncertainty must therefore proceed, strictly speaking, not directly from the analysis of errors in measurement, but rather indirectly from the analysis of observed deviations from an observed model for the true value of the measured variable.

Perhaps the simplest example of this is given by the model used to estimate the true value of a measured variable that is presumed to be independent of time, i.e., the mean value of the observed values of the measured variable. This model can be represented as follows:

$$X_{\text{observed}} = X_{\text{model}} + \delta$$

In this case the error can be expressed as follows:

$$\epsilon = (X_{\text{observed}} - X_{\text{true}}) = (X_{\text{model}} - X_{\text{true}}) + \delta$$

On the assumption that the model is correct, i.e., that the true value of the measured variable is given by X_{model},

$$\epsilon = \delta$$

Furthermore, the assumption that the true value of the measured variable is independent of time can be assessed through an analysis of the time series given by the deviations from the model.

The arguments for constructing an uncertainty interval for the true value of a time independent measured variable by means of the deviations from a model for the "true" value of the variable can be readily extended to the case of constructing an uncertainty interval for the true value of a time-dependent measured variable. In this case one only need model the measured variable as a function of time as follows:

$$Q_{\text{observed},t} = Q_{\text{model},t} + \delta_t$$

So that the error at time t can be expressed as follows:

$$\epsilon_t = (Q_{\text{observed},t} - Q_{\text{true},t}) = (Q_{\text{model},t} - Q_{\text{true},t}) + \delta_t$$

On the assumption that the model is correct, i.e., that the true value of the time-dependent measured variable at time t is given by $Q_{\text{model},t}$,

$$\epsilon_t = \delta_t$$

On assumption that the model is correct, δ_t will be a purely random stationary time series (white noise). The aim is to model the time-dependent behavior of the random variable such that the time series given by the residual deviations from the model is a purely random process. Once an acceptable model has been constructed, the "true" value of the measured variable as a function of time can be estimated by means of the model, and the uncertainty in the true value of the measured variable can be estimated by means of the deviations from the model.

Nomenclature

D = nozzle diameter
K = measurement system static gain
Q_t = random variable for a transient process
R_t = measurement system output variable
r_τ = sample autocorrelation function at time lag τ
Re_D = Reynolds number based on nozzle diameter
S = sample standard deviation
t = time
T = time constant
$t_{v,c}$ = point in t_v-distribution corresponding to level of confidence c
U = uncertainty
X_t = random variable for a stationary process
Y_t = variable for a deterministic process
Z_t = random variable for a purely random process
α = model parameter in an AR process
δ = deviation from a model
δ_t = deviation from a model at time t
ϵ = error
ϵ_t = error at time t
v = degrees of freedom
ρ = autocorrelation function
τ = time lag
θ = model parameter in a deterministic process

Downloaded 03 Jun 2010 to 171.66.16.125. Redistribution subject to ASME license or copyright; see http://www.asme.org/terms/Terms_Use.cfm

Modeling Time Series

In the proposed approach to the assessment of random uncertainty in transient measurements, the primary goal of an uncertainty analysis is to model the time behavior of a given time series such that the deviations from the model represent a purely random process. At the outset of this undertaking, one must have clear definitions of the terms "purely random process," "stationary process," and "transient process." A purely random time series is one in which the members of the sequence are independent and identically distributed random variables. A second-order stationary (or weakly stationary) time series is one in which the members of the sequence have a common mean value and the correlation between any two members of the sequence depends only on the time interval between them (the "time lag"). A transient process can be taken to be simply a non-stationary time series.

Given these definitions of transient, stationary, and purely random processes, the autocorrelation function presents itself as the natural tool for discriminating between these classes of time series. If the autocorrelation function for a process depends not only on the time lag but also on the time (position in the sequence), then the process is transient. If the autocorrelation function depends only on the time lag, then the process is stationary. If the autocorrelation function for a process is zero for a stationary process for all time lags with the exception of zero time lag, then the process is purely random. Of course, whenever one is estimating an autocorrelation function from data one has to allow for the fact that the estimated autocorrelation function will deviate from the true autocorrelation function for the process. For example, one might be justified in declaring a time series to be purely random if the value of the estimated autocorrelation function is not statistically different from zero for all time lags other than $\tau = 0$.

Once a time series has been classified as either transient or stationary but not purely random, an assessment of the random uncertainty associated with the measured variable requires that one model the time behavior of the observed time series. The modeling effort will presume that a transient process can be decomposed into a combination of a strictly deterministic component and a stationary stochastic component, and that the stationary stochastic component can be modeled by an autoregressive process. An autoregressive process of order k, denoted AR(k), is given as follows:

$$X_t = \alpha_1 X_{t-1} + \alpha_2 X_{t-2} + \ldots + \alpha_k X_{t-k} + Z_t$$

Here the process variable X_t is represented as a weighted sum of its past values, X_{t-1}, X_{t-2}, ..., X_{t-k}, combined with the present value of a purely random process, Z_t. One advantage of representing a stationary process as an autoregressive process is that, as the term "autoregressive" suggests, one can estimate the parameters in the model, i.e., the α's, by means of conventional linear regression techniques where X_t is taken to be the response variable and X_{t-1}, X_{t-2}, ..., X_{t-k} are taken to be the regressor variables. An autoregressive process is a special case of a general linear process. [A discussion of general linear processes is given by Box et al. (1994). That any stationary stochastic process has a linear representation has been established by Wold (1938). A discussion of the conditions under which the linear representation of a stationary stochastic process can be represented as an autoregressive process is given by Koopmans (1974).]

As an illustration of the manner in which a transient time series can be composed of a strictly deterministic "transient" component and a stationary "stochastic" component, consider the time series presented in Fig. 1, which represents a series of velocity measurements made in air at 0.0005 s intervals (i.e., 2 kHz sampling rate) with a hot-wire anemometer located 2 diameters from the exit of a nozzle (measured along the axis of the nozzle) of circular cross-section (D = 1.91 cm) as the

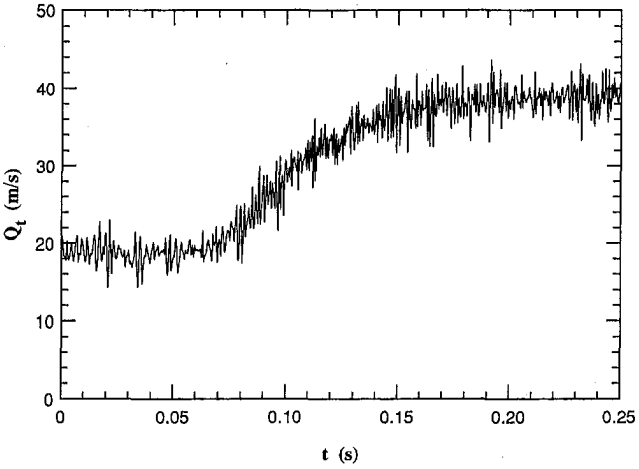


Fig. 1 A time series for a transient process

nozzle undergoes an abrupt change in operating condition (from $Re_D \approx 25{,}000$ to $Re_D \approx 50{,}000$). This time series, Q_t, can be decomposed into a deterministic transient component, Y_t, and a stationary stochastic component, X_t, as follows:

$$Q_t = Y_t + X_t$$

where

$$Y_t = \theta_1 \quad t < \theta_4$$

$$Y_t = \theta_1 + (\theta_2 - \theta_1)(1 - \exp[-\theta_3(t - \theta_4)^2]) \quad t > \theta_4$$

and

$$X_t = \alpha_1 X_{t-1} + \alpha_2 X_{t-2} + \alpha_3 X_{t-3} + \alpha_4 X_{t-4} + \alpha_5 X_{t-5} + \alpha_6 X_{t-6} + Z_t$$

Figure 2 illustrates this decomposition of Q_t into Y_t and X_t. Figure 2(a) presents the underlying deterministic transient component of the process, Y_t, a model in which θ_1 = 18.81 m/s, θ_2 = 38.66 m/s, θ_3 = 300 s^{-2}, and θ_4 = 0.055 s. Figure 2(b) presents the underlying stationary stochastic component of the process, X_t, where X_t has been modeled as an AR(6) process, in which Z_t is a purely random process and $\alpha_1 = -0.47$, $\alpha_2 = -0.21$, $\alpha_3 = 0.17$, $\alpha_4 = 0.20$, $\alpha_5 = 0.25$, and $\alpha_6 = 0.18$. Fig. 3(a) presents the sample autocorrelation function associated with the stationary process X_t, and Fig. 3(b) presents purely random process associated the model for X_t, i.e., Z_t.

In this example, the complete model for the time behavior of the transient process, Q_t, can be re-expressed as follows:

$$Q_{\text{observed},t} = Y_t + \sum_{i=1}^{6} \alpha_i (Q_{\text{observed},t-i} - Y_{t-i}) + Z_t$$

This model can be taken to be a particular instance of a general model for a transient time series, that is

$$Q_{\text{observed},t} = Q_{\text{model},t} + \delta_t$$

where

$$Q_{\text{model},t} = Y_t + \sum_{i=1}^{6} \alpha_i (Q_{\text{observed},t-i} - Y_{t-i})$$

and

$$\delta_t = Z_t$$

This model for Q_t contains both an autoregressive component and a deterministic component. The deviations from the model, δ_t, represent a purely random process. Given that Q_t has been modeled successfully in this example, the true value of Q_t can

Downloaded 03 Jun 2010 to 171.66.16.125. Redistribution subject to ASME license or copyright; see http://www.asme.org/terms/Terms_Use.cfm

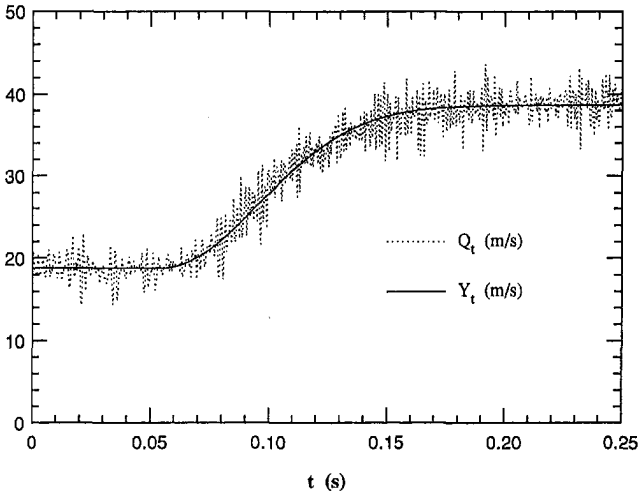


Fig. 2(*a*) A deterministic component

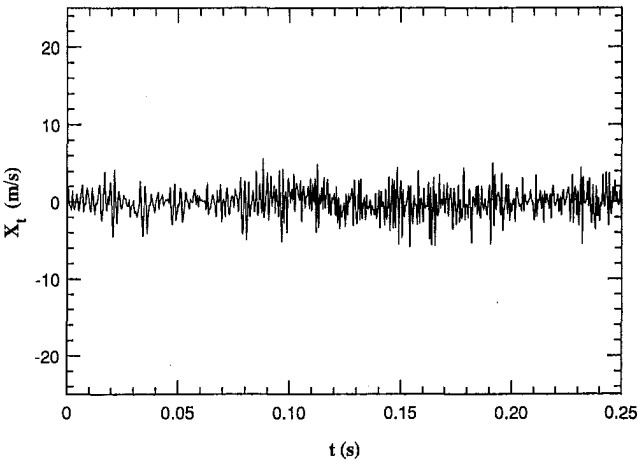


Fig. 2(*b*) A stationary stochastic component

be estimated by means of the model, and the uncertainty in the true value of Q_t can be estimated by means of the deviations from the model.

The random uncertainty in the measurement is given by $U = t_{v,c}S$, where S is the standard deviation for the "observations" in the purely random process that is produced by the analysis, δ_t, and $t_{v,c}$ is the value from the t-distribution corresponding to the number of degrees of freedom, v, in estimating S for this purely random process and corresponding to the desired level of confidence, c. A confidence interval for the measured variable at any given time is constructed as $Q_{\text{observed},t} \pm U$. In the present example, $U = 3.34$ m/s at 95 percent confidence.

Estimation of Model Parameters

The approach presented in the preceding section assumed that a transient process could be modeled as a combination of a deterministic "transient" component and a stationary "stochastic" component, and that the stationary component can be modeled as an autoregressive process. One of the main advantages in making this assumption is that it permits one to estimate all the parameters in the composite model for the time series by conventional regression techniques. The modeling of the overall process will proceed in two stages. In the first stage of the modeling, Q_t is taken as the response variable and functions of time are taken to be the regressor variables. This first stage of the modeling effort will be considered complete when the residual deviations from the model represent a stationary time series, i.e., $Q_t - Y_t = X_t$. In the second stage of the modeling, X_t is taken as the response variable and X_{t-1}, X_{t-2}, etc., are taken to be the regressor variables. This second stage of the modeling effort will be considered complete when the residual deviations from the model represent a purely random time series, i.e., $X_t - X_{\text{model},t} = Z_t$.

As an example of this two stage employment of regression techniques, consider the modeling of the transient process presented in Fig. 1. If the data analyst recognizes that the deterministic component of Q_t, Y_t, may be modeled as follows

$$Y_t = \theta_1 \quad t < \theta_4$$

$$Y_t = \theta_1 + (\theta_2 - \theta_1)(1 - \exp[-\theta_3(t - \theta_4)^2]) \quad t > \theta_4$$

then the analyst can estimate the model parameters θ_1, θ_2, θ_3, and θ_4 by means of a non-linear regression procedure, e.g., one which minimizes the mean squared deviation from the model. This first stage of the modeling effort is taken to be complete if $X_t = Q_t - Y_t$ is a stationary time series. If X_t is not a stationary time series, an alternative deterministic "transient" model for Q_t must be sought. In the second stage of the modeling effort, X_t will be modeled as an autoregressive process. If the data analyst recognizes that the stationary stochastic component of Q_t, X_t, may be modeled as follows

$$X_t = \alpha_1 X_{t-1} + \alpha_2 X_{t-2} + \alpha_3 X_{t-3} + \alpha_4 X_{t-4} + \alpha_5 X_{t-5} + \alpha_6 X_{t-6} + Z_t$$

then the analyst can estimate the model parameters α_1, α_2, α_3, α_4, α_5, and α_6 by means of a linear regression procedure. In

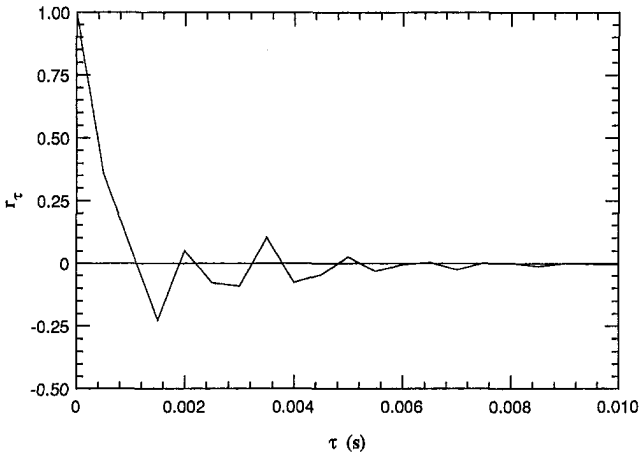


Fig. 3(*a*) An autocorrelation function

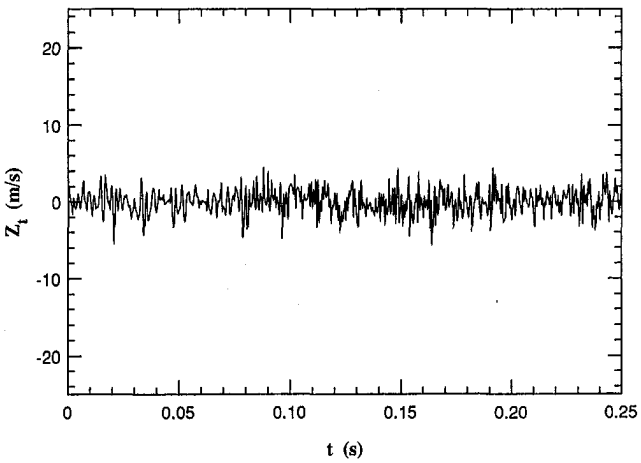


Fig. 3(*b*) A purely random process

Downloaded 03 Jun 2010 to 171.66.16.125. Redistribution subject to ASME license or copyright; see http://www.asme.org/terms/Terms_Use.cfm

this aspect of the modeling, every value of the variable X_t must be treated as being matched with its value at each of the preceding six time steps in order to carry out the regression procedure. Consequently, there will N-6 septuples of observations, $(X_t, X_{t-1}, X_{t-2}, X_{t-3}, X_{t-4}, X_{t-5}, X_{t-6})$, where N is the total number of observations in the time series. This second stage of the modeling is taken to be complete if $Z_t = X_t - (\alpha_1 X_{t-1} + \alpha_2 X_{t-2} + \alpha_3 X_{t-3} + \alpha_4 X_{t-4} + \alpha_5 X_{t-5} + \alpha_6 X_{t-6})$ is a purely random process. If Z_t is not a purely random time series, an alternative autoregressive model for X_t must be sought.

There exists an extensive literature on modeling by means of regression techniques. Anyone who wishes to estimate random uncertainty in transient measurements by the methods outlined here must be sufficiently well versed in the art of regression modeling. A detailed discussion of regression modeling is beyond the scope of this paper.

The Dynamic Response of the Measurement System

Until this point, the proposed method for assessing random uncertainty in transient measurements has presupposed that the time series that one observes is directly representative of the process that one wishes to investigate. In practice, however, the time series that one observes is often only the output of a system of measurement, the unobserved input to which is the time series of interest. If one could reconstruct or estimate the unobserved time series that serves as the input to the system of measurement in terms of the observed time series that results as output from the system of measurement and the dynamic characteristics of the system of measurement, then one would be in a position where one could apply the proposed method of analysis to this reconstructed time series that represents the variable of interest. A key to the success of this proposed project will be one's ability to model the dynamic response of one's system of measurement.

As an example of how the dynamic characteristics of a measurement system can alter the character of a time series, consider the case of a measurement system that can be modeled by means of a linear first order difference equation as follows:

$$T(R_t - R_{t-1})/\Delta t + R_t = KQ_t$$

where R_t is the output from the measurement system, Q_t is the input to the measurement system, Δt is the time interval between successive members in each of the time series, T is the time constant for the measurement system and K is its static gain. This difference equation can be rewritten to express R_t explicitly as follows:

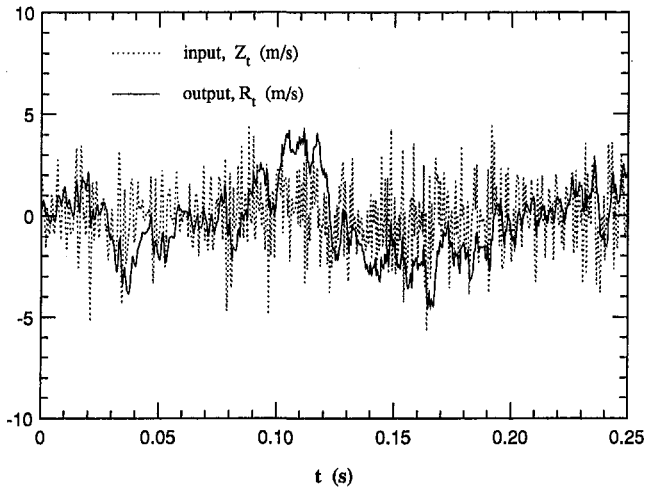


Fig. 4 System output for random input

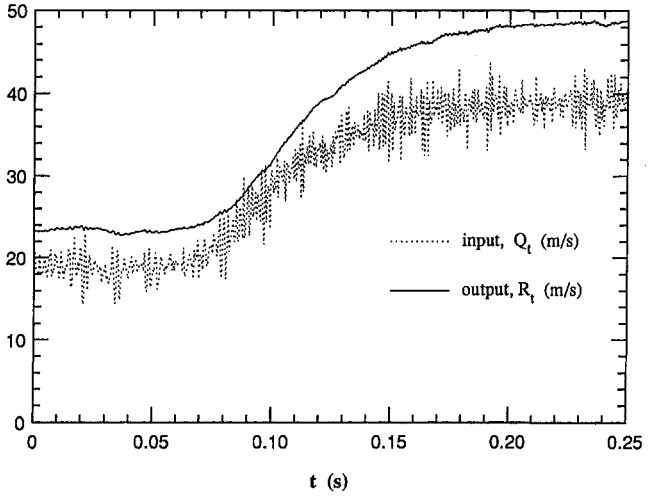


Fig. 5 System output for input given in Fig. 1

$$R_t = [KQ_t + (T/\Delta t)\, R_{t-1}]/(1 + T/\Delta t)$$

If the input to this measurement system is a purely random process, i.e., $Q_t = Z_t$, then this expression for R_t becomes an expression for a first order autoregressive process. In particular, if $Q_t = Z_t$ and if $T/\Delta t = 19$ and $K = \sqrt{39}$, the variance of R_t will be exactly the variance of Q_t and the autocorrelation function for R_t will be given by $\rho = \alpha^\tau$, where $\alpha = 0.95$. An illustration of the input and output to this measurement system for this specific example is given in Figure 4. A white noise input to the measurement system does not result in a white noise output from the system. If the input to the same measurement system is the time series represented in Fig. 1, and if the static gain is adjusted to $K = 1.25$, then the output from the measurement system will be that represented in Fig. 5.

If one knew that one's measurement system could be modeled by means of a first order difference equation, then one would be able to reconstruct an unobserved input time series from an observed output time series and the measurement system parameters T and K as follows:

$$Q_t = [(1 + T/\Delta t)R_t - (T/\Delta t)R_{t-1}]/K$$

More generally, if one could model a measurement system by means of a linear difference equation of any order, then in principle an unobserved input time series could be reconstructed from an observed output time series, provided that all of the parameters associated with the model for the measurement system either were known or could be estimated.

Modeling the dynamic behavior of a given measurement system and estimating parameters for a model of a given measurement system will be essential aspects of an assessment of random uncertainty in transient measurements with a given measurement system. The modeling of a given measurement system will be greatly simplified if the measurement system can be represented as linear and time-invariant. Issues pertaining to the modeling of transfer functions are addressed by Box, Jenkins and Reinsel (1994).

Discussion

The approach to the assessment of random uncertainty in transient measurements advocated in this paper has a number of advantages. Firstly, it provides an acceptable answer to the question "What is the relation between the method of assessment of random uncertainty in a transient process and the method of assessment of random uncertainty in a steady-state process?" The answer to this question is simply that the method of assessment of random uncertainty for a steady-state process

Downloaded 03 Jun 2010 to 171.66.16.125. Redistribution subject to ASME license or copyright; see http://www.asme.org/terms/Terms_Use.cfm

is a special case of the method of assessment of random uncertainty for a transient process, i.e., one in which the observed time series is a purely random process. Secondly, although the proposed approach does require that one fit an empirical model to the data prior to an assessment of random uncertainty, model parameters associated with both the deterministic "transient" component of the composite model and the stationary "stochastic" component of the composite model can be estimated employing conventional regression procedures. Finally, the proposed approach allows one to employ a model for the dynamic characteristics of the measurement system in order to reconstruct a representation of the time series which serves as the unobserved input to the measurement system in terms of the time series that serves as the observed output from the measurement system.

The presentation of the proposed approach to the assessment of random uncertainty in transient measurements has been limited to discrete time series. However, despite the fact that most measured variables in engineering systems are continuous, these variables are quite often observed only at discrete time intervals. The proposed method for the assessment of random uncertainty in transient measurements presupposes that one can adequately model the time-correlated behavior of the random component of the variable of interest, a condition that will be met only if the experimenter ensures that the sampling rate meets the Nyquist criterion for representing the underlying variable by means of a discretely sampled time series. (The application of the proposed method to the case of low frequency sampling of a continuous variable with a significant, high-frequency, time-correlated, random component may lead to the confounding of time-dependent variation in the variable and measurement uncertainty.) Undoubtedly, one could present an approach for the assessment of random uncertainty for transient measurements of a continuous time series which would be an analog to the approach presented here for discrete time series.

The proposed approach to the assessment of random uncertainty in transient measurements may be classified as time series analysis in the time domain. Many researchers, particularly those in engineering disciplines, often prefer to analyze time series in the frequency domain. While it is widely considered a matter of indifference or merely a matter of preference whether one represents their data in the time domain or in the frequency domain, when it comes to matters of modeling, statistics and uncertainty one might find that assessments in the time domain have certain advantages.

The present enquiry has set aside all issues pertaining to the treatment of deterministic uncertainty in transient measurements. There are a number of other issues that touch upon the issue of deterministic uncertainty in transient measurements, for example, issues of standards of measurement and calibration procedures for instruments to be employed in the measurement of transient process variables. These issues remain to be addressed.

Conclusion

This paper has presented an approach to the assessment of random uncertainty in transient measurements that is applicable to both transient and steady-state measurements. In this approach, assessments of random uncertainty for the true value of the measured variable are based on the deviations from a model for the true value of the measured variable, i.e., an assessment of random uncertainty can be made only after the time series representing the variable of interest has been adequately modeled. The approach recommends modeling time series as a combination of a deterministic transient component and a stationary stochastic component such that the estimation of all parameters that appear in the model can be estimated by conventional regression procedures. The criterion for the adequacy of the model for the time series is that the deviations from the model time series represent a purely random process. The approach also allows one to assess random uncertainty in an unobserved time series that serves as an input to a linear and time-invariant measurement system, provided that one observes the output from the measurement system and provided that one has an adequate model for the dynamic behavior of the measurement system.

References

Alwang, W. G., 1991, "The Analysis of Uncertainty in Transient Measurements," ISA Paper No. 91-060.

ANSI/ASME PTC 19.1, 1985, "Measurement Uncertainty, Part 1, Instruments and Apparatus."

Box, G. E. P., Jenkins, G. M., and Reinsel, G. C., 1994, *Time Series Analysis: Forecasting and Control, Third Edition,* Prentice Hall, Englewood Cliffs, NJ.

Koopmans, L. H., 1974, *The Spectral Analysis of Time Series,* Academic Press, New York, NY.

Wold, H. O., 1954, *A Study in the Analysis of Stationary Time Series,* Almqvist & Wiksell, Uppsala, Sweden, 1938, Second Edition.

Downloaded 03 Jun 2010 to 171.66.16.125. Redistribution subject to ASME license or copyright; see http://www.asme.org/terms/Terms_Use.cfm

Unsteady Heat Transfer From a Sphere at Small Peclet Numbers

Zhi-Gang Feng

E. E. Michaelides

Department of Mechanical Engineering,
Tulane University,
New Orleans LA 70118

In a recent paper by Michaelides and Feng (1994) it was discovered that there are history terms in the unsteady heat conduction equation from a small sphere. The history terms are analogous to the terms found in the equation of motion of the sphere, which sometimes are called "Basset terms." An analysis is presented here for the unsteady heat transfer from a sphere, when its surface temperature undergoes a step change. The singular perturbation technique is used to obtain short and long-time solutions, first in the vicinity of the sphere and then far from the sphere. The solution obtained is for finite but low Peclet numbers. It appears that in the case of the step temperature, change, the history terms are reduced to an analytical expression of the error function.

1 Introduction

The dimensionless energy equation of a particle in motion inside a fluid is

$$\frac{\partial \theta}{\partial t} + \mathrm{Pe}\mathbf{v}\cdot\nabla\boldsymbol{\theta} = \nabla^2\theta \tag{1}$$

where θ is a dimensionless temperature and Pe is the Peclet number. It is clear that the Peclet number in the energy equation plays the same role as the Reynolds number in the momentum equation of a particle. At the limit of zero Peclet numbers, when the advection term is neglected, this equation becomes the unsteady heat conduction equation. It was proven by Michaelides and Feng (1994) that the dimensionless rate of heat transfer from a sphere to a fluid of nonuniform temperature is as follows:

$$Q = -\oint_A \mathbf{q}\cdot\mathbf{n}dA = -\frac{4\pi}{3}\frac{d\theta_\infty}{dt} - 4\pi(\theta_s - \theta_\infty - \tfrac{1}{6}\nabla^2\theta_\infty) - 4\pi\int_0^t \frac{\frac{d}{d\tau}[\theta_s - \theta_\infty - \frac{1}{6}\nabla^2\theta_\infty]}{\sqrt{\pi(t-\tau)}}d\tau. \tag{2}$$

The time has been made dimensionless by using the diffusion timescale $t_s = a^2\rho_s c_s/k_f$. Of the terms in the last equation, the first one in the right-hand side is the change of temperature of the fluid in the absence of the sphere; the second term is the usual steady-state conduction term; the third term is a history term, which is analogous to the history term found in the momentum equation of a particle. The history term accounts for the diffusion of temperature gradients inside the fluid. In the particular case of a sphere undergoing a step temperature change inside a fluid of uniform and steady temperature, the last equation yields the following result for the Nusselt number:

$$\mathrm{Nu} = 2\left(1 + \frac{1}{\sqrt{\pi t}}\right) \tag{3}$$

which is consistent with the steady-state conduction results at the limit $t \to \infty$.

The problem of the steady-state convection from a sphere in a viscous fluid was first tackled in the 1960s. Acrivos and Taylor (1962) solved the problem of a sphere in Stokes flow, by employing a singular perturbation expansion technique, first introduced by Proudman and Pearson (1957). Their final result for the Nusselt number is:

$$\mathrm{Nu} = 2(1 + \tfrac{1}{2}\,\mathrm{Pe} + \tfrac{1}{2}\,\mathrm{Pe}^2 \ln \mathrm{Pe} + 0.41465\,\mathrm{Pe}^2 + \tfrac{1}{4}\,\mathrm{Pe}^3 \ln \mathrm{Pe} + O(\mathrm{Pe}^3)) \tag{4}$$

Brenner (1963) extended this solution to the case of particles of arbitrary shapes and presented a general result for steady-state convection from a particle. He used the momentum and energy exchange analogy to derive the following expression for the Nusselt number:

$$\frac{\mathrm{Nu}}{\mathrm{Nu}_0} = 1 + \frac{\mathrm{Nu}_0}{4}\mathrm{Pe} + \frac{\mathrm{Nu}_0}{4} f\,\mathrm{Pe}^2 \ln \mathrm{Pe} + O(\mathrm{Pe}^2) \tag{5}$$

where Nu_0 is the Nusselt number of the arbitrarily shaped particle in the limit of pure conduction and depends only on the geometry of the particle; f is the drag coefficient of the particle.

Batchelor (1979) presented a solution for the problem of an arbitrary particle freely suspended in a linear flow regime. He showed that

$$\frac{\mathrm{Nu}}{\mathrm{Nu}_0} = 1 + \gamma\,\mathrm{Nu}_0\,\mathrm{Pe}^{1/2} + O(\mathrm{Pe}^{1/2}) \tag{6}$$

where γ is a dimensionless shear rate. Shortly thereafter, Acrivos (1980) extended Batchelor's solution to Peclet numbers of higher order:

$$\frac{\mathrm{Nu}}{\mathrm{Nu}_0} = 1 + \gamma\,\mathrm{Nu}_0\,\mathrm{Pe}^{1/2} + \gamma^2\,\mathrm{Nu}_0^2\,\mathrm{Pe} + \gamma^3\,\mathrm{Nu}_0^3\,\mathrm{Pe}^{3/2} + O(\mathrm{Pe}^{3/2}) \tag{7}$$

A summary of the previous work on the steady state convection from a sphere, some of the results and applications may be found in a recent monograph by Leal (1992).

No analytical solutions exist for the unsteady convection from a sphere at finite Peclet numbers. Abramzon and Elata (1984) have presented a numerical study of this problem for a sphere in a Stokesian flow field, which is suddenly introduced into a fluid of different temperature. They found numerically that the advection part of the convection process accelerates the approach to equilibrium.

This paper presents a solution to the problem of the unsteady heat and mass transfer from a sphere to a viscous fluid. The

Contributed by the Fluids Engineering Division for publication in the JOURNAL OF FLUIDS ENGINEERING. Manuscript received by the Fluids Engineering Division October 14, 1994; revised manuscript received October 24, 1995. Associate Technical Editor: M. W. Reeks.

Copyright © 1996 by ASME

Downloaded 03 Jun 2010 to 171.66.16.125. Redistribution subject to ASME license or copyright; see http://www.asme.org/terms/Terms_Use.cfm

analysis is analogous to the one used in the momentum transfer problem by Lovalenti and Brady (1993). The major assumptions of the method of solution are: (*a*) The convection occurs at finite but small Peclet numbers; (*b*) the motion of the sphere in the fluid is Stokesian; and, (*c*) the surface temperature of the sphere is uniform and constant in time. Since the equations for the heat and mass transfer are the same, in order to avoid circumlocution only the terminology of the heat transfer problem will be used in the following sections. We should bear in mind that the heat transfer results may be applied directly to the mass transfer problem, provided that the boundary conditions are similar.

2 Basic Equations and General Method of Solution

We consider the steady-state flow of an incompressible fluid past an isothermal sphere of radius α. Before the inception of the process the sphere and the fluid are in thermal equilibrium. At the inception of the process ($t' = 0$) as a possible result of the action of an internal heat source, the temperature of the sphere undergoes a step change to θ'_{s0}. Hence, an unsteady heat transfer process commences, which will result in the perturbation of the fluid temperature field in the vicinity of the sphere. We decompose the fluid temperature into an undisturbed component, θ'_∞ and the disturbance temperature θ'. The latter is due entirely to the temperature change of the sphere. The energy equation for the perturbation field is as follows:

$$\rho_f c_f \left(\frac{\partial \theta'}{\partial t'} + \mathbf{v}' \cdot \nabla' \theta' \right) = k_f \nabla'^2 \theta' \tag{8}$$

where $\theta' = \theta'_f - \theta'_\infty$.

The initial condition of the problem is: $\theta'_s(t') = \theta'_{s0} H(t') + \theta'_\infty(|x'| = \alpha)$, where $H(t')$ is the Heavyside function, and the boundary conditions for θ' are:

(a) at the surface of the sphere, $\theta' = \theta'_{s0} H(t')$, and
(b) at infinity, $\theta' \to 0$.

We introduce dimensionless quantities for all the parameters in Eq. (8) as follows:

$$\mathbf{x} = \frac{\mathbf{x}'}{\alpha}, \quad t = \frac{t' k_f}{\alpha^2 \rho_f c_f}, \quad \theta(\mathbf{x}, t) = \frac{\theta'(\mathbf{x}', t')}{\theta'_{s0}}$$

$$\mathbf{v} = \frac{\mathbf{v}'}{U_\infty}, \quad \mathrm{Pe} = \frac{\rho_f c_f U_\infty \alpha}{k_f} \tag{9}$$

and, after substitution, we obtain the following energy equation:

$$\frac{\partial \theta}{\partial t} + \mathrm{Pe}\mathbf{v} \cdot \nabla \theta = \nabla^2 \theta \tag{10}$$

and boundary conditions:

(a) $\theta(\mathbf{x}, t) = H(t)$ at $|\mathbf{x}| = 1$;
(b) $\theta(\mathbf{x}, t) \to 0$ as $|\mathbf{x}| \to \infty$. (11)

The characteristic timescale of the process has been taken as the diffusive timescale of the fluid $\tau_f = \alpha^2 \rho_f c_f / k_f$. This is a measure of the time it takes for the thermal effects to diffuse (inside the fluid) to a distance equal to the radius of the sphere. It must be noted that during an established heat advection process, τ_c is of the order of α / U_∞.

It is more convenient to discuss the phenomena pertaining to the timescales of the problem in terms of the equivalent lengthscales. This, because in the analogous momentum transfer problem there is an widely used lengthscale, the Oseen distance $L_{0se} = O(\alpha\, \mathrm{Re}^{-1})$, which is interpreted as the boundary between two regions: one where the purely diffusive processes dominate the momentum transfer process and the other where the process is dominated by the advection effects. We may extend the concept of the Oseen distance to the heat transfer problem by defining a lengthscale $L_l = O(a\, \mathrm{Pe}^{-1})$, which is the analogue of the L_{0se} to the heat transfer problem. Inside L_l conduction is the predominant mechanism of heat transfer to the fluid. The energy transferred to the inner region of the fluid is given to a good approximation by the heat diffusion equation. In the fluid region near L_l the two modes of heat transfer by conduction and thermal advection are of the same order. In this region the appropriate transport equation is the advection/conduction equation. Far from L_l, energy is predominantly advected by the motion of the fluid downstream. The advection is characterized by the existence of a momentum and a thermal wake, which grow across the flow. As with the case of momentum transfer, the temperature disturbance in the thermal wake decays with a Gaussian spread.

In our analysis we assume that the flow is Stokesian. Therefore, the implicit assumption is made that the Reynolds number of the sphere is smaller than one. It must be pointed out, however, that Acrivos and Taylor (1962) have shown that the first order solution is independent of the Reynolds number. The velocity field around a fluid sphere is given as follows in the spherical coordinates (r, β, ϕ):

$$\mathbf{v} = \left(1 - \frac{B}{r} + \frac{2D}{r^3}\right)\zeta \mathbf{e}_r - \left(1 - \frac{B}{2r} - \frac{D}{r^3}\right)\sqrt{1 - \zeta^2}\,\mathbf{e}_\beta \tag{12}$$

Nomenclature

A = area
A^*, B^* = coefficients, functions of time
B, D = constants defined in (11)
c = heat capacity
e = unit vector
f, F = gauge functions
H = Heavyside function
I_n = Bessel functions
k = thermal conductivity
L = coefficients, functions of r
m, n = scaling parameters
Nu = Nusselt number
q = heat flux
Q = rate of heat
P_n = Legendre functions
Pe = Peclet number
r, R = radial distances
s, S = Laplace variables
t, T = time (short and long domains)
U = fluid velocity
$\mathbf{v}$ = particle velocity
W = coefficients, functions of r
α = radius of sphere
β = angular coordinate
γ = dimensionless shear rate
ζ = cos β
θ, Θ = temperature
ρ = density
σ = ratio of viscosities
τ = dummy variable with units of time
ϕ = azimuthal coordinate

Subscripts

f = refers to fluid
s = refers to the particle or surface of particle
∞ = refers to the undisturbed fluid
0 = refers to zeroth-order expansion
1 = refers to first-order expansion

Superscripts

$'$ = refers to dimensional variables
i = includes advection terms
$\bar{}$ = (overbar) denotes Laplace transform

Downloaded 03 Jun 2010 to 171.66.16.125. Redistribution subject to ASME license or copyright; see http://www.asme.org/terms/Terms_Use.cfm

where

$$B = \frac{3 + 2\sigma}{2(1 + \sigma)}; \quad D = \frac{1}{4(1 + \sigma)},$$

$$\zeta = \cos\beta, \quad \sigma = \frac{\mu_f}{\mu_s}. \tag{13}$$

μ_f and μ_s are the viscosities of the fluid and the sphere respectively. For a solid sphere, $\sigma = 0$.

Because of the different mechanisms of heat transfer inside and outside L_l, the usual perturbation methods can not be applied to the unsteady convection problem. The method of singular perturbation will be employed in the solution of the problem at hand. The singular perturbation method was first introduced by Proudman and Pearson (1957) for the steady-state momentum transfer of a sphere and a cylinder. Later Bentwich and Miloh (1978) and Sano (1981) extended the method to the problem of unsteady momentum transfer of a sphere at low Reynolds numbers.

Following the singular perturbation method, we decompose the time-space domain into four parts: (i) short time and inner region; (ii) short time and outer region; (iii) long time and inner region; and (iv) long time and outer region. A measure of the boundary of the inner and outer region is the equivalent Oseen distance L_l.

Shortly after the inception of the heat transfer process the heat diffusion and associated effects on the temperature of the fluid are confined to the inner region, which is in the immediate vicinity of the sphere. The outer region is undisturbed. Hence, at short times the convective terms may be neglected in the entire field. Therefore, the domains defined above as (i) and (ii) may be combined together as one: the short time domain. The solution in this short time domain is constructed by satisfying the boundary conditions, both at the surface of the sphere and at infinity. The construction of the two solutions in the domains (iii) and (iv) are made according to the following matching conditions: (a) the inner expansion $\Theta^{(i)}$ satisfies the boundary condition on the sphere; (b) the outer expansion $\Theta^{(o)}$ satisfies the boundary condition at infinity; (c) both inner and outer expansions match identically in the overlapping space domain, where both expansions are expected to be valid; (d) the long-time expansions also match the short time expansions at small values of T, where T is the time variable used in the long time domains.

3 Short-Time Expansion

Shortly after the inception of the process, the heat transfer from the sphere is dominated by the unsteady conduction. In this domain the time variable is denoted by t and the temperature of the fluid may be given by the following expansion:

$$\theta = \theta_0 + f_1(\mathrm{Pe})\theta_1 + \ldots$$

where $f_1(\mathrm{Pe})$ is the so-called gauge function, whose order in Pe will be determined by a balance of the terms of its governing equation. Substituting this expression in the energy equation we obtain:

$$\nabla^2\theta_0 + f_1(\mathrm{Pe})\nabla^2\theta_1 + \ldots = \frac{\partial\theta_0}{\partial t} + f_1(\mathrm{Pe})\frac{\partial\theta_1}{\partial t} + \mathrm{Pe}\mathbf{v}\cdot\nabla\theta_0 + \ldots \tag{15}$$

A glance at Eq. (15) proves that we have essentially two equations, one for each of the temperature fields θ_0 and θ_1. The first one, which is the zeroth order expansion in Pe is as follows:

$$\nabla^2\theta_0 = \frac{\partial\theta_0}{\partial t} \tag{16}$$

The second equation, which is essentially the governing equation of the first order expansion in Pe, is meaningful (i.e., its terms balance) only if the gauge function $f_1(\mathrm{Pe})$ is actually equal to Pe. Hence, the first order expansion of the temperature field results in the following expression:

$$\nabla^2\theta_1 = \frac{\partial\theta_1}{\partial t} + \mathbf{v}\cdot\nabla\theta_0 \tag{17}$$

A solution of the zeroth order expansion, which is the unsteady conduction equation, may be obtained by first transforming the expression in the Laplace domain. The transformation of the equation and the resulting boundary conditions are:

$$(\nabla^2 - s)\overline{\theta_0} = 0, \quad \text{and} \tag{18}$$

$$\overline{\theta_0}(r, \zeta, s) = \frac{1}{s} \quad \text{at} \quad r = a;$$

$$\overline{\theta_0}(r, \zeta, s) \to 0 \quad \text{as} \quad r \to \infty, \tag{19}$$

where s is the variable in the Laplace domain and the overbar denotes the Laplace transform of a function.

The solution of the equation and boundary conditions in the Laplace domain yield the following expression for the zeroth order expansion of the temperature field in the Laplace domain:

$$\overline{\theta_0}(r) = \frac{1}{sr}\exp[-s^{1/2}(r - 1)] \tag{20}$$

which may be inverted into time domain to yield the following:

$$\theta_0(r) = \frac{1}{r}\,\mathrm{erfc}\left(\frac{r - 1}{2\sqrt{t}}\right) \tag{21}$$

This solution is consistent with the theory of steady-state conduction: When t becomes very long, the above expression yields $\theta_0 = 1/r$, which is the steady-state solution.

The equation for the first-order temperature expansion, θ_1 may be written in the Laplace domain as follows:

$$(\nabla^2 - s)\overline{\theta_1} = -\left(1 - \frac{B}{r} + \frac{2D}{r^3}\right) \times \frac{1 + s^{1/2}r}{sr^2}\exp[-s^{1/2}(r - 1)]P_1(\zeta) \tag{22}$$

where $P_1(\zeta)$ is the Legendre function of order one and $\zeta = \cos\beta$. This expression implies a solution of the form:

$$\overline{\theta_1}(r, \zeta, s) = \bar{g}(r, s)P_1(\zeta) \tag{23}$$

where $g(r, t)$ is an unknown function of r. The last equation may be solved by the variation of constants method. However, it is not necessary to obtain the specific form of the function $g(r, t)$ to calculate the total rate of heat transfer. A glance at equation (22) proves that the expression for the first order contribution to the temperature is symmetric in ζ, because the Legendre function of the first order is one of the factors. Therefore, when the gradient of θ_1 is integrated around the sphere to yield the contribution of this temperature field to the total rate of heat transfer, the net result is zero.

4 Long-Time, Inner Region Expansion

The advection term of the energy equation may also be neglected in this domain, because we are looking for a solution valid in the immediate vicinity of the sphere. For the analysis in this domain, another time variable, T, is chosen defined as follows:

$$T = \mathrm{Pe}^m t. \tag{24}$$

Downloaded 03 Jun 2010 to 171.66.16.125. Redistribution subject to ASME license or copyright; see http://www.asme.org/terms/Terms_Use.cfm

The scaling parameter m is chosen in a way that only the conduction of heat is allowed in the limit $\mathrm{Pe} \to 0$. When (24) is substituted into the dimensionless energy equation, the following expression for the temperature field at long times and in the vicinity of the sphere, $\Theta^{(i)}$, is obtained:

$$\nabla^2\Theta^{(i)} = \mathrm{Pe}^m \frac{\partial\Theta^{(i)}}{\partial T} + \mathrm{Pe}\mathbf{v}\cdot\nabla\Theta^{(i)}. \tag{25}$$

This temperature field is expressed again by an expansion method in terms of a function $\Theta_0^{(i)}$, which is the solution of a zero-order equation and another function $\Theta_j^{(i)}$ multiplied by the gauge functions $F_j^{(i)}(\mathrm{Pe})$, which will be determined later:

$$\Theta^{(i)} = \Theta_0^{(i)} + F_1^{(i)}(\mathrm{Pe})\Theta_1^{(i)} + F_2^{(i)}(\mathrm{Pe})\Theta_2^{(i)} + \ldots \tag{26}$$

It will be proven in the next section that a rational choice of the exponent m is 2. Hence, the gauge functions take the form:

$$F_1^{(i)} = \mathrm{Pe}, \quad F_2^{(i)} = \mathrm{Pe}^2 \tag{27}$$

and the differential equations of the three functions $\Theta_0^{(i)}$, $\Theta_1^{(i)}$, and $\Theta_2^{(i)}$ are written as follows:

$$\nabla^2\Theta_0^{(i)} = 0$$

$$\nabla^2\Theta_1^{(i)} = \mathbf{v}\cdot\nabla\Theta_0^{(i)}$$

and

$$\nabla^2\Theta_2^{(i)} = \frac{\partial\Theta_0^{(i)}}{\partial T} + \mathbf{v}\cdot\nabla\Theta_1^{(i)}$$

The boundary conditions at the surface of the sphere are: $\Theta_0^{(i)} = H(T)$ and $\Theta_j^{(i)} = 0$, $(j = 1, 2)$. Since the solution pertains to the inner region problem alone the boundary conditions at the far field are not necessary to be satisfied. Hence, the solution for

$$\Theta_0^{(i)} = \frac{C_0(T)}{r} + [H(T) - C_0(T)]$$

where $C_0(T)$ is a function of time only, which will be determined by a matching procedure in the next section.

The solution for $\Theta_1^{(i)}$ is:

$$\Theta_1^{(i)} = \sum_{n=0}^{\infty} A_n(T)(r^n - r^{-n-1})P_n(\zeta) + \frac{C_0(T)}{2}\left(1 - \frac{B}{r} + \frac{B + D - 1}{r^2} - \frac{D}{r^3}\right)P_1(\zeta)$$

where $P_n(\zeta)$ are the Legendre functions of the nth order and $A_n(T)$ are coefficients to be determined by a matching procedure (as is the case for $C_0(T)$). Considerations on the solution for Θ will be given in the next section.

5 Long-Time, Outer Region Expansion

In this time domain the heat has already entered the outer region by diffusion. It is expected that both the conduction and advection parts of the energy equation are of the same order of magnitude, even as $\mathrm{Pe} \to 0$. Hence, it is necessary to scale appropriately both the time variable and the length variable. A general form of such a scaling is:

$$R = \mathrm{Pe}^n r, \quad T = \mathrm{Pe}^m t \tag{33}$$

Substituting the scaled variables into the dimensionless energy equation we obtain the following expression for the temperature field of this domain $\Theta^{(o)}$:

$$\mathrm{Pe}^{2n}\nabla_R^2\Theta^{(o)} = \mathrm{Pe}^m \frac{\partial\Theta^{(o)}}{\partial T} + \mathrm{Pe}^{n+1}\mathbf{v}\cdot\nabla_R\Theta^{(o)} \tag{34}$$

It is obvious that the only choice, which retains both the conduction and the advection terms in the equation, is $n = 1$ and $m = 2$. The latter was anticipated in the calculations of the previous section.

The temperature field $\Theta^{(o)}$ may be represented by an asymptotic expansion with gauge functions $F_0(\mathrm{Pe})$ and $F_1(\mathrm{Pe})$. The gauge functions will be determined later by matching.

$$\Theta^{(o)} = F_0(\mathrm{Pe})\Theta_0^{(o)} + F_1(\mathrm{Pe})\Theta_1^{(o)} + \ldots \tag{35}$$

The zeroth-order equation for $\Theta_0^{(o)}$ is:

$$\nabla_R^2\Theta_0^{(o)} = \frac{\partial\Theta_0^{(o)}}{\partial T} + \mathbf{u}_\infty\cdot\nabla_R\Theta_0^{(o)} \tag{36}$$

In a Stokes flow field the fluid velocity vector at infinity, U_∞, is not a function of time. Hence, the Laplace transform of the above equation may be obtained by substituting the Stokes velocity field (Eq. 12) into the Laplace transform of the other terms of the leading order equation. Retaining the leading order terms we obtain the following expression:

$$\nabla_R^2\overline{\Theta_0^{(o)}} = S\overline{\Theta_0^{(o)}} + \zeta\frac{\partial\overline{\Theta_0^{(o)}}}{\partial R} + \frac{1 - \zeta^2}{R}\frac{\partial\overline{\Theta_0^{(o)}}}{\partial\zeta} \tag{37}$$

where S is the variable in the Laplace domain corresponding to the scaled time T.

We use Goldstein's (1929) transformation to solve the last equation. The transformation is written as follows in this particular case:

$$\overline{\Theta_0^{(o)}}(R, \zeta) = \exp\left(\frac{R\zeta}{2}\right)G(R, \zeta). \tag{38}$$

Hence, Eq. (37) becomes:

$$\nabla_R^2 G - (S + \tfrac{1}{4})G = 0 \tag{39}$$

and its general solution is of the following form:

$$\overline{\Theta_0^{(o)}} = \exp\left(\frac{R\zeta}{2}\right)\sum_{n=0}^{\infty}\sqrt{\frac{\pi}{R}}\,[E_n(S)I_{n+1/2}(\kappa R) + D_n(S)I_{-n-1/2}(\kappa R)]P_n(\zeta) \tag{40}$$

where I_n denotes the modified Bessel functions of the first ($n > 0$) and second kind ($n < 0$), $\kappa = (S + \frac{1}{4})^{1/2}$, $E_n(S)$ and $D_n(S)$ are functions of S. Given the properties of the Bessel functions, the boundary condition at infinity is satisfied only if the sum $E_n(S) + D_n(S)$ is equal to zero for all n.

For the matching conditions in the time domain, we require that the solutions in the short and long times are matching in an intermediate time domain. Essentially this is a matching of the expressions in Eqs. (14) and (35) as t becomes long and T becomes short, that is:

$$\theta_0(r, t) + \mathrm{Pe}\theta_1(r, t) + O(\mathrm{Pe}^{1+}) \quad \text{match}$$

$$\text{as} \quad r \to \infty, \quad t \to \infty$$

$$F_0(\mathrm{Pe})\Theta_0^{(0)} + F_1(\mathrm{Pe})\Theta_1^{(o)} + O(\mathrm{Pe}^{1+})$$

$$\text{as} \quad R \to 0, \quad T \to 0 \tag{41}$$

The matching may be performed with the temperature expressions in the Laplace domain by employing the following property of the Laplace transforms:

$$\int_0^\infty \chi(t)e^{-st}dt = \int_0^\infty \mathrm{Pe}^{-2}\chi(\mathrm{Pe}^{-2}T)e^{-sT\mathrm{Pe}^{-2}}dT = \int_0^\infty \mathrm{Pe}^{-2}X(T)e^{-ST}dT \tag{42}$$

Downloaded 03 Jun 2010 to 171.66.16.125. Redistribution subject to ASME license or copyright; see http://www.asme.org/terms/Terms_Use.cfm

The last relationship implies:

$$s = \mathrm{Pe}^2 S, \quad \bar{\chi}(s) = \mathrm{Pe}^{-2}\bar{X}(S) \tag{43}$$

The matching condition may be expressed in the Laplace domain as follows:

$$\left[\frac{1}{\mathrm{PeRS}}\, e^{-\sqrt{S}(R-\mathrm{Pe})} + f_1(\mathrm{Pe})\theta_1\right] \quad \text{match}$$

$$\mathrm{Pe}^{-2}\Bigg[F_0(\mathrm{Pe}) \sum e^{R\zeta/2}\sqrt{\frac{\pi}{R}}\, E_n(S) \times [I_{n+1/2}(\kappa R) - I_{-n-1/2}(\kappa R) + F_1(\mathrm{Pe})\overline{\Theta_1^{(o)}}\Bigg] \tag{44}$$

at the limit $\mathrm{Pe} \to 0$. Comparing the two sides of above relationship, it is evident that the short-time and long-time approximations will match only if:

$$F_0(\mathrm{Pe}) = \mathrm{Pe}, \quad Asmp_{S\gg 1} E_0(S) = \frac{1}{S} \tag{45}$$

and

$$\Theta_0 = \frac{E_0(S)}{R}\exp\left(\frac{R\zeta}{2} - R\sqrt{S + \tfrac{1}{4}}\right) \tag{46}$$

From the matching conditions of (44) it is evident that the inclusion of the gauge function $F_1(\mathrm{Pe})$ would contribute terms, which are of higher order than $O(\mathrm{Pe}^{1+})$. For this reason this function will be neglected in the calculation of $\Theta^{(o)}$ and the heat transfer rate associated with it.

It must be pointed out that the matching condition for $E_0(S)$ is not unique. For example, $E_0(S) = 1/\sqrt{(S(S+\xi))}$, with ξ being a constant, will also satisfy the matching condition. The problem of non-uniqueness of $E_0(S)$ is resolved here by ensuring that the resulting solution in the time domain will satisfy the steady-state solution as $T \to \infty$, obtained by Acrivos and Taylor (1962):

$$\Theta_0^{(o)}(R, \zeta) = \frac{1}{R}\exp\left[-\frac{R(1-\zeta)}{2}\right]. \tag{47}$$

The last expression leads to the following asymptotic limit at long times:

$$\lim_{S=0}[SE_0(S)] = 1 \tag{48}$$

Using Eqs. (45) and (48) it appears that the only rational choice for the function $C_0(S)$ is for it to be equal to $1/S$. Therefore, the first term of the temperature field in the Laplace space is:

$$\overline{\Theta_0^{(o)}}(R, \zeta, S) = \frac{1}{RS}\exp\left[R\left(\frac{\zeta}{2} - \sqrt{S + \tfrac{1}{4}}\right)\right] \tag{49}$$

Upon inversion in the time domain we obtain the following analytical expression for the leading term in the outer region at long times:

$$\Theta_0^{(o)}(R, \zeta, T) = \frac{e^{R\zeta/2}}{R}\left[\frac{e^{-R/2}}{2}\,\mathrm{erfc}\left(\frac{R}{2\sqrt{T}} - \frac{\sqrt{T}}{2}\right) + \frac{e^{R/2}}{2}\,\mathrm{erfc}\left(\frac{R}{2\sqrt{T}} + \frac{\sqrt{T}}{2}\right)\right] \tag{50}$$

In a similar way we may determine the functions $C(T)$ and $A_n(T)$, which were left undetermined in the previous section. We may use the following alternative form of (50):

$$\Theta_0^{(o)} = \frac{1}{2R}\left[e^{R/2(\zeta-1)} + e^{R/2(\zeta+1)}\right] - \frac{1}{2R}\left[e^{R/2(\zeta-1)}\,\mathrm{erf}\left(\frac{R}{2\sqrt{T}} - \frac{\sqrt{T}}{2}\right) + e^{R/2(\zeta+1)}\,\mathrm{erf}\left(\frac{R}{2\sqrt{T}} + \frac{\sqrt{T}}{2}\right)\right] \tag{51}$$

to obtain the asymptotic result for the outer solution $\Theta_0^{(o)}$ in the near region, which is defined by low values of R. This asymptotic result is as follows:

$$Asmp_{R\ll 1}\Theta_0^{(o)} = \frac{1}{R} + \frac{1}{2}P_1(\zeta) - \left[\frac{1}{2}\,\mathrm{erf}\left(\frac{\sqrt{T}}{2}\right) + \frac{1}{2\sqrt{\pi T}}\, e^{-T/4}\right] \tag{52}$$

A matching of the inner solution at long r and of the outer solution at short R, yields the following expressions:

$$A_0(T) = -\tfrac{1}{2}\,\mathrm{erf}\left(\frac{\sqrt{T}}{2}\right) - \frac{1}{\sqrt{\pi T}}\exp\left(-\frac{T}{4}\right),$$

$$A_n(T) = 0, \quad \text{for} \quad n \geq 1$$

$$C_0(T) = H(T) \tag{53}$$

By considering Eq. (32) we obtain the following expression as the first-order contribution to the temperature of the inner region at long times:

$$\Theta_1^{(i)} = \left[\frac{1}{2}\,\mathrm{erf}\left(\frac{\sqrt{T}}{2}\right) + \frac{1}{\sqrt{\pi T}}\exp\left(-\frac{T}{4}\right)\right]\left(\frac{1}{r} - 1\right) + \frac{1}{2}\left(1 - \frac{B}{r} + \frac{B + D - 1}{r^2} - \frac{D}{r^3}\right)P_1(\zeta) \tag{54}$$

Hence, the governing equation for $\Theta_2^{(i)}$ from (30) becomes:

$$\nabla^2\Theta_2^{(i)} = \sum_{k=0}^{2} W_k(r)P_k(\zeta) \tag{55}$$

Among the functions $W_k(r)$, of particular interest for the heat transfer calculations is $W_o(r)$, which is given explicitly as:

$$W_0(r) = \frac{1}{3}\left[\frac{1}{r} - \frac{B}{r^2} + \frac{B^2 + BD - B - D}{2r^4} + \frac{\mathrm{BD}}{r^5} - \frac{3D(B + D - 1)}{r^6} + \frac{4D^2}{r^7}\right] \tag{56}$$

The solution for $\Theta_2^{(i)}$ is:

$$\Theta_2^{(i)} = \sum_{n=3}^{\infty}[A_n^*(T)r^n + B_n^*(T)r^{-n-1}]P_n(\zeta) + \sum_{k=0}^{2} L_k(r)P_k(\zeta)$$

and the first term $L_0(r)$, which is of particular interest is:

$$L_0(r) = \frac{1}{3}\left[\frac{1}{2r} - B\ln r + \frac{B^2 + BD - B - D}{4r^2} + \frac{\mathrm{BD}}{6r^3} - \frac{D(B + d - 1)}{4r^4} + \frac{D^2}{5r^5}\right] \tag{58}$$

Acrivos and Taylor (1962) pointed out that, since $L_0(r)$ contains the term $\ln(r)$, the substitution $R = (\mathrm{Pe})r$ into $\mathrm{Pe}^2\Theta_2^{(i)}$ (after setting $F_2(\mathrm{Pe}) = \mathrm{Pe}^2$) will generate a net contribution

Downloaded 03 Jun 2010 to 171.66.16.125. Redistribution subject to ASME license or copyright; see http://www.asme.org/terms/Terms_Use.cfm

of $O(\mathrm{Pe}^2 \ln \mathrm{Pe})$. Hence, the "outer" solution will not match the last term. It is evident that the long time inner expansion of $\Theta^{(i)}$ should contain an additional term of order $(\mathrm{Pe}^2 \ln \mathrm{Pe})\Theta_*^{(i)}$, which balances the equations. Therefore, the correct expansion for $\Theta^{(i)}$ is:

$$\Theta^{(i)} = \Theta_0^{(i)} + \mathrm{Pe}\Theta_1^{(i)} + (\mathrm{Pe}^2 \ln \mathrm{Pe})\Theta_*^{(i)} + \mathrm{Pe}^2\Theta_2^{(i)} + \ldots \quad (59)$$

The governing equation for the additional term $\Theta_*^{(i)}$ is simply the conduction equation:

$$\nabla^2\Theta_*^{(i)} = 0 \quad (60)$$

The requirement of the absence of any $O(\mathrm{Pe}^2 \ln \mathrm{Pe})$ term in the expression for $\Theta^{(i)}$ given by (59) yields the following solution for $\Theta_*^{(i)}$, which is of interest to this study:

$$\Theta_*^{(i)} = \frac{B}{3}\left(\frac{1}{r} - 1\right) = \frac{3 + 2\sigma}{3(1 + \sigma)}\left(\frac{1}{r} - 1\right) \quad (61)$$

6 Results for the Rate of Heat Transfer and the Nusselt Number

The primary objective for the solution of the energy equation is to calculate the heat flux or the total rate of heat transfer. With the first two terms of the inner solution in hand, we may obtain the total heat transfer rate from the sphere and consequently the Nusselt number, which is defined in terms of the dimensionless variables by the following expression:

$$\mathrm{Nu} = \frac{\int_A \mathbf{q}\cdot\mathbf{n}\,dA}{2\pi}. \quad (62)$$

According to the results of Section 3, the magnitude of the dimensionless heat flux is given in the time domain by the following expression:

$$q(r, t) = \frac{1}{r^2}\,\mathrm{erfc}\left(\frac{r - 1}{2\sqrt{t}}\right) + \frac{1}{r\sqrt{\pi t}}\exp\left(-\frac{(r - 1)^2}{4t}\right). \quad (63)$$

The last equation indicates that the heat flux decays at a fast rate far from the sphere and yields the following equation for the Nusselt number, valid at short times $[t = O(1)]$:

$$\mathrm{Nu} = 2\left(1 + \frac{1}{\sqrt{\pi t}}\right) + O(\mathrm{Pe}^{1+}), \quad t = O(1) \quad (64)$$

It must be pointed out that the accuracy of Eq. (64) is $O(\mathrm{Pe}^{1+})$ as indicated. This is because (notwithstanding the fact that the θ_1 term contributes zero to the total rate of heat transfer) the temperature expansion in θ_0 and θ_1, which eventually results in (64) is of the order of Pe^1.

One may similarly calculate the Nusselt number at long time periods from the inception of the process ($t = O(\mathrm{Pe}^{-2})$. In this case the resulting expression for the Nusselt number in the "stretched" time domain T is:

$$\mathrm{Nu} = 2\left[1 + \frac{\mathrm{Pe}}{2}\,\mathrm{erf}\left(\frac{\sqrt{T}}{2}\right) + \frac{\mathrm{Pe}}{\sqrt{\pi T}}\exp\left(-\frac{T}{4}\right) + \frac{3 + 2\sigma}{6(1 + \sigma)}\mathrm{Pe}^2 \ln \mathrm{Pe}\right] + O(\mathrm{Pe}^{1+}) \quad (65)$$

and its transformation in the actual time domain $t[t = O(\mathrm{Pe}^{-2})]$ is:

$$\mathrm{Nu} = 2\left\langle 1 + \mathrm{Pe}\left[\frac{1}{2}\,\mathrm{erf}\left(\mathrm{Pe}\,\frac{\sqrt{t}}{2}\right) + \frac{1}{\mathrm{Pe}\sqrt{\pi t}}\exp\left(-\frac{\mathrm{Pe}^2 t}{4}\right)\right] + \frac{3 + 2\sigma}{6(1 + \sigma)}\mathrm{Pe}^2 \ln \mathrm{Pe}\right\rangle + O(\mathrm{Pe}^{1+}) - \quad (66)$$

The Nusselt number is a function of the current state of the particle, since it is given by an explicit function of time. It was observed in the general pure conduction case (Michaelides and Feng, 1994) that the unsteady conduction process includes a history term, which accounts for the effect of previous states (or heat transfer at previous times) on the current state. Such a history term does not appear in Eq. (66) because the process (a step function of the temperature) is simple and has been explicitly defined. In this case the effect of the past history of the process is condensed on functions of the current state. It must be recalled that the history term of the momentum equation for a step change of the velocity may also be expressed in terms of state functions only (Clift et al., 1978). One may support the analogy of the momentum and energy equations for a sphere by observing the similar form of the expressions for the drag coefficient and the Nusselt number, for a step-change process.

It appears in Eqs. (65) and (66) that the inclusion of the advection term in the energy equation accelerates the approach to steady state. The approach to equilibrium is as $t^{-1/2}e^{-t}$, rather than $t^{-1/2}$, which is characteristic of the purely diffusion processes. Figure 1 depicts a measure of this approach to steady state as a function Pe. The dimensionless time it takes for a rigid sphere to reach values of 1, 2.5, and 5 percent from the steady-state solution are shown. It is obvious that there is considerably less time required for the approach to steady state as the Peclet number increases. The thermal and momentum wakes, which are formed behind the sphere are the reasons of more rapid heat convection and, hence, for this accelerated approach to equilibrium.

7 Conclusions

There is a length scale, defined by L_I, which is the equivalent of the Oseen distance in the heat transfer problems. It is only outside this distance that the advection effects are important in the energy equation. The singular perturbation method may be used to yield expressions for the rate of heat transfer from a sphere at constant temperature to a viscous fluid at small Peclet numbers. Solutions to the problem were obtained for a step

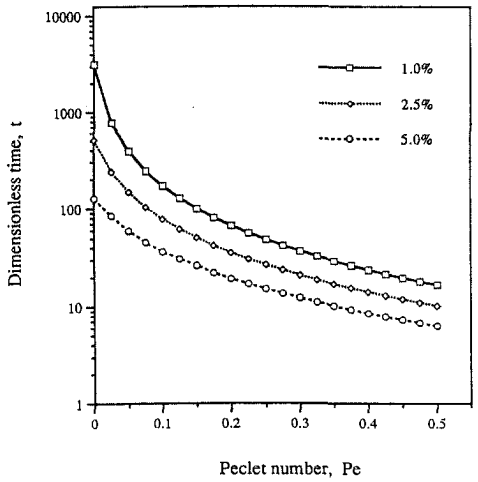


Fig. 1 The dimensionless time it takes for the solution to approach 1, 2.5, and 5 percent from the steady state decreases considerably with the Peclet number

Downloaded 03 Jun 2010 to 171.66.16.125. Redistribution subject to ASME license or copyright; see http://www.asme.org/terms/Terms_Use.cfm

temperature change, for short and long times. It is observed that the first order corrections to the temperature fields do not contribute to the total rate of heat transfer. The history effects of the heat transfer process in this case are condensed to the error function, which is a function of the current state. This is in analogy with the results of the equation of motion for a step change of the velocity.

Acknowledgments

This work was partly supported by grants from the National Science Foundation and the Louisiana Education Quality Support Fund to Tulane University.

References

Abramzon, B., and Elata, C., 1984, "Heat Transfer from a Single Sphere in Stokes Flow," *International Journal of Heat and Mass Transfer,* Vol. 27, pp. 687–695.

Acrivos, A., and Taylor, T. E., 1962, "Heat and Mass Transfer from a Single Spheres in Stokes Flow," *Physics of Fluids,* Vol. 5, pp. 387–394.

Acrivos, A., 1980, "A Note on the Rate of Heat or Mass Transfer from a Small Particle Freely Suspended in Linear Shear Field," *Journal of Fluid Mechanics,* Vol. 98, pp. 299–304.

Batchelor, G. K., 1979, "Mass Transfer from a Particle Suspended in a Fluid with a Steady Linear Ambient Velocity Distribution," *Journal of Fluid Mechanics,* Vol. 95, pp. 369–400.

Bentwich, M. and Miloh, T., 1978, "The Unsteady Matched Stokes-Oseen for the Flow Past a Sphere," *Journal of Fluid Mechanics,* Vol. 88, pp. 17–32.

Brenner, H., 1963, "Forced Convection Heat and Mass Transfer at Small Peclet Numbers from a Particle of Arbitrary Shape," *Chemical Engineering Science,* Vol. 18, pp. 109–122.

Clift, R., Grace, J. R., and Weber, M. E., 1978, *Bubbles, Drops and Particles,* Academic Press, New York.

Goldstein, S., 1929, "The Steady Flow of a Viscous Fluid Past a Fixed Obstacle at Small Reynolds Numbers," *Proceedings of Royal Society,* Series A123, pp. 225–235.

Leal, L. G., 1992, *Laminar Flow and Convective Transport Processes,* Butterworth-Heinemann.

Lovalenti, P. M., and Brady, J. F., 1993, "The Hydrodynamic Force on a Rigid Particle Undergoing Arbitrary Time-dependent Motion at Small Reynolds Number," *Journal of Fluid Mechanics,* Vol. 256, pp. 561–605.

Michaelides, E. E., 1992, "A Novel Way of Computing the Basset Term in Unsteady Multiphase Flow Computations," *Physics of Fluids,* Vol. A4, pp. 1579–1582.

Michaelides, E. E., Li, L., and Lasek, A., 1992, "The Effect of Turbulence on the Phase Change of Droplets and Particles under Non-equilibrium Conditions," *International Journal of Heat and Mass Transfer,* Vol. 34, pp. 601–609.

Michaelides, E. E., and Feng, Z. G., 1994, "Heat Transfer from a Sphere in a Non-uniform Temperature and Velocity Field," *International Journal of Heat and Mass Transfer,* Vol. 37, pp. 2069–2076.

Proudman, I. A. and Pearson, J. R. A., 1957, "Expansions at Small Reynolds Numbers for the Flow Past a Sphere and a Circular Cylinder," *Journal of Fluid Mechanics,* Vol. 2, pp. 237–262.

Sano, T., 1981, "Unsteady Flow Past a Sphere at Low-Reynolds Number," *Journal of Fluid Mechanics,* Vol. 112, pp. 433–441.

Downloaded 03 Jun 2010 to 171.66.16.125. Redistribution subject to ASME license or copyright; see http://www.asme.org/terms/Terms_Use.cfm

On the Virtual Nonexistence of Multiple Instability Regions for Some Heat-Exchanger Arrays in Crossflow

M. P. Païdoussis

S. J. Price

N. W. Mureithi[1]

Department of Mechanical Engineering,
McGill University,
817 Sherbrooke St. W., Montréal, Québec,
H3A 2K6, Canada

In fluidelastic analyses involving a time delay (or phase lag) between the motions of cylinders in an array and the resultant unsteady fluid forces on the cylinders, a succession of instability-stability regions is predicted theoretically at low values of the mass-damping parameter, $m\delta/\rho D^2$, below the "ultimate" fluidelastic instability, beyond which the system is not restabilized. However, as experimenters have had difficulty in verifying the existence of these regions of instability, it is legitimate to ask (i) do these regions really exist, and (ii) why are they so rarely observed? In this paper, with the aid of the quasi-steady model of Price and Païdoussis and with expanded measurements of lift and drag coefficients for a parallel triangular array with $P/D = 1.375$, it is shown that (a) the stability of the array strongly depends on geometric asymmetries; (b) whereas for a perfectly symmetric geometry the system may have several sub-ultimate instability regions, an asymmetry of as little as 0.02D may quench them and leave only the ultimate instability region intact. This suggests a possible explanation as to why the instability regions in question are so difficult to "find" experimentally. It also suggests that they may be of rather less practical importance for operating engineering systems than had heretofore been assumed, at least for some array geometries.

1 Introduction

In all fluidelastic analyses involving a time delay (or phase lag) between the motions of cylinders in an array and the resultant unsteady fluid forces on the cylinders, a succession of instability-stability regions is predicted theoretically, below the "ultimate" fluidelastic instability, beyond which the system is not restabilized (Price, 1995). These regions are predicted to occur at low values of the mass-damping parameter, $m\delta/\rho D^2$. Such multiple sub-ultimate instability regions are predicted by the Lever and Weaver (1982, 1986) and Price and Païdoussis (1986) models; see Fig. 1. Their existence has been explained in terms of the transcendental, periodic nature of the fluidelastic forces, as a result of the sinusoidal terms introduced by the aforementioned time-delay or phase-lag terms. Intriguingly, however, they are also predicted by Chen's (1983) model, in which measured unsteady force coefficients are utilized.

It is seen in Fig. 1 that the sub-ultimate instability regions become progressively thinner as U_c/fD or U_{pc}/fD is reduced, U_c being the critical freestream flow velocity and U_{pc} the value within the pitch of the array. The question arises as to how many of these regions can really materialize. Different empirical suppositions are made by different researchers: e.g., Price and Païdoussis consider only three of these regions in Fig. 1(*b*), since the width of lower ones is so small as to suppose that they would be washed out by fluctuations in U due to interstitial flow turbulence (the intensity of which can be very high). Nevertheless, experimenters have found great difficulty in verifying the existence of any of these sub-ultimate instability regions. Some work by Chen and Jendrzejczyk (1981), Andjelić et al. (1990), and Austermann and Popp (1995) is the exception. Nevertheless, it is not unreasonable to ask the question: do these regions really exist? Also, if they do, why are they not routinely observed in the laboratory?

These questions have been answered in a way that suggests a possible explanation for geometries and intercylinder spacings different from those investigated in this paper. This was done by (i) measuring the fluid force coefficients over a wide range of displacements of one cylinder away from its geometrically perfect equilibrium position in a $P/D = 1.375$ rotated-triangular array; (ii) conducting a linear one-flexible-cylinder stability analysis (Price and Païdousis, 1986), which is reasonable for this array, for various geometrically imperfect locations of the cylinder.

2 The Quasi-Steady Fluid-Dynamic Model

It has been shown (Price and Païdoussis, 1986; Price et al., 1990) that for some array geometries, notably for the rotated triangular array, the theoretical critical flow velocity for fluidelastic instability is virtually the same, whether in the analysis all the cylinders are flexible or one only is flexible and the others rigid. Furthermore, for the rotated triangular array, when the experimental critical flow velocities are plotted in the traditional dimensionless plot of U/fD versus $m\delta/\rho D^2$, results from one-flexible-cylinder and multiple-flexible-cylinder experiments are indistinguishable (Price, 1995). Hence, in view of the simplicity of single-flexible-cylinder analysis, it is justifiable to adopt it for the purpose of this paper.

The reason for the applicability of this analysis to rotated triangular arrays is that the instability is predominantly of the single degree of freedom, negative damping type (Chen, 1983; Païdoussis and Price, 1988). This is also true for in-line square arrays. However, for some array geometries, the instability is substantially of the fluid-stiffness-controlled coupled-mode type, and successful prediction of instability requires at least two and sometimes more flexible cylinders (Païdoussis and Price, 1988; Price, 1995). For instance, it has been shown (Païdoussis and Price, 1988) that for a square array of cylinders with $P/D = 1.5$, the theoretical critical flow velocity for fluidelastic instability is substantially lower when only one cylinder is flexible than when all the cylinders are flexible. Hence, the experimental critical flow velocities for one-flexible-cylinder and multiple-flexible-cylinder experiments are distinguishable (Price, 1995).

[1] Presently with the Takasago R & D Center, Mitsubishi Heavy Industries Ltd, Takasago, Hyogo, Japan.

Contributed by the Fluids Engineering Division for publication in the JOURNAL OF FLUIDS ENGINEERING. Manuscript received by the Fluids Engineering Division December 24, 1994; revised manuscript received October 23, 1995. Associate Technical Editor: F. Giralt.

Copyright © 1996 by ASME

Downloaded 03 Jun 2010 to 171.66.16.125. Redistribution subject to ASME license or copyright; see http://www.asme.org/terms/Terms_Use.cfm

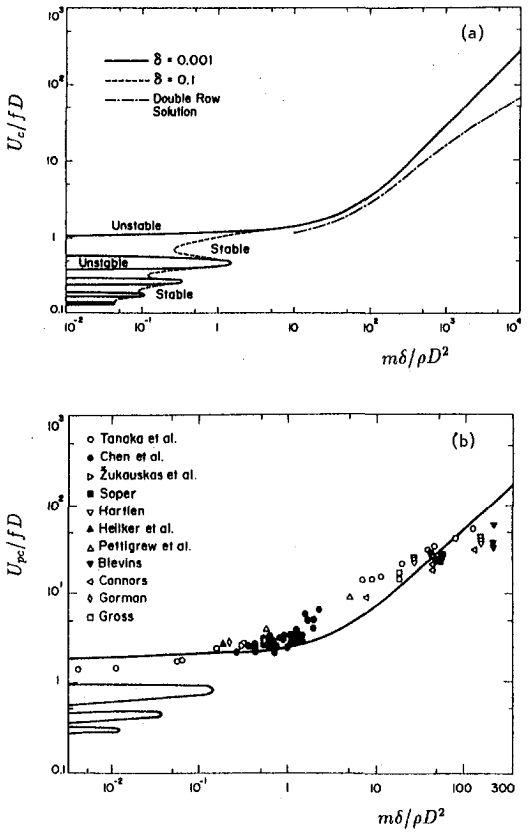


Fig. 1 Multiple sub-ultimate and ultimate fluidelastic instability regions for (*a*) a rotated triangular array with *P/D* = 1.375 and (*b*) an in-line square array with *P/D* = 1.5 (from Price and Païdoussis, 1986)

doussis et al., 1989) that for certain ranges of pitch-to-diameter ratio of the rotated square array, the single-flexible-cylinder analysis predicts no instability at all, whereas analysis with more flexible cylinders does, as confirmed experimentally (Price and Kuran, 1991). Clearly the analysis and results to be presented are not applicable to such arrays.

2.1 The General Model. The quasi-steady approach of Price and Païdoussis (1986) for a single flexible cylinder within an otherwise rigid cylinder array is used, with some modifications. The model used here is a simplified version of that in Mureithi et al. (1994a, b, 1995) where the more complex situation is considered, involving loose supports, impacting, and complex dynamics.

The fluid force components in the x (streamwise) and y (cross-stream) directions may be written as follows (Price and Païdoussis, 1986):

$$F_{xf} = -m_a \frac{\partial^2 x}{\partial t^2} + \frac{1}{2a^2}\rho U_r^2 D[C_L(x_d, y_d)\sin\alpha + C_D(x_d, y_d)\cos\alpha], \quad (1)$$

$$F_{yf} = -m_a \frac{\partial^2 y}{\partial t^2} + \frac{1}{2a^2}\rho U_r^2 D[C_L(x_d, y_d)\cos\alpha - C_D(x_d, y_d)\sin\alpha], \quad (2)$$

where ρ is the fluid density, m_a the added mass, U_r is the flow velocity relative to the moving cylinder, α the flow-approach angle, and C_L and C_D the lift and drag coefficients measured statically. The factor a accounts for the fact that C_L and C_D are based, as measured, on the upstream flow velocity, U_∞; whereas the gap flow velocity, U, used in calculating U_r is assumed to be related to U_∞, by satisfying continuity, via

$$U/U_\infty = T/(T - D) = a, \quad (3)$$

in which T is the center-to-center distance between columns of the cylinders in the same row of the array. In the Price and Païdoussis model, in addition to the effects of incidence inherent in any quasi-steady model, it is necessary to account for a phase lag, or delay, between cylinder motion and the forces generated thereby. Different researchers explain the physical origin of the time delay in different ways: as mainly a retardation of the flow approaching the cylinder (Price and Païdoussis, 1984, 1986), a delay in the redistribution of the flow around the cylinder (Lever and Weaver, 1982, 1986), or, as we shall adopt here, a delay in the reorganization of the viscous flow, notably in the wakes, as the flexible cylinder oscillates (Païdoussis and Price, 1988). Hence, at time t, the lift and drag coefficients are those corresponding to delayed (advanced) cylinder displacements x_d and y_d, i.e.,

$$x_d = x(s, t - \Delta t), \quad y_d = y(s, t - \Delta t), \quad (4)$$

where s is the distance along the cylinder.

Hence, the equations of motion of the cylinder, in the absence of loose-support and impact-related effects (Mureithi et al., 1994a, b), may be written as

$$EI\frac{\partial^4 x}{\partial s^4} + c\frac{\partial x}{\partial t} + m\frac{\partial^2 x}{\partial t^2} = -m_a\frac{\partial^2 x}{\partial t^2} + \frac{\rho U_r^2 D}{2a^2}[C_L(x_d, y_d)\sin\alpha + C_D(x_d, y_d)\cos\alpha], \quad (5)$$

$$EI\frac{\partial^4 y}{\partial s^4} + c\frac{\partial y}{\partial t} + m\frac{\partial^2 y}{\partial t^2} = -m_a\frac{\partial^2 y}{\partial t^2} + \frac{\rho U_r^2 D}{2a^2}[C_L(x_d, y_d)\cos\alpha - C_D(x_d, y_d)\sin\alpha], \quad (6)$$

where EI is the flexural rigidity, m the mass of the cylinder per unit length, c the mechanical damping coefficient, and $x(s, t)$ and $y(s, t)$ are the streamwise and cross-stream cylinder displacements.

Equations (5) and (6) may be rendered dimensionless by introducing the following nondimensional parameters:

$$\tilde{x} = x/D, \quad \tilde{y} = y/D, \quad \tilde{s} = s/l, \quad \tilde{m} = m/\rho UD^2,$$
$$\tau = \omega_1 t, \quad V = U/\omega_1 D, \quad \zeta = c/2m\omega_1,$$
$$C_{ma} = m_a/\rho\pi D^2. \quad (7)$$

Considering a standard Galerkin expansion of cylinder displacements,

$$\tilde{x}(\tilde{s}, \tau) = \sum_{i=1}^{N}\phi_i(\tilde{s})\tilde{p}_i(\tau), \quad \tilde{y}(\tilde{s}, \tau) = \sum_{i=1}^{N}\phi_i(\tilde{s})\tilde{q}_i(\tau), \quad (8)$$

where $\phi_i(\tilde{s})$ are the beam eigenfunctions, the dimensionless equations of motion may be discretized into the following set:

$$\gamma\tilde{p}_i'' + 2\tilde{\zeta}_i\tilde{p}_i' + (\lambda_i/\lambda_1)^4\tilde{p}_i = \frac{1}{2\tilde{m}a^2}\int_0^1\left[\left(V - \frac{\partial\tilde{x}}{\partial\tau}\right)^2 + \left(\frac{\partial\tilde{y}}{\partial\tau}\right)^2\right]^{1/2} \times\left\{C_L\frac{\partial\tilde{y}}{\partial\tau} + \left(V - \frac{\partial\tilde{x}}{\partial\tau}\right)C_D\right\}\phi_i\, d\tilde{s}, \quad (9a)$$

$$\gamma\tilde{q}_i'' + 2\tilde{\zeta}_i\tilde{q}_i' + (\lambda_i/\lambda_1)^4\tilde{q}_i = \frac{1}{2\tilde{m}a^2}\int_0^1\left[\left(V - \frac{\partial\tilde{x}}{\partial\tau}\right)^2 + \left(\frac{\partial\tilde{y}}{\partial\tau}\right)^2\right]^{1/2} \times\left\{\left(V - \frac{\partial\tilde{x}}{\partial\tau}\right)C_L - C_D\frac{\partial\tilde{y}}{\partial\tau}\right\}\phi_i\, d\tilde{s}, \; i = 1, 2, \ldots N, \quad (9b)$$

Downloaded 03 Jun 2010 to 171.66.16.125. Redistribution subject to ASME license or copyright; see http://www.asme.org/terms/Terms_Use.cfm

where $\gamma = [1 + \pi C_{ma}/(4\tilde{m})]$, in which C_{ma} is the added-mass coefficient, and $\tilde{\zeta}_i = \zeta(\lambda_i/\lambda_1)^2$ is the modal damping.

2.2 Reduction to a Two-Degree-of-Freedom System. A natural starting point for the study of the system represented by Eqs. (9) is a linearized stability analysis. For this purpose, it is sufficient to reduce the system to its lowest order, in this case to a two-degree-of-freedom system, in which only the first mode in each of the two orthogonal directions of motion is considered. A further simplification is introduced, by linearizing the position- and velocity-dependent fluid force terms.

To linearize the velocity terms, the approximation

$$\left[\left(V - \frac{\partial \tilde{x}}{\partial \tau}\right)^2 + \left(\frac{\partial \tilde{y}}{\partial \tau}\right)^2\right]^{1/2} \simeq V\left(1 - \frac{1}{V}\frac{\partial \tilde{x}}{\partial \tau}\right) \quad (10)$$

is used. Without loss of generality in the stability analysis, we may also consider planar $(\tilde{x}, \tilde{y})$ tube motion, hence the physical and generalized coordinates are identical; e.g., $\tilde{x} = \tilde{p}_1$, $\tilde{y} = \tilde{q}_1$, which is physically equivalent to analyzing a rigid, flexibly mounted tube. Furthermore, the position-dependent force coefficients are linearized via the Taylor expansions

$$C_L \simeq C_{L0} + e^{-\lambda\Delta\tau}\left(\tilde{p}_1 \frac{\partial C_L}{\partial \tilde{p}_1} + \tilde{q}_1 \frac{\partial C_L}{\partial \tilde{q}_1}\right),$$

$$C_D \simeq C_{D0} + e^{-\lambda\Delta\tau}\left(\tilde{p}_1 \frac{\partial C_D}{\partial \tilde{p}_1} + \tilde{q}_1 \frac{\partial C_D}{\partial \tilde{q}_1}\right). \quad (11)$$

The factor $\exp(-\lambda\Delta\tau)$, where λ is a complex eigenvalue of the system (see Section 4), represents the time-delay effect in the fluid forces; harmonic tube motion, for flow velocities in the neighborhood of the critical instability velocity, is implicitly assumed in this formulation (Price and Païdoussis, 1986).

Equations (10) and (11) are then substituted into (9), and only linear terms are retained. Introducing $\mathbf{w} = \{\tilde{p}_1, \tilde{q}_1\}^T$, the resulting linearized equations may conveniently be expressed in the following vector form:

$$[\mathbf{M}]\ddot{\mathbf{w}} + [\mathbf{D}]\dot{\mathbf{w}} + [\mathbf{K}]\mathbf{w} + \mathbf{F}_0 = 0, \quad (12)$$

where

$$[\mathbf{M}] = \begin{bmatrix} \gamma & 0 \\ 0 & \gamma \end{bmatrix}, \quad [\mathbf{D}] = \begin{bmatrix} 2\tilde{\zeta}_1 + VC_{D0}/(\tilde{m}a^2) & -VC_{L0}/(2\tilde{m}a^2) \\ VC_{L0}/(\tilde{m}a^2) & 2\tilde{\zeta}_1 + VC_{D0}/(2\tilde{m}a^2) \end{bmatrix},$$

$$[\mathbf{K}] = \begin{bmatrix} 1 - \{V^2 e^{-\lambda\Delta\tau}/(2\tilde{m}a^2)\}(\partial C_D/\partial \tilde{p}_1) & -\{V^2 e^{-\lambda\Delta\tau}/(2\tilde{m}a^2)\}(\partial C_D/\partial \tilde{q}_1) \\ 1 - \{V^2 e^{-\lambda\Delta\tau}/(2\tilde{m}a^2)\}(\partial C_L/\partial \tilde{p}_1) & -\{V^2 e^{-\lambda\Delta\tau}/(2\tilde{m}a^2)\}(\partial C_L/\partial \tilde{q}_1) \end{bmatrix} \quad (13)$$

and

$$\mathbf{F}_0 = \begin{bmatrix} -V^2 C_{D0}/(2\tilde{m}a^2) \\ -V^2 C_{L0}/(2\tilde{m}a^2) \end{bmatrix}.$$

For the purpose of a stability analysis, the steady force $\mathbf{F}_0$ determines the tube static equilibrium position, $\mathbf{w}_e$, at which the matrices $[\mathbf{D}]$ and $[\mathbf{K}]$ are evaluated; equivalently, the Taylor series expansions in equations (11) are for a coordinate system centred at this equilibrium position. For a given flow velocity, $\mathbf{w}_e$ may be obtained by solving the non-linear force balance equation

$$\mathbf{w}_e = -[\mathbf{K}(\mathbf{w}_e, V)]^{-1}\,\mathbf{F}_0(\mathbf{w}_e, V). \quad (14)$$

A stability analysis of Eq. (12) is carried out using standard eigenvalue techniques. With the complete position-dependent fluid force-field known, the effect of the tube equilibrium position on the stability flow velocity can also be determined. For the moment, however, we turn to the experimental determination of the fluid force field.

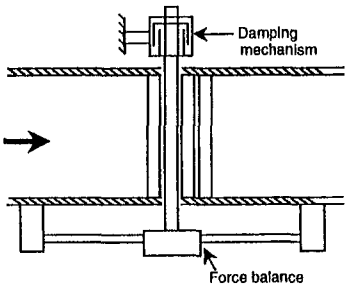


Fig. 2 The test cylinder in the array, in the wind-tunnel test-section, showing the force balance on which the test-cylinder is mounted and the oil-damper on top

3 The Static Fluid-Force Field

The theoretical model developed in Section 2 requires the values of C_L and C_D and their derivatives [see Eqs. (13)] as empirical input. These are generally specified at the symmetric equilibrium position, i.e., $C_L(0, 0)$, $C_D(0, 0)$, and similarly for the derivatives. In this study, however, the static lift and drag field was determined over a wide range of displacements, thus yielding $C_L(\tilde{x}, \tilde{y})$ and $C_D(\tilde{x}, \tilde{y})$ for $-0.23 \leq (\tilde{x}, \tilde{y}) \leq 0.23$.

The measurements were made in a blow-down wind tunnel with a 609 × 914 mm test-section. The free-stream turbulence intensity therein is 0.5 percent or less, outside the boundary layers. Although a maximum wind speed of 40 m/s is possible in the empty test-section, blockage introduced by the cylinder array reduced this to 15 m/s. The array consisted of seven cylinder rows, each containing alternately 14 and 15 cylinders. All cylinders (of diameter 25.4 mm) were rigidly fixed, spanning the 609 mm height of the tunnel. The test cylinder, located centrally in row 3 of the array, protruded outside the test-section and was mounted to the force balance at the bottom. To eliminate any cylinder vibration, a damping device was attached to the upper end of the test cylinder as shown in Fig. 2.

The force balance employs two linear displacement transducers to sense the location of the test-cylinder, vis-à-vis a datum and hence its neighbors, in the two orthogonal (in-flow and cross-flow) directions. The force balance was mounted on a bidirectional traversing mechanism which made accurate cylinder displacement possible. The displacement range, corresponding to an area of 11.7 × 11.7 mm was covered by 625 grid points. With the cylinder positioned at each grid point, a 1 min settling period was allowed. A 10 s time-average of the force outputs was then taken, using a HP 3562A FFT spectrum analyzer (Mureithi, 1993).

First, the effect of Reynolds number on C_L and C_D was checked, for $\tilde{x} = \tilde{y} = 0$. Measurements were made for $2.15 \times 10^3 \leq \mathrm{Re} \leq 1.25 \times 10^4$, where $\mathrm{Re} = U_\infty D/\nu$. It was found

Downloaded 03 Jun 2010 to 171.66.16.125. Redistribution subject to ASME license or copyright; see http://www.asme.org/terms/Terms_Use.cfm

that for Re $> 10^4$, C_L and C_D remained almost constant. The measurements to be presented were all made at Re $= 1.04 \times 10^4$. Other experiments with this and similar arrays have shown (i) no dramatic changes in the lift and drag coefficients up to Re $= 10^5$ and (ii) Re effects on stability are rather weak. The accuracy of the measured C_L and C_D has been estimated to be of the order of 10 percent.

Some typical variations of C_L and C_D with $\tilde{y}$ are shown in Fig. 3, in which, for analytical convenience later, the results were rendered symmetric about $\tilde{y} = 0$ by taking the average of the values for $+\tilde{y}$ and $-\tilde{y}$. Slight asymmetries in C_L and C_D in the measured results do exist, as may be appreciated from Fig. 4.

Figure 3(a, b) shows the variation of C_L and C_D with crossflow displacement $\tilde{y}$ with the movable cylinder at the equilibrium in-flow position ($\tilde{x} = 0$). Most striking is the extreme sensitivity of C_L to $\tilde{y}$ near $\tilde{y} = 0$, the crossflow equilibrium position. As shown by Price and Païdoussis (1986), the large and negative value of $\partial C_L/\partial \tilde{y}$ makes this cylinder location very susceptible to instability. It is also noted that C_L varies nearly linearly at this location; although only three data points show this linearity, repeated tests showed this to be always the case. C_L reaches extremum values of ± 4.1 at $\tilde{y} = \mp 0.055$. This variation in C_L may be associated with the cylinder emerging from the wake of its upstream neighbor and being subjected to the high speed channel flow between the cylinder columns. A gradual drop in $|C_L|$ to an average value of 3.0 occurs as the cylinder approaches either of its row-2 neighbors. The drag coefficient (Fig. 3(b)) shows local maxima, also at $\tilde{y} = \pm 0.055$, with a peak average value of $C_D = 7.0$, again an effect of exposure to the streaming channel flow. At $\tilde{y} = 0$, the test cylinder falls directly behind a row-1 cylinder, resulting in a local minimum in C_D. For $|\tilde{y}| > 0.055$, C_D decreases monotonically, as more of the test cylinder falls in the "shadow" of the neighboring row-2 cylinder.

When the in-flow tube position $\tilde{x}$ is changed, the trends in the variations of C_L and C_D versus $\tilde{y}$ observed in Fig. 3(a, b) are altered, depending on whether for the new in-flow position $\tilde{x} > 0$ (corresponding to a downstream displacement) or $\tilde{x} < 0$ (an upstream displacement). Note, however, that this does not imply the existence of symmetry at $\tilde{x} = 0$, but rather that the neighborhood of $\tilde{x} = 0$ is a transition region. The proximity of the test cylinder to its upstream or downstream neighbors, and the associated intercylinder gaps determine the changes that occur in the force coefficients.

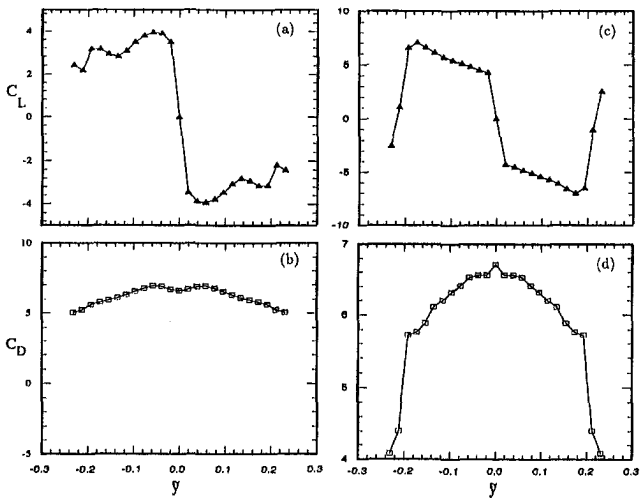


Fig. 3 (a, c) Experimental static lift coefficient and (b, d) drag coefficient variations with cylinder crossflow displacement, $\tilde{y}$, for Re $= 1.04 \times 10^4$: (a, b) for $\tilde{x} = 0$; (c, d) for $\tilde{x} = -0.173$

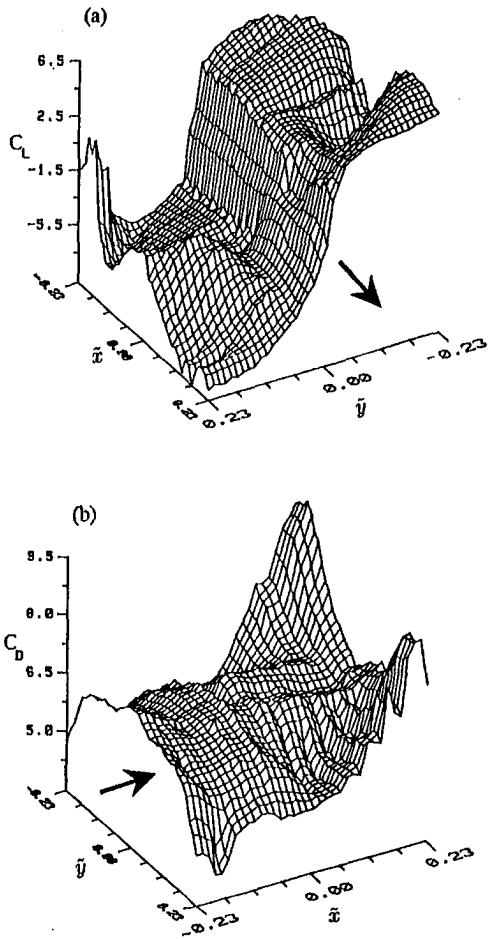


Fig. 4 3-D representation of the experimental (a) lift coefficient, C_L, and (b) drag coefficient, C_D, for a cylinder in the third row of the array at Re $= 1.04 \times 10^4$, as the cylinder is displaced statically in the x and y directions. The arrows indicate the flow direction.

Considering an upstream displacement of the test cylinder to $\tilde{x} = -0.173$, the resulting force coefficient variations are shown in Fig. 3(c, d); both the magnitudes and trends differ appreciably from those at the equilibrium cylinder location $\tilde{x} = 0$. C_L shows increased magnitudes in the range $0.05 < |\tilde{y}| < 0.20$, attaining a maximum absolute value of 7.0. The C_L variation is approximately piecewise linear over the complete $\tilde{y}$ range. Proximity to either of the row-2 cylinders has a drastic effect on C_L, resulting in a reversal of the lift force direction at $\tilde{y} = \pm 0.23$. Coincidentally with this reversal in the lift force direction, a large drop in C_D occurs, see Fig. 3(d). For $\tilde{x} = -0.173$ the test cylinder is located deeper within the wake of the row-1 cylinder, which accounts for the overall reduction in C_D. The drastic drop in C_D and simultaneous vanishing of C_L occur when the cylinder essentially blocks the streaming channel flow on one of its sides while widening the available area on the opposite side.

The force coefficient variation changes significantly for downstream positions of the cylinder, $\tilde{x} > 0$. Results for $\tilde{x} = +0.173$ (not shown here for brevity) indicate that in this case the variation is largely determined by proximity to row-4 and -5 cylinders as well as by the inter-cylinder gap.

Contour plots in 3-D form of the whole set of the results obtained are shown in Fig. 4, already presented by Païdoussis et al. (1993). The large and negative $\partial C_L/\partial \tilde{y}$ in the corridor centred about $\tilde{y} = 0$ (Fig. 4(a)) vanishes downstream, near $\tilde{x} = 0.10$, resulting in a region where the cylinder experiences no lift force (not clearly visible in the 3-D plot). With the exception of the extreme cylinder positions, the overall variation in

Downloaded 03 Jun 2010 to 171.66.16.125. Redistribution subject to ASME license or copyright; see http://www.asme.org/terms/Terms_Use.cfm

C_D magnitude is relatively small (Fig. 4(b)) in comparison to the variations observed for C_L.

A convolution of the lift and drag coefficients gives a net fluid force vector as shown in Fig. 5. The length of the arrows is proportional to a normalized force magnitude. Over most of the test region, the steady force is directed toward the symmetry line $\tilde{y} = 0$. The locations of possible cross-flow static instability are evident at $\tilde{x} = -0.17$, $\tilde{y} = \pm 0.20$ where the net force changes direction and $C_L \simeq 0$. The steady force increases for downstream cylinder positions primarily due to higher C_D values.

4 Stability Analysis

4.1 General Considerations. Restricting the analysis to obtaining a stability boundary, a solution to the linearized Eqs. (12) will suffice. The force $\mathbf{F}_0$ is presumed to give rise to the static equilibrium position $\mathbf{w}_e$ away from the symmetric location $\{0, 0\}^T$. Hence, a stability analysis in the neighborhood of $\mathbf{w}_e$ is conducted by considering solutions of the form

$$\mathbf{w}(\tau) = \mathbf{w}_0 \exp(\lambda\tau), \tag{15}$$

with the aid of Eq. (12) from which $\mathbf{F}_0$ is now eliminated (since its effect has already been accounted for). Alternatively, for fully flexible arrays in which all cylinders are subjected to the effects of $\mathbf{F}_0$ and all are blown back more-or-less equally, $\mathbf{w}_e$ may be considered as due to misalignment, local mean-flow velocity variations or thermal effects.

In this respect, it is important to stress that stability of this new equilibrium position is examined, such that for every value of the flow velocity the same position of the cylinder is being considered as the equilibrium position. This limitation is imposed by the exigencies of a linear analysis. If nonlinear effects had been taken into account, then stability as the cylinder position evolved under the action of $\mathbf{F}_0$ could have been considered; this could lead to different dynamical behavior for a single flexible cylinder in an array of rigid cylinders (if no blow-back correction is made); thus, for instance, stability may not be regained if lost while the cylinder passes through an unstable location, despite a predicted stable final equilibrium position. Hence, the results to be obtained more closely represent the situation of a cylinder deep inside a fully flexible array, in which $\mathbf{F}_0$ causes similar static displacements for all cylinders; yet one of them, the flexible cylinder in this analysis, is $\mathbf{w}_e$ away from the symmetric point due to misalignments and local mean flow variations.

Substituting (15) into (12) with $\mathbf{F}_0 = 0$, we obtain

$$\{\lambda^2[\mathbf{M}] + \lambda[\mathbf{D}(V)] + [\mathbf{K}(\lambda, V)]\}\mathbf{w}_0 \exp(\lambda\tau) = 0. \tag{16}$$

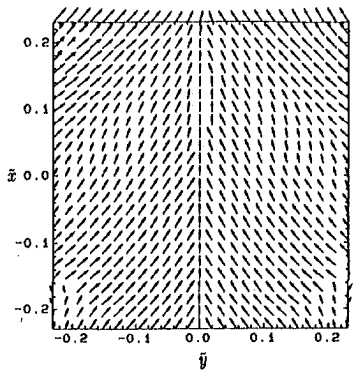


Fig. 5 Fluid-force vector field extracted from the convolution of the experimental lift- and drag-force components (Fig. 4)

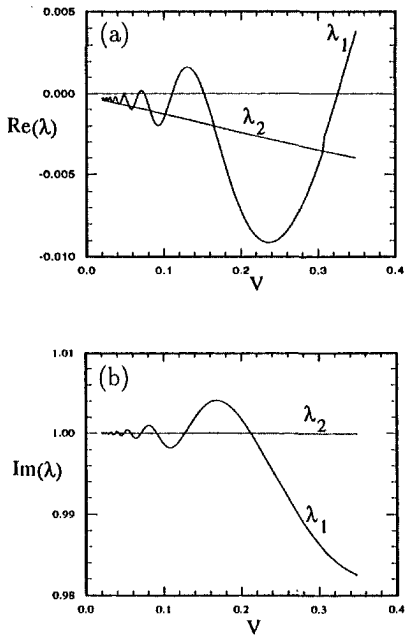


Fig. 6 Theoretical variation of the complex eigenvalues of the first crossflow mode, λ_1, and the first in-flow mode, λ_2, with $V(= U/\omega D)$ for $\tilde{m} = 100$, $\delta = 0.001$, at $\tilde{x} = \tilde{y} = 0$: ($a$) the real parts, $\mathcal{R}e(\lambda)$; (b) the imaginary parts, $\mathcal{I}_m(\lambda)$

For a nontrivial solution to exist we must have

$$\text{Det}\,[\lambda^2[\mathbf{M}] + \lambda[\mathbf{D}(V)] + [\mathbf{K}(\lambda, V)]] = 0. \tag{17}$$

On the stability boundary, purely imaginary or zero eigenvalues exist. An iterative procedure is used to solve Eq. (17), the iteration starting with an initial, assumed value of λ.

4.2 The Effect of Cylinder Misalignment on Stability. Calculations are started with zero misalignment, i.e., for $\tilde{x} = \tilde{y} = 0$ as the mean position of the cylinder. Figure 6 shows plots of $\mathcal{R}e(\lambda)$ and $\mathcal{I}m(\lambda)$ versus $V\ (\equiv U/\omega D)$ for $\tilde{m} = 100$ and $\delta = 10^{-3}$; this corresponds to a mass-damping parameter $\tilde{m}\delta = 0.1$ and is characteristic of low-$\tilde{m}\delta$ behavior. In the figure, λ_1 corresponds to cross-flow motion, while λ_2 to in-flow motion. $\mathcal{I}m(\lambda)$ is proportional to the frequency of oscillation, while $\mathcal{R}e(\lambda)$ is proportional to damping; a positive $\mathcal{R}e(\lambda)$ corresponds to negative damping, hence to fluidelastic instability [see Eq. (15)].

Starting iterations at the low flow velocity $V = 0.020$, the first instability occurs at $V = 0.065$, as evidenced in Fig. 6(a) by $\mathcal{R}e(\lambda_1) > 0$. The instability is the result of a Hopf bifurcation, resulting in a purely imaginary eigenvalue. As V is increased, restabilization occurs ($\mathcal{R}e(\lambda) < 0$) at $V = 0.077$. The alternation between stability and instability is repeated at $V = 0.112$ and $V = 0.153$. Final instability, above which no restabilization occurs, is at $V = 0.343$. This sequence is typical for low mass-damping parameter values, at least when the tube is located at the array equilibrium position. Figure 6(b) shows that the predicted fluidelastic frequency remains within 0.5 percent of the no flow frequency for the cross-flow direction, while essentially no change in in-flow frequency is observed.

For high mass-damping parameter values, $\tilde{m} = 10{,}000$ and $\delta = 0.1$, and tube position $\tilde{x} = 0$, $\tilde{y} = 0$, only one stability boundary exists. A monotonic increase in $\mathcal{R}e(\lambda_1)$ is observed in this case (not shown) and it becomes positive for $V = V_c \simeq 11$, while $\mathcal{R}e(\lambda_2)$ remains negative. A corresponding 11.5 percent increase in frequency is observed in cross-flow at the instability velocity, relative to the no-flow frequency.

We consider next the situation where the cylinder under consideration is misaligned with respect to its neighbors by $\{\tilde{x}, \tilde{y}\}$

Downloaded 03 Jun 2010 to 171.66.16.125. Redistribution subject to ASME license or copyright; see http://www.asme.org/terms/Terms_Use.cfm

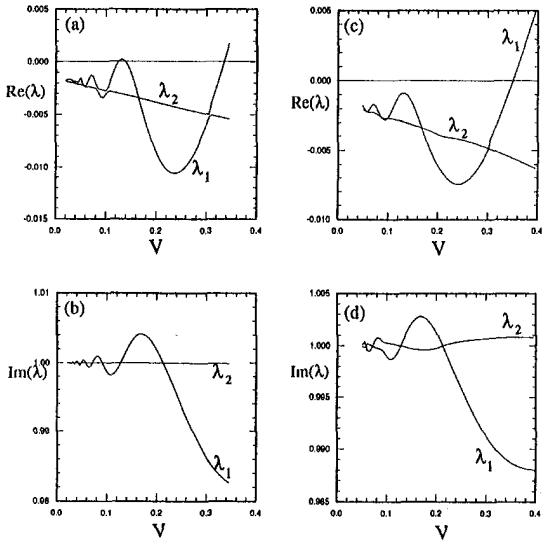


Fig. 7 Theoretical variation of the real and imaginary parts of the cross-flow and in-flow eigenvalues, λ_1 and λ_2, respectively, with V for $\tilde{m} = 100$, $\delta = 0.01$: (*a, b*) for $\tilde{x} = \tilde{y} = 0$; (*c, d*) for $\tilde{x} = 0$, $\tilde{y} = 0.02$ (point labeled A in Fig. 8)

at a given velocity V—in fact, the same $\{\tilde{x}, \tilde{y}\}$ for all V as explained in the foregoing. Typical results for $\tilde{m} = 100$, $\delta = 0.01$ ($\tilde{m}\delta = 1$) are shown in Fig. 7(a, b) when $\{\tilde{x}, \tilde{y}\} = \{0, 0\}$ and Fig. 7(c, d) when $\{\tilde{x}, \tilde{y}\} = \{0, 0.02\}$. From Fig. 7($a$), it is clear that one instability zone below the "final" one is predicted, at $V_c \simeq 0.13$. When the cylinder position is changed in the cross-flow direction by 0.02 cylinder diameters, the low velocity instability region disappears as seen in Fig. 7(c, d).

The disappearance of this instability region for a displacement of only 2 percent of the cylinder diameter is very significant, as it may explain why these instability regions have remained elusive to experimenters, despite their theoretical prediction for geometrically perfect systems in the present work and previously by others, e.g., Price and Païdoussis (1986) and Lever and Weaver (1986). Only in highly specialized and precisely controlled experiments have multiple instability regions been observed (e.g., by Andjelić et al., 1990). For the present array at least, it is clear that the precision in tube positioning (to within $0.02D$), makes it nearly impossible to observe these instabilities in ordinary experiments. More importantly, the same would apply to operational heat exchangers, with tube layout of the type considered here, as discussed at the beginning of Section 2. This, of course, is good news to the designer, since the most important instability (and possibly the only one likely to occur) is the highest-velocity instability.

Figure 8(a) shows contour plots of cylinder instability velocity for the low mass damping parameter, $\tilde{m}\delta = 1$ ($\tilde{m} = 100$, $\delta = 0.01$). The instability boundary considered here is the final one, past which no restabilization occurs. Increasingly darker shades of grey correspond to increased instability (i.e., instability occurs at low flow velocities); the most lightly shaded areas correspond to complete cylinder stability.[2]

As discussed in the foregoing, cylinder position variation markedly affects the resulting stability behavior. The stability behavior not only changes, but in some cases, instabilities no longer occur, e.g., at $\tilde{x} = +0.06$, $\tilde{y} = \pm 0.08$. The corridor $|\tilde{y}| \leq 0.04$ is highly unstable, as are most upstream positions in the range $\tilde{x} < -0.10$, $|\tilde{y}| < 0.20$. For most of the unstable region, the instability is dynamic. In the two small regions centred about $\tilde{x} = -0.18$, $\tilde{y} = \pm 0.20$, however, static instability

[2] A cylinder position was considered stable if no instability occurred at 10 times the instability velocity at $\tilde{x} = \tilde{y} = 0$.

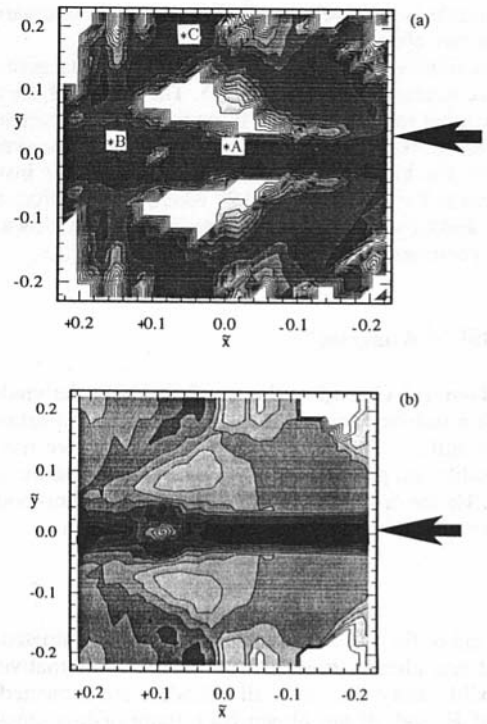


Fig. 8 Theoretical contours of (*a*) the critical flow velocity, V_c, and (*b*) $\partial C_L/\partial\tilde{y}$, as functions of $(\tilde{x}, \tilde{y})$, for $\tilde{m} = 100$, $\delta = 0.01$. In (*a*) darker regions correspond to "more unstable" situations, while in (*b*) to higher negative $\partial C_L/\partial\tilde{y}$. The arrows indicate the direction of the flow.

occurs. This is in agreement with the observation of a vanishing of C_L with $\partial C_L/\partial\tilde{y} > 0$ in this region, as discussed before.

Figure 8(b) shows contours of the derivative $\partial C_L/\partial\tilde{y}$, where darker shades of grey correspond to larger negative values of $\partial C_L/\partial\tilde{y}$. It is thus seen that the dependence of V_c on cylinder position correlates well with the variations in $\partial C_L/\partial\tilde{y}$, by comparison of Figs. 8(a) and 8(b).

At high mass-damping parameter values, i.e., $\tilde{m}\delta = 10^3$ ($\tilde{m} = 10{,}000$ and $\delta = 0.1$), the stability boundary contour plot, Fig. 9, shows overall similarity to the low $\tilde{m}\delta$ case. For the present set of parameters, however, stability is more widespread.

5 Conclusions

The dynamics of a rotated triangular array with pitch-to-diameter ratio of $P/D = 1.375$ was studied theoretically with the aid of the one-flexible-cylinder Price and Païdoussis (1986) model and with empirical input the measured static lift and drag maps corresponding to 625 static cylinder locations in the in-

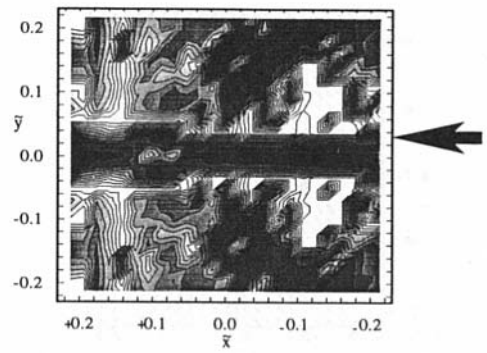


Fig. 9 Theoretical contours of the critical flow velocity, V_c, as a function of $(\tilde{x}, \tilde{y})$ for $\tilde{m} = 10{,}000$, $\delta = 0.1$; darker regions correspond to "more unstable" locations. The arrow indicates the flow direction.

Downloaded 03 Jun 2010 to 171.66.16.125. Redistribution subject to ASME license or copyright; see http://www.asme.org/terms/Terms_Use.cfm

flow and cross-stream directions about the geometrically perfect configuration.

The linear stability of a flexible cylinder in various "deformed" locations in the array was investigated. This could correspond to (i) the case of a single flexible cylinder subjected to blow-back in an otherwise rigid array of cylinders, or to (ii) the more practically interesting case of a cylinder dislocated by thermal, mechanical or local mean-flow effects in a fully flexible array. The questions of primary interest were (i) how sensitive is stability to such geometric imperfection? and (ii) do the instability-stability zones predicted for low $m\delta/\rho D^2$, below the ultimate instability (which is not restabilized at higher flow velocities), really exist? A supplementary question is this: (iii) why is it so rare to find these stability-instability zones in laboratory experiments?

The most important results may be summarized as follows: (a) the stability of the array strongly depends on geometric asymmetries; (b) whereas for a perfectly symmetric geometry the system may have several sub-ultimate instability regions, an asymmetry of as little as $0.02D$ may quench them and leave only the ultimate instability region intact.

The sensitivity in dynamical behavior to geometric imperfections explains why the regions in question are anything but easy to "catch"; precision of better than ± 0.5 mm in positioning the cylinders in the array would be required, and maintaining such geometrical tolerances with increasing flow, which is extremely difficult to achieve even in laboratory experiments. This conclusion applies strictly to arrays of the geometry investigated in this paper, but is expected to apply also to other arrays in which the single-degree-of-freedom negative-damping mechanism is the dominant cause of fluidelastic instability. In engineering practice, for operating heat exchangers, although it cannot be said that these instability zones are impossible to occur, their occurrence must be extremely rare.

Acknowledgments

The authors gratefully acknowledge the support of the Natural Sciences and Engineering Research Council (NSERC) of Canada and Le Fonds FCAR of Québec.

References

Andjelić, M., Austermann, R., and Popp, K., 1990, "Multiple Stability Boundaries of Tubes in a Normal Triangular Cylinder Array," *Flow-Induced Vibration-1990*, S. S. Chen et al., eds., ASME PVP-Vol. 189, New York, pp. 87–98.

Austermann, R., and Popp, K., 1995, "Stability Behaviour of a Single Flexible Cylinder in Rigid Tube Arrays of Different Geometry Subjected to Cross-Flow," *Journal of Fluids and Structures*, Vol. 9, pp. 303–322.

Chen, S. S., 1983, "Instability Mechanisms and Stability Criteria of a Group of Circular Cylinders Subjected to Cross-flow. Parts I and II," ASME *Journal of Vibration, Acoustics, Stress, and Reliability in Design*, Vol. 105, pp. 51–58 and 253–260.

Chen, S. S., and Jendrzejczyk, J. A., 1981, "Flow-Velocity-Dependence of Damping in Tube Arrays Subjected to Liquid Cross Flow," ASME *Journal of Pressure Vessel Technology*, Vol. 103, pp. 130–135.

Lever, J. H., and Weaver, D. S., 1982, "A Theoretical Model for the Fluid-Elastic Instability in Heat Exchanger Tube Bundles," ASME *Journal of Pressure Vessel Technology*, Vol. 104, pp. 147–158.

Lever, J. H., and Weaver, D. S., 1986, "On the Stability Behaviour of Heat Exchanger Tube Bundles. Parts I and II," *Journal of Sound and Vibration*, Vol. 107, pp. 375–392 and 393–410.

Mureithi, N. W., 1993, "Nonlinear Dynamics of a Loosely-Supported Cylinder in Cross-Flow," Ph.D. thesis, Department of Mechanical Engineering, McGill University, Montreal, Québec, Canada.

Mureithi, N. W., Price, S. J., and Païdoussis, M. P. 1994a, "The Post-Hopf-Bifurcation Response of a Loosely-Supported Cylinder in an Array Subjected to Cross-Flow. Part I: Experimental Results," *Journal of Fluids and Structures*, Vol. 8, pp. 833–852.

Mureithi, N. W., Païdoussis, M. P., and Price, S. J., 1994b, "The Post-Hopf-Bifurcation Response of a Loosely-Supported Cylinder in an Array Subjected to Cross-Flow. Part II: Theoretical Model and Comparison with Experiments," *Journal of Fluids and Structures*, Vol. 8, pp. 853–876.

Mureithi, N. W., Païdoussis, M. P., and Price, S. J., 1995, "Intermittency Transition to Chaos in the Response of a Loosely Supported Cylinder in an Array, in Cross-Flow," *Chaos, Solitons and Fractals*, Vol. 5, pp. 847–867.

Païdoussis, M. P., and Price, S. J., 1988, "The Mechanisms Underlying Flow-Induced Instabilities of Cylinder Arrays in Crossflow," *Journal of Fluid Mechanics*, Vol. 187, pp. 45–59.

Païdoussis, M. P., Price, S. J., Nakamura, T., Mark, B., and Mureithi, W. N., 1989, "Flow-Induced Vibrations and Instabilities in a Rotated-Square Cylinder Array in Cross-Flow," *Journal of Fluids and Structures*, Vol. 3, pp. 229–254.

Païdoussis, M. P., Price, S. J., and Mureithi, N. W., 1993, "Nonlinear and Chaotic Dynamics of a Two-Degree-of-Freedom Analytical Model for a Rotated Triangular Array in Cross-Flow," *Journal of Fluids and Structures*, Vol. 7, pp. 497–520.

Price, S. J., 1995, "A Review of Theoretical Models for Fluidelastic Instability of Cylinder Arrays Subject to Cross Flow." *Journal of Fluids and Structures*, Vol. 9, pp. 463–518.

Price, S. J., and Kuran, S., 1991, "Fluidelastic Stability of a Rotated Square Array with Multiple Flexible Cylinders, Subject to Cross-Flow," *Journal of Fluids and Structures*, Vol. 5, pp. 551–572.

Price, S. J., and Païdoussis, M. P., 1984, "An Improved Mathematical Model for the Stability of Cylinder Rows Subject to Cross-Flow," *Journal of Sound and Vibration*, Vol. 97, pp. 615–640.

Price, S. J., Païdoussis, M. P., and Giannias, N., 1990, "A Generalized Constrained-Mode Analysis for Cylinder Arrays in Cross-Flow," *Journal of Fluids and Structures*, Vol. 4, pp. 171–202.

Price, S. J., and Païdoussis, M. P., 1986, "A Single-Flexible Cylinder Analysis for the Fluidelastic Instability of an Array of Flexible Cylinders in Cross-Flow," ASME JOURNAL OF FLUIDS ENGINEERING, Vol. 108, pp. 193–199.

Downloaded 03 Jun 2010 to 171.66.16.125. Redistribution subject to ASME license or copyright; see http://www.asme.org/terms/Terms_Use.cfm

Toshiaki Suzuki

Tomotatsu Nagafuji

Hiroshi Komiya

Takako Shimada

Hydraulic Research Laboratory,
Toshiba Corporation,
Yokohama, 230 Japan

Toshio Kobayashi

Nobuyuki Taniguchi

Institute of Industrial Science,
University of Tokyo,
Tokyo, Japan

Flow Behavior Around Stayvanes and Guidevanes of a Francis Turbine

The three-dimensional computation of steady and incompressible internal flows is of interest in numerical simulations of turbomachinery, and such simulations are currently under investigation, from inviscid to viscous flow analyses. First, surface pressure distributions have been measured for the stayvanes and the guidevanes of a Francis turbine. They are presented to verify the numerical results. Second, both inviscid and viscous three-dimensional flow analyses have been made, so as to predict the flow behavior in the same domain. Comparison of the measured pressure distributions to the predicted pressure distributions has been made to study the usefulness of the present simulations. It can be pointed out that a global analysis which includes a runner flow passage, except runner blades, is necessary to predict the three-dimensional flow characteristics and that inviscid flow analysis has the capability of good prediction for flow without separation. Viscous flow analysis gives similar results, though it is necessary to investigate further the improvement of prediction accuracy. Flow characteristics around the stayvanes and the guidevanes are also discussed.

Introduction

For the performance improvement of the Francis turbine, it is important to study the interaction between guidevanes and runner because the outlet flow from guidevanes significantly influences the flow in the runner. The flow of water turbines is characterized as incompressible, and numerical approaches are in progress from inviscid to viscous flow analyses, e.g., Nagafuji and Morii (1980) for potential flow, Eriksson et al. (1984) for Euler flow, and Vu et al. (1986) for viscous flow. In these studies, efforts are taken to accurately predict the flow behavior in the blade-to-blade passages, but such verification is very rare at the present. This is because accurate measurement of the internal flow of water turbines is very difficult due to the geometric complexity bounded by three-dimensional (3-D) curved blade shapes. In such circumstances, measurements around stayvanes (SV) and guidevanes (GV) are fairly easy because the shapes of such vanes are basically two-dimensional (2-D). Franke et al. (1983) and Matsumoto et al. (1986) have reported 2-D analysis that includes verifications. There are cases where 3-D analysis of the same object is required for a Francis turbine with high specific speed, since the heights of SV and GV increase and a 3-D flow is generated.

In the present study, 3-D measurements for the surface pressure distributions of the SV and GV of a Francis turbine having a high specific speed of 240 (rpm, kW, m) have been carried out in order to study the flow behavior and to verify the accuracy of the analysis. Also, 3-D potential and viscous flow analyses are applied to the same object. A Navier-Stokes equation with turbulence models has been widely used to solve viscous flow problems. However, there remain unknown factors, some of which are caused by problems in the numerical method as much as in the modeling, that must be clarified in order to enhance the ability of actual application; one such example is the complex turbulent flows in water turbines. Otherwise, potential flow analysis does not include such unknown factors and is available for attached (no separation) flows, though it may be bounded by limitations to the potential theory. In order to study the validity of viscous flow simulations with such unknown factors, comparison of the inviscid and viscous flow analyses for the same object will be made, as well as comparisons of the measurements.

Experimental Apparatus and Results

A model which examines the actual flow behavior around the SV and GV of a Francis turbine was designed so that the flow passages from the inlet of a spiral case to the outlet of a draft tube are geometrically homologous to the prototype, as shown in Fig. 1. The model Francis turbine has a runner outlet with a diameter of 350 mm and a high specific speed of 240 (rpm, kW, m). The total number of SV and GV are 20. Two SV and four GV are selected to measure the pressure distributions on their surfaces, as shown in Fig. 2. One SV and two GV are used for the measurement of pressure side, and the others for suction side. Figure 3 shows the locations of pressure measuring points on the SV and GV, where each surface pressure is led from holes having an inner diameter of 0.8 mm to the outside of the model through pressure tubes with an outer diameter of 1.2 mm, which are filled in each vane. In order to make clear the 3-D characteristics of the flow, five measuring sections are set in height direction of each vane. As for GV, a pair of them are used to measure the pressure on one side, for example at the pressure side, because the number of tubes is limited by the size of GV spindle used to move GV. One GV is then used for sections of I–III and the other for III–V of Fig. 3. Section III is used for a pair of GV to check the identity of measuring pressure at both the GV.

The total number of pressure holes is 166, thus necessitating an automatic data acquisition system. The system employed was the same as that used in a previous study (Matsumoto et al., 1986), in which data acquisition is completely controlled by personal computer and the change of measuring point sequentially carried out by multiscanning valves controlled by the computer and connected to pressure tubes. Pressure from the scanning valve is transmitted by a pressure transducer of the semiconduction type and input to a digital-voltmeter, which is connected to the computer through its interface. The directly measured data is stored in the computer's disk memory and

Contributed by the Fluids Engineering Division for publication in the JOURNAL OF FLUIDS ENGINEERING. Manuscript received by the Fluids Engineering Division April 16, 1992; revised manuscript received October 15, 1995. Associate Technical Editor: Wing Ng.

Copyright © 1996 by ASME

Downloaded 03 Jun 2010 to 171.66.16.125. Redistribution subject to ASME license or copyright; see http://www.asme.org/terms/Terms_Use.cfm

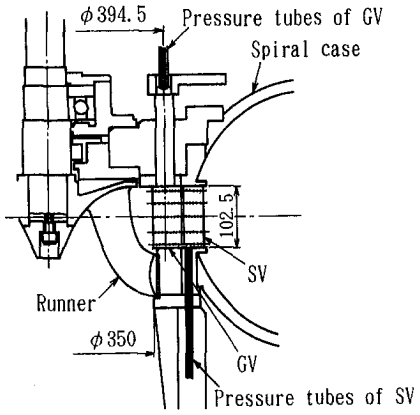


Fig. 1 Configuration of model turbine

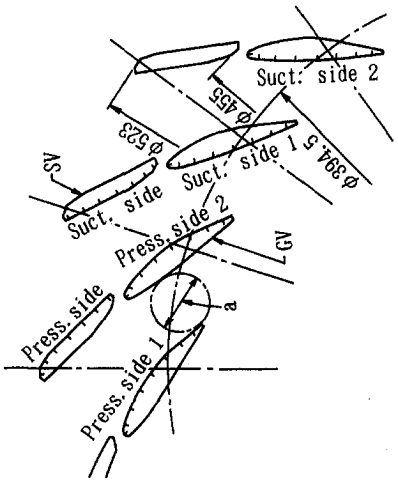


Fig. 2 Arrangement of stay and guidevanes

output to a CRT or line printer after calibration and averaging by the computer. Averaging is done by using 20 instantaneous values per measuring point. The averaged pressure is finally

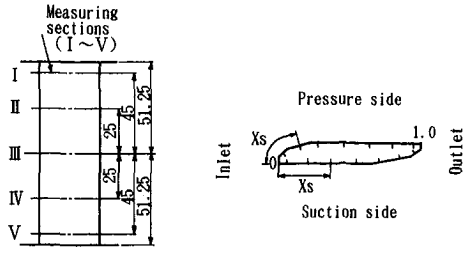


Fig. 3 (a) Stayvane

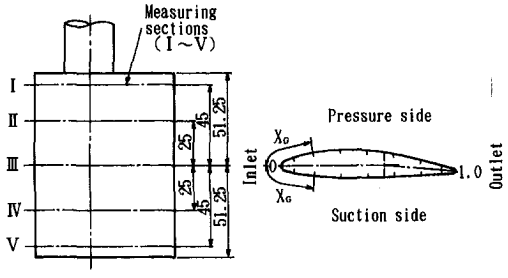


Fig. 3 (b) Guidevane

Fig. 3 Pressure measuring points of stay and guidevanes

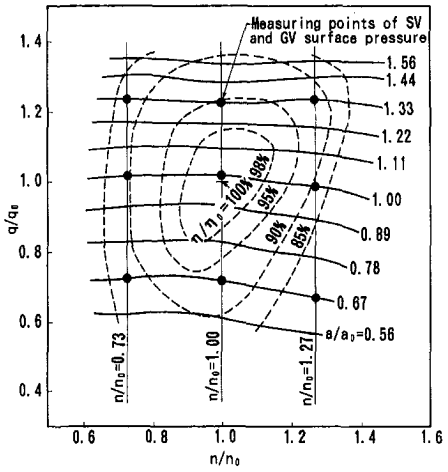


Fig. 4 Performance diagram of model turbine

normalized by a pressure coefficient $C_p = (P - P_i)/(V_i^2/2)$, where P is local static pressure on the SV or GV, P_i and V_i are total pressure and radial velocity at inlet of domain, respectively.

The model turbine was operated under a test head of about 16 m and over a speed range of 600 to 1200 rpm. Operating data of the model, such as inlet/outlet heads, discharge, torque and speed, are automatically recorded and calculated by high-precision measuring instruments. Data acquisition and processing follows by means of a mini-computer attached to the test rig. The operating data is finally normalized using the guidevane opening a_o, unit speed n_o, unit discharge q_o and turbine efficiency η_o corresponding to the optimum point of the model. Figure 4 shows the performance diagram of the model, where $q = Q/\sqrt{H}$, $n = N/\sqrt{H}$. Q, N and H are discharge, rotational speed, and effective head of the model turbine, respectively. The nine points with the symbol (●) are the operating conditions where the pressures of the SV and GV were measured. These points cover the normal operating range of the prototype.

The detailed pressure of vane surfaces obtained by the experiments are represented later with comparison of the experimental and analytical results. Figure 5 shows a typical example of the measured pressure coefficients on the SV and GV at section III of mid-streamline for a GV opening of $a/ao = 0.67$ and three unit speeds. In this figure, X is the length along the surface of the SV or GV as measured from inlet edge of each vane and shown in Fig. 3. L is total length from the inlet to outlet edges. Figure 5 demonstrates that the influence of unit speeds on pressure coefficients of the SV and GV is negligible because the influence on GV, which is strongly affected by runner rotational speed, is very small. It has been verified by the results of other GV openings that this characteristic has generality for flow around SV and GV, and it is furthermore independent of specific speeds because the same characteristic (Matsumoto et al., 1986) has been reported for a Francis turbine having a low specific speed of 100 (rpm, kW, m). These experiments reveal that the pressure difference between the pressure and suction sides of the GV increases when the GV opening becomes small, and is nearly zero when the GV opening is $a/a_o = 1.33$, where a shock-free condition occurs at the inlet of the GV (see Figs. 10 and 11). On the other hand, the pressure distributions of the SV surfaces indicate no changeable characteristic in relation to unit speed or guidevane opening. This observation suggests that the flow from the spiral case is uniform regardless of unit speed or guidevane opening, and the influence of the flow around the GV is very small. Therefore, it is concluded that the flow behavior around the SV and GV of Francis turbines can be influenced only by the GV openings under the given arrangement of the SV and GV.

Downloaded 03 Jun 2010 to 171.66.16.125. Redistribution subject to ASME license or copyright; see http://www.asme.org/terms/Terms_Use.cfm

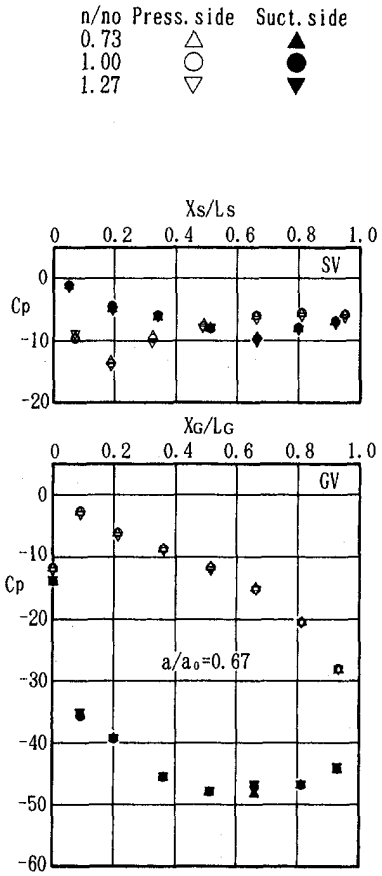


Fig. 5 Typical experimental results for pressure distributions of SV and GV surfaces

Numerical Method and Results

The computational model consists of an inlet, a cascade around the SV and GV, and runner flow passages. In order to reduce computational cost, one pitch of cascade flow passage is used by applying a periodic condition to the boundary surfaces, except of rigid vanes, at both sides in the circumferential direction. The runner flow passage, not including the blades, is added in the computational domain because the outlet flow of the GV is significantly influenced by the runner passage geometry and necessary for the 3-D analysis.

Finite Element Method (FEM). Figure 6 shows the meshes generated in the computational domain for potential flow analysis by FEM, in which 4323 hexahedral elements are used. In general, the mesh discretization of cascade flow passages requires a technique capable of handling a complicated geometry, and FEM is known for its ability to deal with such flow problems.

The flow around SV and GV is governed by the Laplace equation:

$$\nabla^2\phi = 0 \tag{1}$$

where ϕ is the velocity potential function.

The static pressure in the domain can be calculated by using Bernoulli's equation after the computation of ϕ:

$$\frac{1}{2}(\nabla\phi)^2 + U + \frac{P}{\rho} = \text{constant} \tag{2}$$

where U is the potential of an external force and P is the static pressure. The constant value on the right side of Eq. (2) should be determined by specifying a reference datum pressure at an arbitrary node point in the flow field. The details of solution procedures for Eq. (1) under given boundary conditions can be found in Nagafuji and Morii (1980).

The boundary conditions are represented by the following items: (i) the flow at the inlet boundary of the domain is assumed to be uniform, namely, the velocity normal to the boundary is obtained from a given discharge divided by the sectional area and the tangential velocity is determined from the averaged circulation over the sectional area; (ii) the velocities normal to the SV and GV surfaces and to the upper and lower walls are zero, which are naturally satisfied in the computation; (iii) as previously mentioned, the periodic condition is applied to the boundary surfaces extending from the inlet and outlet edges of SV and GV. The circulations on these surfaces, except at the inlet region, are computed from the potential jump across these surfaces which is determined by the Kutta condition at the trailing edges of SV and GV. In the present approach, the Kutta condition is dealt with by considering the outlet velocities on the pressure and suction sides of the vane surfaces to be equal near the trailing edge. This assumption may result in some errors when the spanwise circulation is strong, but is a unique approach to potential flow; (iv) the flow at the outlet boundary has a normal component given in the same manner as that at the inlet, and the tangential component is determined from the Kutta condition of the GV.

Finite Volume Method (FVM) With k-ϵ Turbulence Model. For turbulent flow analysis, a k-ϵ two equation model (Lauder and Spalding, 1972) is used because it is the simplest and most popular model (Rodi, 1980) for turbulent flow with or without flow separations, considering expansion to the simulation of the stalling flows. The basic equations of turbulence model are,

$$\frac{\partial u_i}{\partial x_i} = 0$$

$$\frac{\partial u_i u_j}{\partial x_j} = -\frac{\partial p}{\partial x_i} + \frac{\partial}{\partial x_j}(2\nu_t S_{ij})$$

$$\frac{\partial u_j k}{\partial x_j} = \frac{\partial}{\partial x_j}\left(\frac{\nu_t}{\sigma_k}\frac{\partial k}{\partial x_j}\right) + G - \epsilon$$

$$\frac{\partial u_j \epsilon}{\partial x_j} = \frac{\partial}{\partial x_j}\left(\frac{\nu_t}{\sigma_\epsilon}\frac{\partial \epsilon}{\partial x_j}\right) + C_1\frac{\epsilon}{k}G - C_2\frac{\epsilon}{k^2}$$

$$S_{ij} = \left(\frac{\partial u_i}{\partial x_j} + \frac{\partial u_j}{\partial x_i}\right)\Big/ 2; \quad \nu_t = C_\mu k^2/\epsilon;$$

$$G = 2\nu_t S_{ij} S_{ij} \tag{3}$$

where the five model constants are fixed as the standard values

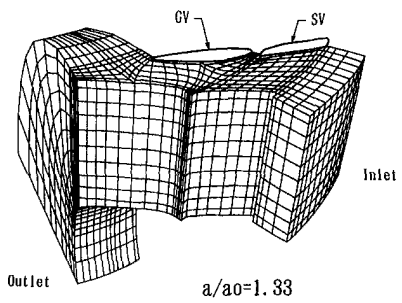


Fig. 6 Finite element model of flow domain

Downloaded 03 Jun 2010 to 171.66.16.125. Redistribution subject to ASME license or copyright; see http://www.asme.org/terms/Terms_Use.cfm

Table 1 Constants of k-ϵ turbulence model

C_μ	C_1	C_2	σ_k	σ_ϵ
0.09	1.44	1.92	1.0	1.3

as shown in Table 1, though they may be valid for the case of high Reynolds number flows around SV and GV with no or small separation. Furthermore, a wall function is adopted for the wall boundary conditions of vanes, upper and lower walls to reduce computational time and storage requirements.

FVM (Taniguchi et al., 1989) is used to discretize the governing equations in the body-fitted grid. The equations are integrated in the generic control cell, shown in Fig. 7, which appears along the nonorthogonal coordinate system. A staggered technique is adopted for velocity components, which are defined as projections on the coordinates. The generalized form derived from the conservation equation is,

$$\iiint_{\mathrm{Vol}} \frac{\partial \phi}{\partial t}\, dV + \iint_{Anb} (\mathbf{J}_{nb} \cdot d\mathbf{n}_{nb}) = \iiint_{\mathrm{Vol}} S dV \quad (4)$$

where $\mathbf{J}(=\mathbf{v}\phi - \Gamma\nabla\phi)$ is the total flux on the cell surface, $\mathbf{n}$ is the unit face vector, ϕ is a general variable (a scalar or a component of vector), $\mathbf{v}$ is the velocity vector, Γ is the diffusive coefficient, S is a source of ϕ and the suffix nb means e, w, n, s, t, and b as shown in Fig. 7. The surface integration is estimated in the following way. An example on the surface "e" is,

$$\iint_{Ae} (\mathbf{J}_e \cdot d\mathbf{n}_e) = JD_e F(|\mathrm{Pe}_e|)(\phi_e - \phi_p) + JM_e \phi_{UP} \quad (5)$$

with

$$JM = \mathbf{v} \cdot \mathbf{A}, \quad JD = (\Gamma/PE)(\mathbf{e} \cdot \mathbf{A})$$

$$\mathrm{Pe} = JM/JD$$

where Pe is the Peclet number, $\mathbf{e}$ is the unit vector along the ξ coordinate axis, $\mathbf{A}$ is the face vector, PE is the segment length from P to E, and ϕ_{UP} means upwind value. Notice that both the velocity and the unit vectors are defined in the direction of the segment P to E, but are not generally normal to the face vector.

A hybrid scheme is adopted in this study, where the function F is switched at Pe = 2 from a central differencing formulation to an upwind scheme to reduce dispersion errors. This method has the advantage that the above formulation can be derived directly from the equation in the physical domain, i.e., it is not transformed into any other coordinate system. The staggered technique effectively suppresses numerical oscillation, though the formulation becomes complicated. For example, the velocity

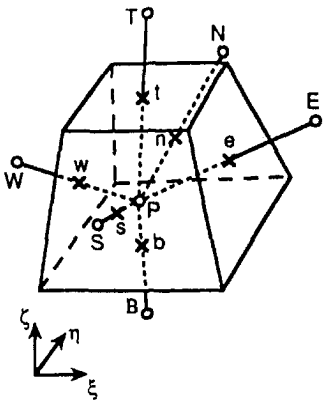


Fig. 7 Control cell of a point "P" and its neighboring points

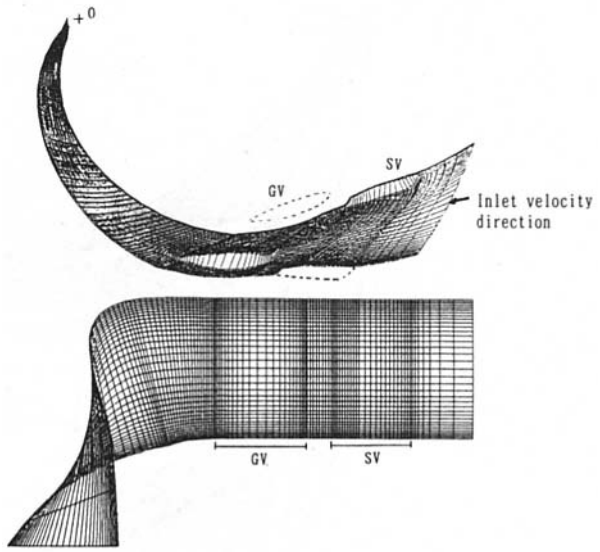


Fig. 8 Computational grid of flow domain

on the cell face is expressed with the one component value defined there, and the interpolation value of the other two components in the neighboring positions in the interporations of flux. The discretized form of the continuity equation is as follows:

$$\sum JM_{NB} = 0 \quad (NB: E, W, N, S, T, \text{and } B) \quad (6)$$

where JM is mass flux on the cell face defined in Eq. (5). The SIMPLE algorithm (Patankar, 1980) can be as valid in the body-fitted grid as in the squared grid along the Cartesian coordinates when the components or velocity is nearly normal to cell faces and angles larger than 60 degrees are expected. Therefore, the present approach uses the same procedure except that relaxation factors for the pressure correction and momentum equations must be decreased to 0.3 and 0.2.

The computational region is the same as that for the inviscid analysis shown in Fig. 8, where $a/a_o = 1.00$. The number of grid points is about 120 thousand (100 in the radial direction, 35 along the height and 35 in the circumferential direction) which are generated by algebraic interporation. Finer grid points ($150 \times 40 \times 40$) are applied to the case of $a/a_o = 1.00$ in order to study the validation of results. Grid points are concentrated on the surfaces of vanes and the upper and lower walls to satisfy the grid condition for the wall function. The Reynolds number defined by the average inlet velocity and the distance between the upper and lower walls is 100,000, which is the same value as that for the experimental condition of the model turbine.

The two opening conditions of $a/a_o = 1.00$ and 1.33 are simulated in vicous analysis, since as the distortion of the grid becomes large it affects the results and could not be ignored in case of $a/a_o = 0.67$. The boundary conditions are represented as follows: (i) the three components of the inlet velocity are estimated from the experimental data of a similar model and the inlet pressure obtained from calculation by means of the continuity equation. Because turbulent information was not measured, a 1 percent fluctuation in velocity and a laminar viscosity equal to 10 times eddy viscosity are assumed; (ii) the outlet pressure is fixed as a constant over the section and other values at the outlet are in the free stream condition; (iii) in the tangential direction, except for vane surfaces, a periodic condition is assumed to be the same as in inviscid analysis; (iv) on the boundaries of the upper and lower walls and the SV and GV surfaces, the wall function is applied as previously explained, with no special treatment adopted at the leading or the trailing edge of vanes.

Downloaded 03 Jun 2010 to 171.66.16.125. Redistribution subject to ASME license or copyright; see http://www.asme.org/terms/Terms_Use.cfm

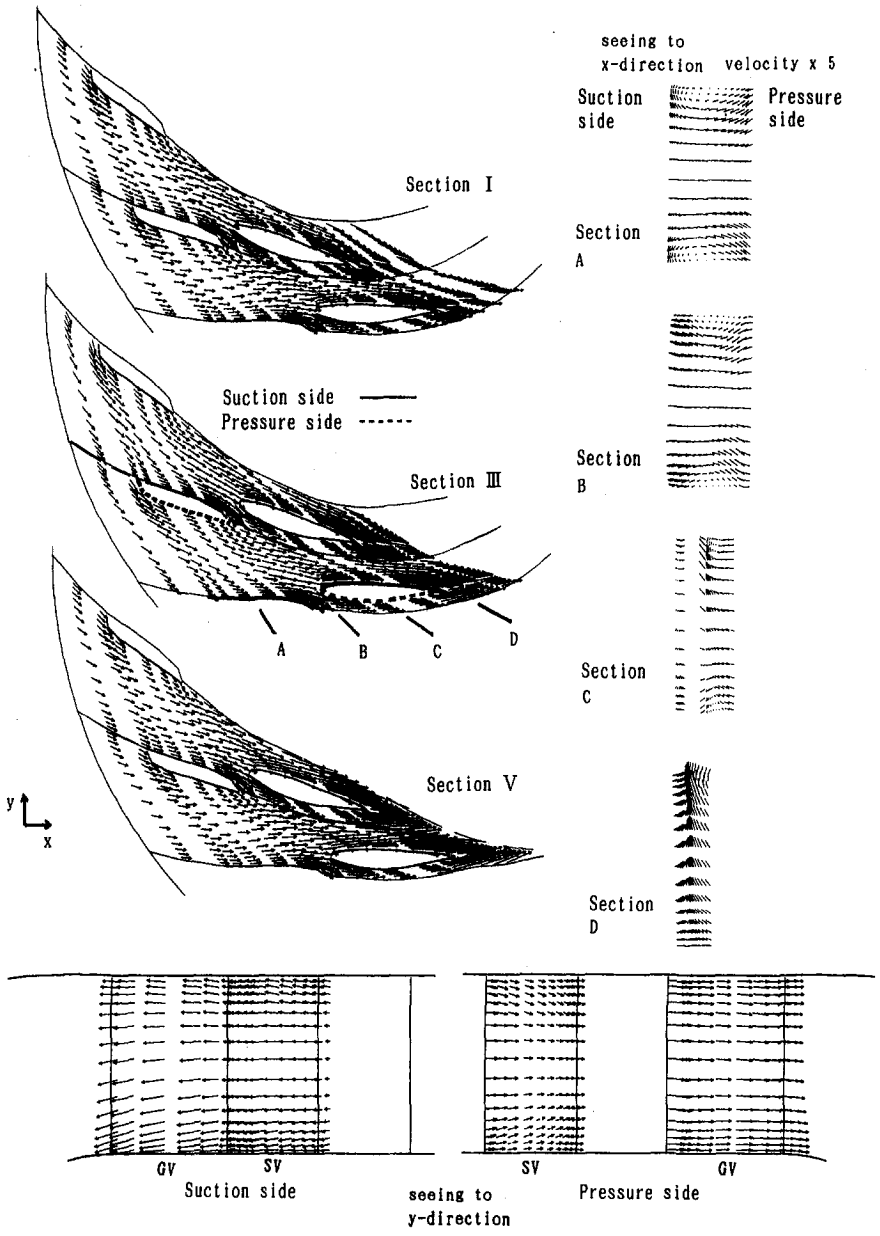


Fig. 9 Typical velocity field (a/a_o = 1.00)

The convergence criterion could be estimated by the residual pressure level, which was less than 0.001 of the pressure drop from the inlet to the trailing edge of the GV. The residual pressure decreased monotonously in the convergence diagram.

Numerical Results and Discussion

Figure 9 shows the predicted velocity fields for the case a/a_o = 1.00, which are the horizontal views in the three sections I, III, and V of Fig. 3, the vertical views in four sections to the flow direction and the flow pattern on the surfaces of SV and GV for viscous analysis. As previously mentioned, the influence of runner rotational speed on the flow fields around SV and GV (see Fig. 5) is very small. As the computations are carried out under the condition where no consideration is given to speed, only the experimental results at n/n_o = 1.00 are used for the following comparisons between the computation and the measurement. The smoothness (no separation) of the flow and the acceleration of the flow in accordance with the circulation around each vane can be seen from Fig. 9, and the secondary vortexes are predicted in the vertical sections, though the 3-D variations are weak in this case. Such a characteristic may caused by the same vane outlet angle on the spanwise, and thus support the validity of potential analysis with the proposed Kutta condition.

Figures 10 and 11 show the pressure distributions on the SV and GV surfaces under the two conditions of a/a_o = 1.00 and 1.33, as compared with experiments. As expected from the flow pattern of Fig. 9, both computations agree with the predictions (typically in section III). As for pressure distributions on the SV surfaces, it can be seen that 3-D characteristics are recognized on the upstream side for the experiments, especially in sections of I and V. On the other hand, the results of potential simulation did not predict such characteristics, even though uniform inlet flow was assumed in the computations. Boundary layers generation on the surfaces of the upper and lower walls of the actual flow should be considered as the prime cause. Indeed, viscous simulation yields fairly good agreement between computation and measurement. The pressure distributions on the downstream side show a uniform pattern from upper to

Downloaded 03 Jun 2010 to 171.66.16.125. Redistribution subject to ASME license or copyright; see http://www.asme.org/terms/Terms_Use.cfm

lower sides, in the measurement as well as in both computations. The abrupt pressure drop on the suction side, which is seen on the viscous analysis, may be caused by the angular surface shape of the SV. Such kinks are mainly due to higher accuracy near the surface in viscous analysis, which has a finer grid than inviscid analysis. Perhaps the actual flow may show a small separation bubble behind the angle, which would have been hardly captured with the turbulent model in the present viscous analysis.

In the GV region, it is recognized that changes in the pressure distributions by the GV openings are remarkable, and the discrepancy between computation and measurement increases when the GV opening becomes small, especially for sections I and V. The whole characteristic of these pressure distributions indicates that 3-D flow is generated in the cascade flow field of the GV. The geometry of a runner flow passage causes an increases in the velocity on the lower side of the GV, and a decrease on the upper side. Therefore, the pressure drop in section V is remarkable for the GV at each GV opening. Potential analysis may overestimate such an effect because the actual viscous flow may restrain the increase in the velocity near the lower wall. The difference between the potential and viscous results for section V may be explained by such an effect. The pressure distributions in sections II, III, and IV show fairly good agreement between computation and measurement. It may be noted that 3-D flow in the main field, except the narrow regions closed at the upper and lower walls, can be accurately predicted by potential analysis.

In viscous analysis, the computational results are more strongly dependent on the grid configurations than in inviscid analysis. In this case, the pressure distributions given by viscous analysis have numerical pseudo peaks at the leading edge of the GV, where the control cells are strongly deformed at the singular points. From this viewpoint, inviscid analysis yielded the better prediction, and it is necessary to improve the treatment of singular points of grid systems for the numerical method of viscous analysis. Numerical diffusion and dissipation due to truncation errors may also have the significant influence on the validation of this analysis. Reference calculation with a finer grid is performed in the case of $a/a_o = 1.00$. As a result, the predictions of static pressure seem to have good agreement between the different grids. But the difference in the variation level of total pressure is not small enough in the GV region. Generally speaking, a strongly nonorthogonal grid causes large numerical errors, and such a grid can be recognized in the GV region. For the precise prediction of energy loss in the cascade, it is necessary to verify numerical methods for strongly deformed grids.

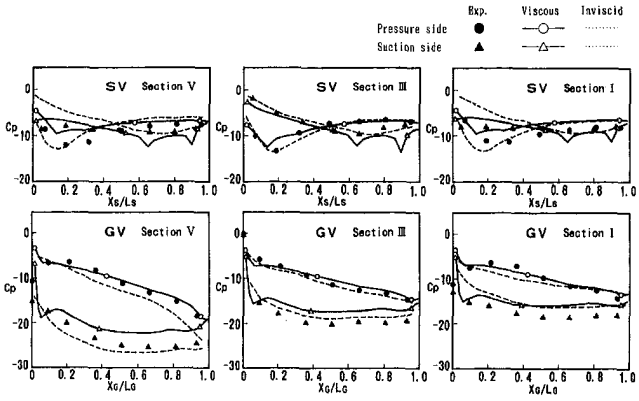


Fig. 10 Distribution of pressure coefficients for SV and GV at a/a_o = 1.00

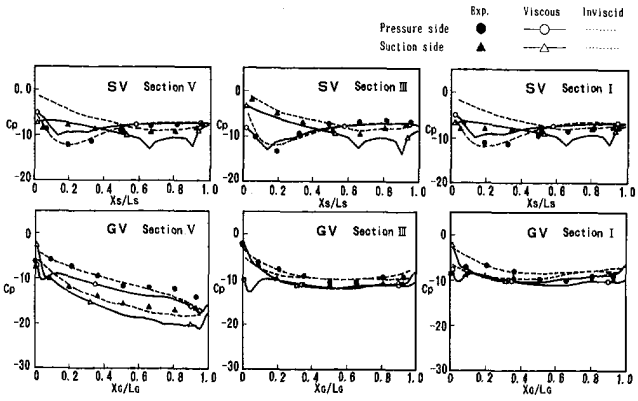


Fig. 11 Distribution of pressure coefficients for SV and GV at a/a_o = 1.33

Conclusions

The hydraulic behavior around the stayvanes and the guidevanes of a Francis turbine with high specific speed was studied experimentally and numerically in this paper. The three-dimensional pressure distributions on stayvane and guidevane surfaces, which were obtained by experiment, were compared with the numerical results of potential and viscous flow analyses.

Based on the experimental results, the flow behavior around stayvanes has no changeable characteristic related to the rotational speed of a runner and guidevane openings, and that around guidevanes can be influenced only by guidevane openings, having a strongly three-dimensional characteristic influenced by the geometry of the runner flow passage downstream.

From the numerical results obtained, it was demonstrated that inviscid analysis had the capability of a good prediction for three-dimensional flow behavior around the stayvanes and the guidevanes of the Francis turbine, except for the narrow regions closed at upper and lower walls where the viscous effect is strong. Viscous analysis offered some modifications in the prediction of three-dimensional characteristics made by inviscid analysis. The validity of viscous analysis is enhanced for separation flow, but the actual flow of the object did not indicate such separation. Viscous simulation also indicates that improvement in dealing with strong deformation of the computational grid is necessary.

References

Eriksson, L. E., Rizzi, A., and Therre, J. P., 1984, "Numerical Solutions of the Steady Incompressible Euler Equations Applied to Water Turbines," AIAA paper 84-2145.

Franke, G. F., Leitner, J. J., and Mount, A. G., 1983, "Application of Flow Analysis to Stay Vane and Wicket Gate Cascades for Hydraulic Turbines and Reversible Pump/Turbines," ASME Winter Annual Meeting, Boston, FED-Vol. 6, pp. 157–163.

Lauder, B. E., and Spalding, D. B., 1972, *Lectures in Mathmatical Models of Turblence,* Academic Press, London, pp. 90–110.

Matsumoto, K., Komiya, H., and Nagafuji, T., 1986, "Measurement and Prediction of the Pressure Distributions on Guide Vanes of a Francis Turbine," *Proceedings, 13th IAHR Symposium,* Montreal, Vol. 2, Paper No. 60.

Nagafuji, T., and Morii, H., 1980, "A Flow Study in Francis Turbine Runner," *Proceedings, 10th IAHR Symposium,* Tokyo, Vol. 1, pp. 583–594.

Patankar, S. V., 1980, *Numerical Heat Transfer and Fluid Flow,* Hemisphere Publishing, New York, pp. 113–135.

Rodi, W., 1980, "Turbulence Models and Their Applications in Hydraulics," IAHR State-of-the-Art Paper, Delft, pp. 26–33.

Taniguchi, N., Arakawa, C., Kobayashi, T., and Tagori, T., 1989, "Numerical Simulations of the Flow Around a Car with Finite Volume Method on General Co-ordinate System," *JSME Transaction,* Series B, Vol. 55, No. 518, pp. 3026–3032. (in Japanese).

Vu, T. C., Shyy, W., Braaten, M. E., and Reggio, M., 1986, "Recent Developments in Viscous Flow Analysis for Hydraulic Turbine Components," *Proceedings, 13th IAHR Symposium,* Montreal, Vol. 2, Paper No. 51.

Downloaded 03 Jun 2010 to 171.66.16.125. Redistribution subject to ASME license or copyright; see http://www.asme.org/terms/Terms_Use.cfm

Experimental and Computational Assessment of Windage Losses in Rotating Machinery

P. M. Wild

N. Djilali

G. W. Vickers

Department of Mechanical Engineering,
University of Victoria, Victoria, B. C.
Canada V8W 3P6

A combined experimental and computational investigation of the flow between a rotating cylinder and a fixed enclosure is presented. The configuration considered is related to the design of a centrifugal desalinator, and includes the flow in the annular as well as in the axial gap regions. The computed flowfield shows significant variations in the axial distribution of the azimuthal shear stress due to the secondary flow associated with Taylor vortices. The averaged azimuthal shear stress (or torque) is however not very sensitive to the number of vortices. Computational results also show that, where the aspect ratio of the annulus (rotor length to radial gap width) is relatively small, this azimuthal variation results in a higher average azimuthal shear stress than for the case where the aspect ratio of the annulus is relatively large. Various functional relations for windage torque of infinite cylinders, developed by other researchers on the basis of power law relations or assuming a log-law velocity distribution, are evaluated. Three such relations are found to be in good agreement with the experimental results when coupled with a correction for end effects. These relations are also the most useful with respect to the design of rotating equipment.

Introduction

The nature of flow in the annular gap between concentric cylinders, where the inner cylinder is rotating and the outer cylinder is stationary, is of general interest in many engineering applications, including the design of rotating equipment such as turbines, pumps, motors, generators and centrifuges as well as the design of the journal bearings which, in some cases, support these various rotors. The flow characteristics of interest vary with the application. In motor design, heat transfer and frictional losses are the key parameters while, in journal bearings, the pressure distribution and thus the load carrying capability are of particular interest. The authors' interest in this problem stems from the development of a sea water desalination technology, Centrifugal Reverse-Osmosis (CRO) (Wild et al., 1989, 1994), in which a centrifuge rotor is a key component. Windage losses are a significant component of the power consumption of this device and an assessment of the effect alternative design configurations have on these losses is therefore an essential component of the design process.

The flow between concentric rotating cylinders has been the subject of numerous studies since the early work of Taylor (1923, 1935) who reported on the transition from laminar Couette flow to laminar Taylor vortex flow, characterized by the formation of an array of toroidal vortices, beyond a critical value of the Reynolds or Taylor number. The spatial frequency of vortices depends on geometric and flow parameters, as well as on the manner of rotor acceleration. At Taylor numbers sufficiently higher than the critical value, instabilities in the form of azimuthal waves develop along the Taylor vortices (Coles, 1965, Fenstermacher et al., 1979, Shultz-Grunow and Hein, 1956). At still higher speeds, the wavy vortices give way to broad band spectrum turbulent flow, in which the vortex structure persists but the azimuthal oscillations are extinguished (Coles, 1965; Fenstermacher et al., 1960). Although extensive work has been done in this area, general criteria for the critical speed at which these upper transitions occur are not available.

As in the Taylor vortex flow regime, both the wavy and turbulent regimes are characterised by nonunique spatial frequencies. Coles' experiments (1965) showed that as many as twenty-six stable spatial states could exist at a given rotor speed. If the rotor is accelerated slowly from rest, there is a preferred spatial frequency called the primary mode. If the manner of rotor acceleration is varied, the resulting spatial frequency may be higher or lower, resulting in what are generally referred to as "anomalous modes" (Benjamin and Mullin, 1981). The non-uniqueness and bifurcation problems related to the determination of the spatial frequency of vortices have been the subject of numerous recent experimental, analytical and numerical studies, most notably by Coles (1965), Benjamin (1978a, 1978b), Mullin (1982), and Cliffe (1989).

Functional Relations for Moment Coefficient of an Infinite Cylinder. From a practical engineering standpoint, the most important issues are the determination of the nondimensional torque, or moment coefficient $C_{M_{CYL}}$ as a function of Reynolds number and annular gap width, and the assessment of end effects. For super critical speeds, the relations in the literature fall into two general categories. Relations falling into the first category assume that the moment coefficient is inversely proportional to the Reynolds number, taken to some power, i.e.

$$C_{M_{CYL}} \propto \mathrm{Re}^{-\alpha} \tag{1}$$

It can be shown that the relation for $C_{M_{CYL}}$ for laminar flow is a special case of this category where $\alpha = 1$ (Donnelly and Simon, 1960). Relations falling into the second category assume that the nature of the drag on the rotating cylinder is fundamentally related to the Prandtl-von Karman logarithmic velocity distributions and are, therefore, characterized by a relation of the form,

$$\frac{1}{\sqrt{C_{M_{CYL}}}} = A + B \ln\left(\mathrm{Re}\sqrt{C_{M_{CYL}}}\right) \tag{2}$$

where A and B are constants.

Contributed by the Fluids Engineering Division for publication in the JOURNAL OF FLUIDS ENGINEERING. Manuscript received by the Fluids Engineering Division November 3, 1994; revised manuscript received August 9, 1995. Associate Technical Editor: L. Nelik.

Copyright © 1996 by ASME

Downloaded 03 Jun 2010 to 171.66.16.125. Redistribution subject to ASME license or copyright; see http://www.asme.org/terms/Terms_Use.cfm

The earliest published relations of the first category were reported in an early experimental study by Wendt (1933), who found that, for supercritical speeds, the moment coefficient varies as $Re^{-0.5}$ for $400 < Re < 10^4$, and as $Re^{-0.3}$ for $Re > 10^4$. Stuart (1958) developed a relation for the moment coefficient for speeds greater than but close to the critical speed and, based on experimental data, Donelly (1960) used a two parameter expression to recast Stuart's solution to apply over a range of supercritical speeds of up to several hundred times the critical speed. Donelly was able to achieve good fits with measurements from a variety of studies. However, the method is of limited practical use because the empirical parameters need to be determined anew for each configuration. Bilgen and Boulos (1973) also attempted to reassess the functional relationship between torque and Reynolds number, and in fact obtained an expression almost identical to that of Wendt (1933). In a recent paper, Lathrop et al. (1992) used a high resolution torque measurement apparatus to investigate large Reynolds number flow. They found that, in fact, the exponent, α, is not constant, but rather varies continuously over two ranges of Reynolds numbers, and they inferred an abrupt change in the exponent at yet another "critical" Reynolds number. Re-examination of Wendt's data confirmed this discontinuous variation.

The earliest relation of the second category was reported by Theodorsen and Regier (1944) who successfully applied the log-law to the open rotating cylinder problem. The enclosed cylinder problem was first considered by Gazely (1958) followed by Vrancick (1968), Ustimenko (cited in Genium, 1969) and, more recently, by Lathrop (1992). Generally good agreement with experimental data was obtained in all studies.

Amongst the relations of both categories, only Wendt, Bilgen and Boulos, Ustimenko and Lathrop include coefficients which are a function of the ratio of the annular gap width to the rotor radius. Only these relations, therefore, have the potential to be applied broadly to a variety of geometries. The moment coefficients calculated from these relations are shown in Fig. 1 for two ratios of radial gap width to rotor radius. With the exception of Lathrop (not plotted), these relations show reasonable agreement over a range of Reynolds numbers.

The Finite Cylinder and "End Effects." Most of the work on Taylor flow neglects the effect of the rotor ends by assuming cylinders of infinite length, and relatively few studies have addressed the complications which the rotor ends introduce. The influence of end effects on Taylor vortex formation and transition was first investigated by Cole (1976). He showed that the onset of wavy vortices was relatively sensitive to rotor length whereas the onset of steady Taylor vortices was not. Burkhalter and Koschmieder (1973) showed that the length of the vortex cells at the ends of an annulus was a function of both rotor speed and of the conditions at the ends of the annulus. Schaefer (1980) and Cliffe and Mullin (1985) have conducted

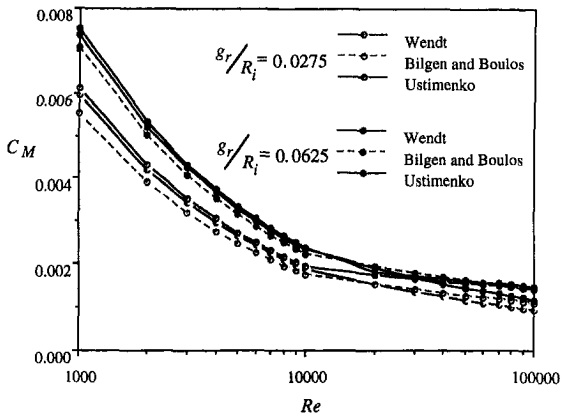


Fig. 1 Calculated moment coefficients using infinite cylinder relations

numerical investigations of the influence of end effects on the stability of anomalous modes. There is, however, no literature which deals directly with the influence of end-gaps on windage torque.

In this paper, a combined experimental and numerical study of turbulent Taylor vortex flow is presented. Experiments are conducted for two relatively low ratios of radial gap width to rotor radius. The computational model accounts for both the finite rotor length and end-gaps between the rotor enclosure.

Computational Analysis

Problem Formulation. The geometry for the rotor-enclosure system is shown in Fig. 2. The flow is assumed to be steady, incompressible and turbulent, and all fluid properties are assumed constant. The flow is also assumed to be axisymmetric, and the problem can therefore be treated as two-dimensional, in the sense that gradients in the azimuthal direction

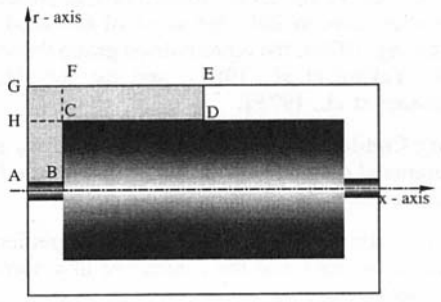


Fig. 2 Computational domain

Nomenclature

C_M = moment coefficient due to entire surface of rotor ($= M_C + M_E/\pi\rho\omega^2 R_i^4 L$)
$C_{M_{CYL}}$ = moment coefficient due to cylindrical surface of rotor ($= M_C/\pi\rho\omega^2 R_i^4 L$)
$C_{M_{DISC}}$ = moment coefficient due to a disc (or rotor ends) ($= M_E/\pi\rho\omega^2 R_i^4 L$)
g_r = radial gap ($= R_o - R_i$)
g_a = axial gap
k = turbulent kinetic energy
L = length of rotor
M_C = moment on outer cylindrical surface of rotor
M_E = moment on ends of rotor
Re = Couette Reynolds number ($= \rho\omega R_i g_r/\mu$)
R_i = inner radius of rotor enclosure
R_o = outer radius of rotor
S_ϕ = source term in transport equations
u_τ = friction velocity ($= \sqrt{\tau_w/\rho}$)
y^+ = nondimensional displacement from the wall ($= yu_\tau/\nu$)
u, v, w = axial, radial and azimuthal velocities
$x, r, \theta,$ = axial, radial and azimuthal coordinates
ϵ = dissipation rate of turbulent kinetic energy
μ_{eff} = effective viscosity ($= \mu + \mu_t$)
μ = dynamic viscosity
μ_t = eddy viscosity
ρ = density of fluid
τ_w = shear stress at rotor surface
ω = angular velocity of rotor

Downloaded 03 Jun 2010 to 171.66.16.125. Redistribution subject to ASME license or copyright; see http://www.asme.org/terms/Terms_Use.cfm

Table 1 Source terms in momentum equations

ϕ	S_ϕ
u	$-\frac{\partial p}{\partial x}$
v	$-\frac{\partial p}{\partial r}+\rho\frac{w^2}{r}-\mu_{eff}\frac{v}{r^2}$
w	$-\rho\frac{vw}{r}-\mu_{eff}\frac{w}{r^2}$

are neglected, but all three velocity components are taken into account. With these assumptions, the time-averaged mass and momentum conservation equations may be written as:

$$\frac{\partial}{\partial x}(\rho u)+\frac{1}{r}\frac{\partial}{\partial r}(\rho r v)=0 \tag{3}$$

$$\frac{1}{r}\left[\frac{\partial}{\partial x}(\rho r u\phi)+\frac{\partial}{\partial r}(\rho r v\phi)\right]$$

$$=\frac{\partial}{\partial x}\left(\mu_{eff}\frac{\partial\phi}{\partial x}\right)+\frac{1}{r}\frac{\partial}{\partial r}\left(r\mu_{eff}\frac{\partial\phi}{\partial r}\right)+S_\phi \tag{4}$$

where $\phi = u, v, w$, respectively, for the three momentum equations in the x, r, and θ directions and S_ϕ is the source term defined in Table 1 for the three components of velocity. μ_{eff} is the sum of the laminar viscosity and turbulent eddy viscosity,

$$\mu_{eff}=\mu+\mu_t. \tag{5}$$

The turbulent eddy viscosity μ_t is obtained from the Prandt-Kolmogorov relation

$$\mu_t=C_\mu\rho\frac{k^2}{\epsilon} \tag{6}$$

where C_μ is an empirically determined constant and the turbulent kinetic energy, k, and its dissipation rate, ϵ, are determined using three alternative models: the standard $k-\epsilon$ model (Launder and Spalding, 1974), the renormalised group theory (RNG) $k-\epsilon$ model (Yakhot et al., 1986), and the Reynolds Stress Model (Launder et al., 1975).

Boundary Conditions. The governing equations are solved in a computational domain shown in Fig. 2, with the following boundary conditions:

(i) At the axis of symmetry, the normal gradients of all variables are set to zero, and the convective flux normal to the boundary is set to zero.

(ii) No slip condition is imposed at all walls for the velocity; the equilibrium wall function treatment (Launder and Spalding, 1974) is adopted to bridge the viscous sublayer. To ensure proper implementation of the wall functions, the grid points

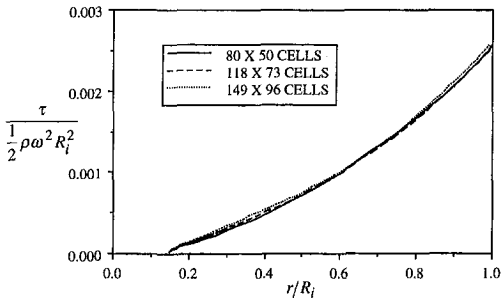


Fig. 3 Effect of grid refinement on computed rotor-end shear stress

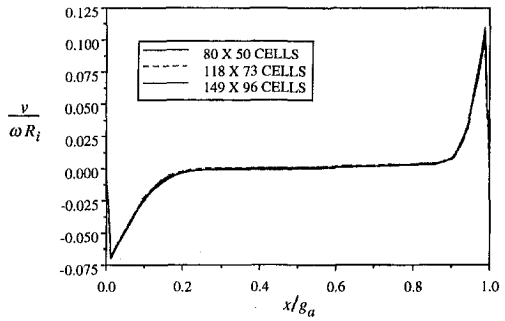


Fig. 4 Effect of grid refinement on computed radial velocity profile in end-gap region

adjacent to solid boundaries were located such that $30 \le (y^+ = yu_\tau/v) \le 100$.

Numerical Solution and Grid Refinement. The equations were solved using the finite volume code FLUENT (Fluent Inc., 1992). This code uses a collocated grid method. The higher order QUICK discretization scheme was employed in conjunction with the SIMPLEC algorithm. A block iterative solution method was used together with a multigrid procedure to accelerate convergence. The calculation procedure was terminated when the normalized residuals were less than 5×10^{-4}. The grid sensitivity of the solutions was assessed at a Couette Reynolds number of 1.7×10^4 (corresponding to 5000 rpm).

Grid refinement was conducted in two stages. First computations were performed for a non-uniform base grid of 80×50, and two successive refinements were performed. The predicted flow field and shear stresses in the radial gap region (CDEF) varied significantly, but the predictions in the axial gap region (ABFG) were essentially identical for the three grids, as shown in Figs. 3 and 4.

Based on these results, a second series of grid refinements was performed in the annular region (DEGH), while keeping the same 18×34 subgrid of the 80×50 grid in the axial gap region (ABCH). The results of this series of grid refinements are summarized in Table 2 in terms of the calculated windage torque for the different surfaces. The streamline patterns obtained with the intermediate grid, shown in Fig. 5, clearly depict the Taylor vortices in the radial gap and the large counterclockwise vortex in the axial gap. The number of vortices obtained with all three grids was identical, but noticeable differences were observed in the wavelengths, particularly for lower grid densities, as shown by the axial distribution of the azimuthal shear stresses presented in Fig. 6(a). When summed along the cylinder, however, the total torque due to this shear stress shows a maximum variation of less than 2 percent from the coarsest to the finest grid, as shown in Table 2. This is consistent with Cole (1974) who found that measured torque was not affected by the number of Taylor vortices occurring at a given speed.

The effect of grid refinement on the radial component of velocity, along the centerline of the radial gap, shows a similar axial distribution, as shown in Fig. 6(b). Again, the variation

Table 2 Average torque (N-m) for each wall segment for four grid densities (5000 rpm)

	Wall segment designations			
Grid size	B-C	C-D	G-E	A-G
109 × 56	−1.93E-02	−7.60E-02	8.35E-02	8.78E-03
140 × 56	−1.93E-02	−7.60E-02	8.41E-02	8.72E-03
170 × 56	−1.93E-02	−7.55E-02	8.38E-02	8.73E-03
230 × 56	−1.93E-02	−7.48E-02	8.29E-03	8.75E-03

Downloaded 03 Jun 2010 to 171.66.16.125. Redistribution subject to ASME license or copyright; see http://www.asme.org/terms/Terms_Use.cfm

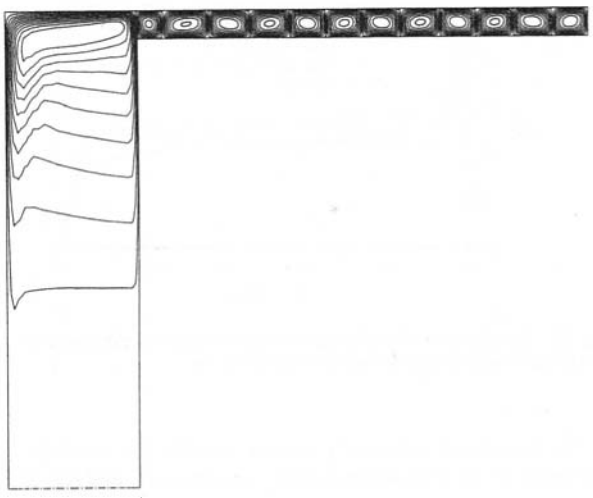


Fig. 5 Computed streamline patterns in the annular and end-gap regions

in wavelengths is noticeable from grid to grid. Also note that the amplitude of the radial velocity component is not negligible, as would be assumed in one-dimensional flow, and is on the order of 7.5 percent of the tangential velocity of the rotating cylinder.

Based on the relative grid-independence of the calculated torques, the intermediate grid, 140 × 56 was selected for parametric studies of the effects of Reynolds number, radial gap width and rotor length.

Experimental Apparatus and Procedure

An experimental test rig was designed and built, consisting of a drive motor connected via a belt drive to a cantilevered cylindrical rotor, housed in a stationary cylindrical enclosure, as shown in Fig. 7. The rotor enclosure is mounted on bearings at either end, and it is restrained from rotating by a length of 0.125 × 1 inch aluminum flat bar. For future work, the enclosure bearings are mounted on vertical and horizontal slides which allow the enclosure to be set eccentric to the rotor. The reaction torque of the rotor enclosure due to windage is measured via strain gages on the flat bar. The dimensions of the rotor and rotor enclosure were determined from similarity considerations with respect to proposed desalinator designs and are shown in Table 3. The maximum operating speed of the rotor was 4750 rpm. The surfaces of the rotor and enclosure are machined to approximately 32 microinches of roughness. Torque data was taken repeatedly at 500 rpm intervals and the resulting moment coefficients were determined to have an uncertainty interval of ±0.00012 (odds of 20 to 1).

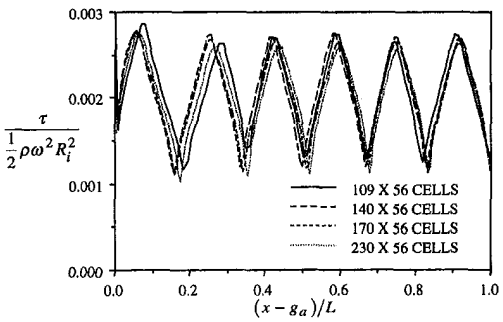


Fig. 6(a)

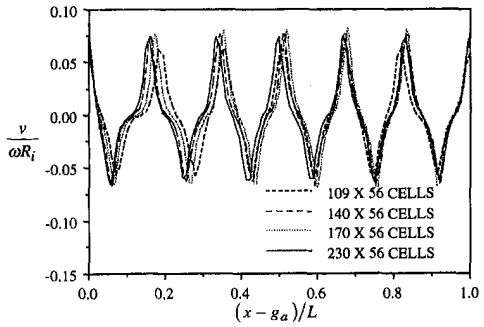


Fig. 6(b)

Fig. 6 Effect of grid refinement on (a) computed azimuthal shear stress along the rotor surface, and (b) on computed radial velocity along center line of radial gap

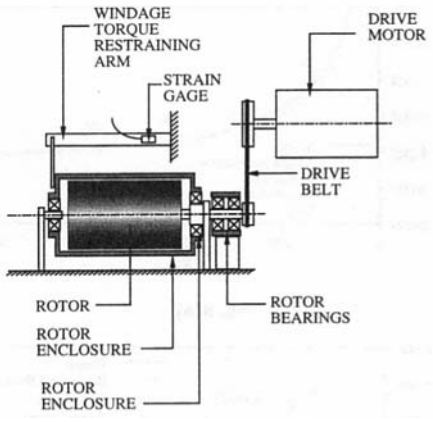


Fig. 7 Schematic view of experimental apparatus

Discussion

Comparison of Windage Data Determined From Functional Relations, CFD Analysis, and Experiments. The moment coefficients computed using the $k-\epsilon$ model are compared to measured data and to the relations of Wendt (1933), Bilgen and Boulos (1973), and Ustimenko (cited in Genium, 1969) in Figs. 8(*a*) and (*b*). Since these relations are for infinite cylinders, a correction for end effects was added. Following Schlichting (1960), the additional torque due to end effects is assumed to be equal to that of an enclosed thin disk. The experimental data for $g_r/R_i = 0.0275$ spans $5{,}000 < \mathrm{Re} < 17{,}000$ and the data for $g_r/R_i = 0.0625$ spans $18{,}000 < \mathrm{Re} < 35{,}000$.

The semi-empirical relations and experiments are in relatively good agreement, while the present computations give values

Table 3 Test rig and rotor enclosure dimensions (all dimensions ± 0.002 in., max. run out 0.004 in.)

	Small rotor	Large rotor
Rotor radius (R_i)	0.1284 m (5.059 in)	0.1328 m (5.231 in)
Housing inner radius (R_o)	0.1364 m (5.375 in)	0.1364 m (5.375 in)
Radial gap width (g_r)	0.008 m (0.316 in)	0.0036 m (0.144 in)
Radial gap width to rotor radius Ratio (gr/R_i)	0.0625	0.0275
Rotor length (L)	0.2568 m (10.118 in)	0.2656 m (10.463 in)
Axial gap width (g_a)	0.0381 m (1.5 in)	0.0381 m (1.5 in)

Downloaded 03 Jun 2010 to 171.66.16.125. Redistribution subject to ASME license or copyright; see http://www.asme.org/terms/Terms_Use.cfm

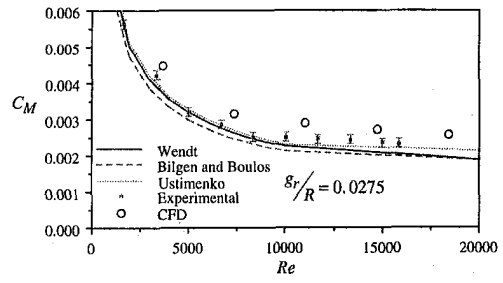


Fig. 8(*a*)

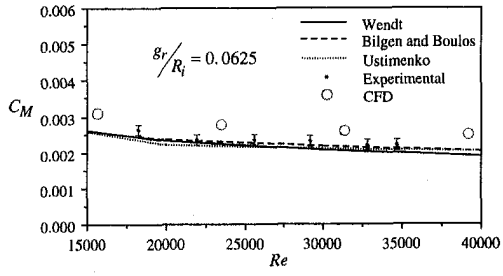


Fig. 8(*b*)

Fig. 8 Comparison of computed, measured and calculated moment coefficients: (*a*) $g_r/R = 0.0275$; (*b*) $g_r/R_i = 0.0625$

which are consistently on the order of 10 percent higher than the experiments. Between 25 and 27 percent of the CFD generated moment coefficients shown in Figs. 8 and 9 is due to the moments on the end surfaces of the rotor whereas, for the functional relations, between 15.5 and 18.5 percent of the moment coefficients is due to the moments on the end surfaces. In order to eliminate any inconsistencies which these differences may be introducing, the CFD data and data calculated after Wendt, for the cylindrical surface of the rotor only, are plotted in Figs. 9(*a*) and (*b*). The spread between these data sets is not significantly different than the spread shown in Figs. 8(*a*) and (*b*).

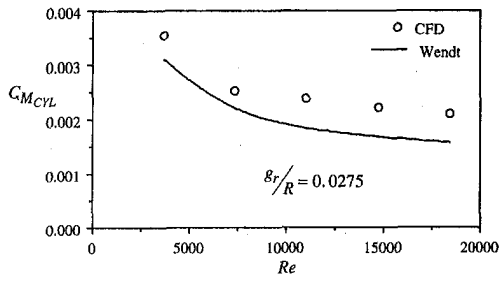


Fig. 9(*a*)

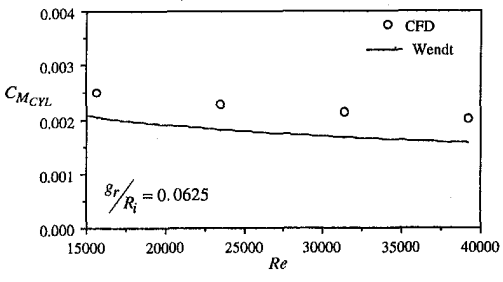


Fig. 9(*b*)

Fig. 9 Cylindrical moment coefficient versus reynolds number: (*a*) $g_r/R = 0.0275$; (*b*) $g_r/R_i = 0.0625$

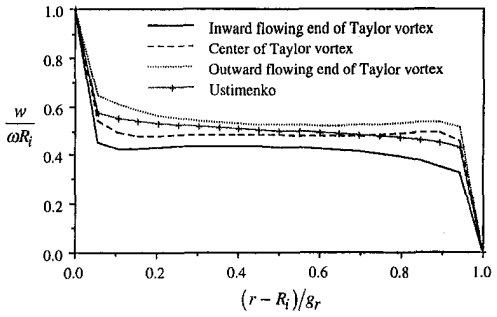


Fig. 10 Comparison of computed azimuthal velocity profiles with log-law profile used in infinite cylinder calculations

The functional relations based on various forms of the log-law assume one-dimensional flow, i.e., the axial and radial gradients associated with the Taylor vortices are neglected. Comparison of the log-law profile used by Ustimenko (cited in Genium, 1969) with computed profiles at three different location in the Taylor vortex at the end of the rotor are presented in Fig. 10. The log-law profile is fairly representative of the average CFD profiles, but does not reproduce the overshoots shown by the CFD profiles near the rotor and enclosure. The higher gradients and shear stresses associated with these overshoots are consistent with the discrepancy between computed and theoretical moment coefficients.

Alternative Turbulence Models. Computations were also performed using the RNG turbulence model (Yakhot and Orzag, 1986), both with and without a wall function, and using the RSM turbulence model (Launder et al., 1975), with a wall function. Where the wall function was used the torques determined using the RNG model were within 2 percent of the torques determined from the standard $k-\epsilon$ model. However, the torques determined using the RSM model were on the order of 40 percent higher than the torques determined from the standard $k-\epsilon$ model. Where the grid was refined so as to allow the RNG model to extend to the wall, the resulting torques were, again, on the order of 40 percent higher than the torques determined from the standard $k-\epsilon$ model. These results are somewhat disappointing in view of the fact that both the RNG and RSM models are defined so as to account for the non-isotropy of strain rates associated with high curvatures and swirl.

Parametric Study of Annulus Length Effects. In most experimental windage studies, the ratios of rotor length to rotor radius and to radial gap-width are set relatively high so as to minimize the effects of the rotor ends and, thereby, to approximate an infinite annulus. The torque due to the rotor ends is either neglected or is, in some manner, estimated and then subtracted from the total rotor torque. The functional relations discussed earlier are based upon data of this kind. In many engineering applications, however, these ratios are relatively low and the contribution to total rotor torque which is due to the rotor ends can be quite significant. If windage torque of such a rotor design is to be estimated using functional relations, the torque due to the rotor ends must also be approximated by a functional relation. In addition, it must be assumed that the interaction between the flow in the axial gap and in the annular gap is negligible.

Using the current CFD model, a numerical study of the effect of annulus aspect ratio (rotor length to radial gap width) on the average windage torque at the outer cylindrical surface of the rotor and on the windage torque at the rotor ends was conducted. Although, as discussed earlier, the quantitative results from the current CFD model are not in complete agreement with the experimental data, the model has shown sufficient accuracy that the trends shown in this study are expected to be reliable. The

Downloaded 03 Jun 2010 to 171.66.16.125. Redistribution subject to ASME license or copyright; see http://www.asme.org/terms/Terms_Use.cfm

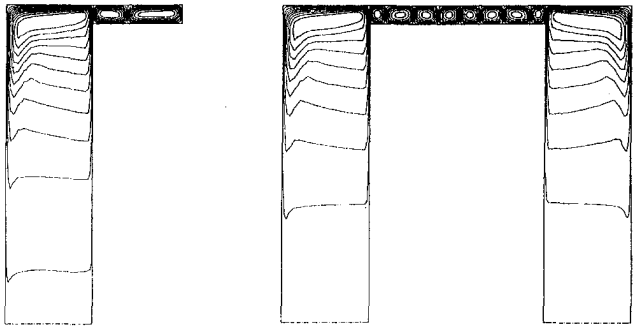


Fig. 11 Stream function patterns for half and full rotor models $(L/2)/g_r = 4.8$

grid density of the 140 × 56 grid was maintained throughout this study.

The results of this study showed that the moment coefficients determined from the half-rotor model, shown in Fig. 2, are erroneous for small annulus aspect ratios. Throughout this work, the symmetry boundary condition at D-E consistently results in an outward flowing Taylor cell, along the boundary D-E. This condition, which is clearly not a physical but rather a numerical phenomenon, restricts the total number of Taylor cells, over the entire length of the rotor, to a multiple of four. A complete Taylor cell is here defined as a single toroidal cell. In the absence of this condition, the total number of Taylor cells can be any multiple of two, excepting anomalous modes (Benjamin and Mullin, 1981). Where the annulus aspect ratio is sufficiently high, this condition does not significantly affect either the individual cell structure or the average azimuthal shear stress. Where the annulus aspect ratio is sufficiently low, however, the individual cell structure becomes distorted, as is shown by comparison of the stream function patterns for the half rotor model with the results from a full-rotor model, as shown in Fig. 11.

The resulting average azimuthal shear stress is underestimated by the half rotor model. This is shown by the divergence of the moment coefficient due to the outer cylindrical surface, $C_{M_{CYL}}$, for the half and full rotor models, shown in Fig. 12(*a*).

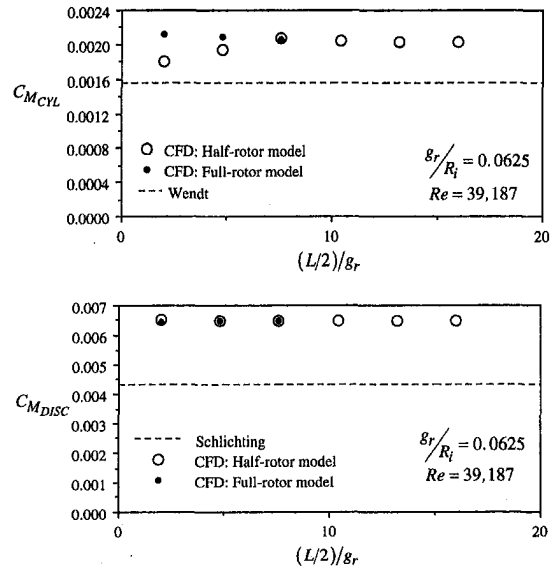


Fig. 12 Variation of moment coefficients with annulus aspect ratio: (*a*) cylindrical surface moment coefficient, (*b*) disk moment coefficient due to torque of rotor end

Neglecting the erroneous half-rotor data, $C_{M_{CYL}}$ is a mildly decreasing function of annulus aspect ratio at relatively low annulus aspect ratios. At higher annulus aspect ratio, the moment coefficient is relatively independent of annulus aspect ratio. The average azimuthal shear stress over the outer two Taylor cells (see the left-most peak in Fig. 6) is higher than the average azimuthal shear stress over the inner cells. As the annulus aspect ratio is increased the effect of these first cells becomes increasingly insignificant. As, however, the annulus aspect ratio becomes increasingly low, these cells significantly elevate the average azimuthal shear stress. The data calculated after Wendt (1933) is, of course, fully independent of rotor length.

The torque on the rotor ends, as determined by the numerical analysis, is relatively independent of the modeled flow in the annular region. As shown in Fig. 12(*b*), the moment coefficients due to the rotor ends, $C_{M_{DISC}}$, are sensitive neither to the annulus aspect ratio nor to the type of numerical model, namely: full or half rotor model. The data calculated after Schlichting (1960) is, of course, independent of annulus aspect ratio.

Concluding Remarks

A computational model of the flow in the annular and axial gaps of a rotor/enclosure arrangement is presented together with experimental torque measurements. The results are compared to various semi-empirical torque calculation methods. The main conclusions are:

- The windage torques computed with the standard $k-\epsilon$ turbulence model are in relatively good agreement (consistently on the order of 10 percent higher) with the experimental data over the range of Couette Reynolds numbers considered.
- The Taylor vortices result in significant axial variations of the azimuthal shear stress distribution but where the annulus aspect ratio is relatively large, this variation is averaged over the length of the rotor, and the resulting torque on the rotor is relatively insensitive to the number of vortices.
- Where the annulus aspect ratio is relatively small, the variation of the azimuthal shear stress results in a higher average azimuthal shear stress than for the case where the annulus aspect ratio is relatively large.
- Of the various functional relations for windage torque, those of Wendt (1933), Bilgen and Boulos (1973) and Ustimenko (cited in Genium, 1969) are the most broadly applicable and these relations, coupled with Schlichting's (1960) relation applied to the rotor ends, show good agreement with the experimental results.

Acknowledgment

The authors wish to thank Professor Frank White for his very useful comments and suggestions on an earlier version of this paper presented at the 1994 ASME Fluids Engineering Summer Meeting.

References

Benjamin, T. B., 1978a, "Bifurcation Phenomena in Steady Flows of a Viscous Liquid. I. Theory," *Proc. Royal Soc.* Series A, Vol. 359, pp. 1–26.

Benjamin, T. B., 1978b, "Bifurcation Phenomena in Steady Flows of a Viscous Liquid. II. Experiments," *Proc. Royal Soc.*, Series A, Vol. 359, pp. 27–43.

Benjamin, T. B., Mullin, T., 1981, "Anomalous Modes in the Taylor Experiment," *Proceedings of the Royal Society of London*, Vol. 377, Part A, pp. 221–249.

Bilgen, E., Boulos, R., 1973, "Functional Dependence of Torque Coefficient of Coaxial Cylinders on Gap Width and Reynolds Numbers," ASME JOURNAL OF FLUIDS ENGINEERING, pp. 122–126.

Burkhalter, J. E., and Koschmieder, E. L., 1973, "Steady Supercritical Flow," *Journal of Fluid Mechanics*, Vol. 53, Part 3, pp. 547–560.

Cliffe, K. A., Mullin, T., 1985, "A Numerical and Experimental Study of Anolmalous Modes in the Taylor Experiment," *Journal of Fluid Mechanics*, Vol. 153, pp. 243–258.

Cliffe, K. A., 1989, "Numerical Calculations of Primary Flow Exchange Process in the Taylor Problem," *Journal of Fluid Mechanics*, Vol. 197, pp. 57–79.20.

Downloaded 03 Jun 2010 to 171.66.16.125. Redistribution subject to ASME license or copyright; see http://www.asme.org/terms/Terms_Use.cfm

Cole, J. A., 1974, "Taylor Vortex Behaviour In Annular Clearances of Limited Length," *Proceedings of the Fifth Australasian Conference on Hydraulics and Fluid Mechanics,* Christchurch, New Zealand, pp. 514–521.

Cole, J. A., 1976, "Taylor Vortex Instability and Annulus Length Effects," *Journal of Fluid Mechanics,* Vol. 75, Part 1, pp. 1–15.

Coles, D., 1965, "Transition in Circular Couette Flow," *Journal of Fluid Mechanics,* Vol. 21, pp. 385–425.

Donelly, R. J., and Simon, N. J., 1960, "An Empirical Torque Relation for Supercritical Flow Between Rotating Cylinders," *Journal of Fluid Mechanics,* Vol. 7, p. 401.

Fenstermacher, P. R., Swinney, H. L., and Gollub, J. B., 1979, "Dynamical Instabilities and the Transition of Chaotic Taylor Vortex Flow," *Journal of Fluid Mechanics,* Vol. 24, Part 1, pp. 103–128.

Fluent Inc., 1992, *Fluent Users Guide,* New Hampshire.

Genium Publishing Corporation, 1969, *Fluid Flow Data Book.*

Gazely, C., 1958, "Heat Transfer Characteristics of the Rotational and Axial Flow Between Concentric Cylinders," *Trans. ASME,* pp. 79–89.

Lathrop, D. P., Fineberg, J., and Swinney, H. L., 1992, "Turbulent Flow Between Concentric Rotating Cylinders at Large Reynolds Number," *Physical Review Letters,* Vol. 68, No. 10, pp. 1515–1518.

Launder, B. E., and Spalding, D. B., 1974, "The Numerical Computation of Turbulent Flow," *Comp. Meths. Appl. Mech. Engng.,* Vol. 3, pp. 269–289.

Launder, B. E., Reece, G. J., and Rodi, W., 1975, "Progress In the Developent of a Reynolds-Stress Turbulence Closure," *Journal of Fluid Mechanics,* Vol. 68, Part 3, pp. 537–566.

Mullin, T., 1982, "Mutations of Steady Cellular Flows in the Taylor Experiment," *Journal of Fluid Mechanics,* Vol. 121, pp. 207–218.

Schaefer, D. G., 1980, "Qualitative Analysis of a Model for Boudary Effects in the Taylor Problem," *Mathematical Proceedings of the Cambridge Philosophical Society,* Vol. 87, pp. 307–337.

Schlichting, H., 1960, *Boundary Layer Theory,* 4th ed., McGraw-Hill, New York, p. 547.

Shultz-Grunow, F., and Hein, H., 1956, "Bietrag zur Couettestromung," *Zeitschrift fur Flugwissenshaften,* Vol. 4, pp. 28–30.

Stuart, T. J., 1958, "On the Non-Linear Mechanics of Hydrodynamic Stability," *Journal of Fluid Mechanics,* Vol. 4, pp. 1–21.

Taylor, G. I., 1923, "Fluid Friction Between Rotating Cylinders," *Philosophical Transactions of the Royal Society of London,* Vol. 223, Feb. 8, pp. 289–343.

Taylor, G. I., 1935, "Distribution of Velocity and Temperature Between Concentric Rotating Cylinders," *Proceedings of the Royal Society of London,* Series A, Vol. 151, No. 874, pp. 494–512.

Theodorsen, T., and Regier, A., 1944, "Experiments on Drag of Revolving Disks, Cylinders, and Streamline Rods at High Speeds," *NACA Report No. 793.*

Vrancik, J. E., 1968, "Prediction of Windage Power Loss in Alternators," *NASA Technical Memorandum D-4849.*

Wendt, F., 1933, "Turbulente Stromungen Zwishen Zwei Rotierender Konaxialen Zylindern," *Ingenieur-Archiv,* Vol. IV, p. 577.

Wild, P. M., Vickers, G. W., Moilliet, A., and Hopkin, D. A., 1989, Centrifugal Reverse-Osmosis Desalination Unit, U.S. Patent No. 4,886,597.

Wild, P. M., 1994, "Development, Optimization and Implementation of the Design for a Centrifugal Reverse-Osmosis Desalination System," Ph.D. thesis, Dept. of Mech. Eng., University of Victoria.

Yakhot, V., and Orszag, S., 1986, "Renormalization Group Analysis of Turbulence," *Journal of Scientific Computing,* Vol. 1, No. 1, pp. 3–57.

Downloaded 03 Jun 2010 to 171.66.16.125. Redistribution subject to ASME license or copyright; see http://www.asme.org/terms/Terms_Use.cfm

Study of Vaneless Diffuser Rotating Stall Based on Two-Dimensional Inviscid Flow Analysis

Yoshinobu Tsujimoto
Professor.

Yoshiki Yoshida
Associate Professor.

Osaka University, Engineering Science,
Toyonaka, Osaka, 560 Japan

Yasumasa Mori
Researcher,
Mitsubishi Motors Corporation,
Ohta, Tokyo, 146 Japan

Rotating stalls in vaneless diffusers are studied from the viewpoint that they are basically two-dimensional inviscid flow instability under the boundary conditions of vanishing velocity disturbance at the diffuser inlet and of vanishing pressure disturbance at the diffuser outlet. The linear analysis in the present report shows that the critical flow angle and the propagation velocity are functions of only the diffuser radius ratio. It is shown that the present analysis can reproduce most of the general characteristics observed in experiments: critical flow angle, propagation velocity, velocity, and pressure disturbance fields. It is shown that the vanishing velocity disturbance at the diffuser inlet is caused by the nature of impellers as a "resistance" and an "inertial resistance," which is generally strong enough to suppress the velocity disturbance at the diffuser inlet. This explains the general experimental observations that vaneless diffuser rotating stalls are not largely affected by the impeller.

Introduction

As we decrease the flow angle in vaneless diffusers, we observe a nonaxisymetric flow pattern rotating with a significantly slower velocity than the tangential mean velocity at the inlet. From the similarity to that in axial flow impellers, this is called "rotating stall" and extensive studies has been made. Jansen (1964) made a two-dimensional inviscid flow analysis using several assumptions and found that inward flow is destabilizing for the case of irrotational flow. Based on this study, Senoo et al. (1977) made an axisymmetric boundary layer analysis and correlated the onset of rotating stall with the reverse flow in the boundary layer. Similar approach was also taken by Tsurusaki et al. (1986). Although this method can predict the critical flow angle fairly well, no explanation has been given to the flow mechanism under the rotating stall.

One of the authors (1987) found that, by a two-dimensional flow analysis, a flow instability similar to vaneless diffuser rotating stall may occur even with outward mean flow. In the present study, it is shown that the onset condition and the propagating velocity ratio are functions of only the radius ratio of the diffuser for the most cases. The effect of the upstream impeller is also discussed. In order to see the validity of the model, onset conditions, propagating velocity ratio, pressure and velocity fields in the vaneless diffuser are compared with experiments.

Similar analyses have been made by Abdelhamid (1980) and Moore (1989), under completely the same conditions and assumptions. Although the method of analysis is different, it is confirmed that the present numerical results agree with those studies. What is new in the present study is the elucidation of the effect of impeller and the understanding of the results based on a simplification of the impeller effect. To the authors' knowledge, the present paper gives the first close comparison with experiments.

Contributed by the Fluids Engineering Division for publication in the JOURNAL OF FLUIDS ENGINEERING. Manuscript received by the Fluids Engineering Division November 9, 1994; revised manuscript received July 7, 1995. Associate Technical Editor: L. Nelik.

Theoretical Model

We consider a two-dimensional vaneless diffuser with outer radius r_3, downstream of an centrifugal impeller with inner and outer radii r_1 and r_2, vane angle β and with infinite number of vanes, rotating with an angular velocity Ω. We work in a stationary frame $z = x + iy = re^{i\theta}$ with its origin at the center of the impeller and diffuser, as shown in Fig. 1. It is assumed that the flow is inviscid and incompressible and that the disturbance is so small that we can make linear analysis.

The unsteady components are represented, for example, by

$$v_r = \tilde{v}_r(r) \exp\{j(\omega t - n\theta)\}$$
$$v_\theta = \tilde{v}_\theta(r) \exp\{j(\omega t - n\theta)\} \quad (1)$$

with an imaginary unit j with respect to time t, the angular frequency ω and the number of rotating stall cell n.

Flows in Vaneless Diffuser. It is assumed that the vorticity is transported on the steady flow $(V_r, V_\theta) = (Q/2\pi r, \Gamma/2\pi r)$ in the vaneless diffuser $(r_2 \leq r \leq r_3)$. Then the linearized vorticity transport equation has a solution represented by

$$\zeta = \tilde{\zeta}_2 \exp\left\{ j\omega\left[t - \frac{\pi}{Q}(r^2 - r_2^2) \right] - jn\left[\theta - \frac{\Gamma}{Q}\log\left(\frac{r}{r_2}\right) \right] \right\} \quad (2)$$

where Q is the flow rate, $\Gamma \equiv 2\pi r_2\{r_2\Omega - (Q/2\pi r_2)\cot\beta\}$ is the circulation of the upstream impeller. The velocity field induced by the vorticity of Eq. (2) can be represented by:

$$v_r^\zeta = \tilde{\zeta}_2(R_R - jR_I) \exp\{j(\omega t - n\theta)\}$$
$$v_\theta^\zeta = \tilde{\zeta}_2(\Theta_R - j\Theta_I) \exp\{j(\omega t - n\theta)\} \quad (3)$$

where

$$R_R - jR_I = -j(F + G), \quad \Theta_R - j\Theta_I = F - G$$

Copyright © 1996 by ASME

Downloaded 03 Jun 2010 to 171.66.16.125. Redistribution subject to ASME license or copyright; see http://www.asme.org/terms/Terms_Use.cfm

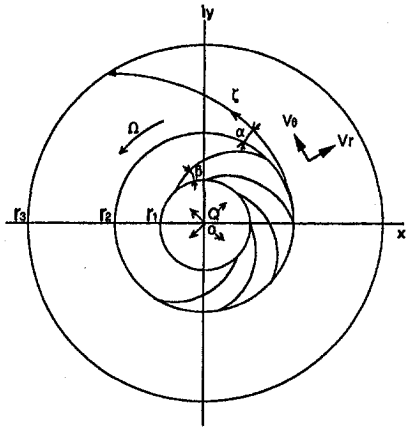


Fig. 1 Impeller and vaneless diffuser

and

$$F(r) = \frac{1}{2}\int_{r_2}^{r} \exp\left\{-j\left[\omega\frac{\pi}{Q}(r_0^2 - r_2^2) - n\frac{\Gamma}{Q}\log\left(\frac{r_0}{r_2}\right)\right]\right\}\left(\frac{r_0}{r}\right)^{n+1} dr_0$$

$$G(r) = \frac{1}{2}\int_{r}^{r_3} \exp\left\{-j\left[\omega\frac{\pi}{Q}(r_0^2 - r_2^2) - n\frac{\Gamma}{Q}\log\left(\frac{r_0}{r_2}\right)\right]\right\}\left(\frac{r}{r_0}\right)^{n-1} dr_0$$

Since we are considering a vaneless diffuser with finite outer radius r_3, an irrotational flow disturbance with the complex conjugate velocity proportional to Z^{n-1} is also possible. We represent the amplitude of this component by $\tilde{A}$. If we assume that the relative flow exits the impeller tangentially to the vanes, we have the following condition at the diffuser inlet.

$$\tilde{v}_{\theta 2} = -\tilde{v}_{r2}\cot\beta \tag{4}$$

In order to satisfy this boundary condition, we add irrotational components proportional to $Z^{-(n+1)}$, to the rotational and the irrotational flow components with amplitudes $\tilde{\zeta}_2$ and $\tilde{A}$.

Finally, the velocity disturbance in the diffuser can be represented by

$$\tilde{v}_r = \tilde{\zeta}_2\left\{(R_R - jR_I) - \left(\frac{r_2}{r}\right)^{n+1} e^{-2j\beta}(R_R - jR_I)_{r2}\right\} + \tilde{A}\left\{\left(\frac{r}{r_2}\right)^{n-1} - \left(\frac{r_2}{r}\right)^{n+1} e^{-2j\beta}\right\}$$

$$\tilde{v}_\theta = \tilde{\zeta}_2\left\{(\Theta_R - j\Theta_I) - j\left(\frac{r_2}{r}\right)^{n+1} e^{-2j\beta}(R_R - jR_I)_{r2}\right\} - j\tilde{A}\left\{\left(\frac{r}{r_2}\right)^{n-1} + \left(\frac{r_2}{r}\right)^{n+1} e^{-2j\beta}\right\} \tag{5}$$

with unknown complex constants $\tilde{\zeta}_2$ and $\tilde{A}$, which will be determined from the conditions described in the following sections (for details, see Tsujimoto and Acosta, 1987).

Boundary Condition at the Diffuser Exit. We assume that the flow is discharged to a space with constant pressure. By putting the expression of Eq. (5) in the θ component of a linearized momentum equation and setting $(\partial p/\partial\theta)_{r=r_3} = 0$, we obtain the following relation.

$$P_\zeta\tilde{\zeta}_2 + P_A\tilde{A} = 0 \tag{6}$$

where

$$P_\zeta = \left\{j\omega - \frac{jn\Gamma}{2\pi r_3^2} + \frac{Q}{2\pi r_3^2}\right\}Z_{\theta 3} + \frac{Q}{2\pi r_3}Z_a$$

$$P_A = \left\{j\omega - \frac{jn\Gamma}{2\pi r_3^2} + \frac{Q}{2\pi r_3^2}\right\}A_{\theta 3} - j\frac{Q}{2\pi r_3}Z_b$$

$$Z_a = \exp\left\{-j\left[\omega\frac{\pi}{Q}(r_3^2 - r_2^2) - n\frac{\Gamma}{Q}\log\left(\frac{r_3}{r_2}\right)\right]\right\} - \frac{n+1}{r_3}F(r_3) + j(n+1)\frac{r_2^{n+1}}{r_3^{n+2}}e^{-2j\beta}(R_R - jR_I)_{r_2}$$

$$Z_b = (n-1)\frac{r_3^{n-2}}{r_2^{n-1}} - (n+1)\frac{r_2^{n+1}}{r_3^{n+2}}e^{-2j\beta}$$

$$\tilde{v}_{\theta 3} = Z_{\theta 3}\tilde{\zeta}_2 + A_{\theta 3}\tilde{A} \quad \text{(from Eq. (5))}$$

Vorticity. The flow in the diffuser is rotational owing to the unsteadiness and the uneven total pressure increase in the impeller. Through the integrations of the momentum equation

Nomenclature

A = complex constant (Eq. (5))
F, G = integral value (Eq. (3))
H = complex constant (Eq. (8))
i = imaginary index in spatial domain
j = imaginary index in time domain
M = effective length of impeller flow channel
n = number of rotating stall cells
p = pressure
P, Z = complex constant (Eq. (6))
ΔP_t = total pressure loss
Q = flow rate
r = radius
R, Θ = complex function (Eq. (3))
t = time
v = unsteady velocity component
V = steady velocity component
$z = x + iy = re^{i\theta}$ = stationary frame (Fig. 1)
α = flow angle
$\bar{\alpha}$ = critical flow angle
β = vane angle
Γ = circulation of the upstream impeller
ζ = vorticity
θ = argument
ρ = density
ϕ = flow coefficient
ω = angular frequency of rotating stall
Ω = angular velocity of impeller

Superscript

$\sim$ = coefficient of unsteady component (function of r)

Subscripts

1 = impeller inlet
2 = impeller outlet, diffuser inlet
3 = diffuser outlet
r = component of r-direction
θ = component of θ-direction
ζ = coefficient of vorticity $\tilde{\zeta}$
A = coefficient of $\tilde{A}$
I = imaginary part
R = real part
p = propagation of disturbance

Downloaded 03 Jun 2010 to 171.66.16.125. Redistribution subject to ASME license or copyright; see http://www.asme.org/terms/Terms_Use.cfm

along the impeller vanes, we obtain the following expression for the vorticity at the impeller discharge.

$$\zeta_2 = -\frac{1}{r_2 v_{r_2}}\left\{\frac{\partial}{\partial t^*}(r_2 v_{\theta_2} - r_1 v_{\theta_1}) - M\frac{\partial}{\partial t^*}\left(\frac{\partial v_{r_2}}{\partial \theta}\right) - \frac{\partial}{\partial \theta}\left(\frac{\Delta P_t}{\rho}\right)\right\} \quad (7)$$

It has been assumed that the upstream flow of the impeller is irrotational. The first term in { } represents the time derivative of Euler's head, the second term is caused by the inertia of the fluid in the impeller with the effective length of impeller flow channel: $M = \int_1^2 (r_2/r \sin\beta)ds$, and the third term represents the effect of total pressure loss in the impeller. $\partial/\partial t^*$ means the time derivative in a frame fixed to the impeller. The unsteady component of Eq. (7) is:

$$\tilde{\zeta}_2 = \frac{1}{r_2 V_{r_2}} H\tilde{v}_{r_2} \quad (8)$$

where

$$H = (\omega - n\Omega)\{r_2(1 + j\cot\beta) + Mn\} + \frac{\partial}{\partial\theta}\left(\frac{\Delta P_t}{\rho\tilde{v}_{r_2}}\right)$$

The first one of Eq. (5) can be represented by $\tilde{v}_{r_2} = Z_{r_2}\tilde{\zeta}_2 + A_{r_2}\tilde{A}$ and is put in Eq. (8). Then we obtain the following relation between $\tilde{\zeta}_2$ and $\tilde{A}$.

$$(r_2 V_{r_2} - HZ_{r_2})\tilde{\zeta}_2 - HA_{r_2}\tilde{A} = 0 \quad (9)$$

Simplified Case

In the general case combined with an impeller, the flow is determined from Eqs. (6) and (9). Here, we consider the simplified case with the boundary conditions

$$\tilde{v}_{r_2} = \tilde{v}_{\theta_2} = 0 \quad (10)$$

along with $\tilde{p}_3 = 0$. The validity of these boundary conditions will be discussed later. Eq. (10) can otherwise be represented by

$$\tilde{v}_{r_2} = Z_{r_2}\tilde{\zeta}_2 + A_{r_2}\tilde{A} = 0 \quad (10a)$$

From Eqs. (10*a*) and (6), representing $\tilde{p}_3 = 0$, the condition for the existence of non-trivial solution can be obtained as follows.

$$P_\zeta A_{r_2} - P_A Z_{r_2} = 0 \quad (11)$$

Once the diffuser radial ratio r_3/r_2 and the number of cell n is given, the flow angle $\alpha = \tan^{-1}(V_r/V_\theta)$ for neutral stability and the frequency ω can be determined so that the real and imaginary parts of Eq. (11) are satisfied. By considering ω to be a complex value, we can show that the disturbance is amplifying in the region of α smaller than that determined as above. Thus, we call it critical flow angle and represent by $\bar{\alpha}$. Since the flow tangency condition of Eq. (4) is always satisfied with the simplified boundary condition of Eq. (10), the simplified flow is completely independent on the impeller. We consider this solution to be representing the "vaneless diffuser rotating stall".

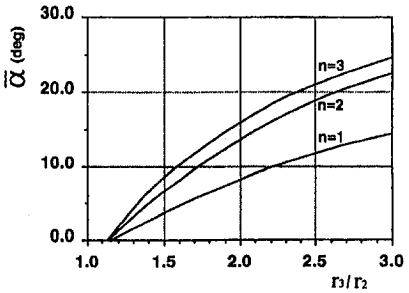


Fig. 2 Critical flow angle $\bar{\alpha}$, Eq. (11)

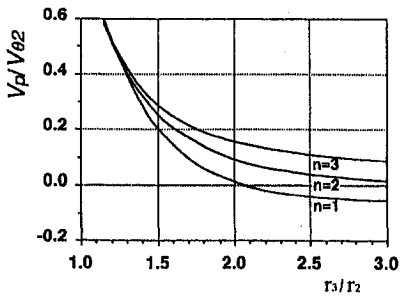


Fig. 3 Propagation velocity ratio V_p/V_{θ_2}, Eq. (11)

Figures 2 and 3 show the critical flow angle $\bar{\alpha}$ and the propagation velocity ratio $V_p/V_{\theta 2} = (r_2\omega)/(nV_{\theta 2})$ as functions of the diffuser radius ratio r_3/r_2 and the number of cell n, determined from Eq. (11). Note that they are independent on β and any other impeller parameters. Equation (11) has also solutions with $n \geq 4$ and higher order radial mode, but only the solutions with fundamental radial mode are shown in the figures. It is interesting to note that the critical flow angle $\bar{\alpha}$ is larger for larger number of stall cell n if we remember that the critical flow rate for impeller rotating stall is independent on the number of cell n. Although the definition and the understanding is different, the phenomena treated in this section is completely the same as the "Resonance" in Moore's analysis (1989).

Comparisons With Experiments

Figure 4 shows the relation of critical flow angle $\bar{\alpha}$ and the propagation velocity ratio $V_p/V_{\theta 2}$ with the diffuser radius ratio r_3/r_2 as a parameter. Experimental propagation velocity ratio

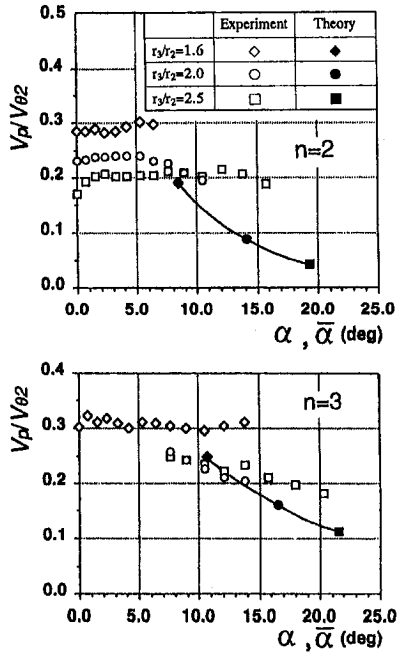
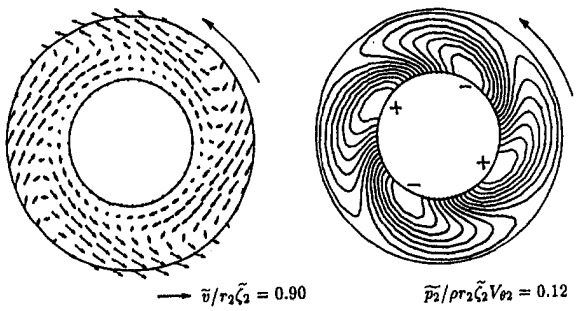
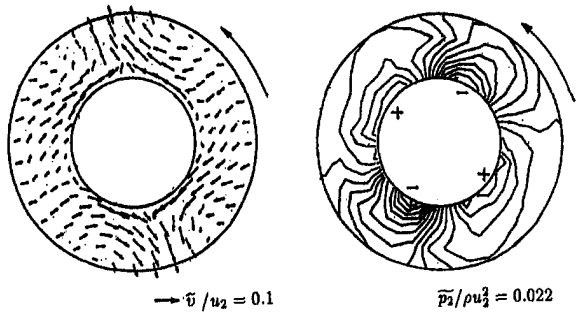


Fig. 4 Comparisons of critical flow angle $\bar{\alpha}$ and the propagation velocity ratio $V_p/V_{\theta 2}$ with experiments (Uncertainty in $V_p/V_{\theta 2}$ is $V_p/V_{\theta 2} = \pm 0.015$, uncertainty in flow rate, from which α is estimated, is ± 2 percent)

Downloaded 03 Jun 2010 to 171.66.16.125. Redistribution subject to ASME license or copyright; see http://www.asme.org/terms/Terms_Use.cfm



(a) Theory ($r_3/r_2 = 2.0, n = 2, \bar{\alpha} = 13.8(deg), V_p/V_{\theta 2} = 0.088$)



(b) Experiment ($r_3/r_2 = 2.0, n = 2, \alpha = 3.3(deg), V_p/V_{\theta 2} = 0.24$)

Fig. 5 Comparisons of the velocity and pressure fluctuation fields with experiments (Uncertainties in experimental velocity and pressure fluctuation are $|\tilde{v}/u_2| = 0.01$, $\tilde{p}/\rho u_2^2 = \pm 0.001$). (a) Theory ($r_3/r_2 = 2.0$, $n = 2$, $\bar{\alpha} = 13.8$ (deg), $V_p/V_{\theta 2} = 0.088$); (b) experiment ($r_3/r_2 = 2.0$, $n = 2$, $\alpha = 3.3$ (deg), $V_p/V_{\theta 2} = 0.24$)

$V_p/V_{\theta 2}$ are also plotted as functions of diffuser inlet flow angle α, for the three cases with $r_3/r_2 = 1.6$, 2.0 and 2.5. Experiments were made with the diffuser breadth ratio $b/r_2 = 0.2$, and an two-dimensional impeller with $\beta = 20$(deg) and $r_1/r_2 = 0.5$.

For the representations of the experimental data, the inlet flow angle α and the steady velocity $V_{\theta 2}$ were estimated from a two-dimensional inviscid flow analysis of the impeller. The propagation velocity ratio $V_p/V_{\theta 2} = r_2\omega/(nV_{\theta 2})$ was determined from the angular frequency ω of pressure fluctuation and the number of cell n estimated from the phase difference of pressure signals at two (or more) circumferential locations. In this experiment no pressure fluctuation with $n = 1$ was observed.

If we compare the experimental critical flow angle $\bar{\alpha}$ (data points with largest α) and the propagation velocity ratio at that flow angle with theoretical values, we observe agreements in the following tendencies.

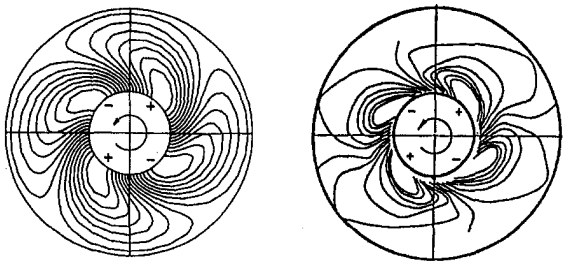
- Larger critical angle $\bar{\alpha}$ with larger radius ratio r_3/r_2
- Smaller propagation velocity ratio $V_p/V_{\theta 2}$ with larger radius ratio r_3/r_2
- Larger critical flow angle $\bar{\alpha}$ with larger number of cell n.

Although the theoretical model predicts larger $V_p/V_{\theta 2}$ at critical $\bar{\alpha}$ for the larger number of cell n, this tendency cannot be observed in the present experiment.

Figure 5 compares the velocity and pressure fluctuation patterns between theory and experiment. We observe:

- Both velocity and pressure patterns are similar between theory and experiment.
- The phase relationships between velocity and pressure patterns are similar between theory and experiment.

However, the amplitude ratio of pressure and velocity fluctuation $|\tilde{p}/\tilde{v}|$ is about 3 times larger in experiment. This may be caused by larger propagation velocity ratio and more radial velocity fluctuation vector in experiment.



(a) Theory (b) Experiment (*1989, Nagashima, T.*)

Fig. 6 Comparisons of pressure fluctuation field with experiment ($r_3/r_2 = 3.0$, $n = 2$). (a) Theory; (b) experiment (1989, Nagashima, T.)

Figure 6 compares the pressure fluctuation pattern with Nagashima et al.'s measurement (1989). They are very similar in that the phase of the pressure fluctuation is advanced at radially outward locations.

As shown above, the results of the present theory can simulate the characteristics of the vaneless diffuser rotating stall fairly well. Although it might be true that the wall boundary layer plays some important role in determining the critical flow angle, the present authors believe that the vaneless diffuser rotating stall itself is basically a two-dimensional inviscid flow instability as treated here. The quantitative disagreements might be attributed to the three-dimensionality and the viscous effects.

Effects of Impeller

In the last section, the simplified case was discussed based on a priori boundary condition $\tilde{v}_{r2} = \tilde{v}_{\theta 2} = 0$. To take into account the upstream impeller effects, it is only necessary to make similar discussions based on Eq. (9) instead of Eq. (10) or (10a), with Eq. (6). Figure 7 compares the results of simplified case and the cases with impellers with $r_1/r_2 = 0.5$, $\beta = 20$(deg) and 90(deg) (with $\Delta P_t = 0$). The effects of the impeller are small and the general tendencies as to r_3/r_2 and n can be represented by the simplified case.

Figure 8 shows the $\tilde{v}_r$ distribution for $n = 2$, $r_3/r_2 = 2.0$. For both cases with $\beta = 20$(deg) and 90(deg) impellers, the velocity distributions are basically the same as that of simplified case, except that $\tilde{v}_{r2}$ is small but finite. These observations can be explained from the larger values of $H/(r_2V_{r2})$ in Eq. (8) for conventional impellers. For small values of β, especially, the negative slope cot β of Euler's head and the inertia effect $M = \int_1^2 (r_2/r \sin\beta)ds$ contribute to the large value of H. That is, the negative slope of pressure performance (resistance) and the inertia of the fluids between impeller vanes (inertial resistance)

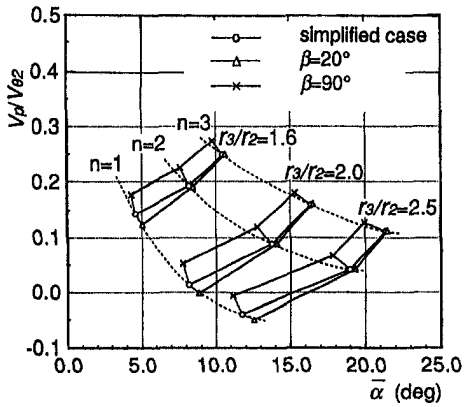
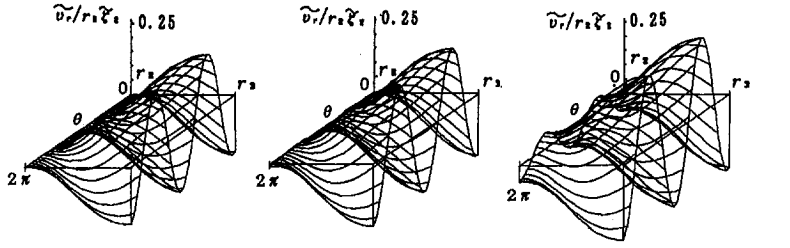


Fig. 7 Effects of impeller on critical flow angle $\bar{\alpha}$ and propagation velocity ratio $V_p/V_{\theta 2}$

Downloaded 03 Jun 2010 to 171.66.16.125. Redistribution subject to ASME license or copyright; see http://www.asme.org/terms/Terms_Use.cfm



(a) Simplified case (b) With an impeller with $\beta = 20(deg)$ (c) With an impeller with $\beta = 90(deg)$

Fig. 8 Effects of impeller on radial velocity distribution $\tilde{v}_r$ ($r_3/r_2 = 2.0$, $n = 2$). (a) Simplified case; (b) with an impeller with $\beta = 20$ (deg); (c) with an impeller with $\beta = 90$ (deg)

has the effects to suppress the fluctuation of the flow through impeller flow channel. These effects, along with the inertia effects of impeller upstream flow (represented by $(\omega - n\Omega)r_2$ in the expression of H), are strong enough to suppress the velocity fluctuation at the diffuser inlet, as shown in Fig. 8. Smaller $\tilde{v}_{r2}$ for $\beta = 20(\text{deg})$ than for $\beta = 90(\text{deg})$ can be explained by these effects. Now we find that the "simplified case" in the last section means "an idealized case when the general effects of impeller appears so strong that the effects of individual impeller parameter can be neglected."

It has been confirmed experimentally that vaneless diffuser rotating stall is nearly unaffected by the upstream impeller (Tsurusaki and Ichihara, 1988). In the experiments with upstream rotating screen, instead of an impeller (Jansen, 1964; Nagashima and Itoh, 1989), the resistance of the screen might have the similar effect on the rotating stall observed.

Conclusion

The main mechanisms of the vaneless diffuser rotating stall can be explained as follows.

The flows in the vaneless diffuser have a two-dimensional, inviscid and rotational flow instability subjected to the boundary conditions of vanishing velocity fluctuation at the diffuser inlet and vanishing pressure fluctuation at the diffuser outlet. The onset conditions and the disturbance fields obtained from the two-dimensional flow analysis are similar to experimental observations. The critical flow angle and the propagation velocity ratio are functions of only diffuser radius ratio and the number of cell, and are independent of impeller parameters. Even if we take account of the upstream impeller, the diffuser rotating stall is nearly unaltered. This is because the "resistance" of the impeller performance and the "inertial resistance" of the impeller flow channel suppress the velocity fluctuation at the diffuser inlet.

From the comparison with experimental results, the authors believe that the above instability is the substance of the vaneless diffuser rotating stall. The quantitative disagreements with experiments, as shown in Fig. 4, and the effects of Reynolds number and diffuser breadth ratio b/r_2 as shown by Kinoshita and Senoo (1985), might be attributed to the 3-D effects of the flow due to wall boundary layer and the nonlinearity of the problem. Further study is needed to elucidate these effects and to fully understand the vaneless diffuser rotating stall. The approach adopted by Frigne and Van den Braembussche (1985) incorporating the interaction between the inviscid flow core and the unsteady boundary layer will be a useful approach for such purpose.

Acknowledgment

The authors are deeply grateful for valuable discussions of Dr. H. Tsurusaki. Experimental data are obtained by Mr. T. Moriai as an undergraduate project. His support is gratefully acknowledged.

References

Abdelhamid, A. N., 1980, "Analysis of Rotating Stall in Vaneless Diffusers of Centrifugal Compressors," ASME Paper 80-GT-184.

Frigne, P., and Van den Braembussche, R., 1985 "A Theoretical Model for Rotating Stall in Vaneless Diffuser of a Centrifugal Compressor," *ASME Journal of Engineering for Gas Turbines and Power,* Vol. 107, No. 2, pp. 507–513.

Jansen, W., 1964, "Rotating Stall in Radial Vaneless Diffuser," ASME JOURNAL OF BASIC ENGINEERING, Vol. 86, No. 4, pp. 750–758.

Kinoshita, Y., and Senoo, Y., 1985, "Rotating Stall Induced in Vaneless Diffusers of Very Low Specific Speed Centrifugal Blowers," ASME JOURNAL OF ENGINEERING FOR GAS TURBINES AND POWER, Vol. 107, pp. 514–521.

Moore, F. K., 1989, "Weak Rotating Stall Flow Disturbance in a Centrifugal Compressor with a Vaneless Diffusers," ASME *Journal of Turbomachinery,* Vol. 111, pp. 442–449.

Nagashima, T., and Itoh, H., 1989, "Radial Swril Flows between Parallel Discs at Critical Flow Rate" (in Japanese), *Journal of the Japan Society for Aeronautical and Space Sciences,* Vol. 37, No. 425, pp. 267–277.

Senoo, Y., and Kinoshita, Y., 1977, "Influence of Inlet Flow Conditions and Geometries of Centrifugal Vaneless Diffusers on Critical Flow Angle for Reverse Flow," ASME JOURNAL OF FLUIDS ENGINEERING, Vol. 99, pp. 98–103.

Senoo, Y., and Kinoshita, Y., 1978, "Limits of Rotating Stall and in Vaneless Diffuser of Centrifugal Compressors," ASME Paper 78-GT-19.

Tsujimoto, Y., and Acosta, A. J., 1987, "Theoretical Study of Impeller and Vaneless Diffuser Attributed Rotating Stalls and Their Effects on Whirling Instability," *Proc. IAHR Work Group on the Behavior of Hydraulic Machinery Under Steady Oscillatory Conditions,* Lille, France.

Tsurusaki, H., Imaichi, K., and Miyake, R., 1986, "A Study on the Rotating Stall in Vaneless Diffusers of Centrifugal Fans (1st. Report; Rotational Speeds of Stall Cells, Critical Inlet Flow Angle)" (in Japanese), *JSME,* Vol. 52B, No. 480, pp. 2930–2938.

Tsurusaki, H., and Ichihara, T., 1988, "A Study on the Rotating Stall in Vaneless Diffusers of Centrifugal Fans (4th. Report; Effect of Impellers)" (in Japanese), *JSME,* Vol. 54B, No. 503, pp. 1661–1668.

Downloaded 03 Jun 2010 to 171.66.16.125. Redistribution subject to ASME license or copyright; see http://www.asme.org/terms/Terms_Use.cfm

P. Chen
School of Mechanical
& Production Engineering,
Nanyang Technological University,
Singapore 2263

M. Soundra-Nayagam
Department of Electrical
& Electronics Engineering,
Loughborough University of Technology,
Loughborough, U.K.

A. N. Bolton
Flow Center, National
Engineering Laboratory,
Glasgow, U.K.

H. C. Simpson
Department of Mechanical
& Processing Engineering,
University of Strathclyde, Glasgow, U.K.

Unstable Flow in Centrifugal Fans

Rotating stall and the inlet vortex in centrifugal fans with inlet vane control has been studied. The advances in stall research in aero-engine compressors are discussed. The present study shows that stall in centrifugal fans can be quite different from that in axial compressors, in that stall can occur in a progressive and intermittent fashion. The study also shows that a discontinuity in the fan characteristic is not necessarily accompanied by rotating stall, unlike the axial machines. Experimental results indicate that the positive prewhirl created by inlet vanes tends to delay the occurrence of stall. Also, dorsal fin devices that are used to control the inlet vortex do not seem to affect the stall point unfavorably. The inlet vortex frequency was found to invariably exhibit a linear relation with the flow rate even when dorsal fins were used. This offers a practical method to distinguish between the inlet vortex and rotating stall.

Introduction

Industrial fans frequently run under part load operating conditions. Unstable flow can occur during these conditions. The three principle types of unstable flow encountered in centrifugal fans are rotating stall, the inlet vortex, and surge. The first two are associated with the fan while surge is due to an interaction between the fan and system.

When rotating stall occurs, one or more retarded flow regions, stall cells, move around the rotor in the direction of the rotation at below the rotor speed. The mechanism of stall cell propagation has been explained by a blockage model (Emmons et al., 1955). The inlet vortex occurs in fans with inlet vane control. Inlet vanes are used to create positive pre-whirl thus reducing the fan pressure rise. However, the high swirl tends to create a central core of near stagnant flow. This core may precess and becomes a whirling helical rope, an inlet vortex.

Unstable flow causes increased noise and vibration levels which can lead to fatigue cracks in ductwork as well as in the rotor. Growing awareness of the problems has led to a demand for fan installations to be free from unstable flow. Fan users have begun to demand acceptance tests for unstable flow in addition to conventional performance tests (Soundra-Nayagam et al., 1990).

Stall research in industrial fans has been quite limited as the production investment levels are low compared with aero-engine compressors. Large fans are custom built and thus production runs are small.

In fan applications, the ductwork configuration varies from one installation to another. Installation effect may affect the stall point. The presence of inlet vortex further complicates the situation, as the inlet vortex represents an inlet distortion. Inlet distortion is expected to have an unfavorable effect on the stall point. On the other hand, the positive prewhirl reduces incidence at low flow rates and thus may have a favorable effect on the stall point.

In the event of unstable flow being detected during fan development, it is necessary to identify whether it is an inlet vortex or a rotating stall. A stall pattern may have one or more cells. A stall cell has a speed below the rotor speed. A vortex cell speed can be below or above the rotor speed depending on the vane angle and flow rate. Vortex cell speeds of between 0.5 to 3 times the rotor speed can be encountered (Bolton, 1975). Thus a flow diagnostic method based on measurement of the cell passing frequency is not adequate.

Madhavan and Wright (1985) pointed out that the high positive pre-whirl, usually present at high flow rates, cause high negative incidence and thus may produce a rotating stall associated with flow separation on the blade pressure side. This type of stall, termed p-stall as opposed to the conventional rotating stall which is associated with flow separation on the suction side, would have a cell speed above the rotor speed.

Rotating stall in aero-engine compressors has received extensive research due to the safety and efficiency concerns as well as their large production runs. Aero-engine compressors have high precision geometry so that the stall behavior is fairly repeatable among same machines. New designs are usually obtained by modifying old versions so that extrapolations of stall behavior can be made.

An elementary stability analysis of the axial compressor indicates that rotating stall should occur when the slope of the pressure rise characteristic becomes zero (Stenning, 1980). However, many machines stall while still on the negatively sloped part of their characteristic. It has been suggested that the local characteristics around the rotor circumference may play an important role in the stall process (MacDougall et al., 1990). For a centrifugal fan, the volute casing represents an asymmetric condition and thus may influence the local characteristics.

A well-known empirical prediction study used the tip clearance and static pressure rise parameters to correlate stall for axial compressors (Koch, 1981). As the majority of axial compressors stall at the discontinuity of their characteristics, deriving a stall correlation is relatively straightforward. Stall in centrifugal fans is less well defined and so it is more difficult to obtain experimental stall correlations.

Recent stall inception research in axial machines using transient measurement techniques points to the important role of the tip clearance flow in the stall inception process (MacDougall et al., 1990; Day, 1993). A method based on a rotor-locked

Contributed by the Fluids Engineering Division for publication in the JOURNAL OF FLUIDS ENGINEERING. Manuscript received by the Fluids Engineering Division October 6, 1994; revised manuscript received February 17, 1995. Associate Technical Editor: L. Nelik.

Copyright © 1996 by ASME

Downloaded 03 Jun 2010 to 171.66.16.125. Redistribution subject to ASME license or copyright; see http://www.asme.org/terms/Terms_Use.cfm

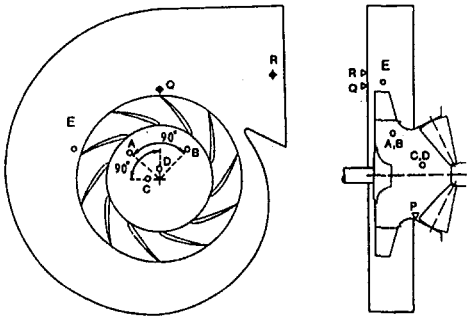


Fig. 1 Fan No 1 and instrumentation (A, B, C, D, E—hot wire probe; P, Q, R—pressure transducer)

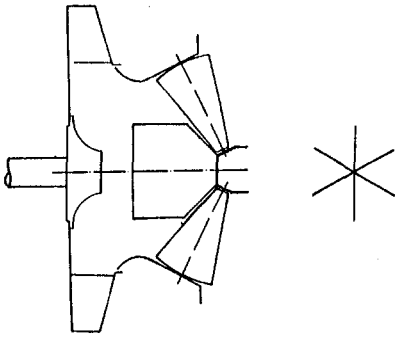


Fig. 1(*a*) Dorsal fin configuration

cross correlation technique (Inoue et al., 1993) indicated another way of studying the stall inception, where the blade-to-blade periodicity (i.e., flow quality) rather than the transient flow events was studied as the stall point was approached.

The inlet vortex behavior in centrifugal fans is fundamentally similar to that in parallel ducts. Experimental and theoretical studies of the vortex breakdown have been carried out in parallel ducts and slightly diverging diffusers (Harvey, 1962; Sarpkaya, 1971; Squire, 1960). These studies showed that vortex breakdown is really an inviscid phenomenon. The critical condition for vortex breakdown mainly depends on the ratio of the angular to axial momentum. Empirical correlations for vortex breakdown have been obtained for parallel ducts (Cassidy and Falvey, 1970). However, these duct correlations are not transferable to centrifugal fans due to their different geometries.

Test Rig and Instrumentation

The present study was carried out on two industrial centrifugal fans (Chen, 1993). Fan No 1 had ten backward curved aerofoil blades. The blade exit and inlet diameters are 690 mm and 440 mm, respectively. The blade exit and inlet angles are 44.1 and 13.9 deg, respectively. The best overall efficiency for fan No 1 was obtained at $\Phi = 0.2$. Fan No 2 had twelve backward curved plate blades, an exit diameter of 610 mm and inlet diameter of 440 mm. Fan No 1 was operated at 1500 rpm with a machine Reynolds number of 2.5×10^6. Fan No 2 was operated at 2600 rpm with a machine Reynolds number of 3.4×10^6. Both fans had a spiral volute casing and an inlet bellmouth with no inlet box.

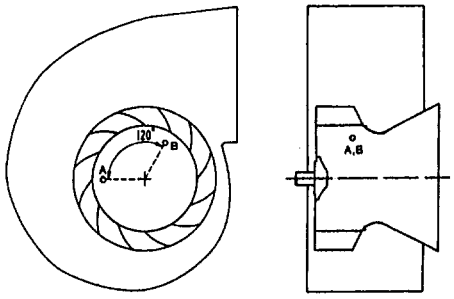


Fig. 2 Fan No 2 and instrumentation (A, B—hot wire probe)

Fan No 1 could be fitted with inlet vane control and dorsal fin devices to study both the inlet vortex and rotating stall. The configuration of the dorsal fin devices used in this study were typical of those used in large centrifugal fans as sketched in Fig. 1(*a*). A variable speed drive attached to fan No 1 allowed a speed change test to be conducted in order to distinguish between the inlet vortex and rotating stall. Fan No 2 was used to study rotating stall only (Fig. 2).

The speed change test makes use of the fact that the vortex speed depends only on the vane angle and flow rate while the stall cell speed will change with rotor speed. During the speed change test the vane angle and flow rate were maintained constant while the largest possible change in rotor speed was performed.

Hot wire probes were used to detect rotating flow disturbances. Spectrum analysis and cross correlation methods were used to obtain both the amplitude and the cell pattern of the disturbance. Pressure transducers were used to record the pressure fluctuations at different locations. Data processing was carried out on-line using FFT analyzers, Advantest TR9402 and Diagnostic Instruments PL22.

The local characteristics around the rotor circumference was studied using a 3-hole wedge probe. The probe was placed at different circumferential locations with the same radial and axial positions.

It is known that the flow quality in the blade passages generally deteriorates as rotating stall is approached. This may appear as a degradation in the blade-to-blade periodicity. It may be assumed that the characteristic distance of the flow disturbance thus caused is related to the blade pitch, rather than the rotor circumference.

The blade-to-blade periodicity was studied using a rotor-locked autocorrelation method. A tangentially orientated hot wire probe was placed at rotor inlet and exit. A single probe was used in order to avoid differences due to different probes and locations. Data were recorded via a microcomputer based data acquisition and control system.

Nondimensional rotor-locked autocorrelation functions, expressed as follows, were calculated and then ensemble averaged over about 80 rotor revolutions.

Nomenclature

C_r = radial velocity, m/s
U_2 = blade speed at rotor exit, m/s
f = frequency, Hz
t = time, s
Q = volume flow rate, m^3/s
P_{ts} = total-to-static pressure rise, Pa
C' = rms amplitude of velocity fluctuations, m/s
p' = rms amplitude of pressure fluctuations, Pa
R_{xy} = cross correlation coefficient, $(m/s)^2$
Φ = flow coefficient ($\Phi = C_{2r}/U_2$)
Ψ_{ts} = total-to-static pressure rise coefficient
r_{xx} = nondimensional autocorrelation coefficient
θ = vane setting angle (90 deg—fully open, 0 deg—fully close)

Downloaded 03 Jun 2010 to 171.66.16.125. Redistribution subject to ASME license or copyright; see http://www.asme.org/terms/Terms_Use.cfm

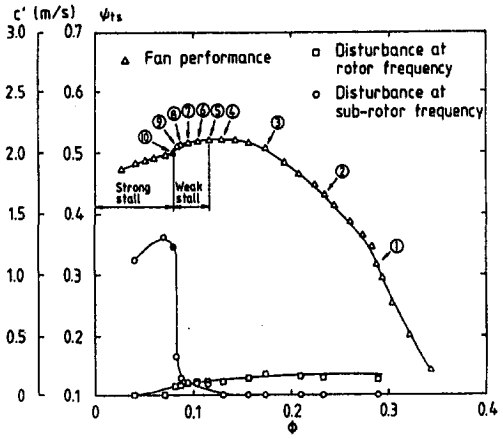


Fig. 3 Development of rotating stall (Fan No 1, probe A)

$$r_{xx}(j) = \frac{\sum_{i=1}^{n-j} (x_i - \bar{x})(x_{i+j} - \bar{x})}{\sum_{i=1}^{n-j} (x_i - \bar{x})^2} \quad j = 1, 2, \ldots m$$

where m is the number of data points over one revolution and n is equal to $\frac{3}{2}$ m.

The uncertainty of the fan overall characteristic measurements was 3%. The uncertainty of the frequency results was 0.25 percent from the FFT analyzer.

Results

The development of rotating stall in fan No 1 is shown in Fig. 3. The spectrograms and correlagrams as shown in Figs. 4–5 were obtained in single cycle, i.e., single shot, as well as in average over 16 cycles.

Near the peak of the fan characteristic, small amplitude sub-rotor frequency peaks began to occur in the averaged spectrogram, e.g., point 7 in Fig. 4(*a*). This suggested rotating stall but could not be confirmed from the accompanying averaged correlogram, Fig. 5(*a*). However, a single cell rotating stall could indeed be confirmed in some single cycle results, e.g., Fig. 5(*b*). This indicated that the stall cell occurred intermittently.

The above intermittent stall behavior persisted for a fairly large of flow rates, between points 5 and 9, but the cell amplitude in the averaged spectrogram increased gradually. This indicated that the stall appeared progressively. The stall cell speed decreased from 80 to 65 percent of the rotor speed from point 5 to 9.

A small discontinuity on the characteristic occurred between points 9 and 10. The flow was seen to alternate between a weak and strong stall condition, Fig. 6, as the fan operating point alternated between the upper and lower points of the discontinuity. Further reduction in flow rate saw a fully developed (strong) single cell rotating stall being established, with a constant cell speed of 65 percent of the rotor speed.

The hot wire spectrograms taken at the rotor exit (not shown) were virtually no use in identifying rotating stall due to the heavy background noises arising from high turbulence at rotor exit.

Fan No 2 exhibited a large discontinuity in its characteristic, Fig. 7. However, hot wire measurements did not indicate rotating stall at this discontinuity. A progressive and intermittent stall behavior similar to that of fan No 1 was observed, between points 6 and 8, while the stall cell speed was almost constant, at about 60 percent of the rotor speed. The stall point, point 6, seemed to be still negatively sloped. A fully developed rotating stall occurred at point 9. However, this was not accompanied by any discontinuity in the overall characteristic.

The progressive and intermittent stall behavior found in the two centrifugal fans is very different from that observed in axial machines. Stall in an axial machine tends to occur abruptly as flow rate is reduced and the stall point is often accompanied by a large discontinuity in the characteristic. The measurement results on fan No 2 also indicates that for a centrifugal fan the discontinuity in the overall characteristic does not necessarily mean the onset of rotating stall and vice versa.

The rotor-locked hot wire autocorrelation results are shown in Figs. 8 and 9. Figure 8 shows that at the rotor inlet the blade-to-blade periodicity was strong even when (weak) stall was present. However, results at the rotor exit showed that the blade-to-blade periodicity degraded substantially as the stall point was approached, Fig. 9. For example, the correlation value at the stall point (point 5) had dropped to 40 percent of the value at a stable operating point (point 3). Compared with the spectrum

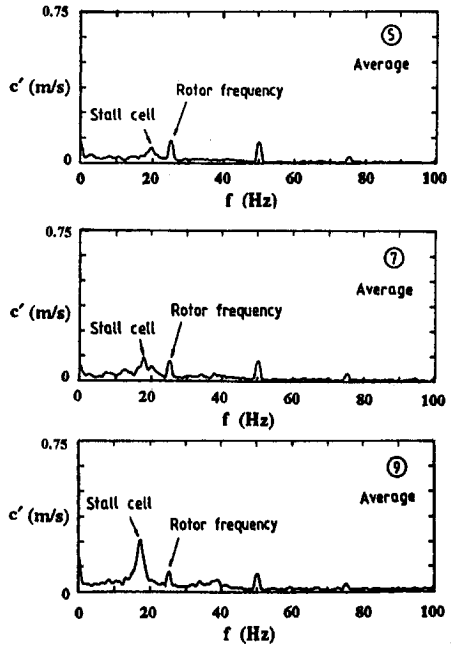


Fig. 4(*a*) Averaged velocity spectrograms (Fan No 1, probe A)

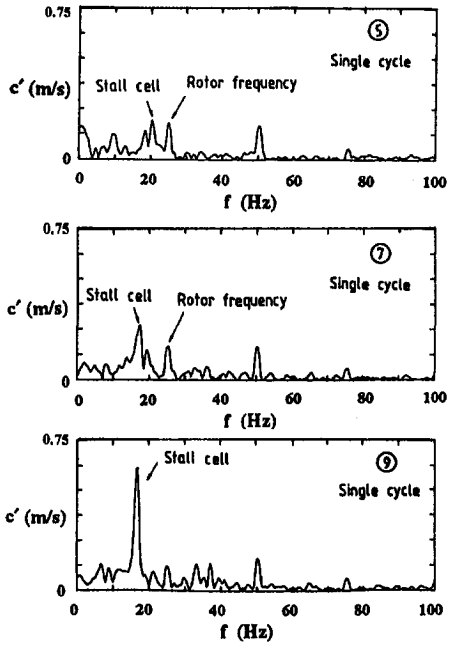


Fig. 4(*b*) Single cycle velocity spectrograms (Fan No 1, probe A)

Downloaded 03 Jun 2010 to 171.66.16.125. Redistribution subject to ASME license or copyright; see http://www.asme.org/terms/Terms_Use.cfm

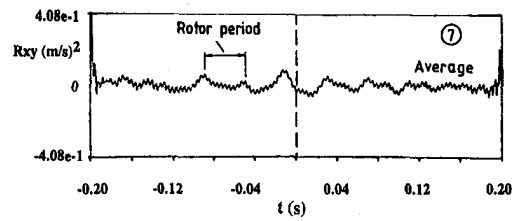


Fig. 5(*a*) Averaged velocity spectrogram (Fan No 1, probes A–B)

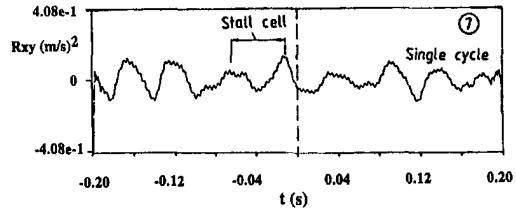


Fig. 5(*b*) Single cycle velocity spectrogram (Fan No 1, probes A–B)

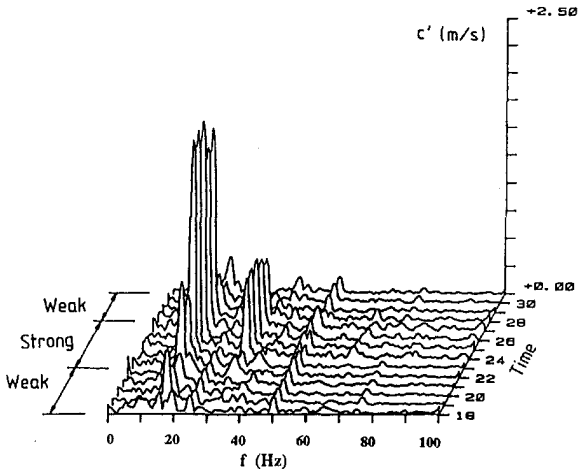


Fig. 6 Waterfall of averaged velocity spectrum (Fan No 1, probe A, point 9)

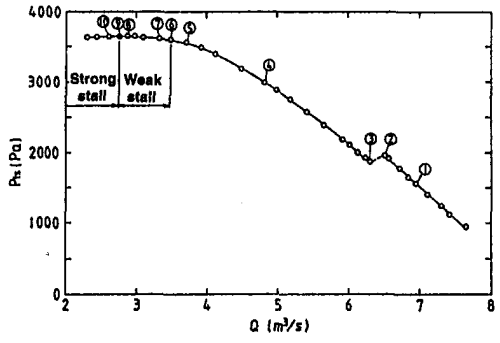


Fig. 7 Development of rotating stall (Fan No 2, probe A)

method for rotor exit measurement, the rotor-locked auto correlation method shows some advantage for machines exhibiting progressive stall behavior.

The measured local characteristics indicates that large variations around the rotor circumference has existed, Fig. 10. In general, a negative slope is more stable than a positive slope. A steep negative slope is more stable than a flatter one. The results therefore suggested that the volute cut-off region was probably the least stable region.

When inlet vane control was used, the inlet vortex and rotating stall conditions were determined by speed change tests.

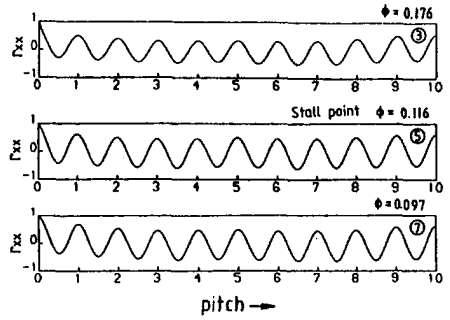


Fig. 8 Rotor-locked autocorrelation functions at rotor inlet (Fan No 1, probe A)

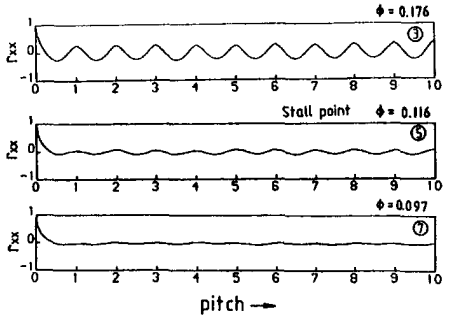


Fig. 9 Rotor-locked autocorrelation functions at rotor exit (Fan No 1, probe E)

Measurements showed no evidence of p-stall existence over the entire range of vane angle and flow rate. Cross correlation results indicated that the inlet vortex and rotating stall had a single cell structure.

Figure 11 shows that the inlet vortex has a linear relationship between its' frequency and flow rate for a given vane angle. This is in qualitative agreement with the parallel duct correlation. This linear frequency behavior may be used to distinguish between the inlet vortex and rotating stall thus avoiding the need for a speed change test.

At high vane angles not capable of producing the inlet vortex (e.g., 90 deg), the progressive and intermittent stall behavior was still observed. No shift in the stall point was observed compared with the case without inlet vanes.

At the vane angles capable of producing the inlet vortex (60–15 deg), the vortex and stall regimes were clearly separated, with vortex occurring at high flow rates while stall at low flow rates. This may suggest that the inlet vortex, existed but was weak in the magnitude, could not have any substantial effect on the stall process. The magnitude of the inlet vortex was seen to decrease rapidly with the reduction in flow rate as is shown in Figs. 12 and 13. Within these vane angles, neither progressive nor intermittent behavior in rotating stall could be observed. This means that stall had occurred abruptly as flow rate was reduced.

It can be seen from Fig. 11 that a reduction in the vane angle has generally shifted the (strong) stall point to a lower flow rate. This was really due to the positive pre-whirl effect which reduced the incidence thus delaying the stall. This result also suggests that the stabilizing effect of the positive prewhirl was stronger than the destabilizing effect of the vortex-caused inlet distortion.

The pressure measurements indicated that strong inlet vortex had occurred in the middle range of vane angles, Fig. 12. The inlet vortex caused the highest pressure fluctuations at the fan inlet with a decay in the amplitude further downstream, Fig. 13. Figure 13 also shows that a strong inlet vortex can even be

Downloaded 03 Jun 2010 to 171.66.16.125. Redistribution subject to ASME license or copyright; see http://www.asme.org/terms/Terms_Use.cfm

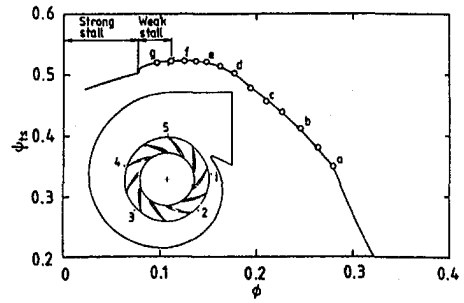


Fig. 10(*a*) Overall total-to-static characteristic (Fan No 1, re-plot of Fig 3)

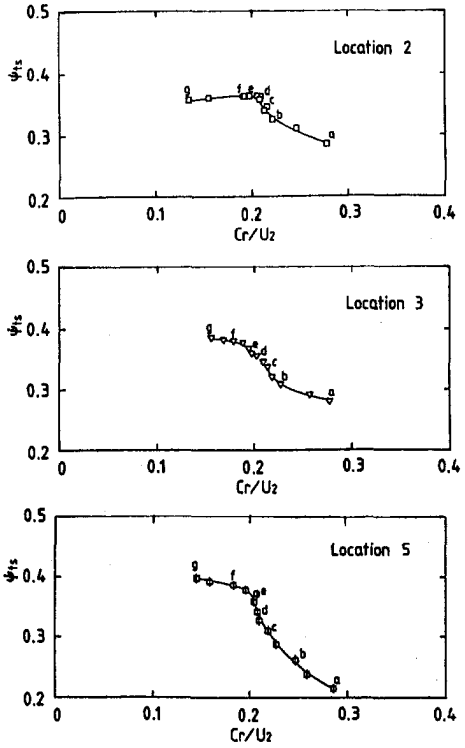


Fig. 10(*b*) Local total-to-static characteristic (Fan No 1)

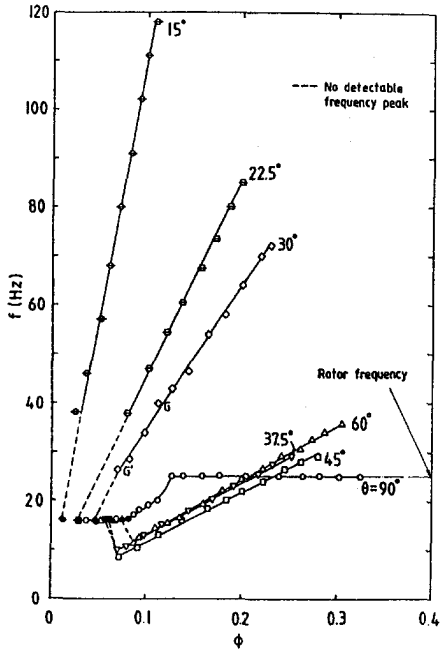


Fig. 11 Inlet vortex and rotating stall frequencies (Fan No 1, solid symbols: onset of strong stall)

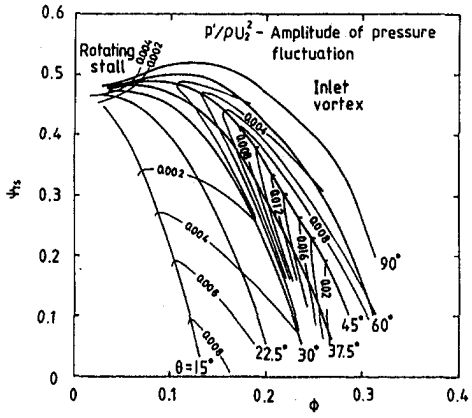


Fig. 12 Amplitude of pressure fluctuations due to inlet vortex and rotating stall (Fan No 1, transducer p)

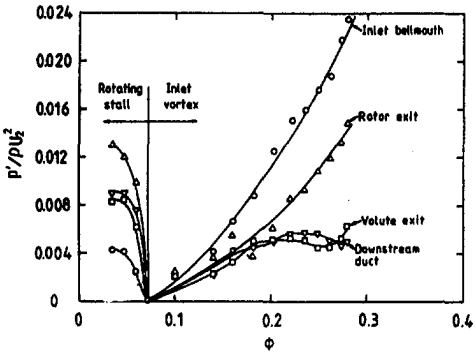


Fig. 13 Amplitude of pressure fluctuations recorded at different locations (Fan No 1, θ = 45°)

detected by a pressure transducer mounted on the casing wall at the rotor exit.

Measurements were also conducted with a number of dorsal fin devices being used. The frequency results as shown in Fig. 14 are typical of the dorsal fin devices used. These results showed that the linear relationship between vortex frequency and flow rate was maintained in the presence of dorsal fins. This is of practical importance to the unstable flow diagnostics as large centrifugal fans with inlet vane control are invariably fitted with dorsal fins. It should also be pointed out that the use of dorsal fins did not appear to have an unfavorable effect on the stall point according to these measurements.

Conclusions

Large commercial centrifugal fans can encounter a complex unstable flow condition due to the likelihood of the occurrence of both rotating stall and the inlet vortex. The present study shows that centrifugal fans can exhibit different stall behaviors from the axial flow machines, in that stall can occur in a progressive and intermittent fashion. In addition, unlike the axial machine a discontinuity in the overall characteristic of a centrifugal fan does not necessarily indicate the onset of a rotating stall and vice versa. Unstable flow diagnostic techniques are therefore essential in the detection of rotating stall for centrifugal fans. The rotor-locked autocorrelation method may provide a method to define the level of rotating stall for machines exhibiting progressive stall. The asymmetry of the volute casing flow may

Downloaded 03 Jun 2010 to 171.66.16.125. Redistribution subject to ASME license or copyright; see http://www.asme.org/terms/Terms_Use.cfm

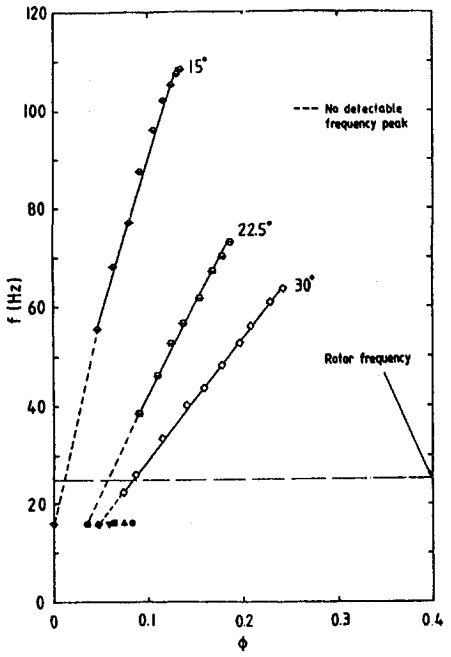


Fig. 14 Inlet vortex and rotating stall frequencies with dorsal fins fitted (Fan No 1, solid symbols: onset of strong stall)

play a rule in the stalling process for centrifugal fans. The present study indicates the existence of large variations in the local characteristics around the rotor circumference, pointing out the volute cut-off region to be the least stable region.

Measurements do not seem to suggest any effect of the inlet vortex on the onset of rotating stall, probably due to the weak magnitude of the inlet vortex being present. This can be seen from the fact that the inlet vortex and rotating stall regimes were clearly separated. It is interesting to note that at the vane setting angles capable of producing an inlet vortex rotating stall occurred abruptly with the reduction in flow rate. It appears that the inlet vanes have an overall effect of delaying the stall due to the presence of the positive pre-whirl they have created.

The inlet vortex maintains a linear relation between its frequency and the flow rate for a given vane angle, even when a vortex control device is used. This linear behavior may be used to distinguish between the inlet vortex and rotating stall.

References

Bolton, A. N., 1975, "Pressure Pulsations and Rotating Stall in Centrifugal Fans," *Proc. of IMechE Conf. on Vibration and Noise in Pump, Fan and Compressor Installations,* Southampton, pp. 175–181.

Cassidy, J. J., and Falvey, H. T., 1970, "Observations of Unsteady Flow Arising after Vortex Breakdown," *Journal of Fluid Mechanics,* Vol. 41, pp. 727–736.

Chen, P., 1993, "Unstable Flow in Centrifugal Fans," Ph.D thesis, University of Strathclyde.

Day, I. J., 1993, "Stall Inception in Axial Flow Compressors," ASME *Journal of Turbomachinery,* Vol. 115, pp. 1–9.

Emmons, H. W., Pearson, C. E., and Grant, H. P., 1955, "Compressor Surge and Stall Propagation," *Trans. ASME,* Vol. 77, pp. 455–469.

Harvey, J. K., 1962, "Some Observations of the Vortex Breakdown Phenomenon," *Journal of Fluid Mechanics,* Vol. 14, pp. 585–592.

Inoue, M., Kuroumaru, M., and Ando, Y., 1993, "Pressure Fluctuation on Casing Wall of Isolated Axial Compressor Rotors at Low Flow Rate," ASME *Journal of Turbomachinery,* Vol. 115, pp. 19–27.

Koch, C. C., 1981, "Stalling Pressure Rise Capability of Axial Flow Compressor Stages," ASME *Journal of Engineering for Power,* Vol. 103, pp. 645–656.

Madhavan, S., and Wright, T., 1985, "Rotating Stall Caused by Pressure Surface Flow Separation on Centrifugal Fan Blades," ASME *Journal of Engineering for Gas Turbines and Power,* Vol. 107, pp. 775–781.

MacDougall, N. M., Cumpsty, N. A., and Hynes, T. P., 1990, "Stall Inception in Axial Compressors," ASME *Journal of Turbomachinery,* Vol. 112, pp. 116–125.

Sarpkaya, T., 1971, "On Stationary and Travelling Vortex Breakdown," *Journal of Fluid Mechanics,* Vol. 45, part 3, pp. 545–559.

Soundra-Nayagam, M., Bolton, A. N., and Margetts, E. J., 1990, "Dynamic Flow Measurements on Model Fan," National Engineering Laboratory, Rept. 272/90.

Squire, H. B., 1960, "Analysis of the Vortex Breakdown Phenomenon," Imperial College, Dept. of Aerospace Engineering, Report No. 102.

Stenning, A. H., 1980, "Rotating Stall and Surge," ASME JOURNAL OF FLUIDS ENGINEERING, Vol. 102, pp. 14–20.

Downloaded 03 Jun 2010 to 171.66.16.125. Redistribution subject to ASME license or copyright; see http://www.asme.org/terms/Terms_Use.cfm

Numerical and Experimental Study of the Propulsive Speed of the Three Joint Bending Propulsion Mechanism

Motomu Nakashima

Kyosuke Ono

Faculty of Engineering, Tokyo Institute of Technology, 2-12-1 Oh-okayama, Meguro, Tokyo 152, Japan

The three joint bending propulsion mechanism as a simplified model of fish propulsion is investigated. A numerical method for a coupled system of the bending propulsion mechanism and the fluid is developed, based on the two-dimensional discrete vortex method. The characteristics of the propulsive speed of the three joint bending propulsion mechanism are numerically and experimentally investigated. It is found that the propulsive speed has a maximum numerical and experimental value when all the phase differences of the joints are about zero for four amplitude patterns. The experimental propulsive speeds are found to be 65 ~ 80 percent of the numerical ones.

1 Introduction

The swimming movements of fish or cetaceans, accompanied with the undulatory motion of their bodies, look so attractive that they have been studied by many researchers. Lighthill (1960) applied the "slender body theory" of aeronautics to transverse oscillatory movements of a slender fish whose cross-section varies gradually along it, and he showed that the propulsive efficiency, which is defined as the ratio of the forward work necessary to overcome frictional drag and the total work necessary to produce both thrust and vortex wake, is essentially very high. This theory is called the Elongated Body Theory; EBT.

Lighthill (1970) further took account of the recoil effect in his EBT, and showed that to reduce the recoil effect, it is necessary to greatly reduce the depth from the immediate anterior part of the body to the caudal fin. Wu (1971c) extended this theory to a slender fish, whose transverse cross-section to the rear of its maximum span section was a lenticular shape with pointed edges. Lighthill (1970) and Newman and Wu (1973) studied the effect of fin appendages. Kambe (1978) considered the dynamics of the slender fish, taking into account the lateral resistance force, the reaction force due to vortex sheets shed from sharp trailing edges, and the inertial force due to its body and fluid. Katz and Weihs (1979) analyzed a slender wing with passive chordwise flexibility.

On the other hand, in the early stage of the development of theories of fish swimming, a two-dimensional model was used in a first attempt to tackle the difficulties of this problem, although these approaches insufficiently represented very slender swimming animals. Wu (1961, 1971a) and Siekmann (1962, 1963) studied the two-dimensional potential flow over a thin waving plate of finite chord as a simplified model of fish propulsion. Uldrick and Siekmann (1964) extended these studies to a waving plate of arbitrary finite thickness and showed that an increase of thickness causes a decrease of thrust. Wang (1966) solved the optimum motion so as to maximize the average thrust in the presence of instantaneous or average power limitation constraints for the case of a two-dimensional oscillating hydrofoil having a finite number of spatial harmonics. Recently, Cheng (1991) developed the fully three-dimensional rectangular or triangular waving plate theory, and showed that important quantities such as thrust can be obtained in a sufficient accuracy by EBT when the aspect ratio of the plate is less than 0.5. In contrast, the transition to results as given by two-dimensional theory takes place only when the aspect ratio is significantly greater than 1.

Another interesting subject which has been investigated by many researchers is about the one organ particular to swimming animals, that is, the lunate tail of a high aspect ratio, which is seen as a common property among fast swimming animals. Lighthill (1970) applied the two-dimensional airfoil theory of aerodynamics to the caudal fin of fish with a high aspect ratio, and investigated the performance of a flat wing of the caudal fin with respect to a ratio of amplitudes and a phase difference between the heaving and pitching motions and with respect to the location of pitching axis. Wu (1971b) also analyzed the two-dimensional flat wing and compared the theory with experimental measurements of a porpoise tail. Katz and Weihs (1978) analyzed the propulsive performance of an airfoil with chordwise flexibility. Chopra (1974, 1976) extended this study to the three-dimensional rectangular wing and the two-dimensional wing with large amplitude. Further, Chopra and Kambe (1977), Cheng and Murillo (1977), and Karpouzian et al. (1990) analyzed the performance of the three-dimensional lunate-tail. Triantafyllou et al. (1993) experimentally showed that the optimal efficiency of an oscillating foil is obtained at the frequency of maximum amplification of wake vortices.

Some of the above-mentioned papers are also available on review papers or books, e.g., Wu (1971d), Lighthill (1975), Wu et al. (1975).

In most of the above-mentioned papers, the undulatory motions of the body are given a priori as a known sinusoidal function in the absolute space coordinate. However, real swimming animals cannot directly control the absolute motion. They control only the bending angles of their many joints, and motions of the whole body are determined as dynamically coupled system of the swimming animal and the fluid. Therefore, the purpose of this study is to analyze the whole body motion of a more dynamically realistic model, that is, we take into account not only the recoil effect, like Lighthill (1970), but also balance in the swimming direction, i.e., the body being self propelled. For this reason, we develop a numerical method for a coupled system of a "bending propulsion mechanism," which is a simplified model of undulatory swimming animals, and is composed of multiple links connected with bending joints, based

Contributed by the Fluids Engineering Division for publication in the JOURNAL OF FLUIDS ENGINEERING. Manuscript received by the Fluids Engineering Division November 5, 1993; revised manuscript received August 9, 1995. Associate Technical Editor: A. Ghoniem.

Copyright © 1996 by ASME

Downloaded 03 Jun 2010 to 171.66.16.125. Redistribution subject to ASME license or copyright; see http://www.asme.org/terms/Terms_Use.cfm

on the discrete vortex method. The discrete vortex method is convenient for extension to the iterative procedure in such a coupled problem, due to its simplicity of formulation. We employ the two-dimensional method, in the tradition of Wu (1961) etc., because it is the first to tackle the dynamically coupled problem, although a two-dimensional model is insufficient for swimming animals. Furthermore, since there is few published experimental data, we develop an experimental setup which consists of a four link and three joint bending propulsion mechanism and a water tank, and numerically and experimentally investigate the characteristics of the propulsive speed of a three joint bending propulsion mechanism.

2 Analytical Model and Theoretical Formulation

Figure 1 illustrates an analytical model of a bending propulsion mechanism in water. The bending propulsion mechanism is streamlined as a whole and is composed of multiple links serially connected with joints. It is assumed that the flow is a two-dimensional incompressible viscous flow. Moreover, the flow is regarded as the potential flow, except in small areas in which the shearing stress from viscosity is not negligible, i.e., the boundary layer around the mechanism and the shear layer shed from the trailing edge of the mechanism, because the Reynolds number of the flow is high enough. Furthermore, by ignoring the thickness of the mechanism, the shear layer shed from the trailing edge of the bending propulsion mechanism and the boundary of the mechanism can be approximately represented by point vortices, i.e., bound vortices $\Gamma_{bv(j)}$ on the centerline of the mechanism and shed vortices $\Gamma_{sv(k)}$, which are, respectively, represented by (large and small) white circles and black circles in Fig. 1. At a point (x, y), the fluid velocities u and v, which are induced by the uniform flow, the bound vortices and the shed vortices, are generally given by

$$u = u_\infty + \sum_{j=1}^{M} \frac{\Gamma_{bv(j)}}{2\pi} \frac{(y - y_{bv(j)})}{(x - x_{bv(j)})^2 + (y - y_{bv(j)})^2} + \sum_{k=1}^{N} \frac{\Gamma_{sv(k)}}{2\pi} \frac{(y - y_{sv(k)})}{(x - x_{sv(k)})^2 + (y - y_{sv(k)})^2} \quad (1)$$

and

$$v = v_\infty - \sum_{j=1}^{M} \frac{\Gamma_{bv(j)}}{2\pi} \frac{(x - x_{bv(j)})}{(x - x_{bv(j)})^2 + (y - y_{bv(j)})^2} - \sum_{k=1}^{N} \frac{\Gamma_{sv(k)}}{2\pi} \frac{(x - x_{sv(k)})}{(x - x_{sv(k)})^2 + (y - y_{sv(k)})^2} \quad (2)$$

In the present case, u_∞ and v_∞ are zero. Using these equations, we can calculate the normal velocities of the mechanism at the M control points represented by '×' in Fig. 1. These normal fluid velocities should be equal to the velocities of the control points themselves, which can be calculated from the differences between the displacements at the previous time step and those at the present time step. These restrictions become M boundary conditions.

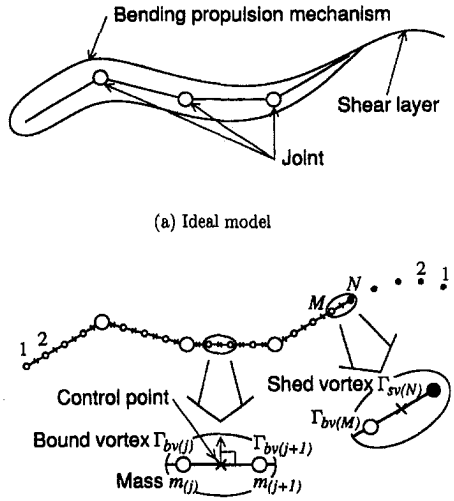


Fig. 1 Analytical model

The forces F'_x and F'_y acting on the bending propulsion mechanism, can be calculated by the following extended Blasius equation:

$$F'_x - iF'_y = \frac{i\rho}{2} \oint_C \left(\frac{dW}{dz}\right)^2 dz - i\rho \frac{\partial}{\partial t} \oint_B \bar{z} d\Phi \quad (3)$$

where C represents a closed stationary curve surrounding the body, and B represents a curve along the body, which is cut at the trailing edge. (See appendix for derivation of Eq. (3)). Using the point vortices, Eq. (3) is rewritten in the form:

$$F'_x - iF'_y = \rho \Bigg[i \sum_{j=1}^{M} \{(u_{bv(j)} - iv_{bv(j)}) \cdot \Gamma_{bv(j)}\} - \frac{1}{2\pi} \sum_{j=1}^{M} \sum_{k=1}^{N} \Gamma_{bv(j)} \Gamma_{sv(k)} \frac{1}{z_{sv(k)} - z_{bv(j)}} - i \sum_{j=2}^{M} \left\{ \left(\sum_{k=j}^{M} \frac{\Delta \Gamma_{bv(k)}}{\Delta t} + \frac{\Gamma_{sv(N)}}{\Delta t} \right) \cdot (\bar{z}_{bv(j-1)} - \bar{z}_{bv(j)}) \right\} - i \frac{\Gamma_{sv(N)}}{\Delta t} \cdot (\bar{z}_{bv(j)} - \bar{z}_{sv(N)}) \Bigg]. \quad (4)$$

Equation (4) is a distributed form, where the first, second and third terms in the square bracket are supposed to act at each jth point and the fourth term is supposed to act at the trailing edge. Hence, the moment of fluid force can also be derived.

Nomenclature

M = number of bound vortices
N = number of shed vortices
x_{bv}, y_{bv} = coordinates of bound vortex
x_{sv}, y_{sv} = coordinates of shed vortex
t = time
Γ_{bv} = strength of bound vortex
Γ_{sv} = strength of shed vortex
m = mass of discretized lumped mass
θ_{bv} = angle from mass center at bound vortex point
I = moment of inertia of lumped mass about mass center
F_x, F_y = fluid force acting on the mechanism
F'_x, F'_y = pressure force acting on the mechanism
T_θ = moment acting on the mechanism
$i = \sqrt{-1}$
$z = x + iy$
W = complex velocity potential
Φ = velocity potential
ρ = fluid density
F_D = drag resulting from fluid viscosity
θ_p = bending angle of pth joint
θ_{max} = amplitude of joint angle
ω = angular frequency of joint angle
ϕ_p = phase difference of pth joint from the first joint
ϕ_0 = uniform phase difference
$\bar{U}$ = average propulsive speed

Downloaded 03 Jun 2010 to 171.66.16.125. Redistribution subject to ASME license or copyright; see http://www.asme.org/terms/Terms_Use.cfm

In the discrete vortex method, however, we cannot theoretically take account of the drag due to fluid viscosity. Therefore, such drag is experimentally measured as a function of the flow speed. By adding the drag, F_x' and F_y', we can then obtain the total forces, F_x and F_y.

The mass of the mechanism is represented by a set of discretized lumped masses ($m_{(j)}$). By assuming predetermined motions for joint angles, the motion of the mechanism is determined by solving the following three equations of motion for the mass center of the mechanism:

$$\sum_{j=1}^{M}\left(m_{(j)}\frac{\partial^2 x_{bv(j)}}{\partial t^2}\right)=F_x \tag{5}$$

$$\sum_{j=1}^{M}\left(m_{(j)}\frac{\partial^2 y_{bv(j)}}{\partial t^2}\right)=F_y \tag{6}$$

$$\sum_{j=1}^{M}\left(I_{(j)}\frac{\partial^2 \theta_{bv(j)}}{\partial t^2}\right)=T_\theta \tag{7}$$

3 Numerical Method

The strength of M bound vortices, and that of one shed vortex, are unknown in the flow field. These unknowns are determined from M boundary conditions and the Kelvin's theorem:

$$\sum_{j=1}^{M}\Delta\Gamma_{bv(j)}+\Gamma_{sv(N)}=0 \tag{8}$$

where $\Delta\Gamma_{bv(j)}$ represents the change in the strength of the jth bound vortex during one discretized time interval. These equations turn into linear algebraic equations of $M+1$ unknown variables. The strength of the vortices must also satisfy the equations of motion of the bending propulsion mechanism, and hence $M+1$ equations of vortices and three equations of motion are solved successively and iteratively at each time step as follows:

From Eqs. (1) and (2), we first calculate the velocity component of the fluid perpendicular to the bending propulsion mechanism at ith control point, using the temporary motion of the bending propulsion mechanism and the temporary strength of the vortices. Assuming that $\Delta u(i)$ represents the difference between this

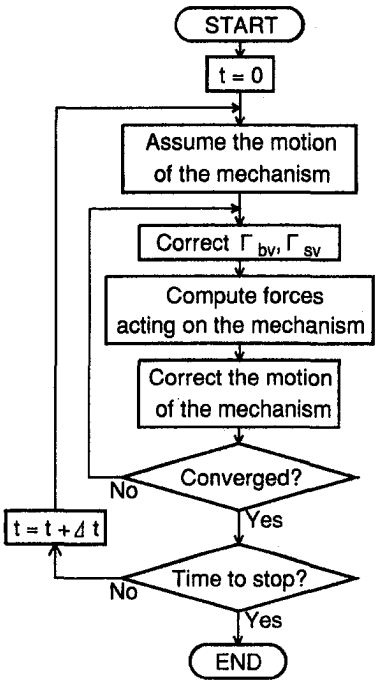


Fig. 2 Computing algorithm

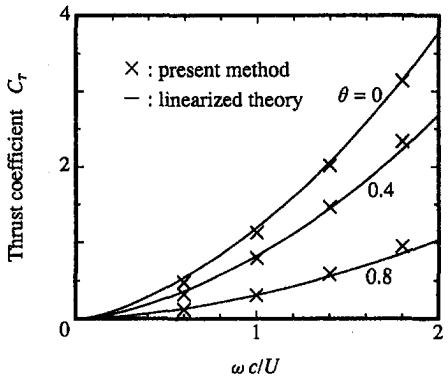


Fig. 3 Comparison of thrust coefficient

velocity and the velocity that will be in the boundary condition, and that $c(i)$ represents the coefficient of the magnitude of the ith bound vortex effect on the velocity of the fluid at the ith control point, the bound vortex is corrected as follows:

$$\Gamma_{bv(i)\text{new}}=\Gamma_{bv(i)\text{old}}-\mathrm{RF}_{bv}\frac{\Delta u(i)}{c(i)}\quad(i=1\sim M) \tag{9}$$

where RF_{bv} is a relaxation factor for the bound vortices. The shed vortex, on the other hand, is corrected as follows when the left side of Eq. (8) becomes $\Delta\Gamma$:

$$\Gamma_{sv(N)\text{new}}=\Gamma_{sv(N)\text{old}}-\mathrm{RF}_{sv}\Delta\Gamma \tag{10}$$

where RF_{sv} is a relaxation factor for the shed vortex.

Next, the fluid forces are calculated using the corrected temporary strength of the vortices and the drag due to fluid viscosity, and the motion of the bending propulsion mechanism is corrected to satisfy the equations of motion Eqs. (5), (6), and (7) using discretized formulas of these equations. Assuming that ΔF_x represents the discrepancy between the left side and the right side of Eq. (5), since $x_{(N)}$ and $x_{(N-1)}$ are known, $x_{(n+1)}$ is corrected as follows:

$$x_{(N+1)\text{new}}=x_{(N+1)\text{old}}-\mathrm{RF}_x\Delta F_x \tag{11}$$

where RF_x is a relaxation factor for the x.

Since the boundary conditions change due to changes in the motion of the mechanism, the strength of the vortices are corrected again.

These corrections are repeated until all the correction amounts $\Delta u(i)$, $\Delta\Gamma$, ΔF_x, ΔF_y, ΔF_θ become smaller than the sufficiently small numbers ϵ_{bv}, ϵ_{sv}, ϵ_x, ϵ_y, ϵ_θ at each time step. The amounts of relaxation factors RF_{bv}, RF_{sv}, RF_x, RF_y, RF_θ are empirically chosen to minimize the iteration. Figure 2 represents the above-mentioned computing algorithm. From many trial computations, we found that this algorithm remains stable unless the mass of the mechanism is extraordinarily small.

We compare the present method with the linearized theory, which uses the Theodorsen function, to verify the accuracy of the present method in the case of a harmonic oscillating flat plate. Since the complete motion of the plate is given, the particular procedure for the present method of solving the motion of the flat plate is omitted in this case. The flat plate moves in the manner of Lighthill (1970), i.e., heaving and pitching motions in a 90 deg phase and with an amplitude ratio defined as the feathering parameter $\theta=U\alpha/\omega h$, where U represents the propulsive speed, α and h represent the amplitude of pitching and heaving motion, respectively, and ω represents the angular frequency of oscillation. Representing the averaged thrust of the plate as $\bar{P}$, the thrust efficient C_T can be defined by the form (Chopra and Kambe, 1977):

$$C_T=\bar{P}/(\tfrac{1}{2}\rho U^2h^2S), \tag{12}$$

where ρ represents the fluid density, and S the area of the plate. Figure 3 shows the thrust coefficient from the present method

Downloaded 03 Jun 2010 to 171.66.16.125. Redistribution subject to ASME license or copyright; see http://www.asme.org/terms/Terms_Use.cfm

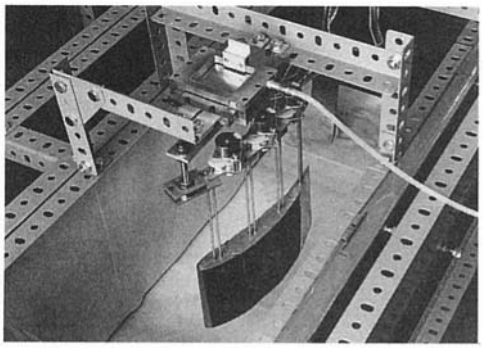


Fig. 4 Three joint bending propulsion mechanism

as the function of the reduced frequency $\omega c/U$ comparing with the linearized theory, where c represents the chord length, and the pitching axis is located at a position of three-quarter chord. An agreement between the two methods indicates the validity of the present method. In the calculation of the present method, $M = 20$, $h = 0.01c$, and one oscillating cycle is divided into 80 time steps.

4 Experimental System and Parameter Identification

4.1 Experimental System. Figures 4 and 5 show the experimental system which consists of a four link and three joint bending propulsion mechanism and a water tank. The speed of water in the tank is controlled by varying the input voltage of a pump. The leading edge of the first link of the mechanism is supported by a vertical shaft through a ball-bearing to rotate freely around a vertical axis. The shaft is fixed to a linear air slider, so that the leading edge point is constrained in a direction perpendicular to that of the flow. The three joints are driven by stepping motors controlled by a personal computer. The streamlined underwater body of the bending propulsion mechanism is handmade according to the profile of NACA0012, which is a common type of wing in aeronautics.

4.2 Parameter Identification. Mass distribution of the bending propulsion mechanism and the drag resulting from fluid viscosity are experimentally identified for the computer simulation. The drag resulting from fluid viscosity is measured as the total fluid force acting on the bending propulsion mechanism. A weight is suspended with a thread so that the weight touches the rear of the air slider. When the mechanism is set in the flow, it moves backward from the force of the drag and the thread inclines from a vertical line until the tangential component of the gravity of the weight balances with the drag. We calculate the drag from the tangent of the inclined thread angle. On the other hand, we measure the velocity of the flow by tracking the displacements of floating markers in the water, using a video tape recorder.

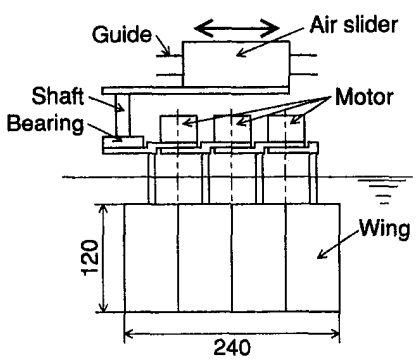


Fig. 5 Schematic side view of the bending propulsion mechanism

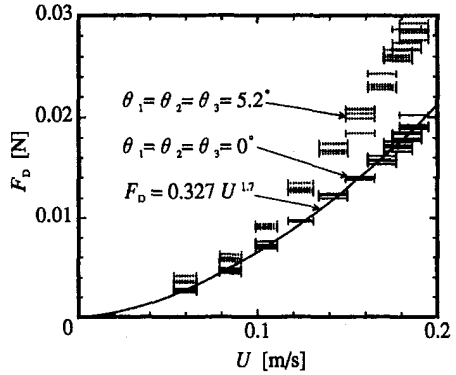


Fig. 6 Experimental relationship between the speed of the flow and the drag resulting from fluid viscosity

Figure 6 shows the experimental results of the steady drag resulting from fluid viscosity when the three joint angles θ_1, θ_2 and θ_3 are fixed at zero (straight case) and 5.2 deg (bending case). In the bending case, the pitching angle of the whole bending propulsion mechanism becomes an equilibrium point at the moment of the fluid force. The horizontal error bars indicate the accuracy of the measurement of the flow velocity. Although the steady drag in the bending case is about 1.5 times larger than the straight case, we cannot say that the unsteady drag of the mechanism in motion changes between two such values, because the condition of the unsteady flow is quite different from that of the steady flow. However, it is difficult to measure the unsteady drag when the mechanism is in motion, because the thrust and the drag cannot be separated. Thus, we simply examine the unsteady effect as follows:

As shown later, we have numerical results that the bending propulsion mechanism almost never generates the thrust when the uniform phase difference is approximately 140 deg. Thus, we have measured the drag in this case and found that it is equal to that of the steady straight case, taking into account our limited ability of measurement. This may be due to the relatively low Reynolds number ($2 \sim 4.5 \times 10^4$) in the experiment, in which a considerable separation of the flow may not occur.

Considering the above discussion, we simply assume that the unsteady drag is equal to that of the steady straight case. For the computer simulation, the drag is regarded as the empirical function of the speed of the flow U m/s, as shown in Fig. 6:

$$F_D = 0.327U^{1.7}\ [N] \tag{13}$$

where the number "0.327" must have a unit N $s^{1.7}/m^{1.7}$ because it is an empirical formula.

5 Analysis of Propulsive Speed

5.1 Motion Patterns. We investigate the steady speed of the bending propulsion mechanism when three joint angles change sinusoidally in the form:

$$\theta_p(t) = \theta_{p\max} \sin(\omega t - \phi_p) \quad (p = 1 \sim 3,\ \phi_1 = 0) \tag{14}$$

where $\theta_p(t)$, $\theta_{p\max}$, ω and ϕ_p represent the bending angle of the pth joint, the amplitude of the pth joint angle, the angular frequency of the joint angles, and the phase difference of the pth joint from the first joint, respectively. Thus the motion of the bending propulsion mechanism depends on six parameters: $\theta_{1\max}$, $\theta_{2\max}$, $\theta_{3\max}$, ϕ_2, ϕ_3, and ω. In this paper, however, we examine the propulsion characteristics of the four particular motion patterns, shown in Table 1.

Motion patterns 1, 2 and 3 have uniform angular amplitudes at three joint angles. They change from a small and quick motion

Downloaded 03 Jun 2010 to 171.66.16.125. Redistribution subject to ASME license or copyright; see http://www.asme.org/terms/Terms_Use.cfm

Table 1 Motion patterns

	$\theta_{1\,\max}$	$\theta_{2\,\max}$	$\theta_{3\,\max}$	$2\pi/\omega$
Pattern 1	2.6°	2.6°	2.6°	0.45 sec
Pattern 2	5.2°	5.2°	5.2°	0.90 sec
Pattern 3	10.4°	10.4°	10.4°	1.80 sec
Pattern 4	2.6°	5.2°	7.8°	0.90 sec

(Pattern 1) to a large and slow motion (Pattern 3), keeping $(\theta_{p\max} \cdot \omega)$ constant, that is, keeping the maximum motion speed of the bending propulsion mechanism constant. In pattern 4, $\theta_{2\max}$ and $\theta_{3\max}$ are two and three times as large as $\theta_{1\max}$, respectively.

The phase differences of the joint angles are varied, keeping the relation:

$$\phi_2 = \phi_0, \quad \phi_3 = 2\phi_0. \tag{15}$$

That is, ϕ_0 represents a "uniform" phase difference.

5.2 Results and Discussion. Figure 7 depicts a typical calculated result of the change in the average propulsive speed of the bending propulsion mechanism after the mechanism begins its bending motion from an initial stationary state (Pattern 1, $\phi_0 = 0$). The number of the spatial division M is 20, and the number of the time division is 20 per cycle of bending motion. As seen in this figure, the propulsive speed converges with a steady limited value after the time has sufficiently elapsed. We denote this steady value of the average propulsive speed as $\bar{U}$. In the experiment, the steady flow speed of the water that makes the propulsion mechanism stand still is regarded as $\bar{U}$.

Figure 8 plots the numerical and experimental results of the relationship between ϕ_0 and $\bar{U}$ for all motion patterns. In the numerical results, $\bar{U}$ has a maximum value when $\phi_0 \approx 0$ deg in all motion patterns; $\bar{U}$ has a minimum value when $\phi_0 = 120 \sim 140$ deg in all motion patterns, except for Pattern 4, where $\bar{U}$ has a minimum value when $\phi_0 \approx 180$ deg.

Let us consider the reason for the above stated results. First, the numerical results of the distribution of the propulsion force are shown in Fig. 9. The abscissa is the normalized length from the leading to the trailing edges of the bending propulsion mechanism. The ordinate is also a normalized propulsive force. As seen in Fig. 9, the propulsive force is mainly produced by the fourth link, while the third link mainly prevents the propulsion of the mechanism.

In the case of Pattern 1, Fig. 10 shows the motion of the bending propulsion mechanism during one period. By comparing Fig. 9 and Fig. 10(a), we conclude that the bending propulsion mechanism is propelled by a reacting force which is induced when the fourth link pushes fluid backward in a fanning motion. This fanning motion of the fourth link of the mechanism

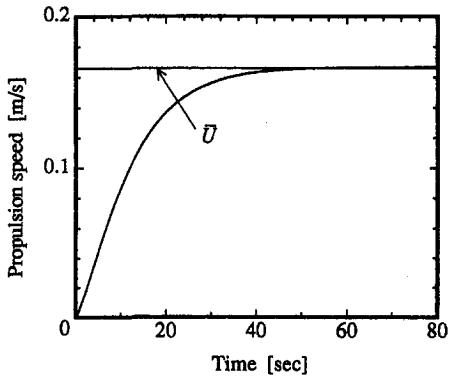
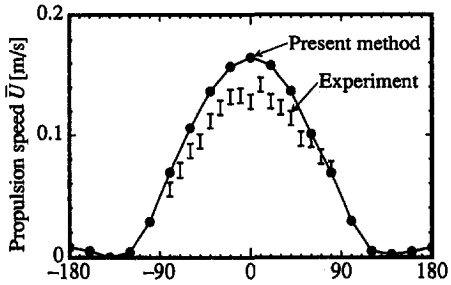
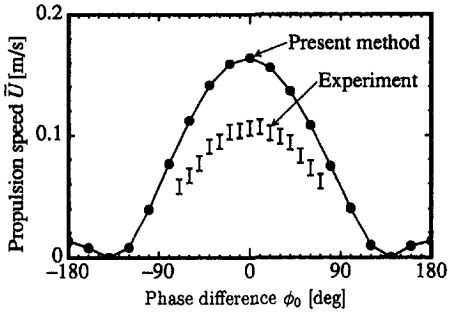


Fig. 7 The relationship between time and the propulsive speed of the bending propulsion mechanism

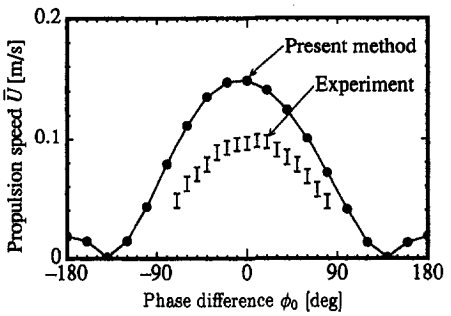


(a) Pattern 1

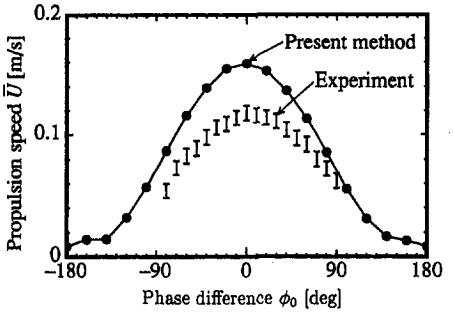


(b) Pattern 2

Fig. 8 (*a* and *b*)



(c) Pattern 3



(d) Pattern 4

Fig. 8 (*c* and *d*)

Fig. 8 The relationship between ϕ_0 and the steady propulsive speed $\bar{U}$

exhibits a maximum amplitude, in particular, when all the joints move in the same phase. Therefore, it is reasonable that $\bar{U}$ has a maximum value when $\phi_0 \approx 0$ deg.

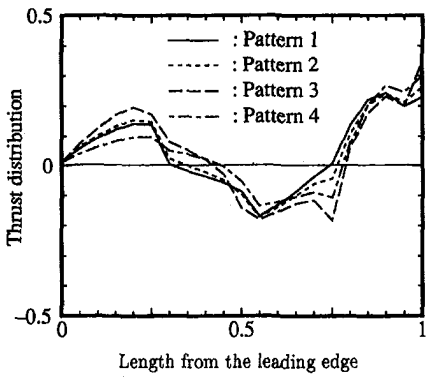
Another explanation of why the propulsive speed reaches its maximum, when all the joints move in phase, can be made from the viewpoint of the EBT. In the EBT, the propulsive efficiency greatly increases when the phase speed is somewhat greater than the swimming velocity. Similar motions to this theory in other observations (Lighthill (1970)) indicate that the fish may

Downloaded 03 Jun 2010 to 171.66.16.125. Redistribution subject to ASME license or copyright; see http://www.asme.org/terms/Terms_Use.cfm

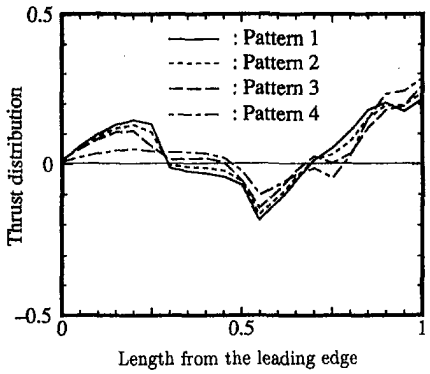
choose the motion to obtain maximum propulsive efficiency. On the other hand, the thrust reaches a finite maximum value when the phase speed reaches infinity in the EBT. Since the motion of $\phi_0 = 0$ in this paper indicates that the phase speed is infinity, it is reasonable to assume that the propulsive speed reaches its maximum when all the joints move in phase.

In the case of $|\phi_0| = 120$ deg, on the other hand, the bending motion of the three joints mostly cancel each other's lateral motion amplitude of the links. Thus, the fanning motion of the fourth link of the mechanism greatly decreases, as seen in Fig. 10(b), resulting in the minimum $\bar{U}$. Moreover, in the case of $|\phi_0| = 180$ deg, the bending motions of the first and the second joints cancel each other's lateral motion amplitude. But the bending motion of the third joint remains effective, and hence the amplitude of the fourth link's motion is larger than that in the case of $|\phi_0| = 120$ deg, resulting in a larger $\bar{U}$. In the case of Pattern 4, however, the motions of the joint angles do not cancel each other out, even when $\phi_0 = 120$ deg, since the amplitudes of the three joint angles are all different. Therefore, we consider that $\bar{U}$ does not have a minimum value when $\phi_0 = 120$ deg in Pattern 4.

By comparing the calculated maximum propulsive speeds of Patterns 1, 2, and 3 to each other, we can find that the maximum propulsive speeds of Patterns 1 and 2 are almost equal. We believe that the reason for this result is as follows: the magnitude of the reacting force in the normal direction of the link is proportional to the acceleration amplitude ($\theta_{p\max} \cdot \omega^2$), and the propulsive force is proportional to (reacting force) $\cdot\, \theta_{p\max}$. Therefore, the propulsive force is proportional to $(\theta_{p\max} \cdot \omega)^2$, making the propulsive speeds become equal when the bending motion speed ($\theta_{p\max} \cdot \omega$) is equal. However, the calculated maximum speed of Pattern 3 is smaller than those of Patterns 1 and 2. The reason

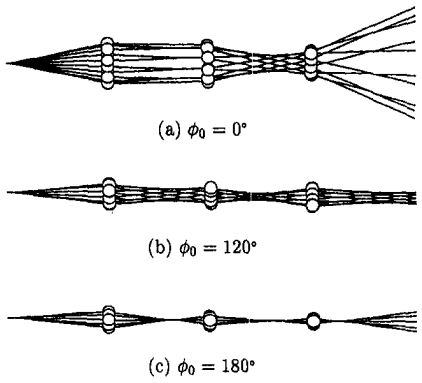


(a) $\phi_0 = 0°$



(b) $\phi_0 = 60°$

Fig. 9 Distribution of the propulsive force along the propulsive mechanism



(a) $\phi_0 = 0°$

(b) $\phi_0 = 120°$

(c) $\phi_0 = 180°$

Fig. 10 Motion of the bending propulsion mechanism during one period

for this may be the reduction of the thrust due to changes in the hydrodynamic characteristics with respect to the frequency of the joints.

In Fig. 8, we find that the experimental values of $\bar{U}$ also reach their maximum when $\phi_0 \approx 0$ deg in all motion patterns. However, the experimental values are quantitatively somewhat smaller than the numerical ones: They are 80 percent of the numerical ones in Pattern 1, 65 percent of those in Patterns 2 and 3, and 75 percent of those in Pattern 4. The reasons for these discrepancies may be due to the three dimensional effect and the unsteady effect on the drag. Although we assume that the unsteady drag is equal to that in the steady straight case, the unsteady drag in the case of $\phi_0 \approx 0$ deg may be larger than that in the straight case.

In this paper, it is found that the bending motion of the three joints in phase is optimum for high speed propulsion, under the condition that each joint amplitude is constant. Further investigation of the optimum motion for varying amplitudes and phases for efficient propulsion will be the next step.

6 Conclusions

A numerical method for a coupled system of the mechanism and fluid for a bending propulsion mechanism is presented. We developed a four link and three joint bending propulsion mechanism, and numerically and experimentally investigated the characteristics of the propulsion speed of the three joint bending propulsion mechanism for four motion patterns, varying the phase difference between the joint motions. The conclusions obtained are summarized as follows:

(1) It is found that the propulsive speed reaches its maximum when the phase differences between adjacent joints are all approximately zero degrees in four motion patterns. The reason for this result appears to be that the fanning motion of the fourth link, which produces the most of the propulsive force, can reach a maximum amplitude when all the joints move in the same phase.

(2) From a numerical analysis it is found that the steady propulsive speed has a minimum value when the absolute values of the phase differences are approximately 120 deg in the motion patterns where all joint motions have the same amplitudes. The reason for this result appears to be that the fanning motion of the fourth link of the mechanism has a minimum amplitude when the absolute values of the phase differences are 120 deg.

(3) From a numerical analysis of the motion patterns which have the same motion speed but different amplitudes and frequencies, it is found that the maximum propulsive speeds are equal when the bending motion and phase are equal. However, the propulsive speed tends to decrease as the motion amplitude greatly increases.

(4) The validity of the numerical method presented in this paper is proven, since the calculated propulsive speeds coincide

Downloaded 03 Jun 2010 to 171.66.16.125. Redistribution subject to ASME license or copyright; see http://www.asme.org/terms/Terms_Use.cfm

with the experimental ones, although the experimental values are 65 ~ 80 percent of the numerical ones.

APPENDIX

We assume a body whose boundary is B in the fluid and assume a stationary closed curve C, which is large enough to surround the body. Curve B is allowed to move and/or deform arbitrarily. The momentum flux which flows into the internal area of C increases the momentum of the area between C and B (this area is denoted as S), and produces force F against body B. This is expressed as the following equation.

$$\mathbf{F} = -\oint_C d\mathbf{G} - \frac{d}{dt}\iint_S \rho \mathbf{v} dS \tag{16}$$

where $d\mathbf{G}$ is the momentum flux which passes through the line element ds of C from left to right.

Using complex variables, Eq. (16) becomes

$$F_x' - iF_y' = -\oint_C (dG_x - idG_y) - \rho \frac{d}{dt}\iint_S w dS \tag{17}$$

where $\mathbf{F} = (F_x', F_y')$, $d\mathbf{G} = (dG_x, dG_y)$, $\mathbf{v} = (u, v)$, and $w = u - iv$ is the complex velocity.

Here, let us demonstrate that the surface integral part of Eq. (17) can be rewritten using curvilinear integrals along B and C. To show this, we note the following general formulas:

$$\iint_S \frac{\partial F}{\partial \bar{z}} dS = -\frac{i}{2}\oint_C F dz \tag{18}$$

$$\iint_S \frac{\partial F}{\partial z} dS = \frac{i}{2}\oint_C F d\bar{z} \tag{19}$$

where $\bar{z}$ is the conjugate of z, $F(z, \bar{z})$ is an arbitrary function of z and $\bar{z}$, C represents a closed curve surrounding the area S, and there is no singularity in area S. Since $w = dW/dz$ is the function of z, the following equation holds:

$$\iint_S w dS = \iint_S \frac{\partial}{\partial \bar{z}}(w\bar{z}) dS = -\frac{i}{2}\oint_C w\bar{z} dz = -\frac{i}{2}\oint_C \bar{z} df. \tag{20}$$

According to Cauchy's integral theorem, the equation

$$\oint_C z df = \oint_C zw dz = 0 \tag{21}$$

holds, and its conjugate becomes

$$\oint_C \bar{z}\bar{df} = 0. \tag{22}$$

Hence, since

$$\oint_C \bar{z} df = \oint_C \bar{z}(df + \bar{df}) = 2\oint_C \bar{z} d\Phi, \tag{23}$$

we obtain the general equation:

$$\iint_S w dS = -\frac{i}{2}\oint_C \bar{z} df = -i\oint_C \bar{z} d\Phi. \tag{24}$$

In the present case, note that the circuit C in Eq. (24) becomes C and B. Thus Eq. (24) becomes

$$\iint_S w dS = -i\left(\oint_C - \oint_B\right)\bar{z} d\Phi. \tag{25}$$

On the other hand, the complex expression of the momentum flux $d\mathbf{G}$ is given by

$$dG_x - idG_y = ipd\bar{z} + \rho w d\Psi = i\left(p + \frac{\rho}{2}q^2\right)d\bar{z} - \frac{i}{2}\rho w^2 dz.$$

Since

$$p + \frac{\rho}{2}q^2 = \rho\left\{F(t) - \frac{\partial \Phi}{\partial t}\right\} \tag{27}$$

where $F(t)$ is an arbitrary function, the curvilinear integral of Eq. (26) becomes

$$\oint_C (dG_x - idG_y) = -\frac{i}{2}\rho\oint_C w^2 dz - i\rho\oint_C \frac{\partial \Phi}{\partial t} d\bar{z}. \tag{28}$$

The last term can be rewritten as

$$\oint_C \frac{\partial \Phi}{\partial t} d\bar{z} = \frac{d}{dt}\oint_C \Phi d\bar{z} = \frac{d}{dt}\left\{[\Phi\bar{z}]_C - \oint_C \bar{z} d\Phi\right\}. \tag{29}$$

Denoting an arbitrary starting point of the surface integral on C as z_1, and considering that $[\Phi\bar{z}]_C$ is the variation of $\Phi\bar{z}$ around C, the following equation holds:

$$[\Phi\bar{z}]_C = [\Phi]_C\bar{z}_1 = \Gamma(C)\bar{z}_1 \tag{30}$$

where $\Gamma(C)$ is the circulation along curve C and is a constant value according to Kelvin's circulation theorem. Hence, the following equation:

$$\oint_C \frac{\partial \Phi}{\partial t} d\bar{z} = -\frac{d}{dt}\oint_C \bar{z} d\Phi \tag{31}$$

holds, and Eq. (28) becomes

$$\oint_C (dG_x - idG_y) = -\frac{i}{2}\rho\oint_C w^2 dz + i\rho\frac{d}{dt}\oint_C \bar{z} d\Phi. \tag{32}$$

Introducing Eq. (32) and Eq. (25) in Eq. (17), finally we obtain

$$F_x' - iF_y' = \frac{i}{2}\rho\oint_C w^2 dz - i\rho\frac{d}{dt}\oint_B \bar{z} d\Phi. \tag{33}$$

References

Cheng, H. K., and Murillo, L., 1984, "Lunate-Tail Swimming Propulsion as a Problem of Curved Lifting Line in Unsteady Flow. Part 1. Asymptotic Theory," *Journal of Fluid Mechanics,* Vol. 143, pp. 327–350.

Cheng, J. Y., Zhuang, L. X., and Tong, B. G., 1991, "Analysis of Swimming Three-Dimensional Waving Plates," *Journal of Fluid Mechanics,* Vol. 232, pp. 341–355.

Chopra, M. G., 1974, "Hydromechanics of Lunate-Tail Swimming Propulsion," *Journal of Fluid Mechanics,* Vol. 64, No. 2, pp. 375–391.

Chopra, M. G., 1976, "Large Amplitude Lunate-Tail Theory of Fish Locomotion," *Journal of Fluid Mechanics,* Vol. 74, No. 1, pp. 161–182.

Chopra, M. G., and Kambe, T., 1977, "Hydromechanics of Lunate-Tail Swimming Propulsion. Part 2," *Journal of Fluid Mechanics,* Vol. 79, No. 1, pp. 49–69.

Kambe, T., 1978, "Dynamics of Carangiform Swimming Motions," *Journal of Fluid Mechanics,* Vol. 87, pp. 533–560.

Karpouzian, G., Spedding, G., and Cheng, H. K., 1990, "Lunate-Tail Swimming Propulsion. Part 2. Performance Analysis." *Journal of Fluid Mechanics,* Vol. 210, No. 4, pp. 329–351.

Katz, J., and Weihs, 1978, "Hydrodynamic Propulsion by Large Amplitude Oscillation of an Airfoil with Chordwise Flexibility," *Journal of Fluid Mechanics,* Vol. 88, No. 3, pp. 485–497.

Katz, J., and Weihs, 1979, "Large Amplitude Unsteady Motion of a Flexible Slender Propulsor," *Journal of Fluid Mechanics,* Vol. 90, No. 4, pp. 713–723.

Lighthill, M. J., 1960, "Note on the Swimming of Slender Fish," *Journal of Fluid Mechanics,* Vol. 9, pp. 305–317.

Lighthill, M. J., 1970, "Aquatic Animal Propulsion of High Hydromechanical Efficiency," *Journal of Fluid Mechanics,* Vol. 44, No. 2, pp. 265–301.

Lighthill, M. J., 1975, *Mathematical Biofluiddynamics,* Society for Industrial and Applied Mathematics, Philadelphia.

Newman, J. N., and Wu, T. Y., 1973, "A Generalized Slender-Body Theory for Fish-Like Forms," *Journal of Fluid Mechanics,* Vol. 57, No. 4, pp. 673–693.

Siekmann, J., 1962, "Theoretical Studies of Sea Animal Locomotion, Part 1," *Ingenieur-Archiv,* Vol. 31, pp. 214–228.

Downloaded 03 Jun 2010 to 171.66.16.125. Redistribution subject to ASME license or copyright; see http://www.asme.org/terms/Terms_Use.cfm

Siekmann, J., 1963, "Theoretical Studies of Sea Animal Locomotion, Part 2," *Ingenieur-Archiv,* Vol. 32, pp. 40–50.

Triantafyllou, G. S., Triantafyllou, M. S., and Grosenbaugh, M. A., 1993, "Optimal Thrust Development in Oscillating Foils with Application to Fish Propulsion," *Journal of Fluids and Structures,* Vol. 7, pp. 205–224.

Uldrick, J. P., and Siekmann, J., 1964, "On the Swimming of a Flexible Plate of Arbitrary Finite Thickness," *Journal of Fluid Mechanics,* Vol. 20, pp. 1–33.

Wang, P. K. C., 1966, "Optimum Propulsion of an Oscillating Hydrofoil," *IEEE Transactions of Automatic Control,* Vol. 11, pp. 645–651.

Wu, T. Y., 1961, "Swimming of a Waving Plate," *Journal of Fluid Mechanics,* Vol. 10, pp. 321–344.

Wu, T. Y., 1971a, "Hydromechanics of Swimming Propulsion. Part 1. Swimming of a Two-Dimensional Flexible Plate at Variable Forward Speeds in an Inviscid Fluid," *Journal of Fluid Mechanics,* Vol. 46, No. 2, pp. 337–355.

Wu, T. Y., 1971b, "Hydromechanics of Swimming Propulsion. Part 2. Some Optimum Shape Problem," *Journal of Fluid Mechanics,* Vol. 46, No. 3, pp. 521–544.

Wu, T. Y., 1971c, "Hydromechanics of Swimming Propulsion. Part 3. Swimming and Optimum Movements of Slender Fish with Side Fins," *Journal of Fluid Mechanics,* Vol. 46, No. 3, pp. 545–568.

Wu, T. Y., 1971d, "Hydromechanics of Swimming of Fishes and Cetaceans," *Advances in Applied Mechanics,* Vol. 11, pp. 1–63.

Wu, T. Y., Brokaw, C. J., and Brennen, C., 1975, *Swimming and Flying in Nature,* Vols. 1 and 2, Prenum Press, New York.

Downloaded 03 Jun 2010 to 171.66.16.125. Redistribution subject to ASME license or copyright; see http://www.asme.org/terms/Terms_Use.cfm

Deformation and Rebounding Processes of a Water Droplet Impinging on a Flat Surface Above Leidenfrost Temperature

Hitoshi Fujimoto
Research Associate.

Natsuo Hatta
Professor.

Department of Mineral Science and Technology, Kyoto University, Kyoto 606, Japan

This paper treats numerical analyses of the deformation and rebounding processes of a water droplet impinging on a flat solid surface above the Leidenfrost temperature with a speed in the order of a few [m/s], as well as the flow field inside the droplet. These calculations were performed using the MAC-type solution method to solve a finite differencing approximation of the axisymmetric Navier-Stokes equations governing incompressible fluid flows. Also, the whole dynamic process of a droplet from the moment of collision with a hot surface including the rebound from it was recorded by using a video camera equipped with a macro lens. First, the water film formed by the droplet impinging on the surface spreads radially in a fairly thin discoid-like shape until it reaches a maximum. Next, the water film begins to recoil backwards towards the center and the recoiling process continues to occur owing to the surface tension effect at the periphery. Subsequently, the center part of the liquid drop begins to elongate upwards and the liquid near the top of the drop pulls up the lower part of the remaining liquid. Finally, a vortical ring structure appearing at the bottom of the elongated droplet induces the rotative motion in such a way as to form the rising flow and the droplet rebounds from the surface as a bowling pin-shaped mass. The numerical model to predict the deformation and rebounding processes was built up by accounting for the presence of viscous and surface tension effects. The numerical results obtained by the model were compared with the experimental data and discussed from a practical point of view.

1 Introduction

The process of cooling a high temperature surface with a water spray or a mist flow is extensively used in iron and steel-making industries. Specifically, these cooling methods are applied to the secondary cooling zone in a continuous casting process. However, there seems to be a conspicuous lack of knowledge concerning the detailed cooling mechanism. To evaluate spray/mist cooling heat transfer, it is indispensable to understand the collision dynamics of liquid droplets on a hot rigid surface systematically.

For an indispensable first approach to the more realistic situation of industrial interest where a droplet impinges against a surface heated above the Leidenfrost temperature, the deformation process of a liquid droplet impacting on a cold surface (at room temperature) has been investigated by a number of researchers. First, the fluid dynamics of droplet splashing were numerically analyzed on the basis of the original MAC method (Harlow and Welch, 1965) by Harlow and Shannon (1967), who neglected viscous and surface tension effects. Turutani et al. (1989) carried out the numerical analysis of the spreading process of a droplet impinging upon a cold flat surface based upon the SMAC method (Amsden and Harlow, 1970), taking into account the surface tension effect and demonstrated that it affects the spreading process of the droplet.

Recently, Fukai et al. (1993) presented a new finite element-based technique to model the droplet spreading process. This technique accounts for the presence of inertial, viscous, gravitational and surface tension effects. Thereafter, this model was enhanced to take into account the wetting effect, which is represented by distinct spreading and recoiling contact angles (Fukai et al., 1995). The wetting effect can be incorporated in theoretical/numerical models if the spreading and recoiling contact angles are measured a priori experimentally. On the other hand, Hatta et al. (1995b, c) calculated the deformation process of a water droplet impacting on an Inconel 625 alloy surface on the basis of the MAC-type solution method. The numerical predictions in terms of droplet deformation, drop radius and height, were found to be in good agreement with the experimental value, at least, in the spreading process, but the difference between the numerical and experimental results was found to be not necessarily negligible in the subsequent process when the wettability is neglected (Hatta et al., 1995b). However, the numerical results obtained by accounting for the slip velocity of contact line corresponding to the degree of wettability on the solid/liquid interface, were found to be in good agreement with experimental data in the whole process (Hatta et al., 1995c). What is carefully taken into account is that this fact can be said, at least, for the case where a water droplet impacts against the Inconel 625 alloy surface. In a strict sense, the combination between liquid and solid phases should be considered to govern the deformation process of the droplet. Also, the deformation process of a water droplet impacting on a cold Inconel 625 alloy surface was compared to that of the droplet colliding with the same surface heated above the Leidenfrost temperature from an experimental point of view. As a result, it was confirmed that good agreement between the cold and hot cases is obtained only in the spreading process, but not in the subsequent (recoiling) process, as will be mentioned later. This above-mentioned fact suggests that the wetting phenomenon can occur even on a hot surface in the spreading process almost until the droplet attains a maximum diameter, and thereafter the droplet does not contact the hot surface through a vapor film.

Contributed by the Fluids Engineering Division for publication in the JOURNAL OF FLUIDS ENGINEERING. Manuscript received by the Fluids Engineering Division September 8, 1994; revised manuscript received August 15, 1995. Associate Technical Editor: R. W. Metcalfe.

Copyright © 1996 by ASME

Downloaded 03 Jun 2010 to 171.66.16.125. Redistribution subject to ASME license or copyright; see http://www.asme.org/terms/Terms_Use.cfm

So far, experimental investigations on the deformation behavior of a droplet impinging on a hot surface have also been performed by many researchers. When the droplet has low Weber numbers corresponding to a low impact energy, the droplet spreads as a lens-shaped mass on the solid surface above the Leidenfrost temperature. The droplet continues to spread up to a maximum diameter. After this time, the liquid begins to flow backwards from the peripheral region towards the center and then swelling in the central region becomes more and more remarkable. Finally, the liquid drop rebounds as a bowling-pin shaped mass from the surface. For higher Weber numbers the droplets shatter during the deformation process (Wachters and Westerling, 1966; Ueda et al., 1979; Akao et al., 1980; Chandra and Avedisian, 1991).

However, it seems that the deformation and rebounding processes of the droplet on/from the surface heated above the Leidenfrost temperature has not been yet clarified, in detail, from analytical as well as experimental aspects. Hence, we have investigated the viscous and surface tension effects on the driving force of flow reversal from the periphery of the circular liquid film towards the central region, and on that of rebounding of the liquid drop from the surface, from the viewpoint of the numerical analysis.

This process of the approach is outlined as follows: The inner pressure in the periphery of the liquid film formed by the droplet impinging on a hot surface can be considered to be much higher than that in the central region. This is because the radius of curvature in the periphery is extremely small in comparison with that in the central region. Therefore, the flow reversal is induced owing to the pressure difference. This leads to the recoiling process of the liquid film. Even when the central region of the liquid film commences to swell, the recoiling continues to occur due to the fact that the pressure is still higher at the periphery. Subsequently, the center part of the liquid drop continues to elongate upwards. Finally, the preceding liquid at the top of the drop, which has a large upward velocity component, pulls up the bottom part of the remaining liquid on the surface and then the droplet rebounds from the surface.

In the present numerical simulation, the no-slip condition is adopted in the spreading process at the liquid/solid interface until the droplet reaches a maximum and thereafter the bottom boundary condition is switched to slip on the premise that the drop does not contact the surface in the recoiling process, as mentioned above.

In addition to this, it is reasonable to consider that heat transfer from the hot surface to the droplet causes temperature gradients through the droplet. The temperature variation along the surface of the droplet must lead to the surface tension variations; with higher surface tension on the upper, colder side of the droplet and lower surface tension on the lower, hotter side of the droplet. However, it is very tedious to exactly estimate temperature gradient through an extremely deformable droplet within very short time scales in comparison with the time scales of the associated heat transfer processes. Then, a simple thermal distribution such that temperature becomes lower (higher) on the upper (lower) side of the droplet and higher with time is assumed. In this case, the bottom surface of the droplet is fixed at the water saturation temperature (=100°C). The validity of the foregoing hypothesis has been examined by numerical experiments. In order to inspect whether or otherwise the droplet rebounds from the surface only by the surface tension effect, the numerical analysis of the flow field inside the liquid drop has been performed neglecting the evaporation loss of the droplet. Also, the numerical results obtained by the present numerical model have been compared with the experimental data and discussed from a practical point of view. In passing, the computations were performed on the Fujitsu super computer VP2600 at the Data Processing Center of Kyoto University.

2 Conservation Equations

It is assumed that the flow fields obey the axisymmetric Navier-Stokes equations governing incompressible viscous flows. The equations to be solved are expressed nondimensionally in terms of the following dimensionless variables:

$$\left.\begin{aligned} t &= \bar{t}/(\bar{D}_p/\bar{u}_0), \quad x = \bar{x}/\bar{D}_p, \quad y = \bar{y}/\bar{D}_p \\ u &= \bar{u}/\bar{u}_0, \quad v = \bar{v}/\bar{u}_0, \quad p = \bar{p}/(\bar{\rho}\bar{u}_0^2) \end{aligned}\right\} \tag{1}$$

in which t is the time; (x, y) denote the coordinates in the radial and axial directions, respectively; (u, v) denote the velocity components in the x- and y-directions, respectively; p is the pressure. $\bar{D}_p$, $\bar{u}_0$, and $\bar{\rho}$ denote the initial droplet diameter, the impacting velocity and the material density of droplet, respectively. Here, overbars denote the dimensional quantities.

Also, the Reynolds number Re, the Weber number We, and the Froude number Fr are defined as

$$\mathrm{Re} = \frac{\bar{u}_0\bar{D}_p}{\bar{\nu}}, \quad \mathrm{We} = \frac{\bar{\rho}\bar{u}_0^2\bar{D}_p}{\bar{\sigma}}, \quad \mathrm{Fr} = \frac{\bar{u}_0}{\sqrt{\bar{g}\cdot\bar{D}_p}} \tag{2}$$

Here, $\bar{\nu}$ and $\bar{g}$ denote the liquid kinematic viscosity and the gravitational acceleration, respectively; $\bar{\sigma}$ is the surface tension. It should be noted that both $\bar{\nu}$ and $\bar{\sigma}$ are temperature-dependent.

The system of equations governing the droplet deformation is given by

$$\frac{\partial u}{\partial x} + \frac{\partial v}{\partial y} + \frac{u}{x} = 0 \tag{3}$$

Nomenclature

$\bar{a}$ = constant in thermal function of Eq. (7), K
c = distance from a solid surface to a bottom of droplet
$\bar{D}_p$ = initial droplet diameter, m
$\bar{g}$ = gravitational acceleration, m/s^2
Fr = $\bar{u}_0/\sqrt{\bar{g}\cdot\bar{D}_p}$ Froude number
f = CFL number
h = droplet height
p = dimensionless pressure
R_1, R_2 = principal radii of curvature at a point on free surface
Re = $(\bar{u}_0\bar{D}_p/\bar{\nu})$ Reynolds number
r = droplet radius
$\bar{T}$ = liquid temperature, K
$\bar{T}_{ini}$ = initial droplet temperature, K
$\bar{T}_{sat}$ = saturation temperature of a liquid droplet, K
t = time
U_η = velocity component in η direction
u, v = velocity components
u_s, v_s = velocity components on free surface
$\bar{u}_0$ = impinging velocity, m/s
We = $\bar{\rho}\bar{u}_0^2\bar{D}_p/\bar{\sigma}$ Weber number
x, y = coordinates
x_s, y_s = surface position
Δx, Δy = mesh size
ξ = length from the central axis to a point along the free surface
η = coordinate normal to surface
$\bar{\rho}$ = material density of droplet, kg/m^3
$\bar{\nu}$ = kinematic viscosity, m^2/s
$\bar{\sigma}$ = surface tension, Newton/m
$(\bar{\ })$ = dimensioned quantities

Downloaded 03 Jun 2010 to 171.66.16.125. Redistribution subject to ASME license or copyright; see http://www.asme.org/terms/Terms_Use.cfm

$$\frac{\partial u}{\partial t} + \frac{\partial u^2}{\partial x} + \frac{\partial uv}{\partial y} + \frac{u^2}{x} = -\frac{\partial p}{\partial x} + \frac{1}{\mathrm{Re}}\left[\frac{\partial^2 u}{\partial x^2} + \frac{\partial^2 u}{\partial y^2} + \frac{\partial}{\partial x}\left(\frac{u}{x}\right)\right] \quad (4)$$

$$\frac{\partial v}{\partial t} + \frac{\partial uv}{\partial x} + \frac{\partial v^2}{\partial y} + \frac{uv}{x} = -\frac{\partial p}{\partial y} - \frac{1}{\mathrm{Fr}^2} + \frac{1}{\mathrm{Re}}\left[\frac{\partial^2 v}{\partial x^2} + \frac{\partial^2 v}{\partial y^2} + \frac{1}{x}\frac{\partial v}{\partial x}\right] \quad (5)$$

Next, the normal stress balance condition on the free surface is given by

$$p_s - p_\infty + \frac{1}{\mathrm{Re}}\frac{\partial U_\eta}{\partial \eta} = \frac{1}{\mathrm{We}}\left(\frac{1}{R_1} + \frac{1}{R_2}\right) \quad (6)$$

in which p_s and p_∞ are the surface pressure and the atmospheric one, respectively. R_1 and R_2 are the principal radii of curvature at a given point along the free surface, respectively. η is the coordinate normal to the surface and U_η is the component of velocity in the η-direction. Obviously, the sign of the left hand side of Eq. (6) depends upon the sign of R_1 and R_2, that is, whether a concave or convex surface.

3 Numerical Procedure

The deformation and rebounding processes of a droplet impacting on a heated solid surface are basically solved by the same method as shown in the previous paper (Hatta et al., 1995b). Namely, the simulation of the deformation and rebounding processes on the hot surface is performed using the MAC-type solution method to solve a finite-differencing approximation of the Navier-Stokes equations governing an axisymmetric incompressible fluid flow.

Now, let us describe briefly the calculating procedure of the free surface configuration. It is assumed that the free surface consists of a large number of segments and the two-end points of each segment are located on the underlying lines of the rectangular cell system (Miyata, 1986). The time evolution of the free surface is pursued by the Lagrangian movement of the segments that form the free surface configuration. Here, it is worthy to note that the submesh system, whose mesh size is half that of the main system, is introduced in the present calculation (see Fig. 1). Because the free surface configuration is represented by a succession of line segments, it becomes smoother due to the fact that the number of the intersecting points between the segments and the underlying mesh lines increases to twice those of the main mesh system alone. It should be borne in mind that the calculation of the velocity vector and pressure fields is performed only on the main mesh system.

Next, the value of pressure on the free surface is calculated based on Eq. (6). However, the third term in the left hand side of Eq. (6) is neglected because there are some cases where it is impossible to calculate exactly this term, particularly at a sharply concave/convex region.

A droplet impinging on a surface above the Leidenfrost temperature makes direct contact with it within a very short time. As Fukai et al. (1993) stated, a comparison of the time scales of fluid dynamics of droplet spreading to the time scales of the associated heat transport processes shows that the former scales are markedly smaller. Accordingly, it is reasonable to consider that the wetting phenomenon occurs in the early period of impact at the liquid/solid interface, but the vapor film is soon formed and the liquid drop is insulated from the hot surface through it. Let us denote the time required from the moment of collision of a droplet with the surface up to the formation of a vapor film between the liquid drop and the surface by t_c. The determination of t_c will be discussed in the later section.

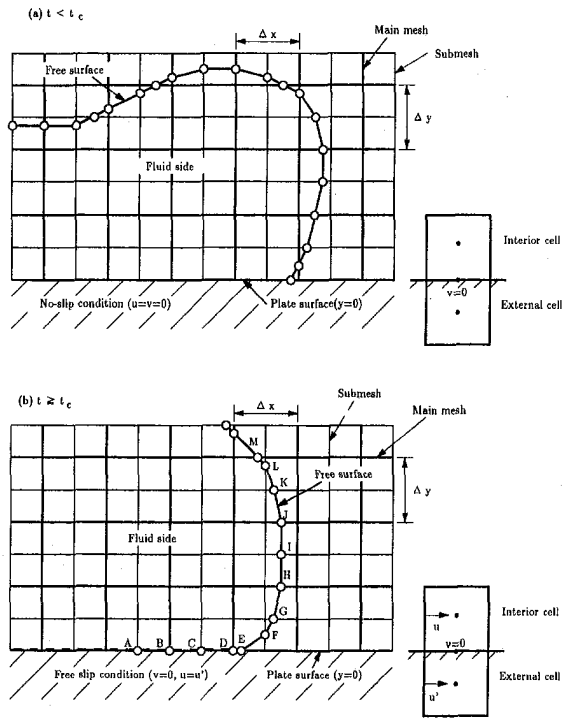


Fig. 1 Indication of boundary conditions for droplet contacting solid surface (*a*) and for droplet being separated from surface by a vapor film (*b*)

In the time range of $t < t_c$, the no-slip condition is adopted ($u = v = 0$ at the wall) at the liquid/solid interface. In the time range of $t \geq t_c$, the free-slip condition ($v = 0$, $u' = u$; $u' =$ velocity component at the external cell contacting the solid wall, see Figure 1(b)) is adopted at the liquid/solid interface, because it is assumed that there is no friction owing to the formation of a vapor film. Furthermore, it may be justifiable to assume that the liquid drop is insulated with the hot solid surface through a thin vapor film and that the diameter of the circular area contacting the vapor film is always smaller than the maximum diameter of the liquid film because the significant mass accumulation around the periphery of the liquid film is formed on the hot surface (see Figs. 6, 8, and 10). Therefore, the free surface near the periphery of the area contacting the vapor film can be regarded as the region with a very large curvature. By so doing, the principal radii of curvature near the periphery of the liquid film are calculated by renewing the mesh points A, B, C, . . . etc. indicating the free surface at the vapor/solid interface, as shown in Fig. 1(b). Thereby, the peripheral zone with a large curvature is considered to play an important role of the driving force to make the liquid drop rebound from the surface.

Next, it is anticipated that heat transfer from the hot surface to the droplet occurs and causes temperature gradients through the droplet. However, it is very tedious to perform an unsteady heat transfer analysis of the droplet accompanied by the large deformations in a very short time. On the premise that the temperature variation along the surface of droplet leads to surface tension variations, a simple distribution function such that the temperature $\bar{T}$ becomes lower (higher) on the upper (lower) side of the droplet and higher with time is assumed as

$$\bar{T} = \bar{T}_{sat} - \frac{y - c}{h - c}\{(\bar{T}_{sat} - \bar{T}_{ini}) - \bar{a}t\} \quad (7)$$

Downloaded 03 Jun 2010 to 171.66.16.125. Redistribution subject to ASME license or copyright; see http://www.asme.org/terms/Terms_Use.cfm

in which $\bar{T}_{sat}$ and $\bar{T}_{ini}$ are the saturation and initial temperatures, respectively. h is the nondimensional maximum droplet height at a given time t, and $\bar{a}$ is an appropriate constant. c denotes the nondimensional distance between the bottom of droplet and the solid surface, if the droplet rebounds from the surface (see Figure 4). Again, the evaporation loss is neglected.

The calculation starts at the moment of impact of a droplet with a hot surface ($t = 0$). The mesh size is selected to be $\Delta x(= \Delta y) = 1/100$ according to the previous paper (Hatta et al., 1995b). Also, the computational time interval Δt is determined by the CFL (Courant-Friedrichs-Lewy) condition and CFL number f is set at $f = 0.05$ according to the previous paper.

4 Experimental Apparatus

Figure 2 shows a schematic diagram of the experimental apparatus by which the deformation process of a droplet impinging on a rigid surface heated above the Leidenfrost temperature can be measured. By this experimental apparatus, droplets of 300 μm to 700 μm in diameter can be generated in the impinging velocity range between 1.2 m/s and 6.0 m/s. Also, throughout the present paper, the surface temperature is fixed at 500°C. But, it should be noted that the temperature change during the experiments is confirmed to be within ±20°C.

The time variation of the droplet height and radius during the deformation on the hot surface is recorded by many double exposure video images on the basis of the statistical procedure. Again, the measurement accuracy determined by the resolution of the video image is within ±0.006 mm in the present measurement unit. At any rate, the apparatus as well as the measurement method is described in detail elsewhere (Hatta et al., 1995a).

5 Results and Discussion

It is well-known that with lower We numbers a droplet strikes and spreads and eventually rebounds as a bowling pin-shaped mass from a hot surface, while for a high We number the droplet shatters during the deformation process (Wachters and Westerling, 1966; Ueda et al., 1979). The critical Weber number We_c, which specifies the boundary between rebounding and disintegrating, was proposed by some researchers. Ueda et al. (1979) gave $We_c = 70$ on the basis of the empirical results obtained on condition that the droplets of 1 mm to 3 mm in diameter fell on the flat stainless steel and copper surface heated to 300°C. Again, Shoji et al. (1984) proposed $We_c = 80 \sim 90$ on condition that the droplets of 0.3 mm to 3.5 mm in diameter impinged on the flat nickel surface heated in the temperature range from 300°C to 800°C. Hence, we also investigated the deformation and rebounding phenomena of the droplet after making contact with an Inconel 625 alloy surface heated to 500°C under the experimental condition that the initial droplet size $\bar{D}_p = 330$ μm to 600 μm in diameter and the impact velocity $\bar{u}_0 = 1.7$ m/s to 5.7 m/s. As a result, $We_c \simeq 50$ at 20°C (the Weber number is commonly defined as a function of liquid temperature and here We is given by the water droplet temperature before impinging on a hot plate) was obtained (Hatta et al., 1995a). We consider that the rebounding condition is influenced not only by the We number, but also by other parameters such as the surface temperature, the surface roughness, the affinity at the liquid/solid interface, etc.. Then, the water droplets of $We \leq 50$ are treated in the present investigation.

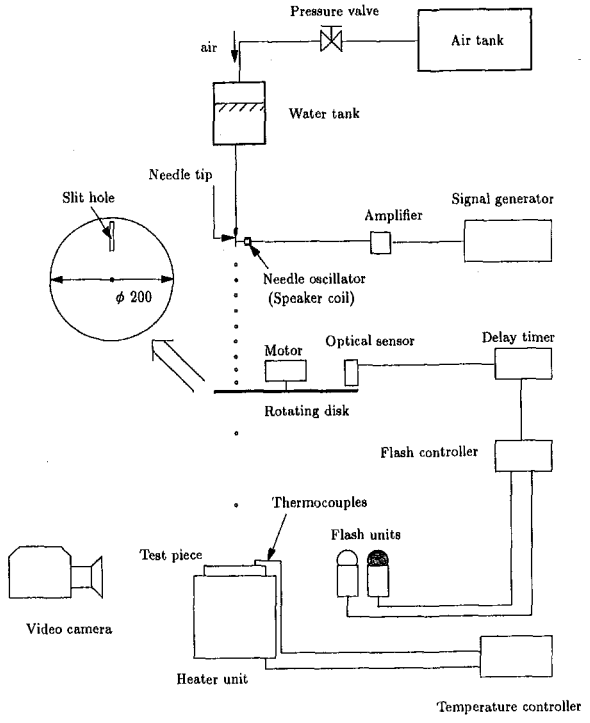


Fig. 2 Schematic diagram of experimental apparatus

First, in order to identify the time t_c required from the moment of impact up to the formation of a vapor film, the deformation process of a droplet impacting on a cold Inconel 625 alloy surface (at room temperature) was compared to that of the droplet colliding with the hot surface of the same material heated to 500°C, from an experimental point of view. These experiments were performed on condition that $\bar{D}_p = 0.50$ [mm] and $\bar{u}_0 = 2.32$ [m/s]. Figure 3 gives the comparison of the time evolution of the height h and the radius r of the droplet between the cold and hot cases. Here, it is noted that h and r are normalized by the preimpact droplet diameter; $h \equiv \bar{h}(t)/\bar{D}_p$ and $r \equiv \bar{r}(t)/\bar{D}_p$ (see Fig. 4). The solid and empty circles in Figure 3 denote the experimental data of h and r, respectively, for the cold surface and the solid and empty triangles for the hot surface. The comparisons demonstrate that the hot case agrees well with the cold one only in the spreading process, but not in the recoiling process.

Furthermore, we found in the previous work (Hatta et al., 1995a) that the nondimensional maximum diameter of droplet impinging on a hot surface above the Leidenfrost temperature is given by a function of the Weber number alone. The results of this formula for the hot surface case were found to be close to the experimental values for the cold case on condition that water droplets impact on an Inconel surface (Hatta et al., 1995c). Additionally, it was confirmed in the previous work (Hatta et al., 1995b) that the numerical predictions in terms of the droplet deformation, drop radius and height, are in good agreement with the experimental data, at least, in the spreading process, although the wetting effect was not taken into account.

The following three conclusions are drawn from the above-mentioned facts. First, the wetting phenomenon occurs in the spreading process almost until the droplet reaches a maximum diameter, even though the surface is heated above the Leidenfrost temperature. Second, the use of the no-slip condition is allowed, at least, in the spreading process. In other words, the wetting effect is not needed in the present model, although this effect is involved in the model of Fukai et al. (1995). Third, the critical time t_c, defined in the third section, at which the bottom boundary condition is switched from the no-slip to the free-slip corresponds to the moment at which the spreading of the droplet is terminated.

Next, the numerical procedure of the boundary condition at the liquid/solid interface is of much importance in the time interval after the droplet reaches a maximum diameter. Judging from the experimental results in Fig. 3, it must be recognized that the deformation process of the drop after the spreading process is entirely different between the cold and hot cases. It is reasonable to suspect that the wide difference in the deformation

Downloaded 03 Jun 2010 to 171.66.16.125. Redistribution subject to ASME license or copyright; see http://www.asme.org/terms/Terms_Use.cfm

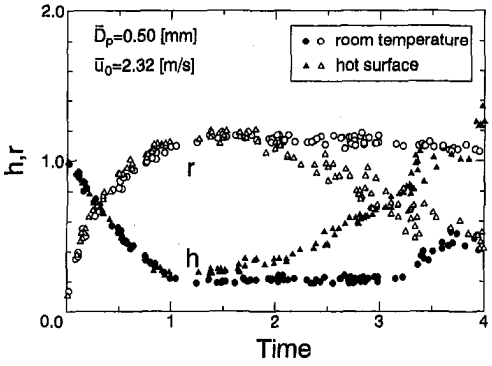


Fig. 3 Time history of droplet deformation process impinging on cold and hot surfaces on condition that $\bar{D}_p$ = 0.50 [mm] and $\bar{u}_0$ = 2.32 [m/s]. Note that the experimental uncertainties in both the droplet radius *r* and height *h* are kept within ±0.021 on a nondimensional scale.

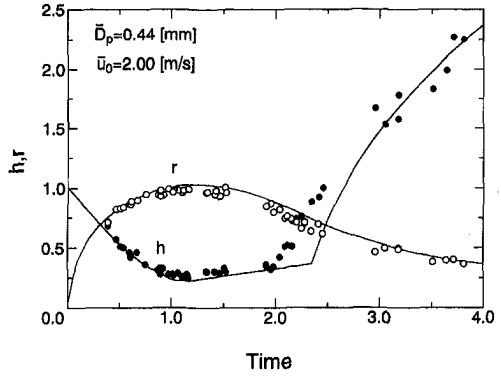


Fig. 5 Numerical and experimental time evolutions of the droplet hight h and radius r on condition that $\bar{D}_p$ = 0.44 [mm] and $\bar{u}_0$ = 2.00 [m/s]. Note that the experimental uncertainties in both the droplet radius r and height h are kept within ±0.023 on a nondimensional scale.

process is attributed to the problem of the interface between the droplet and the surface of the solid, and that the droplet does not contact the surface through a very thin vapor film. Although it is likely that the vaporization into the narrow gaseous layer, between the droplet and the solid surface, increases the pressure in the confined region and therefore leads to the rebound of the droplet, we believe that the whole bottom area of the droplet is not in contact with the solid surface, at least, after the spreading process. The experimental measurement indicates that the bottom surface area of the drop decreases and the height increases within very short time scales. Furthermore, the configuration in the lower part of the drop is observed to be roundish at the moment of rebounding from the hot solid surface. Therefore, we believe that the vapor layer is not confined but open in the whole range from the bottom center to the contact line and that the effect of vaporization on the driving force of rebounding from the hot solid surface is not so strong. At this regard, it may not be erroneous that the free slip condition is applied at the liquid/solid interface after the time t_c defined above. At any rate, the comparison of the results calculated on the above-mentioned condition with the experimental ones determines the validity.

Figure 5 gives the time evolution of the maximum height h and radius r of the droplet on condition $\bar{D}_p$ = 0.44 [mm] and $\bar{u}_0$ = 2.0 [m/s]. Here, the value of $\bar{a}$ appearing in Eq. (7) is fixed at 5[K] throughout the present simulations. The solid and empty circles denoted in this figure indicate the experimental data of h and r, respectively and solid lines show the calculated time history of h and r (see Fig. 4). No difference in h is observed almost until t = 1, both theoretically and experimentally. This result suggests that the initial rate of change of h is directly proportional to the impact velocity. This fact is in agreement with the results obtained by Fukai et al. (1993) and Hatta et al. (1995b). The minimum point along the curve presenting the time variation of h corresponds to the first critical time at which the location of the maximum height of the drop shifts from the centerline to the apex of the ring structure (see Fig. 6). In the time span between t = 0 and $t \simeq 2$, indicated in Fig. 6, the centerline height of the drop decreases rapidly. At the same time, the height of the ring structure increases at a slower rate until it surpasses the centerline height. At the next stage, the sharply increasing point along the calculated curve of h corresponds to the second critical time at which the location of the maximum height of the drop shifts from the apex of the ring structure to the centerline. The calculated critical time at which the height of the drop increases sharply is estimated to be $t \simeq 2.3$, while the experimental critical time corresponds to $t = 2$. Therefore, a difference is observed between the calculated and experimental second critical times and the former is slightly slower than the latter. Again, the centerline height increases in a rapid rate, as soon as the centerline height surpasses that of the ring structure. The calculated increasing rate is observed to be faster than the experimental one. Next, the drop radius increases sharply, as soon as the droplet impacts on the hot surface. No difference in the radius r is observed both theoretically and experimentally until the droplet reaches the peak radius ($t \simeq 1.2$). The simulations predict well the time history of the drop deformation in the radial direction even after this time, although the calculated result is observed to be a little larger than the experimental one in the time span between t = 1.2 and 3.

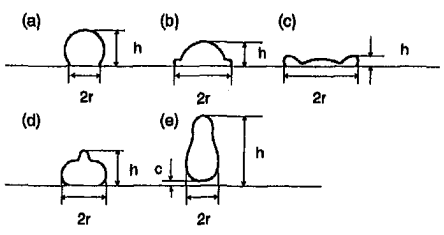


Fig. 4 Definition of droplet height *h*, radius *r* and distance between droplet and plate surface *c*

Figure 6 gives the time evolution of the velocity vector and pressure fields calculated by the present numerical model on the same condition as in Fig. 5. It is noted that the pressure contours in the left side of each droplet configuration are plotted by $p = p_\infty \pm 0.1k$ (k = 1, 2, . . .), and the length of arrows showing the magnitude of the velocity vector is not comparable at every time stage. It is apparent that a thin water film is formed around the droplet immediately after impact. In the subsequent process, the mass accumulation around the periphery of the droplet occurs and a ring structure is initiated in an early stage. The centerline height decreases rapidly while the height of the ring structure increases slowly. Also, the latter is almost equal to the former at about t = 1.0. A comparison between the drop configurations at t = 1.6 and 2.0 shows that the ring structure develops at the periphery of the droplet as the fluid in the ring structure flows reversely towards the inner side and the recoiling occurs. Also, the radial distance from the centerline to the contact line is decreasing in the time range of $t > 1.6$. The ring structure around the liquid film is observed to be roundish owing to the surface tension effect. Therefore, the inner pressure in the roundish ring structure is higher than the atmospheric pressure. The liquid film is divided into two regions. One of which is the part of the convex lens-like shape located in the central region. The other is the part of the doughnut-like shape in the peripheral region. There can be seen a trough between the above mentioned two parts. The free surface of the trough is sharply

Downloaded 03 Jun 2010 to 171.66.16.125. Redistribution subject to ASME license or copyright; see http://www.asme.org/terms/Terms_Use.cfm

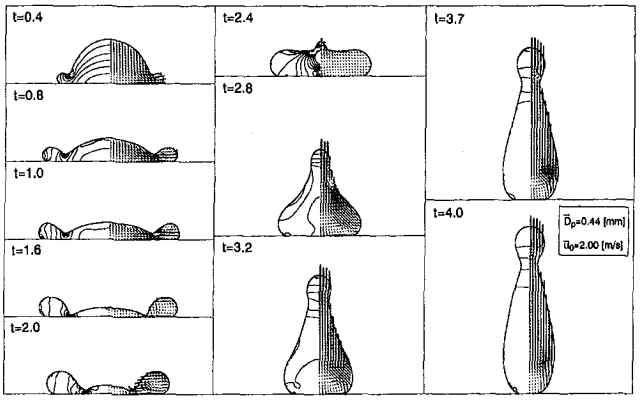


Fig. 6 Numerical free surface configuration and velocity vector field of a droplet impinging on a hot plate and pressure distribution along the surface with $\bar{D}_p$ = 0.44 [mm] and $\bar{u}_0$ = 2.00 [m/s]

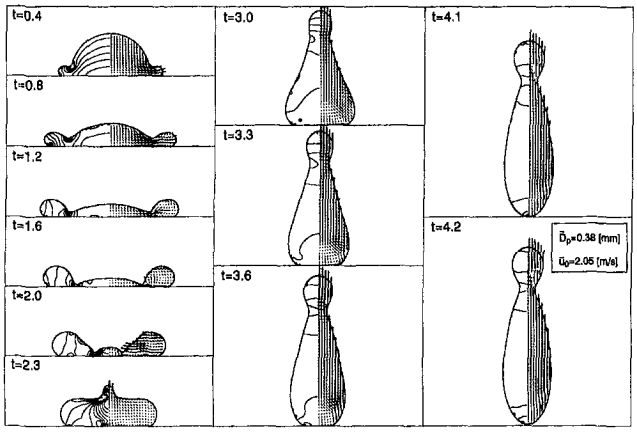


Fig. 8 Time history of numerical velocity vector fields and pressure contours of droplet for $\bar{D}_p$ = 0.38 [mm] and $\bar{u}_0$ = 2.05 [m/s]

concave and its inner pressure must be remarkably lower than the atmospheric pressure. After the liquid film diameter reaches a maximum value at $t \simeq 1.2$, the high pressure liquid at the periphery begins to flow backwards towards the trough whose inner pressure is relatively low. At the same time, the liquid in the central region continues to flow outwardly towards the trough in an appreciably slow rate. As a result, the reversal flow from the peripheral region comes into collision with another flow from the center, at the concave region. Finally, the collision of the flows keeps the position of the trough moving towards the center and thereby the ring structure grows in both thickness and width. This may be due to the fact that the flow induced by the surface tension effect is superior to the flow from the center. At $t \simeq 2.4$, the convexity is seen at the center. Subsequently, the liquid flowing from the periphery to the centerline is concentrated at the center and the rising flow is formed there at $t \simeq 2.8$. The top part of the liquid pulls upwardly the lower part and then the liquid droplet is elongated longitudinally at $t \simeq 2.8 \sim 4.0$.

Next, the numerical accuracy of the volume conservation of the liquid droplet must be checked, because the evaporation loss of the drop is neglected in the present simulation on the basis of the fact that the ratio of the time scales of the fluid dynamics of droplet deformation to the time scales of the associated heat transfer processes is negligibly small even on a hot surface. The numerical error of the liquid volume during deformation was at most within ±1% on the same condition as in Fig. 5.

Figure 7 indicates the comparison of the calculated time evolution of h, r, and c with the experimental data on condition that $\bar{D}_p = 0.38$ [mm] and $\bar{u}_0 = 2.05$ [m/s]. The results calculated by the present model show the following two weak points in the time evolution of the droplet height. First, the second critical time at which the location of the maximum height returns from the apex of the ring structure to the centerline tends to be slow in comparison to the measured data. Second, the increasing rate of the drop height after the second critical time tends to be fast in comparison to the experimental data. With the exception of the above two trends, the present model predicts well the deformation process of a droplet impacting on a hot surface. Also, the time variation of the deformation in the radial direction gives almost complete fit to the experimental data. A comparison between the calculated and experimental data, indicated in Fig. 7, also shows the above-mentioned tendency clearly. What is very interesting in this case is that the rebounding process is observed in a relatively early stage. The rebounding phenomenon shown in Fig. 7 occurs at t = 3.7 to 4.0 experimentally.

Figure 8 gives the sequence of drop configurations showing the predicted deformation along with the velocity vector and pressure fields at different time stages. The rebounding is observed to occur at t = 4.1 to 4.2 numerically. Figure 9 shows the detailed formation process of the vortical structure inside the droplet. A thermal function such that temperature becomes

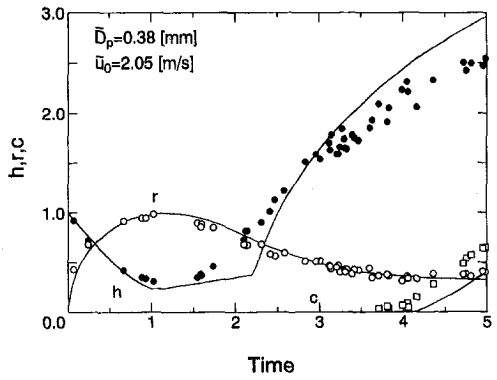


Fig. 7 Comparison of numerical time histories of droplet height h, radius r and the distance between the droplet and a plate c with experimental values for $\bar{D}_p$ = 0.38 [mm] and $\bar{u}_0$ = 2.05 [m/s]. Note that the experimental uncertainties in r, h and c are kept ±0.026 on nondimensional scale.

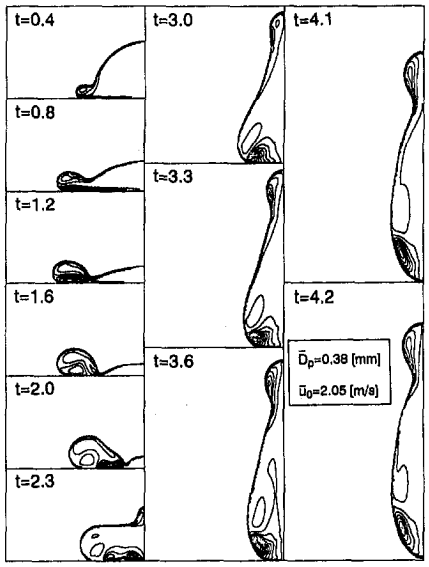


Fig. 9 Time history of vorticity contour on the same condition as shown in Fig. 7

Downloaded 03 Jun 2010 to 171.66.16.125. Redistribution subject to ASME license or copyright; see http://www.asme.org/terms/Terms_Use.cfm

lower (higher) on the upper (lower) side of the droplet and higher with time is introduced to the present simulation in the form of Eq. (7). Therefore, the temperature variation is formed along the surface of droplet, which leads to surface tension variations; with higher surface tension on the upper, colder side of the droplet and lower surface tension on the lower, hotter side of the droplet. The induced flow resulting from the various surface tension augments the vortex strength that is being created. In fact, a ring vortical structure is formed at the bottom of the elongated droplet and induces the rotative motion there in such a way as to induce the rising flow. Eventually, the droplet rebounds as a bowling pin-shaped mass at $t = 4.1 \sim 4.2$. Figure 10 shows the deformation and rebounding behaviors on the same condition as shown in Figs. 7 and 8. All the photographs shown here were obtained by double exposure video images. It is noted that the time interval of two flashes is not common for each picture. The time indicated in every photograph corresponds to the time elapsed from the moment of impacting of the droplet on the hot surface. By comparing these photographs to the configuration shown in Figure 8, it is apparent that the simulation can predict fairly well the droplet shape, considering the complexity of the problem. Also, the drop is observed to rebound from the hot surface at $t = 4.0$ experimentally, but at $t = 4.1 \sim 4.2$ numerically.

As mentioned previously, we believe that the model presented herein agrees fairly well with the experiments, considering the difficulties of the problem. However, it is also true that a few important physical effects are simplified, assumed or neglected in the present model. In fact, the formation process of vapor film between the droplet and the solid surface as well as the time variation of the vapor film thickness could not be clarified from a quantitative point of view. Therefore, the complicated problem of heat transfer from the solid surface to the deformable droplet through the vapor film could not be introduced to the present model, although heat transfer seems to be important, including the problem of thermal radiation. Then, a simple thermal function given by Eq. (7) is instead adopted to the model. The results calculated by the present model show the two weak points in the time evolution of the droplet height as mentioned already, regardless of the fact that the calculated time variation of the radius gives almost complete fit to the experimental data. An unsteady heat transfer analysis of the droplet is needed in order to reduce the difference between the calculated and experimental data. This problem will be addressed in future studies, although this is a tough problem.

Next, a thinning film of ambient gas was reported to develop between the droplet and the solid by Pozrikidis (1990). It is very difficult to introduce the effect of the interaction with the external gas, as the droplet is approaching and rebounding from the surface, to the boundary condition at the liquid/solid (or liquid/vapor) interface. On the other hand, according to Makino and Michiyoshi (1987), the visual observations show that even if the surface temperature is very high above the Leidenfrost point, the droplet makes contact first and then bounces or floats. At any rate, in the present simulations, the no-slip condition was adopted at the liquid/solid interface in the spreading process until the drop reaches a maximum diameter and thereafter the boundary condition was switched to the free-slip. A comparison of the numerical results to the measured ones shows the validity for the boundary condition used in the present simulation.

Furthermore, the evaporation loss is neglected in the present model. As pointed out by Fukai et al. (1993), a comparison of the time scales of the fluid dynamics the drop deformation to the time scales of the associated heat transfer processes shows that the former scales are extremely smaller. Hence, it appears that the droplet spreading occurs, to a larger extent, first, and the heat transfer follows. In this sense, it may not be erroneous to consider that the droplet volume is kept constant, because the period from the moment of impact, at most, to the rebounding is only in the order of 1 [ms].

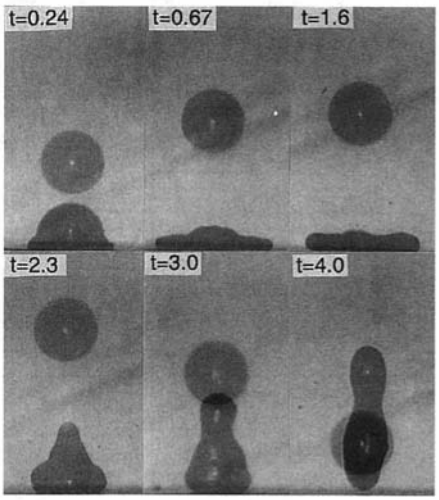


Fig. 10 Deformation process of droplet impinging on a flat plate with $\bar{D}_p = 0.38 \pm 0.01$ [mm] and $\bar{u}_0 = 2.05 \pm 0.01$ [m/s]

6 Conclusion

The deformation and subsequent rebounding processes of a droplet impacting on a hot surface above the Leidenfrost temperature were investigated from numerical as well as experimental points of view. The analytical model of the flow field inside the droplet was established by accounting for the effects of viscous and surface tension, but neglecting the heat transfer from the hot surface to the liquid droplet and the evaporation loss of the droplet.

The droplet impinging on the hot surface spreads in the shape of a flattened disk during the early stage of impact and reaches a maximum diameter. The inner pressure in the periphery of the liquid is much higher than that of the central region, because the radius of curvature in the periphery is extremely small in comparison with that in the central region. This causes to the reversal flow from the periphery towards the center. As a result, the swelling process in the central region occurs and the center part of the liquid drop continues to elongate upwards. Finally, the liquid drop rebounds as a bowling-pin shaped mass from the surface.

The numerical time evolution of the liquid drop was compared with the experimental ones. It was found that the time history of the droplet height is fairly matchable between the calculated and experimental results, although the numerical second critical time tends to slow compared with the experiment. Particularly, the time history of the droplet radius was found to give almost complete fit to the experimental data.

It was confirmed that the surface tension effect on the driving force of the droplet deformation and rebounding from the surface plays a paramount role while the effect of the vaporization owing to the heat transfer from the hot surface to the droplet on the droplet deformation is not so strong.

The final objective of the present work is to enhance the current version of the model. In this sense, the problem of the unsteady heat transfer analysis, including the phase change, will be addressed in future studies.

Acknowledgment

The authors would like to note that this study was supported through a Grant in Aid for Scientific Research (07455287) of the Ministry of Education, Science and Culture in Japan and the Kawakami Memorial Foundation.

Downloaded 03 Jun 2010 to 171.66.16.125. Redistribution subject to ASME license or copyright; see http://www.asme.org/terms/Terms_Use.cfm

References

Akao, F., Araki, K., Mori, S., and Moriyama, A., 1980, "Deformation Behaviors of a Liquid Droplet Impinging Onto Hot Metal Surface," *Transaction of ISIJ,* Vol. 20, pp. 737–743.

Amsden, A. A., and Harlow, F. H., 1970, "The SMAC Method: A Numerical Technique for Calculating Incompressible Fluid Flows," Los Alamos Scientific Laboratory Report LA-4370.

Chandra, S., and Avedisian, C. T., 1991, "On the Collision of a Droplet with a Solid Surface," *Proceedings of the Royal Society London,* Series A, 432, pp. 13–41.

Fukai, J., Zhao, Z., Poulikakos, D., Megaridis, C. M., and Miyatake, O., 1993, "Modeling of the Deformation of a Liquid Droplet Impinging Upon a Flat Surface," *Physics of Fluids A,* Vol. 5, pp. 2588–2599.

Fukai, J., Shiiba, Y., Yamamoto, T., Miyatake, O., Poulikakos, D., Megaridis, C. M., and Zhao, Z., 1995, "Wetting Effects on the Spreading of a Liquid Droplet Colliding With a Flat Surface: Experiment and Modeling," *Physics of Fluids,* Vol. 7, pp. 236–247.

Harlow, F. H., and Welch, J. E., 1965, "Numerical Calculation of Time Dependent Viscous Incompressible Flow of Fluid with Free Surface," *Physics of Fluids,* Vol. 8, pp. 2182–2189.

Harlow, F. H., and Shannon, J. P., 1967, "The Splash of a Liquid Drop," *Journal of Applied Physics,* Vol. 38, pp. 3855–3866.

Hatta, N., Fujimoto, H., Takuda, H., Kinoshita, K., and Takahashi, O., 1995, "Collision Dynamics of a Water Droplet Impinging on a Rigid Surface Above the Leidenfrost Temperature," *ISIJ International,* Vol. 35, pp. 50–55.

Hatta, N., Fujimoto, H., and Takuda, H., 1995, "Deformation Process of a Water Droplet Impinging on a Solid Surface," ASME JOURNAL OF FLUIDS ENGINEERING, Vol. 117, pp. 394–401.

Hatta, N., Fujimoto, H., Takuda, H., Yamamoto, K., Kinoshita, K., and Takahashi, O., 1995, "Numerical Analysis of Deformation Behavior of a Water Droplet Impinging on a Solid Surface at Room Temperature," *ISIJ International,* Vol. 35, pp. 1094–1099.

Makino, K., and Michiyoshi, I., 1987, "Discussions of Transient Heat Transfer to a Water Droplet on Heated Surfaces Under Atmospheric Pressure," *International Journal of Heat and Mass Transfer,* Vol. 30, pp. 1895–1905.

Miyata, H., 1986, "Finite-Difference Simulation of Breaking Waves," *Journal of Computational Physics,* Vol. 65, pp. 179–214.

Nichols, B. D., Hirt, C. W., and Hotchikiss, R. S., 1980, "SOLA-VOF, A Solution Algorithm for Transient Fluid Flow with Multiple Free Boundaries," Los Alamos Scientific Laboratory Report LA-8355.

Pozrikidis, C., 1990, "The Deformation of a Liquid Drop Moving Normal to a Plane Wall," *Journal of Fluid Mechanics,* Vol. 215, pp. 331–363.

Shoji, M., Wakunaga, T., and Kodama, K., 1984, "Heat Transfer Between a Heated Surface and Impinging Droplet (in Japanese)," *Transaction of the Japan Society of Mechanical Engineers Series B,* Vol. 50, pp. 716–723.

Turutani, K., Yao, M., Senda, J., and Fujimoto, H., 1989, "Numerical Analysis of the Deformation Process of a Droplet Impinging Upon a Surface (in Japanese)," *Transaction of the Japan Society of Mechanical Engineers Series B,* Vol. 55, pp. 814–819.

Ueda, T., Enomoto, T., and Kanetsuki, M., 1979, "Heat Transfer Characteristics and Dynamic Behavior of Saturated Droplets Impinging on a Heated Vertical Surface," *Bulletin of the JSME,* Vol. 22, pp. 724–732.

Wachters, L. H. J., and Westerling, N. A., 1966, "The Heat Transfer from a Hot Wall to Impinging Water Drops in the Spheroidal State," *Chemical Engineering Science,* Vol. 21, pp. 1047–1056.

Downloaded 03 Jun 2010 to 171.66.16.125. Redistribution subject to ASME license or copyright; see http://www.asme.org/terms/Terms_Use.cfm

Tuncay Yilmaz
Professor.

Saban Ünal
Research Assistant.

Çukurova University,
Department of Mechanical Engineering,
01330 Balcalı-Adana, Turkey

General Equation for the Design of Capillary Tubes

Capillary tubes are used widely in small refrigeration systems. It is necessary to design the capillary tube, but there does not exist any analytical equation which allows the determination of capillary tube length or mass flow rate for all refrigerants. In this work, an analytical equation is derived which allows to design the capillary tubes. The comparison with existing methods and experimentally obtained values using the refrigerants R12, R22, R113, R114, R134a, and R600a has turned out to be satisfactory.

1 Introduction

Capillary tubes are used as a refrigerant controlling device in some small refrigeration systems. These tubes have inner diameters around 1 mm. Most used diameters are between 0.6 and 1 mm. They have found general acceptance because of their reliability and low cost.

A lot of research works have been carried out since 1940 on capillary tubes both in experimental and theoretical way. The first comprehensive theoretical and experimental work has been done by Bolstad and Jordan (1948), Cooper et al. (1957), and Whitesel (1957a, 1957b). Their results are only valid for the refrigerants R12 or R22. In addition, the calculation procedures are very complicated.

Mikol (1963) showed that two-phase friction coefficient in small bore tubes can be calculated approximately like the one-phase friction coefficient. Lin et al. (1991) investigated the friction coefficient through capillary tubes and suggested a new form of dynamic viscosity calculation.

The metastable flow in capillaries was first treated by Bolstad and Jordan (1948). Some proposals for taking the metastable flow into consideration are suggested by Kuijper and Janssen (1983). Maczeh et al. (1983), Li et al. (1990) showed experimentally the complication of this matter and were not able to give any correlation for metastable flow condition.

A new method of calculation of capillary tube parameters is given by Gorasia et al. (1991). But this method, again, is too complicated and is valid only for R12. A very simple correlation obtained from experimental values is given by Schulz (1987). The correlation of Schulz is only valid for very high values of subcooling and not useful for general applications.

In this work, a simple analytical equation is developed for the design of capillary tubes, which is valid for all refrigerants.

2 Mathematical Formulation

In capillary tubes, we have one-phase and two-phase flow. The flow is accelerated in flow direction. Two-phase flow can be treated as a homogeneous flow because of the very small tube diameters (Mikol, 1963). Therefore, we can write for the pressure difference for the capillary tube of dL

$$-dp = G^2 dv + \frac{1}{2}\frac{\lambda}{d} v G^2 dL \tag{1}$$

Here, are p the pressure, G mass velocity, v specific volume, λ the friction factor, d the diameter, L the length of the capillary tube.

We assume further that the process in capillary tube is isenthalpic. Beside this, we treat horizontal capillary tubes. In Fig. 1, p-h diagrams are shown for different fluid inlet conditions to the capillary tube. Figure 1(a) shows the state where the condensation ends at the saturation curve. In Fig. 1(b) is seen the state of subcooled liquid entering the capillary tube. In Fig. 1(c) is the very rare state of two-phase fluid flowing into the capillary tube.

To solve the differential Eq. (1) we need a simple function between v and p. Therefore, we will first try to get a relation between p and v. The quality x is defined as $x = (v - v_l)/(v_v - v_l) = (h - h_l)/(h_v - h_l)$. Indices v and l denote the saturated vapor and saturated liquid. From this equation we get for v with $h = h_1$ and $h_v - h_l = r$

$$v = v_l + \frac{h_1 - h_l}{r}(v_v - v_l) \tag{2}$$

Assuming to be far from the critical point, we can write $v_v \gg v_l$ and $v_l \approx v_1$. With the above assumption and with the relationship $h_1 - h_l = c_p(T_1 - T)$, it follows from Eq. (2) that $v = v_1 + (c_p v_v/r)(T_1 - T)$. For a finite change of state we can use the ideal gas equation for saturated vapor $v_v = RT/p$ and also the Clausius Clapeyron equation $\ln(p/p_1) = (r/R)(1/T_1 - 1/T)$ so that $(v/v_1) = 1 - [(c_p R^2 T^2)/(r^2 p v_1)]T_1 \ln(p/p_1)$. With the definition of the dimensionless parameters

$$k_1 = [(c_p R^2 T^2)/(r^2 p_1 v_1)]T_1 \tag{3}$$

$$p^* = p/p_1; \quad v^* = v/v_1 \tag{4}$$

we get the simple relationship $v^* = 1 - (k_1 \ln p^*)/p^*$. For low pressure changes one obtains from the above equation

$$v^* = 1 + k_1(1/p^* - 1) \tag{5}$$

The dimensionless parameter k_1 is dependent on the properties at the point 1 and the properties R, T, r, c_p of the following process in capillary tube.

To see the practical application of Eq. (5), $v^* - 1$ is shown to be dependent on $1/p^* - 1$ in Fig. 2 for different refrigerants. One can see from these figures that k_1 can be considered for all refrigerants independent of the pressure p^* itself. This is, therefore, because the variables in Eq. (3) are balancing each other so that k_1 does not change with pressure and can be considered only dependent on the initial pressure p_1. In Fig. 3, k_1 values which are calculated numerically for different refrigerants are shown to be dependent on p_1. One can give a very accurate relation for k_1 as follows:

$$k_1 = 2.62 \cdot 10^5 / p_1^{0.75} \tag{6}$$

We have tried to give k_1 as a function of dimensionless pressure p_1/p_{cr} where p_{cr} is the critical pressure of the refrigerant. But the accuracy got worse. Through the differentiation of Eq. (5) one gets

Contributed by the Fluids Engineering Division for publication in the JOURNAL OF FLUIDS ENGINEERING. Manuscript received by the Fluids Engineering Division November 5, 1993; revised manuscript received August 24, 1995. Associate Technical Editor: O. C. Jones.

Copyright © 1996 by ASME

Downloaded 03 Jun 2010 to 171.66.16.125. Redistribution subject to ASME license or copyright; see http://www.asme.org/terms/Terms_Use.cfm

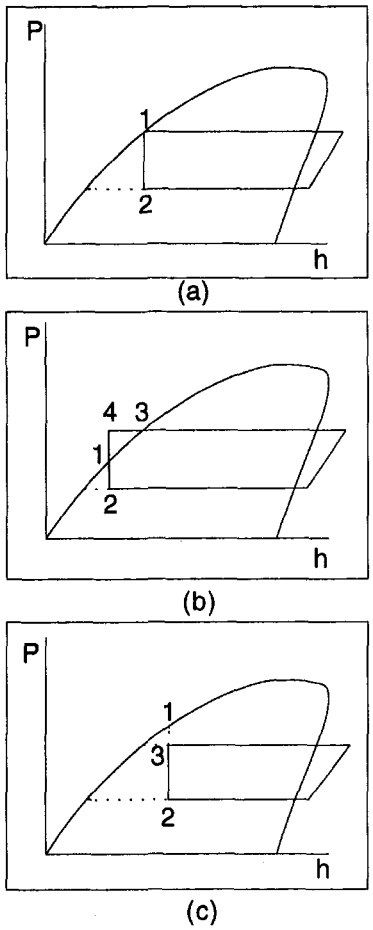


Fig. 1 Processes in capillary tubes for various inlet conditions of refrigerants. (*a*) saturated liquid, (*b*) subcooled liquid, (*c*) two-phase flow

$$dv = -k_1 v_1 p_1 \frac{dp}{p^2} \tag{7}$$

substituting Eq. (5) and (7) into Eq. (1) it follows:

$$-dp\left[1 - \frac{G^2 k_1 p_1 v_1}{p^2}\right] = \frac{1}{2}\frac{\lambda}{d} G^2 v_1 \left[k_1 \frac{p_1}{p} - k_1 + 1\right] dL \tag{8}$$

We assume here further that λ is independent of p. With the definitions

$$k_2 = v_1 G^2 / p_1 \tag{9}$$

$$L^* = \frac{\lambda}{2}\frac{L}{d} \tag{10}$$

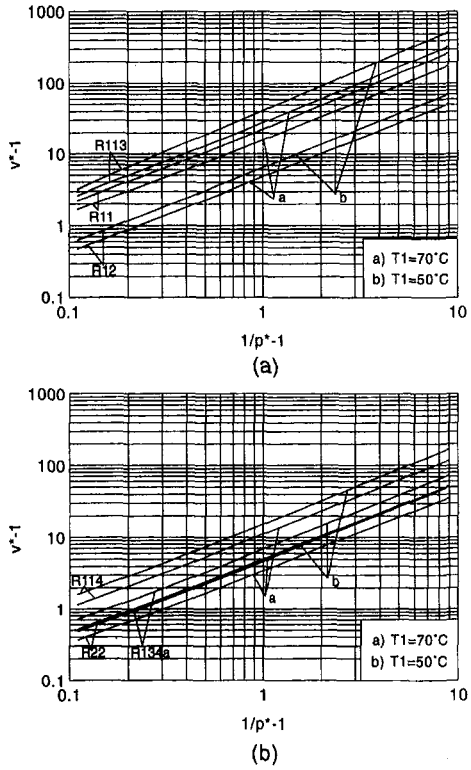


Fig. 2 Variation of $v^* - 1$ with $1/p^* - 1$. (*a*) For R11, R12, and R113, (*b*) For R114, R22, and R134a.

we obtain from Eq. (8), $-dp^*[1 - k_1 k_2/p^{*2}] = k_2[k_1/p^* - k_1 + 1]dL^*$. We can rewrite this equation as

$$[(1 - k_1 k_2/p^{*2})/(k_2[k_1/p^* - k_1 + 1])]dp^* = -dL^* \tag{11}$$

We can normally neglect the pressure loss of the fluid at the capillary tube inlet. Therefore, this differential equation can be integrated with the following boundary condition for the case in Fig. 1(*a*). $L^* = 0$; $p^* = 1$. So, one gets from Eq. (11)

$$L^* = \ln\left(\frac{p^*}{k_1 + (1 - k_1)p^*}\right) - \frac{1}{k_2(1 - k_1)}\left\{p^* - 1 - \frac{k_1}{1 - k_1}\ln\left[k_1 + (1 - k_1)p^*\right]\right\} \tag{12}$$

3 Physical Properties and Other Needed Parameters

In Eq. (12), k_1 and k_2 can be considered as given because the point 1 is known. We can calculate then L^* as a function

Nomenclature

A = defined in Eq. (14)
B = defined in Eq. (15)
c_p = specific heat capacity
d = capillary tube diameter
G = mass velocity
h = enthalpy
k_1 = defined in Eq. (6)
k_2 = defined in Eq. (9)
L = capillary tube length
m = mass flow rate
p = pressure
r = specific latent heat
R = gas constant
Re = Reynolds number
T = temperature
x = quality
v = specific volume
Δp = pressure difference
ΔT = subcooling of the liquid
ϵ = roughness
η = dynamic viscosity
λ = friction factor
υ = kinematic viscosity

Subscripts

a = average
cr = critical point
l = saturated liquid
v = saturated vapour
1 = point 1
2 = point 2
3 = point 3
4 = point 4

Superscripts

* = dimensionless parameter

Downloaded 03 Jun 2010 to 171.66.16.125. Redistribution subject to ASME license or copyright; see http://www.asme.org/terms/Terms_Use.cfm

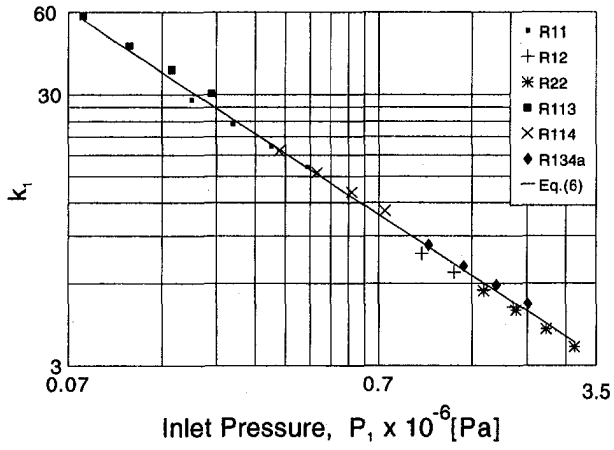


Fig. 3 Dependence of k_1 on the inlet pressure p_1

of p^*. But for the determination of L we need the value of λ. λ will be calculated from an equation given by Churchill (1977). This equation is valid for laminar and turbulent flow.

$$\lambda = 8[(8/\mathrm{Re})^{12} + 1/(A + B)^{3/2}]^{1/12} \quad (13)$$

$$A = \{2.457 \ln (1/[(7/\mathrm{Re})^{0.9} + 0.27(\epsilon/d)])\}^{16} \quad (14)$$

$$B = (37530/\mathrm{Re})^{16} \quad (15)$$

Here, ϵ is roughness of the tube inner surface. Reynolds number Re is defined as $\mathrm{Re} = Gd/\eta_a$. For the calculation of Re, an average dynamic viscosity η_a is needed. It is calculated from the equation $\eta_a = \eta_a^* \eta_l$. η_a^* takes into consideration the change of viscosity along the capillary tube. The dimensionless viscosity of two-phase flow in a capillary tube is calculated for different refrigerants according to the equation $\eta^* = [x\eta_v + (1 - x)\eta_l]/\eta_l$, where η_l and η_v are the saturated liquid and saturated vapor dynamic viscosities (Wallis, 1969). η_a^* is an average value in the capillary tube. We assume further that the velocity in the capillary tube remains below the sound velocity and

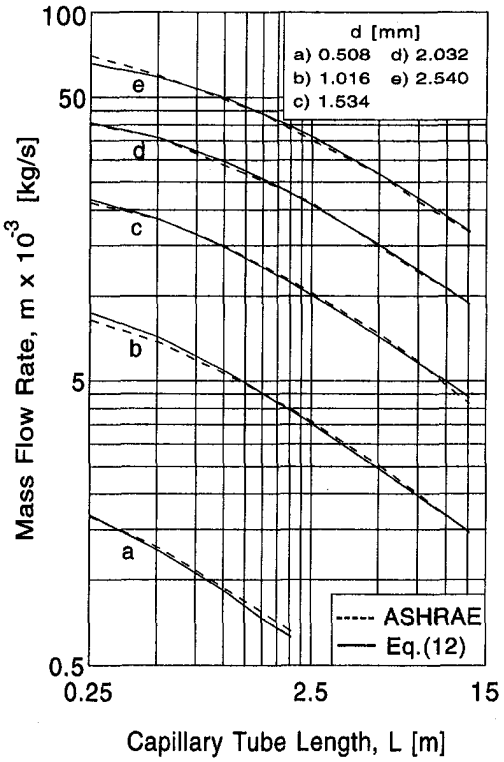


Fig. 5 Variation of refrigerant mass flow rate with capillary tube length for the inlet condition in Fig. 1(*b*) with ΔT = 5.6°C

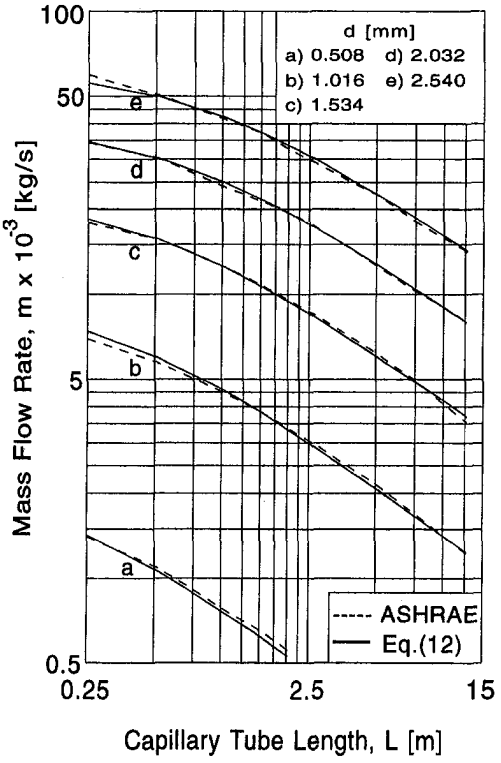


Fig. 4 Variation of refrigerant mass flow rate with capillary tube length for the inlet condition in Fig. 1(*a*)

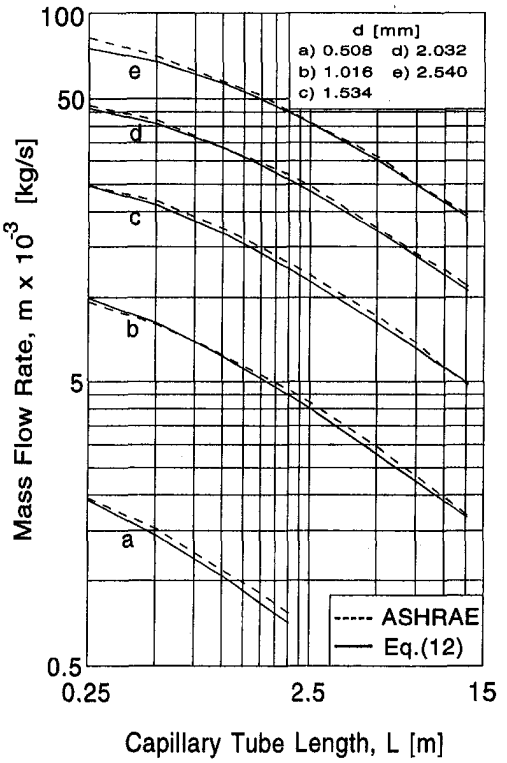


Fig. 6 Variation of refrigerant mass flow rate with capillary tube length for the inlet condition in Fig. 1(*b*) with ΔT = 11.1°C

Downloaded 03 Jun 2010 to 171.66.16.125. Redistribution subject to ASME license or copyright; see http://www.asme.org/terms/Terms_Use.cfm

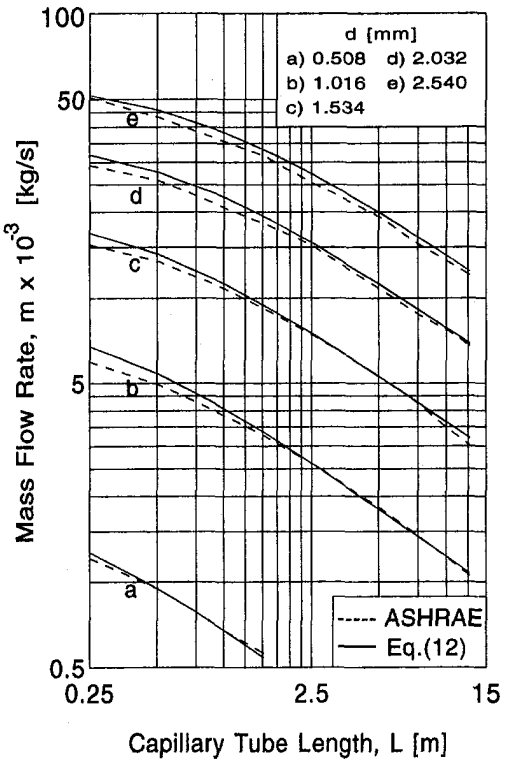


Fig. 7 Variation of refrigerant mass flow rate with capillary tube length for the inlet condition in Fig. 1(c) with $x = 0.05$

therefore the exit pressure can be taken equal to the pressure p_2 in the evaporator. We get then:

$$\eta_a^* = \frac{1}{(1 - p_2^*)} \int_{p_2^*}^{1} \eta^* dp^* \qquad (16)$$

η^* is a function of p_2^*. The integration in Eq. (16) is carried out numerically for different refrigerants and different inlet pressure conditions. The numerical results can be represented by the following equation.

$$\eta_a^* = (8/7)[(1 - p_2^{*7/8})/(1 - p_2^*)] \qquad (17)$$

This equation can be used for all refrigerants. The saturated liquid dynamic viscosity at the point 1 is calculated with $\eta_l = \upsilon_l/v_l$, where υ_l and v_l are, respectively the kinematic viscosity and specific volume of the saturated liquid. Kinematic viscosity, enthalpy, specific heat capacity of the saturated liquid and saturation pressure and temperature can be calculated for all refrigerants by equations given in literature (Downing, 1974; Yilmaz and Ünal, 1992).

4 Comparison With Known Methods

The most accepted and practically used method for dimensioning capillary tubes is the method described by ASHRAE (1979). The result of this work will be compared with the method described by ASHRAE for different fluid inlet conditions into capillary tube shown in Fig. 1. The comparisons will be made as given by ASHRAE for R12. Equation (12) is derived for saturated liquid entering the capillary tube but the method is valid for both subcooled liquid entrance and two-phase mixture entering the capillary tube as will be explained in the following. The inlet pressure is assumed to be 17.22 bar. The evaporation is taken at 10°C. The relative roughness is taken as $\epsilon/d = 3.27 \cdot 10^{-4}$ (Mikol, 1963; Lin et al., 1985).

4.1 Saturated Liquid Inlet Condition. This state is demonstrated in Fig. 1(*a*). Point 1 shows the saturated liquid state at the end of condensation. The liquid enters the capillary tube and exits to the evaporator at point 2. For this condition the refrigerant flow rate m is given in Fig. 4 as a function of the capillary tube length L where the capillary tube diameter is the parameter. The curves calculated using the equation (12) are given as solid and dashed curves show the values calculated according ASHRAE. From this figure we can see that both methods yield similar results. Only for large tube diameters and very short tube lengths there are some differences.

4.2 Subcooled Liquid Entering the Capillary Tube. Equation (12) can be applied to the case of subcooled liquid entering the capillary tube. For this case the capillary tube length includes the portion necessary for subcooled liquid to become saturated between the points 4 and 1. This length is designated as L_{41}, which can be calculated with the equation of one-phase flow

$$L_{41} = (2\Delta p_{41} d)/(\lambda G^2 v) \qquad (18)$$

Here Δp_{41} is the pressure difference between the points 4-1. At the point 1 the liquid is at saturated state.

The capillary tube length necessary between the points 1-2 can be determined using Eq. (12). Before doing it, we have to get the pressure at point 1. We can calculate the enthalpy at point 1 as $h_1 = h_4 = h_3 - c_p \Delta T$. ΔT is the subcooling of the liquid. Using equations for the enthalpy and specific heat capacity one can determine the temperature T_1 iteratively. From the temperature we can then get the pressure at point 1. Using this calculated pressure at point 1, capillary tube length L_{12} necessary between the points 1 and 2 can be calculated according to Eq. (12). At last, we can determine the capillary tube length as $L = L_{41} + L_{12}$. Similar to the saturated liquid inlet case, the mass flow rate calculated with this method (solid curves) is compared in Figs. 5 and 6 with the curves given by ASHRAE (dashed

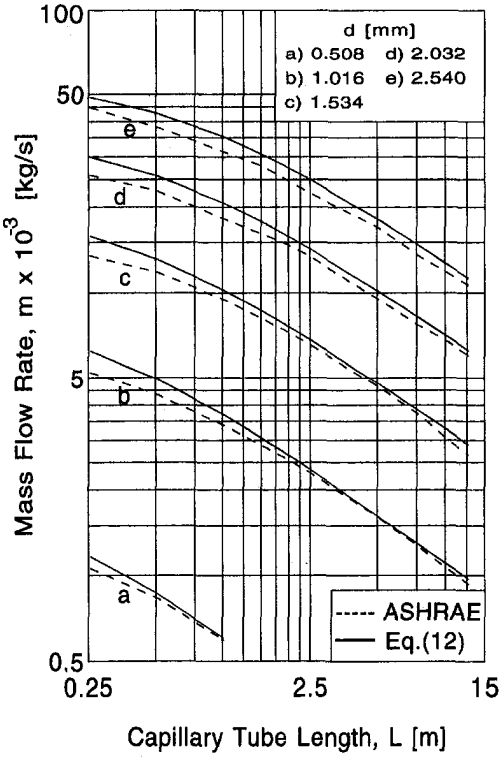


Fig. 8 Variation of refrigerant mass flow rate with capillary tube length for the inlet condition in Fig. 1(c) with $x = 0.10$

Downloaded 03 Jun 2010 to 171.66.16.125. Redistribution subject to ASME license or copyright; see http://www.asme.org/terms/Terms_Use.cfm

Table 1 Comparison of the mass flow rates between our analytical method and experimentally obtained

Refrigerants	ΔT [°C]	P_1 [bar]	P_2 [bar]	d [mm]	L [m]	m [kg/s] Eq.(12)	[kg/s] Lit.	Dev. [%]	Literature
R12	2.0	10.55	1.456	0.74	2.9	0.913	0.940	-2.87	Maczeh,K., et al., 1983
	6.0	10.55	1.698	0.74	2.9	1.059	0.940	12.63	
R22	8.5	10.10	3.0	1.25	0.747	8.241	9.167	-10.10	Schulz, U.W., 1987
	8.5	10.10	3.0	1.62	0.747	15.43	18.06	-14.53	
	6.0	10.12	3.0	1.25	0.747	7.638	8.611	-11.3	
	6.0	10.12	3.0	1.62	0.747	14.31	16.11	-11.19	
	33	14.80	3.0	1.25	0.747	14.89	17.05	-12.64	
	33	14.80	3.0	1.40	0.747	19.61	21.67	-9.50	
R114	13	6.91	1.5	1.62	0.747	13.42	15.83	-15.22	
	13	6.91	1.5	1.62	0.838	12.94	14.44	-10.44	
	8.5	10.10	3.0	1.25	0.747	8.241	9.167	-10.10	
R12	4	9.20	4.23	0.77	2.926	1.01	1.01	-0.05	Melo, C., et al., 1994
	12	9.20	4.23	0.77	2.926	1.30	1.19	8.77	
	4	11.23	4.23	0.77	2.926	1.17	1.08	7.79	
	12	11.23	4.23	0.77	2.926	1.46	1.28	14.17	
	4	9.20	4.23	0.77	2.009	1.24	1.20	3.52	
	12	9.20	4.23	0.77	2.009	1.59	1.43	11.00	
	4	11.23	4.23	0.77	2.009	1.43	1.35	5.51	
	12	11.23	4.23	0.77	2.009	1.79	1.59	12.69	
R134a	4	9.21	4.12	0.77	2.926	0.97	0.94	4.01	
	12	9.21	4.12	0.77	2.926	1.26	1.12	13.00	
	4	11.26	4.12	0.77	2.926	1.13	0.95	18.07	
	12	11.26	4.12	0.77	2.926	1.43	1.20	19.17	
	4	9.21	4.12	0.77	2.009	1.20	1.0	12.63	
	12	9.21	4.12	0.77	2.009	1.56	1.32	17.90	
	4	11.26	4.12	0.77	2.009	1.38	1.28	7.60	
	12	11.26	4.12	0.77	2.009	1.75	1.50	16.64	
R600a	4	9.26	2.22	0.77	2.926	0.66	0.64	2.08	
	12	9.26	2.22	0.77	2.926	0.83	0.79	4.83	
	4	11.25	2.22	0.77	2.926	0.75	0.68	10.20	
	12	11.25	2.22	0.77	2.926	0.93	0.82	13.03	
	4	9.26	2.22	0.77	2.009	0.80	0.76	5.17	
	12	9.26	2.22	0.77	2.009	1.01	0.89	13.38	
	4	11.25	2.22	0.77	2.009	0.91	0.87	4.18	
	12	11.25	2.22	0.77	2.009	1.12	1.02	10.58	
R134a	5.56	9.67	4.12	0.838	3.048	1.27	1.47	-13.83	Wijaya, H., 1992
	5.56	11.12	4.12	0.838	3.048	1.40	1.64	-14.61	
	5.56	14.76	4.12	0.838	3.048	1.68	1.96	-14.10	
	11.11	9.61	4.12	0.838	3.048	1.50	1.66	-9.78	
	11.11	11.12	4.12	0.838	3.048	1.64	1.88	-12.53	
	11.11	14.76	4.12	0.838	3.048	1.94	2.18	-11.09	
	16.67	9.70	4.12	0.838	3.048	1.70	1.82	-6.51	
	16.67	11.12	4.12	0.838	3.048	1.84	2.02	-8.63	
	16.67	14.81	4.12	0.838	3.048	2.17	2.38	-8.96	

curves). The subcooling in these figures are 5.6°C and 11.1°C, respectively.

4.3 Two-Phase Mixture Entering the Capillary Tube. Even though this case is not often encountered in practical application, we still have considered it. In Fig. 1(*c*) this case is shown. Two-phase mixture at the point 3 enters the capillary tube. The point 1 has the same enthalpy as point 3 and lies at the saturation curve. We can find T_1 iteratively and then p_1. Applying this p_1 to Eq. (12) we can calculate the capillary tube length L_{13} necessary between the points 1-3, and L_{12} between the points 1-2. The total capillary tube length between the points 3-2 is then $L_{32} = L_{12} - L_{13}$. In Figs. 7 and 8 the values calculated with this method (solid curves) and with ASHRAE (dashed curves) are given. The quality in these figures are 0.05 and 0.10 respectively. The deviations are larger than for saturated and subcooled liquid inlet cases. Our method yields approximately 8 and 10 percent more mass flow rates than the curves given by ASHRAE.

4.4 Other Comparisons. The mass flow rates determined using our analytical method are compared in Table 1 with the experimentally-obtained values given in the literature (Maczeh et al., 1983; Schulz, 1987; Wijaya, 1992; Melo et al., 1994). Values are given for subcooled liquid entering the capillary tube. One can see from this table that our analytical method yields in most cases lower mass flow rates than experimentally obtained values. The deviations (Dev.) may be considered to be reasonable and satisfactory on account of the simplicity of the present analytical method.

5 Conclusions

For the design of capillary tubes an analytical method is given. This method can be applied to different liquids such as R11, R113, R114, R12, R22, and as well as to alternative refrigerants such as R134a and R600a. The mass flow rates using our methods and that which is given by ASHRAE have been compared. We have found maximum of ±6 percent deviations between the mass flow rates calculated with these methods for saturated and subcooled liquid entering the capillary tube. For a two-phase mixture entering the capillary tube we have determined an average deviation of +8 and +10 percent for the qualities 0.05 and 0.10. On the other hand, the mass flow rates determined using our simple analytical method yields up to 15 percent lower values than the experimentally-obtained values given by Schulz and Wijaya. This is contrary to the comparison of our results with those of Melo's obtained experimentally; the values determined for mass flow rate using Eq. (12) were up to 19 percent higher than Melo's experimental data. According to these comparisons, a general equation is developed which can be applied to all refrigerants for all kinds of fluid conditions entering the capillary tube.

References

ASHRAE, 1979, *Handbook Equipment 1979,* pp. 20.20–20.28.

Bolstad, M. M., and Jordan, R. C., 1948, "Theory and Use of the Capillary Tube Expansion Device," *Refrigerating Engineering,* pp. 519–552.

Churchill, S. W., 1977, "Frictional Equation Spans All Fluid Flow Regimes," *Chemical Engineering,* Vol. 84, pp. 91–92.

Cooper, L., Chu, C. K., and Brisken, W. R., 1957, "Single Selection Method for Capillaries Derived from Physical Flow Conditions," *Refrigerating Engineering,* pp. 37–107.

Downing, R. C., 1974, "Refrigerating Equations," *ASHRAE Transactions,* Vol. 80, Part 2, pp. 158–168.

Gorasia, J. N., Dubey, N., and Jain, K. K., 1991, "Computer-Aided Design of Capillaries of Different Configurations," *ASHRAE Transactions, Research,* Vol. 97, Part 1, pp. 132–138.

Kuijpers, L. J. M., and Janssen, M. J. P., 1983, "Influence of Thermal Non-Equilibrium on Capillary Tube Mass Flow," *XIVth International Congress of Refrigeration,* Paris, Proceedings Commission B2, Vol. 2, pp. 689–698.

Li, R. Y., Lin, S. L., Chen, Z. Y., and Chen, Z. H., 1990, "Metastable Flow of R12 Through Capillary Tubes," *International Journal of Refrigeration,* Vol. 13, pp. 181–186.

Lin, S., Kwork, C. C. K., Li, R. Y., Chen, Z. H., and Chen, Z. Y., 1991, "Local Frictional Pressure Drop During Vaporization of R12 Through Capillary Tubes," *International Journal of Multiphase Flow,* Vol. 17, pp. 95–102.

Maczeh, K., Krolicki, Z., and Sochanecka, E., 1983, "Model of Throttling Capillary Tube With Metastable Process," *XIVth International Congress of Refrigeration,* Paris, Proc, Commission B2, Vol. 2, pp. 699–707.

Melo, C., Ferreira, R. T. S., Neto, C. B., Gonçalves, J. M., Pereira, R. H., and Thiessen, M. R., 1994, "Evaluation of HC-600a, R134a and CFC-12 Mass Flow Rates Through Capillary Tubes," *New Applications of Natural Working Fluids in Refrigeration and Air Conditioning,* IIR Meeting, 10–13 May 1994, Hannover, Germany.

Mikol, E. P., 1963, "Adiabatic Single and Two-Phase Flow in Small Bore Tubes," *ASHRAE Journal,* pp. 75–86.

Schulz, U. W., 1987, PhD - thesis, University of Essen, Untersuchung des Expansionsprozesses nichtazeotroper Kaeltemittelgemische im Kapillarrohr Kaeltetechnischer Anlagen, *published by* C. F. Müller Verlag, Karlsruhe.

Wallis, G. B., 1969, "*One-Dimensional Two-Phase Flow,*" McGraw-Hill, New York, NY.

Whitesel, H. A., 1957a, "Capillary Two-Phase Flow, Part I," *Refrigerating Engineering,* pp. 42–99.

Whitesel, H. A., 1957b, "Capillary Two-Phase Flow, Part II," *Refrigerating Engineering,* pp. 35–40.

Wijaya, H., 1992, "Adiabatic Capillary Tube Test Data for HFC-134a," *Proceedings of the IIR-Purdue Refrigeration Conference,* Vol. 1, pp. 63–71, West Lafayette, Ind.

Yilmaz, T., Ünal, Ş., 1992, "General Equations for Thermodynamical and Physical Properties of Refrigerants," (in Turkish), *Proceedings of 2. National Refrigeration and Air Conditioning Congress,* Adana, pp. 93–113.

Downloaded 03 Jun 2010 to 171.66.16.125. Redistribution subject to ASME license or copyright; see http://www.asme.org/terms/Terms_Use.cfm

Buoyant Convection During the Growth of Compound Semiconductors by the Liquid-Encapsulated Czochralski Process With an Axial Magnetic Field and With a Non-Axisymmetric Temperature

Nancy Ma

J. S. Walker

Department of Mechanical and Industrial Engineering, 140 Mechanical Engineering Building, University of Illinois, Urbana, IL 61801

This paper treats the buoyant convection of a molten semiconductor in a cylindrical crucible with a vertical axis, with a uniform vertical magnetic field, and with a non-axisymmetric temperature. Most previous treatments of melt motions with vertical magnetic fields have assumed that the temperature and buoyant convection were axisymmetric. In reality, the temperature and resultant buoyant convection often deviate significantly from axisymmetry. For a given non-axisymmetric temperature, the electromagnetic suppression of the axisymmetric part of the buoyant convection is stronger than that of the non-axisymmetric part, so that the deviation from an axisymmetric melt motion increases as the magnetic field strength is increased. The non-axisymmetric part of the buoyant convection includes relatively strong azimuthal velocities adjacent to the electrically insulating vertical crucible wall, because this wall blocks the radial electric currents needed to suppress azimuthal velocities.

Introduction

Many advanced computer circuits and electro-optical devices are produced on wafers sliced from crystals of compound semiconductors, such as gallium-arsenide and indium-phosphide. In the Czochralski process, a crystal is grown from a melt contained in a cylindrical crucible which is surrounded by a heater. A layer of liquid boron oxide on top of the melt prevents evaporation of the volatile component and reduces the dislocation-producing axial temperature gradient in the crystal. An oscillatory melt motion produces temporal oscillations in the transport of a dopant to the growing crystal, so that the final crystal has undesirable spatial oscillations in dopant concentration, which are called striations. The application of a uniform vertical magnetic field eliminates turbulence and all other unsteadiness in the melt motion, and suppresses the remaining laminar steady motion. The benefits of a magnetic field in semiconductor crystal growth have been reviewed by Series and Hurle (1991) and by Langlois et al. (1993).

Many heaters have a gap between the electrical leads, so that there is significantly less heat input to the melt at one azimuthal position, and the temperature in the melt is not axisymmetric. Bachmann et al. (1975) reported large deviations from axisymmetry in the temperatures measured during the liquid encapsulated Czochralski growth of indium-phosphide crystals. Hurle et al. (1987) stated that "the temperature distribution in the melt . . . is normally non-axisymmetric." The crystal is rotated, so that the local growth rate averaged over one rotational period is the same for each point on the growth interface. Therefore the crystal-melt interface remains axisymmetric, and the crystal remains cylindrical.

We assume that the magnetic field is sufficiently strong that the inertial term in the Navier-Stokes equation and the convective term in the heat equation can both be neglected everywhere. With these assumptions, the governing equations are linear, and the melt motions driven by buoyant convection and by the crystal and crucible rotations are decoupled. Here we only consider the buoyant convection because the non-axisymmetric temperature has no effect on the rotationally driven motion. The remaining dimensionless parameter is the Hartmann number, $\mathrm{Ha} = BR(\sigma/\mu)^{1/2}$. Here B is the magnetic flux density of the externally applied magnetic field, and R is the inside radius of the crucible, while σ and μ are the electrical conductivity and absolute viscosity of the melt. For the typical growth of compound semiconductors with $B = 0.2$ tesla, $\mathrm{Ha} = 300$.

In a previous paper (Ma and Walker, 1995), we presented a large Hartmann number asymptotic solution. For the buoyant convection, the melt is divided into (1) an inviscid core, (2) Hartmann layers with $O(\mathrm{Ha}^{-1})$ thickness adjacent to the crucible bottom, crystal-melt interface and encapsulant-melt interface, and (3) a parallel layer with $O(\mathrm{Ha}^{-1/2})$ thickness adjacent to the vertical crucible wall, which is parallel to the applied magnetic field. The asymptotic solution involves expansions in powers of $\mathrm{Ha}^{-1/2}$, and our previous paper presented the first non-zero term in the expansion for each variable in each subregion of the melt. The asymptotic solution provides physical insights into the complex three-dimensional buoyant convection driven by the non-axisymmetric temperature.

The problem with the large Hartmann number asymptotic solution of Ma and Walker (1995) is that $\mathrm{Ha}^{-1/2} = 0.06$ is not really small for the typical crystal-growth value of $\mathrm{Ha} = 300$. Therefore the neglected $O(\mathrm{Ha}^{-1/2})$ terms may not be much smaller than the $O(1)$ terms, and the parallel layer with a thick-

Contributed by the Fluids Engineering Division for publication in the JOURNAL OF FLUIDS ENGINEERING. Manuscript received by the Fluids Engineering Division March 20, 1995; revised manuscript received November 6, 1995. Associate Technical Editor: Jong H. Kim.

Copyright © 1996 by ASME

Downloaded 03 Jun 2010 to 171.66.16.125. Redistribution subject to ASME license or copyright; see http://www.asme.org/terms/Terms_Use.cfm

ness of roughly 3 $Ha^{-1/2}$ is not really distinct from the core. One alternative would be a numerical solution of the fully viscous equations with Ha as an arbitrary parameter. The problem with a fully viscous solution is that most of the computational resources would be consumed in the resolution of the Hartmann layers because their $O(Ha^{-1})$ thickness is quite small for Ha = 300. The Hartmann layers have a simple local exponential structure which matches any tangential velocities in the core or parallel layer and which satisfies the no-slip conditions at the crucible bottom, crystal-melt interface and encapsulant-melt interface. Since the Hartmann layers are well developed for Ha = 300, there is no need to waste computational resources to duplicate numerically the structure given by a simple analytical expression.

Like ordinary hydrodynamic boundary layers, Hartmann layers match any tangential velocities in the adjacent region, satisfy the no-slip conditions at the boundary, and produce a certain normal velocity into or out of the adjacent region. In addition Hartmann layers adjacent to an electrically insulated boundary involve tangential electric currents whose continuity implies a certain normal electric current into or out of the adjacent region. Therefore the solution in the adjacent region need only satisfy certain conditions on the normal velocity and electric current, called the Hartmann conditions, and need not satisfy the no-slip conditions (Walker et al., 1972). Ting et al. (1993) used the analytical Hartmann-layer solutions to derive Hartmann conditions on a solution which combined the core and parallel layer solutions. Since their Hartmann conditions neglected $O(Ha^{-1})$ terms, they neglected any term in an expression which was $O(Ha^{-1})$ smaller than other terms for both the core and parallel layer. We use the same approach with a composite core-parallel-layer solution. For our problem, the neglected terms include the axial derivatives in the viscous term because the composite solution does not satisfy the no-slip conditions at the crucible bottom, crystal-melt interface or encapsulant-melt interface. In terms of the asymptotic solution of Ma and Walker (1995), the composite solution combines the leading term and the $O(Ha^{-1/2})$ perturbation to the leading term for each variable in both the core and parallel layer. There is no distinction between the core and parallel layer, so that we have a continuous solution from the vertical centerline to the vertical crucible wall. While Ha remains as a parameter in the boundary value problem, the composite solution assumes that Ha is sufficiently large that the Hartmann layers have negligible thickness and that an $O(Ha^{-1})$ error is acceptable.

Composite Core-Parallel-Layer Solution

The characteristic velocity for magnetically damped buoyant convection is

$$U = \rho g \beta (\Delta T)/\sigma B^2, \tag{1}$$

where ρ is the melt's density at the solidification temperature T_S, $g = 9.81\ m/s^2$, β is the melt's volumetric expansion coefficient, and (ΔT) is the characteristic temperature difference (Hjellming and Walker, 1987). We assume (1) that the magnetic Reynolds number $R_m = \mu_p \sigma U R$ is sufficiently small that the magnetic field produced by the electric currents in the melt is negligible, (2) that the interaction parameter $N = \sigma B^2 R/\rho U$ is sufficiently large that the inertial term in the Navier-Stokes equation is negligible, and (3) that the Péclét number $Pe = \rho c_h U R/k$ is sufficiently small that convective heat transfer in the melt is negligible. Here μ_p, c_h and k are the magnetic permeability, specific heat and thermal conductivity of the melt.

With these assumptions and the Boussinesq approximation, the dimensionless governing equations are

$$0 = -\nabla p + T\hat{\mathbf{z}} + \mathbf{j} \times \hat{\mathbf{z}} + Ha^{-2}\nabla^2 \mathbf{v}, \quad \nabla \cdot \mathbf{v} = 0, \tag{2a, b}$$

$$\nabla \cdot \mathbf{j} = 0, \quad \mathbf{j} = -\nabla\phi + \mathbf{v} \times \hat{\mathbf{z}}, \quad \nabla^2 T = 0. \tag{2c-e}$$

Here $\mathbf{v}$, $\mathbf{j}$, and ϕ are the melt velocity, electric current density and electric potential function (voltage), normalized by U, σUB, and UBR, while p is the deviation of the dimensional pressure from the hydrostatic pressure for ρ, normalized by $\sigma UB^2 R$, and T is the deviation of the dimensional temperature from T_S, normalized by (ΔT). Also $\hat{\mathbf{r}}$, $\hat{\theta}$, $\hat{\mathbf{z}}$ are the unit vectors for the dimensionless cylindrical coordinates r, θ, z with the z axis along the common vertical centerline of the crystal and crucible.

In the bulk flow approximation, the crystal-melt interface and the encapsulant-melt interface lie in the same horizontal plane at $z = b$, while the crucible bottom lies in the plane at $z = -b$, where $2bR$ is the instantaneous dimensional melt depth, which decreases as crystal growth progresses. The crucible and encapsulant are electrical insulators. The electrical conductivity of a compound semiconductor crystal can be as large as 0.2σ, but here we treat the crystal as an insulator. The encapsulant is so viscous that its velocity is negligible compared to the magnetically damped melt velocity. Therefore all three components of $\mathbf{v}$ and the normal component of $\mathbf{j}$ must be zero at $r = 1$ and at $z = \pm b$.

For the composite core-parallel-layer solution, we neglect any term in Eqs. (2) which is $O(Ha^{-1})$ smaller than other terms in the same expression for both the core and parallel layer. Equations (2) yield expressions for all other variables in terms of ϕ and an integration function h for p and v_z (Ting et al., 1993):

$$\nu_z = \frac{\partial^2 h}{\partial r^2} + \frac{1}{r}\frac{\partial h}{\partial r} + \frac{1}{r^2}\frac{\partial^2 h}{\partial \theta^2}, \quad p = \frac{\partial h}{\partial z}, \tag{3a, b}$$

$$j_\theta = \frac{\partial^2 h}{\partial r \partial z}, \quad j_z = -\frac{\partial \phi}{\partial z}, \quad \nu_r = -\frac{1}{r}\frac{\partial \phi}{\partial \theta} - \frac{\partial^2 h}{\partial r \partial z}, \tag{3c-e}$$

$$\nu_\theta = \frac{\partial \phi}{\partial r} - \frac{1}{r}\frac{\partial^2 h}{\partial \theta \partial z}, \tag{3f}$$

$$j_r = -\frac{1}{r}\frac{\partial^2 h}{\partial \theta \partial z} + Ha^{-2}\left(\frac{\partial^3 \phi}{\partial r^3} + \frac{1}{r}\frac{\partial^2 \phi}{\partial r^2}\right). \tag{3g}$$

The z-component of Eq. (2a) and Eq. (2c) give the equations governing h and ϕ,

$$\frac{\partial^2 h}{\partial z^2} - Ha^{-2}\left(\frac{\partial^4 h}{\partial r^4} + \frac{2}{r}\frac{\partial^3 h}{\partial r^3}\right) = T, \tag{4a}$$

$$\frac{\partial^2 \phi}{\partial z^2} - Ha^{-2}\left(\frac{\partial^4 \phi}{\partial r^4} + \frac{2}{r}\frac{\partial^3 \phi}{\partial r^3}\right) = 0. \tag{4b}$$

The composite solution must satisfy all the boundary conditions at the vertical crucible wall,

$$\nu_r = \nu_\theta = \nu_z = j_r = 0, \quad \text{at} \quad r = 1, \tag{5a-d}$$

but need only satisfy the Hartmann conditions at the crystal-melt interface, encapsulant-melt interface and crucible bottom (Walker et al., 1972),

$$\nu_z = 0, \quad j_z = \pm Ha^{-1} r^{-1}\left(\frac{\partial \nu_r}{\partial \theta} - \frac{\partial}{\partial r}(r\nu_\theta)\right),$$

$$\text{at } z = \pm b. \tag{6a, b}$$

The only inhomogeneous term in the boundary value problem for h and ϕ is the T in Eq. (4a).

We assume that the heat flux from the vertical crucible wall to the melt is independent of z and is symmetric about a vertical plane through the gap in the heater where the heat flux is smallest. Since the problem is linear, the variables associated with each Fourier component of the heat flux are decoupled from

Downloaded 03 Jun 2010 to 171.66.16.125. Redistribution subject to ASME license or copyright; see http://www.asme.org/terms/Terms_Use.cfm

those for the other components. The first two terms in the Fourier series, namely 1 and cos θ, illustrate the effects of a non-axisymmetric temperature. We choose $(\Delta T) = qR/k$, where q is the average heat flux from the vertical crucible wall. We assume that the crucible bottom is thermally insulated. The boundary conditions on T are,

$$\frac{\partial T}{\partial r} = 1 + \alpha \cos\theta, \quad \text{at} \quad r = 1, \tag{7a}$$

$$\frac{\partial T}{\partial z} = 0, \quad \text{at} \quad z = -b, \tag{7b}$$

$$T = 0, \quad \text{at} \quad z = b, \quad \text{for} \quad 0 \le r \le a, \tag{7c}$$

$$\frac{\partial T}{\partial z} = -1.2 - 0.35T, \quad \text{at} \quad z = b, \quad \text{for} \quad a \le r \le 1. \tag{7d}$$

Here aR is the dimensional radius of the crystal, and the dimensional heat flux at the vertical crucible wall varies from $(1 + \alpha)q$ at $\theta = 0$ to $(1 - \alpha)q$ at $\theta = \pm\pi$, which is the azimuthal position of the gap in the heater. The coefficients in Eq. (7d) represent estimates of the radiative and conductive heat losses from the melt at the encapsulant interface. These estimates are based on experimentally measured temperatures in a furnace (Prasad et al., 1994) and in an encapsulant (Bachowski et al., 1990).

For our two-component model, the Fourier series for T, p, h, v_r, v_z, and j_θ all have the form

$$T = T_a(r, z) + \alpha \cos\theta T_n(r, z), \tag{8a}$$

while the series for ϕ, v_θ, j_r and j_z all have the form

$$\phi = \alpha \sin\theta \phi_n(r, z). \tag{8b}$$

Here the subscripts a and n denote the axisymmetric and non-axisymmetric components, while $\phi = v_\theta = j_r = j_z = 0$ for an axisymmetric buoyant convection.

In the boundary value problem, **v** and **j** are uniquely defined, but arbitrary constants can be added to p and ϕ. Equation (8b) makes ϕ_n unique. Equations (3a,b) indicate that $(C_1 r^{-1} + C_2 z + C_3)$ can be added to h_a, while $C_4 r$ can be added to h_n, for any constants C_1, C_2, C_3, C_4 and that the arbitrary constant in p is C_2. We make h_a and h_n unique by requiring that h_a is bounded at $r = 0$, and with the conditions

$$h_a(0, \pm b) = 0, \quad \frac{\partial h_n}{\partial r}(1, b) = 0. \tag{9a, b}$$

Chebyshev spectral collocation methods are used to determine T_a, T_n, h_a, h_n, and ϕ_n (Ting et al., 1993), and the other variables are then given by Eqs. (3), (8).

Results

For all the results presented here, $a = b = 0.5$. The isotherms for T_a and T_n are presented in Fig. 1. The values of T_a are the same in every θ = constant plane, while the values of T_n are multiplied by $\alpha \cos\theta$. If the top surface were thermally insulated, T_n would be r, and the isotherms in Fig. 1(b) would be equally spaced vertical lines. The isothermal crystal-melt interface produces the largest distortion from vertical isotherms for T_n.

Since $v_\theta = 0$ for the axisymmetric buoyant convection driven by T_a, there is a stream function for v_{ra} and v_{za}, and the streamlines for Ha = 200 are presented in Fig. 2. An axisymmetric radial velocity across the axial magnetic field drives an azimuthal electric current, which produces an electromagnetic (EM) body force opposing the radial velocity. Since the melt provides a low-resistance circuit for azimuthal electric currents, the EM suppression of the axisymmetric buoyant convection is strong. In the large Ha asymptotic solution, the axisymmetric

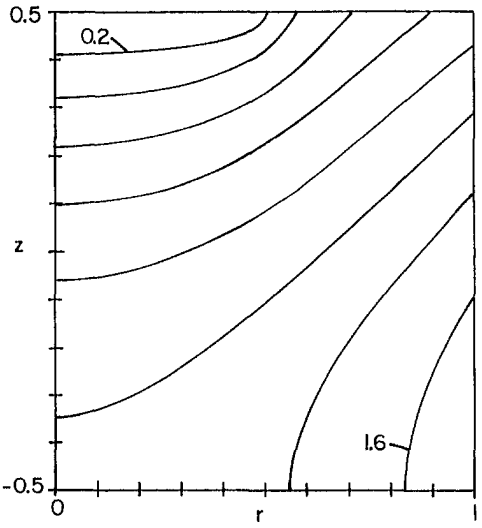


Fig. 1(a) Isotherms for T_a: T_a = 0.2 m, for m = 1 to 8

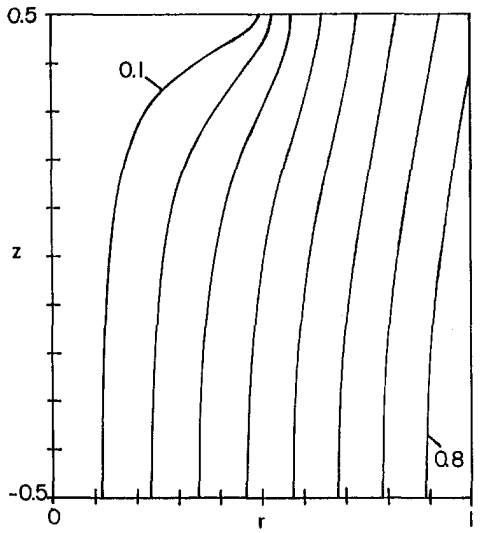


Fig. 1(b) Isotherms for T_n: T_n = 0.1 m, for m = 1 to 8

convection consists of a vertically upward flow with an $O(\mathrm{Ha}^{1/2})$ v_{za} inside the parallel layer and $O(1)$ v_{ra} and v_{za} in the core. The only difference between the axisymmetric flow streamlines for Ha = 100, 500, and 1000 and those in Fig. 2 is that the streamlines for the vertically upward flow become more compressed near $r = 1$ as Ha increases. For Ha = 100 and 200, the maximum values of v_{za} are 8 and 3 percent below 0.09363 $\mathrm{Ha}^{1/2}$, which holds for Ha $\ge$ 500. The maximum and minimum values of v_{ra} approach 0.5 and -0.58 near the crucible bottom and crystal edge, respectively, as Ha increases.

For the non-axisymmetric buoyant convection driven by $\alpha \cos\theta\, T_n$, the highest and lowest temperatures on the vertical crucible wall occur at $\theta = 0$ and at $\theta = \pm\pi$, respectively. We expect vertically upward and downward flows near the vertical crucible wall for $|\theta| < \pi/2$ and for $|\theta| > \pi/2$, respectively. We also expect a transverse horizontal flow from the crucible at $|\theta| < \pi/2$ to the crucible at $|\theta| > \pi/2$ for $z > 0$, and opposite transverse flow for $z < 0$. There are two possible paths for the opposite transverse flows: across the core or around the vertical crucible wall inside the parallel layers with large values of v_θ. The electrically insulating vertical crucible wall blocks the radial electric currents j_r which would produce an EM body force opposing azimuthal velocities inside the parallel layer. The asymptotic analysis showed that v_θ inside the parallel layer

Downloaded 03 Jun 2010 to 171.66.16.125. Redistribution subject to ASME license or copyright; see http://www.asme.org/terms/Terms_Use.cfm

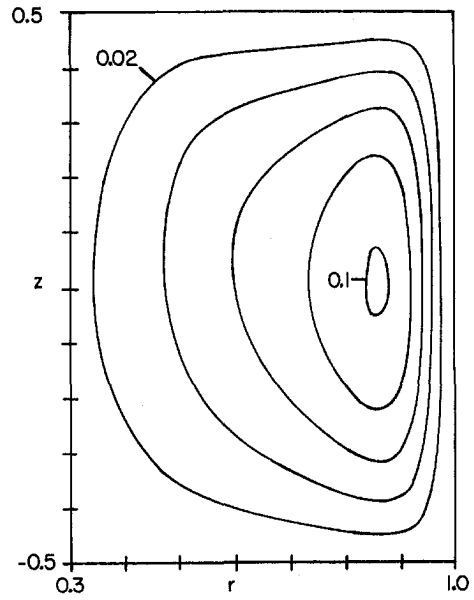


Fig. 2 Streamlines for v_{ra} and v_{za}: ψ = 0.02 m, for m = 1 to 5. Ha = 200

is $O(\mathrm{Ha})$, so that the dimensionless volumetric flow swirling around the vertical crucible wall inside the parallel layer is $O(\mathrm{Ha}^{1/2})$, while the transverse flow across the core is $O(1)$, like the axisymmetric flow (Ma and Walker, 1995).

The contours of $v_{\theta n}$ for Ha = 200 are presented in Fig. 3, and these values are multiplied by $\alpha \sin\theta$. The only differences between the contours for Ha = 100, 500, and 1000 and those in Fig. 3 are that the contours are compressed toward $r = 1$ and the magnitudes increase as Ha increases. The asymptotic solution gave the extreme values of $v_{\theta n} = \pm 0.023\mathrm{Ha}$, while the composite solution gives values whose magnitudes are 19 and 15 percent smaller than $\pm 0.023\mathrm{Ha}$ for Ha = 200 and 500, respectively. The composite solution includes both the $O(\mathrm{Ha})$ and $O(\mathrm{Ha}^{1/2})$ $v_{\theta n}$ inside the parallel layer, while the asymptotic solution neglects the $O(\mathrm{Ha}^{1/2})$ term. Obviously Ha must be extremely large before the $O(\mathrm{Ha}^{1/2})$ term is negligible compared to 0.023Ha, so that the composite solution is more accurate for the values of Ha in crystal growth.

The contours of v_{rn} for Ha = 200 are presented in Fig. 4, and these values are multiplied by $\alpha \cos\theta$. The only change as Ha increases from 100 to 1000 is that the vertical parts of the contours on the right become compressed toward $r = 1$. These contours reflect the transverse flow across the core from the crucible for $|\theta| < \pi/2$ to the crucible for $|\theta| > \pi/2$ for $z > 0$ and in the opposite direction for $z < 0$. If the transverse flow went straight across the core, the contours in Fig. 4 would be horizontal lines except near $r = 1$. However, the transverse flow from the crucible for $|\theta| < \pi/2$ and for $z > 0$ encounters the relatively isothermal region in Fig. 1(*b*) near the crystal-melt interface, so that part of the transverse flow descends across the $z = 0$ plane and returns to the crucible for $|\theta| < \pi/2$ without crossing the vertical plane at $\theta = \pm\pi/2$. Thus the contours in Fig. 4 spread out near $r = 0$, reflecting the decrease in v_{rn} as part of the transverse flow turns back toward the crucible. For a transverse flow, the v_r in the $\theta = 0$ and $\theta = \pm\pi$ planes should have similar values of v_θ in the $\theta = \pm\pi/2$ plane, and these values do exist in $v_{\theta n}$, but they are lost in Fig. 3 with contours at $\Delta v_{\theta n} = 1$. Technically the composite solution includes the $O(\mathrm{Ha}^{1/2})$ and $O(1)$ terms in the core. The asymptotic solution gave a transverse core velocity of $0.000164\ \alpha\mathrm{Ha}^{1/2}$ for this T_n, but we see no evidence of this transverse core flow in the composite solution, even for Ha = 1000. The asymptotic solution neglects any $O(1)$ term compared to an $O(\mathrm{Ha}^{1/2})$ term, but the $O(1)$ flow is actually much larger than $0.000164\mathrm{Ha}^{1/2}$ for realistic values of Ha for crystal growth.

The contours of v_{zn} for Ha = 200 are presented in Fig. 5, and these values are multiplied by $\alpha \cos\theta$. As Ha increases from 100 to 1000, the contours are compressed toward $r = 1$ and the maximum value of v_{zn} increases from 1.726 to 10.578. This vertically upward or downward flow inside the parallel layer for $|\theta| < \pi/2$ or $|\theta| > \pi/2$, respectively, completes the flow circuit for both the azimuthal velocity inside the parallel layer and the transverse flow across the core. Therefore v_{zn} in the parallel layer combines an $O(\mathrm{Ha})$ term for the azimuthal parallel-layer flow and an $O(\mathrm{Ha}^{1/2})$ term for the transverse core flow. The asymptotic solution only included the $O(\mathrm{Ha})$ term, while the composite solution includes both. The asymptotic solution gave a maximum value of $v_{zn} = 0.008588\mathrm{Ha}$ at $r = 1 - 0.65\mathrm{Ha}^{-1/2}$, while the maximum values of v_{zn} from the composite solution exceed 0.008588Ha by 101, 71, 41, and 23 percent for Ha = 100, 200, 500 and 1000, respectively. This excess

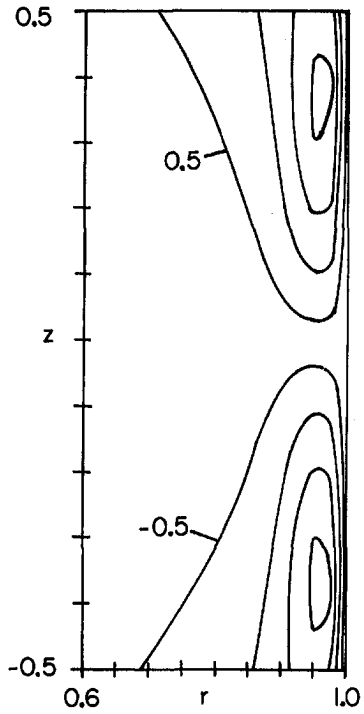


Fig. 3 Contours of $v_{\theta n}$ for Ha = 200: $v_{\theta n} = -3.5 + m$, for m = 0 to 7

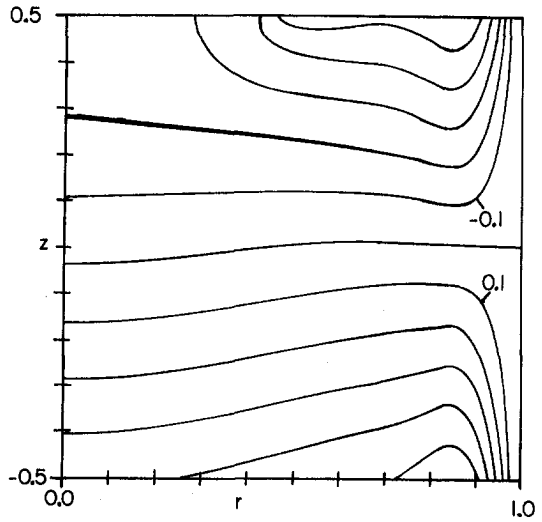


Fig. 4 Contours of v_{rn} for Ha = 200: $v_{rn} = \pm 0.1$ m, for m = 0 to 5

Downloaded 03 Jun 2010 to 171.66.16.125. Redistribution subject to ASME license or copyright; see http://www.asme.org/terms/Terms_Use.cfm

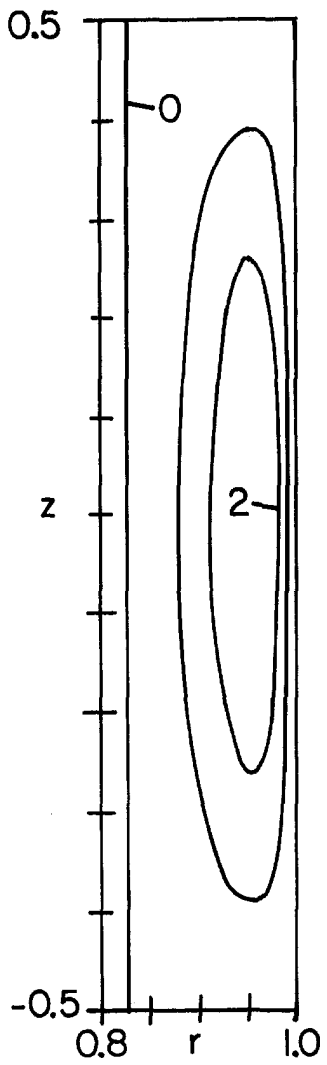


Fig. 5 Contours of v_{zn} for Ha = 200: $v_{zn} = m$, for $m = 0$ to 2

reflects the $O(\mathrm{Ha}^{1/2})$ v_z to complete the flow circuit for the transverse core flows between the crucible wall for $|\theta| < \pi/2$ or $|\theta| > \pi/2$. The fact that part of the transverse core flow returns to the crucible without crossing the plane at $\theta = \pm\pi/2$ is reflected by the negative values of v_{zn} in the core for $r < 0.82$, with a minimum value of -0.178 near $r = 0.5$, but these small values are lost in Fig. 5 with its $\Delta v_{zn} = 1$.

Conclusions

An axisymmetric buoyant convection is strongly suppressed because the melt provides a low-resistance circuit for the azimuthal electric current. A non-axisymmetric temperature drives transverse flows between the hot and cold sides of the crucible. For these transverse flows, a flow path along the vertical crucible wall is favored because the electrically insulating wall blocks the radial electric currents which would produce the EM body force opposing local azimuthal velocities. The nondimensionalization with Eq. (1) assumes that all melt velocities vary as B^{-2} as B is increased. The azimuthal and axial velocities very near the vertical crucible wall actually vary as B^{-1}, so that they become relatively larger as B is increased. The actual comparison of the axisymmetric and non-axisymmetric buoyant convection depends on α which reflects the relative deviation from axisymmetry in the heating and which scales the combination of our two solutions of the linear problem. For the temperatures reported by Bachmann et al. (1975), α would be rather large, but their early experiment probably does not reflect the current state of the art. Most crystal growers probably design heaters to minimize the deviation from axisymmetry, thus making α small. If a large deviation from axisymmetry is unavoidable, the swirling flows around the vertical crucible wall can be eliminated by using a non-uniform magnetic field with a nonzero radial component at the vertical crucible wall.

Acknowledgments

This research was supported by the National Science Foundation under Grants CTS 94-19484 and CTS 95-0010N. The calculations were performed on the CONVEX 3880 supercomputer at the National Center for Supercomputing Applications at the University of Illinois at Urbana-Champaign. Drs. David Bliss and Andrew Anselmo of the U.S. Air Force Rome Laboratory provided information about the thermal environment in indium-phosphide crystal growth.

References

Bachman, K. J., Buehler, E., Shay, J. L., and Strnad, A. R., 1975, "Liquid Encapsulated Czochralski Pulling of InP Crystals," *Journal of Electronic Materials,* Vol. 4, pp. 389–406.

Bachowski, S., Bliss, D. F., Ahern, B., Hilton, R. M., Adamski, J., and Carlson, D. J., 1990, "Magnetically Stabilized Kyropoulos and Czochralski Growth of InP," *Proc. 2nd Int. Conf. on InP and Related Materials,* pp. 30–34.

Hjellming, L. N., and Walker, J. S., 1987, "Melt Motion in a Czochralski Crystal Puller with an Axial Magnetic Field: Motion due to Buoyancy and Thermocapillarity," *Journal of Fluid Mechanics,* Vol. 182, pp. 335–368.

Hurle, D. T. J., Müller, G., and Nitsche, R., 1987, "Crystal Growth from the Melt," *Fluid Sciences and Materials Science in Space,* H. U. Walter, ed., Springer-Verlag, pp. 313–354.

Langlois, W. E., Kim, K. M., and Walker, J. S., 1993, "Hydromagnetic Flows and Effects on Czochralski Silicon Crystals," *Journal of Crystal Growth,* Vol. 126, pp. 352–372.

Ma, N., and Walker, J. S., 1995, "Liquid-Metal Buoyant Convection in a Vertical Cylinder with a Strong Vertical Magnetic Field and with a Non-Axisymmetric Temperature," *Physics of Fluids,* Vol. 7, No. 8, pp. 2061–2071.

Prasad, V., Bliss, D. F., and Adamski, J. A., 1994, "Thermal Characterization of the High Pressure Crystal Growth System for In-Situ Synthesis and Growth of InP Crystals," *Journal of Crystal Growth,* Vol. 142, pp. 21–30.

Series, R. W., and Hurle, D. T. J., 1991, "The Use of Magnetic Fields in Semiconductor Crystal Growth," *Journal of Crystal Growth,* Vol. 113, pp. 305–328.

Ting, A., Hua, T. Q., Walker, J. S., and Picologlou, B. F., 1993, "Liquid-Metal Flow in a Rectangular Duct with Thin Metal Walls and with a Non-Uniform Magnetic Field," *International Journal of Engineering Science,* Vol. 31, pp. 357–372.

Walker, J. S., Ludford, G. S. S., and Hunt, J. C. R., 1972, "Three-Dimensional MHD Duct Flows with Strong Transverse Magnetic Fields. Part 3. Variable-Area Rectangular Ducts with Insulating Walls," *Journal of Fluid Mechanics,* Vol. 56, pp. 121–141.

Downloaded 03 Jun 2010 to 171.66.16.125. Redistribution subject to ASME license or copyright; see http://www.asme.org/terms/Terms_Use.cfm

Enhanced Axial Dispersion in Oscillating Pipe Flow With Different Solute Concentrations at Its Ends

J. G. Zhang
Research Engineer.

W. C. Zegel
President, Research Scientist.

Water and Air Research, Inc.,
6821 SW Archer Road,
Gainesville, FL 32608

U. H. Kurzweg
Professor.
Department of Aerospace Engineering,
University of Florida,
Gainesville, FL 32011

The problem of the enhanced axial contaminant dispersion by sinusoidal oscillation of fluid in a cylindrical pipe connected to reservoirs filled with contaminated groundwater involving different concentrations of species has been examined. It is found that the axial contaminant transfer along the pipe can be greatly enhanced by the fluid oscillation, which leads to a rapid removal of contaminants from groundwater and develops a relative low concentration region in the neighborhood of the subsurface collector. The enhanced dispersion coefficients, D_{eff}, of several heavy metal ions and organic compounds with water as carrying fluid were computed, and the results show they are about four to six orders of magnitude larger than those in the absence of fluid oscillation. The operational energy cost is low. For example, by operating the presented U-type enhanced mass pump, whose total cross-section area in one leg is 0.0154 m^2, it takes 15 days to extract and remove acetone from a contaminated groundwater body that is 12 m below grade and 10 m^3 in volume, such that the acetone concentration can be decreased from 650 mg/l to 325 mg/l (i.e., 50 percent lower than its original level) and the averaged daily (24 hours) operational energy cost is only 12.6 kJ (1.56 Btu).

Introduction

This paper presents a study into the problem of enhanced axial dispersion by sinusoidal oscillation of fluid in pipes connected to a clean water tank at one end and to a subsurface reservoir (collector) filled with contaminated groundwater at the other end, in which the concentrations of various hazardous contaminants are uncontrolled and, hence, time-dependent. The described pipe system in which the fluids oscillate is called the Enhanced Mass Pump (EMP), which is a key component of our currently studied hydrodynamic enhanced barrier system (HEBS), designed to improve the effectiveness of the existing groundwater containment units. The HEBS generally includes a slurry wall, a subsurface groundwater collector installed parallel to the slurry wall at the contaminated groundwater site, an at-grade tank that supplies unlimited clean water or treatment liquid, and a U-type EMP which can be operated in either oscillating-flow mode or circulating-flow mode.

Figure 1 shows the schematic of a U-type EMP geometry, which essentially consists of two bundles of small diameter, open-ended thin pipes attached to the at-grade tank at one end and to the collector at the other. Assuming the groundwater flowing into the subsurface collector is small and negligible, the extraction of contaminants from groundwater by oscillation of fluid in pipes can be several orders of magnitudes larger than those in the absence of oscillations. This rapid removal of contaminants from groundwater creates a very low contaminant concentration zone at or near the subsurface collector, which acts like a hydrodynamic barrier superimposed on the existing groundwater containment units and effectively prevents the hazardous substances from further dispersing outward into the surrounding groundwater. When it is operated in the circulating flow mode, the contaminated groundwater is continuously pumped into the at-grade tank or treatment units. After proper treatment, the relative "clean" groundwater then will be routed back to the collector and mixed there. This continuing groundwater "replacement" depresses the concentration of contaminant in the groundwater and eventually results in a low concentration zone or a hydrodynamics barrier. Moreover, the HEBS also can be used as an injector to constantly deliver the treatment agents to places where human approach is restricted, such as the radioactive-related areas in power plants and/or groundwater systems.

Theoretical studies of dispersion for unidirectional laminar flows in straight pipes have been made by Taylor (1953) and showed that when a small quantity of diffusing substance is introduced into a fluid flowing along a circular pipe, the spreading of the cloud of the species is enhanced by the flow of the fluid. A similar effect occurs for oscillating flows, as pointed out by Bowden (1965) and later by Harris (Harris and Goren, 1967). The enhanced axial dispersion of contaminants in the presence of laminar oscillatory flow within a thin pipe was studied by Chatwin (1975), who suggested that the assumption of constant time-averaged axial contaminant gradient can be made. Watson (1983) showed that the effective axial dispersion of contaminants is proportional to the square of the tidal displacement, and the theoretical prediction was successfully tested experimentally by Joshi et al. (1983) and by Jaeger (Jaeger and Kurzweg, 1983; Jaeger et al., 1991). In the 1980s, studies were extended to the biomechanics area by Jaeger and Kurzweg (1983) and to the heat transfer field by Kurzweg and Zhao (1984), Kaviany (1986), and Zhang and Kurzweg (1991; Zhang, 1988). This later problem led to the interesting observation that the effective axial heat conduction rates increase some five orders of magnitude over those in the absence of oscillations, and the process does not require a convective mass exchange. In these studies, a constant concentration (or temperature in heat transfer) existing in the end-reservoir fluids was assumed. For many applications, including this one, however, the solutes concentration in the end-reservoirs are time-depen-

Contributed by the Fluids Engineering Division for publication in the JOURNAL OF FLUIDS ENGINEERING. Manuscript received by the Fluids Engineering Division March 13, 1994; revised manuscript received November 6, 1995. Associate Technical Editor: O. C. Jones.

Copyright © 1996 by ASME

Downloaded 03 Jun 2010 to 171.66.16.125. Redistribution subject to ASME license or copyright; see http://www.asme.org/terms/Terms_Use.cfm

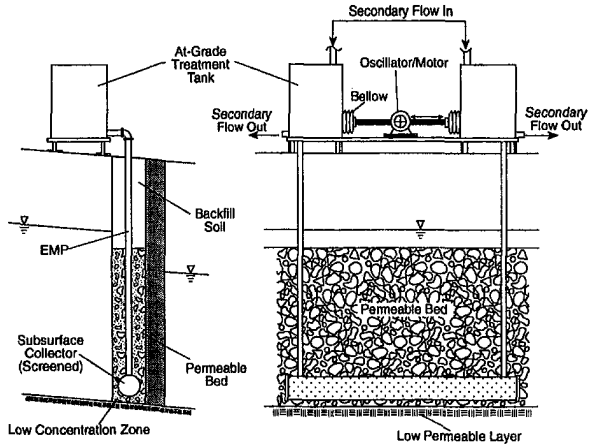


Fig. 1 Schematic of U-type EMP geometry

dent. Studies of the enhanced axial dispersion by oscillation of fluid in pipes that are connected to end reservoirs filled with a variable solutes concentration is of particular interest in designing the hydrodynamics enhanced barrier unit for groundwater remediation at hazardous waste landfill sites. The EMP works like a smart mass pump, it extracts and removes the contaminants only from the source, not the whole water body. Apparently, this will greatly reduce the "clean-up" costs in the remediation activities at a hazardous wastes landfill site.

Formulation of the Problem

1. End-Reservoir Concentration. Because of the U-type EMP design (Fig. 1), the fluid static pressure is self-balanced during the oscillations, and the analysis of EMP can be simplified by examining only its one leg. Since gravity force is self-balanced, it will not appear in the analysis. Figure 2 shows the schematic of a one-leg EMP rotated 90 deg from its vertical orientation. This figure presents one leg of the system in Fig. 1. The system in Fig. 2 has been previously analyzed (Zhang, 1988), although not for this application, and provides a mathematical approach to the problem. The mechanisms associated with Tank 1 in Fig. 2 do not exist in the collector of Fig. 1. In operation, the system shown in Fig. 1 will be removing contaminated water in one leg while injecting cleaner water from the other leg. The precise response of a contaminated aquifer to these imposed flows depends upon the aquifer's hydraulic characteristics. More often than not, contamination occurs in a surficial aquifer. It is expected, but not known as yet, that the water in the screened sub-surface collector will be refreshed through the screening by the surrounding contaminated aquifer water. The major focus of planned bench and pilot-scale experiments is to gain an understanding of this part of the system and what limitations it imposes.

With this understanding of the differences between the proposed system and previously analyzed mechanisms, we assume that the time-dependent groundwater solute concentration in or near the subsurface collector is $C_1(t)$ and that it is C_{01} at $t = 0$. The solute concentration in the at-grade tank fluid is C_2, which is held constant by properly adjusting the secondary flow rate, Q_2. The contaminated groundwater of concentration C_1^i flows freely into the subsurface collector at a constant flow rate, Q_1, and exits from it at the same flow rate; the solute concentration is the same as that in the collector (i.e., $C_1(t)$). The oscillator near the at-grade tank can set the working fluid in pipes into sinusoidal axial motion at an angular frequency, ω. The tidal displacement Δx, which is proportional to the amplitude of the applied periodical pressure, is always kept relatively small so that the condition of zero net convection between the pipe ends is maintained. In practice, the volume of the subsurface collector, V_1, is often quite large, so that the variation of solute concentration in the collector within a single oscillatory period is very small and negligible, which assures a nearly constant time-averaged axial solute concentration gradient between the pipe ends. With these assumptions, the time-averaged enhanced axial contaminant flux in oscillatory flow can be estimated by

$$q_{eff}(t) = D_{eff}\gamma A \tag{1}$$

where $\gamma = (C_1(t) - C_2)/L$ is the time-averaged axial concentration gradient between end-reservoirs, A is the total cross section area of pipes, L is the pipe length, and D_{eff} is the effective dispersion coefficient obtained from Equation 4. The concentration in the contaminated groundwater at or near the subsurface collector is described by the Volterra integral equation

$$C_1(t) = C_{01} + \frac{1}{V_1}\int \{Q_1[C_1^i - C_1(t)] - q_{eff}\}dt \tag{2}$$

By solving Eq. (2) with the initial condition of $C_1(t) = C_{01}$, the time-dependent concentration, $C_1(t)$, in the subsurface collector has the form

$$C_1(t) = (C_{01} - C_{tr})e^{-\kappa t} + C_{tr} \tag{3}$$

where $C_{tr} = (C_1^i Q_1 + C_2 Q_p)/(Q_1 + Q_p)$, $\kappa = (Q_1 + Q_p)/V_1$, and $Q_p = D_{eff}A/L$. The time required to achieve such a solute concentration can also be easily estimated from Eq. (3).

2 Effective Axial Dispersion Coefficient. The values of the effective axial dispersion coefficient, D_{eff}, can be determined from existing theory of contaminant dispersion by oscillating flow in pipes, as first done by Harris and Goren (1967) and later in more detail by Chatwin (1975) and Watson (1983), provided the restriction is made that one is dealing with dilute mixtures where the flow hydrodynamics are essentially controlled by the properties of the carrier fluid. By neglecting the direct axial molecular diffusion and end effects, and assuming laminar conditions, the effective axial dispersion coefficient for incompressible flow in a cylindrical pipe of radius a is

$$D_{eff} = \Phi(\alpha, \sigma)\omega\Delta x^2 \tag{4}$$

where ω is the oscillating frequency and Δx is the tidal displacement. The dimensionless enhanced axial dispersion coefficient, $\Phi(\alpha, \sigma)$, can be estimated from (Jaeger and Kurzweg, 1983):

$$\Phi(\alpha, \sigma) = \frac{1}{4\alpha\sigma(1 - \sigma^{-2})}\left[F_1(\alpha) - \frac{F_1(\alpha\sqrt{\sigma})|F(\alpha)|^2}{\sqrt{\sigma}|F(\alpha\sqrt{\sigma})|^2}\right] \div \left(\left|1 + \frac{2}{\alpha}F(\alpha)\right|^2\right) \tag{5}$$

where $\alpha = a\sqrt{\omega/\nu}$ is the Womersley number, $\sigma = \nu/D_m$ is the Schmidt number, ν is the kinematic viscosity of the carrier fluid,

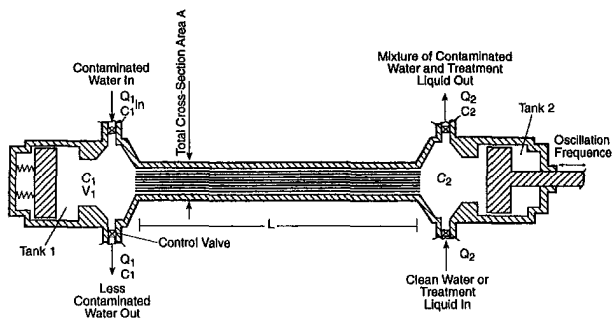


Fig. 2 A simplified one-leg EMP device

Downloaded 03 Jun 2010 to 171.66.16.125. Redistribution subject to ASME license or copyright; see http://www.asme.org/terms/Terms_Use.cfm

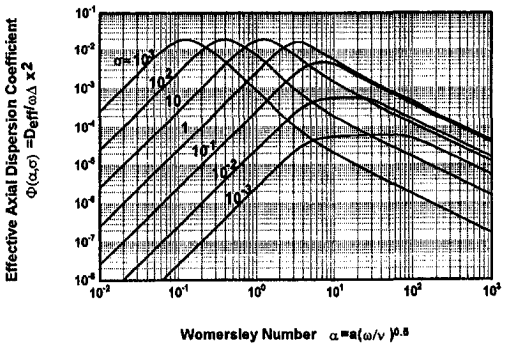


Fig. 3 Effective axial dispersion coefficient versus Womersley number

a is the pipe radius, D_m is the molecular diffusivity, and $F_I(\alpha)$ represents the imaginary part of the complex function

$$F(\alpha) = -\frac{J_0'(\sqrt{-i}\alpha)}{J_0(\sqrt{-i}\alpha)} = i\left[\frac{ber'\alpha + ibei'\alpha}{ber\alpha + ibei\alpha}\right] \tag{6}$$

The first order Bessel function, J_0, is related to the Kelvin functions by $J_0(\sqrt{-i}\alpha) = ber\alpha + ibei\alpha$. The enhanced axial dispersion coefficient $\Phi(\alpha, \sigma)$ described in Eq. (5) can be derived by reformulation of Watson's original result, first derived by Jaeger and Kurzweg (1983). It has the advantage that derivatives no higher than the first order of the Kelvin functions are needed.

3 Power Input Calculation. The rate of work done by the piston (or oscillator) to support the oscillation of the carrier fluid per unit length can be found by integrating the product of pressure and velocity over the pipe cross-section; the mean rate of power input for a single pipe is (Jaeger et al., 1991):

$$W_{pipe}(\alpha) = \frac{\pi\alpha^4 F_I(\alpha)}{8\left|1 + \frac{2}{\alpha}F(\alpha)\right|^2}\frac{\rho v^3 L\Delta x^2}{a^4} \tag{7}$$

The power required to extract a unit mass of contaminants from the end-reservoir and deliver it to the other end-reservoir by the carrier fluid through a parallel bundle of n pipes (radius $r = a$) within the EMP conduit is

$$W_{\text{EMP}} = \frac{nW_{\text{pipe}}}{q} = \mathcal{L}(\alpha, \sigma)\frac{\mu\omega L}{\gamma a^2} \tag{8}$$

where q = mass of contaminants delivered by n pipes and

$$\mathcal{L}(\alpha, \sigma) = \frac{2}{\sigma\alpha^2(1 - \sigma^{-2})}\left[1 - \frac{F_I(\alpha\sqrt{\sigma})|F(\alpha)|^2}{\sqrt{\sigma}F_I(\alpha)|F(\alpha\sqrt{\sigma})|^2}\right] \tag{9}$$

Equation (8) shows that the power required to abstract a unit of contaminant from groundwater with EMPs is directly proportional to the viscosity of the carrier fluid, the pipe length, and the oscillation frequency, while inversely proportional to time-averaged axial concentration gradient and the pipe's cross-section. For a given pipe length and axial concentration gradient, which are often constrained by design conditions, the use of lighter carrier fluid or a lower oscillation frequency will result in a more cost-effective manner of operation. However, to optimize the performance of the EMP device, one has to choose a compatible pipe diameter for which a reasonable oscillation frequency produces maximum mass transfer per energy cost. This is called tuning the apparatus. Rapid removals can be accomplished by increasing the oscillation frequency and the tidal displacement. However, if this is done in an untuned condition, the rapid removal may occur but an energy penalty must be paid and the possibility of turbulent flow must be considered. Tuning reduces the energy penalty by making maximum use of axial dispersion, and in reasonable systems does not lead to turbulent flow.

4 Limits of Laminar Flow. The foregoing analysis is based upon the assumption of laminar oscillating flow over the full length of the pipe. Transition to turbulent flow occurs when the Reynolds number exceeds a critical value that is generally accepted to be approximately 2,000, although some studies indicate larger values are possible (Hino et al., 1976; Ohmi and Iguchi, 1982). Thus, as a minimum condition for laminar flow:

$$\text{Re} = vD/\nu \leq 2{,}000$$

Assuming water as the working fluid, $\nu = 10^{-6}$ sq m/s yields:

$$vD \leq 0.002 \text{ sq m/s}$$

for laminar flow to occur.

The general range of reasonable small pipe diameters is 0.003 to 0.0125 m ($\frac{1}{8}$ in to $\frac{1}{2}$ in). Thus, fluid velocity within these pipes cannot exceed 0.67 to 0.16 m/s, respectively, if laminar flow is to be assured. If we assume a Δx of 4 m, oscillation frequency would be limited to approximately 0.17 to 0.04 rad/s to assure laminar flow.

Using a Womersley number of 0.14, the oscillation frequency is limited to 0.0022 to 0.00013 rad/s (about 8 to 0.5 rad/hr), respectively. In the untuned case where the Womersley number is 1.0, the oscillation frequency is limited to 0.11 to 0.0064 rad/s (approximately 400 to 23 rad/hr), respectively. Based on this, the maintenance of laminar flow must be considered but appears not to limit the present analysis.

Results and Discussion

The function $\Phi(\alpha, \sigma)$, described in Eq. (5), has been programmed, and the results of computer evaluations of the effective axial dispersion coefficients as a function of Womersley number, α, for several different values of Schmidt numbers, σ, are given in Fig. 3. The curves show a single maximum that shifts to a lower value of the Womersley number as σ is increased. These curves are called tuning curves, since for a fixed oscillating frequency their peak indicates the pipe diameter at which contaminants extracted from the end reservoirs is optimized. Physically, the tuning condition implies that the optimum enhanced axial contaminants transfer can be achieved only when the radial molecular diffusion time is equal to one half of the oscillation period, or $\sigma\alpha^2 = \pi$. For Schmidt numbers greater than 1, these tuned values of $\Phi = D_{eff}/\omega\Delta x^2$ are approximately 0.02. The observed drop-off in the peak values of $\Phi(\alpha, \sigma)$ for very small σ is attributed to an inability to store contami-

Table 1 Tuning values of several heavy metals and organic compounds

	Cs	Ag	Cd	Pyridine	Acetone	HCl
σ (10^{-4} m^2/s)	489.3	610.4	635.1	1734.5	785.9	381.06
Φ_{max}	0.0191	0.0196	0.0195	0.0195	0.0192	0.0196
α (for tuned Φ_{max})	0.158	0.158	0.158	0.1	0.14	0.2

[1] With water as working fluid ($\nu H_2O = 10^{-6}$ m^2/s)

Downloaded 03 Jun 2010 to 171.66.16.125. Redistribution subject to ASME license or copyright; see http://www.asme.org/terms/Terms_Use.cfm

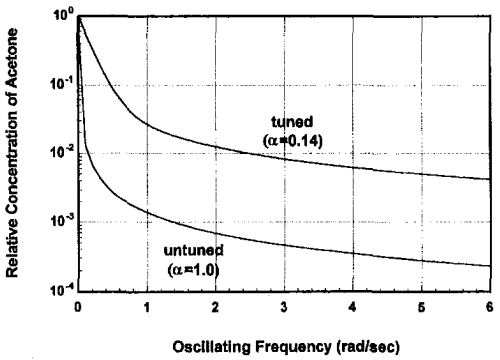


Fig. 4 The relative acetone concentrations versus oscillating frequency under tuned and untuned conditions (t = 15 days, V_1 = 10 m^3, Δx = 4 m)

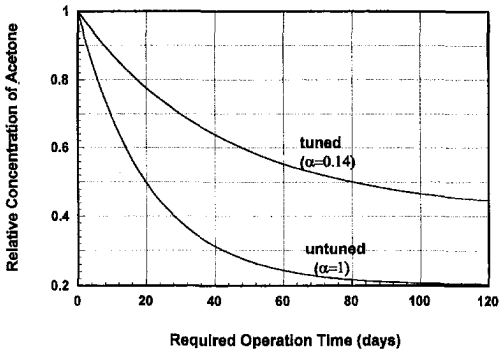


Fig. 5 Relative acetone concentration as a function of operation time

nants in the thin boundary layer that occurs in a fluid of low kinematic viscosity.

Table 1 presents the enhanced axial dispersion coefficient at the tuning point for several toxic heavy metals and organic compounds, which often are observed in contaminated groundwater. As a comparison, the tuning curve for HCl also is tabulated. The tuned values of the enhanced axial dispersion coefficients are seen to lie between 0.0191 and 0.0196, which agrees with the observations illustrated in Fig. 3. Note that, for the three metals, the tuning occurs at a Womersley number of 0.158, while for pyridine the Womersley number is 0.1, and for acetone, 0.14. Since optimum contaminants extraction from contaminated groundwater, for fixed oscillation frequency, can occur only at or near the tuning point, Fig. 3 suggests a pipe size for which a given oscillation frequency produces a tuned condition. In engineering practices, however, the tuning condition may not be achievable and the system may have to be operated at a larger α. Although this will decrease D_{eff}, the enhancement can be still very large.

It is pointed out that the effective dispersion coefficient, D_{eff}, at the tuning point is directly proportional to the product of the oscillation frequency and the square of the tidal displacement. Accordingly, the increase in the tidal displacement can always lead to a large augmentation in the solutes extraction rate from the contaminated groundwater, but at a significant energy penalty compared to the tuned condition. To illustrate the theoretical predictions, we have computed, as a sample, the variation of acetone concentration in groundwater at or near the subsurface collectors (see Fig. 2). We assume that the volume of the subsurface collector, V_1, is 10 m^3 and that it is located 12 m below grade. The tidal displacement used in the study is 4 m, the acetone concentration at t = 0 is 650 mg/l, the inflow concentration remains 650 mg/l at all times during the operation, and the inflow rate is $Q_1 = 1.157 \times 10^{-6}$ m^3/s. This flow represents the rate at which the water in the underground collector is refreshed. It has little effect unless it becomes too small to maintain contaminant concentration in the collector at levels sufficient to drive the desired diffusion. The selected value for this flow (0.1 m^3/day) is somewhat arbitrary, but is felt to be within a range of reasonable values for field conditions. The value is controlled by aquifer conditions and the surface area of the underground collector. Under realistic operating conditions, we only have limited control over the latter of these.

Figure 4 shows the relative acetone concentration, $C_1(t)/C_{01}$, curves as a function of oscillation frequency under tuned (α = 0.14) and untuned (α = 1) conditions. These curves represent the relative concentrations of acetone in groundwater after 15 days of EMP operation. The acetone concentration decreases drastically as the oscillating frequency increases; for example, if ω = 1 rad/sec, the relative acetone concentration, $C_1(t)/C_{01}$, observed at the end of the 15 days of EMP operation is approximately 0.001 under untuned conditions, while it is 0.027 under tuned conditions. Actual operation levels would likely be one to four orders of magnitude smaller than this frequency. The relatively lower residual solute concentration of the EMP operating under untuned conditions is due to the use of a larger oscillating frequency for a given small-diameter pipe. However, running at a still higher oscillating frequency would mean the use of even smaller-diameter pipes in the U-type EMP conduit, higher operational energy cost, and hence inefficiency.

The effect of tidal displacement is the larger the displacement, the lower the remaining contaminant concentration remaining in groundwater. In the acetone example, simulation shows acetone concentration in the groundwater after the EMP has been operating for 15 days. Under the untuned condition (Womersley number, α = 1, ω = 0.001 rad/s), the acetone concentration decreases from 650 mg/l to 380 mg/l, which is quite low in comparison with the surrounding groundwater.

The depth from the earth's surface to the collector, which is also the pipe length in the EMP, will affect the rate of contaminant removal from groundwater. For a given tidal displacement, the deeper the collector is located, the less efficient the EMP technique becomes. However, if a variable tidal displacement is used, the depth of the water table will not be a problem in the EMP process. For example, the device might be designed in which the tidal displacement is always equal to one-third of the depth. In an acetone example, the acetone concentration in groundwater decreases as the depth of collector increases. When the depth is equal to 30 m, the acetone concentration is reduced to 400 mg/l under tuned condition and to 175 mg/l under untuned conditions, which is about 28 percent of its original level with 15 days of EMP operation.

The residual acetone concentration in groundwater is a function of the length of time that the EMP is operated. As shown in Fig. 5, under untuned conditions, the acetone concentration can be reduced to 50 percent of its original level after 20 days

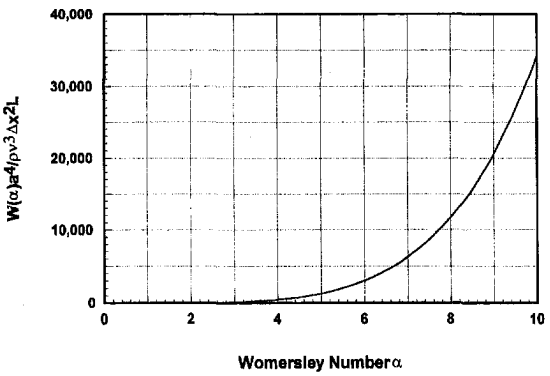


Fig. 6 Dimensionless operational costs as a function of Womersley number

Downloaded 03 Jun 2010 to 171.66.16.125. Redistribution subject to ASME license or copyright; see http://www.asme.org/terms/Terms_Use.cfm

Table 2 Operating energy costs for removal of acetone in a single pipe under tuned and untuned conditions (with EMP leg's conduit diameter of 14 cm [5.5 in])

	Pipe diameter (cm)	Oscillating frequency (rad/s)	Power input for two legs (watts)	Total daily energy costs (J)	Average daily acetone removed (g/day)
Tuned	0.63 ($\frac{1}{4}$")	0.002	9.2×10^{-6}	0.79	75.3
($\alpha = 0.14$)	0.32 ($\frac{1}{8}$")	0.008	1.5×10^{-3}	12.67	170.1
Untuned	0.63 ($\frac{1}{4}$")	0.099	0.043	3688	82.3
($\alpha = 1$)	0.32 ($\frac{1}{8}$")	0.397	0.683	59013	245.6

of operation and to about 30 percent after 40 days of operation. Under tuned conditions, the corresponding relative acetone concentrations are about 77 percent and 64 percent, respectively. As shown by Eq. (3), the contaminant concentration is an inverse exponential function of time; it will not be a cost-effective way to achieve an even lower concentration level by solely increasing the EMP operation time. A lower concentration of certain solute or hazardous substances in the groundwater can be achieved by adjusting some other factors, such as the total cross-section area of the EMP, the tidal displacement, and the oscillatory frequency.

It is important to note that, for a fixed pipe diameter, the energy requirement increases as $\omega^{5/2}$, and the rate of contaminants removed from groundwater under tuned conditions increases in direct proportion to $\omega\Delta x^2$. Therefore, an increasing contaminant removal rate will be accompanied by a more rapidly increasing power import at a high oscillation frequency, thus making the EMP process inefficient there. Fortunately, in most of the discussed cases, the Schmidt numbers of various solutes in groundwater are from several hundreds to more than one thousand, and the tuning points for α are approximately or less than one (Fig. 3). Figure 6 shows the dimensionless energy curve as a function of Womersley number in a single pipe, which can be used to estimate the operational energy requirement of EMP. For the discussed case, the estimated operational energy costs of EMP are presented in Table 2.

Table 2 shows that the energy cost for a single pipe is lower under tuned conditions than under untuned conditions and that the use of larger pipes generally leads to lower energy costs, but they will also decrease the contaminant transport rate. For example, if $\frac{1}{4}$ in. (0.00625 m) diameter pipes are used, the averaged daily solute extraction is 75.3 grams under tuned conditions and 82.3 grams under untuned conditions, their ratio is approximately 1.09. However, the daily energy cost for the untuned operation is about 4,688 times higher than those of tuned operation. This implies that with $\frac{1}{4}$ in. (0.00625 m) pipes, to remove the same amount of hazardous substances from the contaminated groundwater with EMP being operated under untuned conditions will be 4300 times more expensive than under tuned conditions. For $\frac{1}{8}$ in. (0.003175 m) diameter pipes, this ratio is 3,234. However, to achieve the same solute concentration level, the operational energy cost with the U-type EMP being operated under tuned conditions is less than one-third of the pumping cost, which agrees with the findings by Jaeger (Jaeger et al., 1991).

Conclusions

Earlier studies have shown that oscillation of fluid columns in appropriately sized pipes greatly increases axial diffusion. This paper studied the application of this result to the removal of contaminants from groundwater by simulation using a mathematical model.

Application of oscillating pipe flow to the removal of water soluble contaminants from groundwater offers a means of essentially pumping contaminants out of the ground. Using the contaminated water as a working fluid, the contaminants can be removed as they are brought up without the problem of disposal of large amounts of water. The mathematical simulation indicates that this can be a viable method for removal of contamination.

The optimum harnessing of the enhancement of the axial transfer of contaminants in the system can be realized when the ratio of the pipe radius, a, to the boundary layer thickness, $\delta = \sqrt{2\nu/\omega}$, satisfies the tuning condition, $\delta/a = \sqrt{\sigma}/\pi$. This means that the optimum effect for low-energy removal of contaminants from the contaminated reservoir liquid by oscillation of fluids in pipes can be achieved only if the solute radial diffusion time, $t_d = a^2/D_m$, is equal to the half period of the oscillation, $t_h = \pi/\omega$.

The operational energy cost is low; for the discussed acetone case, to reduce the acetone concentration in groundwater to 50 percent of its original level (650 mg/l), the enhanced axial acetone flux over the entire EMP cross-section area (0.031 m^2) is 4.45 g/hour, which is about 2.986×10^5 larger than that in the absence of oscillation, and the power required is only 0.145 watts under tuned conditions and 677 watts under untuned conditions.

The energy analysis shows that operation in a tuned mode will result in slower removal of contamination, but dramatically reduces the energy cost of operation. This opens the possibility of remote, solar-powered units slowly pumping contaminants out of contaminated aquifers for storage in activated carbon or other appropriate absorbent or adsorbent. In some cases, solar energy or an other active agent may be used to directly destroy the contaminants.

The next step is to conduct bench and pilot-scale experiments to verify the simulation and test assumptions made regarding the influence of aquifer characteristics upon the process.

Acknowledgment

The work presented here was funded by a SBIR grant from the Department of the Navy, Office of the Chief of Naval Research, under Contract No. N47408-93-C-7360 with Naval Civil Engineering Laboratory. This support is gratefully acknowledged.

References

Bowden, K. F., 1965, "Horizon Mixing in the Sea Due to Shearing Current," *Journal of Fluid Mechanics,* Vol. 21, p. 84.

Chatwin, P. C., 1975, "On the Longitudinal Dispersion of Passive Contaminant in Oscillatory Flow in Pipes," *Journal of Fluid Mechanics,* Vol. 71, Part 3, pp. 513–527.

Harris, H. G., Jr., and S. L. Goren, 1967, "Axial Diffusion in a Cylinder with Pulsed Flow," *Chemical Engineering Science,* Vol. 22, pp. 1571–1576.

Jaeger, M. J., and U. H. Kurzweg, 1983, "Determination of the Longitudinal Dispersion Coefficient in Flows Subjected to High Frequency Oscillations," *Physics Fluids,* Vol. 26, No. 6, pp. 1380–1382.

Jaeger, M. J., T. Soepardi, A. Maddahian, and U. H. Kurzweg, 1991, "Diffusional Separation of Gases and Solutes in Oscillatory Flow," *Separation Science and Technology,* Vol. 26, No. 4, pp. 503–514.

Jefferis, S., 1991, "Slurry Trench Cut-Offs for Gas and Leachate Control," in *Land Reclamation—An End to Dereliction,* M. C. R. Davies, ed., Elsevier Applied Science Publishers, London.

Joshi, C. H., R. D. Kamm, J. M. Drazen, and A. S. Slutsky, 1983, "An

Downloaded 03 Jun 2010 to 171.66.16.125. Redistribution subject to ASME license or copyright; see http://www.asme.org/terms/Terms_Use.cfm

Experimental Study of Gas Exchange in Laminar Oscillatory Flow," *Journal of Fluid Mechanics,* Vol. 133, pp. 245–254.

Kaviany, M., 1986, "Some Aspects of Heat Diffusion in Fluids Subjected to Sinusoidal Oscillations," *International Journal of Heat and Mass Transfer,* Vol. 29, pp. 2002–2006.

Kurzweg, U. H., and L. D. Zhao, 1984, "Heat Transfer by High-Frequency Oscillations: A New Hydrodynamic Technique for Achieving Large Effective Thermal Conductivities," *Physics of Fluids,* Vol. 27, pp. 2624–2627.

Kurzweg, U. H., and M. J. Jaeger, 1987, "Diffusional Separation of Gases by Sinusoidal Oscillations," *Physics of Fluids,* Vol. 30, pp. 1023–1026.

Taylor, F. R. S., 1953, "Dispersion of Soluble Matter in Solvent Flowing Slowly Through a Pipe," *Proceedings of the Royal Society,* pp. 186–203.

Watson, E. J., 1983, "Dispersion in Oscillatory Pipe Flow," *Journal of Fluid Mechanics,* Vol. 133, pp. 233–244.

Zhang, J., and U. H. Kurzweg, 1991, "Numerical Simulation of Time-Dependent Enhanced Axial Heat Transfer in Oscillating Pipe Flow," *Journal of Thermal Physics and Heat Transfer,* Vol. 5, No. 3, pp. 401–406.

Zhang, J., 1988, "Time-Dependent Enhanced Heat Transfer in Oscillating Pipe Flow," Doctoral Dissertation, Department of Mechanical Engineering, University of Florida, Gainesville, FL. Apr.,

Downloaded 03 Jun 2010 to 171.66.16.125. Redistribution subject to ASME license or copyright; see http://www.asme.org/terms/Terms_Use.cfm

Effect of Branch Orientation on Annular Two-Phase Flow in T-Junctions

(Data Bank Contribution)*

F. Peng

M. Shoukri

Department of Mechanical Engineering, McMaster University, Hamilton, Ontario, Canada L8S 4L7

A. M. C. Chan

Ontario Hydro Research Division, Toronto, Ontario, Canada M8Z 5S4

Experimental data on dividing steam-water two-phase annular flow in T-junctions with horizontal inlet and downwardly inclined branches were obtained. The experiments were performed under experimental conditions which have not been examined before. The branch orientation was found to be a significant parameter affecting phase redistribution in the junction. Increasing the downward inclination of the branch was found to reduce the degree of phase separation in the junction under the present test conditions. This is caused by the nonuniform distribution of the liquid film thickness associated with the horizontal inlet annular flow. The phase redistribution data were compared with available models. The need for additional modelling studies was evident. The pressure changes of two-phase flow in the junction were closely correlated with the phase redistribution phenomenon. The data on pressure changes in the junction were correlated using simple models based on momentum and mechanical energy balances.

1 Introduction

The ability to predict the phase redistribution and pressure changes when two-phase flow is divided in a T-junction is of considerable importance in many applications in the power and process industries. However, owing to the large number of variables affecting the phenomena, our understanding and the data base on the subject remain rather incomplete. A typical dividing T-junction is shown in Fig. 1.

Reported experimental and analytical studies have shown that phase separation and pressure distribution in T-junctions are complex functions of inlet flow regime, inlet quality x_1, inlet mass flux G_1, branch flow split ratio G_3/G_1, conduit geometry etc. Important experimental investigations on the subject are due to Collier (1976), Hong (1978), Henry (1981), Azzopardi and Whalley (1982), Saba and Lahey (1984), Seeger et al. (1986), Ballyk et al. (1988), Rubel et al. (1988), McCreery and Banerjee (1990), and Davis and Fungtamasan (1990). Comprehensive reviews of the topic are available by Azzopardi (1986), Lahey (1986) and recently by Müller and Reimann (1991). Most of the existing experimental data on the subject were obtained from low pressure air-water flow in horizontal junctions. The effect of the branch orientation on phase separation was studied by a few researchers under limited test conditions. Recently, experiments on the effect of upward branch orientation were reported by Azzopardi and Smith (1992) for annular and stratified air-water flows. The present work focuses on the effect of branch downward orientation on phase redistribution and pressure changes in T-junctions having horizontal inlet, and accordingly it complements the recent results of Azzopardi and Smith (1992). Referring to Fig. 1, the present experiments were carried out for T-junctions having $\alpha = \gamma = 90$ deg, while θ was varied from 0 to 90 deg. Moreover, current knowledge on the subject shows clearly that phase redistribution in a T-junction is a strong function of the inlet phase distribution, i.e., flow regime in the inlet pipe. Hence, in performing experiments it is essential that the inlet flow regime be clearly defined.

The work presented herein is an extension of that reported by Ballyk et al. (1988) and Ballyk (1992). The data obtained in this work, together with that of Ballyk et al. (1988), are amongst the few sets of data in which the void fraction in each leg of the junction was measured and the inlet flow regime is directly defined, i.e. not through the use of flow regime maps.

2 Experimental Arrangements

2.1 Experimental Facility and Measurements. The present investigation was performed on the steam-water two-phase flow loop of McMaster University, illustrated schematically in Fig. 2. Preheated water and steam were mixed in the two-phase mixer. The mixture reached thermodynamic equilibrium through approximately 3 m of piping before entering the test section. The test sections used were T-junctions wherein the flow was split and passed from each downstream leg to condensers. The condensates were then metered and delivered back to an open storage tank. The entire loop is insulated to minimize heat losses with the exception of a 10 cm transparent section at the test section inlet for flow regime visualization. The test sections were made from 25.65 mm I.D. stainless steel tubing. The tests were carried out with horizontal inlet ($\alpha =$ 90 deg and $\gamma = 90$ deg) and three branch downward orientations ($\theta = 0$, 45, and 90 deg).

Within the test sections, the pressure distribution was measured by means of pressure taps in all three legs of the T. Five pressure taps were located in each of the inlet and branch sections over approximately 600 mm. Due to slower flow development, the run section contained up to fifteen pressure taps over approximately 2.4 m to ensure that a fully developed pressure profile was obtained. The pressure distribution was measured by means of differential pressure transducers with measurement uncertainty of ± 0.5 percent of the measurement. The flow rates were measured by turbine flow meters with uncertainty of ± 1.0 percent of measurement, while the temperature was measured at fifteen stations throughout the loop using E type thermocouple with uncertainty of ± 2.0 percent. The void fraction in each

* Data have been deposited with JFE Data Bank. To access the file for this paper, see instructions on p. 213 of this issue.

Contributed by the Fluids Engineering Division for publication in the JOURNAL OF FLUIDS ENGINEERING. Manuscript received by the Fluids Engineering Division August 22, 1995; revised manuscript received November 6, 1995. Associate Technical Editor: D. P. Telionis.

Copyright © 1996 by ASME

Downloaded 03 Jun 2010 to 171.66.16.125. Redistribution subject to ASME license or copyright; see http://www.asme.org/terms/Terms_Use.cfm

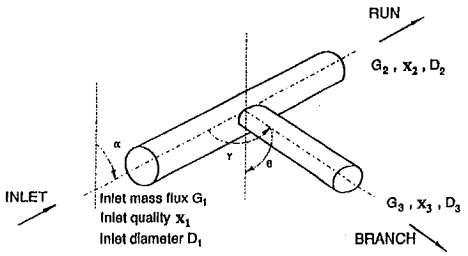


Fig. 1 T-junction geometry

leg, at a location corresponding to the fully developed pressure profile, was measured using a single beam gamma densitometer. It consisted of a 75 mCi Cobalt-57 sealed line source and a NaI(T1) scintillator. The system had a 26 percent sensitivity to water content and static calibration showed the measured void fraction to be accurate within ±8.0 percent of measurement. Details of the experimental arrangements and measuring equipment were given by Ballyk et al. (1988) and Peng (1994).

2.2 Data Reduction. The thermodynamic equilibrium quality in the three legs of the T was evaluated from energy balances. The inlet quality x_1 was calculated by simple energy balance on the mixer. The run and branch qualities, x_2 and x_3 respectively, were calculated by performing energy balances at the two condensers. The pressure changes at the junction were obtained by extrapolating the fully developed pressure profiles in each leg to the junction using the least-squares method. The pressure rise in the run $\Delta P_{2\text{-}1}$ and pressure drop in the branch $\Delta P_{1\text{-}3}$ were calculated from the extrapolated values as shown by Ballyk et al. (1988).

Detailed error analysis was carried out by Peng (1994) to evaluate the uncertainties in the various derived parameters. The uncertainties in the pressure changes $\Delta P_{2\text{-}1}$ and $\Delta P_{1\text{-}3}$ were ±13.1 and ±11.9 percent, respectively. The uncertainties in the calculated qualities x_1, x_2, and x_3 were within ±7.2, ±5.7, and ±6.1 percent, respectively. In presenting the results, the experimental errors are noted at representative data points in the figures.

In order to provide needed information for others who are working on modeling the phase separation phenomena in T-junctions, the data obtained in this work are available in the JFE Data Bank.

3 Phase Redistribution Results

In annular flow, a substantial part of the liquid flows as a thin liquid film along the tube wall. It is, therefore, expected that the liquid film in the main tube segment that is intercepted by the branch will be the first component to be extracted into the branch. At low branch flow rate, most of the branching flow is removed from the liquid film and the branch quality is expected to be below that of the inlet flow. Increasing the branch flow, which corresponds to decreasing the branch downstream pressure, causes more vapour to be extracted through the branch, raising the branch quality. It should be noted that increasing the branch flow is associated with a pressure rise through the junction run due to Bernoulli effect. This adverse pressure rise yields an additional force which tends to drive the flow through the branch. Since the vapor phase in the inlet tube has lower axial momentum than the liquid phase, it tends to respond more readily allowing more vapour flow into the branch. Accordingly, increasing the branch flow tends to result in an increase in the branch flow quality. At a certain branch flow split ratio, G_3/G_1, almost all of the inlet vapour will be extracted through the branch. As shown by Ballyk et al. (1988), the critical branch flow split ratio, at which almost all the vapour is extracted through the branch, i.e. complete phase separation, depends upon the inlet quality and mass flux, the branch to inlet diameter ratio and the conduit geometrical parameters.

3.1 Effect of Branch Orientation. Under the horizontal annular inlet flow condition, the orientation of the branch has a significant influence on the redistribution of the two phases in the T-junction due to the non-uniform distribution of the liquid film caused by gravity. In horizontal annular flow the liquid film is expected to drain toward the bottom of the pipe under the influence of gravitational forces, resulting in a thicker film at the bottom. Typical results showing the effect of branch orientation on phase redistribution are shown in Figs. 3(*a*) to 3(*d*). The branch quality and mass flux are normalized with respect to the inlet conditions, i.e. x_3/x_1 versus G_3/G_1. Equal phase distribution is represented by the horizontal line $x_3/x_1 = 1$, while complete vapour extraction is represented by the curve $x_3/x_1 = G_1/G_3$. The results for three branch orientations, i.e. $\theta = 0$, 45, and 90 deg, under various inlet flow conditions are presented. In the range of the present experimental study, the results show significant effect of branch orientation on phase separation. It is clear that the horizontal branch causes the highest degree of phase separation. For the same inlet condition, the results show that rotating the branch downward from the horizontal orientation results in lower branch quality through the entire range of flow split ratio. The maximum normalized branch quality is also reduced. Moreover, the flow split ratio at which equal phase distribution and complete vapour extraction occur is moved to higher value with increasing the downward branch orientation angle θ.

The observed trends are explained in terms of the asymmetrical distribution of the liquid film in the annular inlet flow, having a very thin film at the top with increasing thickness toward the bottom. By downward rotation of the branch, more liquid becomes readily available for extraction resulting in higher liquid content in the branch flow at any given flow split ratio. The results of Azzopardi and Smith (1992) for upward branches appear as natural extension of the trends described above for downwardly inclined branches. Azzopardi and Smith (1992) showed that for an upward branch, the branch quality increased significantly over that for a horizontal branch under the same conditions of inlet annular flow. However, direct comparison with the present results cannot be carried out since their results were obtained for air-water annular flow at low inlet mass flux, $G_1 < 100$ kg/m^2·s, and high quality $0.60 < x_1 < 0.90$.

3.2 Effect of Inlet Mass Flux and Quality. The results showed clearly that, independent of branch orientation, the inlet mass flux has very little effect on the phase redistribution phenomenon. This can be shown by comparing the data in Figs.

Nomenclature

D = pipe diameter [m]
G = mass flux [kg/m^2·s]
K_{12} = momentum correction factor
K_{13} = energy loss coefficient
P = pressure [Pa]
u = velocity [m/s]
x = thermodynamic quality
α = void fraction
ρ = density [kg/m^3]
θ = orientation angle
ϕ = two-phase multiplier

Subscripts

1, 2, 3 = inlet, run, branch flow regions
e = energy weighted
g = vapour phase
h = homogeneous flow
L = liquid phase

Downloaded 03 Jun 2010 to 171.66.16.125. Redistribution subject to ASME license or copyright; see http://www.asme.org/terms/Terms_Use.cfm

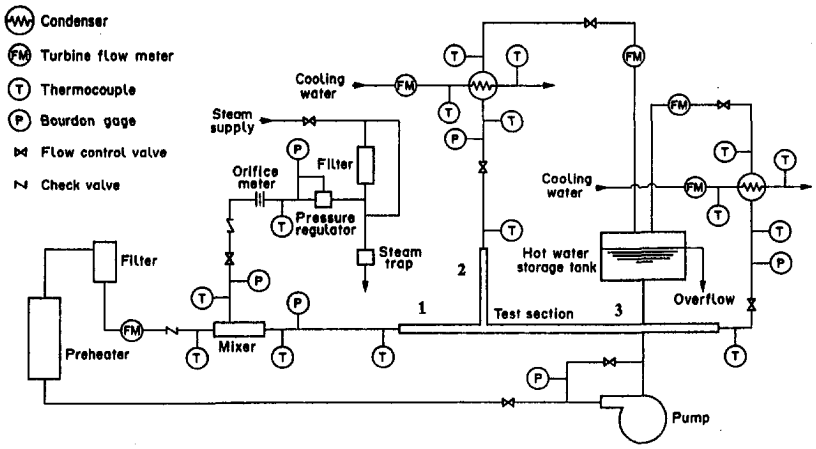


Fig. 2 Steam-water loop

3(*c*) and 3(*d*) obtained for the same inlet quality, $x_1 = 2$ percent, and for mass fluxes of 600 and 900 kg/m^2·s, respectively. This trend is consistent with earlier data published in the literature.

It is also interesting to note that the effect of inlet quality on phase redistribution is dependent on branch orientation. This effect is seen from the results shown in Figs. 4(*a*) to 4(*c*) for a given inlet mass flux; $G_1 = 600$ kg/m^2·s. For a horizontal branch, an increase in inlet quality resulted in reduction of the peak phase separation ratio and increase in the flow split ratio at which complete phase separation is encountered (Fig. 4(*a*)). This is caused by the increase in the thickness of the liquid film available for extraction as the liquid film will tend to be more uniform with increasing vapour velocity, i.e., increasing inlet quality. However, increasing inlet quality and the associated more uniform film thickness cause the liquid film thickness at the bottom to decrease with increasing quality. As a result less liquid becomes available for extraction to the downwardly inclined branches. Accordingly, the effect of inlet quality is reversed for the 90 deg downward branch as shown in Fig. 4(*c*), i.e., the peak branch quality ratio increases with increasing inlet quality. The same effect is seen to a less extent for the 45 deg inclined branch. One would expect that at angle less than 45 deg, the effect of inlet quality will diminish.

3.3 Comparison With Available Models. Seeger et al. (1986) developed empirical relations for phase separation in horizontal T-junctions and T-junctions having horizontal inlet and a 90 deg downwardly inclined branches. The present data are compared with these correlations in Fig. 5. Although the correlations appear to capture the general trends, they clearly underpredict the horizontal T-junction results and overpredict the results of the junction having 90 deg branch. It should be noted that these empirical correlations were developed using high pressure experimental data ($P = 0.7$ MPa). For the present low pressure study ($P = 0.1$–0.2 MPa), the deviation between the predictions and experimental data is not unexpected due to the empirical nature of the correlations which did not account for the effect of pressure on the vapour density.

Ballyk and Shoukri (1990) presented a model for phase redistribution in piping junctions. The model is based on solving a set of mixture conservation equations at the junction. The model uses semi-empirical equations for pressure changes across the junction and uses a closure equation to link the phase separation characteristics of the junction with the associated pressure changes. The model requires prior knowledge of the phase distribution in the inlet pipe to the junction. This model has been tested successfully against data obtained for steam-water and air-water annular flow in horizontal T-junctions. The model can be easily extended to downwardly inclined branches. Taking into account the effect of gravity in downward branches, the predictions of this model are compared with the experimental data obtained in the present work as shown in Figure 6. It is shown that the model is capable of predicting the general trends observed in the present results. However, the model, as presented by Ballyk and Shoukri (1990), clearly overpredicts the phase separation results for the downwardly inclined branches. This is believed to be due to a number of reasons related to the input to the model and its assumptions. The model requires detailed description of the inlet phase distribution, i.e. film thickness distribution and entrainment. Currently, a simple model suggested by Butterworth (1974) is used. The model also uses empirical relations for the flow development lengths in both the run and the branch which were developed from data obtained with horizontal branches. No attempt was made here to adjust the empirical parameters to fit the present data.

Based on the above, additional work is needed in characterizing the phase distribution at the inlet, through the development or use of an accurate annular flow model. Moreover, other empirical correlations used in the model need to be refined.

4 Junction Pressure Changes

When flow is divided in a T-junction the deceleration of the fluid causes a reversible pressure rise in the run and branch due to the Bernoulli effect. Previous studies have shown that the irreversible pressure drop is much higher than the reversible pressure rise in the branch and hence there is a net pressure drop in the branch. The pressure change in the run, however, is dominated by the reversible rise due to Bernoulli effect. Detailed discussion of the pressure changes in T-junctions and comparisons between the present data and all available correlations were given by Peng (1994). A summary of the findings is presented here.

4.1 Single-Phase Flow. By applying simplified momentum and mechanical energy equations to model the run pressure rise and the branch pressure drop respectively, it can be shown that for single-phase flow (see Collier, 1976 and Ballyk et al., 1988)

$$\Delta P_{2\text{-}1} = K_{12}\rho(u_1^2 - u_2^2) \tag{1}$$

$$\Delta P_{1\text{-}3} = \frac{\rho}{2}(u_3^2 - u_1^2) + K_{13}\frac{\rho u_1^2}{2} \tag{2}$$

where $\Delta P_{2\text{-}1}$ and $\Delta P_{1\text{-}3}$ are the run pressure rise and branch pressure drop respectively. K_{12} is known as the run momentum correction factor, which accounts for the indeterminant axial momentum carried out of the control volume by the branching flow, and K_{13} is the mechanical energy loss coefficient due to the

Downloaded 03 Jun 2010 to 171.66.16.125. Redistribution subject to ASME license or copyright; see http://www.asme.org/terms/Terms_Use.cfm

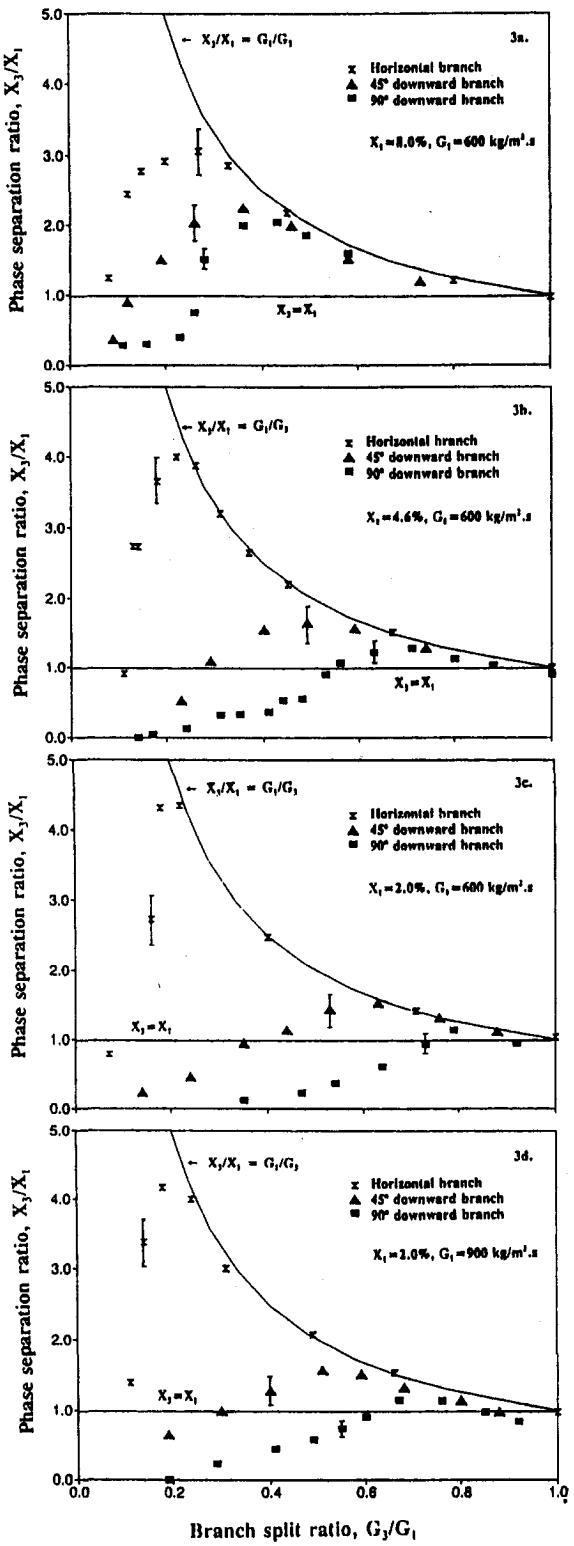


Fig. 3 Effect of branch orientation

dissipation in the T-junction. The single phase run momentum correction factor K_{12} and branch energy loss coefficient K_{13} were obtained in the present work using the above equations. They were found to be in good agreement with the following correlations suggested by Ballyk et al. (1988).

$$K_{12} = 0.704 - 0.320\left(\frac{G_3}{G_1}\right) - 0.028\left(\frac{G_3}{G_1}\right)^2 \quad (3)$$

$$K_{13} = 1.081 - 0.914\left(\frac{G_3}{G_1}\right) + 1.050\left(\frac{G_3}{G_1}\right)^2 \quad (4)$$

4.2 Two-Phase Flow. Most available models for two-phase pressure changes in T-junctions are simple extensions of Eqs. (1) and (2). As suggested by Fouda and Rhodes (1974), Collier (1976), and Ballyk et al. (1988), the axial pressure recovery can be described by,

$$\Delta P_{2\text{-}1} = P_2 - P_1 = K_{12s}\left(\frac{G_1^2}{\rho_{m1}} - \frac{G_2^2}{\rho_{m2}}\right) \quad (5)$$

where K_{12s} is the two-phase momentum correction factor and ρ_m is the momentum density defined by,

$$\rho_{mi} = \left[\frac{x_i^2}{\alpha_i \rho_g} + \frac{(1-x_i)^2}{(1-\alpha_i)\rho_L}\right]^{-1}, \quad i = 1, 2 \quad (6)$$

Several two-phase momentum correction factors have been suggested by different researchers for a T-junction with a horizontal branch. Fouda and Rhodes (1974) recommended that $K_{12s} = 0.533$. Madden and St. Pierre (1969) and Ballyk et al. (1988) showed that $K_{12s} = 1.0$ for T-junctions having a hori-

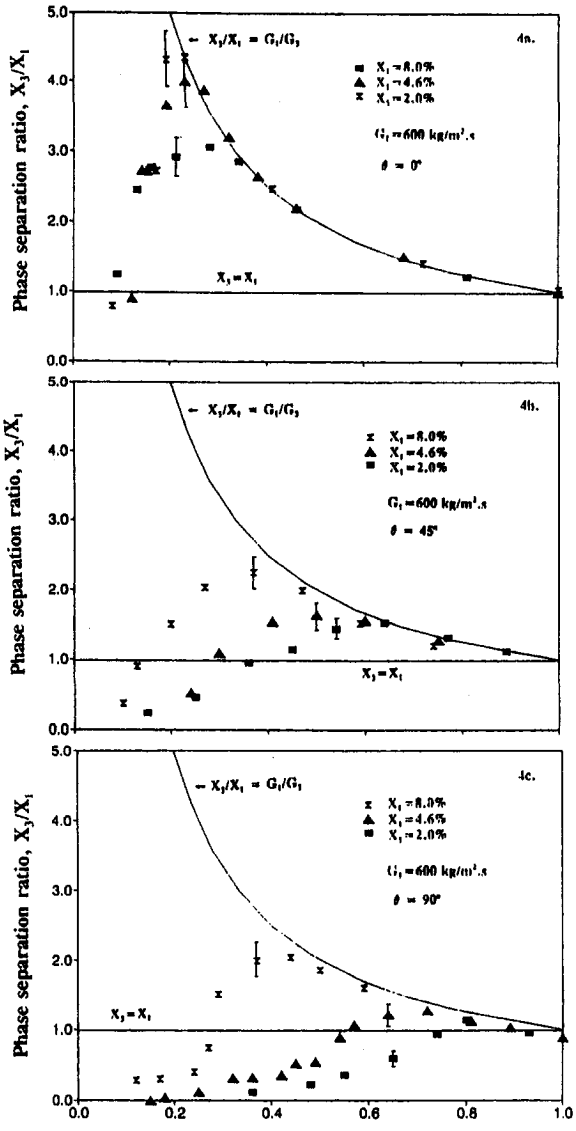


Fig. 4 Effect of inlet quality

Downloaded 03 Jun 2010 to 171.66.16.125. Redistribution subject to ASME license or copyright; see http://www.asme.org/terms/Terms_Use.cfm

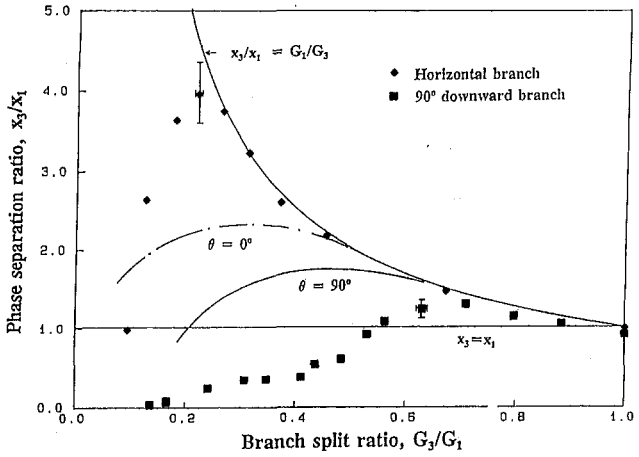


Fig. 5 Comparison of Seeger et al. (1986) model with present data (G_1 = 600 kg/m^2·s, x_1 = 4.6 percent)

zontal branch under annular inlet flow conditions. The work of Ballyk et al. (1988) was the only one in which the momentum density was calculated based on actual measurement of void fraction. The others used empirical correlations for calculating the mixture density.

The two-phase momentum correction factor K_{12s} was calculated from the present data, based on the measured void fraction, for the T-junctions with the branch downwardly inclined by 90 and 45 deg. Physically, K_{12s} is the correction factor which accounts for the axial momentum flux taken off by the branching flow. For a horizontal branch, Ballyk et al. (1988) showed that K_{12s} equals unity, which indicates that the axial momentum flux carried by the branch is insignificant. In the case of downwardly oriented branches more water is extracted into the branch due to gravitational forces. As the water film has higher axial momentum, due to its high density, than the vapour phase, more axial momentum flux will be taken off the control volume. Consequently, the axial momentum correction factor should be less than that for junctions with a horizontal branch. The present investigation showed that K_{12s} can be approximated by 0.78 and 0.42 for junctions with 45 and 90 deg downward branches, respectively, as shown by Peng (1994).

The models used for two-phase pressure drop in the branch are also extensions of the single phase case, and can generally be written in the mechanical energy balance form,

$$\Delta P_{1\text{-}3} = P_1 - P_3 = \frac{\rho_{h3}}{2}\left(\frac{G_3^2}{\rho_3^2} - \frac{G_1^2}{\rho_1^2}\right) + K_{13}\frac{G_1^2}{2\rho_L}\bar{\phi}_{tp} \quad (7)$$

where K_{13} is the single-phase energy loss factor and $\bar{\phi}_{tp}$ is a two-phase multiplier. Available models differ in their definitions of the densities, ρ_1 and ρ_3, and the multiplier $\bar{\phi}_{tp}$.

Saba and Lahey (1984) and Reimann and Seeger (1986) recommended the use of the homogeneous density ρ_h given by:

$$\rho_{hi} = \left[\frac{x_i}{\rho_g} + \frac{(1 - x_i)}{\rho_L}\right]^{-1}, \quad i = 1, 3 \quad (8)$$

On the other hand, Saba and Lahey (1984) correlated the two-phase multiplier by, $\bar{\phi}_{tp} = \rho_L/\rho_{h1}$, while Reimann and Seeger (1986) suggested that $\bar{\phi}_{tp} = \rho_L\rho_{h3}/\rho_{h1}^2$. The predictions of the above two correlations were compared by Peng (1994) with the present data for downwardly inclined branches. Both models predicted the data well in the range of high branch split ratio, $G_3/G_1 > 0.6$. The phase redistribution data shows that this is the range of complete phase separation. In the lower range of branch split ratio, Peng (1994) showed that the two models were very inadequate.

Through a consistent application of the mechanical energy balance, Ballyk et al. (1988) derived an equation for the branch pressure drop similar to Eq. (7). However, the branch and inlet densities were defined by

$$\rho_3 = \rho_{e3} = \left[\frac{x_3^3}{\alpha_3^2\rho_g^2} + \frac{(1 - x_3)^3}{(1 - \alpha_3)^2\rho_L^2}\right]^{-0.5} \quad (9)$$

and

$$\rho_1 = \rho^* = \left[\frac{x_1^2 x_3}{\alpha_1^2\rho_g^2} + \frac{(1 - x_1)^2(1 - x_3)}{(1 - \alpha_1)^2\rho_L^2}\right]^{-0.5} \quad (10)$$

Moreover, Ballyk et al. (1988) defined the multiplier $\bar{\phi}_{tp}$ by,

$$\bar{\phi}_{tp} = \frac{\rho_L\rho_{h3}}{\rho^{*2}}\phi_{tp} \quad (11)$$

where ϕ_{tp} was experimentally determined for horizontal T-junctions. It is interesting to note that the above model and that of Reimann and Seeger (1986) include characteristics of the branch flow in the irreversible pressure drop term. This was shown by Ballyk et al. (1988) to be consistent with the mechanical energy balance assumptions.

The present data were used to calculate the multiplier ϕ_{tp} using Eqs. (7), (9), (10), and (11). The results were empirically correlated, independent of branch orientation, by the following expression,

$$\phi_{tp} = 0.603 + 3.193\left(\frac{G_3}{G_1}\right) + 14.210\left(\frac{G_3}{G_1}\right)^2 + 10.354\left(\frac{G_3}{G_1}\right)^3 - 20.730\left(\frac{G_3}{G_1}\right)^4 \quad (12)$$

The comparison between the branch pressure drop calculated by this correlation and the experimental measurements is presented in Fig. 7 where 75 percent of the data lies within ±50 percent of the predictions. Although this may not be very good, it is far superior to available correlations. Equation (12) is an updated correlation from that presented earlier by Ballyk et al. (1986).

5 Concluding Remarks

Detailed experimental data on dividing steam-water annular flow in T-junctions having horizontal inlet and downwardly inclined branches were obtained. The branch orientation was

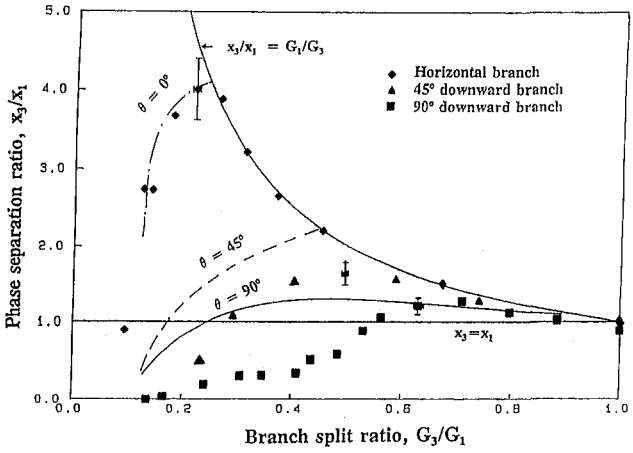


Fig. 6 Comparison of Ballyk and Shoukri (1990) model with present data (G_1 = 600 kg/m^2·s, x_1 = 4.6 percent)

Downloaded 03 Jun 2010 to 171.66.16.125. Redistribution subject to ASME license or copyright; see http://www.asme.org/terms/Terms_Use.cfm

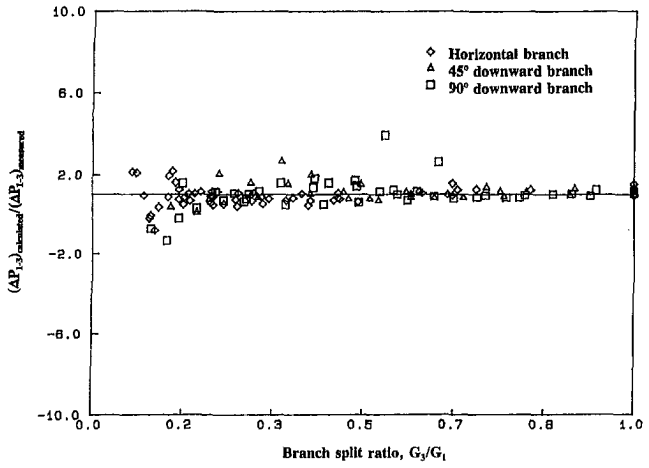


Fig. 7 Comparison of Ballyk and Shoukri (1988) correlation with present experimental data

found to be a significant parameter affecting phase redistribution under a horizontal annular inlet flow condition. The effect of branch orientation on phase redistribution is mainly caused by the non-uniform thickness distribution of the liquid film in the inlet tube; typical of horizontal annular flow. The results showed that, in general, downward rotation of the branch results in less vapor extraction as the liquid film available for extraction is thicker. The inlet mass flux was found to have no effect on the phase separation phenomenon under the present test conditions. However, the inlet quality has a pronounced effect. Changing the inlet quality affects the liquid film thickness distribution and accordingly affects the phase separation phenomenon.

The data on pressure changes through the junction were correlated using simple models based on momentum and mechanical energy balances. The run pressure recovery data was correlated using a momentum balance model. The momentum correction factor was found to depend on branch orientation. The branch pressure drop was correlated using a mechanical energy-based model and a two-phase multiplier which was found to be independent of branch orientation.

JFE Date Bank Contribution

The data presented in this paper have been saved in the JFE Data Bank for the use of other readers. The data included inlet mass flux G_1, qualities x_1, x_2, x_3, void fractions α_1, α_2, α_3, branch flow split ratio G_3/G_1, branch orientation angle θ, phase separation ratio x_3/x_1, pressure changes $\Delta P_{2\text{-}1}$ and $\Delta P_{1\text{-}3}$ and system pressure P.

References

Azzopardi, B. J., and Whalley, P. B., 1982, "The Effect of Flow Patterns on Two-Phase Flow in a T-Junction," *International Journal of Multiphase Flow,* Vol. 8, pp. 491–507.

Azzopardi, B. J., 1986, "Two-Phase Flows in Junctions," *Encyclopedia of Fluid Mechanics,* Vol. 3, Chapter 25, N. Cheremisinoff, ed.

Azzopardi, B. J., and Smith, P. A., 1992, "Two-Phase Flow Split in T Junctions: Effect of Side Arm Orientation and Downstream Geometry," *International Journal of Multiphase Flow,* Vol. 18, pp. 861–875.

Ballyk, J. D., Shoukri, M., and Chan, A. M. C., 1988, "Steam-Water Annular Flow in a Horizontal Dividing T-Junction," *International Journal of Multiphase Flow,* Vol. 14, pp. 265–285.

Ballyk, J. D., 1992, "Dividing Annular Two-Phase Flow in Horizontal T Junctions," Ph.D. thesis, McMaster University.

Ballyk, J. D., and Shoukri, M., 1990, "On the Development of a Model for Predicting Phase Separation Phenomena in Dividing Two-Phase Flow," *Nuclear Engineering and Design,* Vol. 123, pp. 67–75.

Butterworth, D., 1974, "An Analysis of Film Flow and Its Application to Condensation in a Horizontal Tube," *International Journal of Multiphase Flow,* Vol. 1, pp. 671–682.

Collier, J. G., 1976, "Single-Phase and Two-Phase Flow Behaviour in Primary Circuit Components," *Proceedings of NATO Advanced Institute on Two-Phase Flow and Heat Transfer,* Vol. 1, pp. 313–365, Hemisphere, Washington, D.C.

Davis, M. R., and Fungtamasan, B., 1990, "Two-Phase Flow Through Pipe Branch Junctions," *International Journal of Multiphase Flow,* Vol. 16, pp. 799–817.

Fouda, A. E., and Rhodes, E., 1974, "Two-Phase Annular Flow Stream Division in a Simple Tee," *Transactions of the Institute of Chemical Engineers,* Vol. 52, pp. 354–360.

Henry, J. A. R., 1981, "Dividing Annular Flow in a Horizontal Tee," *International Journal of Multiphase Flow,* Vol. 7, pp. 342–355.

Hong, K. C., 1978, "Two-Phase Flow Splitting at a Pipe Tee," *Journal of Petroleum Technology,* pp. 290–296.

Lahey, R. J., Jr., 1986, "Current Understanding of Phase Separations Mechanisms in Branching Conduits," *Nuclear Engineering and Design,* Vol. 95, pp. 145–161.

Madden, J. M., and St. Piere, C. C., 1969, "Two-Phase Flow in a Slot-Type Distributor," *Institute of Mechanical Engineers,* 184, Part 3C.

McCreery, G. E., and Banerjee, S., 1990, "Phase Separation of Dispersed Mist and Dispersed Annular (Rivulet or Thin Film) Flow in a Tee—I, Experiments," *International Journal of Multiphase Flow,* Vol. 16, pp. 429–445.

Müller, U., and Reimann, J., 1991, "Redistribution of Two-Phase Flow in Branching Conduits: A Survey," *Proceedings of the International Conference on Multiphase Flows,* 91-TSUKUBA, Vol. 3, pp. 85–107, Sept. 24–27, 1991, Tsukuba, Japan.

Peng, F., 1994, "A Study of Dividing Two-Phase Flow in Horizontal Inlet T-Junctions: Experiments and Analyses," Ph.D. thesis, McMaster University.

Reimann, J., and Seeger, W., 1986, "Two-Phase Flow in a T-Junction with a Horizontal Inlet Part II: Pressure Differences," *International Journal of Multiphase Flow,* Vol. 12, pp. 587–608.

Reimann, J., Binkmann, H. J., and Domanski, R., 1988, "Gas-Liquid Flow in Dividing Tee-Junction with Horizontal Inlet and Different Orientations and Diameters," Karlsruhe, Report K f K 4399.

Rubel, M. T., Soliman, H. M., and Sims, G. E., 1988, "Phase Distribution During Steam-Water Flow in a Horizontal T-Junction," *International Journal of Multiphase Flow,* Vol. 14, pp. 425–438.

Saba, N., and Lahey, R. T. Jr., 1984, "The Analysis of Phase Separation Phenomena in Branching Conduits," *International Journal of Multiphase Flow,* Vol. 10, pp. 1–20.

Seeger, W., Reimann, J., and Müller, U., 1986, "Two-Phase Flow in a T-Junction with a Horizontal Inlet Part I: Phase Separation," *International Journal of Multiphase Flow,* Vol. 12, pp. 575–585.

Downloaded 03 Jun 2010 to 171.66.16.125. Redistribution subject to ASME license or copyright; see http://www.asme.org/terms/Terms_Use.cfm

Yongliang Chen
Graduate Research Assistant.

S. D. Heister
Associate Professor.

School of Aeronautics and Astronautics,
Purdue University,
1282 Grissom Hall, West Lafayette,
IN 47907

Modeling Hydrodynamic Nonequilibrium in Cavitating Flows

A nonlinear numerical model has been developed to assess nonequilibrium effects in cavitating flows. The numerical implementation involves a two-phase treatment with the use of a pseudo-density which varies between the liquid and gas/vapor extremes. A new constitutive equation for the pseudo-density is derived based on the bubble response described by a modified form of the Rayleigh-Plesset equation. Use of this constitutive equation in a numerical procedure permits the assessment of nonequilibrium effects. This scheme provides a quantitative description of scaling effects in cavitated flows. With minimal modifications, the model can also be used for bubbly two-phase flows.

1 Introduction/Background

Two-phase flows involving gas or vapor bubbles suspended in a liquid medium commonly occur in underwater vehicles, high speed pumps, aeration devices, and many other applications. Using numerical techniques to predict flowfields of this type is much more challenging than a single-phase flow calculation. Hydrodynamic and thermodynamic nonequilibrium, slip between bubbles and liquid, bubble breakup and coalescence, and turbulence effects can all play critical roles in defining flowfields of this nature. Clearly this most general situation is far beyond the current modeling capabilities. However, for some problems, such as cavitation or bubbly flows in "cold" liquids, the hydrodynamic nonequilibrium effects can play a pivotal role in defining flowfield characteristics.

Traditionally, researchers have attempted to quantify the extent of the hydrodynamic nonequilibrium by assuming a passive pressure field and applying the Rayleigh-Plesset equation (Lamb, 1932) to analyze the volume change of a bubble. While one can argue that this approach may produce adequate results when bubbles are very small (near inception), there are considerable errors introduced by neglecting the displaced liquid when the bubbles are of finite size. In fact, recent evidence indicates that bubble/liquid interactions may be important even during the inception process (D'Agostino et al., 1988).

The bulk of the research performed to date on flows of this nature deals with attached cavitating flows. These flows are characterized by a vapor forebody attached to the surface of some object. At the rear part of the attached cavitation, there is an unsteady, two-phase and turbulent wake region where the cavitation bubble begins to collapse under the influence of increasing external pressure. The wake region may also be characterized by the presence of an unsteady re-entrant jet (Furness and Hutton, 1975; Delannoy and Kueny, 1990) as a result of the pressure recovery in this region. Periodic bubble shedding may also be present in internal flows (Chen and Heister, 1994a). The extent of the wake depends on the rate of increase of the external pressure (as determined by the body shape) as well as Reynolds number and local turbulence levels. Physically, there is no well-defined interface in this region.

Experimental evidence indicates that there may be considerable pressure difference between vapor and liquid at the leading edge and trailing edge of cavitation region (Rood, 1991; Kato, 1985). At leading edge, viscous effects (Arakeri, 1975) or surface tension may explain this phenomena; At the trailing edge, thermodynamic effects can be important. However, in both regions, the hydrodynamic nonequilibrium, may play an important role in causing the deviation of the liquid pressure from the vapor pressure.

One popular numerical treatment presumes that the cavitation region is described as a large bubble with a distinct interface followed by a two-phase collapse region. Typically, the interface is described by assuming the cavitating region is at a constant pressure equal to the local vapor pressure. Predictions using potential flow models (Furness and Hutton, 1975; Lemonnier and Rowe, 1988; Ingber and Hailey, 1991; Kinnas and Fine, 1993) and more recently Navier-Stokes and Euler solutions (Chen and Heister, 1994b; Deshpande et al., 1992 and 1993) have been successful in describing this flow under these assumptions. These "interface tracking schemes" must employ a wake model to approximate the behavior at the aft end of the region where local pressure recovery invalidates the constant pressure assumption. Unfortunately, it is difficult to introduce physics into the wake model since the single phase flow solution cannot address two-phase effects. This fact, along with the constant pressure assumption applied at the cavity initiation point, makes these schemes unsuitable for investigation of non-equilibrium and unsteady effects.

The other distinct class of numerical methods applied to cavitation problems makes no attempt to track an interface, but instead treats the flow as two-phase with a pseudo-density which varies between liquid and vapor extremes. These two-phase approaches have the advantage that no special wake treatment is required, but have the disadvantage in that the interface of gas and liquid is not determined and must be inferred from density values in neighboring cells. These methods are attractive in that they can treat both traveling and attached cavitation. Also, the elimination of the wake model permits these methods to address unsteady and non-equilibrium effects. These schemes can also be applied to turbulent flows, in which the attached cavitation film may not be represented by a discontinuity, but is more likely a cluster of tiny vapor bubbles (Kato, 1985).

The greatest challenge in the implementation of the two-phase methods is in deriving a suitable constitutive relationship for the pseudo-density. To trace the evolution of every bubble is definitely out of reach at current stage since a single bubble may need a fully 3-D calculation (Chahine, 1989). A wide array of analytic solutions have been constructed for linearized forms of the governing equations under the assumption of a disperse bubble field (van Wijngaarden, 1968; Chahine and Lie,

Contributed by the Fluids Engineering Division for publication in the JOURNAL OF FLUIDS ENGINEERING. Manuscript received by the Fluids Engineering Division January 16, 1995; revised manuscript received November 6, 1995. Associate Technical Editor: R. Arndt.

Copyright © 1996 by ASME

Downloaded 03 Jun 2010 to 171.66.16.125. Redistribution subject to ASME license or copyright; see http://www.asme.org/terms/Terms_Use.cfm

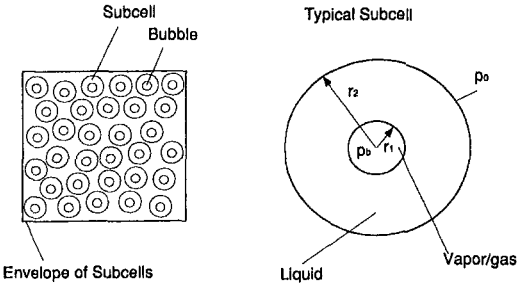


Fig. 1 A computational cell is presumed to contain a large number of spherical subcells for determination of pseudo-density in cavitated regions

1985; D'Agostino and Brennen, 1989). However, if one desires a full nonlinear simulation in which bubbles may be closely spaced, a different approach must be employed.

Delannoy and Kueny proposed a nonlinear treatment in which the pseudo-density is simply a function of the pressure. While this approach gives some encouraging results, it seems to be oversimplified since the density here must be related not simply to the local pressure, but to the time-dependent bubble evolution caused by the changing pressure field. In a significant effort by Kubota et al. (1992), the Rayleigh-Plesset equation is used to introduce bubble dynamics into the problem. However, the assumption of constant bubble number density employed by these researchers is not desirable in regions of higher void fraction since clearly the number density should decrease if bubbles are large. The simple treatment in Chen and Heister (1994a) gives a practical numerical tool to analyze cavitating flows. However, it is essentially based on hydrodynamic equilibrium. In this work, we extend the models of Kubota et al. for the case of variable bubble number density.

Section 2 describes the derivation of a new constitutive relation for the pseudo-density which allows for interactions between liquid and bubbles during nonequilibrium processes for arbitrary bubble spacing. Implementation of this model in a numerical flow solver is also discussed in Section 2. In Section 3, we discuss application to several cavitating flows. Conclusions from the study are presented in Section 4.

2 Model Development

Consider the laminar flow of a viscous two-phase mixture in which body forces are negligible. We choose the liquid density, a characteristic length (or diameter) of a body in the flow, and a characteristic velocity as dimensions. We presume that the gas or vapor density is negligible compared to that of the liquid so that the dimensionless pseudo-density, ρ, varies over the range $0 \leq \rho \leq 1$ between gas/vapor and liquid extremes. Following the treatment due to Kubota et al. (1992), we write the viscosity of the mixture:

$$\mu = \alpha\mu_g + (1 - \alpha)\mu_l \tag{1}$$

where μ_g and μ_l are vapor and liquid viscosities, respectively, and α is the local void fraction. Since $\mu_g \ll \mu_l$, and $1 - \alpha$ is simply the dimensionless density, we have $\mu \approx \rho\mu_l$. We still employ the incompressible form of viscous terms instead of compressible form. The rationale here is that the viscosity of gas-liquid mixture is still to be investigated and actually the eddy viscosity, which is even unclear in one phase flow, may exceed the molecular viscosity. Since the focus of this work is on hydrodynamic nonequilibrium, a simple form of the viscous terms was deemed to be acceptable.

Under this assumption, the dimensionless axisymmetric, laminar Navier Stokes equations are:

$$\frac{\partial(r\rho)}{\partial t} + \frac{\partial(r\rho v)}{\partial r} + \frac{\partial(r\rho u)}{\partial z} = 0 \tag{2}$$

$$\frac{\partial(r\rho v)}{\partial t} + \frac{\partial(r\rho v^2)}{\partial r} + \frac{\partial(r\rho vu)}{\partial z} = -r\frac{\partial p}{\partial r} + \frac{1}{\mathrm{Re}}\left(r\frac{\partial}{\partial r}\left[\frac{\rho}{r}\frac{\partial}{\partial r}(rv)\right] + \frac{\partial}{\partial z}\left[\rho\frac{\partial(rv)}{\partial z}\right]\right) \tag{3}$$

$$\frac{\partial(r\rho u)}{\partial t} + \frac{\partial}{\partial r}(r\rho vu) + \frac{\partial(r\rho u^2)}{\partial z} = -r\frac{\partial p}{\partial z} + \frac{1}{\mathrm{Re}}\left(\frac{\partial}{\partial r}\left(r\rho\frac{\partial u}{\partial r}\right) + \frac{\partial}{\partial z}\left[\rho\frac{\partial(ru)}{\partial z}\right]\right) \tag{4}$$

We also require the Lagrangian form of the continuity equation (Eq. (2)):

$$r\frac{D\rho}{Dt} + \rho\left(\frac{\partial(rv)}{\partial r} + \frac{\partial(ru)}{\partial z}\right) = 0 \tag{5}$$

Here we note that the technique to be described below is not limited to axisymmetric problems, we have simply chosen this coordinate system for our implementation. To close the equation system, an additional relation is needed since we have introduced a new variable, the pseudo-density, ρ. In the following subsection, we discuss a new constitutive relation for this parameter which reflects nonequilibrium hydrodynamic interactions between the liquid and gas/vapor components of the mixture.

2.1 Constitutive Relation for Pseudo-Density. Consider the motion of a locally homogeneous cloud of spherical bubbles. We assume that surface tension and mass transfer between phases are negligible, and that no bubble breakup or coalescence occurs. Furthermore, we neglect any relative motion (slip) between the bubbles and liquid. Under these assumptions, the schematic representation of the flowfield is shown in Fig. 1. We envision a finite-volume numerical implementation which requires a relationship between the pseudo-density and average pressure within an "envelope of subcells." To this end, we assume that there are a sufficient number of subcells (each of which contains a single bubble) to provide an accurate spatial average of the pressure as it is affected by neighboring subcells. Under this assumption, the average pressure in the liquid within a given subcell will be equivalent to the average pressure in the envelope shown in Fig. 1. Further, we assume that each subcell is spherical (Fig. 1). This simplification permits the prediction of the equivalent bubble response to the liquid pressure variations with a one-dimensional analysis.

Nomenclature

f = frequency of oscillation
n = bubble number density in the non-cavitating fluid
K = cavitation number
P = pressure
r = radial coordinate
S = distance from the body's leading edge
T = dominant period of cavitation oscillation
u = axial velocity
v = radial velocity
z = axial coordinate
Re = Reynolds number
α = void fraction
δ = height of cavitation bubble
μ = viscosity

Downloaded 03 Jun 2010 to 171.66.16.125. Redistribution subject to ASME license or copyright; see http://www.asme.org/terms/Terms_Use.cfm

This approach is consistent with following a given mass of liquid and bubbles in a Lagrangian sense through a flowfield. As the bubbles expand or contract in response to local pressure variations, the size of the envelope used to define the pseudo-density also changes. Therefore, in our formulation, the bubble number per unit mass of fluid will be constant.

In previous work, van Wijngaarden, (1968), employed a similar assumption for a linearized analysis valid for small void fraction. Under these conditions, there is little difference between the per unit mass and per unit volume treatments. Since the current approach will be used for large void fraction, the difference is significant. Using the mass basis, the bubble number density continually changes as void fraction changes in the flow. This treatment differs significantly from that of Kubota et al. (1992) in which the bubble number density must be input as an assumed constant. In the case of small void fraction, the two assumptions converge to the same result which is analogous to the treatment of van Wijngaarden, (1968).

When a spherical cavitation bubble is in an infinite domain of liquid, its movement is governed by the Rayleigh-Plesset equation. It is commonplace to use this relation to describe bubble dynamics when the void fraction is low. However, in many gas/liquid flows, the void fraction can approach unity (pure vapor region). If the distance between bubbles is comparable to the bubble radius, the pressure at the outer boundary of the liquid surrounding the bubble cannot be considered as farfield pressure. While the flowfield at the edge of a subcell is three-dimensional, we presume that an average pressure p_o characterizes the outer boundary (at $r = r_2$). We can relate this pressure to the average pressure in the subcell ($\bar{p}$) by solving a finite-domain form of the Rayleigh-Plesset equation as described in the following paragraphs.

Neglecting viscous terms, the nondimensional governing equations for a spherical subcell may be written:

$$\frac{\partial v}{\partial r} + \frac{2v}{r} = 0 \tag{6}$$

$$\frac{\partial v}{\partial t} + v\frac{\partial v}{\partial r} = -\frac{\partial p}{\partial r} \tag{7}$$

Integrating Eq. (6), we can solve for the radial velocity:

$$v = \frac{1}{r^2}C(t) \tag{8}$$

We can solve for the time-dependent constant $C(t)$ by substituting this result into Eq. (7) and integrating over the liquid domain $r_1 \le r \le r_2$ to obtain:

$$\frac{\partial v}{\partial t} = \frac{(r_1^{-4} - r_2^{-4})r^4v^2/2 + p_b - p_0}{r^2(1/r_1 - 1/r_2)} \tag{9}$$

Since $Dr_1/Dt = v_1$ (i.e. the notation D/Dt denotes differentiation in a Lagrangian reference), we have:

$$\frac{D^2r_1}{Dt^2} = \frac{Dv_1}{Dt} = \frac{\partial v_1}{\partial t} + v_1\cdot\nabla v_1 = \frac{(r_1^{-4} - r_2^{-4})r^4v^2/2 + p_b - p_0}{r^2(1/r_1 - 1/r_2)} - \frac{2v_1^2}{r_1} \tag{10}$$

This result is simply a Rayleigh-Plesset equation for a finite domain. As $r_2 \to \infty$, we recover the original result due to Rayleigh.

Using Eq. (9), we can integrate the momentum equation (Eq. (7)) to determine the pressure behavior in the liquid domain:

$$p - p_b = \frac{1}{2}r_1^4v_1^2\left(r_1^{-4} - r^{-4} - (r_1^{-4} - r_2^{-4})\frac{1/r_1 - 1/r}{1/r_1 - 1/r_2}\right) - \frac{p_b - p_0}{1/r_1 - 1/r_2}(1/r_1 - 1/r) \tag{11}$$

which is valid over the range $r_1 \le r \le r_2$. Inside the bubble ($r < r_1$), we assume a constant pressure $p = p_b$. Using this assumption and Eq. (11), we can determine the average pressure within a subcell, $\bar{p}$, from:

$$\bar{p} = \frac{\int_0^{r_2} p\cdot 4\pi r^2 dr}{4/3\pi r_2^3} = \frac{\int_0^{r_1} p_b\cdot 4\pi r^2 dr + \int_{r_1}^{r_2} p\cdot 4\pi r^2 dr}{4/3\pi r_2^3} = p_b + \frac{3}{4\pi r_2^3} \times \int_{r_1}^{r_2}\left(\frac{1}{2}r_1^4v_1^2\left(r_1^{-4} - r^{-4} - (r_1^{-4} - r_2^{-4})\frac{1/r_1 - 1/r}{1/r_1 - 1/r_2}\right) - (p_b - p_0)\frac{1/r_1 - 1/r}{1/r_1 - 1/r_2}\cdot 4\pi r^2\right)dr \tag{12}$$

Note that we employ a volume-weighted average which is consistent with our finite-volume numerical implementation. In the following, it is useful to define a modified void fraction, α':

$$\alpha' = \frac{r_1}{r_2} = \sqrt[3]{1 - \rho} = \sqrt[3]{\alpha} \tag{13}$$

Using this definition, Eq. (12) can be written:

$$p_0 - p_b = \frac{\bar{p} - p_b - v_1^2\alpha'(1 + 4\alpha' + \alpha'^2)(1 - \alpha')^3/4}{(2 + \alpha')(1 - \alpha')/2} \tag{14}$$

Equation 14 relates the pressure at the outer boundary of subcells to the average pressure within the cell. Note that as void fraction approaches unity, we recover the result $\bar{p} = p_b$. This feature is important because the size of the envelope of subcells may be comparable to the size of the computational cell in this limit and errors in the spatial averaging are expected to be large. We get the correct answer in this limit because the subcell is nearly filled with constant pressure vapor/gas so that errors from integration in the liquid region are negligible. In the low void fraction limit, Eq. (14) is also correct since the assumption of bubble sphericity is valid. Since the equation is correct in both of these limits, we presume that the largest errors attributable to the sphericity assumption will occur at moderate void fractions.

2.2 Density Equation. At this point, we are able to relate the pseudo-density to the average pressure and void fraction from mass balance considerations. Since the assumption of a locally homogeneous bubble field implies that the number of bubbles per unit mass is fixed, we require a constant liquid volume within a subcell:

$$r_2^3 - r_1^3 = C \tag{15}$$

so that the pseudo-density may be written:

$$\rho = \frac{C}{C + r_1^3} \tag{16}$$

Differentiating this result noting that r_1 varies with time, we get:

$$\frac{D\rho}{Dt} = -\frac{C}{(C + r_1^3)^2}\cdot 3r_1^2\frac{Dr_1}{Dt} \tag{17}$$

A second Lagrangian differentiation gives:

$$\frac{D^2\rho}{Dt^2} = -\frac{3Cr_1^2}{(C + r_1^3)^2}\frac{D^2r_1}{Dt^2} - 3C\cdot\frac{2Cr_1 - 4r_1^4}{(C + r_1^3)^3}\left(\frac{Dr_1}{Dt}\right)^2 = 3\alpha'^3(\alpha'^3 - 1)\frac{1}{r_1}\frac{D^2r_1}{Dt^2} - \frac{2 - 6\alpha'^3}{3(1 - \alpha'^3)\alpha'^3}\left(\frac{D\rho}{Dt}\right)^2 \tag{18}$$

Downloaded 03 Jun 2010 to 171.66.16.125. Redistribution subject to ASME license or copyright; see http://www.asme.org/terms/Terms_Use.cfm

Substituting (10) into (18) introducing α',

$$\frac{D^2\rho}{Dt^2} = \frac{3\alpha'^3(1+\alpha'+\alpha'^2)}{r_1^2}\left(\frac{1}{2}(\alpha'^4-1)v_1^2 + p_0 - p_b\right)$$

$$+ \frac{6\alpha'^3(1-\alpha'^3)}{r_1^2}v_1^2 - \frac{2-6\alpha'^3}{3(1-\alpha'^3)\alpha'^3}\left(\frac{D\rho}{Dt}\right)^2 \quad (19)$$

Since

$$v_1 = \frac{Dr_1}{Dt} = -\frac{(C+r_1^3)^2}{3Cr_1^2}\frac{D\rho}{Dt} = -\frac{r_1}{3(1-\alpha'^3)\alpha'^3}\frac{D\rho}{Dt} \quad (20)$$

we may write the result in Eq. (19) as:

$$\frac{D^2\rho}{Dt^2} = \frac{3\alpha'^3}{r_1^2}(1+\alpha'+\alpha'^2)(p_0-p_b)$$

$$+\left(\frac{2}{1-\alpha'^3} - \frac{(\alpha'^2+1)(\alpha'+1)}{6\alpha'^3(1-\alpha'^3)}\right)\left(\frac{D\rho}{Dt}\right)^2 \quad (21)$$

which gives changes in density in terms of void fraction and the pressure at the edge of the subcell. Since the numerical procedure will return an average cell pressure, we substitute for p_0 to give the constitutive equation for density:

$$\frac{D^2\rho}{Dt^2} = \frac{6\alpha'^3(1+\alpha'+\alpha'^2)}{r_1^2(2+\alpha')(1-\alpha')}(\bar{p}-p_b)$$

$$+\left(\frac{2}{1-\alpha'^3} - \frac{(\alpha'^2+1)(\alpha'+1)}{6\alpha'^3(1-\alpha'^3)}\right.$$

$$\left.-\frac{1+4\alpha'+\alpha'^2}{6\alpha'^2(2+\alpha')(1+\alpha'+\alpha'^2)}\right)\left(\frac{D\rho}{Dt}\right)^2 \quad (22)$$

This equation has the same fundamental features as the Rayleigh-Plesset equation in that the bubble response (in pseudo-density) is reflected by changes in pressure and inertial effects. The expression is a general result applicable to both bubbly and cavitated flows with a suitable choice for p_b.

In this equation, r_1 is the local characteristic radius of cavitation bubbles. This quantity can be evaluated in terms of initial conditions in the bubble/cavitation field if we invoke the homogeneity assumption. Since this assumption is tantamount to maintaining constant liquid volume in a subcell, we may write:

$$r_{20}^3 - r_0^3 = r_2^3 - r_1^3 \quad (23)$$

where r_{20} and r_0 are the initial subcell and bubble radii, respectively. Writing this requirement in terms of void fraction, we get:

$$r_1 = r_0\sqrt[3]{\frac{\alpha_0^{-1}-1}{\alpha^{-1}-1}} \quad (24)$$

If we let

$$L_0 = r_0\left(\frac{1}{\alpha_0}-1\right)^{1/3} \quad (25)$$

then:

$$r_1^2 = L_0^2\left(\frac{\alpha}{1-\alpha}\right)^{2/3} \quad (26)$$

Substituting (26) into (22), we have the final form of the density equation:

$$\frac{D^2\rho}{Dt^2} = \frac{6\alpha'(1+\alpha+\alpha'^2)^2}{L_0^2(2+\alpha')(1-\alpha'^3)^{1/3}}(\bar{p}-p_b)$$

$$+\left(\frac{2}{1-\alpha'^3} - \frac{(\alpha'^2+1)(\alpha'+1)}{6\alpha'^3(1-\alpha'^3)}\right.$$

$$\left.-\frac{1+4\alpha'+\alpha'^2}{6\alpha'^2(2+\alpha')(1+\alpha'+\alpha'^2)}\right)\left(\frac{D\rho}{Dt}\right)^2 \quad (27)$$

This is the density equation employed in the two-phase model.

Here it should be noted that the scale effects in bubbly or cavitating flows are reflected by L_0. In Eq. (25), r_0 is nondimensional. For a given fluid under certain conditions, $\bar{r}_0$, the dimensional value of r_0 will be constant regardless of the length scale of flowfields. If the characteristic length is L^*, then $L_0 = \bar{r}_0(1/\alpha_0 - 1)^{1/3}/L^*$. So, for a larger L^*, we have a smaller L_0, and integration of Eq. (27) reveals an increase of importance of the pressure term. This implies that large bodies can exhibit large density fluctuations (i.e., cavitation) with only moderate pressure changes, while smaller bodies can tolerate larger pressure variations (i.e., nonequilibrium effects) before the onset of cavitation. These characteristics have been noted by numerous researchers in connection with cavitating flows.

For bubbly flows, we presume that an average bubble size and void fraction are specified at some flow entry condition. This information permits the calculation of L_0 in this case. In case of cavitating flows, the fluid at the inlet is practically liquid, so α_0 is almost zero. If the bubble density at the inlet is n, then $\alpha_0 = n \cdot 4/3\pi r_0^3$. Therefore:

$$L_0 = r_0(1/(n\cdot 4/3\pi r_0^3))^{1/3} = (3/(4\pi n))^{1/3} \quad (28)$$

L_0 is only a function of the inflow bubble density n which is the number of nucleation sites per unit volume. In Eq. (28), the bubble density n has been nondimensionalized. If we let $\bar{n}$ represent the dimensional value, then $n = \bar{n}(L^*)^3$ and the effect of scale becomes apparent. From this result, Eq. (28) shows that larger bodies will have smaller L_0 values than a small-scale body.

It should be noted that even though there are excellent works on cavitation nuclei population (Liu et al., 1993), we have difficulty in using this information in the context of this model. In deriving Eq. (27) we have assumed that all bubbles, no matter how small, will serve as nucleation sites. At the same time, it is practically impossible to measure bubbles whose sizes are below a certain value (say 5 μm). Actually, the surface tension which is currently neglected in current approach will be important for extremely small bubbles. We leave this problem for future development.

2.3 Solution Procedure. The Navier Stokes equations are solved using the Marker and Cell method (Peyret and Taylor, 1986). The discretized equations for the continuity and momentum are similar to those in Chen and Heister (1994). Density nodes are placed at the same location as pressure nodes. An upwind scheme is used for the density when calculating the flux through the control face at which there is no density point. We notice that in Eq. (5), $D\rho/Dt$ is needed, while in Eq. (27) we have an expression for $D^2\rho/Dt^2$. We rewrite the substantial derivative in Eq. (27) in Euler form, and use the $D\rho/Dt$ at previous time step to calculate the current values. The rather

Downloaded 03 Jun 2010 to 171.66.16.125. Redistribution subject to ASME license or copyright; see http://www.asme.org/terms/Terms_Use.cfm

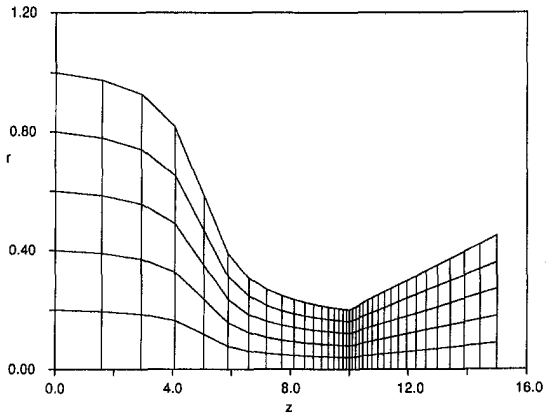


Fig. 2 Mesh and geometry of pseudo-one-dimensional nozzle

long and tedious differencing equations will not be shown here in the interest of brevity.

The overall solution procedure is:

1. Calculate the new density from continuity (Eq. (2))
2. Express u, v as functions of p by using momentum Eqs. (3) and (4) and the new density
3. Combine the expressions for u, v, the additional Eq. (27) and the Lagrangian form continuity Eq. (5) to get the equation for pressure
4. Solve for new pressures by using the Successive Line Over-Relaxation method (SLOR)
5. Update u, v from Eqs. (3) and (4)
6. Return to step 1 for next time step

2.4 Model Validation. Grid function convergence studies were conducted for a 1-D homogeneous bubbly flow. We choose this flow (rather than a cavitated flow) for validation because steady solutions can be obtained and computational costs are more modest. The current code is axisymmetric, so we choose a nozzle with small wall slope for the quasi-one-dimensional simulation. The geometry of the nozzle and a typical mesh are shown in Fig. 2. For all the calculations, three inflow conditions are specified: total pressure, flow angle (horizontal), and void fraction. At the outlet, the back pressure is specified. Pressures of two phases are assumed to be the same at the inlet. The p_b may be expressed by the polytropic relation of index q: $p_b = p_1(v_1/v_b)^q$. If we assume isothermal flow, $q = 1$. From Eq. (24), we can show that the bubble pressure is a function of inlet conditions and the local density:

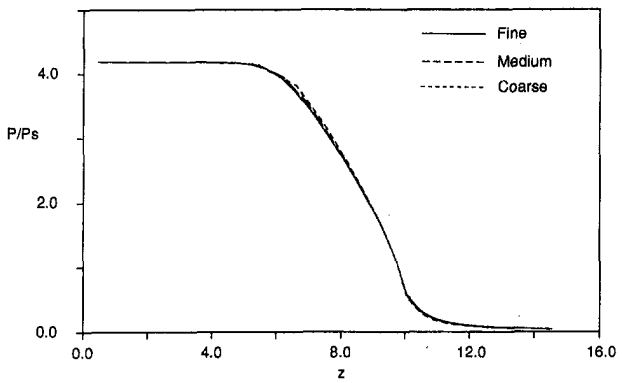


Fig. 3 Grid function convergence study for bubbly flow. Pressure distribution as a function of axial location in the pseudo-one-dimensional nozzle for three separate grids.

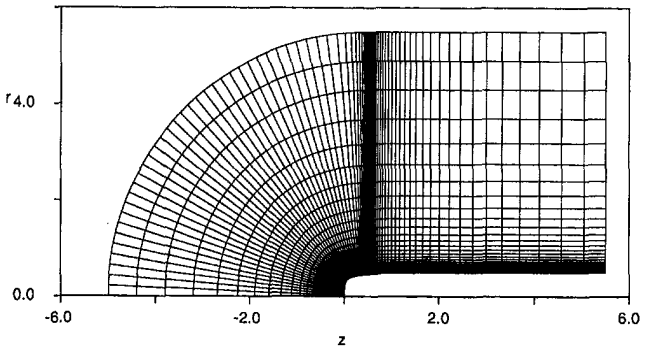


Fig. 4 Typical computational mesh for a Schiebe body headform

$$p_b = \frac{p_1 v_1}{v_b} = p_1 \frac{\rho(1-\rho_1)}{\rho_1(1-\rho)} \tag{29}$$

This expression is used to calculate p_b in Eq. (27).

The grid function convergence test is conducted for an inflow void fraction $\alpha_0 = 0.05$ and L_0^2 of 0.1. We use only five points in the radial direction in order to simulate a one-dimensional flow. Calculations are carried out on three meshes: 54×5, 36×5 and 24×5. Back pressure is set to be zero for non-choking calculations. The results are shown in Fig. 3. The solutions on fine and medium mesh are almost on top of each other indicating that the solution is mesh-independent.

3 Results

Since the bulk of experimental data for axisymmetric objects exists for external flows over various headforms, we choose this flow as a basis for computations. The computational domain and a typical mesh (75×40) are shown in Fig. 4. We enforce a no-slip boundary condition at solid surfaces and a symmetry condition at the centerline. We assume that the flow is undisturbed and steady in applying the farfield boundary conditions. In these flows, the cavitation number, K, is defined:

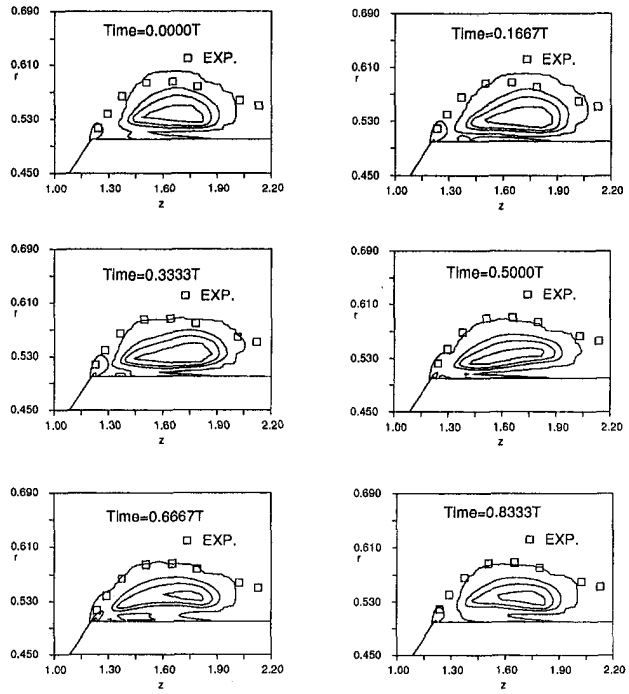


Fig. 5 Density contour evolution during one oscillation: conic headform

Downloaded 03 Jun 2010 to 171.66.16.125. Redistribution subject to ASME license or copyright; see http://www.asme.org/terms/Terms_Use.cfm

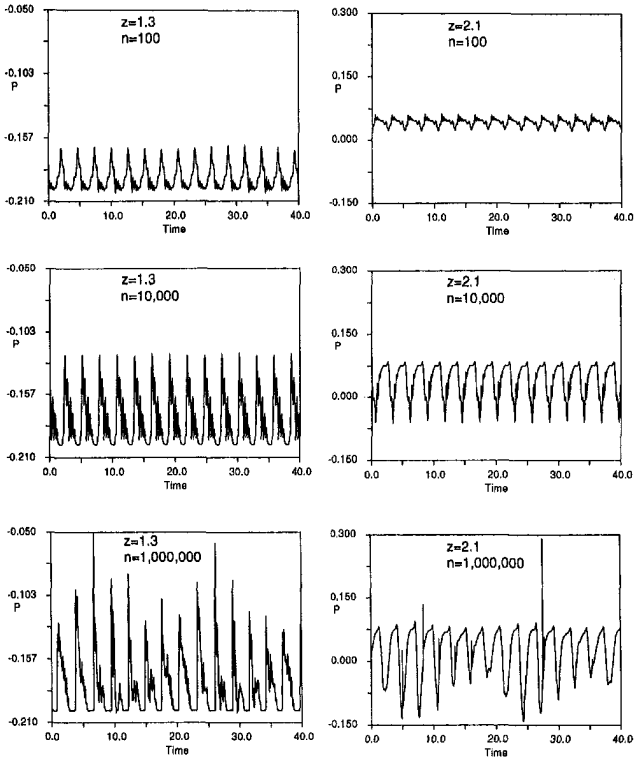


Fig. 6 Pressure oscillations at various axial locations and for various bubble number densities for a conic headform

$$K = (P_\infty - P_v)/(P_0 - P_\infty) \tag{30}$$

where P_0 is the total pressure, P_v is the vapor pressure, and P_∞ is the freestream pressure. Calculations have been performed for cavitating flows around the 45 deg conic headform with $K = 0.4$ which was tested by Rouse and Mcnown (1948). Since experimental data are incomplete, we pick Re $= 1.36 \times 10^5$ (following Ingber and Hailey, 1991).

The computational mesh is 75×40 and L_0^2 is chosen to be 0.0008291, which corresponds to 10^4 nucleation sites (n) per cubic inch. It is interesting to note that the unsteadiness in cavitating flows observed in experiments (Hammitt, 1980) is observed in current calculations. The density contour evolution over one oscillation is shown in Fig. 5. In all the density contour plots, the outermost density contour is $\rho = 0.99$, and contour increments of 0.3 are utilized. While the cavitation region remains nearly fixed, there are slight oscillations about its shape and position. Since the inflow boundary conditions are steady, the inherent unsteadiness of cavitating flows is caused by the nonlinear interaction between the bubbles and the liquid. Numerical experiments have verified that this oscillation is independent of grid.

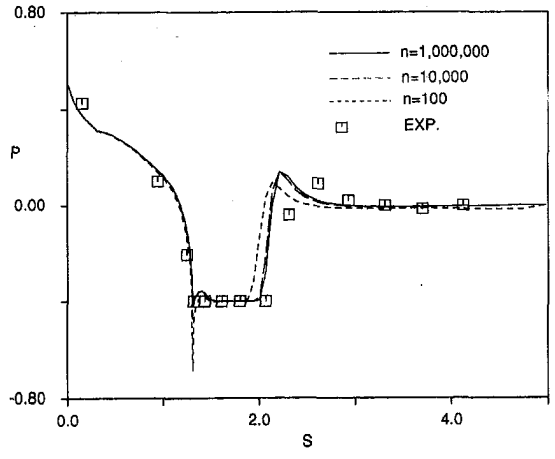


Fig. 7 Time averaged surface pressure comparisons for various bubble number densities for a conic headform

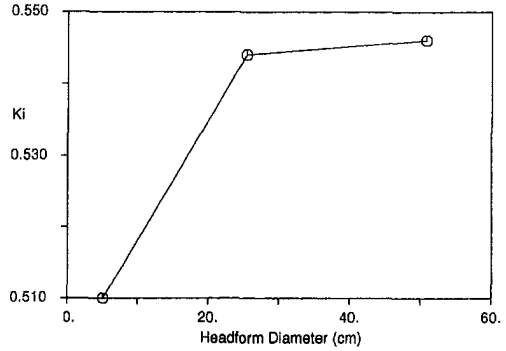


Fig. 8 Predicted cavitation inception number (K_i) as a function of body size for Schiebe bodies

To evaluate the hydrodynamic nonequilibrium, we also conducted calculations with $L_0^2 = 0.01786$ and 0.00003848, which correspond to n values of 10^2 and 10^6 nucleation sites per cubic inch. The pressure oscillations at $z = 1.3$ (just after the inception point) and $z = 2.1$ (in the wake) are shown in Fig. 6. For the low number density ($n = 100$) case corresponding to a smaller body, we see a very regular and moderate oscillation. Nonequilibrium effects in this case are very important and tend to damp out larger pressure fluctuations. In contrast, the high number density case ($n = 10^6$) corresponding to a larger body demonstrates a more violent and irregular oscillation due to the close proximity of the bubbles.

The dominant frequencies are almost the same in all three cases, and approximately equal to 0.35 (nondimensional value). If we define St (Strouhal number) $= f\,\delta/U$ as Ceccio and Brennen (1992), we obtain St ≈ 0.028. In experiments conducted by Ceccio and Brennen (1992) on Schiebe and I. T. T. C. bodies, St numbers are reported to be in the range St $= 0.002$ to 0.02. This comparison is quite good considering the fact that our numerical model assumes a uniform size bubble field.

The average wall pressure distribution comparison for the three L_0 values given above is plotted in Fig. 7. When L_0 is small, variations in this quantity have only a minor influence on the average pressure distribution. In this case we have a pressure dominated density response (see Eq. (27)). Therefore, as the body grows in size, nonequilibrium effects will have a vanishing influence on the average pressure along it's surface. In this case, we should see only minor differences between the fluid and vapor pressures in the cavitated region. If L_0 is large, (corresponding to a small body) inertial effects will dominate the bubble response (see Eq. (27)), and nonequilibrium effects will be important. The cavitation region will be significantly smaller and the minimum pressure may be significantly smaller than the vapor pressure in

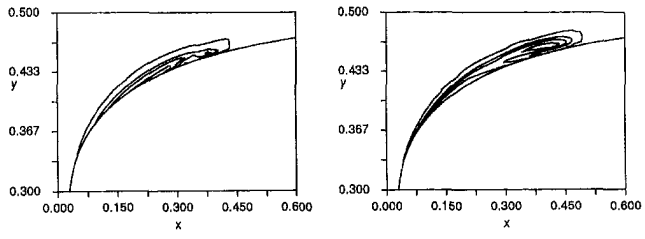


Fig. 9 Density contour comparison between small and large Schiebe bodies for $K = 0.51$, $n = 10^8/m^3$

Downloaded 03 Jun 2010 to 171.66.16.125. Redistribution subject to ASME license or copyright; see http://www.asme.org/terms/Terms_Use.cfm

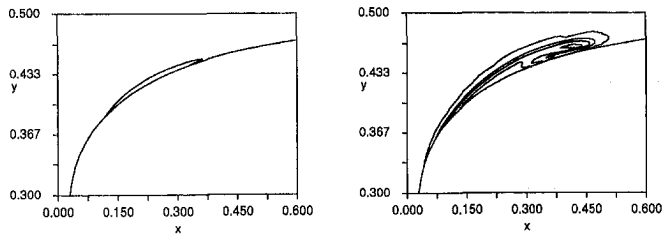


Fig. 10 Density contour comparison between small and large Schiebe bodies for $K = 0.51$, $n = 10^6/m^3$

this case. Figure 7 also shows that the minimum pressure decreases dramatically for conditions associated with a small body. These predictions are consistent with the scale effects mentioned by Rood (1991) and Chizelle et al. (1994).

Chizelle et al. (1994) have conducted experiments on three sizes of Schiebe bodies ($C_{pmin} = -0.75$) to observe the scale effects of traveling bubble cavitation. In our current model, we may evaluate the scale effects quantitatively. Unfortunately, it is difficult to give an uniform, exact definition of cavitation inception for both experiments and computations. Also, as mentioned in Section 2.2, more study is needed to utilize the measured nucleation information in the current model. These factors inhibit quantitative comparisons with the experiments. However, we may use the current model to predict scaling behavior.

We have performed computations for the three Schiebe bodies tested by Chizelle et al. (1994). The nucleation density is assumed to be $10^8/m^3$. Thus, for the bodies with diameters of 5.08 cm, 25.4 cm, 50.8 cm, L_0^2 would be 6.9217×10^{-4}, 2.7687×10^{-5}, and 6.9217×10^{-6}, respectively. We define the inception cavitation number K_i as the point at which the total vapor volume in the cavitation has reached a critical threshold value. Presently, we arbitrarily set this threshold at 0.16 percent of the volume of a sphere of diameter equivalent to that of the body. In the experiments, the inception cavitation number is defined as that at which, 50 cavitation events per second are detected. The latter definition is very difficult to apply in the computational model.

The predicted curve K_i versus body diameter is plotted in Fig. 8. Both experiments and computations show that the inception cavitation number will increase when the body becomes larger. We predict an insensitivity of K_i to body diameter as the body grows large. This asymptotic behavior is realistic since sufficient nuclei will be present to make the hydrodynamic nonequilibrium effects unimportant.

The density contours of smallest and the largest bodies at $K = 0.51$ are plotted in Fig. 9. We can see that the cavitation region is larger for the large body than for the small body as observed in experiments. For a very low bubble density ($10^6/m^3$), the difference is much more significant as is shown in Fig. 10. It is interesting to note that the cavitation inception is affected by the tunnel pressure in the experiments. The possible explanation, that it is caused by the changing nuclei concentration under different pressure, given by Chizelle et al. (1994), appears reasonable. In this case, the inclusion of surface tension and the relationship between the nuclei distribution and the pressure may be required to predict the observed phenomena.

4 Conclusions

A two-phase, nonlinear computational model has been developed to address hydrodynamic nonequilibrium effects in either cavitated or bubbly flows. The new constitutive relationship derived for the pseudo-density (Eq. (27)) properly reflects nonequilibrium and scaling effects under the assumption of a uniform size, locally homogeneous bubble field.

Results indicate good comparisons of the overall extent of the cavitated region in flows over various axisymmetric headforms. In this case, the flowfield oscillates due to nonlinear interactions between the bubbles and pressure field. The predicted period of the oscillation is in reasonable agreement with the recent measurements of Ceccio and Brennen (1992). The model predicts an increased importance of non-equilibrium effects with decreasing body size. While the period of the oscillations is not particularly affected, nonequilibrium effects tend to diminish the amplitude of pressure variations along smaller bodies.

The model also is capable of providing a quantitative description of cavitation inception for bodies of various sizes. While it is difficult to incorporate the definition of Chizelle et al. (1994) in the numerical predictions, results clearly indicate an increase in the inception cavitation number with growing body size. Moreover, an asymptotic behavior is present for larger bodies such that above a certain threshold size insignificant changes in the inception cavitation number are predicted. However, for smaller bodies, the nonequilibrium processes can lead to a great sensitivity of inception cavitation number with changes in size.

References

Arakeri, V. H., 1975, "Viscous Effects on the Position of Cavitation Separation from Smooth Bodies," *Journal of Fluid Mechanics,* Vol. 68, pp. 779–799.

Ceccio, S. L., and Brennen, C. E., 1992, "Dynamics of Attached Cavities on Bodies of Revolution," ASME JOURNAL OF FLUIDS ENGINEERING, Vol. 114, pp. 93–99.

Chen, Y., and Heister, S. D., 1994a, "Two-Phase Modeling for Cavitating Flows," *Cavitation and Gas-Liquid Flows in Fluid Machinery and Devices.* FED-Vol. 190, pp. 299–307.

Chen, Y., and Heister, S. D., 1994b, "A Numerical Treatment for Attached Cavitation," to appear in ASME JOURNAL OF FLUIDS ENGINEERING.

Chahine, G. L., 1989, "A Numerical Model of Three-Dimensional Bubble Dynamics in Complex Flow Configurations," Twenty Second Meeting of the American Towing Tank Conference, St. John's, Newfoundland.

Chahine, G. L., and Lie, H. L., 1985, "A Singular-Perturbation Theory of the Growth of a Bubble Cluster in a Superheated Liquid," *Journal of Fluid Mechanics,* Vol. 156, pp. 257–279.

Chizelle, Y. K., Ceccio, S. L., and Brennen, C. E., 1994, "Observations, Scaling and Modelling of Traveling Bubble Cavitation," submitted to *Journal of Fluid Mechanics.*

D'Agostino, L., and Brennen, C. E., 1989, "Linearized Dynamics of Spherical Bubble Clouds," *Journal of Fluid Mechanics,* Vol. 199, pp. 155–176.

D'Agostino, L., Brennen, C. E., and Acosta, A. J., 1988, "Linearized Dynamics of Two-Dimensional Bubbly and Cavitating Flows Over Slender Surfaces," *Journal of Fluid Mechanics,* Vol. 192, pp. 485–509.

Delannoy, Y., and Kueny, J. L., 1990, "Two Phase Flow Approach in Unsteady Cavitation Modeling," *Cavitation and Multiphase Flow Forum,* FED-Vol. 98, pp. 153–158.

Deshpande, M., Feng, J., and Merkle, C. L., 1992, "Nonlinear Euler Analysis of 2-D Cavity Flow," *Cavitation and Multiphase Flow Forum,* FED-Vol. 135, pp. 213–219.

Deshpande, M., Feng, J., and Merkle, C. L., 1993, "Navier-Stokes Analysis of 2-D Cavity Flow," *Cavitation and Multiphase Flow Forum,* FED-Vol. 153, pp. 149–155.

Furness, R. A., and Hutton, S. P., 1975, "Experimental and Theoretical Studies of Two-Dimensional Fixed-Type Cavities," ASME JOURNAL OF FLUIDS ENGINEERING, pp. 515–522, Dec.

Hammitt, F. G., 1980, Cavitation and Multiphase Flow Phenomena, p. 7.

Ingber, M. S., and Hailey, C. E., 1991, "A Numerical Approach for Modeling Cavitating Flows," *Computational Modeling of Free and Moving Boundary Problems: Proceeding of the First International Conference,* held on July 2–4, Southampton, U.K.

Kinnas, S. A., and Fine, N. F., 1993, "A Numerical Nonlinear Analysis of the Flow Around Two- and Three-Dimensional Partially Cavitating Hydrofoils," *Journal of Fluid Mechanics,* Vol. 254, pp. 151–181.

Kubota, A., Kato, H., and Yamaguchi, H., 1992, "A New Modelling of Cavitating Flows: A Numerical Study of Unsteady Cavitation on a Hydrofoil Section," *Journal of Fluid Mechanics,* Vol. 240, pp. 59–96.

Lamb, H., 1932, *Hydrodynamics,* Dover Pub., pp. 112.

Lemonnier, H., and Rowe, A., 1988, "Another Approach in Modelling Cavitating Flows," *Journal of Fluid Mechanics,* Vol. 195, pp. 557–580.

Liu, Z., Sato, K., and Brennen, C. E., 1993, "Cavitation Nuclei Population Dynamics in a Water Tunnel," *Cavitation and Multiphase Flow Forum,* FED-Vol. 153, pp. 119–125.

Peyret, R., and Taylor, T. D., 1986, *Computational Methods for Fluid Flow,* Springer-Verlag.

Rood, E. P., 1991, "Mechanism of Cavitation Inception," ASME JOURNAL OF FLUIDS ENGINEERING, Vol. 113, pp. 163–175.

Rouse, H., and Mcnown, J. S., 1948, "Cavitation and Pressure Distribution. Head Forms at Zero Angle of Yaw," State University of Iowa, Engrg. Bull., No. 32.

Wijngaarden, L. Van, 1968, "On the Equations of Motion for Mixtures of Liquid and Gas Bubbles," *Journal of Fluid Mechanics,* Vol. 33, pp. 465–474.

Downloaded 03 Jun 2010 to 171.66.16.125. Redistribution subject to ASME license or copyright; see http://www.asme.org/terms/Terms_Use.cfm

Compressible Dusty-Gas Boundary-Layer Flow Over a Flat Surface

Ali J. Chamkha
Department of Mechanical and Industrial Engineering, P.O. Box 5969, Kuwait University, Safat, 13060, Kuwait

Equations governing compressible boundary-layer laminar flow of a two-phase particulate suspension are developed based on a continuum representation of both phases. These equations include such effects as particle-phase viscous stresses, variable position-dependent particle slip coefficient, and general power-law viscosity-temperature and thermal conductivity-temperature relations. The dimensionless form of the equations are applied to the problem of flow over a semi-infinite flat surface. An appropriate transformation is employed to allow proper comparison with previously published results for special cases of this problem. The full coupled system of equations is solved numerically via an implicit finite-difference method. Graphical results for the density, and temperature profiles as well as the displacement thicknesses, skin-friction coefficients, and the wall heat transfer coefficient for both the fluid and particle phases are presented and discussed in detail. In addition, a parametric study is performed to illustrate the influence of the particle to fluid viscosity ratio and the viscosity-temperature power exponent on the flow properties.

Introduction

The problem considered in this paper is that of a steady, compressible, laminar, boundary-layer, two-phase (particle-fluid) flow over a semi-infinite flat surface. This type of flow occurs in many industrial applications. These include fluidized beds and environmental pollutant motions (Rudinger, 1980), gas purification, conveying of powdered materials and transport processes (Soo and Tien, 1960 and Soo, 1961). Special cases of this problem have been considered by Singleton (1965) and Wang and Glass (1988). Singleton (1965) uses a series method and obtains asymptotic solutions for the large-slip region (near the leading edge of the flat plate or surface) and the small-slip region far downstream. Wang and Glass (1988) obtains asymptotic solutions using a series expansion method similar to that of Singleton (1965). In addition, they report finite-difference-based numerical results for the whole computational domain. Their asymptotic large-slip solution provided the initial profiles of flow properties for their numerical finite-difference solution. There have been investigations dealing with the incompressible version of the present problem due to its importance as a fundamental problem in fluid-particle mechanics. Some employed the integral method (Soo, 1967) in obtaining their solutions, others used a series expansion method (see, Soo, 1968; and Datta and Mishra, 1982) and others utilized the finite-difference method (Osiptsov, 1980; Prabha and Jain, 1982; and Chamkha and Peddieson, 1989). Most of these investigators reported that when the dusty-gas model (Marble, 1970) is used to represent the two-phase suspension, a singularity exists in which the particle-phase density distribution at the wall becomes infinite somewhere downstream of the plate's leading edge. This singular behavior in the wall density is believed to be related to the particle-phase tangential velocity at the wall which vanishes at the singularity point. This catastrophic growth in the particle-phase wall density was shown to be of physical nature by imposing fluid-phase suction at the plate's surface and gradually reducing it to approach the impermeable plate solution (Chamkha and Peddieson, 1992). Refinements of the dusty-gas model to include particle-phase diffusive effects were reported and applied to the incompressible problem by Chamkha and Peddieson (1989) which resulted in a singularity-free flow solution. Chamkha (1994) reported the thermal aspects of the problem using the refined model.

It is of special interest in this paper to investigate whether the singular behavior observed in the problem of incompressible two-phase flow over a semi-infinite plate still exists for the compressible version and to understand the effects of particle-phase viscosity on the flow and heat transfer properties. Inclusion of the particle-phase viscous stresses in the dusty-gas model requires the use of additional boundary conditions on the particle phase. The proper boundary conditions to be satisfied by a solid particle phase at a surface are not understood at present. However, there is some experimental evidence that the particles experience some slip at the wall. In the present model, boundary conditions similar to those known from rarefied gas-dynamics with a wall slip coefficient dependent on the axial position of the plate is employed for the particle phase. A numerical method based on the finite-difference algorithm similar to that used by Wang and Glass (1988) is used for the solution of the present problem. Contrary to Wang and Glass (1988), a special modified Blasius transformation is employed which allows exact solutions for the initial profiles which are needed to start the numerical computations.

Problem Formulation

The dusty-gas model discussed by Marble (1970) is widely used in modeling two-phase particulate suspension flow situations. This model is restricted to small particle volume fraction and represents both phases as two interacting continua. Similar continuum models have been reported by other authors (see, for instance Soo, 1967 and Ishii, 1975). Other models based on the Lagrangian modeling approach have also been reported (Berlemont et al., 1990). Both modeling approaches have proven to be successful for modeling two-phase suspensions. However each approach may be more convenient than the other depending on the application. Since the individual motion of each particle is of no interest in the present work, and to allow comparisons between models in the solution of this problem, the continuum or the Eulerian approach will be employed in the present paper.

Contributed by the Fluids Engineering Division for publication in the JOURNAL OF FLUIDS ENGINEERING. Manuscript received by the Fluids Engineering Division August 26, 1994; revised manuscript received August 24, 1995. Associate Technical Editor: O. C. Jones.

Copyright © 1996 by ASME

Downloaded 03 Jun 2010 to 171.66.16.125. Redistribution subject to ASME license or copyright; see http://www.asme.org/terms/Terms_Use.cfm

Consider steady, compressible, laminar, boundary-layer two-phase flow in a half space bounded by a semi-infinite flat surface. The surface or plate is coincident with the plane $y = 0$ and the flow is a uniform stream in the plane $y > 0$ parallel to the surface. Far from the surface, both phases are in both hydrodynamic and thermal equilibrium. The particles are all assumed to be of one size and spherical in shape and moving with the same velocity. Besides, there is no radiative heat transfer from one particle to another, chemical reaction, coagulation, phase change, and deposition. The fluid phase is assumed to behave as a perfect gas. The fluid and particles motions are coupled only through drag and heat transfer between them. The drag force is modeled using Stokes linear drag theory and the small particle volume fraction assumption inherent in the dusty-gas model (Marble, 1970) is retained in this problem.

The governing equations for this investigation are based on the balance laws of mass, linear momentum, and energy for both phases. These can be written

$$\vec{\nabla}\cdot(\rho\vec{V}) = 0 \tag{1a}$$

$$\vec{\nabla}\cdot(\rho_p\vec{V}_p) = 0 \tag{1b}$$

$$\rho\vec{V}\cdot\vec{\nabla}\vec{V} = \nabla\cdot\underline{\underline{\sigma}} - \vec{f} \tag{1c}$$

$$\rho_p\vec{V}_p\vec{\nabla}\cdot\vec{V}_p = \vec{\nabla}\cdot\underline{\underline{\sigma}}_p + \vec{f} \tag{1d}$$

$$\rho c\vec{V}\cdot\vec{\nabla}T = \vec{\nabla}\cdot k\vec{\nabla}T + \underline{\underline{\sigma}}:\vec{\nabla}\vec{V} + (\vec{V} - \vec{V}_p)\cdot\vec{f} + Q_T \tag{1e}$$

$$\rho_p c_p\vec{V}_p\cdot\vec{\nabla}T_p = \underline{\underline{\sigma}}_p:\vec{\nabla}\vec{V}_p - Q_T \tag{1f}$$

where ρ, $\vec{V}$, $\underline{\underline{\sigma}}$, c, k, and T denote, density, velocity vector, stress tensor, specific heat, thermal conductivity, and temperature for the fluid phase, respectively. Properties and variables with subscript p denote the same thing for the particle phase. $\vec{\nabla}$ is the gradient operator. $\vec{f}$ and Q_T are the interphase drag force per unit volume of suspension, and the interphase heat transfer, respectively.

To completely define the problem, the following equations are used

$$\underline{\underline{\sigma}} = -P\underline{\underline{I}} + \mu(T)(\vec{\nabla}\vec{V} + \vec{\nabla}\vec{V}^T) \tag{2a}$$

$$\underline{\underline{\sigma}}_p = \mu_p(T_p)(\vec{\nabla}\vec{V}_p + \vec{\nabla}\vec{V}_p^T) \tag{2b}$$

$$\vec{f} = \rho_p(\vec{V} - \vec{V}_p)/\tau_v \tag{2c}$$

$$Q_T = \rho_p c_p(T_p - T)/\tau_T \tag{2d}$$

$$P = \rho RT \tag{2e}$$

In Eqs. (2), P is the fluid pressure, $\underline{\underline{I}}$ is the unit tensor, μ and μ_p are the fluid and particle dynamic viscosities, respectively, τ_v, τ_T, and R are the momentum and temperature relaxation times and the gas constant, respectively, and a superposed T denotes the transpose of a second-order tensor.

It is seen from Eqs. (2) that the particle phase is assumed to have viscous effects which are not present in the models reported by Singleton (1965) and Wang and Glass (1988). These effects can model particle-particle interaction and particle-wall interaction. They can also be thought of as a natural consequence of the averaging processes involved in representing a discrete system of particle as a continuum (Drew, 1983; and Drew and Segal, 1971). The particle-phase viscous effects have been investigated by many previous investigators (Gidaspow, 1986; Tsuo and Gidaspow, 1990; and Gadiraju et al., 1991). Also, the particles are assumed to be dragged along by the fluid and, therefore, have no analog of pressure.

Substituting the following dimensionless variables

$$s = x/(\tau_v U_\infty),\quad n = y\,\mathrm{Re}_\infty^{1/2}/(\tau_v U_\infty),\quad \Gamma(H) = \mu/\mu_\infty$$

$$\Gamma_p(H_p) = \mu_p/\mu_{p\infty},\quad \mathrm{Pr} = \mu c/k,\quad \mathrm{Ec} = U_\infty^2/(cT_\infty)$$

$$\beta = \mu_{p\infty}/\mu_\infty,\quad \gamma = c/c_p$$

$$\vec{V} = U_\infty(u(s,n)\vec{e}_x + v(s,n)/\mathrm{Re}_\infty^{1/2}\vec{e}_y),$$

$$\vec{V}_p = U_\infty(u_p(s,n)\vec{e}_x + v_p(s,n)/\mathrm{Re}_\infty^{1/2}\vec{e}_y)$$

$$H = T/T_\infty,\quad H_p = T_p/T_\infty,\quad Q = \rho/\rho_\infty,\quad Q_p = \rho_p/\rho_\infty \tag{3}$$

(where $\mathrm{Re}_\infty = (\rho_\infty U_\infty^2\tau_v)/\mu_\infty$, e denotes a unit vector, and U_∞, ρ_∞, μ_∞, and T_∞ are the freestream velocity, density, viscosity, and temperature, respectively) along with Eqs. (2) into Eqs.

Nomenclature

C = fluid-phase skin-friction coefficient
c = fluid-phase specific heat at constant pressure
Ec = fluid-phase Eckert number
e_x, e_y = unit vectors in x and y directions, respectively
F = nondimensionalized fluid-phase tangential velocity
f = interphase force per unit volume acting on the particle phase
G = nondimensionalized fluid-phase transformed normal velocity
H = nondimensionalized fluid-phase temperature
$\underline{\underline{I}}$ = unit tensor
k = fluid-phase thermal conductivity
P = fluid-phase pressure
Pr = fluid-phase Prandtl number
Q = nondimensionalized fluid-phase density
Q_T = interphase heat transfer rate per unit volume to the particle phase
r, S_R = constants defined in Eq. (18)
q_w = wall heat transfer
R = ideal gas constant
Re = Reynolds number
S = particle-phase slip parameter
t_o = nondimensionalized fluid-phase wall temperature
T = fluid-phase temperature
u = x-component of velocity
U_∞ = free stream velocity
v = y-component of velocity
V = fluid-phase velocity vector
x, y = Cartesian coordinate variables
β = viscosity ratio
γ = specific heat ratio
Δ = fluid-phase displacement thickness
η = transformed normal coordinate
Γ = fluid-phase viscosity coefficient
κ = particle mass loading ratio
μ = fluid-phase viscosity coefficient
ρ = fluid-phase density
$\underline{\sigma}$ = fluid-phase stress tensor
τ_T = temperature relaxation time
τ_v = momentum relaxation time
ω = power index for viscosity relation
ξ = transformed tangential coordinate
∇ = gradient operator

Subscripts

∞ = free stream
p = particle phase

Superscripts

T = transpose of a second-order tensor

Downloaded 03 Jun 2010 to 171.66.16.125. Redistribution subject to ASME license or copyright; see http://www.asme.org/terms/Terms_Use.cfm

(1) and performing the usual boundary-layer order of magnitude analysis give

$$\partial_s(Qu) + \partial_n(Qv) = 0 \quad (4a)$$

$$\partial_s(Q_p u_p) + \partial_n(Q_p v_p) = 0 \quad (4b)$$

$$Q(u\partial_s u + v\partial_n u) = \Gamma\partial_n^2 u + (d_H\Gamma\partial_n H)\partial_n u + Q_p\Gamma(u_p - u) \quad (4c)$$

$$Q_p(u_p\partial_s u_p + v_p\partial_n u_p) = \beta(\Gamma_p\partial_n^2 u_p + (d_{H_p}\Gamma_p\partial_n H_p)\partial_n u_p) + Q_p\Gamma(u - u_p) \quad (4d)$$

$$Q_p(u_p\partial_s v_p + v_p\partial_n v_p) = \beta(\Gamma_p\partial_n^2 v_p + (d_{H_p}\Gamma_p\partial_n H_p)\partial_n v_p) + Q_p\Gamma(v - v_p) \quad (4e)$$

$$\mathrm{Pr}Q(u\partial_s H + v\partial_n H) = \Gamma\partial_n^2 H + d_H\Gamma(\partial_n H)^2 + \mathrm{Ec\ Pr}\Gamma(\partial_n u)^2 + \mathrm{EcPr}Q_p\Gamma(u_p - u)^2 + 2Q_p\Gamma(H_p - H)/3 \quad (4f)$$

$$Q_p(u_p\partial_s H_p + v_p\partial_n H_p) = \beta\,\mathrm{Ec}\Gamma_p\gamma(\partial_n u_p)^2 + 2\gamma Q_p\Gamma(H - H_p)/(3\ \mathrm{Pr}) \quad (4g)$$

$$QH = 1 \quad (4h)$$

It should be noted in Eqs. (3) that x and y and, hence, s and n are tangential and normal coordinates and that u and v are corresponding velocities.

The physics of the present problem suggests the following boundary conditions:

$$u(s, 0) = 0, \quad u(s, \infty) = 1, \quad v(s, 0) = 0$$

$$H(s, 0) = t_o, \quad H(s, \infty) = 1, \quad v_p(s, \infty) = 1$$

$$v_p(s, 0) = 0, \quad v_p(s, \infty) = v(s, \infty), \quad H_p(s, \infty) = 1$$

$$Q_p(s, \infty) = \kappa, \quad Q(s, \infty) = 1 \quad (5)$$

where t_o is a dimensionless constant and $\kappa = \rho_{p\infty}/\rho_\infty$ is the mass loading ratio of the particles. In all the work to be presented later in this paper, κ is taken to be unity (Wang and Glass, 1988).

In the present work it is assumed that the viscosity-temperature relations for both phases are of the forms:

$$\Gamma = H(s, n)^\omega, \quad \Gamma_p = H_p(s, n)^\omega, \quad 0.5 \le \omega \le 1 \quad (6a, b)$$

where ω is a power index. It is assumed herein that both power indices for the fluid and particle phases are identical, and that the particle phase is treated as a viscous fluid. This would justify the pseudo particle viscosity which behaves as described in Eq. (6b). Singleton (1965) restricted his work to $\omega = 0.5$ while Wang and Glass (1988) allowed for different values of ω as is the case in the present work.

Substituting Eqs. (6) and the following modified Blasius transformations

$$s = \xi/(1 - \xi), \quad n = (2\xi/(1 - \xi))^{1/2}\eta$$

$$u = F(\xi, \eta), \quad v = ((1 - \xi)/(2\xi))^{1/2}(G(\xi, \eta) + \eta F(\xi, \eta))$$

$$u_p = F_p(\xi, \eta),$$

$$v_p = ((1 - \xi)/(2\xi))^{1/2}(G_p(\xi, \eta) + \eta F_p(\xi, \eta)) \quad (7)$$

into Eqs. (4) and (5) and rearranging result

$$\partial_\eta(QG) + QF + 2\xi(1 - \xi)\partial_\xi(QF) = 0 \quad (8)$$

$$\partial_\eta(Q_pG_p) + Q_pF_p + 2\xi(1 - \xi)\partial_\xi(Q_pF_p) = 0 \quad (9)$$

$$H^\omega\partial_\eta^2 F + (\omega H^{\omega-1}\partial_\eta H - QG)\partial_\eta F - 2\xi/(1 - \xi)((1 - \xi)^2 QF\partial_\xi F - Q_pH^\omega(F_p - F)) = 0 \quad (10)$$

$$\beta H_p^\omega\partial_\eta^2 F_p + (\beta\omega H_p^{\omega-1}\partial_\eta H_p - Q_pG_p)\partial_\eta F_p - 2\xi/(1 - \xi)((1 - \xi)^2 Q_pF_p\partial_\xi F_p + Q_pH^\omega(F_p - F)) = 0 \quad (11)$$

$$\beta H_p^\omega\partial_\eta^2 G_p + (\beta\omega H_p^{\omega-1}\partial_\eta H_p - Q_pG_p)\partial_\eta G_p - \beta\mathrm{H}_p^\omega\partial_\eta^2(\eta F_p) + \beta\omega H_p^{\omega-1}\partial_\eta H_p\partial_\eta(\eta F_p) - \eta Q_pG_p\partial_\eta F_p + \eta Q_pF_p^2 - 2\xi(1 - \xi)Q_pF_p\partial_\xi(G_p + \eta F_p) - 2\xi/(1 - \xi)Q_pH^\omega(G_p - G + \eta(F_p - F)) = 0 \quad (12)$$

$$H^\omega\partial_\eta^2 H + (\omega H^{\omega-1}\partial_\eta H - \mathrm{Pr}QG)\partial_\eta H - 2\xi(1 - \xi)\ \mathrm{Pr}QF\partial_\xi H + \mathrm{EcPr}H^\omega(\partial_\eta F)^2 + 2\xi/(1 - \xi)(\mathrm{EcPr}Q_pH^\omega(F_p - F)^2 + 2Q_pH^\omega(H_p - H)/3) = 0 \quad (13)$$

$$Q_pG_p\partial_\eta H_p - \beta\mathrm{Ec}\gamma H_p^\omega(\partial_\eta F_p)^2 + 2\xi(1 - \xi)Q_pF_p\partial_\xi H_p + 4\xi/(1 - \xi)\gamma Q_pH^\omega(H_p - H)/(3\ \mathrm{Pr}) = 0 \quad (14)$$

$$QH = 1 \quad (15)$$

$$F(\xi, 0) = 0, \quad F(\xi, \infty) = 1, \quad G(\xi, 0) = 0$$

$$H(\xi, 0) = t_o, \quad H(\xi, \infty) = 1, \quad F_p(\xi, \infty) = 1$$

$$G_p(\xi, 0) = 0, \quad G_p(\xi, \infty) = G(\xi, \infty), \quad H_p(\xi, \infty) = 1$$

$$Q_p(\xi, \infty) = 1, \quad Q(\xi, \infty) = 1 \quad (16)$$

Equations (8) through (16) represent general equations for steady, compressible, boundary-layer flow of a particle-fluid suspension over a flat surface. They represent a generalization of the dusty-gas model employed by Wang and Glass (1988) to include particle-phase viscous effects. In fact, they reduce to the equations given previously by Wang and Glass (1988) in the absence of the particle-phase viscosity. The advantage of using the modified Blasius transformations (Eq. (7)) is that they allow the closed-form solutions $Q_p = 1$, $H_p = 1$, $F_p = 1$, $G_p = -\eta$ at $\xi = 0$ and they convert the computational region from semi-infinite ($0 \le x < \infty$) to finite ($0 \le \xi \le 1$).

The exact form of boundary conditions to be satisfied by a particle phase at a surface are unknown at present. Since the particle phase may resemble a rarefied gas, a boundary condition borrowed from rarefied-gas dynamics is utilized in the present work. This can be written in the new variables as

$$F_p(\xi, 0) = S((1 - \xi)/(2\xi))^{1/2}\partial_\eta F_p(\xi, 0) \quad (17)$$

where S is a particle-phase slip parameter which is dependent on the coefficient of viscosity and wall slip velocity (difference between particle and fluid velocities). However, no attempt was made to relate S to the internal properties of the suspension.

In reality the particle-phase tangential velocity at the wall is controlled by many physical effects such as sliding friction, the nature of particle/surface collision, etc. It is not possible to model such effects with precision at present. To allow for a variety of particle-phase wall tangential velocity profiles, it is assumed that the wall slip parameter S is a function of the wall position ξ (since the wall slip velocity is related to ξ). A general function of the form

$$S = S_R((1 - \xi)/\xi)^r \quad (18)$$

(where S_R and r are constants) is employed in the present work. It can be seen that the form of Eq. (18) allows perfect particulate slip at $\xi = 0$ followed by approach to no-slip at a rate controlled by the values of S_R and r.

Of practical interest are the fluid- and particle-phase displacement thicknesses, the skin-friction coefficients, and the wall heat transfer coefficient. These are defined, respectively, as

Downloaded 03 Jun 2010 to 171.66.16.125. Redistribution subject to ASME license or copyright; see http://www.asme.org/terms/Terms_Use.cfm

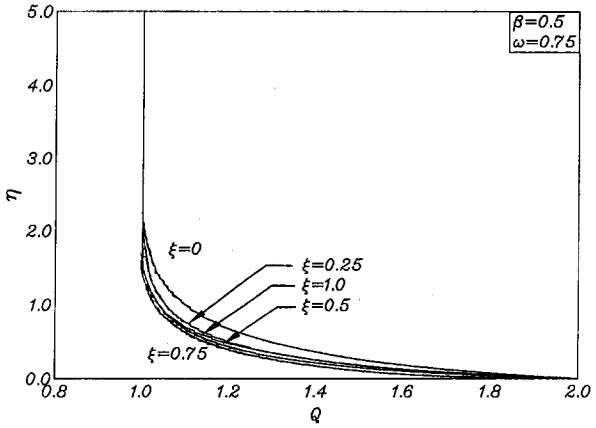


Fig. 1 Fluid-phase density profiles

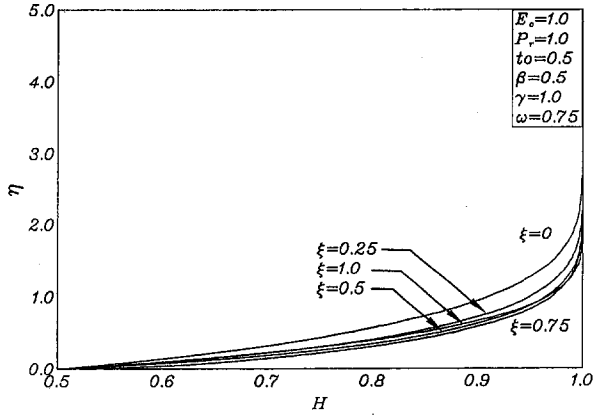


Fig. 3 Fluid-phase temperature profiles

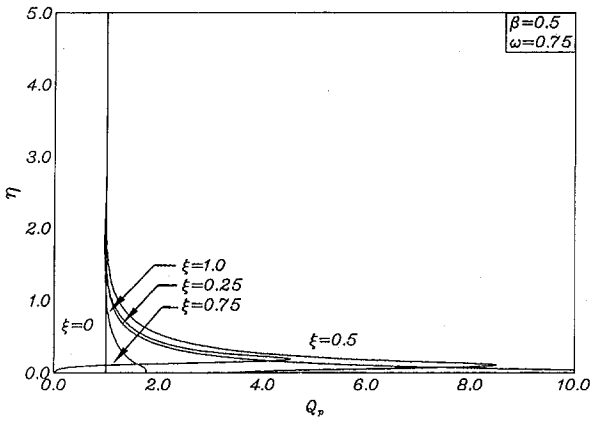


Fig. 2 Particle-phase density profiles

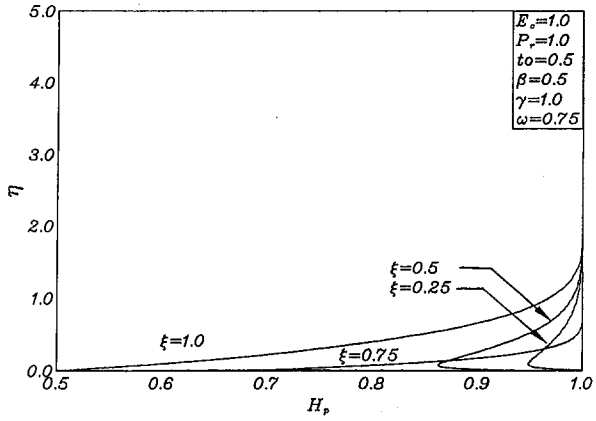


Fig. 4 Particle-phase temperature profiles

$$\Delta(\xi) = \int_0^\infty (1 - QF)d\eta \tag{19a}$$

$$\Delta_p(\xi) = \int_0^\infty (1 - Q_pF_p)d\eta \tag{19b}$$

$$C(\xi) = H(\xi, 0)^\omega \partial_\eta F(\xi, 0) \tag{19c}$$

$$C_p(\xi) = \beta H_p(\xi, 0)^\omega \partial_\eta F_p(\xi, 0) \tag{19d}$$

$$q_w(\xi) = H(\xi, 0)^\omega \partial_\eta H(\xi, 0)/(\mathrm{EcPr}) \tag{19e}$$

Results and Discussion

Equations (8) through (15) are obviously nonlinear and exhibit no closed-form or similar solution. They, therefore, must be solved numerically. The tri-diagonal, implicit, iterative, finite-difference method discussed by Blottner (1970) and similar to that used by Wang and Glass (1988) has proven to be successful in the solution of boundary-layer problems. For this reason, it is adopted in the present work.

All first-order derivatives with respect to ξ are represented by two-point backward difference formulas. All second-order differential equations in η are discretized using a three-point central difference quotients while all first-order differential equations in η are discretized using the trapezoidal rule. The computational domain was divided into 1001 nodes in the ξ direction and 195 nodes in the η direction. Since it is expected that most changes in the boundary layer occur in the vicinity of the wall, variable step sizes in η are utilized with $\Delta\eta_1 = 0.001$ and a growth factor of 1.03. Also, constant small step sizes in ξ with $\Delta\xi = 0.001$ are used. The governing equations are then converted into sets of linear tri-diagonal algebraic equations which are solved by the Thomas Algorithm (Blottner, 1970) at each iteration. The convergence criterion required that the difference between the current and the previous iterations be 10^{-5}. It should be mentioned that many numerical experimentations were performed by altering the step sizes in both directions to ensure accuracy of the results and to assess grid independence. For example, when $\Delta\eta_1$ was set to 0.01 instead 0.001, an average error of about eight percent was observed in the results with the maximum error being close to $\xi = 1$. Also, when $\Delta\eta_1$ was equated to 0.0001 no significant changes of results were observed. For this reason $\Delta\eta_1 = 0.001$ was chosen and employed in producing the numerical results. The flow and heat transfer parameter are not as sensitive to $\Delta\xi$ as they are sensitive to $\Delta\eta_1$. For this reason, a constant step size was used in the ξ direction. The sensitivity analysis of the results to changes in $\Delta\xi$ was also performed. For instance, when $\Delta\xi$ was set to 0.01, an average deviation of five percent from the results with $\Delta\xi = 0.001$. Smaller values of $\Delta\xi$ than 0.01 produced no changes in the results and, therefore, $\Delta\xi$ was set to 0.001 in all the produced results. As far as the convergence criterion is concerned, two types were tried. One was based on the percentage error between the previous and the current iterations and the other was based on their difference. Since we are not dealing with very small numbers, the convergence criterion based on the difference between the previous and current iterations was employed in the present study. No convergence problems were encountered even with the small value of 10^{-5} used in this work. It should be mentioned that when a second-order ξ-derivative is used, a slight enhancement of results (within two percent) was predicted. However, all results to be presented are based on the first-order-accurate approximation of ξ derivatives. Equations

Downloaded 03 Jun 2010 to 171.66.16.125. Redistribution subject to ASME license or copyright; see http://www.asme.org/terms/Terms_Use.cfm

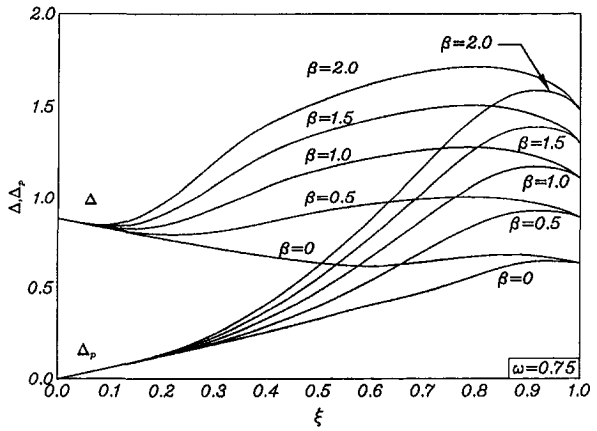


Fig. 5 Fluid and particle-phase displacement thicknesses profiles

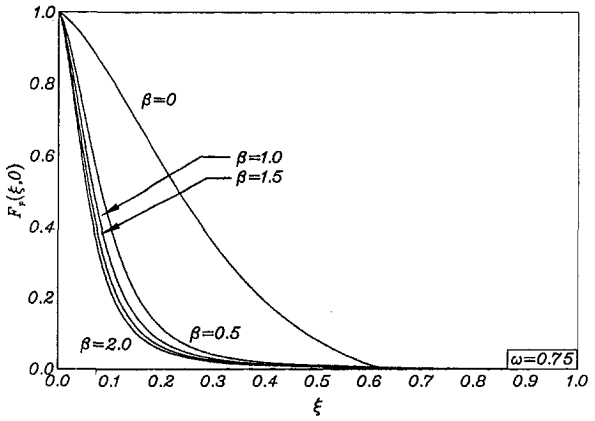


Fig. 8 Wall particle-phase tangential velocity profiles

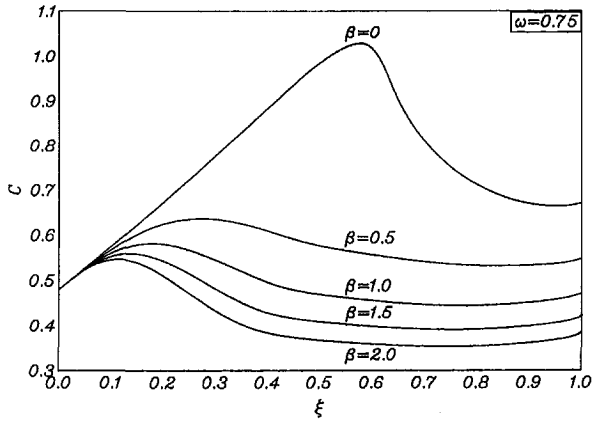


Fig. 6 Fluid-phase skin friction coefficient profiles

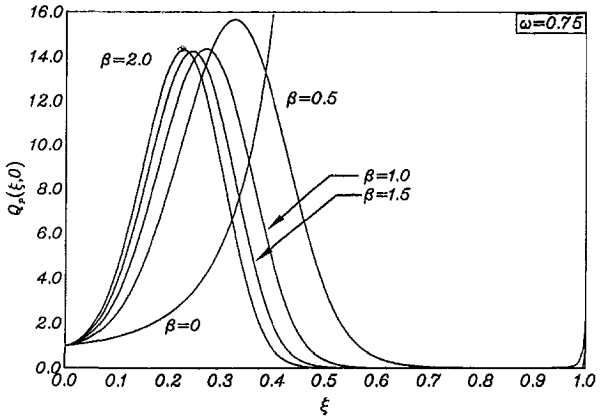


Fig. 9 Wall particle-phase density profiles

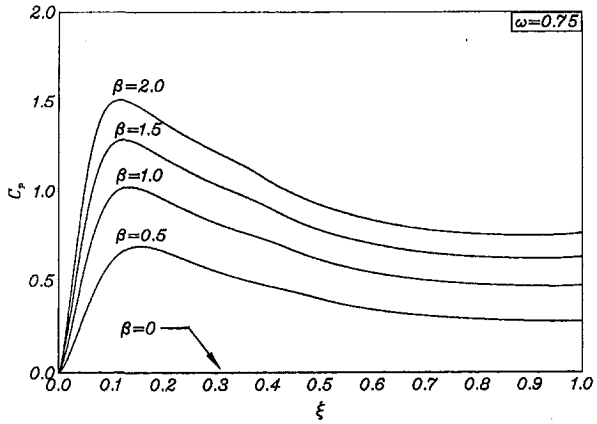


Fig. 7 Particle-phase skin friction coefficient profiles

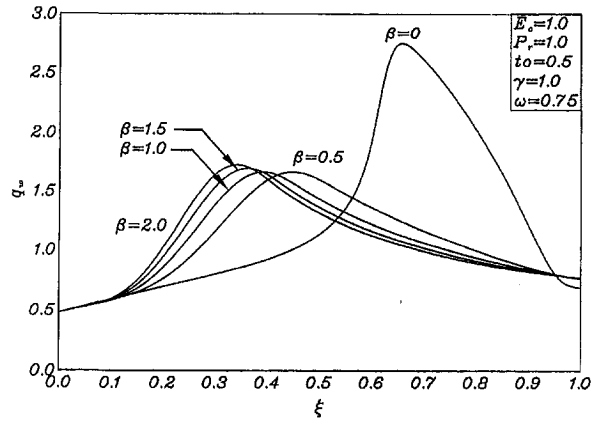


Fig. 10 Wall heat transfer coefficient profiles

(8) through (15) were solved for G, Q_p, F, F_p, G_p, H, H_p, and Q, respectively. Many results were obtained throughout the course of this work. A representative set is presented in Figs. 1 through 10 to show the effects of the viscosity ratio β. In all these figures $S_R = 50$ and $r = 1$.

Figures 1 and 2 present representative fluid- and particle-phase density profiles, respectively. It is seen from these figures that most changes occur in a small region in the vicinity of the wall and uniform conditions exist above it. Since the wall temperature t_O is taken to be 0.5, Eq. (15) implies that the fluid density at the wall must be equal to 2 as is shown in Fig. 5. Figure 6 shows that the particle-phase density at the wall becomes relatively large in the region $0.25 \leq \xi \leq 0.5$ and then its value vanishes for $\xi = 0.75$ and reaches its expected value at $\xi = 1$. This suggests the existence of a particle-free zone near $\xi = 0.75$. This will be discussed later.

Figures 3 and 4 show temperature profiles for both the fluid and particle phases, respectively. Like the velocity profiles, these figures show a complete transition to equilibrium conditions. It is seen that the particle-phase temperature profiles at $\xi = 0.25$ and $\xi = 0.5$ decrease in value close to the wall and then increase to reach the free-stream value. This behavior probably occurs as these profiles are being adjusted to reach equilibrium conditions with the fluid phase. It should be noted that while

Downloaded 03 Jun 2010 to 171.66.16.125. Redistribution subject to ASME license or copyright; see http://www.asme.org/terms/Terms_Use.cfm

the fluid-phase temperature is diffusive and, thus, requires a wall boundary condition, the particulate temperatures do not. In general, if particulate-phase stresses are included in the mathematical model, then a thermal conductivity for particles arises (Soo, 1990). However, this was neglected in the present work compared with other effects and to allow the particle-phase wall temperature to adjust itself through the energy coupling mechanism between the phases.

Figures 5 through 10 are presented to illustrate the effect of the particle-phase viscosity on the flow properties. Figures 5 through 7 show the behavior of the displacement thicknesses of both phases Δ and Δ_p, the fluid-phase skin-friction coefficient C, and the particle-phase skin-friction coefficient C_p along the flat surface for various values of β, respectively. At $\xi = 0$, the drag force between the phases is maximum and it decreases as ξ increases until it vanishes at $\xi = 1$ where equilibrium between the phases exists. This momentum exchange mechanism causes the fluid-phase displacement thickness to decrease (which causes an increase in the fluid-phase skin friction) and the particle-phase displacement thickness to increase until equilibrium is reached. However, as β increases the effective viscosity of the mixture increases and causes a rapid increase in the values of Δ as the flow moves downstream toward equilibrium. It should be noted that the particle-phase streamlines are completely unaffected by the fluid-phase displacement. This is because of the frozen condition (where both phases move independently) existing at $\xi = 0$. These behaviors are evident from Fig. 5. As β increases, the domain of particle-phase viscous effects increases causing an increase in the region close to the wall where significant deviations from uniformity occur. This results in increases in the values of Δ and Δ_p and decreases in the values of C as shown in Figs. 5 and 6. In addition, the values of C_p shown in Fig. 6 increases as β increases since C_p is directly proportional to β (see Eq. (19d)).

Figures 8 and 9 present the wall particle-phase tangential velocity and density profiles for various values of β, respectively. The transition from a perfect slip condition at $\xi = 0$ to a no-slip condition downstream at about $\xi \geq 0.6$ is shown in Fig. 8. Figure 9 shows that for an inviscid particle phase ($\beta = 0$) the particle-phase wall density becomes large in the vicinity of $\xi = 0.5$. This behavior was also observed for the case of incompressible flow (Ospitsov, 1980 and Chamkha and Peddieson, 1989). However, in the present work a continuous solution for $Q_p(\xi, 0)$ is predicted in the entire range $0 \leq \xi \leq 1$ unlike the incompressible case where no continuous solutions existed. The peak value of $Q_p(\xi, 0)$ for $\beta = 0$ is large and falls outside the range of the figure. It has a value of 240 occurring at $\xi = 0.62$ and approaches the equilibrium conditions at $\xi = 1$ without going below unity. This indicates that a particle-free zone does not exist for $\beta = 0$. It is seen that as the particulate slip decreases, lower peak values for $Q_p(\xi, 0)$ are predicted. However, for $\beta > 0$ (viscous particle phase) $Q_p(\xi, 0)$ vanishes over a big region far from the leading edge of the surface and then approaches the equilibrium conditions at $\xi = 1$. The vanishing of $Q_p(\xi, 0)$ is suggestive of the formation of a particle-free zone at the wall somewhere downstream. This phenomenon has been predicted by the work of Young and Hanratty (1991). It is seen from Fig. 9 that as β increases the peaks in the $Q_p(\xi, 0)$ profiles move toward the leading edge of the plate and the particle-free region increases.

If the vanishing of the particle-phase density at the wall represents a physical phenomenon, then the dusty-gas model employed in the present work may be inadequate because the equations of this model are derived under the assumption that the entire space is occupied by both phases. Enhancements to the model which eliminates the existence of the particle-free zone will be discussed in another contribution.

Figure 10 illustrates the changes in the wall heat transfer coefficient q_w as the viscosity ratio β is altered. It is seen that a sharp peak in the values of q_w exits for $\beta = 0$ and this peak moves upstream and its value decreases as β increases. The behavior of q_w with respect to ξ observed in the figure is a property of relaxation type problems.

More graphical results were obtained (and not presented herein for brevity) illustrating the influence of varying ω, S_R, and r. Increasing the power index ω causes the fluid- and particle-phase viscosities to decrease. This reduces the fluid and particle domain of viscous effects which result in decreases in the values of Δ and Δ_p. Both C and C_p are directly proportional to the wall viscosities which are related to the wall temperatures of both phases. The fluid phase has a constant wall temperature ($t_O = 0.5$) while the particle phase has a variable wall temperature. Thus, increasing ω causes $H(\xi, 0)^\omega$ and $H_p(\xi, 0)^\omega$ to decrease and increase, respectively. This causes a decrease in C and an increase in C_p. It is expected that ω has a negligible effect on the particle-phase wall tangential velocity and a slight effect on its wall density. Decreases in the fluid-phase wall viscosity caused by increasing ω, as mentioned earlier, cause decreases in the fluid thermal conductivity at the wall. This causes the wall heat transfer to decrease. All these statements are consistent with predicted results.

In addition, it was observed that as either S_r or r is increased, the values of Δ, Δ_p, and C_p were increased while those of C and q_w decreased. Also, some adjustments were made in the computer program and results for the incompressible case were obtained. These results were in excellent agreement with those reported by Chamkha and Peddieson (1989) and Chamkha (1994). The velocity and temperature fields reported by Wang and Glass (1988) were compared with the present results and were found to be in good agreement. These comparisons gave some confidence in the numerical procedure. No comparisons with experimental data were made since these data are lacking at present.

Conclusion

A continuum dusty-gas model modified to include particle-phase viscous effects was employed in analyzing steady, compressible, laminar, boundary-layer flow of a particulate suspension over a flat surface. The mathematical model included conservation equations for mass, momentum, and energy for each phase where diffusive transport of thermal energy in the particle phase was neglected and where thermal and momentum exchange between the phases was specified in terms of relaxation time constants. Similar to the carrier fluid, the particle phase was assumed to have a general power-law viscosity-temperature relation. The governing equations were solved numerically via an implicit, iterative, finite-difference method and numerical solutions for the flow and heat transfer aspects of the problem were reported and discussed. A parametric study was performed to show the effects of the particle-phase viscosity and the viscosity-temperature power index. In contrast with the incompressible version of the current problem, it was found that continuous solutions existed throughout the computational domain. Another major prediction of the present work was that for a viscous particle phase a particle-free zone was formed at the plate surface. This prediction could not be verified by experimental data due to the absence of such data at present. Favourable comparisons with previously published results on special cases of this problem were made which gave confidence in the accuracy of the numerical method. It is hoped that the present results be of use for environmental agencies in validating computer routines and serve as a stimulus for experimental work on the present problem.

Acknowledgments

The author wishes to thank the Research Administration at Kuwait University for funding the work presented in this paper under Contract EPM079. Also, thanks are due to Engineer

Downloaded 03 Jun 2010 to 171.66.16.125. Redistribution subject to ASME license or copyright; see http://www.asme.org/terms/Terms_Use.cfm

Khalil Khanafer for preparing the graphs used in this manuscript.

References

Berlemont, A., et al., 1990, "Particle Lagrangian Simulation in Turbulent Flows," *International Journal of Multiphase Flow,* Vol. 16, pp. 19–34.

Blottner, F. G., 1970, "Finite-Difference Methods of Solution of the Boundary-Layer Equations," *AIAA Journal,* Vol. 8, pp. 193–205.

Chamkha, A. J., and Peddieson, J., 1992, "Singular Behavior in Boundary-Layer Flow of a Dusty Gas," *AIAA Journal,* Vol. 30, pp. 2966–2968.

Chamkha, A. J., and Peddieson, J., 1989, "Boundary-Layer Flow of a Particle-Fluid Suspension Past a Flat Plate," *Developments in Mechanics,* Vol. 15, pp. 315–316.

Chamkha, A. J., 1994, "Effects of Particulate Diffusion on the Thermal Flat Plate Boundary Layer of a Two-Phase Suspension," ASME *Journal of Heat Transfer,* Vol. 116, pp. 236–239.

Datta, N., and Mishra, S. K., 1982, "Boundary Layer Flow if a Dusty Fluid Over a Semi-Infinite Flat Plate," *Acta Mechanica,* Vol. 42, pp. 71–83.

Drew, D. A., 1983, "Mathematical Modeling of Two-phase Flow," *Annual Review of Fluid Mechanics,* Vol. 15, pp. 261–291.

Drew, D. A., and Segal, L. A., 1971, "Analysis of Fluidized Beds and Foams Using Averaged Equations," *Studies in Applied Mathematics,* Vol. 50, pp. 233, 252.

Gadiraju, M., and et al., 1992, "Exact Solutions for Two-Phase Vertical Pipe Flow," *Mechanics Research Communications,* Vol. 19, pp. 7–13.

Gidaspow, D., 1986, "Hydrodynamics of Fluidization and Heat Transfer: Super Computer Modeling," *Applied Mechanics Reviews,* Vol. 39, pp. 1–23.

Ishii, M., 1975, Thermo-Fluid Dynamic Theory of Two-Phase Flow, Eyrolles, Paris.

Marble, F. E., 1970, "Dynamics of Dusty Gases," *Annual Review of Fluid Mechanics,* Vol. 2, pp. 297–446.

Osiptsov, A. N., 1980, "Structure of the Laminar Boundary Layer of a Disperse Medium on a Flat Plate," *Fluid Dynamics,* Vol. 15, pp. 512–517.

Prabha, S., and Jain, A. C., 1980, "On the Use of Compatibility Conditions in the Solution of Gas Particulate Boundary Layer Equations," *Applied Scientific Research,* Vol. 36, pp. 81–91.

Rudinger, G., 1980, *Fundamentals of Gas-Particle Flow,* Elsevier.

Singleton, R. E., 1965, "The Compressible Gas-Solid Particle Flow Over a Semi-Infinite Flat Plate," *Zamp,* Vol. 16, pp. 421–449.

Soo, S. L., 1990, Multiphase Fluid Dynamics, Science Press, Beijing, China.

Soo, S. L., 1961, "Boundary Layer Motion of a Gas-Solid Suspension," University of Illinois, Project Squad Report Ill-3p.

Soo, S. L., 1967, *Fluid Dynamics of Multiphase Systems,* Blaisdell Publishing, Waltham, Mass.

Soo, S. L., 1968, "Non-Equilibrium Fluid Dynamics-Laminar Flow Over a Flat Plate," *ZAMP,* Vol. 19, pp. 545–563.

Soo, S. L., and Tien, C. L., 1960, "Effect of the Wall on Two-Phase Turbulent Motion," *Journal of Fluid Mechanics,* Vol. 27: ASME *Journal of Applied Mechanics,* Vol. 82, Series E, pp. 5–11.

Tsuo, Y. P., and Gidaspow, D., 1990, "Computation of Flow Patterns in Circulating Fluidized Beds," *AIChE Journal,* Vol. 36, pp. 88–896.

Wang, B. Y., and Glass, I. I., 1988, "Compressible Laminar Boundary-Layer Flows of a Dusty Gas Over a Semi-Infinite Flat Plate," *Journal of Fluid Mechanics,* Vol. 186, pp. 223–241.

Young, J. B., and Hanratty, T. J., 1991, "Trapping of Solid Particles at a Wall in a Turbulent Flow," *AIChE Journal,* Vol. 37, pp. 1529–1536.

Downloaded 03 Jun 2010 to 171.66.16.125. Redistribution subject to ASME license or copyright; see http://www.asme.org/terms/Terms_Use.cfm

On the Application of the Method of Landau and Lifshitz to Sonic Velocities in Homogeneous Two-Phase Mixtures

Joseph C. Leung
Leung Inc.,
1521 Evergreen Lane,
Darien, IL 60561

A theoretical sonic velocity correlation for homogeneous two-phase mixtures under thermal equilibrium is proposed. By application of the method of Landau and Lifshitz, a dimensionless correlating parameter ω is found whereby different fluid properties and vapor mass fraction (quality) can be adequately accounted for by the simple correlation.

Introduction

The purpose of this note is to propose an appropriate scaling law for sonic velocities in homogeneous (bubbly) two-phase mixtures under saturated equilibrium. This similarity approach follows closely the method of Landau and Lifshitz (1959) but the present result also yields a simpler correlation for sonic velocities. In general, the sonic velocity can be given by

$$c = v\left[-\left(\frac{\partial v}{\partial P}\right)_s^{-1}\right]^{1/2} \tag{1}$$

where for a homogeneous two-phase fluid (with $v = v_f + xv_{fg}$) in phase equilibrium under constant entropy constraint (i.e., $S = S_f + xS_{fg}$ = constant), the above equation can be shown to yield (see Moody, 1990),

$$c = v\left\{-\left[\frac{dv_f}{dP} - \frac{d}{dP}\left(\frac{S_f v_{fg}}{S_{fg}}\right) + S\frac{d}{dP}\left(\frac{v_{fg}}{S_{fg}}\right)\right]^{-1}\right\}^{1/2} \tag{2a}$$

or equivalently,

$$c = v\left\{-\left[\frac{dv_f}{dP} + x\frac{dv_{fg}}{dP} - \frac{v_{fg}}{S_{fg}}\left(\frac{dS_f}{dP} + x\frac{dS_{fg}}{dP}\right)\right]^{-1}\right\}^{1/2} \tag{2b}$$

Here the property derivatives are to be evaluated along the saturation line. More recently, Michaelides and Zissis (1983) gave a somewhat different form:

$$c^2 = \frac{\frac{v^2}{T^2}\left(\frac{h_{fg}}{v_{fg}}\right)^2}{\frac{C_{pf}}{T} + xv_{fg}\frac{d}{dT}\left(\frac{h_{fg}}{Tv_{fg}}\right) - \frac{h_{fg}}{Tv_{fg}}\frac{dv_f}{dT}} \tag{3}$$

However, this equation can be readily derived from Eq. (2) by using the thermodynamic relations $dP/dT = S_{fg}/T$, $S_{fg} = h_{fg}/T$, and $dS_f/dT = C_{pf}/T$ (generally a good approximation). They also proposed a scaling law based on reduced temperature ($T_r = T/T_c$) and rewrote Eq. (3) as

$$\frac{c^2}{h_{fg}} = \frac{\frac{v^2}{T_r^2}\left(\frac{h_{fg}}{v_{fg}^2}\right)}{\frac{C_{pf}T_c}{T_r} + xv_{fg}\frac{d}{dT_r}\left(\frac{h_{fg}}{T_r v_{fg}}\right) - \frac{h_{fg}}{T_r v_{fg}}\frac{dv_f}{dT_r}} \tag{4}$$

Their analyses of the data for water, ammonia (NH_3), Freon-12 (R-12 or dichlorodifluoromethane) and isobutane (iC_4) showed that Eq. (4) is only marginally successful with standard deviations in the 5–10 percent range.

Both Eqs. (2) and (3) require extensive thermodynamic property data (tabulation or curve fits) for their evaluation and great care needs to be exercised regarding data accuracy since derivatives are present.

Theoretical Development

The present development follows quite closely (though not exactly the same) the method of Landau and Lifshitz (1959). For completeness, we shall detail the derivation below. For a homogeneous equilibrium two-phase mixture the specific volume derivative in Eq. (1) can be given by

$$\left(\frac{\partial v}{\partial P}\right)_s = x\frac{dv_g}{dP} + v_{fg}\left(\frac{dx}{dP}\right)_s + (1-x)\frac{dv_f}{dP} \tag{5}$$

Using ideal gas assumption and the Clapeyron relation, dv_g/dP becomes

$$\frac{dv_g}{dP} = -\frac{v_g}{P} + \frac{v_g}{T}\frac{dT}{dP} = -\frac{v_g}{P} + \frac{v_g v_{fg}}{h_{fg}} \tag{6}$$

The $(dx/dP)_s$ derivative can be written as

$$\left(\frac{dx}{dP}\right)_s = \left(\frac{dx}{dT}\right)_s \Big/ \left(\frac{dP}{dT}\right) = \frac{v_{fg}T}{h_{fg}}\left(\frac{dx}{dT}\right)_s \tag{7}$$

where from constant entropy constraint

$$\left(\frac{dx}{dT}\right)_s = -\left[\frac{C_{pf}}{T} + x\frac{d}{dT}\left(\frac{h_{fg}}{T}\right)\right]\frac{T}{h_{fg}} \tag{8a}$$

$$\left(\frac{dx}{dT}\right)_s = -\frac{C_{pf}}{h_{fg}} + \frac{x}{T} \tag{8b}$$

Contributed by the Fluids Engineering Division for publication in the JOURNAL OF FLUIDS ENGINEERING. Manuscript received by the Fluids Engineering Division September 23, 1993; revised manuscript received August 15, 1995. Associate Technical Editor: O. C. Jones.

Copyright © 1996 by ASME

Downloaded 03 Jun 2010 to 171.66.16.125. Redistribution subject to ASME license or copyright; see http://www.asme.org/terms/Terms_Use.cfm

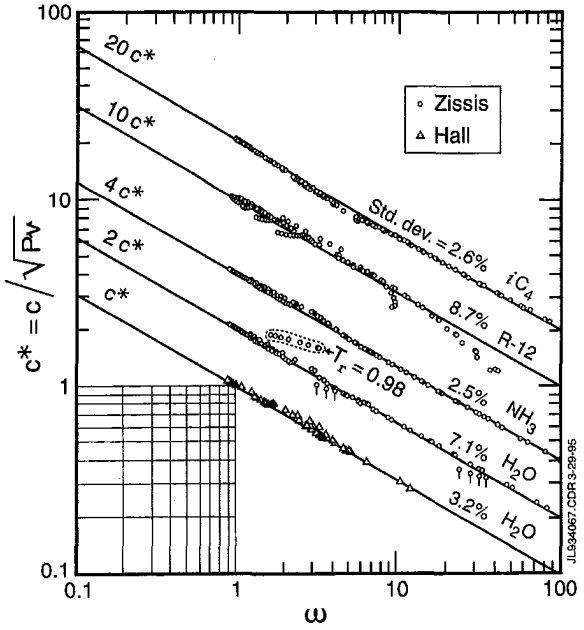


Fig. 1 Comparison of sonic velocity data of Zissis and Hall against present correlation

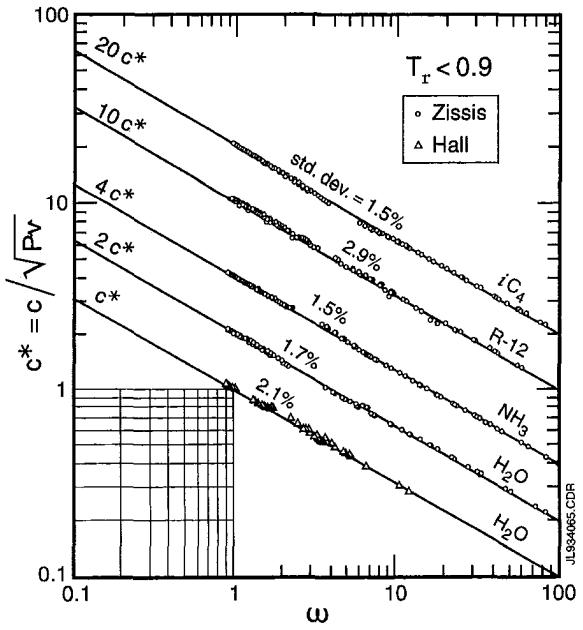


Fig. 2 Corrected R-12 data and other data at $T_r < 0.9$ versus present correlations

In arriving at Eq. (8*b*), the latent heat of vaporization h_{fg} has been assumed to be constant. Finally, the derivative dv_f/dP (reflecting liquid compressibility along the saturation line) is deemed negligible in comparison with other derivatives.

Substituting Eqs. (6), (7), and (8*b*) into Eq. (5) yields the specific volume derivative as

$$\left(\frac{\partial v}{\partial P}\right)_s = -\frac{xv_g}{P}\left[1 - \frac{Pv_{fg}}{h_{fg}}\left(1 + \frac{v_{fg}}{v_g}\right)\right] - C_{pf}T\left(\frac{v_{fg}}{h_{fg}}\right)^2 \quad (9)$$

A dimensionless sonic velocity can now be written as

$$\frac{c}{\sqrt{Pv}} = \left\{\frac{xv_g}{v}\left[1 - \frac{Pv_{fg}}{h_{fg}}\left(1 + \frac{v_{fg}}{v_g}\right)\right] + \frac{C_{pf}TP}{v}\left(\frac{v_{fg}}{h_{fg}}\right)^2\right\}^{-1/2} \quad (10a)$$

Recalling $xv_g/v = \alpha$, the void fraction, and that $v_{fg}/v_g \approx 1$, Eq. (10*a*) can be simplified to

$$\frac{c}{\sqrt{Pv}} = \left[\alpha\left(1 - 2\frac{Pv_{fg}}{h_{fg}}\right) + \frac{C_{pf}TP}{v}\left(\frac{v_{fg}}{h_{fg}}\right)^2\right]^{-1/2} \quad (10b)$$

Thus Eqs. (10*a*) or (10*b*) provide the scaling law for sonic velocity of a homogeneous two-phase fluid in thermodynamic equilibrium. At both saturated liquid cases ($x = 0$, $\alpha = 0$) and saturated vapor case ($x = 1$, $\alpha = 1$), the present equation reduces to the limiting solutions given by Landau and Lifshitz. We can therefore define an appropriate scaling parameter as

$$\omega \equiv \alpha\left(1 - 2\frac{Pv_{fg}}{h_{fg}}\right) + \frac{C_{pf}TP}{v}\left(\frac{v_{fg}}{h_{fg}}\right)^2 \quad (11)$$

thus resulting in a simple sonic velocity correlation

$$c^* = \frac{c}{(Pv)^{0.5}} = \omega^{-0.5} \quad (12)$$

A scaling parameter of similar form has been proposed by the author to correlate successfully critical (choked) flow data of homogeneous two-phase fluid in thermodynamic equilibrium (Leung, 1986). In that work, ω was defined in terms of inlet stagnation properties and the first term was given by $x_o v_{fgo}/v_o$ (which can be approximated by α_o).

Data Comparison

The two-phase sonic velocity data of Michaelides and Zissis (1983) as tabulated in Zissis's (1982) thesis are compared against the present correlation in Fig. 1. Also shown are selected data from the critical flow tables for water by Hall and Czapary (1980). (Note that Hall and Czapary's compilation is very extensive—every 10°C interval in the steam table—and the tabulation was for critical flow in accordance with the homogeneous-equilibrium model based on upstream stagnation conditions. To yield good representation of their data, stagnation temperatures T_o from 400 K–620 K in 20 K interval and stagna-

Nomenclature

c = sonic velocity
C_p = specific heat at constant pressure
h = specific enthalpy
P = pressure
S = specific entropy
T = absolute temperature
v = specific volume
x = static quality or vapor mass fraction
α = void fraction
ω = scaling parameter, Eq. (11)

Subscripts

c = thermodynamic critical point
f = liquid phase
fg = difference between vapor and liquid phase property
g = vapor phase
o = upstream stagnation condition
r = reduced thermodynamic property
s = under constant entropy path

Downloaded 03 Jun 2010 to 171.66.16.125. Redistribution subject to ASME license or copyright; see http://www.asme.org/terms/Terms_Use.cfm

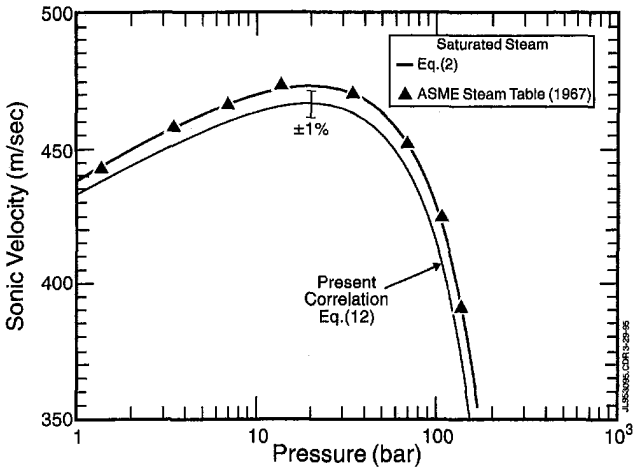


Fig. 3 Comparison of saturated steam sonic velocity data against present correlation

tion quality x_o at 0, 0.01, 0.1, and 1.0 were chosen. Of course the sonic velocity data were taken at the throat condition from their tabulation.) The physical properties used in ω evaluation were interpolated from the thermodynamic tables published by Reynolds (1979). Here we noted that the discrepancy in Zissis's water data occurred at $T_r = 0.98$, where the present simplifying assumptions would break down near this critical region, and at low qualities low temperature subatmospheric region, where only one or two significant figures for the sonic velocity were reported. These data are tagged for identification in Fig. 1. As for R-12, the agreement with the present correlation is poor. After extensive comparison with well-established thermodynamic properties published by DIPPR (1982), ASHRAE (1985), and Reynolds (1979), it was found that the property curve fits for v_g and h_{fg} as employed in Zissis's work were inaccurate at temperatures below 260 K for R-12. Hence revised sonic velocity data for R-12 at 223–253 K were generated using their formula, Eq. (3), together with curve fits taken from DIPPR publication and with vapor-phase compressibility based on Redlich-Kwong equation of state. After replacing Zissis's data below 260 K, a marked improvement in the agreement with the present correlation is obtained as illustrated in Fig. 2. Also only data of $T_r < 0.9$ are shown together with the individual standard deviations for all five sets of data. The Zissis's subatmospheric water data which contain only two significant figures are also excluded in this figure.

As a further comparison the sonic velocity data for saturated steam ($x = 1$) are shown in Fig. 3 as a function of pressure. Equation (2) was used in conjunction with the ASME Steam Table (1967) to generate the sonic velocity data for steam ($x = 1.0$). Also shown are values taken from Fig. 12 of the 1967 ASME Steam Table—confirming the data thus generated are consistent. The present correlation predicts the data trend satisfactory and underpredicts the sonic velocity by only 1–2 percent up to 150 bar (at $T_r = 0.95$).

Comments on Equilibrium

Note that the assumption of equilibrium implies thermodynamic equilibrium phase change processes here and, as pointed out by Moody, should only be associated with decompressive disturbances, which drop the two-phase mixture into the saturation region, where equilibrium is more closely approached. On the other hand compressive disturbances momentarily drive the liquid phase into the subcooled region, and the vapor phase into the super-heated region; such a configuration is not conducive to heat and mass transfer processes required to achieve thermodynamic equilibrium. In the absence of any phase change, the scaling parameter as defined by Eq. (11) would reduce to

$$\omega = \frac{\alpha}{k} \tag{13}$$

where k is the specific heat ratio for the gas. This stems from the fact that the only remaining term in Eq. (5) is $x(dv_g/dP)_s$ and the isentropic process for the gas requires $P(v_g)^k = \text{constant}$.

The present correlation, Eq. (12), then becomes

$$c = \left(\frac{kP}{\alpha\rho}\right)^{1/2} \tag{14}$$

By ratioing this sonic velocity in a homogeneous mixture to that of the gas alone (i.e., at $\alpha = 1$, and $\rho = \rho_g$), and making the usual approximation that $\rho = (1 - \alpha)\rho_f$, we arrive at the well-known results (Wallis, 1969):

$$\frac{c}{c_g} = \left[\frac{\rho_g/\rho_f}{\alpha(1-\alpha)}\right]^{0.5} \tag{15}$$

Conclusion

The proposed scaling law and correlation for sonic velocity of a homogeneous equilibrium two-phase mixture is demonstrated to correlate previously published data to within 3% spanning the entire range of quality. The scaling parameter ω can be evaluated readily without any property derivatives involving temperature or pressure. Due to the imbedded simplifying assumptions ($dv_f/dP = 0$, $v_g \gg v_f$, $dh_{fg}/dT = 0$), this correlation is recommended for reduced temperature less than 0.9.

References

ASHRAE Handbook 1985 Fundamentals, 1985, p. 17.5, published by American Society of Heating, Refrigerating, and Air-Conditioning Engineers Inc.

ASME 1967 Steam Tables, 1967, "Thermodynamic and Transport Properties of Steam," published by the American Society of Mechanical Engineers, 2nd ed.

Design Institute for Physical Property Data, DIPPR Data Compilation, 1982, edited by T. E. Daubert and R. P. Danner, American Institute of Chemical Engineers Publication.

Hall, D. G., and Czapary, L. S., 1980, "Tables of Homogeneous Equilibrium Critical Flow Parameters for Water in SI Units," Report No. EGG-2056, EG&G Idaho Inc., Sept.

Landau, L. D., and Lifshitz, E. M., 1959, *Fluid Mechanics,* Vol. 6 of *Course of Theoretical Physics,* Trans. from Russia by Sykes, J. B. and Reid, W. H., Pergamon Press, pp. 248–249.

Leung, J. C., 1986, "A Generalized Correlation for One-Component Homogeneous Equilibrium Flashing Choked Flow," *American Institute of Chemical Engineers Journal,* Vol. 32(10), p. 1743.

Michaelides, E. E., and Zissis, K. L., 1983, "Velocity of Sound in Two-Phase Mixtures," *International Journal Heat & Fluid Flow,* Vol. 4, No. 2, pp. 79–84.

Moody, F. J., 1990, *Introduction to Unsteady Thermofluid Mechanics,* Chapter 2, John Wiley & Sons, pp. 72–75.

Reynolds, W. C., 1979, *Thermodynamic Properties in SI,* Dept. of Mechanical Engineering, Stanford University.

Wallis, G. B., 1969, *One-Dimensional Two-Phase Flow,* Chapter 2, p. 25, Chapter 6, p. 144, McGraw-Hill.

Zissis, K. L., 1982, "The Velocity of Sound in Two-Phase Mixtures," M.S. thesis, Dept. of Mechanical and Aerospace Engineering, University of Delaware.

Downloaded 03 Jun 2010 to 171.66.16.125. Redistribution subject to ASME license or copyright; see http://www.asme.org/terms/Terms_Use.cfm

Calculations of Wall Shear Stress in Harmonically Oscillated Turbulent Pipe Flow Using a Low-Reynolds-Number k-ϵ Model

J. O. Ismael

M. A. Cotton

School of Engineering,
University of Manchester,
Manchester M13 9PL, United Kingdom

The low-Reynolds-number k-ϵ turbulence model of Launder and Sharma is applied to the calculation of wall shear stress in spatially fully-developed turbulent pipe flow oscillated at small amplitudes. It is believed that the present study represents the first systematic evaluation of the turbulence closure under consideration over a wide range of frequency. Model results are well correlated in terms of the parameter $\omega^+ = \omega\nu/\bar{U}_\tau^2$ *at high frequencies, whereas at low frequencies there is an additional Reynolds number dependence. Comparison is made with the experimental data of Finnicum and Hanratty.*

Introduction

The present paper is concerned with the calculation of wall shear stress in fully-developed turbulent pipe flow in which the mass flow rate is oscillated harmonically about a mean value. The corresponding flow in the laminar regime can be treated analytically and has been considered in detail by Uchida (1956). In the turbulent regime, however, the problem is not amenable to direct analysis and the essential trends in the response of the wall shear stress have been revealed principally by experimental investigations undertaken in pipes (Ronneberger and Ahrens, 1977; Tu and Ramaprian, 1983; Mao and Hanratty 1986; Finnicum and Hanratty, 1988), channels (Binder et al., 1985; Tardu et al., 1994), and boundary layers (Cousteix and Houdeville, 1985). The main features of the observed response are, firstly, that the time-averaged value of the wall shear stress is little affected by pulsation. Secondly, the oscillations of wall shear stress, as characterized by the first harmonic phase and amplitude, appear to be reasonably well correlated by the non-dimensional frequency ω^+ $(=\omega\nu/\bar{U}_\tau^2$, where ω is the pulsation frequency, ν the kinematic viscosity and the friction velocity is formed from the time-average of the wall shear stress $(\bar{U}_\tau^2 = -\overline{\tau}_w/\rho))$. For low values of $\omega^+(\omega^+ \lesssim 0.001)$ an approximately "quasi-steady" response (instantaneously identical to steady flow at the same Reynolds number) is obtained. An increase in ω^+ causes the velocity field to respond in such a way that a "turbulent Stokes layer" is confined to progressively narrower near-wall regions (see Tu and Ramaprian, 1983). At sufficiently high values of $\omega^+(\omega^+ \gtrsim 0.05)$ this layer resides completely within the viscous sublayer so that the oscillations of velocity and therefore wall shear stress are effectively governed by unsteady laminar flow analysis. This behavior is termed "quasi-laminar." Between these limiting responses the oscillation of wall shear stress is observed to undergo a development whereby it exhibits a phase lead in advance of the bulk velocity which changes monotonically from the quasi-steady value of 0° to the quasi-laminar value of approximately 45°; the amplitude varies in a non-monotonic fashion, initially reducing below the quasi-steady value and subsequently asymptoting to quasi-laminar behavior.

In attempting to understand the behavior of wall shear stress in pulsatile flows, researchers have applied a range of turbulence models to the problem. Ronneberger and Ahrens (1977) and Mao and Hanratty (1986) found that Prandtl's mixing length hypothesis was unable to capture the measured behavior of the wall shear stress. In the same paper Mao and Hanratty reported more successful results obtained using modifications of the basic mixing length model intended to take account of the effect of rapidly-varying pressure gradient. The application of more advanced models of turbulence to this problem appears to have been restricted to the examination of individual cases: Blondeaux and Colombini (1985) and the present authors (Cotton and Ismael, 1991) applied two-equation models of the k-ω and k-ϵ type respectively to the calculation of two cases of periodic pipe flow over a cycle measured by Tu and Ramaprian (1983). Kebede et al. (1985) applied a Reynolds stress closure to the computation of the same data. Despite these studies, the extent to which such transport models of turbulence may be applied over a wide range of conditions remains unknown. The present work seeks to address this question by examining the ability of the low-Reynolds-number k-ϵ model of Launder and Sharma (1974) to reproduce experimental wall shear stress data for fully-developed harmonically pulsating pipe flow. Consideration is given to the behavior of the wall shear stress oscillation as characterized by the time-averaged value and first harmonic over a range of values of ω^+ which span conditions from the quasi-steady to quasi-laminar regimes.

Analysis

Model Formulation. Solution is obtained below for phase-averages of various flow quantities. In a flow oscillated periodically with fundamental radian frequency ω the phase-average of an instantaneous turbulent quantity $\hat{\phi}$ at phase position ωt is defined as

$$\langle\phi\rangle = \lim_{N\to\infty} \frac{1}{N} \sum_{n=0}^{N-1} \hat{\phi}(\omega t + 2\pi n) \qquad (1)$$

Consider now the pulsation of an incompressible fluid of density ρ and kinematic viscosity ν within a pipe of diameter

Contributed by the Fluids Engineering Division for publication in the JOURNAL OF FLUIDS ENGINEERING. Manuscript received by the Fluids Engineering Division April 21, 1994; revised manuscript received May 25, 1995. Associate Technical Editor: R. W. Metcalfe.

Copyright © 1996 by ASME

Downloaded 03 Jun 2010 to 171.66.16.125. Redistribution subject to ASME license or copyright; see http://www.asme.org/terms/Terms_Use.cfm

D. The flow is subjected to an oscillatory pressure gradient which causes the bulk velocity U_b to vary harmonically as

$$U_b = \bar{U}_b + \tilde{U}_b = \bar{U}_b + |U_b| \cos(\omega t) \tag{2}$$

where an overbar denotes a long time mean and a tilde denotes the phase-averaged departure from the mean. Attention is restricted to positions along the pipe sufficiently far downstream from the entry region for the flow to be considered spatially fully-developed. Under these conditions the axial momentum equation reads

$$\frac{\partial U}{\partial t} = -\frac{1}{\rho}\frac{dp}{dx} + \frac{1}{r}\frac{\partial}{\partial r}\left[r\left(\nu\frac{\partial U}{\partial r} - \langle uv\rangle\right)\right] \tag{3}$$

where velocity U, pressure gradient dp/dx and Reynolds stress $-\langle uv\rangle$ are phase-averages. U and $-\langle uv\rangle$ are functions of radial position and time, whereas the pressure gradient is a function of time only. Turbulent viscosity in periodic flow is here defined as the ratio of the phase-averages of Reynolds stress and velocity gradient such that the Reynolds stress appearing in Eq. (3) may be written

$$-\langle uv\rangle = \nu_t\frac{\partial U}{\partial r} \tag{4}$$

Equations (3) and (4) are solved subject to the constraint that the velocity should satisfy the overall continuity condition such that $U_b(t)$ is given by Eq. (2). Closure of these equations requires only that the turbulent viscosity ν_t be determined. In the present study ν_t is supplied by the low-Reynolds-number k-ϵ model of Launder and Sharma (1974). The model equations are written for phase-averaged turbulent kinetic energy k and the dissipation variable $\tilde{\epsilon}$ as follows:

$$\nu_t = C_\mu f_\mu\frac{k^2}{\tilde{\epsilon}} \tag{5}$$

$$\frac{\partial k}{\partial t} = \nu_t\left(\frac{\partial U}{\partial r}\right)^2 + \frac{1}{r}\frac{\partial}{\partial r}\left[r\left(\nu + \frac{\nu_t}{\sigma_k}\right)\frac{\partial k}{\partial r}\right] - (\tilde{\epsilon} + D_\epsilon) \tag{6}$$

$$\frac{\partial \tilde{\epsilon}}{\partial t} = C_{\epsilon 1}\frac{\tilde{\epsilon}}{k}\nu_t\left(\frac{\partial U}{\partial r}\right)^2 + \frac{1}{r}\frac{\partial}{\partial r}\left[r\left(\nu + \frac{\nu_t}{\sigma_\epsilon}\right)\frac{\partial \tilde{\epsilon}}{\partial r}\right] - C_{\epsilon 2}f_2\frac{\tilde{\epsilon}^2}{k} + 2\nu\nu_t\left(\frac{\partial^2 U}{\partial r^2}\right)^2 \tag{7}$$

$$f_\mu = e^{-3.4/(1+\mathrm{Re}_t/50)^2}$$

$$f_2 = 1 - 0.3e^{-\mathrm{Re}_t^2};\quad \mathrm{Re}_t = k^2/\nu\tilde{\epsilon}$$

where

$$D_\epsilon = \begin{cases} 2\nu(\partial\sqrt{k}/\partial y)^2 \text{ for } y^+_{\max} \geq 1.5 \\ 2\nu k/y^2 \text{ for } y^+_{\max} < 1.5 \end{cases}$$

$$C_\mu = 0.09;\quad \sigma_k = 1.0;\quad \sigma_\epsilon = 1.3;$$

$$C_{\epsilon 1} = 1.44;\quad C_{\epsilon 2} = 1.92. \tag{8}$$

The model equations are unchanged from those presented by Launder and Sharma with the exception that a "switch" is applied to alter D_ϵ from the published differential form to an algebraic form very close to the wall (Eq. (8): $y^+_{\max} = 1.5$ defines a wall distance $y = 1.5\ \nu/U_{\tau,\max}$ where the friction velocity is the maximum occurring over a quasi-steady cycle as calculated from the Blasius equation). This practice has been adopted to assist convergence of the discretized equation set. (Ismael, 1993a demonstrates that, in fact, neither definition of D_ϵ is consistent with the asymptotic quadratic variation of k in the limit $y \to 0$ when solution is obtained using a linear discretization scheme.) The closed set of equations, Eqs. (2) to (8), are solved numerically using a finite volume/finite difference method adapted from the PASSABLE scheme of Leschziner (1982). Full details of the solution method are given by Ismael (1993b). Considerable care has been taken to ensure that the results presented below are sensibly independent of the final numerical values assigned to various computational parameters and the authors have lodged a "Statement on Numerical Accuracy" with the *Journal of Fluids Engineering*.

Dimensional Analysis. The behavior of the flows considered depends on the dimensional quantities ρ, ν, D, $\bar{U}_b$, $|U_b|$ and ω. Dimensional analysis then gives the following independent groups:

$$\text{Reynolds number, } \overline{\mathrm{Re}} = \bar{U}_b D/\nu$$

$$\text{Strouhal number, } \omega D/\bar{U}_b$$

$$\text{relative amplitude, } \gamma = |U_b|/\bar{U}_b$$

In the most general case, all characteristics of the oscillation of wall shear stress, appropriately non-dimensionalized, will depend on these three groups. However, a more restricted framework in which to consider the dependence of quantities on the above groups exists if it is assumed that the deviation of the wall shear stress from the steady value at $\overline{\mathrm{Re}}$ responds linearly to oscillation of bulk velocity about its mean value. Thus, for the nominally positive quantity $-\tau_w$,

$$-\tau_w = -\tau_w(\overline{\mathrm{Re}}) - \Delta_\tau \tag{9}$$

and

$$-\Delta_\tau = A_0 + A_1\tilde{U}_b + A_2\frac{d\tilde{U}_b}{dt} + A_3\frac{d^2\tilde{U}_b}{dt^2} + \cdots \tag{10}$$

It follows formally that $-\bar{\Delta}_\tau = A_0$ so that $-\bar{\tau}_w = -\tau_w(\overline{\mathrm{Re}}) + A_0$. Now, in the limit of vanishingly small amplitude of pulsation ($\gamma \to 0$), $U_b \to \bar{U}_b$ and therefore $-\bar{\tau}_w \to -\tau_w(\mathrm{Re})$ and $\bar{\Delta}_\tau \to 0$. In other words, the true mean of the unsteady variation of the wall shear stress is the same as the value in steady flow at Re. It is then seen from Eq. (10) that Δ_τ is a pure harmonic with zero mean and that the decomposition of Eq. (9) may be rewritten as follows:

$$-\tau_w = -\bar{\tau}_w + |-\tau_w| \cos(\omega t + \phi) \tag{11}$$

where $-\bar{\tau}_w$, $|-\tau_w|$ and ϕ are the time-average, amplitude and phase of the oscillation of wall shear stress. It follows from Eq. (10) that, with $A_0 = 0$, the amplitude of the wall shear stress oscillation will vary linearly with the relative amplitude of the bulk velocity oscillation while the phase will be independent of γ. It is then possible to form the following non-dimensional quantities dependent on Reynolds number and Strouhal number:

$$-\bar{\tau}_w/\rho\bar{U}_b^2 = f_1(\overline{\mathrm{Re}})$$

$$|-\tau_w|/\gamma\rho\bar{U}_b^2 = f_2(\overline{\mathrm{Re}},\ \omega D/\bar{U}_b)$$

$$\phi = f_3(\overline{\mathrm{Re}},\ \omega D/\bar{U}_b) \tag{12}$$

The explicit dependence on the relative amplitude of pulsation is thus eliminated and the three parameter problem is reduced to one involving only two parameters.

In the present study attention is restricted to small amplitudes of pulsation ($\gamma \leq 0.2$) and results are analyzed initially in terms of the dependencies given in Eqs. (12).

Asymptotic Low and High Frequency Response. Following an approach pursued by Mao and Hanratty (1986), useful analytical expressions for the mean level, amplitude and phase of the wall shear stress oscillation may be obtained in the limits of low and high frequency.

Downloaded 03 Jun 2010 to 171.66.16.125. Redistribution subject to ASME license or copyright; see http://www.asme.org/terms/Terms_Use.cfm

At sufficiently low frequencies of oscillation, the variation of wall shear stress may be expected to follow the variation occurring under quasi-steady conditions. Expressions for $-\bar{\tau}_w/\rho\bar{U}_b^2$, $|-\tau_w|/\gamma\rho\bar{U}_b^2$ and ϕ may then be derived on the assumption of a power law variation of wall shear stress with bulk velocity (cf. the Blasius equation for friction coefficient). Thus, in the limit of very low frequencies we assume

$$c_f = -\tau_w/0.5\rho U_b^2 = \alpha\ \mathrm{Re}^m \tag{13}$$

(where in the Blasius equation $\alpha = 0.079$ and $m = -0.25$). It follows that

$$-\bar{\tau}_w/\rho\bar{U}_b^2 = 0.5\alpha\ \overline{\mathrm{Re}}^m$$

$$|-\tau_w|/\gamma\rho\bar{U}_b^2 = 0.5(m+2)\alpha\ \overline{\mathrm{Re}}^m$$

$$\phi = 0 \tag{14}$$

Values are required for the quasi-steady quantities of Eqs. (14) which are appropriate for comparison with the present unsteady computations. In order to provide such values for the time-averaged shear stress and oscillation amplitude, α and m are determined by fitting a function of the form of Eq. (13) to computed steady flow results using the method of least squares.

At high oscillation frequencies it is to be expected that the effects of oscillating shear will be confined to a near-wall Stokes layer. The present analysis pertains to the case in which the oscillation frequency is sufficiently high for the Stokes layer to lie completely within the viscous sublayer: neglecting curvature effects, the oscillation of velocity about the time-averaged profile is then determined from the following equation:

$$\frac{\partial\tilde{U}}{\partial t} = -\frac{1}{\rho}\frac{d\bar{p}}{dx} + \nu\frac{\partial^2\tilde{U}}{\partial y^2} \tag{15}$$

The amplitude and phase of the oscillation of the wall shear stress at high frequencies are obtained as

$$|-\tau_w|/\gamma\rho\bar{U}_b^2 = \frac{\sqrt{\omega\nu}}{\bar{U}_b} = (1/\overline{\mathrm{Re}} \times \omega D/\bar{U}_b)^{1/2}$$

$$\phi = 45^\circ \text{ (leading } U_b) \tag{16}$$

Derivations of Eqs. (14) and (16) are provided in greater detail by Ismael (1993b).

Results

Computational Conditions. The form of the functional dependence of the wall shear stress on $\overline{\mathrm{Re}}$ and $\omega D/\bar{U}_b$ as calculated using the present model is considered next. The behavior of these quantities is examined for $\overline{\mathrm{Re}} = 8 \times 10^3$, 2×10^4, 6×10^4 and 1×10^5 over a range of values of $\omega D/\bar{U}_b$ between those at which the limiting low frequency (quasi-steady) and high frequency (quasi-laminar) responses are approached. In each Reynolds number series of tests the only dimensional quantity varied is the frequency ω. Calculations are reported for 11 values of Strouhal number for each series; $\omega D/\bar{U}_b$ values for the individual tests are detailed in Table 1. All calculations are performed for $\gamma = 0.2$, a value which was found to be sufficiently small for the wall shear stress to oscillate approximately as a pure harmonic. (Quantitatively, the r.m.s. deviation of the computed oscillation of the wall shear stress from its first harmonic was found to be less than 5 percent of the amplitude of pulsation of the wall shear stress for all computations.)

Table 1 Strouhal number values for wall shear stress calculations. (An asterisk denotes the calculational points plotted on Figs. 6 and 7; all points are plotted on Figs. 1 to 5.)

Series 1 $\overline{\mathrm{Re}}=1\times10^5$	Series 2 $\overline{\mathrm{Re}}=6\times10^4$	Series 3 $\overline{\mathrm{Re}}=2\times10^4$	Series 4 $\overline{\mathrm{Re}}=8\times10^3$
22.22	13.50	5.278	2.365*
14.02	8.516	3.330	1.493*
8.847	5.373	2.101*	0.942*
5.582	3.390	1.326*	0.594*
3.522	2.139*	0.836*	0.375*
2.222	1.350*	0.528*	0.237*
1.402	0.852*	0.333*	0.149*
0.885	0.537*	0.210*	0.094*
0.558	0.339*	0.133*	0.059
0.352	0.214*	0.084*	0.037
0.222	0.135*	0.053	0.024

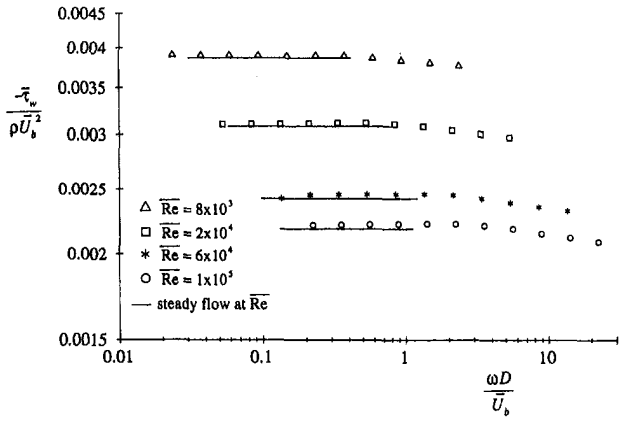


Fig. 1 Variation of time-averaged wall shear stress with Strouhal number

Strouhal Number Dependence of the Harmonic Wall Shear Stress Oscillation. Figure 1 examines the computed variation of $-\bar{\tau}_w/\rho\bar{U}_b^2$ as a function of Strouhal number for the four Reynolds number series. Comparison is made with the computed quasi-steady values given by Eq. (14). It is seen that the time-averaged values of oscillating wall shear stress do not differ greatly from the quasi-steady values over the range of conditions considered. The results do, however, indicate a slight reduction of approximately 5 percent at the highest Strouhal numbers examined.

Corresponding results for the amplitude of oscillation of the wall shear stress, normalized as $|-\tau_w|/\gamma\rho\bar{U}_b^2$, are shown in Fig. 2. Quasi-steady values of oscillation amplitude, given by Eq. (14), are indicated by chained lines at the lower end of the

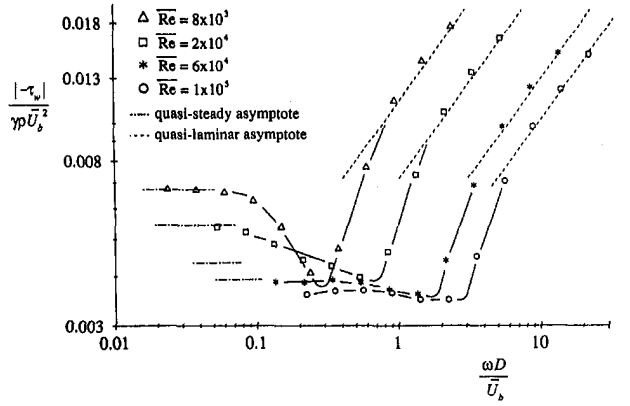


Fig. 2 Variation of the amplitude of wall shear stress with Strouhal number

Downloaded 03 Jun 2010 to 171.66.16.125. Redistribution subject to ASME license or copyright; see http://www.asme.org/terms/Terms_Use.cfm

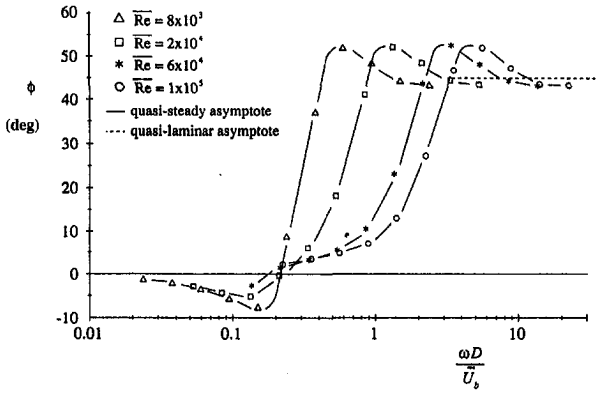


Fig. 3 Variation of the phase of wall shear stress with Strouhal number

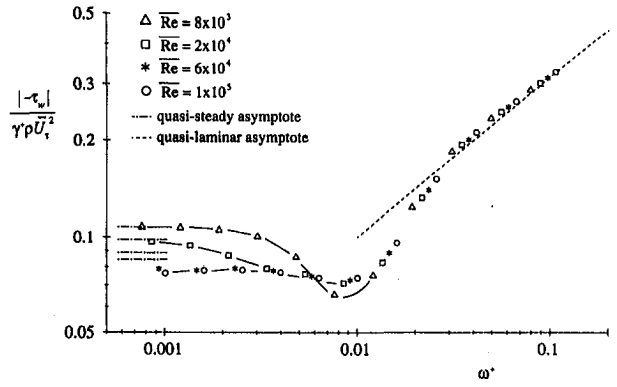


Fig. 4 Variation of the amplitude of wall shear stress with ω^+

Strouhal number axis. The quasi-laminar amplitude asymptote given by Eq. (16) may be rearranged to read

$$\log\left(|-\tau_w|/\gamma\rho\bar{U}_b^2\right) = -0.5\log\overline{\mathrm{Re}} + 0.5\log\left(\omega D/\bar{U}_b\right) \quad (17)$$

which represents a straight line on a logarithmic plot of amplitude versus Strouhal number. Lines given by Eq. (17) at each Reynolds number are shown at the higher frequency end of the Strouhal number axis (dashed lines). It is evident from Fig. 2 that present results span the Strouhal number range between quasi-steady and quasi-laminar oscillation. (However, at $\overline{\mathrm{Re}} = 6 \times 10^4$ and 1×10^5 the lowest Strouhal number calculations do differ from the quasi-steady value indicating that completely quasi-steady oscillation was not achieved over the range of Strouhal number of these calculations.) Between the two limiting responses the computed oscillation amplitude varies in a similar manner for different values of $\overline{\mathrm{Re}}$, however the curves are displaced relative to one another on the Strouhal number axis. There is an initial reduction in amplitude as the Strouhal number is increased from quasi-steady values followed by an increase towards the quasi-laminar asymptotes. The minimum in the oscillation amplitude is most pronounced at the lowest Reynolds number ($\overline{\mathrm{Re}} = 8 \times 10^3$) in which case the minimum is 60 percent of the quasi-steady value.

Results for the phase of the oscillation of wall shear stress are examined in Fig. 3. The quasi-steady and quasi-laminar values of 0 and 45 deg, respectively (Eqs. (14) and (16)) are also indicated. The calculated variation of oscillation phase follows a similar pattern for different Reynolds numbers and shows curves displaced relative to one another on the Strouhal number axis in a similar manner to the amplitude results of Fig. 2. Results for $\overline{\mathrm{Re}} = 8 \times 10^3$ and 2×10^4 at the lower end of the Strouhal number range lag the bulk velocity oscillation (results for $\overline{\mathrm{Re}} = 6 \times 10^4$ and 1×10^5 are limited to a higher Strouhal number range). At the higher end of the Strouhal number range results for all Reynolds number series exhibit similar behavior, first rising above the quasi-laminar phase lead of 45 deg by approximately 7 deg and then falling back toward the asymptote with increasing Strouhal number. Calculated results at the highest frequencies show a phase lead of approximately 2 deg below the quasi-laminar lead.

ω^+ Dependence of Amplitude and Phase Results. It was noted in the Introduction that experimental studies have indicated that frequency made dimensionless as $\omega^+ = \omega\nu/\bar{U}_\tau^2$ may be the principal similarity parameter correlating the phase and amplitude response of the wall shear stress oscillation. The extent to which present results can be correlated in terms of this parameter is examined below.

Amplitude results are considered first: Eq. (16) which governs the quasi-laminar oscillation of wall shear stress may be arranged into the following form:

$$|-\tau_w|/\gamma^+\rho\bar{U}_\tau^2 = \sqrt{\omega^+} \quad \text{where} \quad \gamma^+ = |U_b|/\bar{U}_\tau \quad (18)$$

Thus, for oscillation frequencies sufficiently high to give quasi-laminar oscillation the analysis indicates that a collapse of data should be obtained when $|-\tau_w|/\gamma^+\rho\bar{U}_\tau^2$ is plotted against ω^+. For oscillation frequencies sufficiently low to give quasi-steady oscillation, the following relation may be obtained from Eqs. (14) and (18):

$$|-\tau_w|/\gamma^+\rho\bar{U}_\tau^2 = (m+2)(0.5\alpha)^{1/2}\,\overline{\mathrm{Re}}^{m/2} \quad (19)$$

In view of the explicit appearance of Reynolds number on the right of Eq. (19), a complete collapse of amplitude data plotted as $|-\tau_w|/\gamma^+\rho\bar{U}_\tau^2$ against ω^+ cannot be expected at quasi-steady frequencies.

Figure 4 examines the dependence of $|-\tau_w|/\gamma^+\rho\bar{U}_\tau^2$ on ω^+ as computed by the present model. It can be seen that a collapse of results is obtained at high ω^+ values in accordance with Eq. (18). At low values of ω^+ the results exhibit some Reynolds number dependence as indicated by Eq. (19). In between these two limiting responses a collapse of data is obtained, the collapse extending over a progressively greater ω^+ range as $\overline{\mathrm{Re}}$ is increased.

The phase of the oscillation of wall shear stress is plotted as a function of ω^+ in Fig. 5. It is again evident that a collapse of the results extends over progressively greater ω^+ ranges as $\overline{\mathrm{Re}}$ is increased. Thus, the suggestion that phase and amplitude results may be correlated in terms of ω^+ is supported by the present model, at least at higher values of ω^+ and more particularly at higher Reynolds number.

Comparison With the Data of Finnicum and Hanratty and Remarks on Flow Profiles. Comparison is next made between the present computations and experimental data re-

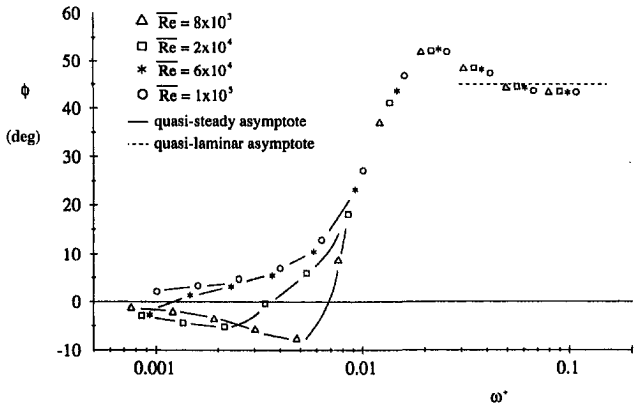


Fig. 5 Variation of the phase of wall shear stress with ω^+

Downloaded 03 Jun 2010 to 171.66.16.125. Redistribution subject to ASME license or copyright; see http://www.asme.org/terms/Terms_Use.cfm

ported by Finnicum and Hanratty (1988). The data were obtained for harmonically oscillated flow of water in a pipe of diameter $D = 0.0508$ m at small amplitudes of bulk velocity oscillation. Test conditions spanned the ranges $8650 < \overline{\mathrm{Re}} < 44900$ and $0.2\ \mathrm{Hz} < f < 1.5\ \mathrm{Hz}$ corresponding to a maximum possible Strouhal number range of $0.07 < \omega D/\bar{U}_b < 2.8$. Present results used in comparison with the data of Finnicum and Hanratty are marked by an asterisk in Table 1. These selected calculations span the Reynolds number range of the data and lie within the maximum possible Stouhal number range. (Note that experimental conditions for individual data points are not matched.) Furthermore, it should be noted that the experiments of Finnicum and Hanratty were carried out for a fixed fractional amplitude of center-line velocity oscillation equal to 10 percent and differ in this respect from the conditions of the present calculations which were for a constant fractional amplitude of bulk velocity oscillation equal to 20 percent. The normalization of data employed can, however, be expected to largely eliminate any dependence on pulsation amplitude for small amplitudes of pulsation.

Comparisons with the amplitude and phase data reported by Finnicum and Hanratty are shown in Figs. 6 and 7, respectively. Amplitude data are normalized, following Finnicum and Hanratty, as $|-\tau_w|/\gamma^+\rho\bar{U}_\tau^2$ where γ^+ is now defined alternatively in terms of the amplitude of pulsation of the center-line velocity, $|U_c|$, as $\gamma^+ = |U_c|/\bar{U}_\tau$. The presentation of phase results also differs from that used previously in the respect that the results indicate leads relative to $-dp/dx$ (the negative values obtained indicating lags). Phase and amplitude results are plotted against ω^+ from which it is evident that a reasonable collapse of results is obtained over the parameter range considered. The quasi-laminar amplitude and phase asymptotes are also shown in the figures and are seen to be in fair agreement with both calculations and data at high frequencies of oscillation.

The main conclusion to be drawn from these comparisons is that the Launder and Sharma model does quite reliably capture the variation of wall shear stress amplitude and phase for small amplitude pulsation. The only significant discrepancy between the present computations and data occurs as the quasi-laminar phase asymptote is approached where the calculated overshoot of the quasi-laminar value is not supported by experimental evidence (Fig. 7).

Significant Reynolds stress profile distortions across the pipe radius were measured by Tu and Ramaprian (1983) and Burnel et al. (1990) for values of ω^+ equal to approximately 0.0013 and 0.0011, respectively (slightly above the approximate upper frequency limit for quasi-steady response of the wall shear stress). In confirmation of the generally satisfactory performance of the Launder and Sharma model reported here, Cotton and Ismael (1991) found acceptably close agreement between the model and the two sets of measurements. At frequencies

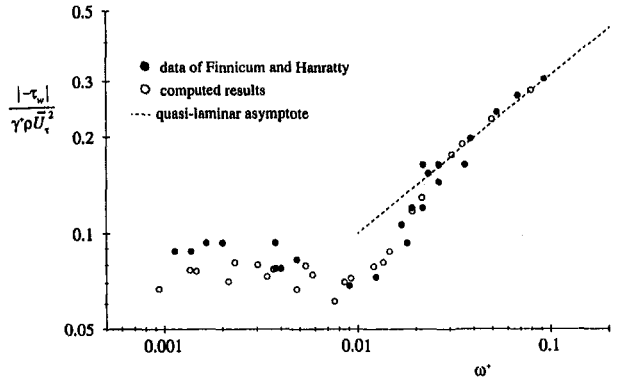


Fig. 6 Comparison of the calculated amplitude of wall shear stress with the data of Finnicum and Hanratty

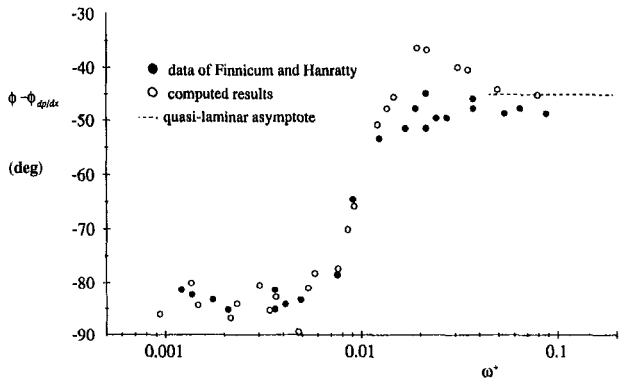


Fig. 7 Comparison of the calculated phase of wall shear stress with the data of Finnicum and Hanratty

between those associated with the limiting responses (Tu and Ramaprian's data for $\omega^+ \simeq 0.009$ and the data of Burnel et al. for $\omega^+ \simeq 0.012$) comparisons with data indicated that the principal features of the Reynolds stress profiles measured by Burnel et al. were resolved, whereas poor agreement was obtained between the Launder and Sharma model and the data of Tu and Ramaprian. It is believed, however, that the indirect measurement technique employed by Tu and Ramaprian is the major cause of these latter discrepancies (Cotton and Ismael, 1991, Ismael, 1993b).

Conclusions

The foregoing results serve to indicate that the low-Reynolds-number k-ϵ model of Launder and Sharma can reproduce the oscillation of wall shear stress in periodic flow over a wide range of conditions. It should be borne in mind, however, that in the limit of quasi-laminar oscillation ($\omega^+ \gtrsim 0.05$) the details of a turbulence model are not critical to the calculation of the wall shear stress. Also, in the limit of quasi-steady oscillation ($\omega^+ \lesssim 0.001$) a model capable of computing wall shear stress in steady flow will continue to give the correct behavior. That the behavior is reasonably well captured in the region ($0.001 \lesssim \omega^+ \lesssim 0.05$) is, however, significant because over this range of conditions the unsteady dynamics of turbulence have an important influence on the oscillation of wall shear stress.

References

Binder, G., Tardu, S., Blackwelder, R. F., and Kueny, J. L., 1985, "Large Amplitude Periodic Oscillations in the Wall Region of a Turbulent Channel Flow," *Proc. 5th Symposium on Turbulent Shear Flows,* Cornell University, Ithaca, NY.

Blondeaux, P., and Colombini, M., 1985, "Pulsatile Turbulent Pipe Flow," *Proc. 5th Symposium on Turbulent Shear Flows,* Cornell University, Ithaca, NY.

Burnel, S., Raelison, J. C., and Thomas, J. M., 1990, "Radial Distribution of the Reynolds Stress in a Turbulent Pulsating Flow in a Pipe," *Engineering Turbulence Modelling and Experiments,* (Rodi, W., and Ganic, E. N., eds.), Elsevier, New York, pp. 419–427.

Cotton, M. A., and Ismael, J. O., 1991, "An Examination of Periodic Turbulent Pipe Flow Using a Low-Reynolds-Number k-ϵ Turbulence Model," *Proc. 8th Symposium on Turbulent Shear Flows,* Technical University of Munich, Germany.

Cousteix, J., and Houdeville, R., 1985, "Turbulence and Skin Friction Evolutions in an Oscillating Boundary Layer," *Proc. 5th Symposium on Turbulent Shear Flows,* Cornell University, Ithaca, NY.

Finnicum, D. S., and Hanratty, T. J., 1988, "Influence of Imposed Flow Oscillations on Turbulence," *Physico-Chemical Hydrodynamics,* Vol. 10, pp. 585–598.

Ismael, J. O., 1993a, "Discretization of the Generic Transport Equation at the Near-Wall Control Volume Using a Quadratic Approximation to the Near-Wall Derivative," School of Engineering, University of Manchester.

Ismael, J. O., 1993b, "Theoretical Studies of Unsteady Turbulent Pipe Flow," Ph.D thesis, University of Manchester.

Kebede, W., Launder, B. E., and Younis, B. A., 1985, "Large-Amplitude Periodic Pipe Flow: A Second Moment Closure Study," *Proc. 5th Symposium on Turbulent Shear Flows,* Cornell University, Ithaca, NY.

Launder, B. E., and Sharma, B. I., 1974, "Application of the Energy Dissipation Model of Turbulence to the Calculation of Flow Near a Spinning Disc," *Lett. Heat Mass Transfer,* Vol. 1, pp. 131–138.

Downloaded 03 Jun 2010 to 171.66.16.125. Redistribution subject to ASME license or copyright; see http://www.asme.org/terms/Terms_Use.cfm

Leschziner, M. A., 1982, "An Introduction and Guide to the Computer Code PASSABLE," Dept. Mech. Eng., University of Manchester Institute of Science and Technology.

Mao, Z-X., and Hanratty, T. J., 1986, "Studies of the Wall Stress in a Turbulent Pulsating Pipe Flow," *J. Fluid Mech.,* Vol. 170, pp. 545–564.

Ronneberger, D., and Ahrens, C. D., 1977, "Wall Shear Stress Caused by Small Amplitude Perturbations of Turbulent Boundary-Layer Flow: An Experimental Investigation," *J. Fluid Mech.,* Vol. 83, pp. 433–464.

Tardu, S., Binder, G., and Blackwelder, R. F., 1994, "Turbulent Channel Flow with Large-Amplitude Velocity Oscillations," *J. Fluid Mech.,* Vol. 267, pp. 109–151.

Tu, S. W., and Ramaprian, B. R., 1983, "Fully Developed Periodic Turbulent Pipe Flow. Part 1: Main Experimental Results and Comparisons with Predictions. Part 2: The Detailed Structure of the Flow," *J. Fluid Mech.,* Vol. 137, pp. 31–81.

Uchida, S., 1956, "The Pulsating Viscous Flow Superposed on the Steady Laminar Motion of Incompressible Fluid in a Circular Pipe," *ZAMP,* Vol. 7, pp. 403–422.

Downloaded 03 Jun 2010 to 171.66.16.125. Redistribution subject to ASME license or copyright; see http://www.asme.org/terms/Terms_Use.cfm

Journal of Fluids Engineering

Technical Briefs

An Experimental Investigation of Buoyant Transient Cavity Collapse Near Rigid Cylindrical Boundaries

J. P. Best,[1] W. K. Soh,[2] and C. F. Yu[2]

An experimental investigation was carried out upon spark discharge generated transient cavities undergoing motion in the neighborhood of a rigid cylinder, in order to investigate the interaction between the Bjerknes attraction of the rigid cylinder and the buoyancy force. It was found that upon collapse, the direction of migration and liquid jet formation occurs at a characteristic angle. The experimental observations support the postulate that the direction of the Kelvin impulse at collapse bears close correlation with the direction of migration and jet formation.

1 Introduction

The collapse of transient cavities near surfaces has received considerable attention due to the destructive nature of this process. Experimental studies involving kinetic impulse, spark discharge or laser generated bubbles and high speed photography are commonplace (Benjamin and Ellis, 1966; Gibson, 1968; Kling and Hammitt, 1972; Lauterborn and Bolle, 1975; Tomita and Shima, 1986; Vogel et al., 1989). The particular feature of the collapse event that has caused this interest is the formation of a liquid jet directed toward the boundary. Indeed, the experiments of Tomita and Shima (1986) demonstrated the pitting of a soft boundary material by microjet impact. This jetting behavior is also exhibited during the collapse of the bubble caused by an underwater explosion (Wilkerson, 1989), the fluid dynamics of this phenomenon being very similar to that of cavitation.

Theoretical investigations have been conducted in parallel with these studies, and boundary integral methods utilized upon assumption of ideal fluid flow (Guerri et al., 1981; Blake et al., 1986, 1987; Chahine and Perdue, 1988; Wilkerson, 1989; Best and Kucera, 1992; Best, 1993). Of relevance to this paper are the calculations of buoyant transient cavity collapse above a plane rigid boundary presented by Blake et al. (1986), and particularly those illustrated by Fig. 5 of that paper. In this flow field geometry, the Bjerknes attraction of the boundary which tends to cause jet formation toward it, and the buoyancy force which tends to cause jet formation upwards, act in opposition. The calculations reveal two regimes: that in which buoyancy is dominant and the jet forms upwards, and that in which the Bjerknes attraction of the rigid boundary is dominant and the jet forms downwards. The calculations also reveal a transition zone between these regimes, where very weak jetting is evident. In order to provide an elementary classification of this behavior, Blake et al. (1986) invoked the concept of the Kelvin impulse and proposed that the direction of jet formation upon collapse should be closely correlated with the direction of the Kelvin impulse at the time of collapse. Recently, Best and Blake (1994) have presented a general theory for approximating the Kelvin impulse of a transient cavity in quite general flow field geometries, including those that are fully three dimensional.

In this paper, the Kelvin impulse theory is reviewed and its applicability investigated experimentally. A spark discharge method was used to generate transient cavities near a rigid cylindrical body and the collapse behavior recorded using high speed photography. The theory of Best and Blake (1994) is used to estimate the direction of the Kelvin impulse at the time of collapse and good agreement is found with the direction of liquid jet formation.

2 The Kelvin Impulse

The Kelvin impulse of a transient cavity may be introduced in the context of ideal fluid flow described by a velocity potential ϕ, and is defined as

$$\mathbf{I} = \rho \oint_S \phi \mathbf{n} dS, \tag{1}$$

where ρ is the fluid density, S is the bubble surface, and $\mathbf{n}$ is the normal to S, directed interior to the bubble. The velocity potential is chosen so that the fluid velocity is $\mathbf{u} = \nabla\phi$. Physically, the Kelvin impulse is the impulse that would have to be applied over the surface of the bubble in order to generate the observed flow field from rest. This physical interpretation has motivated application of the Kelvin impulse in characterising the behaviour of transient cavities upon collapse. Considering a cavity pierced by a liquid jet upon collapse, it is physically plausible to suppose that to generate such a flow field from rest would require application of an impulse in a direction closely correlated with the jet direction. Axisymmetric calculations of jet formation (Blake et al., 1986, 1987) are in accord with this hypothesis, with the theory for obtaining analytical estimates of the Kelvin impulse of a transient cavity in simple flow geometries developed by Blake and his collaborators (Blake and Cerone, 1982; Blake et al., 1986, 1987).

Fully three-dimensional flow geometries are addressed in this paper and the consideration motivated by the general theory for

[1] Senior Research Scientist, Aeronautical and Maritime Research Laboratory (AMRL)-DSTO, P.O. Box 4331, Melbourne, VIC, 3001, Australia.

[2] Senior Lecturer and Research Fellow, respectively, Department of Mechanical Engineering, University of Wollongong, Northfields Ave., Wollongong, NSW, 2522, Australia. The present address of Dr. Yu is: Department of Mechanical and Production Engineering, National University of Singapore, Singapore.

Contributed by the Fluids Engineering Division of THE AMERICAN SOCIETY OF MECHANICAL ENGINEERS. Manuscript received by the Fluids Engineering Division February 8, 1995; revised manuscript received September 21, 1995. Associate Technical Editor: O. C. Jones.

Copyright © 1996 by ASME

Downloaded 03 Jun 2010 to 171.66.16.125. Redistribution subject to ASME license or copyright; see http://www.asme.org/terms/Terms_Use.cfm

Table 1 Values of the complete Beta function appearing in Eqs. (3)-(5)

B (11/6, 1/2)	1.400	B (13/6, 1/2)	1.275
B (7/6, 3/2)	0.546	B (3/2, 3/2)	0.393
B (5/6, 1/2)	2.241	B (7/6, 1/2)	1.821

approximating the Kelvin impulse of a transient cavity, given recently by Best and Blake (1994). This theory permits estimates of the Kelvin impulse to be routinely made in complex flow geometries. It is pertinent to review the key elements of that theory.

To approximate the Kelvin impulse, Best and Blake assume that for much of the cavity life its velocity potential may be approximated by a source at the point of inception, along with images of this source such that appropriate boundary conditions are satisfied at surfaces of the flow domain, excluding the bubble surface, which are denoted by Σ. Expressions may then be derived for the Kelvin impulse and bubble lifetime. For convenience, the following impulse and time scales are introduced:

$$I_{sc} = R_m^3(\rho\Delta p)^{1/2}, \quad T_{sc} = R_m(\rho/\Delta p)^{1/2}, \tag{2}$$

where R_m is the maximum bubble radius and $\Delta p = p_\infty - p_c$, with p_∞ the hydrostatic pressure where cavity inception occurs and p_c is the vapor pressure exerted by the bubble contents and assumed to be constant. In analyzing the experiments performed here, p_c is taken to be the vapor pressure of the water at its ambient temperature. The contributions to the final Kelvin impulse due to buoyancy and nearby boundaries are, respectively, denoted by $\mathbf{I}^g$ and $\mathbf{I}^\Sigma$ and given by

$$\mathbf{I}^g(T) = (4\sqrt{6}\pi/9)\delta^2[B(11/6, 1/2) + (1/2)\mu B(13/6, 1/2)]\mathbf{e}_z \tag{3}$$

and

$$\mathbf{I}^\Sigma(T) = (2\sqrt{6}\pi/9)\boldsymbol{\Gamma}[B(7/6, 3/2) - (1/2)\mu B(3/2, 3/2)], \tag{4}$$

where T is the nondimensional period of the bubble given as

$$T = (2/\sqrt{6})[B(5/6, 1/2) + (1/2)\mu B(7/6, 1/2)]. \tag{5}$$

The total Kelvin impulse is equal to $\mathbf{I}^g + \mathbf{I}^\Sigma$. In these expressions δ is the buoyancy parameter given by

$$\delta = (\rho g R_m/\Delta p)^{1/2}, \tag{6}$$

with g the gravitational acceleration and $\mathbf{e}_z$ is a unit vector in the vertical direction. $B(x, y)$ is a complete Beta function (Abramowitz and Stegun, 1965) and the relevant values are listed in Table 1. In (3)–(5) μ is a constant and $\boldsymbol{\Gamma}$ a constant vector that depend solely upon the geometry of the flow domain. For simple geometries, such as plane boundaries and spheres, image theory can be used to calculate these constants analytically. For more general cases, such as collapse near a cylinder considered here, a numerical approach is required and that utilized is described in detail by Best and Blake (1994).

Best and Blake (1994) considered in their paper the examples of transient cavity collapse near a spherical body and also a prolate spheroid, the latter example motivated by the problem of underwater explosion bubble collapse near marine vessels. In the context of these examples, the concept of a zone of attraction surrounding the body has been introduced. Throughout the bubble motion, the buoyancy force tends to cause jet formation upwards, whereas the Bjerknes attraction of the rigid body tends to cause jet formation toward it. These influences combine to cause a final Kelvin impulse in some well defined direction. In some circumstances this direction is toward the body, and in others it is away. The region from which the final Kelvin impulse is directed towards the body is termed the zone of attraction. Based upon the postulate that the final Kelvin impulse of the cavity is closely correlated with the jet direction, Best and Blake inferred that the jetting behavior would correlate with this behavior of the Kelvin impulse.

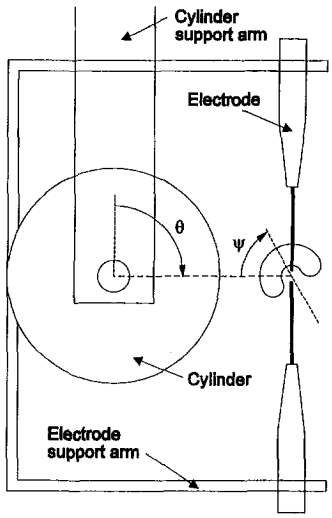


Fig. 1 Schematic representation of the integrated cylindrical target—electrode apparatus. The orientation of the inception point is θ measured with respect to the vertical and the jet direction is ψ measured with respect to the horizontal.

3 Experimental Method

The bubbles studied in this experiment were generated using the spark discharge technique described by Gibson (1968). This technique utilizes electric current at high potential difference to create a thermal impulse which causes inception of a vapor bubble in a very short time. All experiments were conducted using distilled water and at reduced pressure, in order to increase the size and lifetime of the bubbles generated. The experimental facility consists of a large rectangular prism tank with internal dimensions 1 m × 1 m × 1.2 m, which allows placement of targets of various sizes and geometries. The water is contained in an inner perspex tank, which itself is contained in a steel outer shell. Portholes of 400 mm diameter on the four vertical sides of the tank facilitate photography of the bubble motion event. The bubble was created by the discharge either of an 8.3 μF capacitor charged to 8 kV or a 1.0 μF capacitor charged to 10 kV. The pressure in the tank was reduced to between 21 kPa and 27 kPa with an uncertainty of ±0.25 kPa in the pressure measurement. In this regime, bubbles with maximum radii in the range 11 mm–43 mm were generated. The cylindrical target is 315 mm in length, with a diameter of 110 mm.

A significant feature of this experiment is the construction of the cylindrical target and electrode apparatus as shown in Fig 1. The electrodes and cylinder are integrated so that the cylinder may be rotated to give inception at the required orientation, θ, to the vertical, measured as shown in the figure. For the purposes of this investigation the direction of the final Kelvin impulse is measured with respect to a horizontal axis directed from the inception point towards the cylinder. This angle is denoted by ψ and the convention for its definition is illustrated in Fig. 1. Since the only horizontal component of the Bjerknes force is directed toward the cylinder, ψ lies between −90 and 90 deg. In addition to being able to vary the orientation of the inception point, the standoff of the inception point from the cylinder may also be adjusted. Furthermore, the manner in which the electrodes are arranged ensures that they do not significantly obscure observation of the bubble collapse event.

Downloaded 03 Jun 2010 to 171.66.16.125. Redistribution subject to ASME license or copyright; see http://www.asme.org/terms/Terms_Use.cfm

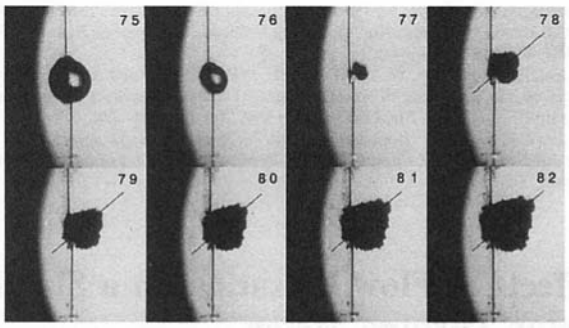


Fig. 2 Cavity collapse and rebound adjacent to a rigid cylinder located to the right of the bubble and out of frame. The rear porthole of the tank is visible to the left of each frame. The standoff is 70 mm and the maximum bubble radius is 35 mm. The time interval between frames is 0.168 ms. Inception occurs at $\theta = 90$ deg and outside the zone of attraction. The direction of jet formation does not intersect the cylinder.

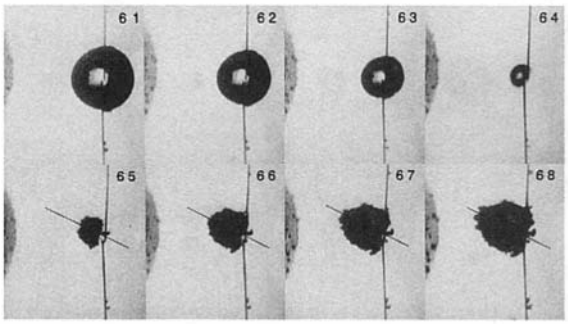


Fig. 3 Cavity collapse and rebound adjacent to a rigid cylinder located to the left of the bubble. The standoff is 58 mm and the maximum bubble radius is 31 mm. The time interval between frames is 0.169 ms. Inception occurs at $\theta = 90$ deg and close to the boundary of the zone of attraction. The direction of jet formation approximately intersects the boundary of the cylinder.

The bubble was illuminated using continuous diffuse backlighting in order that a well-defined silhouette of the bubble was recorded on the cine film. The event was filmed using a NAC model E-10 high speed cine camera operating at nearly 6000 frames per second (fps). To obtain the necessary experimental data, the film record of the bubble motion event was digitally analysed to determine bubble shape profiles. Initiation of the bubble is evident by the film (negative) being blacked out due to the high intensity light emitted by the spark discharge. Since initiation of the bubble may have occurred anywhere within the time interval between successive frames, zero time for the event is taken to be halfway between this frame and the preceding one, with an absolute error of $\pm\delta t/2$, with δt the time interval between frames. For bubble motion near the cylindrical target, it is not possible to precisely determine the volume from the bubble profile, due to the three dimensional character of the flow field. Under these circumstances the area of the profile was used to determine an equivalent radius and the maximum over all frames taken to well approximate the maximum bubble radius. This should give an accurate estimate since the cine film records indicate that the bubble remains close to spherical in shape during its first expansion.

4 Experimental Results

The collapse and rebound of a cavity whose inception point is at $\theta = 90$ deg to the vertical is shown in Fig. 2 with the experimental data describing this example recorded in Table 2. The edge of the rear porthole of the tank can be seen in the left hand side of each frame. The cylindrical target is not shown but is located to the right of each frame. After the collapse depicted in the first two frames the bubble rebounds. This phase is characterized by instability of the bubble surface which appears to cause formation of many small bubbles. These are swept along by the flow caused by the bubble collapse and jet formation processes and are a valuable aid in visualization of the flow. The early rebound is characterized by an elongation of the bubble along a characteristic direction, with the bubble exhibiting a pointed shape in the direction of jet formation. This direction arises from the interaction of the buoyancy force, tending to cause jet formation upwards, and the Bjerknes attraction of the rigid cylinder, tending to cause jet formation toward it. The theoretical estimate of the direction of the final Kelvin impulse in this case is 40 deg as indicated by the line drawn on the figure. This direction approximates closely the direction of jet formation upon collapse. Furthermore, the collapse geometry is such that the final impulse direction does not intersect the cylinder, so this example illustrates cavity inception outside the zone of attraction.

The next example is shown in Fig. 3. Notice in this case that inception occurs on the opposite side of the cylinder but still at $\theta = 90$ deg to the vertical. The character of the collapse is similar to the previous case with instability of the bubble surface evident after rebound from frame 65 onwards. The bubble is elongated along a characteristic direction which is identified as the direction of jet formation. Inception here occurs closer to the cylinder, which is relatively larger than the bubble, compared to the previous case. Furthermore, the buoyancy force, as characterized by the buoyancy parameter, is less. Consequently, the Bjerknes force dominates the buoyancy force and yields a theoretical prediction of the final Kelvin impulse direction as 26 deg. The photographic record indicates excellent agreement. This example illustrates a case where the direction of jet formation is approximately tangential with the cylinder. Inception would here be considered to have taken place around the boundary of the zone of attraction.

The final example is shown in Fig. 4 with inception occurring at an even smaller standoff, and consequently greater Bjerknes force. In this case the cylinder is located on the left-hand side of the bubble and inception occurs at $\theta = 90$ deg. The buoyancy force is slightly larger than in the previous example, however the Bjerknes force is clearly dominant. Although a jet tip is not clearly seen, the motion of the center of volume of the bubble is in accordance with the direction of 15 deg predicted by the Kelvin impulse theory. Furthermore, a feature of the surface instability often evident upon rebound is the formation of a collection of micro bubbles at the rear of the jet, this phenomenon having been documented elsewhere, particularly in a number of the experimental records of Vogel et al. (1989). In this example, the collection of micro bubbles at the rear of the large bubble becomes evident from frame 74 and defines a direction consistent with that predicted by the Kelvin impulse theory. In

Table 2 Experimental data for the bubble motion events illustrated in Figs. 2-4

Figure	R_m mm	Standoff mm	Period msec	δ	p_∞ kPa	p_c kPa	Water temperature °C
2	35	70	13	0.12	25.2	1.6	14
3	31	58	11	0.10	29.3	1.5	13
4	34	47	12	0.11	29.2	1.7	15

Downloaded 03 Jun 2010 to 171.66.16.125. Redistribution subject to ASME license or copyright; see http://www.asme.org/terms/Terms_Use.cfm

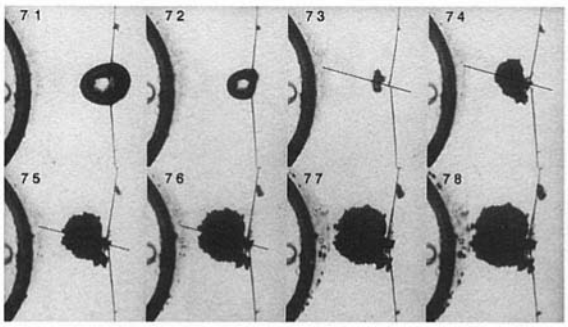


Fig. 4 Cavity collapse and rebound adjacent to a rigid cylinder located to the left of the bubble. The standoff is 47 mm and the maximum bubble radius is 34 mm. The time interval between frames is 0.168 ms. Inception occurs at $\theta = 90$ deg and inside the zone of attraction. The direction of jet formation clearly intersects the cylinder.

this example the direction of migration and jet formation clearly intersects the cylinder and thus illustrates inception inside the zone of attraction.

Other examples for inception at different orientations θ, with differing standoffs and bubble radii, showed similar good agreement between theory and experiment and demonstrate the validity of the zone of attraction concept and the value of the Kelvin impulse theory in quantitatively estimating the direction of jet formation upon the collapse of transient cavities.

Acknowledgments

The contribution of Mr. Darren Wiese, who carried out the digital image analysis, is gratefully acknowledged, as is the advice on high speed photography provided by Mr. Trevor Kinsey. The construction of the experimental apparatus was performed by the Department of Mechanical Engineering workshop at the University of Wollongong. These experiments were funded by the Aeronautical and Maritime Research Laboratory, Defence Science and Technology Organisation.

References

Abramowitz, M., and Stegun, I. A., 1965, *Handbook of Mathematical Functions,* Dover.

Benjamin, T. B., and Ellis, A. T., 1966, "The Collapse of Cavitation Bubbles and the Pressures Thereby Produced Against Solid Boundaries," *Philosophical Transactions of the Royal Society of London A,* Vol. 260, pp. 221–240.

Best, J. P., 1993, "The Formation of Toroidal Bubbles upon the Collapse of Transient Cavities," *Journal of Fluid Mechanics,* Vol. 251, pp. 79–107.

Best, J. P., and Blake, J. R., 1994, "An Estimate of the Kelvin Impulse of a Transient Cavity," *Journal of Fluid Mechanics,* Vol. 261, pp. 75–93.

Best, J. P., and Kucera, A., 1992, "A Numerical Investigation of Non-Spherical Rebounding Bubbles," *Journal of Fluid Mechanics,* Vol. 245, pp. 137–154.

Blake, J. R., and Cerone, P., 1982, "A Note on the Impulse Due to a Vapour Bubble Near a Boundary," *Journal of the Australian Mathematical Society Series B,* Vol. 23, pp. 383–93.

Blake, J. R., Taib, B. B., and Doherty, G., 1986, "Transient Cavities Near Boundaries. Part 1. Rigid Boundary," *Journal of Fluid Mechanics,* Vol. 170, pp. 479–497.

Blake, J. R., Taib, B. B., and Doherty, G., 1987, "Transient Cavities Near Boundaries. Part 2. Free Surface," *Journal of Fluid Mechanics,* Vol. 181, pp. 197–212.

Chahine, G. L., and Perdue, T. O., 1988, "Simulation of the Three-Dimensional Behaviour of an Unsteady Large Bubble Near a Structure," *Proceedings of the 3rd International Colloquium on Drops and Bubbles,* Monterey, CA.

Gibson, D. C., 1968, "Cavitation Adjacent to Plane Boundaries," *Proceedings of the 3rd Australasian Conference on Hydraulics and Fluid Mechanics,* Institution of Engineers, Sydney, pp. 210–214.

Guerri, L., Lucca, G., and Prosperetti, A., 1981, "A Numerical Method for the Dynamics of Non-Spherical Cavitation Bubbles," *Proceedings of the 2nd International Colloquium on Drops and Bubbles,* CA, pp. 175–181.

Kling, C. L., and Hammitt, F. G., 1972, "A Photographic Study of Spark-Induced Cavitation Bubble Collapse," ASME *Journal of Basic Engineering,* Vol. 94, pp. 825–833.

Lauterborn, W., and Bolle, H., 1975, "Experimental Investigations of Cavitation Bubble Collapse in the Neighbourhood of a Solid Boundary," *Journal of Fluid Mechanics,* Vol. 72, pp. 391–399.

Tomita, Y., and Shima, A., 1986, "Mechanisms of Impulsive Pressure Generation and Damage Pit Formation by Bubble Collapse," *Journal of Fluid Mechanics,* Vol. 169, pp. 535–564.

Vogel, A., Lauterborn, W., and Timm, R., 1989, "Optical and Acoustic Investigations of the Dynamics of Laser-Produced Cavitation Bubbles Near a Solid Boundary," *Journal of Fluid Mechanics,* Vol. 206, pp. 299–338.

Wilkerson, S., 1989, "Boundary Integral Technique for Explosion Bubble Collapse Analysis," *ASME Energy-Sources Technology Conference and Exhibition,* Houston, Texas.

Effects of Flow Pulsation on a Single-Rotor Turbine Meter

Wiktor M. Jungowski[1] and Marvin H. Weiss[1]

The effects of pulsating flow on a single-rotor turbine meter with a rotor response parameter greater than unity were investigated experimentally. Oscillating velocities and pressures at various pipe cross-sections were measured which enabled characterization of flow properties at the turbine meter and their effect on meter error. Measurements confirmed that meter error depends primarily on the velocity amplitude of the flow pulsation at the rotor. Moreover, it was shown that the velocity amplitude at the rotor results from the system response, which is determined by the system geometry, pulsation frequency, flow velocity, and sound speed. Lastly, a technique was developed to determine the meter error from measurements of dynamic pressure in the pipe upstream or downstream of the turbine meter.

Nomenclature

a = sound speed
C = correction coefficient
D = pipe diameter
D_1 = rotor response parameter
E = meter error
f = pulsation frequency
I = pulsation index, U_a/U_o
J = mass moment of inertia of rotor system
M = Mach number, U_o/a
Q_o = reference time average volume flow rate measured with the critical flow nozzle
Q_t = time average volume flow rate indicated by the turbine meter
r = radial distance
$\bar{r}$ = normalized radius, r/R
$\hat{r}$ = root mean square of r_i and r_o
r_i = hub (blade root) radius of the rotor
r_o = outer (blade tip) radius of rotor
R = pipe radius, $D/2$
Re = Reynolds number, $\rho U_o D/\mu$
St = Strouhal number, fD/U_o
U = flow velocity
$\bar{U}$ = normalized flow velocity, U/U_o
U_o = bulk velocity
x = axial distance along the pipe measured from the rotor midpoint

[1] Research Fellow (retired) and Research Scientist, respectively, Fluid Dynamics Group, Novacor Research & Technology Corporation, 2928-16th Street N.E., Calgary, Alberta, Canada T2E 7K7.

Contributed by the Fluids Engineering Division of THE AMERICAN SOCIETY OF MECHANICAL ENGINEERS. Manuscript received by the Fluids Engineering Division April 15, 1994; revised manuscript received August 15, 1995. Associate Technical Editor: H. Hashimoto.

Downloaded 03 Jun 2010 to 171.66.16.125. Redistribution subject to ASME license or copyright; see http://www.asme.org/terms/Terms_Use.cfm

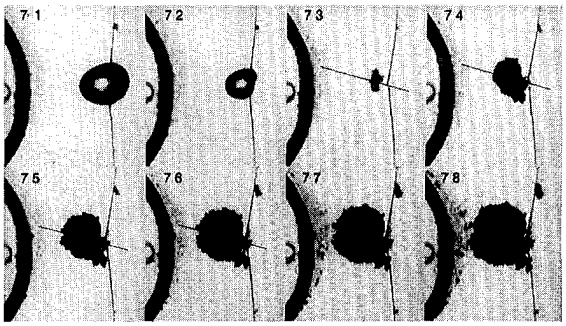


Fig. 4 Cavity collapse and rebound adjacent to a rigid cylinder located to the left of the bubble. The standoff is 47 mm and the maximum bubble radius is 34 mm. The time interval between frames is 0.168 ms. Inception occurs at $\theta = 90$ deg and inside the zone of attraction. The direction of jet formation clearly intersects the cylinder.

this example the direction of migration and jet formation clearly intersects the cylinder and thus illustrates inception inside the zone of attraction.

Other examples for inception at different orientations θ, with differing standoffs and bubble radii, showed similar good agreement between theory and experiment and demonstrate the validity of the zone of attraction concept and the value of the Kelvin impulse theory in quantitatively estimating the direction of jet formation upon the collapse of transient cavities.

Acknowledgments

The contribution of Mr. Darren Wiese, who carried out the digital image analysis, is gratefully acknowledged, as is the advice on high speed photography provided by Mr. Trevor Kinsey. The construction of the experimental apparatus was performed by the Department of Mechanical Engineering workshop at the University of Wollongong. These experiments were funded by the Aeronautical and Maritime Research Laboratory, Defence Science and Technology Organisation.

References

Abramowitz, M., and Stegun, I. A., 1965, *Handbook of Mathematical Functions,* Dover.

Benjamin, T. B., and Ellis, A. T., 1966, "The Collapse of Cavitation Bubbles and the Pressures Thereby Produced Against Solid Boundaries," *Philosophical Transactions of the Royal Society of London A,* Vol. 260, pp. 221–240.

Best, J. P., 1993, "The Formation of Toroidal Bubbles upon the Collapse of Transient Cavities," *Journal of Fluid Mechanics,* Vol. 251, pp. 79–107.

Best, J. P., and Blake, J. R., 1994, "An Estimate of the Kelvin Impulse of a Transient Cavity," *Journal of Fluid Mechanics,* Vol. 261, pp. 75–93.

Best, J. P., and Kucera, A., 1992, "A Numerical Investigation of Non-Spherical Rebounding Bubbles," *Journal of Fluid Mechanics,* Vol. 245, pp. 137–154.

Blake, J. R., and Cerone, P., 1982, "A Note on the Impulse Due to a Vapour Bubble Near a Boundary," *Journal of the Australian Mathematical Society Series B,* Vol. 23, pp. 383–93.

Blake, J. R., Taib, B. B., and Doherty, G., 1986, "Transient Cavities Near Boundaries. Part 1. Rigid Boundary," *Journal of Fluid Mechanics,* Vol. 170, pp. 479–497.

Blake, J. R., Taib, B. B., and Doherty, G., 1987, "Transient Cavities Near Boundaries. Part 2. Free Surface," *Journal of Fluid Mechanics,* Vol. 181, pp. 197–212.

Chahine, G. L., and Perdue, T. O., 1988, "Simulation of the Three-Dimensional Behaviour of an Unsteady Large Bubble Near a Structure," *Proceedings of the 3rd International Colloquium on Drops and Bubbles,* Monterey, CA.

Gibson, D. C., 1968, "Cavitation Adjacent to Plane Boundaries," *Proceedings of the 3rd Australasian Conference on Hydraulics and Fluid Mechanics,* Institution of Engineers, Sydney, pp. 210–214.

Guerri, L., Lucca, G., and Prosperetti, A., 1981, "A Numerical Method for the Dynamics of Non-Spherical Cavitation Bubbles," *Proceedings of the 2nd International Colloquium on Drops and Bubbles,* CA, pp. 175–181.

Kling, C. L., and Hammitt, F. G., 1972, "A Photographic Study of Spark-Induced Cavitation Bubble Collapse," ASME *Journal of Basic Engineering,* Vol. 94, pp. 825–833.

Lauterborn, W., and Bolle, H., 1975, "Experimental Investigations of Cavitation Bubble Collapse in the Neighbourhood of a Solid Boundary," *Journal of Fluid Mechanics,* Vol. 72, pp. 391–399.

Tomita, Y., and Shima, A., 1986, "Mechanisms of Impulsive Pressure Generation and Damage Pit Formation by Bubble Collapse," *Journal of Fluid Mechanics,* Vol. 169, pp. 535–564.

Vogel, A., Lauterborn, W., and Timm, R., 1989, "Optical and Acoustic Investigations of the Dynamics of Laser-Produced Cavitation Bubbles Near a Solid Boundary," *Journal of Fluid Mechanics,* Vol. 206, pp. 299–338.

Wilkerson, S., 1989, "Boundary Integral Technique for Explosion Bubble Collapse Analysis," *ASME Energy-Sources Technology Conference and Exhibition,* Houston, Texas.

Effects of Flow Pulsation on a Single-Rotor Turbine Meter

Wiktor M. Jungowski[1] and Marvin H. Weiss[1]

The effects of pulsating flow on a single-rotor turbine meter with a rotor response parameter greater than unity were investigated experimentally. Oscillating velocities and pressures at various pipe cross-sections were measured which enabled characterization of flow properties at the turbine meter and their effect on meter error. Measurements confirmed that meter error depends primarily on the velocity amplitude of the flow pulsation at the rotor. Moreover, it was shown that the velocity amplitude at the rotor results from the system response, which is determined by the system geometry, pulsation frequency, flow velocity, and sound speed. Lastly, a technique was developed to determine the meter error from measurements of dynamic pressure in the pipe upstream or downstream of the turbine meter.

Nomenclature

a = sound speed
C = correction coefficient
D = pipe diameter
D_1 = rotor response parameter
E = meter error
f = pulsation frequency
I = pulsation index, U_a/U_o
J = mass moment of inertia of rotor system
M = Mach number, U_o/a
Q_o = reference time average volume flow rate measured with the critical flow nozzle
Q_t = time average volume flow rate indicated by the turbine meter
r = radial distance
$\bar{r}$ = normalized radius, r/R
$\hat{r}$ = root mean square of r_i and r_o
r_i = hub (blade root) radius of the rotor
r_o = outer (blade tip) radius of rotor
R = pipe radius, $D/2$
Re = Reynolds number, $\rho U_o D/\mu$
St = Strouhal number, fD/U_o
U = flow velocity
$\bar{U}$ = normalized flow velocity, U/U_o
U_o = bulk velocity
x = axial distance along the pipe measured from the rotor midpoint

[1] Research Fellow (retired) and Research Scientist, respectively, Fluid Dynamics Group, Novacor Research & Technology Corporation, 2928-16th Street N.E., Calgary, Alberta, Canada T2E 7K7.

Contributed by the Fluids Engineering Division of THE AMERICAN SOCIETY OF MECHANICAL ENGINEERS. Manuscript received by the Fluids Engineering Division April 15, 1994; revised manuscript received August 15, 1995. Associate Technical Editor: H. Hashimoto.

Copyright © 1996 by ASME

Downloaded 03 Jun 2010 to 171.66.16.125. Redistribution subject to ASME license or copyright; see http://www.asme.org/terms/Terms_Use.cfm

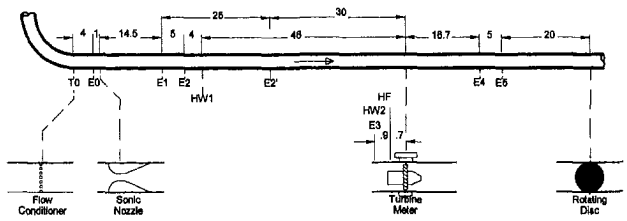


Fig. 1 Schematic of the test rig: E—pressure transducers; HF—hot-film sensor; HW—hot wire sensors; TO—temperature sensor; (dimensions are in terms of the pipe diameter).

α = curve-fit coefficient
η = flow deviation factor
μ = dynamic viscosity
ρ = density

Subscripts

a = amplitude
h = from hot-film measurement
m = time-mean
p = from pressure measurement
r = rms

Introduction

Turbine meters are widely used flow measurement devices for which theoretical models, based on the consideration of momentum or airfoil theory, have been developed to predict their performance. Furthermore, Haalman (1965) and Lee et al. (1975) have analyzed pulsating flow effects utilizing the momentum equation and have shown that periodic or pulsating flow will result in meter overspeeding, thus indicating a net positive error in the meter reading. This meter error depends primarily on the amplitude of the velocity pulsations and on the rotor response parameter D_1 defined by Lee et al. (1975) as:

$$D_1 = f\frac{(1+\eta)J}{\hat{r}^2\rho Q_o} \tag{1}$$

When the rotor response parameter is greater than unity, the speed fluctuations of the rotor are negligible—due to rotor inertia—and the error is manifested simply as a rotor overrun. In such a case, the error depends only on the velocity pulsation amplitude and wave form shape, and is essentially independent of the rotor response parameter (i.e., independent of frequency).

It is of considerable practical interest to be able to correct for pulsation errors in actual turbine meter installations. However, the most important parameter—the character of the velocity fluctuation at the meter—is difficult to measure in an industrial environment. Attempts have been made to determine the velocity pulsation amplitude and frequency directly from the modulation of the rotor blade-passing frequency and thus predict the error in meter reading (Atkinson, 1992; McKee, 1992). However, such an approach becomes increasingly difficult when the rotor response parameter is greater than unity and the rotor is no longer able to respond to velocity fluctuations.

The measurements in the present study were designed not only to determine the characteristic features of a pulsating flow at the rotor and its subsequent effect on the meter error, but also to determine the meter error based on measurements of the oscillating pressures in the piping upstream or downstream of the turbine meter.

Experimental Apparatus

For the investigation, a commercial 4 inch single-rotor turbine meter was connected to a Roots-type blower, which drew atmospheric air through the 4 in. piping (see Fig. 1 where distances are given in terms of the inside pipe diameter). The rotor of the turbine meter had 16 blades with a hub to blade-tip radius ratio $r_i/r_o = 0.72$ and a width of blade to blade-tip radius ratio of 0.21. A calibrated mass flow rate (± 0.5 percent) which did not vary with pulsations was obtained by locating a choked nozzle upstream of the turbine meter. Nozzles with throat diameters of 13, 19, 23 and 27 mm were used, thus providing flow velocities at the rotor ranging from 8.7 to 37.8 m/s. Flow pulsations in the frequency range 5 to 185 Hz were generated by a 4 inch rotating disk located downstream of the turbine meter. The amplitude of the generated pulsations were proportional to the flow velocity in the test section and could not be varied independently. In Table 1, the resulting ranges of several experimental parameters are given. Radial distributions of the mean and rms flow velocity were measured in the annulus preceding the rotor and in the pipe upstream of the turbine meter (using hot film sensor HF and hot-wire sensors HW1 and HW2, respectively) and oscillating pressures were measured by five high frequency response transducers (E1-E5). Density at the rotor was determined from the pressure signal measured with transducer E3. The frequency response (amplitude ratio and phase) from two dynamic pressure transducer pairs, E1-E2 and E4-E5, was utilized for computation of plane wave pressure and velocity amplitude distributions along the pipe. Knowing the pressure amplitude ratio and phase between two pressure transducers located a fixed distance apart, the impedance at either pressure transducer can be calculated using an acoustic transfer matrix model for a pipe (Kinsler et al., 1982; Munjal, 1987). Then, utilizing the calculated impedance, the same transfer matrix model is used to predict the fluctuating pressure and velocity amplitude at any point along the pipe. To improve the accuracy of the predicted plane wave distributions, in particular the velocity amplitude at the rotor, the distance between transducers E1 and E2 was increased for lower pulsation frequencies to monitor pressures further apart on the distribution.

Properties of Flow at the Turbine Meter

Measurements of several different quantities provided a characterization of the flow at the turbine meter for various flow conditions and pulsation frequencies. Radial distributions of the fluctuating velocity were measured in the annulus just preceding the rotor and spectra were obtained from Fourier transforms of the time traces. Axial plane wave pressure and velocity distributions for dominant harmonics of the pulsating flow were calculated from the measured frequency response between pairs of dynamic pressure transducers along the pipe. A few insightful results will be discussed.

The calculated distributions of velocity amplitudes (first harmonic) along the pipe are given in Fig. 2 for two extreme cases. With a pulsation frequency equal to 25 Hz, a velocity node is located at the rotor while at 60 Hz an antinode is observed. In Fig. 2, the axial distance along the pipe (in diameters) was measured from the rotor midpoint (negative values indicate distance upstream of the rotor). The solid lines represent the calculated distribution using frequency response measurements from transducers E1 and E2 while the dotted lines refer to the distribution calculated using measurements from transducers E4 and E5. Vertical dashed lines mark the position of the pressure

Table 1 Ranges of similarity numbers and rotor response parameter[1] D_1 for the present study

M	0.012–0.051
Re	20000–80000
St	0.027–4.61
D_1	2–296

[1] To determine D_1 the mass moment of inertia J of the rotor system was measured using a torsional oscillation test and the flow deviation factor η was estimated from the rotor blade geometry (Cohen et al., 1987).

Downloaded 03 Jun 2010 to 171.66.16.125. Redistribution subject to ASME license or copyright; see http://www.asme.org/terms/Terms_Use.cfm

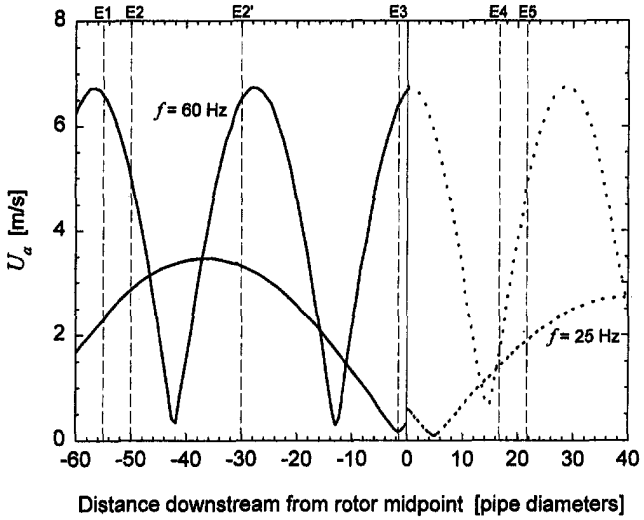


Fig. 2 Velocity amplitude distributions along the pipe for two frequencies: f = 25 Hz; f = 60 Hz. (Uncertainty in U_a = ±4 percent)

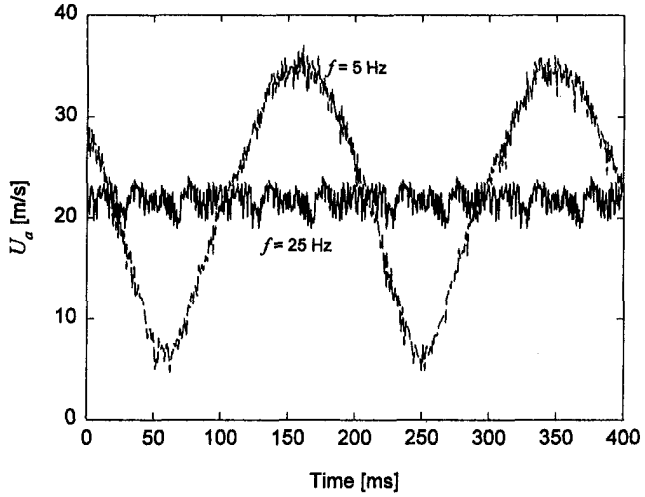


Fig. 4 Time-traces of velocity oscillations at the rotor for two frequencies: f = 5 Hz; f = 25 Hz. (Uncertainty in U_a = ±2 percent)

transducers in the system. A slight discrepancy of the calculated amplitudes at the rotor midpoint was observed when using the two different transducer pairs: this was due to acoustic reflection at the rotor. In general, the calculated distributions varied with pulsation frequency and were also affected by the critical nozzle throat diameter.[2] Specifically, the nozzle throat diameter determines not only the velocity through the test section, but also the upstream acoustic boundary condition. Thus, the calculated axial distributions vary somewhat with different nozzle throat diameters and, since the generated pulsations are proportional to flow rate, the peak velocity amplitude in the pipe increases with nozzle throat diameter.

Using a hot-film probe, radial distributions of the normalized time-mean velocity $\bar{U}_m$ and of the normalized rms velocity $\bar{U}_r$ (see Fig. 3) were acquired in the annular space just upstream of the rotor. From Fig. 3 it is obvious that the radial distribution of mean axial velocity $\bar{U}_m$ is not affected by flow pulsation in contrast to the rms velocity $\bar{U}_r$ which is strongly dependent on flow pulsation. It is important to note that although Fig. 3 would indicate that the rms level depends on frequency, it is actually the *system response* which determines the rms level at the rotor. That is to say, the rms velocity level at the rotor is determined by the plane wave distribution of oscillating velocity (which depends on frequency) in conjunction with the amplitude of the generated pulsation. This concept is clearly illustrated by the presence of a node at the rotor for one frequency while for another an antinode is present (Fig. 2). With no pulsations present, the radial distribution of rms velocity was in good agreement with turbulence intensity measurements found in the literature. At some frequencies the rms level increased towards the walls, likely due to a complex interaction of the pulsating flow with the turbulence production mechanisms near the wall.

Figure 4 presents two hot-film time traces of the fluctuating velocity measured in the annulus just upstream of the rotor. Typically, an almost sinusoidal wave form was generated for the lower frequencies while at higher frequencies the spectrum was characterized by a dominant second harmonic and a significant third harmonic. For two signals with the same rms level, it was generally observed that 'noisier' wave forms were associated with a smaller meter error. This result is consistent with the predictions of Haalman (1965) and Lee et al. (1975) which indicate that a triangular wave form results in a smaller meter error whereas a square wave produces a larger meter error when compared with a purely sinusoidal wave form of the same amplitude and frequency.

[2] In general, the axial distribution of oscillating velocity will also depend on the sound speed, which was essentially constant for the range of experiments performed in the present study.

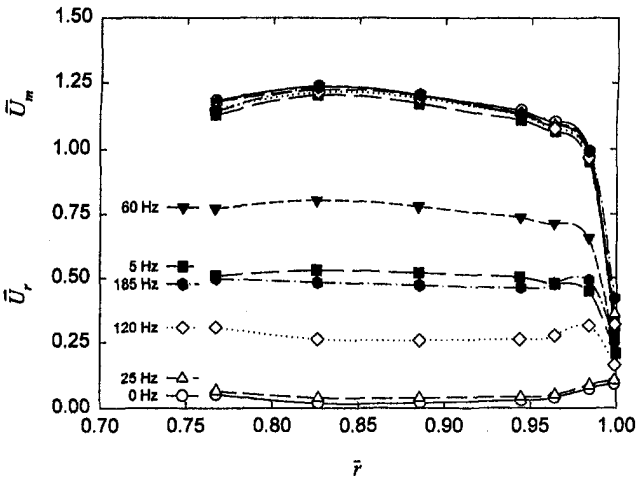


Fig. 3 Time-mean and rms velocity profiles at the rotor from hot-film traverse. (Uncertainty in $\bar{U}_m$ = ±2 percent, in $\bar{U}_r$ = ±5 percent)

Effects of Flow Parameters on the Meter Error

In established standards for flow rate measurement it is common practice to define correction coefficients which account for nonstandard conditions. For the present study with pulsating flows, the ratio of the reference flow rate measured with the critical flow nozzle Q_o to the flow rate indicated by the turbine meter Q_t, is defined as the correction coefficient C. This coefficient is akin to the "square root correction factor" typically used in assessing the effect of pulsations on orifice metering (Mottram, 1974). A simple relationship exists between the correction coefficient C and the meter error E adopted in previous studies (e.g., Lee et al., 1975):

$$C = \frac{Q_o}{Q_t} = \frac{1}{1+E} \tag{2}$$

The dependence of the correction coefficient on Reynolds number Re and Strouhal number St for various frequencies was investigated for all four nozzles tested. A trend of decreasing correction coefficient with increasing Reynolds number for a constant frequency was found. This trend is due to the fact

Downloaded 03 Jun 2010 to 171.66.16.125. Redistribution subject to ASME license or copyright; see http://www.asme.org/terms/Terms_Use.cfm

that the amplitude of the generated pulsations increased with increasing flow velocity (i.e., Reynolds number) which simply indicates that the correction coefficient is inversely related to the pulsation amplitude. This interpretation was confirmed by an increasing correction coefficient with increasing Strouhal number St. From both trends it is evident that the values of C vary with frequency, however, the variation results from the velocity amplitude distribution along the pipe which leads to different velocity amplitude levels at the rotor. In other words, the meter error is the consequence of the system response and not of the rotor response to various frequencies. In the range of experiments performed, no *direct* effect of pulsation frequency, Reynolds number or Strouhal number on the correction coefficient C was observed: the velocity amplitude at the rotor determined the meter error.

In Fig. 5 the strong dependence of C on the rms velocity is explicitly exposed, thus confirming the above conclusions. The rms velocities from a hot-film traverse in the annulus just upstream of the rotor were integrated to obtain the mean normalized value of rms velocity $\bar{U}_{rh}$, i.e.

$$\bar{U}_{rh} = \frac{2}{1 - (r_i/R)^2} \int_{r_i/R}^{1} \bar{U}_r \bar{r} d\bar{r} \tag{3}$$

The normalized rms velocity $\bar{U}_{rp}$ at the rotor can also be calculated by applying plane wave acoustic theory as described earlier. The results are plotted in Fig. 6, which indicate that the correction coefficient can be accurately determined from frequency response measurements using a pair of dynamic pressure transducers suitably located in the piping upstream or downstream of the turbine meter.

Referring to Figs. 5 and 6, a curve fit of the form

$$C = \frac{1}{1 + \alpha \bar{U}_r^2} \tag{4}$$

was suggested by Lee et al. (1975). The curve fits using both the measured and calculated rms velocity at the rotor are shown in Figs. 5 and 6, respectively. Although some scatter in the experimental data is evident—most likely due to differing wave form characteristics of the velocity fluctuation caused by varying reflectivity at the nozzle exit—the functional form of the expression in (4) appears to capture the actual trend quite well.

Conclusions

The present experimental study of flow pulsation effects on a single-rotor turbine meter resulted in several important conclusions. It was confirmed that the correction coefficient C primarily depends on the rms velocity amplitude of the flow pulsation at the rotor when the rotor response parameter D_1 is greater than unity. More importantly, the level of rms velocity at the meter results from the system response which is determined by the system geometry, pulsation frequency, flow velocity, and sound speed. However, no *direct* effect on C of flow velocity, pulsation frequency, Reynolds number and Strouhal number was observed in the range of the experiment. The character of the oscillating velocity wave form was also found to have an effect on the correction coefficient. Lastly, the same observed dependence of C on the rms velocity resulting from either direct hot-film measurements or calculated from frequency response pressure measurements (using plane wave acoustic theory) indicated that the correction for pulsation effects can be based on frequency response measurements of the oscillating pressure using a pair of dynamic pressure transducers suitably located in the piping upstream or downstream of the turbine meter. The accuracy of the correction coefficient could be improved further by systematically determining the effects of the velocity fluctuation wave form.

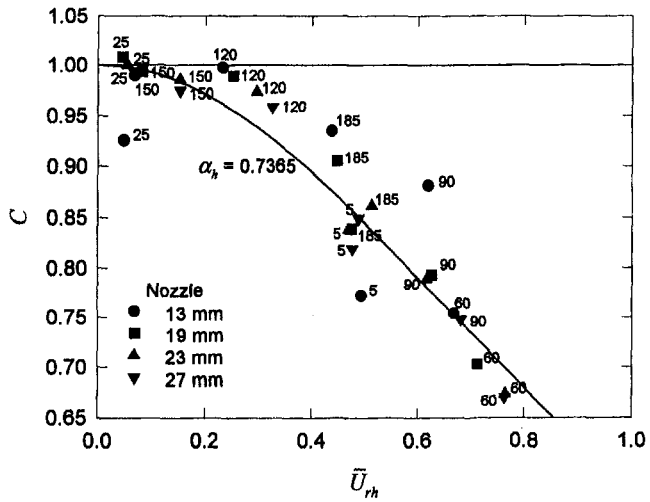


Fig. 5 Correction coefficient versus measured rms velocity from hot-film traverse: numbers refer to frequency values and symbols to nozzle diameters. (Uncertainty in C = ±1.5 percent, in $\bar{U}_{rh}$ = ±5 percent)

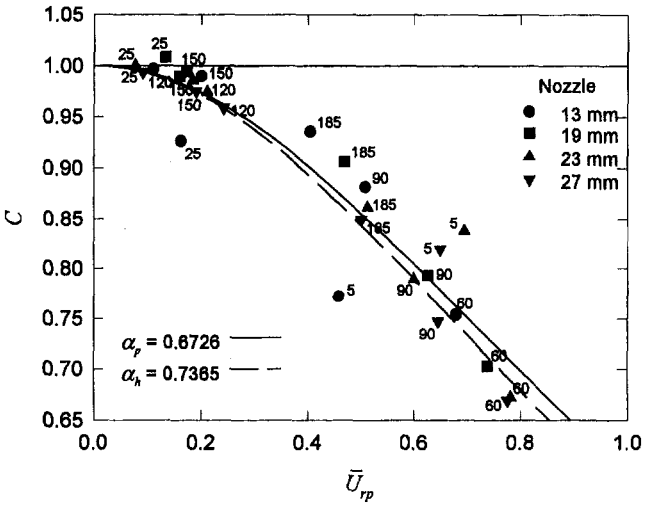


Fig. 6 Correction coefficient versus rms velocity calculated from pressure measurements: numbers refer to frequency values and symbols to nozzle diameters. (Uncertainty in C = ±1.5 percent, in $\bar{U}_{rp}$ = ±4 percent)

Acknowledgments

The work presented here is based on a research project performed for NOVA Gas Transmission Ltd. Permission to publish the results is gratefully acknowledged. The authors are also grateful to Jason Szabo and Pete Tetreau for their contributions in performing measurements and processing experimental data.

References

Atkinson, K. N., 1992, "A Software Tool to Calculate the Over-Registration Error of a Turbine Meter in Pulsating Flow," *Flow Measurement and Instrumentation,* Vol. 3, No. 3, 167–172.

Cohen, H., Rogers, G. F. C., and Saravanamuttoo, H. I. H., 1987, *Gas Turbine Theory—3rd Ed.,* Longman.

Haalman, A., 1965, "Pulsation Errors in Turbine Flowmeters," *Control Engn.,* May, pp. 89–91.

Kinsler, L. E., Frey, A. R., Coppens, A. B., and Sanders, J. V., 1982, *Fundamentals of Acoustics—3rd Ed.,* John Wiley & Sons.

Lee, W. F. Z., Kirik, M. J., and Bonner, J. A., 1975, "Gas Turbine Flowmeter Measurement of Pulsating Flow," ASME JOURNAL OF ENGINEERING FOR POWER, Oct. 531–539.

McKee, R. J., 1992, "Pulsation Effects on Single- and Two-Rotor Turbine Meters," *Flow Measurement and Instrumentation,* Vol. 3, No. 3, 151–166.

Mottram, R. C., 1974, "The Measurement of Pulsating Flows Using Orifice Plate Meters," *Flow, Its Measurement and Control in Science and Industry,* Pittsburgh, Vol. 1, ISA, 197–208.

Munjal, M. L., 1987, *Acoustics of Ducts and Mufflers,* Wiley-Interscience.

Downloaded 03 Jun 2010 to 171.66.16.125. Redistribution subject to ASME license or copyright; see http://www.asme.org/terms/Terms_Use.cfm